CONF-9705115
ORNL/FMP-97/1

U.S. Department of Energy
Fossil Energy
Advanced Research and Technology Development

Proceedings of the Eleventh Annual Conference On Fossil Energy Materials

May 20-22, 1997
Knoxville, Tennessee

Fossil Energy AR&TD Materials Program

OAK RIDGE NATIONAL LABORATORY
MANAGED BY
LOCKHEED MARTIN ENERGY RESEARCH CORP.
FOR THE
U.S. DEPARTMENT OF ENERGY
UNDER CONTRACT DE-AC05-96OR22464

Fossil Energy Program

CONF-9705115
ORNL/FMP-97/1

PROCEEDINGS OF THE ELEVENTH ANNUAL CONFERENCE ON FOSSIL ENERGY MATERIALS

May 20-22, 1997
Knoxville, Tennessee

Compiled by
R. R. Judkins

Date Published: December 1997

Prepared by the
Department of Energy
Fossil Energy Office of Advanced Research
and
Oak Ridge Operations Office
AA 15 10 10 0

Prepared by the
OAK RIDGE NATIONAL LABORATORY
Oak Ridge, Tennessee 37831-6285
managed by
LOCKHEED MARTIN ENERGY RESEARCH CORP.
for the
U. S. DEPARTMENT OF ENERGY
under Contract DE-AC05-96OR22464

PREFACE

The Eleventh Annual Conference on Fossil Energy Materials was held in Knoxville, Tennessee, on May 20-22, 1997. The meeting was sponsored by the U.S. Department of Energy's (DOE) Office of Fossil Energy through the Advanced Research and Technology Development (AR&TD) Materials Program. The objective of the AR&TD Materials Program is to conduct research and development on materials for longer-term fossil energy applications as well as for generic needs of various fossil fuel technologies. The management of the program has been decentralized to the DOE Oak Ridge Operations Office and Oak Ridge National Laboratory (ORNL). The research is performed by staff members at ORNL and by researchers at other national laboratories, universities, and in private industry. The work is divided into the following categories: (1) structural ceramics, (2) new alloys and coatings, (3) functional materials, and (4) technology development and transfer.

This conference is held each year to review the work on all of the projects of the program. The final program for the meeting is given in Appendix A, and a list of attendees is presented in Appendix B.

These proceedings have been published from camera-ready masters supplied by the authors. All of the contributions have been checked for errors but have not been subjected to peer reviews. However, most of the papers have already undergone technical review within the individual organizations before submission to the Program Office.

The successful completion of the conference and publication of the proceedings has required help from several people. The organizers with to thank Judy Fair for her superb coordination work; Gloria Donaldson and Judy for their excellent work at the registration desk; Thelma Garrett for her help in the many arrangements; and the numerous staff and support personnel associated with the conference. Finally, we express our sincere appreciation to the authors whose efforts are the very basis of the conference.

TABLE OF CONTENTS

SESSION II - CERAMICS, NEW ALLOYS, AND FUNCTIONAL MATERIALS

SESSION I

CERAMIC COMPOSITES AND FUNCTIONAL MATERIALS

FABRICATION OF FIBER-REINFORCED COMPOSITES BY CHEMICAL VAPOR INFILTRATION

T. M. Besmann and J. C. McLaughlin
Metals and Ceramics Division
Oak Ridge National Laboratory
P.O. Box 2008, Oak Ridge, TN 37831-6063
e-mail: tmb@ornl.gov

K. J. Probst and T. J. Anderson
Department of Chemical Engineering
University of Florida
Gainesville, FL 32611

T. L. Starr
Department of Materials Science and Engineering
Georgia Institute of Technology
Atlanta, GA 30332-0245

ABSTRACT

Silicon carbide-based heat exchanger tubes are of interest to energy production and conversion systems due to their excellent high temperature properties. Fiber-reinforced SiC is of particular importance for these applications since it is substantially tougher than monolithic SiC, and therefore more damage and thermal shock tolerant. This paper reviews a program to develop a scaled-up system for the chemical vapor infiltration of tubular shapes of fiber-reinforced SiC. The efforts include producing a unique furnace design, extensive process and system modeling, and experimental efforts to demonstrate tube fabrication.

INTRODUCTION

Fiber-reinforced SiC-matrix composites are candidates for a number of high temperature applications due to their high-temperature strength, high thermal conductivity, light weight, thermal shock resistance, creep resistance, and damage tolerance. However, in the current commercial isothermal, isobaric chemical vapor infiltration process, thick-walled parts are difficult to densify. A leading alternative process is forced chemical vapor infiltration (FCVI).[1,2] In FCVI, a preform is placed in a reactor where one side is heated and the other side is cooled, resulting in a thermal gradient across the preform. The reactant gases are constrained to flow from the cooled to the heated side, undergoing a surface, chemical vapor deposition reaction forming the ceramic matrix and an effluent gas. In the case of SiC deposited from chlorosilanes, the effluent HCl gas, has a poisoning effect on the reaction rate. This poisoning, combined with the depletion of the reactant, tends to retard the deposition rate. However, since the gases are traveling toward the hot side of the preform their temperature increases, resulting in faster deposition rates due to the Arrhenius behavior of the deposition reaction. Control over deposition is thus maintained by using the increase in temperature to offset reactant depletion and effluent gas buildup and poisoning effect.

In the current work, emphasis is on the development of composites with tubular geometries. In order to demonstrate the fabrication of a prototypical tube, the efforts have centered on component diameters approaching 100 mm with a 6.4 mm wall thickness. As a result, a unique furnace system was designed and constructed that facilitates the FCVI of such tubes with lengths of 300 mm. Supporting the developmental effort has been extensive process modeling which has successfully described and aided in the optimization of the FCVI of composite plates.[3,4]

CVI MODEL

The modeling of CVI involves the mathematical description of transport and reaction phenomena within a simulation domain. The simulation domain for the tube FCVI system includes the fibrous preform, fixturing, and open gas space. The open spaces include the gas injection system and the area between the preform and the heating element. Fundamental processes to be modeled include heat transfer by conduction, convection, and radiation, transport and reaction of gaseous reactant species, and pressure-driven flow of the gas. Differential equations representing these phenomena can be written in the following steady-state form:

$$\nabla(\rho u \phi) = \nabla \cdot (\Gamma \nabla \phi) + S \qquad [1]$$

where ϕ is temperature, pressure, or concentration, u is the gas velocity, ρ and Γ are constants, and S is a source term. Using the finite volume method of Patankar, the discretized version of this equation is solved over the simulation domain which is divided into control volumes.[5]

Heat Transfer

The heat transfer equation contains both diffusion and convection components,

$$\nabla\left(C_p\, u\, T\right) = \nabla \cdot (\mathrm{K} \nabla T) + S \qquad [2]$$

and a source term:

where C_p is the heat capacity of the flowing gas and K is the thermal conductivity of the material. The source term S contains any heat generated or absorbed by the volume

element, such as heat from chemical reactions or from absorption of microwave energy. This source term also will be used to account for the thermal radiation.

Calculation of the diffusive and convective contributions to the heat balance for each volume element is straightforward given the flow rate and heat capacity of the gas, the thermal conductivities of the materials, and the thermal boundary conditions. The heat flux terms for each volume element depend only on these quantities and on the temperatures of the adjoining volume elements. Since the radiation contribution may depend on the temperatures of more distant volume elements, these cannot be included as flux terms in the same manner. Instead, these are calculated and included as a source term. To do this a ray tracing program is coupled to the main finite-volume program as a pre-processing step. Based on the discretization of the simulation domain the ray tracing program calculates the view factors of the control volume surfaces. The view factors are then stored for later use. During the solution of the heat transfer equation the view factors are used to calculate the energy exchange between the radiating surfaces by standard formulas based on the nodal temperatures. The radiant energy is then added as a source term to the heat flow equation. To obtain a self-consistent solution several iterations of the heat flow equation are required to incorporate the non-linear behavior of the radiant energy exchange.

Mass Transport and Reaction

The flow of the carrier gas and the concentrations of reacting species are determined by differential equations in the form of equation [1]. For pressure-driven gas flow,

$$\nabla \cdot \left(\frac{k}{\mu V} \nabla P \right) = 0 \qquad [3]$$

where k is the Darcy permeability for the material of each volume element, V is the gas molar volume, and μ is the gas viscosity. This formulation of gas transport does not include source or convective (inertial) terms. It will not be accurate for high velocity gas flow in open reactors but is suitable for the pressure-driven gas flow through semi-permeable materials as is the case for FCVI.

The transport equation for the reacting species includes convection, diffusion, and

$$\nabla(u\ C_i) = \nabla\cdot\left(D_i^{eff}\nabla C_i\right)+S \qquad [4]$$

source terms,

where C_i is the species concentration and D_i^{eff} is the effective diffusion coefficient for species i.

Two species are included in the relationship for SiC deposition, methyltrichlorosilane (MTS) and HCl. The MTS is the input species which decomposes into solid SiC which deposits on the preform fibers and gaseous HCl, which is a by-product. The matrix deposition rate depends on the concentrations of both species. The carrier hydrogen, while playing a catalytic role, is not considered.

The coupled systems of differential equations for temperature, pressure, and chemical species concentration are solved in the steady-state. For a selected time increment the local reaction rate is used to calculate a new density for each preform volume element. A new steady-state solution is then calculated and the density incremented again, producing a series of "snap shots" of the densification process.

MODELING TUBULAR GEOMETRY

In a preliminary effort, the CVI model has been applied to a system for preparation of tubular composites by FCVI. The preform is made up of seven layers of

Nextel 312™ (alumino-borosilicate fiber, 3M Company, Minneapolis, MN) cloth. The calculations are performed in cylindrical geometry due to its ease of use and symmetry. The preform, fixturing, and open gas space are discretized into a grid of radial and axial volume elements. No discretization in the θ-direction is considered. The grid size chosen for the modeling domain is 31 radial volume elements by 49 axial volume elements. The preform itself is discretized into six radial volume elements and 29 axial volume elements. The preform is 37 cm in length and 6.4 mm in thickness with an inside diameter of 4.8 cm, and has a 40% fiber volume.

The transport properties for all materials in the modeling domain are defined in separate material files. The thermal conductivities for the graphite, stainless steel, preform, and ceramic fiberboard which make up the structure of the system are functions of temperature. The hydrogen heat capacity, viscosity, and binary diffusivities of MTS and HCl in hydrogen are also functions of temperature. The, thermal conductivity, permeability, and surface area of the preform are functions of fractional density.

Several key boundary conditions are applied to the model. The preform is heated by a cylindrical furnace which surrounds it and is lined with a graphite coating chamber. The thermal gradient is imposed by a stainless steel cooling line that is positioned along the centerline of the system. The temperatures of the graphite coating chamber and stainless steel cooling line are fixed. The total molar flux and mole fraction of MTS are specified at the gas inlet, which is at the centerline on the left side of the preform. Atmospheric pressure is fixed at the gas exhaust and the ends of the domain are specified as adiabatic.

The modeling considered in this paper investigates three key parameters that affect the CVI process: The temperature of the graphite coating chamber; the ratio of hydrogen to MTS (alpha), and the hydrogen flow rate. The temperature range is 1100°C to 1200°C, the alpha range is 5 to 10, and the hydrogen flow rate range is 2.5 to 7.5 l/min.

Figure 1 shows the preform density profile after 24 hours of infiltration at the baseline modeling parameter values of 1200°C, an alpha of 5, and a hydrogen flow rate of 5 l/min. The profile represents a longitudinal section of the tube with the hot side at the

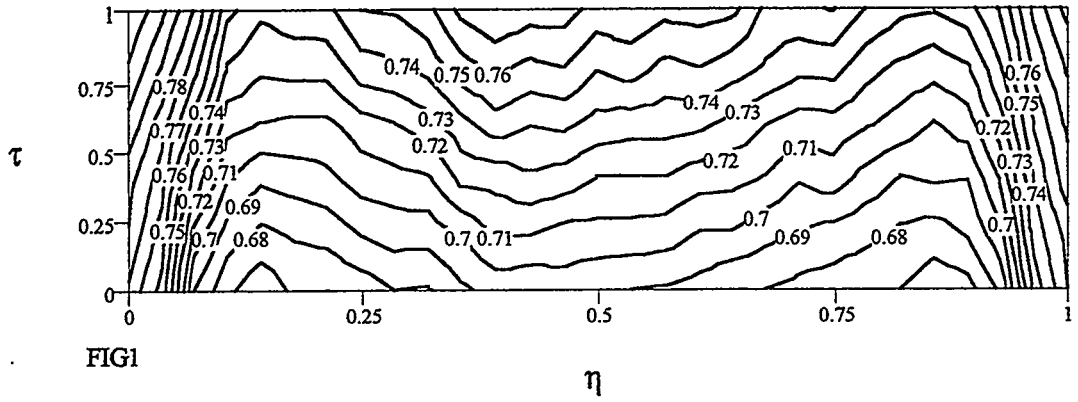

Figure 1: Density profile at baseline conditions.

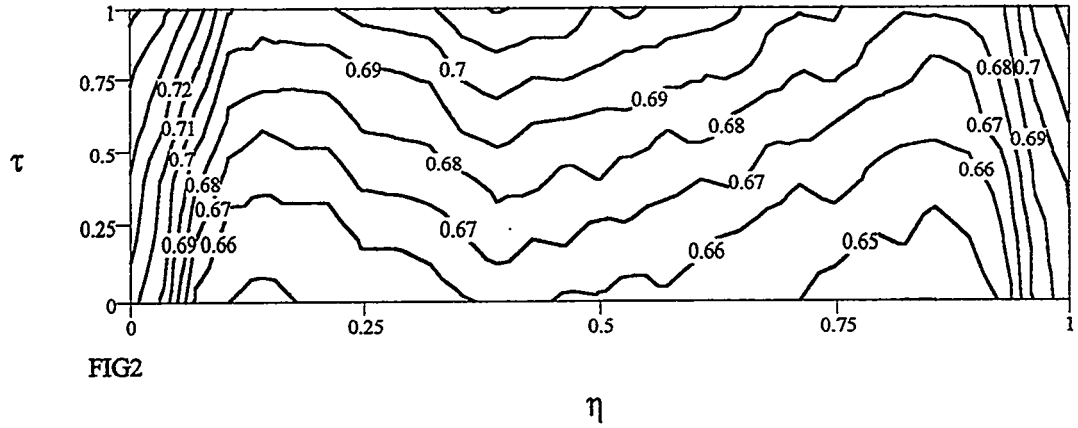

Figure 2: Density profile when alpha = 10.

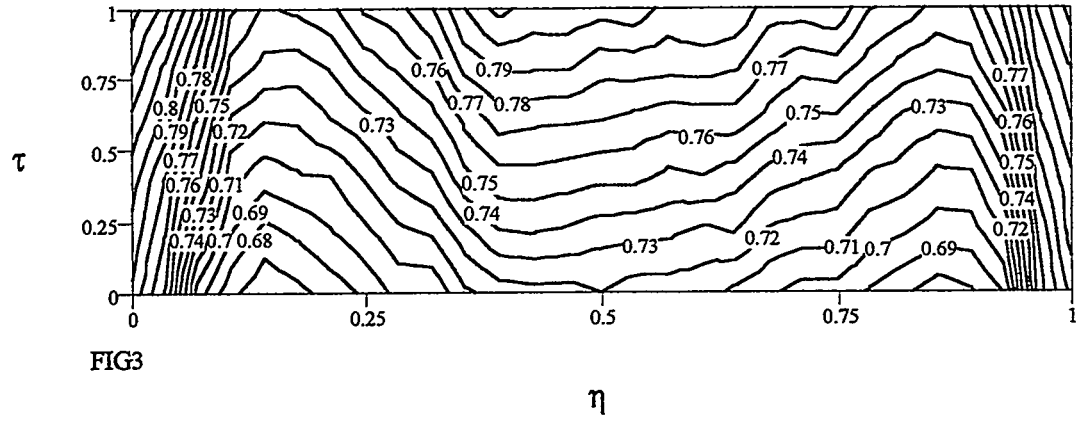

Figure 3: Density profile when hydrogen flow rate = 7.5 l/min.

top and the cooled side at the bottom. τ is the dimensionless thickness and η is the dimensionless length. Figure 2 illustrates an increase in alpha to 10 and Fig. 3 uses a hydrogen flow rate of 7.5 l/min. Figures 4 and 5 show preform temperature profiles at the baseline conditions at the start of infiltration and after 12 hours, respectively.

The density profiles in Figs. 1-3 show approximately the same radial and axial gradients. The densities are highest at τ=1 and η=0 and 1. The fractional density is higher in these areas because of the higher temperature. The higher temperature at the ends is due to the graphite felt insulation placed just outside the preform. In Fig. 2, the absolute density values are somewhat lower across the preform. The higher alpha used in Fig. 2 lowers the MTS concentration in the gas phase and thus lowers the SiC deposition rate. Due to the greater reactant flux, the absolute densities in Fig. 3 are slightly higher than those of Fig. 1.

In Fig. 4, the temperature gradient across the preform thickness at η=0.5 is about 80°C. At lower η, near the gas inlet, the gradient is greater due to the radial convective gas cooling. Figure 5 shows the temperature profile after 12 hours of infiltration. The radial temperature gradient is reduced to 50°C due to enhanced radial heat conduction by the SiC matrix in the gas inlet region.

EXPERIMENT

An initial infiltration experiment has been attempted utilizing a tubular preform of the same material and dimensions as that described in the modeling efforts. The Nextel™ preform was rigidized by impregnation with a resin to prevent it from sagging in the horizontal furnace. The infiltration conditions utilized were a hydrogen flow of 5 l/min, an alpha of 4.5, a coating chamber temperature of 1200°C, and a centerline coolant temperature of 50°C. The infiltration time was 24 hours.

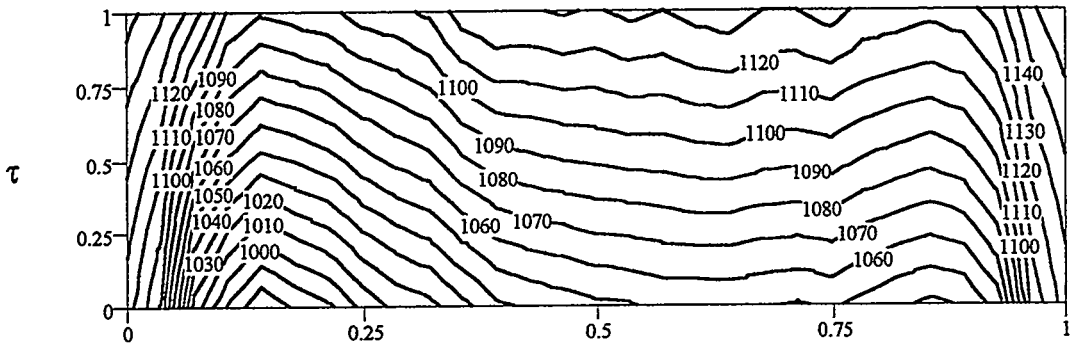

FIG4

Figure 4: Baseline temperature profile at the start of infiltration.

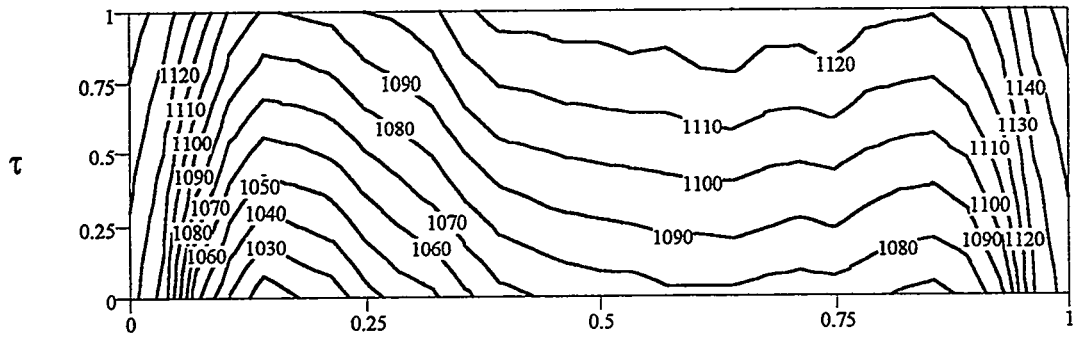

FIG5

Figure 5: Baseline temperature profile after 12 hours of infiltration.

Figure 6: Photograph of Nextel 312™, SiC matrix composite tube fabricated by FCVI.

Figure 6 is a photograph of the tube showing that, at least superficially, it is well-infiltrated. The average fractional density based on weight is approximately 80%. However, adjustments for the somewhat heavy overcoating of the inner surface of the tube may cause some uncertainty. The model estimated an average preform fractional density of 76% after 24 hours of infiltration.

CONCLUSIONS

The efforts to model the FCVI of tubular geometries has indicated generally successful conditions for infiltration. Decreasing the coating chamber temperature increases the densification time. This reduces the temperature across the preform, causing slower deposition rates. Increasing alpha also increases the densification time. At higher hydrogen flow rates, the densification time decreases. However, a higher gas flow imposes a higher temperature gradient near the gas inlet.

Application of the modeling conditions to experiment gave initial indications that high quality composite tubes can be fabricated, which is also indicated by the experimental results. Future efforts will be focused on better validating the model through comparison with experiment, optimizing processing time and composite density, and increasing the preform outer diameter to 10 cm.

ACKNOWLEDGEMENTS

The comments and suggestions of T. N. Tiegs and L. L. Snead are gratefully acknowledged.

REFERENCES

1. W. J. Lackey and A. J. Caputo, *U. S. Patent No. 4,580,524* (April 8, 1986).

2. T.M. Besmann, B.W. Sheldon, R.A. Lowden, and D.P. Stinton, *Science* **253**, 1104 (1991).

3. T.M. Besmann, in *Proc. High Temperature Matrix Composites II, Ceramic Transactions,* A. G. Evans and R. Naslain, Editors, **58**, p. 1, American Ceramic Society, Westerville, OH (1995).

4. W.M. Matlin, D.P. Stinton, T.M. Besmann, and P.K. Liaw, in Ceramic Matrix *Composites - Advanced High-Temperature Structural Materials*, R.A. Lowden, M.K. Ferber, J.R. Hellman, K.K. Chawla, and S.G. DiPietro, Editors, **365,** p. 309, Materials Research Society, Pittsburgh, PA (1995).

5. S. V. Patankar, *Numerical Heat Transfer and Fluid Flow*, Hemisphere Publishing Corp., New York (1980).

MASS TRANSPORT MEASUREMENTS AND MODELING FOR CHEMICAL VAPOR INFILTRATION

T.L. Starr, D.Y. Chiang, O.G. Fiadzo and N. Hablutzel

School of Materials Science and Engineering
Georgia Institute of Technology
Atlanta, Georgia 30332-0245

ABSTRACT

This project involves experimental and modeling investigation of densification behavior and mass transport in fiber preforms and partially densified composites, and application of these results to chemical vapor infiltration (CVI) process modeling. This supports work on-going at ORNL in process development for fabrication of ceramic matrix composite (CMC) tubes.

Tube-shaped composite preforms are fabricated at ORNL with Nextel™ 312 fiber (3M Corporation, St. Paul, MN) by placing and compressing several layers of braided sleeve on a tubular mandrel. In terms of fiber architecture these preforms are significantly different than those made previously with Nicalon™ fiber (Nippon Carbon Corp., Tokyo, Japan) square weave cloth. We have made microstructure and permeability measurements on several of these preforms and a few partially densified composites so as to better understand their densification behavior during CVI.

INTRODUCTION

The success of forced flow-thermal gradient chemical vapor infiltration (FCVI) for ceramic matrix composites is strongly influenced by the densification behavior and mass transport properties of the preform and partially densified composite. The densification behavior of a particular preform is controlled by the fiber geometry and the weave architecture, and how the residual porosity evolves with increasing density. Gas permeability is a critical factor for FCVI, controlling the movement of reactant within the preform and determining the ultimate density limit for a particular preform in a particular

FCVI reactor. This effort involves experimental measurement of densification behavior and transport properties of CVI preforms. In particular, we have investigated preforms fabricated from Nextel 312 braided sleeve from 3M Company. These results are used in process modeling for optimization of tube fabrication at ORNL. More generally, we are developing models for prediction of these properties and of densification performance.

PREFORM AND COMPOSITE MATERIALS

Freestanding tube preforms are fabricated from Nextel 312 fiber in the form of triaxial braided sleeve. This material is commercially available and is used for electrical insulation, hose protection, fire zone cable protection and thermocouple insulation, and is available in sizes ranging from approximately 1" to 3" ID. The diameter of the sleeve in somewhat variable and can be adjusted by elongating or compressing the sleeve. The different size sleeves are formed by including different numbers of tows in each yarn and by using different numbers of yarns in the braider. The individual Nextel 312 filaments are oval in shape, have an equivalent diameter of 11 μm and are fabricated in tows of 390 filaments. In the braiding operation 6 to 12 tows are combined and these yarns are placed with a spacing of 8 to 12 picks per inch. Figure 1 shows the structure of this weave for a nominal 2-1/2" ID sleeve. This braid pattern yields closely packed yarns with a crossing pattern of "two-over, two-under" and a crossing angle of approximately 90°. This architecture differs substantially from that of square weave Nicalon fiber cloth which has a "one-over, one-under" crossing pattern and non-close-packed yarns consisting

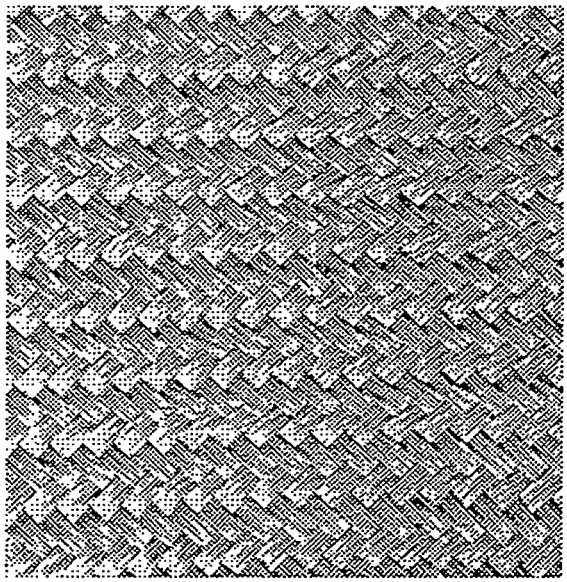

Figure 1. Triaxial braided sleeve is fabricated from Nextel 312 fiber.

of a single tow of 500 15 μm filaments.

In fabricating the tube preform several of these sleeves are placed over a tubular mandrel, compressed by stretching and stabilized with a thermoset resin. Locally the preform microstructure is a cloth layup with no rotation between adjacent layers. In order to measure the densification behavior and gas permeability of this type of preform, specimens were fabricated by stacking and compressing disks 1.9 cm diameter in an aluminum ring and securing with perforated metal lids. Preform specimens were fabricated with 1", 1-1/2", 2-1/2" and 3" sleeve and with fiber loading of 35 to 40 %v. Composite specimens were extracted from larger disks fabricated at ORNL. These composite all were fabricated with 2-1/2" sleeve, stacked to yield 35, 39 and 43 %v fiber and infiltrated for 5 or 10 hours with conditions of 1200°C furnace temperature, 500 sccm hydrogen and 0.3 g/min MTS. At Georgia Tech we sampled these infiltrated disks by coring out cylindrical specimens 1.4 cm in diameter with a diamond coated core drill. Some of these specimens were mounted for gas permeability measurements while others were mounted and polished for microstructure measurements.

DENSIFICATION BEHAVIOR

Chemical vapor infiltration is, fundamentally, chemical vapor deposition where the deposition surface is, initially, the surface of the reinforcement fibers and, ultimately, the surfaces of the residual pores. Thus, the volume deposition rate consists of two factors: the deposition rate which depends on temperature, pressure and reactant composition and the pore surface area which depends on the fiber architecture and degree of densification of the preform. In developing infiltration conditions for a new type of fiber or preform, one must understand the latter factor.

The surface area function relates the volume of matrix deposited to the deposit thickness. While the initial value of this function can be estimated from fiber size and loading the value after partial densification depends in a complicated way on the architecure. While surface area measurements can be accomplished with high resolution

X-ray tomography[1] or by standard stereology methods[2] we use a method more directly related to the CVI process by measuring the deposit thickness as a function of composite density.

Figure 2 shows the typical microstructure of a partially infiltrated CVI composite. the deposit thickness is measured in the channels between layers where the deposition is not inhibited geometrically by neighboring fibers. Figure 3 shows these measurements for two composite specimens. There is significant scatter among individual values but the overall average for the two infiltration times is clearly different. Figure 4 shows all of these average values plotted versus the density. Density was measured from the mass and geometric volume. The volume fraction solid in the composite calculated from the preform fiber volume fraction plus the volume of matrix deposited assuming silicon carbide at 3.2 g/cm^3. These data include three different packing fractions each at two intermediate densities. The trend is similar to that seen

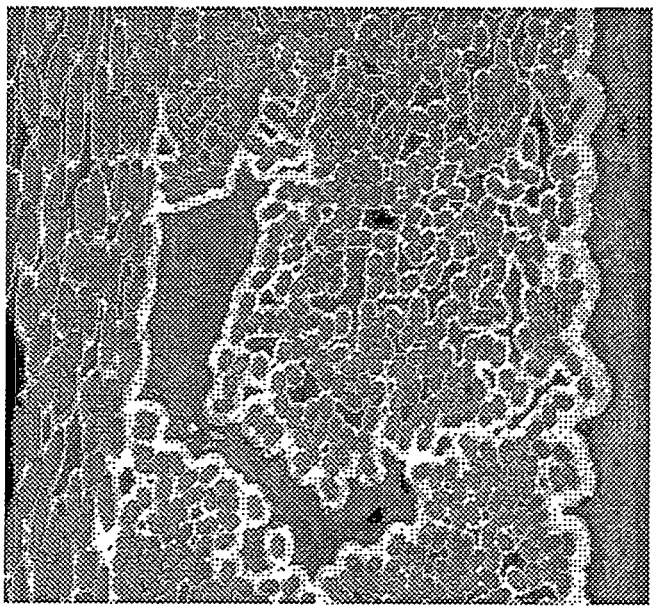

Figure 2. Optical micrograph shows deposition thickness.

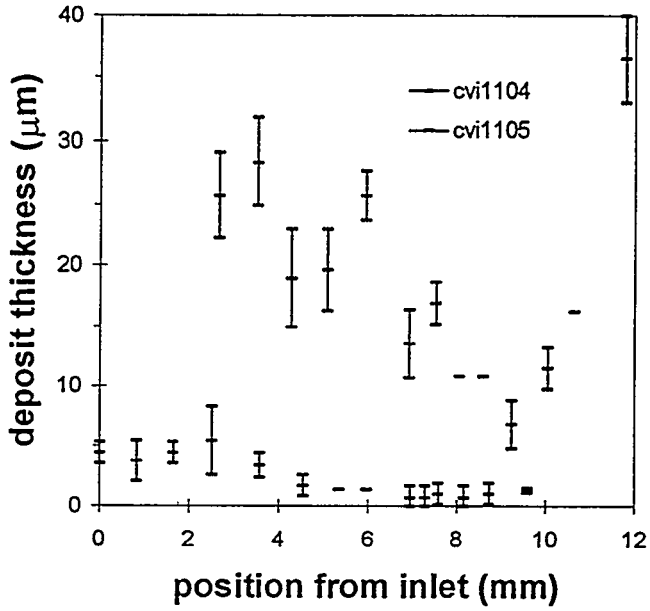

Figure 3. Deposit thickness measurements show significant scatter but average relates to deposition time.

previously with other woven preforms - rapid initial densification as the volume between filaments within the tows is filled, followed by a more gradual densification as the larger spaces between tows (or yarns) is filled.

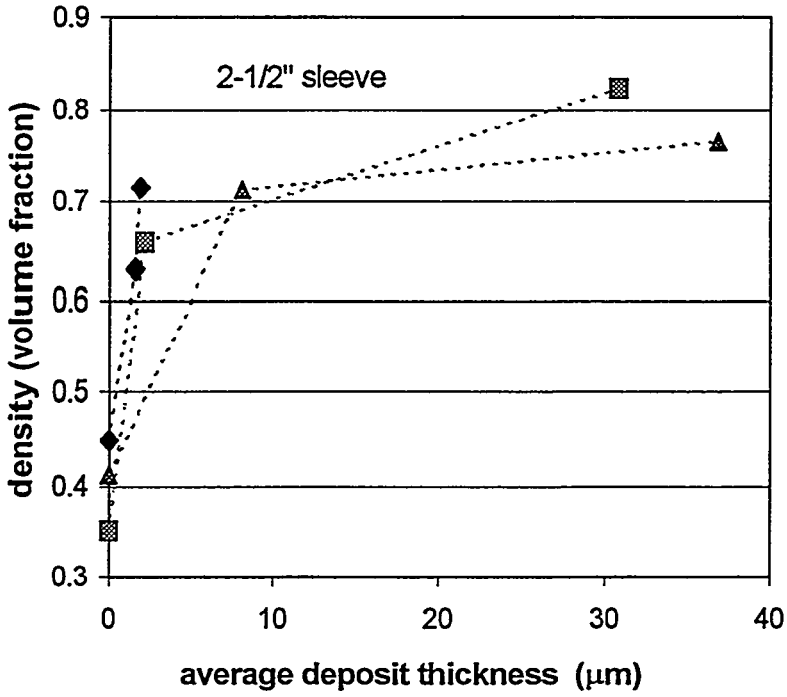

Figure 4. Composite density increases with increasing deposit thickness.

In order to make these results more useful we fit the data to a semi-empircal interpolation function. The form of this function is based on an understanding of the densification process. There are two scales of porosity: between filaments and between tows. At each scale the initial densification is linear with deposit thickness i.e. the volume deposited is proportional to the thickness deposited. The constant of proportionality is equal to the initial surface area per unit volume S_o. At each scale the deposition rate approaches zero at a maximum value of coating thickness x_c yielding a maximum volume deposited. As a "critical" phenomenon this approach to x_c (the percolation limit) is expected to have an exponential dependence. A functional form that meets these criteria is:

$$V_m = \frac{S_o(1-1/n)x}{\left(1-1/n(x/x_c)^n\right)} \quad for\, x \le x_c$$

where x is the deposit thickness and n is the exponent controlling the approach to the maximum volume. While there appear to be three parameters in this equation only two

are independent due to the requirement that the derivative with respect to x must be zero at x_c. The value of the initial surface area for the tow is calculated from the fiber diameter and packing fraction. Our "fit" to the experiments involves selecting only two values: n (the same for both tow and weave) and the critical thickness for the weave deposit. These are tabulated below and the resulting curve shown in figure 5 where the plot is versus matrix deposited. A better fit could be obtained recognizing that the experimental measurements are for three different initial fiber loadings and different values of S_o and x_c should be specified for each.

The function need for CVI process modeling is the surface area function. This is obtained by differentiating the curve in Figure 5 yielding Figure 6. These results show maximum densification at 40 μm deposition and leaving closed porosity of approximately 20 v%.

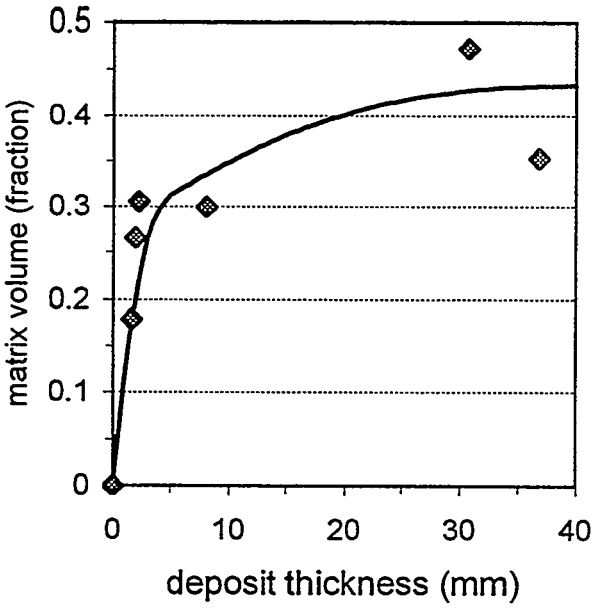

Figure 5. Model compares to experiment with only two empirical parameters.

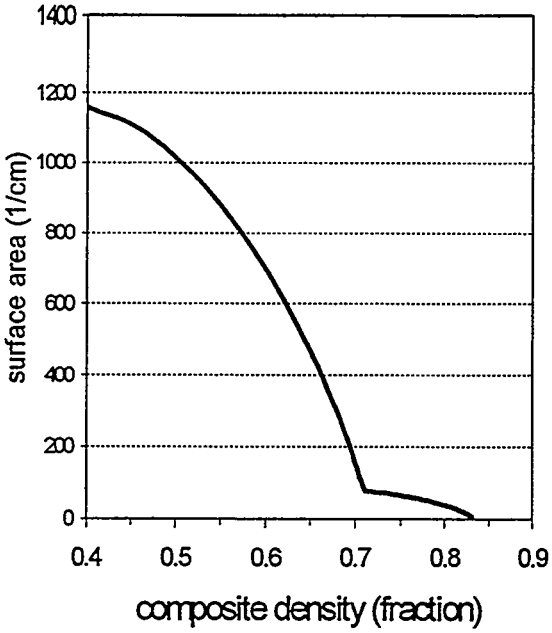

Figure 6. Derivative of densification curve yields surface area function.

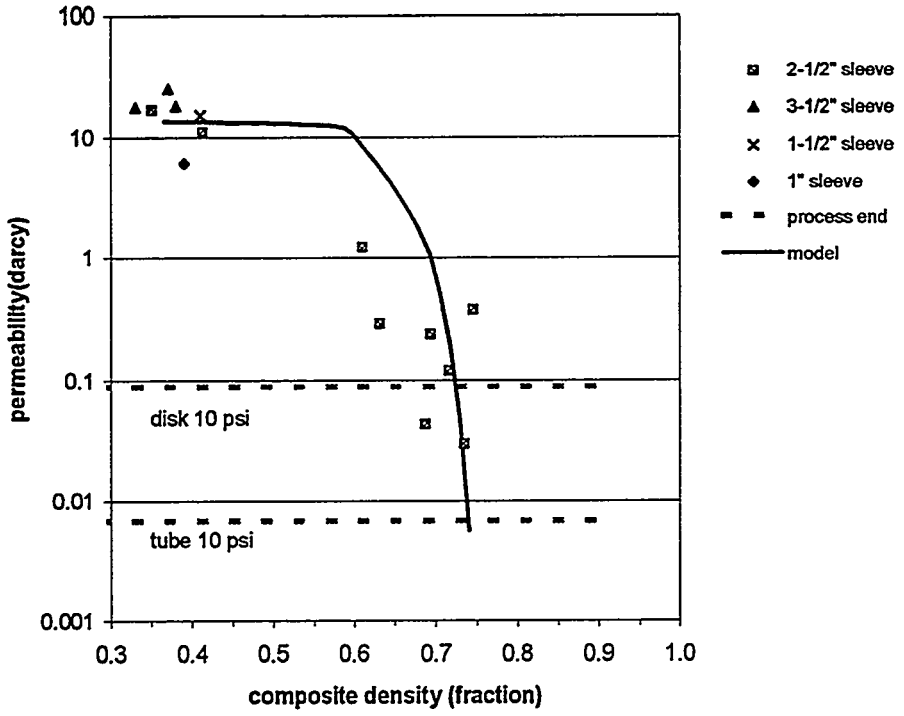

Figure 7. Permeability measurements show more than 20% porosity at end of process.

MASS TRANSPORT MEASUREMENTS

The apparatus and method for measurement of gas permeability has been describe previously[3]. A specimen of preform or porous composite is mounted in an aluminum ring and held in the specimen chamber with o-ring seals top and bottom. The helium gas flow rate is adjusted using a needle valve and the differential pressure across the specimen is recorded for each flow level. The gas permeability is calculated from a linear fit to the flow versus pressure data, the specimen dimensions and the viscosity of helium.

Measurements have been completed for preforms of four different braided sleeve and seven specimens cored from the infiltrated composites. These data are shown in Figure 7. These data are compared to permeability results calculated using a node-bond model[4]. The permeability approaches zero at approximately 80% full density.

DISCUSSION AND CONCLUSIONS

Both the microstructure and the permeability measurements indicate that the maximum density achievable with the braided sleeve preform leaves approximately 20% porosity. This result is in agreement with results for tube infiltration at ORNL reported elsewhere in this proceedings and is in contrast to previous densification with Nicalon square weave cloth preforms which yield densities of up to 95 %. The difference between these is traced to the packing density of yarns within the cloth layers. For the Nicalon cloth yarns are space about 300 μm apart leaving a square through-hole at each yarn crossing point. This hole is wider than the interlayer spacing. Densification can continue until this interlayer channel is filled since the through-holes remain open. For standard Nextel braided sleeve the yarns are tightly packed and the angled through-hole at crossing points is less than 100 μm in diameter, much smaller than the interlayer channel. The maximum density occurs when the through-hole is sealed leaving significant amount of residual porosity between layers.

Other non-standard braid of Nextel are available including a 2" diameter sleeve with 7 picks per inch as shown in Figure 8. This weave provides a significant through-hole in each layer and tube preforms of this braid would be expected to densify to higher density.

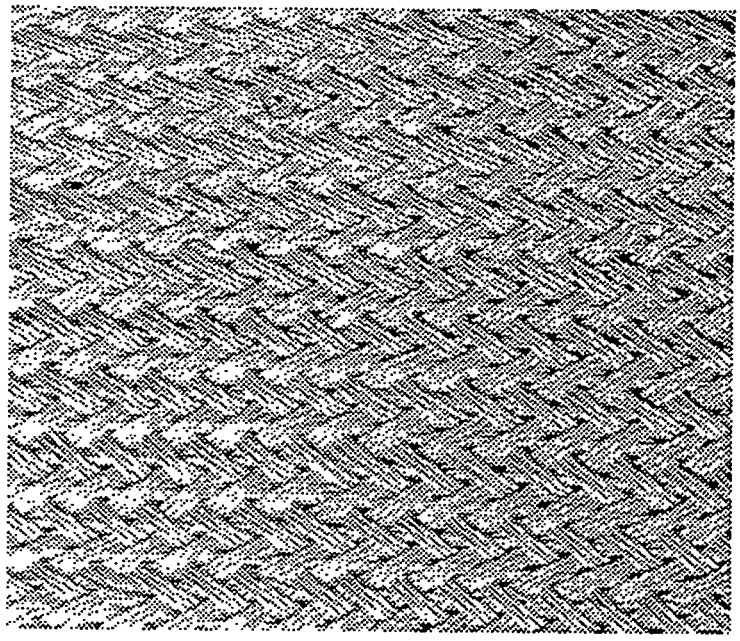

Figure 8. Non-standard braided sleeve (7 picks per inch) should provide better through-cloth transport.

Measurement of densification behavior and gas permeability for the fiber preforms fabricated from braid sleeve provide date for CVI process modeling. These results indicate, however, that a large amount of residual porosity is inevitable for tubes fabricated using the standard sleeve material. Better composite densification should result from using a more open braid pattern.

ACKNOWLEDGEMENTS

We acknowledge the assistance of T.M. Besmann and K.J. Probst at ORNL in providing the partially infiltrated composites and of R.G. Smith of 3M in providing braided sleeve materials.

REFERENCES

1. S-B. Lee, S.R. Stock, M.D. Butts, T.L. Starr, T.M. Breunig and J.H. Kinney, "Pore Geometry in Woven Fiber Structures: 0°/90° Plain-weave Cloth Lay-up Preform," Journal of Materials Research, accepted for publication (1997)
2. E. E. Underwood, Quantitative Stereology, Addison-Wesley, Reading, Mass., 1970
3. T.L. Starr and N. Hablutzel, "Measurement of Gas Transport Through Fiber Preforms and Densified Composites for Chemical Vapor Infiltration," Journal of the American Ceramic Society, accepted for publication (1997)
4. T.L. Starr, "Gas Transport Model for Chemical Vapor Infiltration," Journal of Materials Research 10(9) 1-7 (1995)

OXIDATION-RESISTANT INTERFACE COATINGS FOR NICALON/SiC COMPOSITES

D. P. Stinton, T. M. Besmann, and R. A. Lowden

Oak Ridge National Laboratory
Oak Ridge, Tennessee

P. K. Liaw and S. Shanmugham

University of Tennessee
Knoxville, Tennessee

ABSTRACT

Nicalon/SiC composites with thin C and C/oxide/C interfaces were fabricated. The oxide layers, mullite and Al_2O_3-TiO_2, were deposited by a sol-gel process, while the C layer was deposited by a chemical vapor infiltration method. The fabricated composites were flexure tested in both as-processed and oxidized conditions. Composites with C and C/oxide/C interfaces retained graceful failure even after 500 h oxidation at 1000°C, but with reduced flexural strengths.

INTRODUCTION

It is well established that the fiber-matrix interface plays a key role in determining the mechanical properties of ceramic matrix composites [1-3]. Currently, Nicalon-fiber/SiC-matrix composites owe their good mechanical properties at room temperature to either carbon © or boron nitride (BN) interfaces, which provide a weak interfacial bond. However, C and BN oxidize at elevated temperatures resulting in degradation of mechanical properties of these composites in oxidizing environments [3]. Hence, alternative oxidation-resistant interface materials need to be identified and developed.

Recent analytical and finite element modeling studies have indicated that low modulus interfacial coatings may be desirable to reduce residual radial compressive stresses at fiber-matrix interfaces which develop upon cooling from processing to room temperature [4, 5]. Two oxides, mullite and aluminum titanate, were chosen as interface materials for Nicalon/SiC and Nextel/SiC composites based on their relatively low modulus and their good oxidation resistance at elevated temperatures.

Mullite and aluminum titanate precursor sols were developed for coating applications [6, 7]. High temperature X-ray diffraction studies in air identified that mullite crystallizes at or above

950°C, while aluminum titanate forms at or above 1300°C. Nicalon tows were embrittled during the formation of mullite at 1000°C, and hence, there is a need to protect the fibers by an inert material during the sol-gel oxide processing. The aluminum titanate formation temperature is high and would damage the Nicalon fibers. However, Nicalon fibers dip-coated in an aluminum titanate sol and heat treated at 1000°C for 10 h in air, forming an Al_2O_3-TiO_2 mixture, were not embrittled. Based on the non-embrittlement of the fibers, the Al_2O_3-TiO_2 mixture was chosen as an alternative to aluminum titanate for an interface material. Thermochemical analysis also identified the need to protect the oxide coatings from the HCl attack, a by-product of the SiC matrix deposition reaction. In order to protect the fibers and oxides during processing, a C coating was selected because of its inertness and ease of processing.

To study the effect of protecting the fibers by an inert material during sol-gel oxide coating, oxide/C, and C/oxide/C interfaces were used with Nicalon/SiC composites, and the results were reported earlier [8]. Since composites with C/oxide/C interfaces exhibited higher flexural strengths than composites with oxide/C interfaces in the as-processed condition, C/oxide/C interfaces were given further consideration. On this basis, Nicalon/SiC composites with C/oxide/C interfaces were chosen for further investigation and a control sample, Nicalon/SiC composite with a thin C (40 nm) interface, was also fabricated.

EXPERIMENTAL PROCEDURE

Table 1 summarizes the fabricated Nicalon/SiC composites along with their interfaces, sols used for the deposition of oxides, and the C deposition time. The mullite coating was deposited using either an ethanol or 2-methoxy ethanol based mullite precursor sol, while the Al_2O_3-TiO_2 coating was deposited from an aluminum titanate precursor sol. The C layer was deposited using argon and propylene as reactants for either 15 or 30 min.

Processing of Nicalon/SiC composites involve three steps: preparation of the Nicalon preform, deposition of the interface coatings, and the infiltration of the SiC matrix. The procedure used for fabricating Nicalon/SiC composites is described in detail elsewhere [6, 8], however, a brief description is given below. Fibrous preforms were prepared by stacking 50 layers of Nicalon cloth (45 mm in dia) in a 0°/30°/60° sequence in graphite holders to a thickness of 12.5 mm thick. The C coating was deposited under isothermal and reduced pressure conditions using argon and propylene on the virgin as well as oxide-coated Nicalon preforms. The oxide precursor coatings were

produced on C-coated Nicalon preforms by vacuum infiltration of the oxide sol followed by drying at 110°C in air. This process was repeated 3-4 times till a desired coating thickness of 150-300 nm was obtained (determined by weight gain). Then, the oxide precursor coatings obtained on the preforms were heat treated in argon at 1050°C for 1 h to produce the oxide coatings. This was followed by the deposition of the outer C layer. Finally, the SiC matrix was deposited using a forced-flow thermal gradient chemical vapor infiltration process, with methyltrichlorosilane and hydrogen as reactants.

Table 1: Nicalon/SiC composites samples

CVI#	Interface	Sol used for oxide deposition	C deposition time	Oxidation time (h) at 1000°C in air
1077	C	-	30 min	24, 200, and 500
986	C/mullite/C	Ethanol based mullite precursor sol	Inner C: 15 min Outer C: 15 min	24, 200, and 500
1080	C/mullite/C	2-methoxy ethanol based mullite precursor sol	Inner C: 15 min Outer C: 15 min	24, 200, and 500
1002	C/Al_2O_3-TiO_2/C	Aluminum titanate precursor sol	Inner C: 15 min Outer C: 15 min	24, 200, and 500
1066	C/Al_2O_3-TiO_2/C	Aluminum titanate precursor sol	Inner C: 15 min Outer C: 15 min	24, 200, and 500

24 flexure bars of dimensions ~ 2.5 x 3.0 x > 33 mm were obtained from each of the fabricated composites using a standard grinding and cutting procedure. The geometrical density was determined from the weight and dimension measurements of each bar. Four to six specimens were flexure tested at room temperature in the as-processed condition and again after oxidation at 1000°C for 24 h, 200 h, and 500 h. Flexural strengths of composite bars were determined using a four-point bend test fixture (with 20 or 30 mm outer span and 10 mm inner span) on an Applied Testing System machine equipped with a 4375 N load cell. The specimen was placed in the fixture and loaded during the downward motion of the crosshead. The crosshead speed utilized was 2.54 mm/min.

After flexure testing, samples which did not completely fracture were broken by hand for fracture surface examination. The fracture surfaces were examined using a Hitachi S-800 SEM equipped with an energy dispersive X-ray system. The fiber-matrix interfaces of selected samples were examined by transmission electron microscopy using a Hitachi HF-2000 cold field emission gun microscope at 200 kV, which is equipped with a Noran/4 II EDX system. EDS patterns were obtained on fiber-matrix interfaces and were used to identify the coatings.

RESULTS AND DISCUSSION

Table 2 summarizes the geometrical density of fabricated composites along with the inner and outer C layer coating thickness, based on weight gain. The C in the control sample, composite with a C interface, was 43 nm thick. In other composites, the inner C and outer C coatings were each < 30 nm thick. The oxide coating thickness values are not indicated in Table 2 since some of the oxide coatings adhere to the graphite holder, and hence, a good estimate of their thickness cannot be obtained from the weight gain measurements.

Table 2. Density of the fabricated composites along with the C coating thickness (based on weight gain)

CVI #	Density (g/cm^3)	Inner C layer thickness (nm)	Outer C layer thickness (nm)
1077	2.36±0.14	43**	-
986	2.47±0.06	22	21
1080	2.40±0.11	22	21
1002	2.46±0.06	28	27
1066	2.45±0.07	16	16

** control sample where the total C thickness was 43 nm

Table 3 summarizes the flexural strength results of fabricated composites. It should be noted that all the fabricated composites exhibited graceful failure (composite behavior) in both as-processed and oxidized conditions. In the as-processed condition, flexural strengths of composites

were between 255 to 311 MPa, and the CVI 1080 composite (C/mullite/C interface) had the highest flexural strength. The control sample, composite with a C interface, had a flexural strength of 311±74 MPa, and is comparable to the value obtained by Walukas [9] for a composite with a 40 nm thick C interface (325±8 MPa). Flexural strengths of the composites decreased with increasing exposure time at 1000°C in air. The CVI 1066 composite (C/Al_2O_3-TiO_2/C interface) and the CVI 1080 composite (C/mullite/C interface) underwent the minimum (21%) and maximum percentage reduction (40%) in flexural strength, respectively, after 500 h oxidation at 1000°C. The composite with a C interface had a 32% strength reduction after 500 h oxidation at 1000°C.

Table 3. Flexural strengths of fabricated composites in the as-processed as well as oxidized conditions

CVI #	Interface	Flexural Strength (MPa) Oxidation at 1000°C in air			
		As-processed	24 h	200 h	500 h
1077	C	311±74	238±43	224±62	214±68
986	C/mullite/C	268±52	260±61	200±47	184±28
1080	C/mullite/C	320±24	238±54	239±39	193±27
1002	C/Al_2O_3-TiO_2/C	255±35	189±45	217±35	159±20
1066	C/Al_2O_3-TiO_2/C	298±23	314±29	257±64	234±52

In the as-processed condition, the fracture surfaces of composites with C, C/mullite/C, and C/Al_2O_3-TiO_2/C interfaces displayed considerable amount of fiber pullout. However, with increased exposure time at 1000°C, the fracture surfaces revealed reduced fiber pullout, and the fiber pullout was confined to the interior. The samples displayed only brittle fracture along the periphery. An illustration of this effect is shown in Fig. 1.

The persistence of graceful failure in a composite with a C interface even after 500 h oxidation at 1000°C in air, is similar to that reported by Walukas [9]. Walukas [9] observed substantial amount of fiber pullout in the interior in a composite with a thin C interface (40 nm)

even after 1000 h oxidation at 1000°C yet with 42% strength reduction, while the regions near the edges were embrittled. His TEM study identified that C was retained in the interior, and hence, the graceful behavior might have been due to the remaining presence of a C interface in the composite.

The TEM study of a CVI 986 composite (C/mullite/C interface) sample in the as-processed condition indicated that the mullite coatings were non-uniform i.e., the mullite layer was absent in many fiber-matrix interfaces. In fiber-matrix interfaces where the C/mullite/C interface was observed, the inner and outer C coatings were each 20 nm thick, while the mullite was ~70 nm thick.

In the CVI 1002 composite, the TEM study identified that the C/Al_2O_3-TiO_2/C interface was present and appeared uniform. The inner and outer C layers were each 30 nm thick, while the Al_2O_3-TiO_2 interface was 30-50 nm thick. Both Al_2O_3 and TiO_2 were crystalline. After oxidation at 1000°C for 500 h in air, the TEM images indicated that the C layers were replaced by SiO_2, but the Al_2O_3-TiO_2 layer was intact. Hence, in the oxidized condition, only a SiO_2/Al_2O_3-TiO_2/SiO_2 interface was observed. Further, the Nicalon fiber surface was oxidized such that 30-50 nm of SiO_2 was observed on the fiber. Thus, the decrease in strength of composite with a C/Al_2O_3-TiO_2/C interface may also be attributed to fiber degradation. Interface C layers may have been retained in the interior of the C/Al_2O_3-TiO_2/C sample after oxidation since it was not clear where the TEM images were obtained. Hence, there is uncertainty involved in the extent to which C is replace by SiO_2.

Nicalon/SiC composites with C, C/mullite/C, and C/Al_2O_3-TiO_2/C interfaces retained damage-tolerant behavior even after 500 h oxidation at 1000°C in air. As examples, Figs. 2 and 3 show the load vs. displacement curves of a CVI 1077 composite (C interface), and a CVI 1066 (C/Al_2O_3-TiO_2/C interface) composite as-processed and after oxidation at 1000°C for up to 500 h in air.

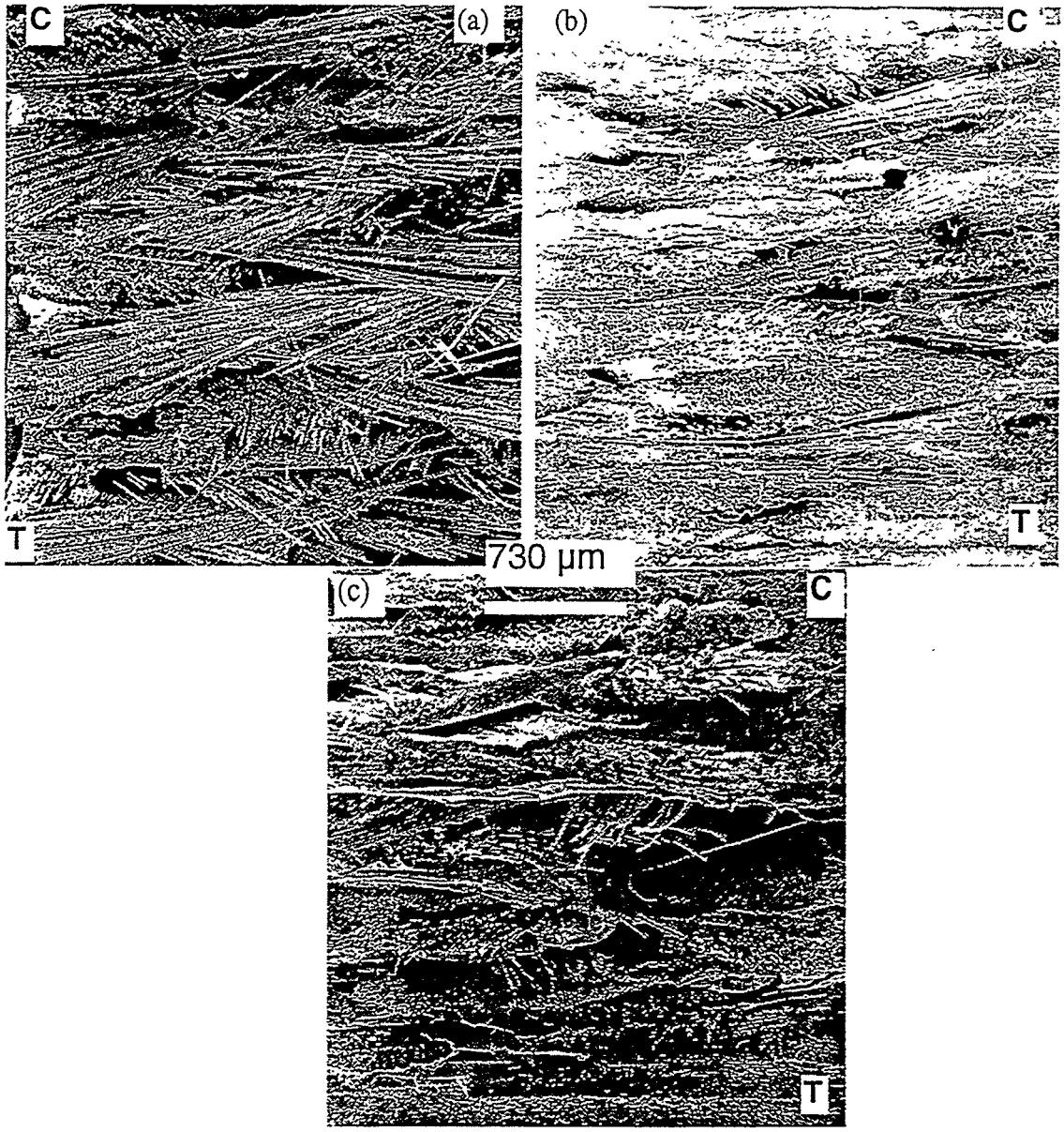

Fig. 1. Fracture surface of a CVI 986 composite sample (a) as-processed condition, (b) after 24 h oxidation at 1000°C, and (c) after 500 h oxidation at 1000°C

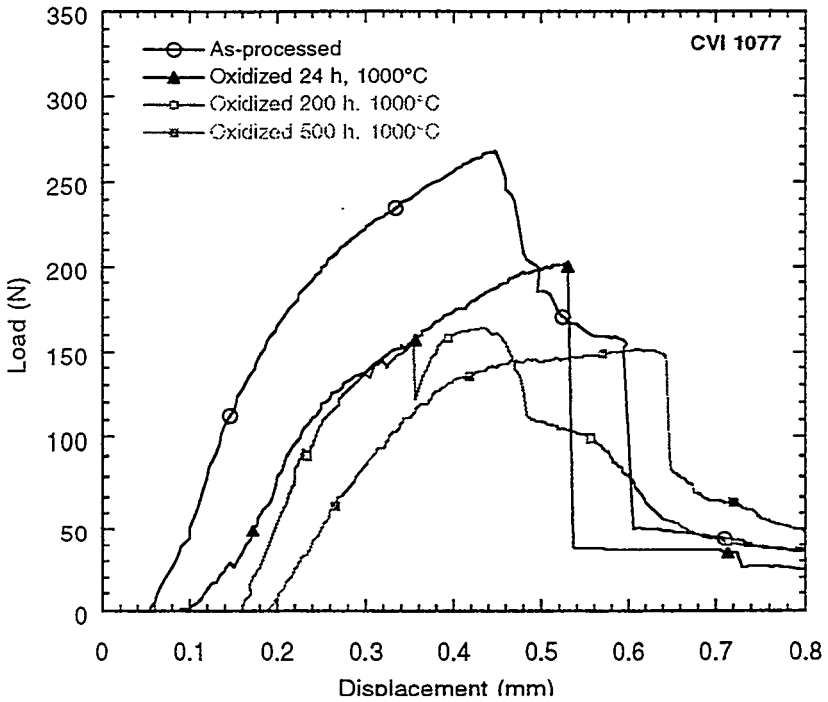

Fig. 2. Representative load vs displacement curves for a CVI 1077 (C interface) composite in the as-processed and oxidized conditions

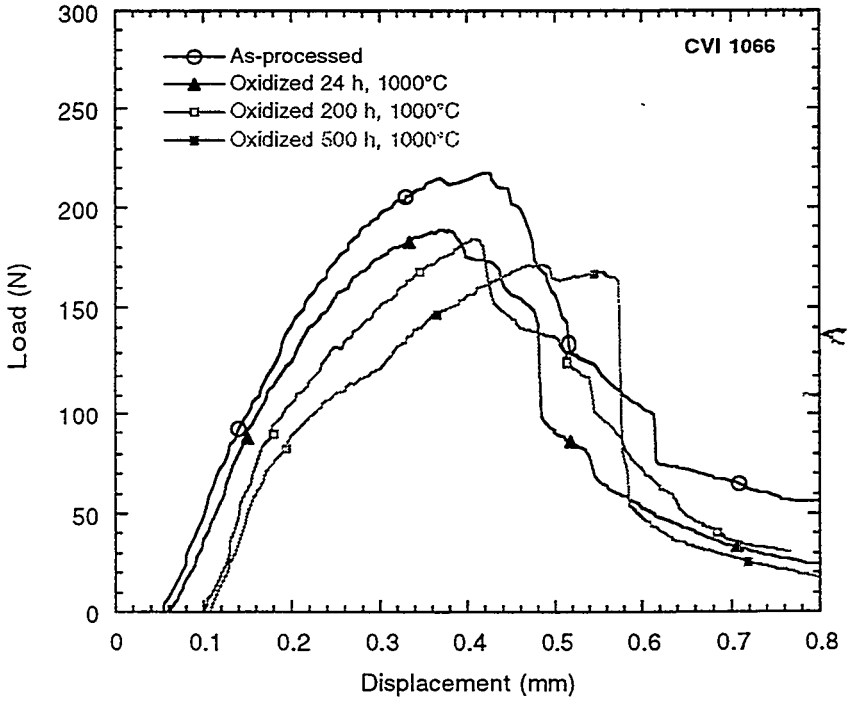

Fig. 3. Load vs displacement curves for a CVI 1066 (C/Al_2O_3-TiO_2-C interface) composite as-processed and after oxidation at 1000°C for up to 500 h in air

CONCLUSIONS

Nicalon/SiC composites with thin C and C/oxide/C interfaces retained damage-tolerant behavior even after 500 h oxidation at 1000°C, but with reduced flexural strengths (21-40%). With increased exposure time at 1000°C, flexural strengths as well as fiber pullout amounts were reduced, and the fiber pullout was confined to the sample interior. TEM analysis indicated that the C layers were replaced by SiO_2, however, there is uncertainty involved in the extent of SiO_2 replacement.

REFERENCES

1. R. J. Kerans, "Issues in the Control of Fiber-Matrix Interface Properties in Ceramic Composites," Scripta Metall. et Mater., 31 [8], 1079-84 (1994).

2. J. J. Brennan, "Interfacial Characteristics of Glass-Ceramic Matrix/SiC Fiber Composites," J. de Physique, Colloque C5 Suppl., 10 [49], 791-809 (1988).

3. R. Naslain, "The Concept of Layered Interphases in SiC/SiC Composites," pp. 23-40 in High Temperature Ceramic Matrix Composites II: Manufacturing and Materials Development in Ceramic Transactions, Vol. 58, Edited by A. G. Evans and R. Naslain, The American Ceramic Society, Ohio, 1995.

4. C. H. Hsueh, P. F. Becher, and P. Angeline, "Effects of Interfacial Films on Thermal Stresses in Whisker-Reinforced Ceramics," J. Am. Ceram. Soc., 71 [11], 929-33 (1988).

5. S. Shanmugham, D. P. Stinton, F. Rebillat, A. Bleier, T. M. Besmann, E. Lara-Curzio, and P. K. Liaw, "Oxidation-Resistant Interfacial Coatings for Continuous Fiber Ceramic Composites," Ceram. Eng. Sci. Proc., 16 [4], 389-99 (1995).

6. S. Shanmugham, P. K. Liaw, D. P. Stinton, T. M. Besmann, K. L. More, W. D. Porter, A. Bleier, and S. T. Misture, "Development of Sol-Gel Derived Coatings for Nicalon/SiC Composites," pp. 71-78 in Advanced Synthesis and Processing of Composites and Advanced Ceramics II, Ceramic Transactions, Vol. 79, The American Ceramic Society, 1996.

7. S. Shanmugham, "Processing and Mechanical Behavior of Nicalon/SiC and Nextel/SiC Composites with Sol-Gel Derived Oxide Interfacial Coatings," Doctoral Dissertation, The University of Tennessee, Knoxville, Tennessee, May 1997.

8. D. P. Stinton, E. R. Kupp, J. W. Hurley, R. A. Lowden, S. Shanmugham, and P. K. Liaw, "Oxidation-Resistant Interface Coatings for SiC/SiC Composites," Fossil Energy Program Annual Progress Report for April 1995 Through March 1996, ORNL-6902, pp. 21-29, June 1996.

9. D. Walukas, "A Study of the Mechanical Properties and Oxidation Resistance of Nicalon/SiC Composites with Sol-Gel Derived Oxide Interfacial Coatings," Masters Thesis, The University of Tennessee, Knoxville, Tennessee, May 1993.

CORROSION PROTECTION OF SIC-BASED CERAMICS WITH CVD MULLITE COATINGS

M.L. Auger and V.K. Sarin

Boston University
Department of Manufacturing Engineering
Boston, MA 02215

For the first time, crystalline mullite coatings have been chemically vapor deposited on SiC substrates to enhance its corrosion and oxidation resistance. Thermodynamic and kinetic considerations have been utilized to produce mullite coatings with a variety of growth rates, compositions, and morphologies. The flexibility of processing can be exploited to produce coated ceramics with properties tailored to specific applications and varied corrosive environments.

INTRODUCTION

Power plants with increased efficiency, fewer emissions, and lower costs has lead to the current development of a new generation of materials. Ceramic coatings are being considered for turbine components such as combustors, blades, stators, seals, and bearings [1]. Under such conditions ceramics are better suited to high temperature environments than metals. Silicon-based ceramics are currently the leading candidate materials for high temperature applications because of their unique combination of high strength and low thermal conductivity, low thermal expansion, good high temperature stability and oxidation

resistance. SiC is limited by its susceptibility to specific high temperature corrosive environments. These environments include but are not limited to hot gas streams containing trace amounts and combinations of impurities such as SO_x, NaCl, and O_2 [2]. Combined with the inherent liability of monolithic ceramics to contact stress failure, this corrosion resistance limitation has lead to the development of protective coatings. Innumerable coatings have been developed yet none has met the complex requirements of high temperature engines [3].

Mullite has been targeted as a potential coating material for silicon based ceramics such as SiC. In addition to traditional refractory applications, mullite has received considerable attention as a high temperature material because of its unique ability to retain its strength, resist creep, and avoid thermal shock failure at elevated temperatures [4,5,6,7]. Stoichiometric mullite is quoted as $3Al_2O_3 \bullet 2SiO_2$ yet exists between 57 and 74 mole% Al_2O_3. The crystal structure of mullite is a modified defect structure of sillimanite ($Al_2O_3 \bullet SiO_2$) in which the mullite stoichiometry is achieved by substituting Si^{4+} ions with Al^{3+} ions in the tetrahedral sites and forming an oxygen vacancy [8,9]. The well accepted defect structure is expressed as $Al^{VI}_2(Al^{IV}_{2+2X}Si_{2-2x})O_{10-x}$ where x denotes the amount of missing oxygen and VI and IV denote six-fold and four-fold coordination. Stoichiometric mullite is orthorhombic and theoretically fits between sillimanite (x=0) and alumina (x=1). Solid solubility depends on the formation process and the cooling rate with extreme Al_2O_3 concentrations resulting from temperatures in excess of 2000°C and rapid cooling rates.

Previous attempts to grow mullite coatings by various processing methods have met with limited success [10]. Most commonly reported techniques require a post deposition heat treatment to convert the amorphous alumina-silicate into crystalline mullite [11,12]. Deposition of plasma sprayed mullite coatings was reported; however, inherent porosity in the coatings resulted in the migration of corrodants through the coating after a few hundred hours [13]. To overcome these deficiencies, the direct formation of chemically vapor deposited (CVD) mullite coatings has been investigated. The CVD process results in dense adherent coatings with the ability to control microstructural and morphological properties.

THERMODYNAMIC ANALYSIS

Equilibrium thermodynamics was performed on the $AlCl_3$-$SiCl_4$-CO_2-H_2 system to establish equilibrium reaction products at various operating conditions. This analysis has been detailed in previous publications [14,15]. and were used to create CVD phase diagrams that help establish guidelines for input conditions for producing mullite and other compounds at equilibrium. The overall equilibrium reaction yielding mullite from the reactant gases utilized in the CVD process is theorized to be the following:

$$6AlCl_3 + 2SiCl_4 + 13CO_2 + 13H_2 \rightarrow 3Al_2O_3 \bullet 2SiO_2 + 13CO + 26HCl \quad (1)$$

The results of the previous analysis determined that low concentrations of chlorides need to be used to obtain high deposition efficiency and carbon free deposits.

KINETIC CONSIDERATIONS

A comprehensive thermodynamic analysis is necessary but not sufficient for understanding the CVD process parameters required to grow mullite coatings. Analyzing the kinetic steps, in particular the rate limiting step, involved in the coating deposition is also essential. Current studies focus on collecting experimental data concerning the kinetics of CVD mullite formation using $AlCl_3$, $SiCl_4$, H_2, and CO_2. Kinetic considerations are being taken from the formation of the well established oxide coatings Al_2O_3 and SiO_2 using chloride reactants. The formation of Al_2O_3 proceeds via this hydrolysis reaction:

$$CO_2(g) + H_2(g) \rightarrow CO(g) + H_2O(g) \quad (2.1)$$

$$2AlCl_3(g) + 3H_2O(g) \rightarrow Al_2O_3(g) + 6HCl(g) \qquad (2.2)$$

It has been shown that the reaction rate of $AlCl_3$ with O_2 is extremely slow while $AlCl_3$ reacts vigorously with H_2O. $AlCl_3$, H_2, and CO_2 exhibit a moderate reaction rate and avoid homogenous nucleation [16]. The reaction proceeds via reaction (2) where reaction (2.1)is labeled the water-gas shift reaction. It has also been stated that SiO_2 is formed via the hydrolysis mechanism at 1000°C, yet it is unclear whether SiO2 can easily form via another mechanism [17]. Experimentally it has been found that the rate is proportional to the concentration of both reactants (assuming the reaction is irreversible). Hence the rate equation for H_2O production is

$$R_{H2O} = k[CO_2]^n[H_2]^m \qquad (3)$$

In this equation, k is called the rate constant for this reaction. It is independent of concentration yet will vary with temperature according to the Arrhenius relation. The factors n and m refer to the rates of the equation and are not necessarily equal to the stoichiometry of the formation equation. For instance if $n = 1$ the reaction is considered first order with respect to carbon dioxide.

The water-gas shift reaction has been extensively studied due to its applicability to metal oxide reactions [18]. Analysis of the reaction over the temperature range 400 to 1050°C suggest separate low temperature and high temperature reaction paths. The low temperature reaction path is dominant at temperatures below 800°C and is extremely sensitive to trace impurities such as oxygen. The high temperature reaction is homogenous and dominant at temperatures in excess of 800°C. The respective low and high temperature mechanisms (determined by measuring CO concentration) are as follows:

$$\text{Low Temperature: } dC_{CO}/dt = 7.6\text{x}10^4 \text{Exp}\left(\frac{-39{,}200}{RT}*\right)[H_2]^{1/3}[CO_2] \qquad (4)$$

$$\text{High Temperature: } dC_{CO}/dt = 1.2\text{x}10^{13}\text{Exp}(\frac{-78{,}000}{RT}*)[H_2]^{1/2}[CO_2] \qquad (5)$$

*activation energy is stated in cal/mole

The activation energy of SiO_2 and Al_2O_3 on Si substrates varies according to experimental conditions. Two similar studies performed in cold-walled CVD reactors state an SiO_2 activation energy of 82kcal/mol [19]. and an Al_2O_3 activation energy of 34.8kcal/mol [20]. These separate studies agree with numerous experimental observations in which Al_2O_3 deposition is particularly sensitive to trace impurities in the gas mixture resulting in homogenous (powdery) nucleation [21]. These previous kinetic studies have been used as guides for CVD mullite yet may not be used directly as the kinetics of the mixed chloride reaction will vary from the kinetics of the separate systems.

EXPERIMENTAL METHODS

A CVD reactor consisting of a vertically hot-walled reactor with a resistively heated three-zoned furnace was used for the experiments. Polished bars of 3 x 4 x 20 mm Hexaloy SiC (Carborundum Company, Niagara Falls, NY) were used as substrates. $AlCl_3$ was formed *in situ* by flowing Cl_2 with Ar as a carrier and dilutant through heated Al chips. $SiCl_4$ vapor was introduced by evaporating the liquid at room temperature. CO_2 and H_2 were mixed with the chlorides prior to entering the deposition reactor. Excess H_2 was present to ensure complete reduction of the metal chlorides to form HCl before exiting the reactor. The deposition technique is detailed in previous literature [22]. All depositions were performed at 950°C and a pressure of 75 torr. All coatings were characterized using x-ray diffraction (XRD) and scanning electron microscopy (SEM). Selected coatings were analyzed with electron diffraction, transmission electron microscopy (TEM), and scanning transmission electron microscopy (STEM).

RESULTS AND DISCUSSION

The effect of the input Al:Si ratio on the resultant mullite coating was investigated. The ratio of Al:Si was varied from pure SiO_2 to pure Al_2O_3 with composite coatings varying between 1:1 to 4:1. Experimentally there are numerous methods to achieve the desired input Al:Si molar ratios. The two methods explored in this study are 1) varying the total partial pressure of metallic chlorides (P_{MClx}) by altering the flow rate of $AlCl_3$ and holding the flow rate of $SiCl_4$ constant and 2) holding P_{MClx} constant and varying both $AlCl_3$ and $SiCl_4$ to achieve the desired ratio. The effect of varying the Al:Si ratio through varying P_{MClx} is shown in Figure 1. An initial increase in growth rate is seen as $AlCl_3$ is introduced at an Al:Si ratio of 1:1 and P_{MClx} of 0.33 torr The coatings produced at a 1:1 ratio and P_{MClx} of 0.33 torr were not usually mullite when examined through XRD and exhibited a high degree of non-uniformity. TEM analysis reveled that these coatings were a nano-crystalline mixture of γ-Al_2O_3 and amorphous SiO_2. This nano-crystalline layer was evident in all samples tested at all input ratios. Details of similar structural analysis may be found in a previous study [23]. The growth rate of the coating continues to decrease as the $AlCl_3$ flow rate is increased to an Al:Si ratio of 4:1 and P_{MClx} of 0.93 torr.

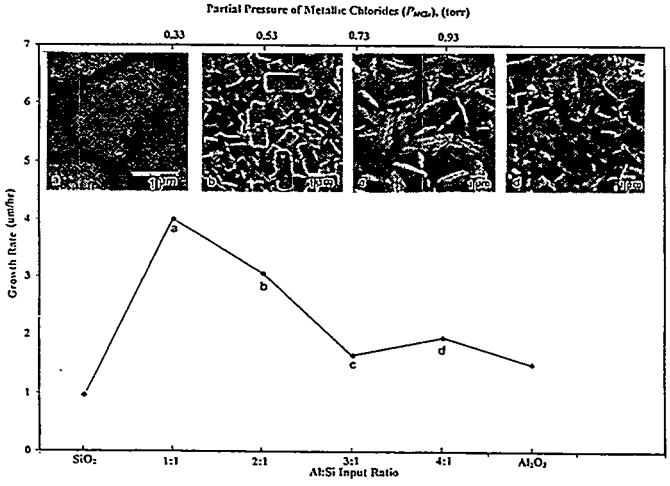

Figure 1: Growth rate of mullite vs. reactant Al:Si ratio and variable metallic chloride partial pressure

The degree of homogenous nucleation (powder formation) and non-uniformity in the coating continued to increase as the Al:Si ratio increased. The surface morphology of the coating becomes more faceted as the input Al:Si ratio increases. Previous studies of CVD mullite coatings have shown that increased Al content increases the faceted nature of the coating [17]. Mullite coatings grown with an input Al:Si ratio of 2:1 were uniform, fine grained, and highly faceted with a growth rate of 3 μm/hr. The growth rate for Al_2O_3 stated in Figure 1 is an average value taken from several literature sources under similar conditions. Attempts to deposit Al_2O_3 using mullite processing conditions resulted in significant homogenous nucleation. Pure SiO_2 coatings under these conditions were found to be amorphous.

The effect of varying the Al:Si ratio by increasing P_{MCl_x} on the initial nano-crystalline region is shown in Figure 2. The thickness of the nano-crystalline region decreases as the input Al:Si ratio increases. Compositional analysis on the 2:1 and 3:1 samples, carried out in an STEM using a 40nm electron probe, indicate a variation in the Al:Si ratio across the thickness of the coatings. The Al:Si ratio near the substrate is very low, a typical value is 0.326 and is presumed to be SiO_2 at the substrate coating interface. The Al:Si ratio increases as the analysis proceeds through the nano-crystalline region. The coating begins to grow as (001) textured columnar mullite at the point where the Al:Si ratio is between 2.93 and 3.77. This ratio overlaps with the known Al_2O_3 solid solubility of mullite (2.76-3.33). The Al:Si ratio continues to increase through the nano-crystalline region with maximum values approaching 7:1 at the top of the coating. The presence of a nano-crystalline region suggests that mullite is not forming directly as thermodynamics suggests but rather as Al_2O_3 and SiO_2 separately. These molecules are absorbed on the surface of the silicon-based substrate with SiO_2 initially preferred. Mullite nucleates when the Al:Si ratio of the initial nano-crystalline coating reaches a critical value close to that of stoichiometric mullite.

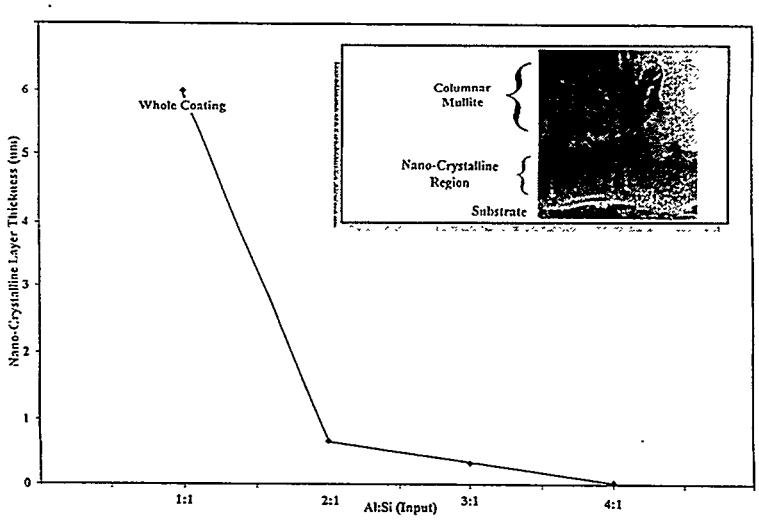

Figure 2: Nano-crystalline layer thickness of mullite coatings vs. reactant Al:Si ratio. Inset is the typical microstructural evolution of mullite coatings on silicon-based materials.

Figure 3 illustrates the effect of growth rate upon the second method of controlling the input Al:Si ratio by maintaining the P_{MCl_x} at 0.53 torr and varying both $AlCl_3$ and $SiCl_4$ to achieve the desired ratio. The constant P_{MCl_x} value was 0.53 torr , the same value for the 2:1 coatings grown in Figure 1. Unlike in the varying P_{MCl_x} matrix the coatings grown at all mixed oxide compositions were uniform, fine-grained, and faceted mullite coatings. The degree of homogenous nucleation did not visually change throughout the mixed oxide range

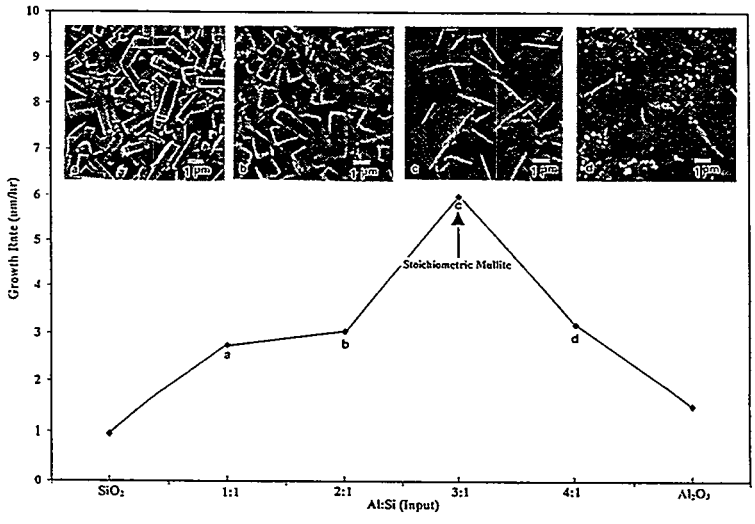

Figure 3: Growth rate of mullite vs. reactant Al:Si ratio at a constant metallic chloride partial pressure (P_{MCl_x}) of 0.53torr

Post-deposition heat treatments were conducted on SiC coated samples with coatings grown by varying P_{MClx} to achieve different Al:Si input ratios. Studies were conducted on mullite coatings grown at Al:Si input ratios of 1:1, 2:1, 3:1, and 4:1, as well as SiO_2. Separate coating sets were thermally treated in a vacuum tight chamber at atmospheric pressure in a flowing Ar environment at 1000°C for 100 hours, 1200°C for 100 hours, and 1350°C for 4 hours. The structures of mullite coatings on SiC grown at an input Al:Si ratio of 2:1 and heat treated under these conditions are shown in Figure 4. As the temperature of the annealing treatment increased the surface structure became increasingly featureless. X-ray diffraction of the coatings after heat treatment indicated that the only crystalline phases present were mullite and SiC.

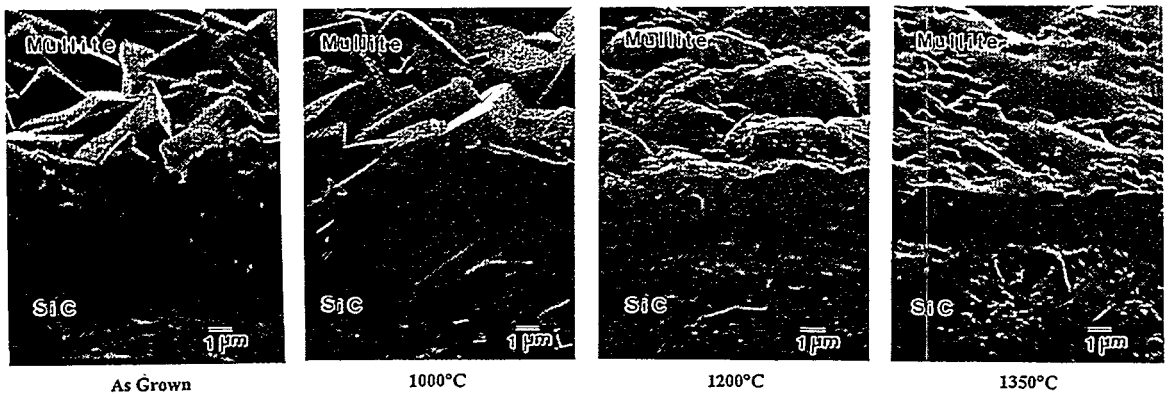

Figure 4: Surface structure of mullite a) as deposited, annealed in Ar @ b) 1000°C for 100hr, c) 1200°C for 100hr, c) 1350°C for 4hr

Preliminary experimentation has begun to determine the degree of protection provided by mullite coatings on silicon-based ceramics in corrosive environments. Different corrosive environments may require mullite coatings with slightly different properties. This degree of control may be achieved with CVD mullite coatings. CVD mullite coated SiC was tested in an O_2 rich environment at 1000°C for 100 hours [24]. As shown in Figure 5 an extremely low weight gain is observed past 30 hours of exposure. The extremely low weight change (little formation of oxide) is shown as the weight change versus square root of time(assuming

parabolic oxide growth kinetics) for times greater than 30 hours. At this point, there is no statistical difference in the growth kinetics between mullite coated with an input Al:Si ratio of 2:1 (P_{MCl_x} = 0.53 torr), 3:1 (P_{MCl_x} of 0.53 torr), and the slow diffusion rate of O_2 through the protective SiO_2 layer that forms on SiC.

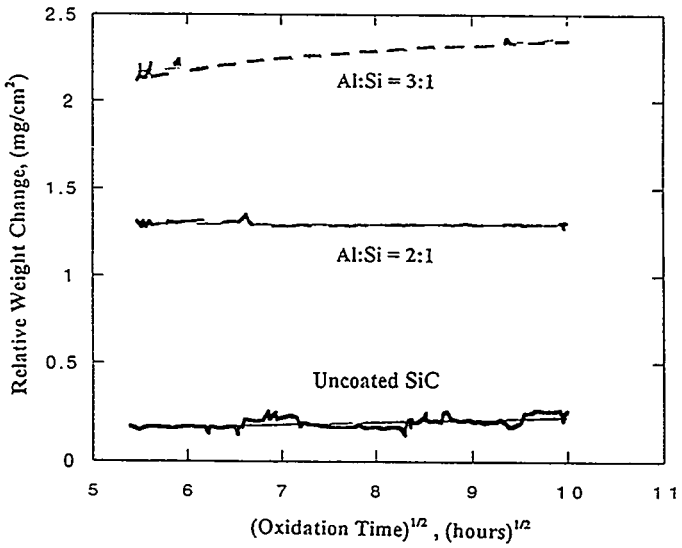

Figure 5: Relative weight change of uncoated SiC and mullite coatings grown at reactant Al:Si ratios of 2:1 and 3:1 on SiC vs. (oxidation time)1/2 in a flowing air environment at 1000°C. [Tortorelli Ref. 24]

CVD mullite coated Si_3N_4 was subjected to a corrosive environment containing Na_2SO_4 and O_2 at 1000°C for 100 hours [25]. The specimens were typically loaded with about 5 mg/cm^2 of Na_2SO_4 and exposed to a flowing oxygen environment in a quartz tube heated to 1000°C. The use of an oxygen environment results in a basic molten salt (i.e., high Na_2O activity), thus facilitating the corrosive reaction of Na_2O with native SiO_2.

The results of uncoated Si_3N_4 and mullite coated Si_3N_4 after exposure are shown in Figure 6. The presence of a Na-containing glassy phase is observed to a depth of $\approx$ 20 μm below the initial substrate surface in the uncoated sample. Yttrium (used as a sintering aid in Si_3N_4) migrated through the grain boundaries of the substrate to the substrate surface, resulting in the formation of a yttrium depleted zone of $\approx$ 10 μm. The mullite coated sample

was relatively unaffected by the corrosive environment. It was found from TEM study that the remainder of the coating as well as the underlying Si_3N_4 substrate were not affected either microstructurally or compositionally by the corrosion exposure.

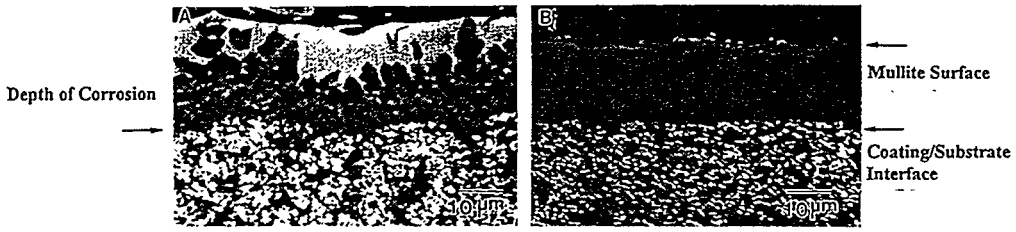

Figure 6: Comparison between a) uncoated Si3N4 and b) mullite coated Si3N4 subjected to a Na2SO4-O2 environment at 1000°C. White areas on surface are corrosion. [W.Lee Ref. 25]

With the desire to tailor CVD mullite coatings on ceramic heat exchangers in coal-fired systems for power production, CVD mullite coated SiC samples were exposed to corrosive coal slag at 1260°C for 300 hours [26]. Corrosive coal slag will form extreme porosity and dramatic pit formation in unprotected SiC. After 300 hours of exposure all mullite coatings (Al:Si input ratios 2:1, 3:1, 4:1 achieved through varying P_{MClx}.) exhibited excellent protection. Generally, mullite grown with a lower input Al:Si ratio exhibited a more corrosion resistant surface as shown in Table I. This trend agrees with the as deposited SEM analysis of mullite coatings in which an input Al:Si ratio of 2:1 (P_{MClx} 0.53 torr) produced a more uniform coating than an input Al:Si ratio of 4:1 (P_{MClx}. 0.93 torr).

Al:Si (Input Ratio)	Observations
2:1	Very Clean, no pitting
3:1	Clean, possible beginning of pit formation
4:1	Clean, possible beginning of pit formation
Uncoated SiC	Corrosion beginning

Table I: Observations of mullite grown with different input Al:Si ratios on SiC and exposed to Baldwin coal slag for 300 hr at 1260°C. [Breder Ref. 26]

CONCLUSIONS

Through the use of thermodynamic and kinetic analysis crystalline mullite coatings have been deposited via chemical vapor deposition upon silicon based materials such as SiC. Altering process parameters such as deposition temperature and reactant partial pressure has resulted in mullite coatings with varied physical and chemical properties such as crystal structure, surface morphology, and chemical composition. Preliminary results have indicated that mullite coatings form an effective barrier to corrosion in high temperature corrosive environments including Na_2SO_4-O_2, oxidation, and coal slag.

ACKNOWLEDGMENTS

Research sponsored by the U.S. Department of Energy, Assistant Secretary for Energy Efficiency and Renewable Energy, Office of Transportation Technologies, as part of the Ceramic Technology Project of the Propulsion System Materials Program, and Fossil Energy AR&TD Materials Program under contract numbers DE-AC05-840R21400 and SC-19X-SS110C with Martin Marietta Energy Systems, Inc. The authors would like to acknowledge Dr. Woo Lee, Dr. Kristen Breder, and Dr. Peter Tortorelli for corrosion testing, Ping Hou for TEM analysis, and Dr. S. Basu for invaluable discussions.

REFERENCES

1. W.J. Lackey, D.P. Stinton, et.al., *Advanced Ceram. Mat.*, **2** [1], 24-30, (1987)
2. N.S. Jacobson, *J.Am. Ceram. Soc.*, **76** [1], 3-28, (1993)

3. W.J. Lackey, D.P. Stinton, et.al., ORNL/TM-8959 (1984)
4. I.A. Aksay, D.M.Dabbs, M. Sarikaya, *J. Am. Ceram. Soc.*, **74** [10] 2343-58(1991)
5. P.F.Becher, *J. Am. Ceram. Soc.*, **74** [2] 255-69 (1991)
6. S.Somiya, Y. Hirata, *Am. Ceram. Soc. Bull.*, **70** [10] 1624-32 (1991)
7. R.D. Nixon, S. Chevacharoenkul, R.F. Davis, and T.N. Tiegs, pp. 579-603 in Ceramic Transactions, Vol. 6, *Mullite and Mullite Matrix Composites*, Edited by S. Somiya, R.F. Davis, and J.A. Pask, American Ceramic Society, Westerville, OH, 1990
8. D.G.W. Smith and J.D.C. McConnel, *Mineral. Mag.*, **35** [274] 810-14 (1966)
9. T. Epicier, *J. Am. Ceram. Soc.*, **74** [10] 2359-66 (1991)
10. J. Schienle, and J. Smyth, Final Report, ORNL/Sub/84-47992/1 (1987)
11. K. Okada, N. Otsuka, pp.425-34 in Ceramic Transactions, Vol. 6, *Mullite and Mullite Matrix Composites*, Edited by S. Somiya, R.F. Davis, and J.A. Pask, American Ceramic Society, Westerville, OH, 1990
12. O.R. Monteiro, Zhi Wang, Ian G. Brown, *J. Mat. Res.*, To be Published
13. K.N. Lee, N.S. Jacobson, R.A. Miller, *MRS Bulletin* **19** [10], 35-38, (1994)
14. R.P. Mulpuri, and V.K. Sarin, 19th Annual Cocoa Beach Conference and Exposition on Engineering Ceramics, Cocoa Beach, FL, The American Ceramic Society, Westerville, OH, (Jan. 1995)
15. R.P. Mulpuri, and V.K. Sarin, *J. Mater. Res.*, 11 (6), 1315-24, (1996)
16. Ph, Wong, M. Robinson, *J.Am Ceram. Soc.*, **53**, 617-21, (1970)
17. W.Steinmaier, J.Bloem, *J. Electro. Soc.*,**111** (2), 206-209, (1964)
18. G.L. Tingey, *J. Phy. Chem.*, **70** (5), 1406-1412, (1966)
19. W.Steinmaier, J.Bloem, *J. Electro. Soc.*,**111** (2), 206-209, (1964)
20. S.W. Choi, C. Kim, et.al., pp.233-41 in the proceedings of the IX International Conference on CVD (CVD-IX) , ed. McD. Robinson, The Electrochemical Society Inc., Pennington, NJ, 1984
21. H. Altena, K. Stjernberg, B. Lux, pp. 381-90 in the proceedings of the V European Conference on CVD (Euro-CVD-V), ed. J. -O. Carlsson, Uppsala University, Department of Chemistry, Uppsala, Sweden
22. V.K. Sarin and R.P. Mulpuri, *U.S. Pat. Pending*
23. D.Doppalaupudi, et.al., pp. 664-70 in the proceedings of the XIII Annual CVD Conference, ed. T.M.Besmann, The Electrochem. Soc. Inc. Pennington, NJ, 1996
24. Testing performed by Dr. Tortorelli of ORNL, Oak Ridge, TN
25. W.Y. Lee, K.L. More,Y.W. Bae, *J. Am. Ceram. Soc.*, **79** (9), 2489, (1996)
26 Testing performed by Dr. Breder of ORNL Oak Ridge, TN

THERMAL CYCLING CHARACTERISTICS OF PLASMA SYNTHESIZED MULLITE FILMS

O.R. Monteiro, P.Y. Hou and I.G. Brown

Lawrence Berkeley National Laboratory, University of California, Berkeley, CA 94720

ABSTRACT

We have developed a plasma-based technique for the synthesis of mullite and mullite-like films on silicon carbide substrate material. The method, which we refer to as MePIIID (for Metal Plasma Immersion Ion Implantation and Deposition), uses two vacuum arc plasma sources and simultaneous pulse biasing of the substrate in a low pressure oxygen atmosphere. The Al:Si ratio can be controlled via the separate plasma guns, and the film adhesion, structure and morphology can be controlled via the ion energy which in turn is controlled by the pulse bias voltage. The films are amorphous as-deposited, and crystalline mullite is formed by subsequent annealing at 1000° C for 2 hours in air. Adhesion between the aluminum-silicon oxide film and the substrate increases after this first annealing. We've tested the behavior of the films when subjected to repetitive thermal cycling between room temperature and 1100°C, and found that the films retain their adhesion and quality. Here we review the plasma synthesis technique and the characteristics of the mullite films prepared in this way, and summarize the status of the thermal cycling experiments.

INTRODUCTION

Thin films have been formed by a wide variety of plasma methods[1]. We have developed a plasma-based thin film deposition technique that has the important feature that the ion energy can be controlled widely. Highly adherent, fully-dense films of metals, alloys (including non-equilibrium alloys) and other conducting materials, and their oxides and nitrides, can be formed. In the early stages of the process the ion energy is held in the keV range so as to produce atomic mixing at the film-substrate interface, and in the latter stages of deposition the energy is reduced so as to optimize the film structure and morphology.

We've drawn upon previously existing technology to form a new plasma technique that is a hybrid of several more commonly know methods, including filtered cathodic arc deposition[2,3], ion beam assisted deposition (IBAD)[4-7], ion beam mixing[4-6,8], and plasma immersion ion implantation (piii)[9,10]. In our method, which we've dubbed Mepiiid (*Me*tal *p*lasma *i*mmersion *i*on *i*mplantation and *d*eposition), the object to be implanted is immersed in a plasma of the desired species, formed by a vacuum arc plasma gun and repetitively pulse-biased to a negative voltage[11-15]. A high voltage sheath rapidly forms at the substrate-plasma boundary, and plasma ions are accelerated through the sheath and into the substrate, thereby accomplishing implantation into the substrate of plasma ions at an energy determined by the bias voltage. Because of the surface retention of condensed metal plasma, the process in a metal plasma is quite different from in a gaseous plasma. Ions that are deposited during the pulse-off part of the cycle are deposited on the surface as a monolayer or sub-monolayer film, and ions that are accelerated from the

plasma and bombarded into the substrate during the high voltage bias part of the cycle suffer collisions with previously-deposited neutral metal atoms and thus also produce recoil implantation. By varying the proportions of the direct and recoil implantation parts of the cycle (ie, the duty cycle of the pulse biasing) one can tailor the shape of the implantation depth profile, and the range can be tailored by the amplitude of the applied pulse voltage. The whole operation can be time-varied throughout the processing duration, starting for example with a high energy phase so as to create a deep buried layer of the implanted species an ion mixing phase) and slowly changing to a low energy phase whereby a surface film is built up by plasma deposition (an ion beam assisted deposition phase). By controlling the plasma ion energy we thus acquire control over two very important features to the deposition process: the interface width can be tailored, and the film morphology and structure can be controlled. In this way one can synthesize a surface metallic film of precisely controllable thickness having a well-determined and controllable atomically mixed interface with the substrate, and the parameters of the film and the interface can be tailored over a wide range. For purely metallic films, the process is carried out at a vacuum in the 10^{-6} Torr range; oxides and nitrides can be formed by doing the deposition at the appropriate background pressure of oxygen or nitrogen, typically a few tens of microns

In our plasma materials synthesis research program we have shown that highly adherent, high quality films of many different kinds of materials can be formed in this way, including films of metals[16-18], metal oxides[19,20] and oxide ceramics[21-24], optoelectronic materials[25], high-Tc superconductors[26,27], diamond-like carbon[28-30], and multilayer structures with complex layer structures[31-33]. Concise reviews have been presented of the method and applications[34,35].

Of relevance to the present work, we have previously formed alumina films[21,24] and mullite films[22,23], and some observations of the behavior of these films in a high temperature environment and their value as high temperature oxidation resistant coatings have been made. Near-stoichiometric alumina films of thickness ~0.2 - 1 μ on substrates of FeAl (containing ~0.1% Zr) were prepared; the films were amorphous prior to heat treatment and showed an α-alumina phase after heat treating at 1000°C for up to 16 hours. The film substrate adhesion was typically greater than ~70 Mpa (the limit of our measurement) prior to heating, and the adhesion was maintained after repetitive cycling in temperature between ambient and 1000°C. Also, mullite ($3Al_2O_3.2SiO_2$) films have been formed on SiC substrates by mixing together separately produced plasmas of aluminum and silicon. The Al to Si ratio was controlled by the plasma gun parameters and the plasmas blended together in a magnetic multipole plasma homogenizer device. Deposition was done onto appropriately positioned SiC substrates.

Here we report on our evaluation of the performance of plasma-synthesized mullite films on SiC subject to repetitively cycled high temperature excursions. In the following we firstly summarize the plasma synthesis technique as applied for the present purpose, and outline the characteristics of the mullite films formed, followed by a description of the testing processes and the experimental results obtained.

OUTLINE OF THE PLASMA SYNTHESIS TECHNIQUE

Our approach is to immerse the substrate in the dense metal plasma formed by one or more vacuum arc plasma guns while controlling the energy of the depositing ions by the application of a high frequency, repetitively pulsed bias voltage to the substrate during the plasma deposition. Oxygen is added at a suitable low pressure and is incorporated in the growing film primarily by surface oxidation and subsequent recoil implantation. Ion energy is controlled as a function of time, and the film-substrate interface can be tailored and the film structure optimized by the ion beam assist that is inherent to the process.

The vacuum arc is a high current discharge between two electrodes in vacuum in which metal plasma is produced in abundance[2,36-38]. We have made several different embodiments of vacuum arc plasma guns. Here we used a small, repetitively pulsed version operated at a pulse length of 5 ms and repetition rate 1 Hz with arc current typically 300 A. Along with the metal plasma that is generated, a flux of macroscopic droplets (resolidified cathode debris) of size in the range 0.1 - 10 microns is also produced[36-40]. In general it is desirable to remove the solid particulate contamination and this can be done by using a curved magnetic duct (bent solenoid of magnetic field strength a few hundred gauss) which stops line-of-sight transmission of macroparticles while allowing the transport of plasma[41-43]. The overall plasma formation system thus consists of the repetitively pulsed plasma gun in conjunction with a 90° magnetic filter.

Metal oxides can be formed by carrying out the deposition not in a high vacuum environment but in a somewhat higher pressure ambient of oxygen gas; we have found empirically that a pressure in the range 1 - 100 mTorr is suitable for most purposes. In the present work the oxygen background pressure was 5 to 25 mTorr. The oxygen is both entrained in the plasma stream, ionized, and deposited in the plasma state, as well as reacting at the freshly-deposited metallic surface to form aluminum oxide or silicon dioxide. In either case, for the optimal oxygen pressure a near-stoichiometric film of the metal oxide is formed.

Ion energy of the depositing plasma flux is controlled by repetitively pulse biasing the substrate. The pulse duration is ~10 μs and the duty cycle ~10–50%. Pulsing the bias is necessary (for all but the lowest bias voltages) because a high-voltage dc bias would cause a discharge between the substrate and the vessel or the plasma gun; the plasma would be grossly perturbed (because the plasma sheath would expand from the substrate to large distances). The solution is to switch off the bias before a discharge can occur (to limit the sheath expansion to modest distances), let the plasma recover, and then repeat the process; ie, to do the biasing in a repetitively pulsed mode. For the early stages of the deposition the pulse bias is held at a relatively high voltage of -2.2 kV. The mean aluminum ion energy is then 3.75 keV, because the mean ion charge state of the aluminum plasma is 1.7 and $E_i = QV$; for silicon the mean charge state is 1.4 and the mean ion energy 3.1 keV; (the charge state spectra of vacuum arc produced plasmas have been discussed in detail in refs. 44,45). At this energy ions are implanted into the substrate to a depth of up to ~100 Å. The film thus grows on the SiC substrate from a highly mixed interface. When a film thickness of just a few tens of angstroms has accumulated, the pulse bias voltage is reduced, since intermixing with the

substrate is no longer a factor and the higher ion energy would sputter away the already-deposited film. Moreover, it is known from a large body of work on ion assisted deposition that a modest ion energy can be highly advantageous for controlling characteristics such as the density, morphology and structure of the film. For the bulk of the plasma deposition process the pulse amplitude is kept at -200 volts.

To deposit films containing several different metallic elements we have combined the operation of two plasma sources, with their magnetic ducts, so that the plasma streams of different elements are mixed together before reaching the substrate. Optionally, a short magnetic multipole "plasma homogenizer" structure can be used also, to better blend the two plasmas and to produce a more uniform plasma density profile; we have incorporated this feature in some of our work [46]. A schematic diagram of the dual-plasma deposition apparatus is shown in Figure 1. The deposition can be carried out synchronously or asynchronously, i.e. the plasma sources can be operated simultaneously or sequentially. Depending on the deposition rate, asynchronous operation may lead to stratification of the film in layers, whereas synchronized operation results in a greater degree of mixing. In the films described here the latter operating mode was chosen so as to maximize the intermixing of the atoms in the solid phase.

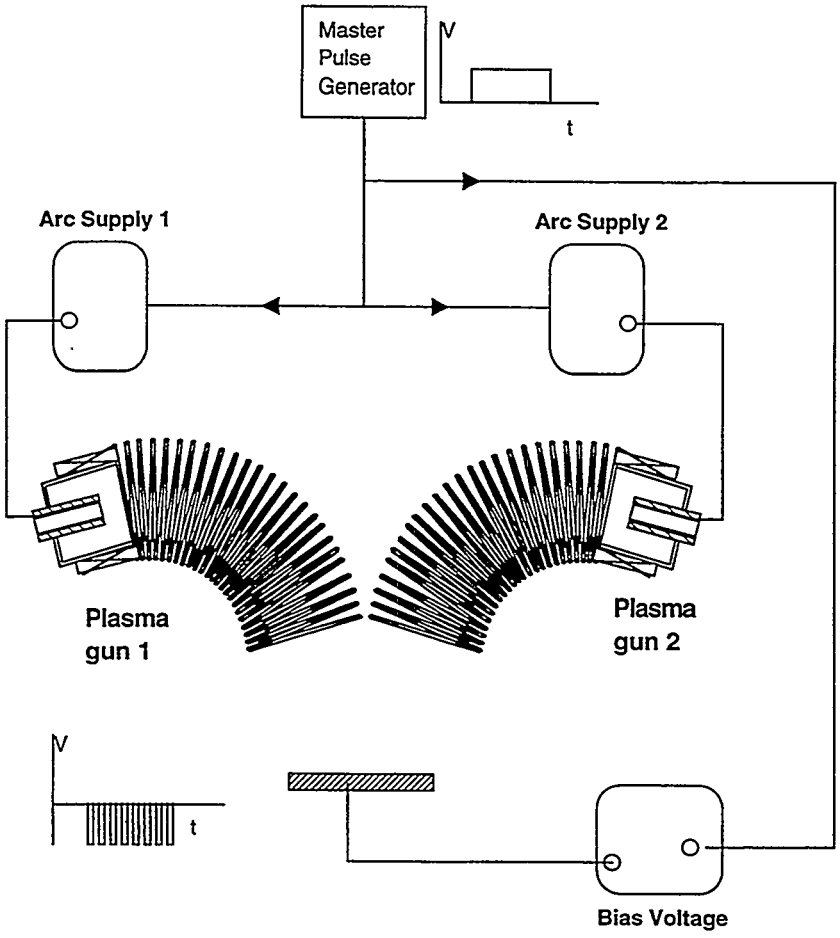

Figure 1 Simplified schematic of the plasma configuration used to form the films.

CHARACTERISTICS OF THE SYNTHESIZED FILMS

Films of silicon-aluminum oxide were synthesized on polished SiC substrates. An edge-on SEM photograph of a typical film is shown in Figure 2. The details of our Mepiiid technique as applied for this specific application have been described elsewhere[22,23]. The films are typically of thickness in the range 0.2 - 2 microns. X-ray diffraction analysis has shown that the as-deposited films are amorphous, with no evidence of crystalline structure or phase separation. Annealing of the films at 1100°C in air for 2 hours results primarily in the formation of crystalline mullite, $3Al_2O_3.2SiO_2$.

Adhesion of the films to the substrate has been investigated using a Sebastian-type pull-tester having an instrumental limit of measurement of about ~70 MPa. We have found that adhesion strength of the as-deposited films is generally in the range 10 - 40 MPa, and the post-annealing adhesion strength is equal to or greater than the instrumental limit of ~70 MPa – i.e., the annealed samples when subjected to a normal pull-test of epoxied studs show failure at the epoxy-film interface and not the film-substrate interface.

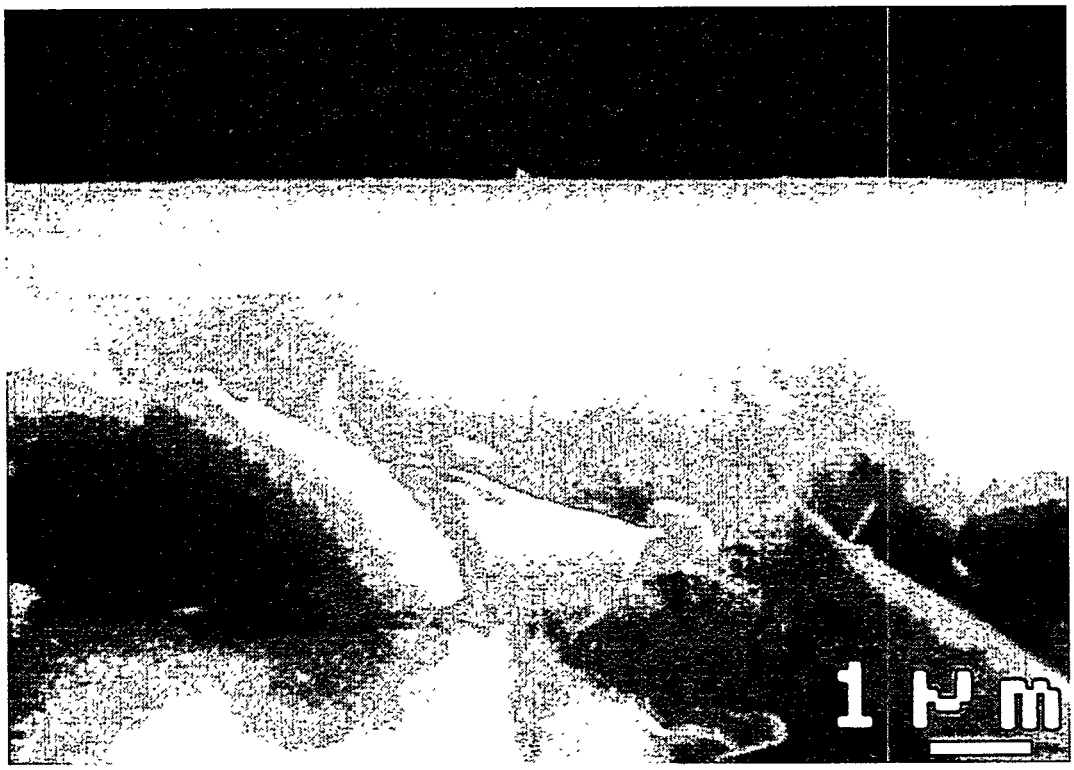

Figure 2. Edge-on scanning electron microscope photograph of a thin film of mullite formed by the dual-source MePIIID process on a silicon carbide substrate. Aluminum and silicon plasmas were combined in the appropriate proportions in a low pressure background of oxygen to form the $3Al_2O_3.2SiO_2$ mullite structure. The film is somewhat over 1 micron in thickness, and is fully dense, non-columnar, highly adherent, smooth, and exceptionally resistant to repeated thermal cycling between room temperature and 1100°C.

THERMAL CYCLING CHARACTERISTICS

We have investigated the adhesion of the mullite films to silicon carbide when subjected to thermal cycling. Each cycle consisted of heating the samples to 1100°C at a rate of 9°C/min, maintaining the substrate at 1100°C for 18 h in air, and cooling it down at a rate of approximately 4°C/min. For the first 5 cycles, adhesion was measured after each heat cycle, and after that adhesion was measured after the 15th and 20th cycle.

In order to characterize the adhesion after thermal cycling we used our Sebastian pull tester. However, in our early work[22,23] we showed that the stress required to debond the mullite film from the SiC substrate often exceeds the maximum strength of the epoxy used (this is the limit of measurement of this technique). Therefore these measurements can provide only a lower limit for the adhesion strength. This has prompted us to use an additional method for characterizing the strength of the bonding between film and substrate.

The method used here for characterizing the interface toughness is based on the indentation method developed by Evans and co-workers[47-49]. This technique involves making micro-indentations in the surface of the oxide film. The indentation creates a plastically deformed zone immediately beneath the surface. Residual stresses developed in the plastic zone provide the driving force for lateral and radial crack growth[50]. If the interface toughness is lower than the toughness of both the film and the substrate, lateral cracks will develop and propagate along the interface, as indicated in Figure 3. Evans and co-workers[47-49] have developed fracture mechanics solutions that allow interfacial fracture energies to be calculated from the size of these cracks. In order for the model to be realistic, the depth of the indent should be less than the film thickness.

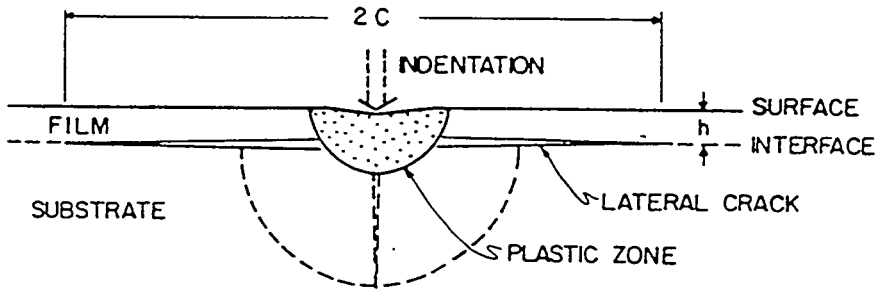

Figure 3: Schematic of an indentation made on a film-substrate sample, showing the lateral crack propagating preferentially along the interface.

Due to the small thickness of the mullite films produced here, the indents did perforate through the film, and therefore our estimates of the interface strength should not be taken too quantitatively. One can make arguments that would imply that perforation of the layer would lead either to an underestimate or to

an overestimate of the toughness. Figure 4 is an optical micrograph of an indentation mark, with the lateral crack visible. According to the model presented in Figure 3, this determines the end of the delaminated region. We used a load of 1 kg with a Vickers indenter. In spite of these limitations, the test can still be used comparatively, to show trends. The results of both kinds of tests are shown in Table 1 for the thermal cycling tested. The result of the indentation tests in this Table are shown in terms of the radius of the debonded region observed. A value of zero indicates that no crack was observed upon application of the load. Appearance of lateral cracks after cycling the temperature 15 times suggests some weakening of the interface, though still below the detection limit of the Sebastian pull-test. We plan to extend the thermal cycling to see if the adhesion further deteriorates.

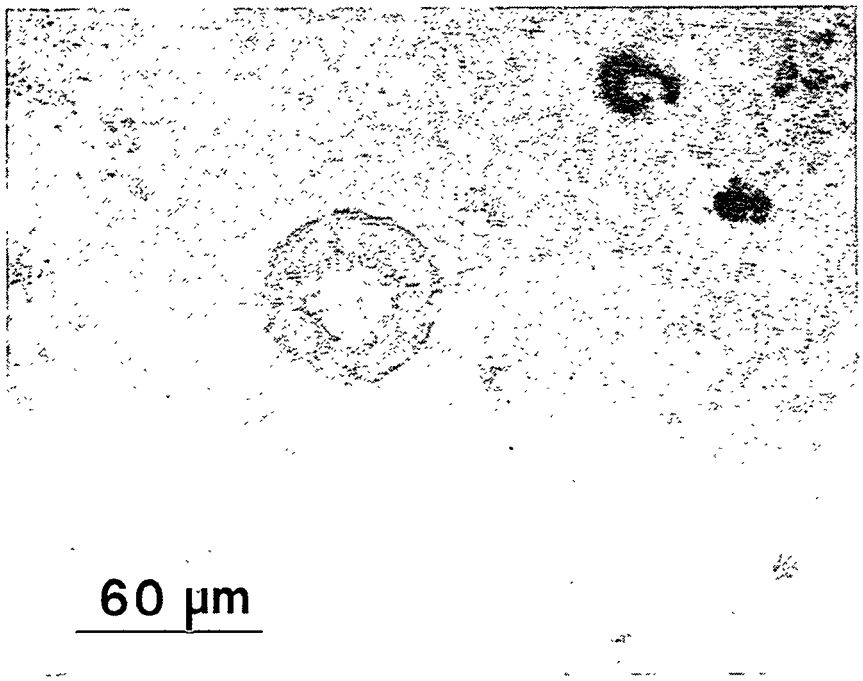

Figure 4: Optical micrograph of a Vickers indent on a mullite film on a SiC substrate. Indentation load was 1000 g.

To illustrate the order of magnitude of the interface strengths determined by the indentation method, we carried out an analysis according to ref. 47 using the model for lateral crack expansion. The following parameters were used for this calculation: crack radius 30 µm, contact load 1000 g, film thickness 0.2 µm, film hardness 30 GPa. The calculated interfacial fracture resistance was then $K_{IC,interface}$ = 0.8 MPa $m^{1/2}$. Despite the uncertainties in this value, it compares highly favorably with the fracture toughness for SiC ($K_{IC,SiC}$ = 4.6 MPa $m^{1/2}$) and mullite[51] ($K_{IC,mullite}$= 2 MPa $m^{1/2}$).

Cycle No.	Sebastian Pull Test (MPa)	Indentation Test lateral crack size
1	> 70	0
2	> 70	0
3	> 70	0
4	> 70	0
5	> 70	0
10	> 70	0
15	> 70	30 μm
20	> 70	30 μm

Table 1: Film-substrate adhesion strength as determined by a Sebastian-type pull-test, and lateral crack size as determined by a microindentation test, as a function of number of 24-hour thermal cycles between room temperature and 1100 °C.

CONCLUSION

We have successfully deposited mullite films on silicon carbide by combining plasma streams of Al and Si ions produced by vacuum arc plasma guns in a background atmosphere of oxygen. The films are of the stoichiometric $3Al_2O_3.2SiO_2$ composition and fully dense, non-columnar, and smooth. Application of high negative bias voltage to the substrate (ie, high ion energy) is essential for good adhesion between the film and substrate. The adhesion of the as-deposited mullite is high, increases upon annealing of the film, and remains high over subsequent thermal cycling at 1100°C.

Evaluation of sample properties following thermal cycling through a yet greater number of heat cycles is presently under way. Future studies will include: extension of the number of thermal cycles that the coated samples experience in order to determine whether any degradation takes place; detailed microstructural characterization of the mullite-SiC interface; and more accurate determination of interface strength.

ACKNOWLEDGMENTS

We are indebted to Bob MacGill and Mike Dickinson for their support of the LBNL experimental equipment. This work was supported by the U.S. DOE, Office of Advanced Research, Fossil Energy, under Contract Number DE-AC03-76SF00098.

REFERENCES

1. See, for example, the Proceedings of the annual International Conferencer on Metallurgical Coatings and Thin Films (ICMCTF), published as special issues of *Thin Solid Films* and *Surface and Coatings Technology*.
2. R.L. Boxman, P. Martin and D. Sanders (eds), *Vacuum Arc Science and Technology*, Noyes, New York, 1995.
3. D. M. Sanders, J. Vac. Sci. Tech. A7, 2339 (1989).
4. See, for instance, Ion Implantation and Plasma Assisted Processes, edited by R.F. Hochman, H. Solnick-Legg and K.O. Legg, (ASM, Ohio, 1988).
5. *Plasma Processing and Synthesis of Materials*, edited by D. Apelian and J. Szekely, Mat. Res. Soc. Symp. Proc. Vol 98, (MRS, Pittsburgh, 1987).
6. See, for instance, the proceedings of conferences such as those on Ion Implantation Technology, and Ion Beam Modification of Materials, in Nucl. Intrum. Methods, Part B.
7. M. Iwaki, Critical Rev. in Solid State and Mat. Sci. 15 (1989) 473.
8. G.K. Wolf and W. Ensinger, Nucl. Instr. and Meth. B59/60, 173 (1991).
9. J.R. Conrad, J.L. Radtke, R.A. Dodd, F.J. Worzala and N.C. Tran, J. Appl. Phys. 62, 4591 (1987).
10. See the proceedings of the First and Second International Workshops on Plasma-Based Ion Implantation, J. Vac. Sci. Tech. B12, 815-998 (1994), and Surface and Coatings Technol. 85, 1-124 (1996), resp.
11. I.G. Brown. X. Godechot and K.M. Yu, Appl. Phys. Lett. 58, 1392 (1991).
12. I.G. Brown, A. Anders, S. Anders, M.R. Dickinson, I.C. Ivanov, M.A. MacGill, X. Yao and K.M. Yu, Nucl. Instrum. Meth. Phys. Res. B80/81, 1281 (1993).
13. I.G. Brown, in *Plasma Synthesis and Processing of Materials*, edited by K. Upadhya (pub. TMS, Warrendale, PA, 1993).
14. A. Anders, S. Anders, I.G. Brown and I.C. Ivanov, Mat. Res. Soc. Symp. Proc. 316, 833 (1994).
15. A. Anders, S. Anders, I.G. Brown, M.R. Dickinson and R.A. MacGill, J. Vac. Sci. Tech. B12, 815 (1994).
16. S. Anders, A. Anders, I. Brown, F. Kong and F. McLarnon, Surface and Coatings Technol. 85, 75-79 (1996).
17. I. Brown, A. Anders, S. Anders, M.R. Dickinson and R.A. MacGill, J. Vac. Sci. Tech. B12, 823 (1994).
18. M.A. Otooni, I.G. Brown, S. Anders and Z. Wang, Mat. Res. Soc. Symp. Proc. 396, 649 (1996).
19. R.A. MacGill, S. Anders, A. Anders, R.A. Castro, M.R. Dickinson, K.M. Yu and I.G. Brown, Surface and Coatings Technol. 78, 168 (1996).
20. S. Anders, A. Anders, M. Rubin, Z. Wang, S. Raoux, F. Kong and I.G. Brown, Surface and Coatings Technol. 76-77, 167 (19950.
21. I.G. Brown and Z. Wang, 9th Annual Conference on Fossil Energy Materials, Oak Ridge, TN, May 16-18, 1995, Proceedings of conference (U.S. Dept. of Energy, Conf-9505204, ORNL/FMP-95/1), p. 239.
22. O.R. Monteiro, Z. Wang, K.-M. Yu, P.Y. Hou, I.G. Brown, B.H. Rabin and G.F. Kessinger Proc. 10th Annual Conference on Fossil Energy Materials, Knoxville, TN May 14-16, 1996, (Pub. Conf-9605167, ORNL/FMP-96/1, published by US DOE). p. 97.
23. O.R. Monteiro, Z. Wang and I.G. Brown, J. Mat. Res., to be published (1997).
24. P.Y. Hou, K.B. Alexander, Z. Wang and I.G. Brown, in *Elevated Temperature Coatings: Science and Technology II*, edited by N.B. Dahotre and J.M. Hampikian (pub. The Minerals, Metals and Materials Society, 1996); p. 187.
25. S. Raoux, I. Brown, S. Anders, K.M. Yu and I.C. Ivanov, Mat. Res. Soc. Symp. Proc. 392, 241 (1995).
26. M.S. Chae, M.T. Simnad, M.B. Maple, S. Anders, A. Anders and I.G. Brown, Physica C 270, 173-179 (1996).
27. M. S. Chae, M. B. Maple, M. T. Simnad, S. Anders, A. Anders and I. G. Brown, IEEE Trans. Appl. Supercon. 5, 2011 (1995).
28. O.R. Monteiro, I.G. Brown, R. Sooryakumar and M. Chirita, Mat. Res. Soc. Symp. Proc. 444, 93-98 (1997).
29. G.M. Pharr, D.L. Callahan, S,D. McAdams, T.Y. Tsui, S. Anders, A. Anders, J.W. Ager III, I.G. Brown, C.S. Bhatia, S.R.P. Silva and J. Robertson, Appl. Phys. Letters 68, 779 (1996).

30. S. Anders, A. Anders, I.G. Brown, B. Wei, K. Komvopoulos, J.W. Ager III and K.M. Yu, Surface and Coatings Technol. 68/69 388 (1994).
31. O.R. Monteiro, M.-P. Delplancke-Ogletree, J.W. Ager and I.G. Brown, Mat. Res. Soc. Symp. Proc. 438, 599-604 (1997).
32. M.-P. Delplancke-Ogletree, O.R. Monteiro and I.G. Brown, Mat. Res. Soc. Symp. Proc. 438, 639-644 (1997).
33. S. Anders, D.L. Callahan, G.M. Pharr, T.Y. Tsui and C.S. Bhatia, J. Mat. Res., to be published.
34. I.G. Brown, A. Anders, S. Anders, M.R. Dickinson, R.A. MacGill, O.R. Monteiro, E.M. Oks, S. Raoux, Z. Wang and G. Yushkov, Mat. Res. Soc. Symp. Proc. 396, 467-477 (1996).
35. J.V. Mantese, I.G. Brown, N.W. Cheung and G.A. Collins, in: "Plasma Processing of Advanced Materials", MRS Bulletin 21(8), 52-56 (1996).
36. J.M. Lafferty (ed.), *Vacuum Arcs - Theory and Application*, Wiley, New York, 1980.
37. For a most impressive and comprehensive bibliography of the vacuum arc literature see H.C. Miller, *A Bibliography and Author Index for Electrical Discharges in Vacuum (1897 - 1986)*, pub. by the General Electric Co., document No. GEPP-TIS-366e (UC-13), March 1988; also published in part in IEEE Trans. Elec. Insul. 25(5),765 (1990) and 26(5), 949 (1991).
38. See the Special Issues on Vacuum Discharge Plasmas in IEEE Trans. Plasma Sci. These issues contain selected papers from the biennial International Symposium on Discharges and Electrical Insulation in Vacuum, usually in the October issues in odd-numbered years.
39. D.T. Tuma, C.L. Chen and D.K. Davies, J. Appl. Phys. 49, 3821 (1978).
40. J.E. Daalder, Physica 104C, 91 (1981).
41. I.I. Aksenov, A.N. Belokhvostikov, V.G. Padalka, N.S. Repalov and V.M. Khoroshikh, Plasma Physics and Controlled Fusion 28, 761 (1986).
42. A. Anders, S. Anders and I.G. Brown, Plasma Sources Sci. & Technol. 4, 1 (1995).
43. S. Anders, A. Anders and I.G. Brown, J. Appl. Phys. 75, 4895 (1994).
44. I.G. Brown and X. Godechot, IEEE Trans. Plasma Sci. PS-19, 713 (1991).
45. I.G. Brown, Rev. Sci. Instrum. 10, 3061 (1994).
46. S. Anders, S. Raoux, K. Krishnan, R.A. MacGill and I.G. Brown, J. Appl. Phys. 79, 6785 (1996).
47. S.S. Chiang, D.B. Marshall and A. G. Evans in "Surfaces and Interfaces in Ceramic and Ceramic-Metal Systems" (Eds J. Pask and A.G. Evans), Plenum Press, New York, 1981, p. 603.
48. D.B. Marshall, B.R. Lawn and A.G. Evans, J. Am. Ceram. Soc. 65, 561 (1982).
49. D.B. Evans and A.G. Evans, J. Appl. Phys. 24, 209 (1984).
50. P.Y. Hou and A. Atkinson, Mater. at High Temp. 12, 119 (1994).
51. R. Torrecillas, G. Fantozzi, S. de Aza and J.S. Moya, Acta Mater. 45, 897 (1997).

INFLUENCE OF WATER VAPOR AND SLAG ENVIRONMENTS ON CORROSION AND MECHANICAL PROPERTIES OF CERAMIC MATERIALS*

by

K. Natesan and M. Thiele
Energy Technology Division
Argonne National Laboratory
Argonne, IL 60439

ABSTRACT

Conceptual designs of advanced combustion systems that utilize coal as a feedstock require high-temperature furnaces and heat transfer surfaces that can operate at temperatures much higher than those prevalent in current coal-fired power plants. The combination of elevated temperatures and hostile combustion environments requires the development and application of advanced ceramic materials in these designs. The objectives of the present program are to evaluate the corrosion behavior of candidate ceramic and metallic materials in air and slag environments and evaluate the residual mechanical properties of the materials after corrosion. The program emphasizes temperatures in the range of 1000-1400°C for ceramic materials and 600-1000°C for metallic alloys. Coal/ash chemistries based on thermodynamic/kinetic calculations and slags from actual combustors are used in the program. The materials being evaluated include monolithic silicon carbide from several sources, silicon carbide in a silicon matrix, silicon carbide in alumina composites, silicon carbide fibers in a silicon carbide-matrix composite, and some advanced nickel-base alloys. This paper presents results from an ongoing study of the corrosion performance of candidate ceramic materials exposed to dry air, air with water vapor, and slag environments and the effects of these environments on the flexural strength and energy absorbed during fracture of these materials.

INTRODUCTION

Coal is a complex and relatively dirty fuel that contains varying amounts of sulfur and a substantial fraction of noncombustible mineral constituents, commonly called ash. Conceptual designs of high-performance power systems (HIPPS) that utilize coal as a feedstock require high-temperature furnaces and heat transfer surfaces capable of operating at higher temperatures than those used in conventional coal-fired power plants. The combination of elevated temperatures and hostile combustion environments requires the use of ceramic materials in at least the first few passes of the heat exchangers in these designs.

In addition to conventional steam turbines, HIPPS would employ a combined cycle that uses a gas turbine driven by a working fluid (air) that is separately heated in a high-temperature advanced furnace.[1] The ultimate goal is to produce electricity from coal with an overall thermal efficiency of 47% or greater (compared with ≈35% for current systems) and to reduce CO_2 emissions by 25-30%. The pulverized-coal high-temperature advanced furnace (HITAF) in the HIPPS concept will heat air to an intermediate temperature of ≈1000°C and burn supplemental clean fuel to boost the temperature of air to a turbine inlet temperature of ≥1300°C. Use of supplemental fuel can be reduced as the HITAF technology evolves to permit the heating of air to higher temperatures in the furnace. The HITAF represents a major departure from conventional pulverized-coal-fired boilers in which only steam is raised to a maximum of 530-620°C. The purpose of the HITAF is to heat the clean working fluid, air, to the required turbine inlet temperatures. At the elevated temperatures of the HITAF, transfer of heat from the combustion gases to the working fluid will be dominated by radiative heat transfer, and the design of the heat transfer surface will be critical for the success of the

system. Several concepts are under development for the design of the heat transfer surfaces in the HITAF system.[2]

For any of the concepts to be viable for a commercial-scale HIPPS, the heat transfer surfaces must be exposed to much higher temperatures than are prevalent in conventional coal-fired steam-turbine systems. For temperatures of 1000-1300°C, conventional metallic materials do not possess adequate strength properties and/or corrosion resistance for long-term service. In addition, an important difference between the conventional boiler system and the HIPPS is seen in the chemical and physical characteristics of the ash layers that can deposit on the heat transfer surfaces. The deposits are likely to be dominated by alkali sulfates and coal slags in HIPPS rather than by pyrosulfates or alkali-iron-trisulfates (which are prevalent in conventional pulverized coal-fired boilers) and by increased mobility of corrosion-accelerating agents in the deposit layers due to the much higher temperature of the heat transfer surfaces in the HIPPS. It is major challenge to develop methods to combat severe deposition, erosion, and corrosion of heat transfer surfaces that are exposed to higher-than-normal temperatures. These methods could include fuel selection, cleaning of aggressive contaminants from coal, fine grinding of coal, use of additives, and selection of advanced corrosion-resistant ceramic materials, coatings, and advanced alloys for vulnerable heat transfer sections.

In earlier studies, several ceramic materials were examined to evaluate their performance after exposure to dry air, salt environments that contained Na_2SO_4 or a 75 wt.% Na_2SO_4-25 wt.% NaCl mixture, and three coal slags that simulated slags obtained from combustion of coals from eastern and western U.S.[3-5] The results showed that the materials exposed to an air environment undergo passive oxidation of SiC to SiO_2. Exposure of these materials to salt environments led to catastrophic corrosion, especially if the sodium activity of the condensed salt was high, by enabling formation of low-melting corrosion products. The mode of degradation of SiC-based materials involves reactions between the ceramic materials and alkali sulfates such as Na_2SO_4 and K_2SO_4, and alkali chlorides such as NaCl and KCl. In the combustion gas environment, the concentrations of oxygen and of sulfur as SO_2 and SO_3 determine the sodium oxide activity via the reaction $Na_2SO_4 = Na_2O + SO_3$. Subsequently, the silica phase that forms on the ceramic materials reacts with Na_2O to form compounds such as $Na_2O{\cdot}XSiO_2$, where X can be 0.5, 1, 2, or 4. These sodium silicates exhibit melting temperatures of 875-1110°C. This mode of degradation of ceramic materials requires sufficiently high Na_2O activity and is usually possible in gas turbine systems where slag constituents are virtually absent. In such instances, the liquid phase can dissolve the protective SiO_2 scale and also cause the liquid reaction products to penetrate into the substrate ceramic material and thereby mechanically weaken the material.

In coal-fired combustion systems, the presence of slag constituents determines the thermodynamic activity of various deposit constituents, and alkali-sulfate-induced corrosion is generally not dominant. The mode of degradation of ceramic materials in coal-fired combustion systems is via reactions with coal ash. This type of degradation depends on material composition, slag chemistry (acidic or basic), and gas-phase environment (either oxidizing or reducing). The slags generally contain phases such as SiO_2, Al_2O_3, CaO, Fe_2O_3, Na_2O, a combination of these phases, and other ash constituents, depending on the coal feedstock. X-ray diffraction (XRD) data for deposits, that were obtained during a Combustion and Environmental Research Facility (CERF) run with combustion of Pittsburgh coal showed the dominant phases to be mullite

($3Al_2O_3 \cdot 2SiO_2$), ordered calcian albite ([Na,Ca] Al $[Si,Al]_3O_8$), and hematite (Fe_2O_3). The melting temperatures of these phases are >1400°C; reactions between these compounds and the ceramic materials occur primarily in the solid state, and little or no penetration of the ceramics by liquid phase from coal combustion environment occurs.

Similarly, XRD data for the deposits, obtained during a CERF run with combustion of Alaskan/Russian blend coal, showed the dominant phases to be anorthite ($CaO \cdot Al_2O_3 \cdot 2SiO_2$), calcium aluminum silicate ($CaO \cdot Al_2O_3 \cdot SiO_2$), and ordered sodium anorthite (Ca,Na) $(Al,Si)_2$ Si_2O_8. These calcium-rich silicates also have melting temperatures >1400°C, and reactions between the coal ash deposit and the ceramics occur predominantly in the solid state. The experimental results also indicate that Na_2O activity in the deposits (with combustion of coals that contain Fe_2O_3 and CaO) is sufficiently low to form liquid sodium silicates of various types in coal-fired systems.

On the other hand, exposure of the materials to slags obtained from typical coal ashes had very little effect on the corrosion performance of the materials, especially at 1200°C, where the reactions do not involve formation of liquid corrosion products. Four-point bend tests, conducted on several of the materials after exposure to dry air, salt, and slag environments, indicated that sodium salts (both sulfates and chlorides) have the greatest degrading effect on corrosion properties of the materials, whereas exposures to air and slag environments had minimal effect on the properties at 1200°C.

The objectives of the work presented here were to (a) evaluate the influence of water vapor in the environment on the oxidation behavior of SiC-based materials, (2) assess the effect(s) of simultaneous presence of coal slag and combustion gas (with water vapor) on the corrosion behavior of materials, and (c) determine the residual mechanical properties of the materials after exposure to the above-mentioned environments.

EXPERIMENTAL PROCEDURE

Materials

The materials selected for the laboratory experimental program include monolithic ceramic materials and ceramic-matrix ceramic composites.

Sintered alpha SiC is a fully densified (>98% of theoretical density) ceramic material produced by sintering. It is a single-phase material that has a very fine grain structure (8 μm) for excellent wear resistance, contains no free silicon, and has been reported to be chemically resistant in both oxidizing and reducing environments. The density of this material is ≈3.1 g/cm^3.

SiC in a silicon matrix is a material that consists of silicon carbide in a silicon matrix. The silicon metal phase provides good fracture toughness and resistance to thermal shock, oxidation, and creep without the extreme brittleness of many ceramic materials. The material exhibits a density of 2.8 g/cm^3, 0% porosity, and contains ≈47% silicon.

Siliconized SiC consists of 90 vol.% SiC, 8 vol.%Si metal, and 2 vol.% pores. The material has a density of 3.1 g/cm^3.

The SiC(f)/SiC matrix material contains ≈40 vol.% SiC fibers (criss crossed in two dimensions) in a SiC matrix with a 10 vol% porosity. The density of the material is 2.5 g/cm^3 and it exhibits excellent compressive and interlamellar shear strength, high stiffness, and good oxidation resistance.

SiC(p) in Al_2O_3 is a composite material that contains SiC particulates in an alumina matrix. The material contains some free aluminum in the matrix becausee the material is made by direct metal oxidation. The material combines the thermal properties of SiC and corrosion resistance of alumina. Particulate loading is in the range of 50-55 vol.%; particle diameter is 5-20 μm. The material contains ≈40 vol.% alumina, ≈10 vol.% Al, and 1 vol.% of ores.

Oxidation and Corrosion Tests

Coupon specimen 25.4 x 4.76 x 1.6 mm were prepared from several of the above–listed materials for oxidation experiments at 1000, 1200, and 1400°C in dry air. In addition, experiments were performed at 1200°C in air that contained water vapor. Dimensions and initial weights of the specimens were measured prior to exposure. Before the oxidation treatment, all but the SiC(f)/SiC specimens were ground on 1200-grit SiC paper and cleaned with alcohol. The specimens were placed in an alumina holder that was suspended into an alumina chamber inside a resistance-wound furnace. The heating was conducted at a rate of 5°C/min in the exposure environment. Water vapor was introduced into the air stream by passing the air through a heated water bath. In this study, the air was saturated with water at 46 and 69°C, which resulted in 10 and 30 vol.% water vapor in the air, respectively. Each experimental series consisted of five cycles of 100 h each. An electrobalance with a sensitivity of 0.1 mg was used after each cycle to determine weight change of the specimens that was due to oxidation.

Exposures in the presence of three slags were conducted at 1200°C for 200 h. Table 1 lists the compositions of the slags and the coals that were combusted to obtain these slags. Analysis shows that the slag obtained from Illinois #6 coal was richer in Fe_2O_3 and leaner in CaO and MgO, whereas the reverse was seen for slag from Rochelle coal. Slags #43 and XX typify the slags derived from coals in the eastern U.S., whereas the slag #47 is typical of that derived from western coals. Slag exposure tests were conducted in a flowing gas mixture of air-1 vol.% SO_2 with and without 10 vol.% water vapor.

Table 1. Compositions of slags for laboratory study

Compound	Slag 43/ Illinois #6	Slag 47/ Rochelle	Slag XX/ Illinois #6
SiO_2	52.9	47.1	53.3
Al_2O_3	16.6	18.8	18.6
Fe_2O_3	12.9	5.2	17.6
CaO	13.0	19.6	7.2
MgO	1.3	5.8	1.0
Na_2O	0.8	0.9	0
K_2O	1.6	0.3	1.7
SO_3	0.1	0.3	0

Mechanical Tests

The effect of air oxidation, water vapor additions, and exposures to slag from Illinois #6 and Rochelle coals on the flexural strength of four candidate materials was evaluated by preexposure to the specific environment and postexposure four-point bend testing of the specimens in vacuum. For these evaluations, the temperature was maintained at 1200°C during both the preexposure and the mechanical testing. The flexural test involved bending a specimen of rectangular cross section until fracture. The specimen dimensions were 25.4 x 4.76 x 1.6 mm and the slag-exposed surface was maintained under tension during the test. The data on the load that was necessary to cause fracture and the area under the load-displacement curves were used to calculate the flexural strength of the material and the energy absorbed during the fracture.

Microstructural analysis

Upon completion of the oxidation experiments, slag exposures, and mechanical testing, fracture surfaces and polished cross sections of several of the specimens were analyzed by scanning electron microscopy (SEM), energy dispersive X-ray (EDX) analysis, and XRD.

EXPERIMENTAL RESULTS

Oxidation in Dry and Wet Air

Oxidation of ceramic materials, such as monolithic and composite SiC and SiC-dispersed Al_2O_3, involves reaction of carbide phases to silicon-rich oxides. The rate of oxidation is generally influenced by the porosity of the material, the amount of free silicon and/or aluminum in the material, and exposure temperature. Earlier work showed a low rate of oxidation for these materials when exposed in dry air at 1200°C.[4,5] One exception was SiC(p) in Al_2O_3 material, which exhibited a large increase in weight gain in the early stage of exposure, due to oxidation of free aluminum in the surface region of the sample. After ≈100 h of exposure, the oxidation rate slowed but was still higher than in other materials, indicating oxidation of free aluminum in the interior of the material, dictated by the diffusion of oxygen. The results also established that these ceramic materials undergo passive oxidation at temperatures in the range of 1000-1400°C in a dry-air environment.

Figure 1 shows weight-change-versus-time data for specimens of several ceramic materials exposed to air with 0, 10, and 30 vol.% water vapor at 1200°C. It is generally accepted that during oxidation of silicon-based materials, the mobile species is oxygen and not silicon. Several reactions are possible for the oxidation of SiC to SiO_2:

$$SiC + 3/2\ O_2 = SiO_2 + CO \quad (1)$$

$$SiC + O_2 = SiO(g) + CO \quad (2)$$

$$SiC + O_2 = SiO_2 + C \quad (3)$$

$$SiC + 2\ O_2 = SiO_2 + CO_2 \quad (4)$$

$$SiC + 2\ H_2O = SiO_2 + C + 2\ H_2 \quad (5)$$

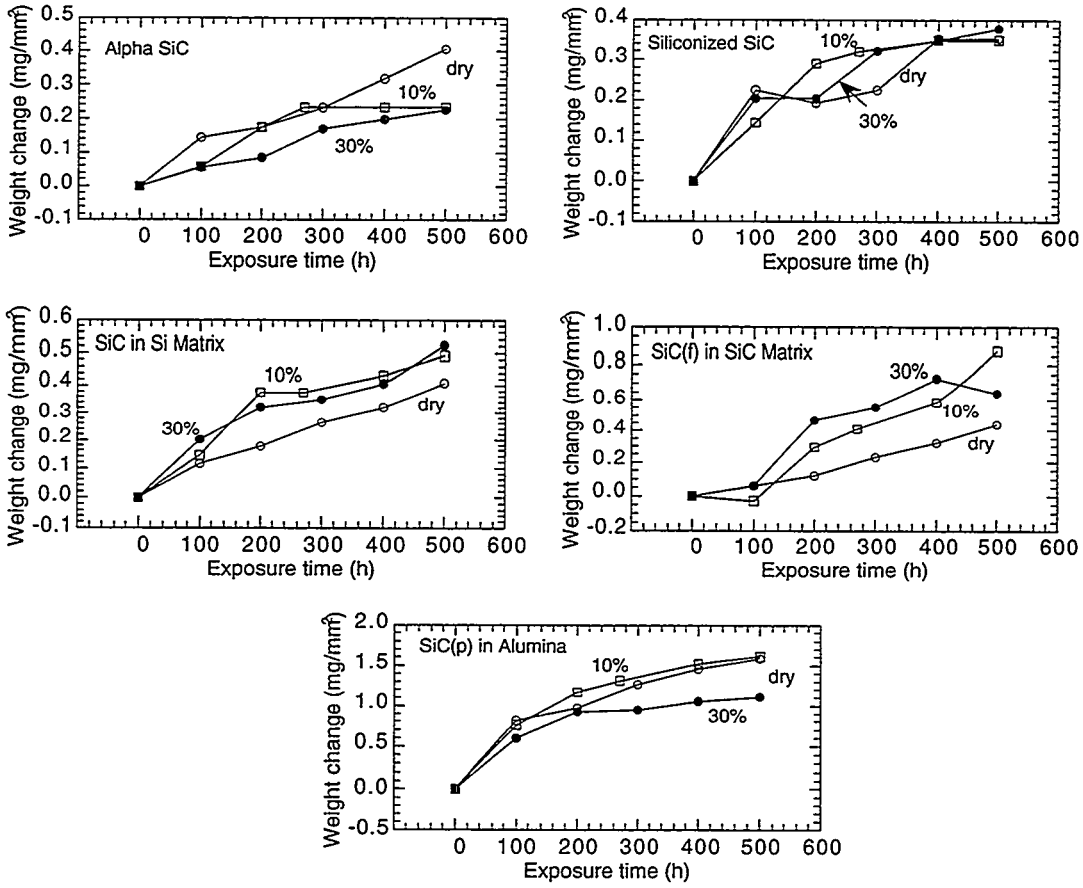

Figure 1. Influence of water vapor on the oxidation performance of several SiC-containing materials

All of the listed reactions are thermodynamically favored, but the kinetics of these reactions are dictated primarily by temperature. Uncertainties, however, exist as to whether molecular oxygen diffuses through silica scale or if oxygen ion diffusion is the rate determining step. At 1200°C in an air environment with and without water vapor, reaction 2 was not observed because the vapor pressure of SiO is negligible. Furthermore, the kinetics of carbide oxidation are influenced by the rate of transport of CO and/or CO_2 through the silica scale, because the new oxide generally grows on the SiC/SiO_2 side of the interface. The kinetics of reaction 3 are dictated by the oxygen transport through silica scale and lead to carbon deposition. None of the ceramic materials examined in the present work showed a significant influence of water vapor partial pressure on the oxidation rate at 1200°C. The oxidation rates of alpha SiC (with no free silicon and ≈0% porosity) and siliconized SiC (with 8% free silicon and 2% porosity) in air with and without water vapor are similar. SiC in a silicon matrix (47% free silicon and no porosity) showed a slight increase in absolute weight gain but the oxidation rate was similar in dry air and in air with water vapor. Only the fiber-reinforced SiC material (with 10% porosity) showed a slight increase in oxidation rate when air contained 10 vol.% water vapor. The increase in water vapor content up to 30 vol.% did not further enhance the oxidation rate at 1200°C. Extensive microstructural analysis of oxidized specimens showed a continuous silica scale on all of the specimens and the thickness of oxide scale was similar for specimens exposed in dry air and in air that contained 10 and 30 vol.% water vapor (see Fig. 2, typical of monolithic materials). Only the fiber-reinforced SiC material became thicker with an increase in water vapor content (see Fig. 3).

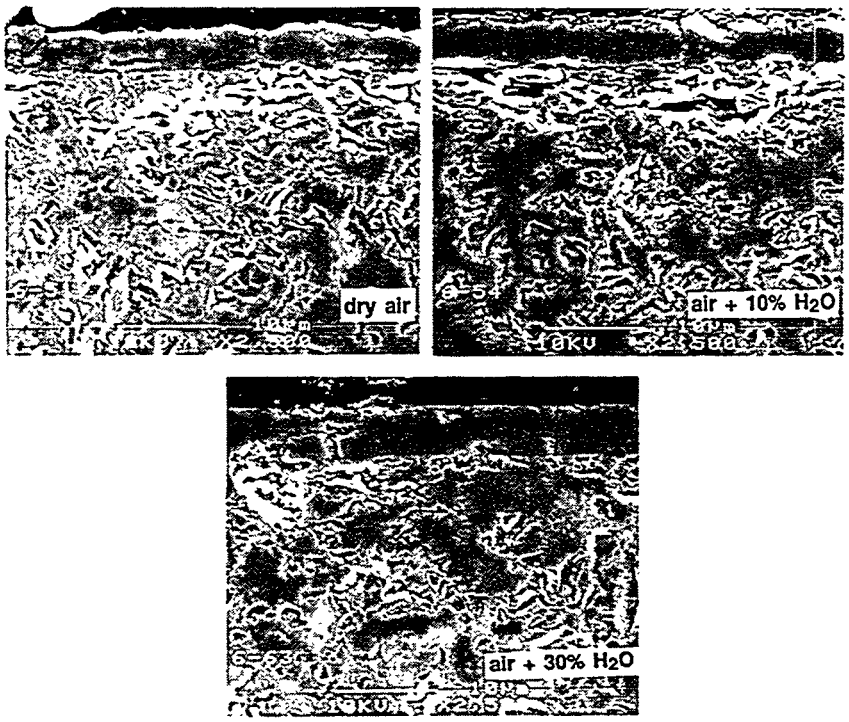

Figure 2. Scanning electron photomicrographs of cross sections of siliconized SiC material after 500-h exposure at 1200°C in dry air and in air that contained 10 and 30 vol.% water vapor

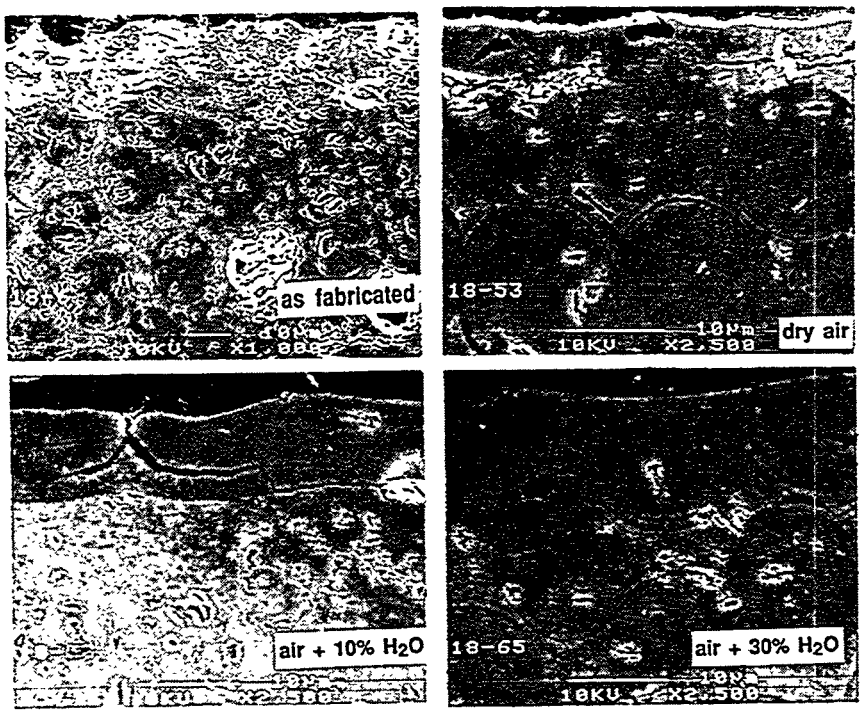

Figure 3. Scanning electron photomicrographs of cross sections of SiC(f)/ SiC matrix material in as-fabricated condition and after 500-h exposure at 1200°C in dry air and in air that contained 10 and 30 vol.% water vapor

Exposure in Slag Environments

In laboratory slag tests, specimens showed significant surface cracking but the slag itself did not seem to penetrate the specimens, as indicated by EDX analysis of specimen cross sections. Because Na_2O activity in the slag is relatively low, the deposit did not melt, but significant bubbling of the slag, probably due to evolution of CO and CO_2, was noted. All three slags exhibited a similar appearance after the test and all three specimens exposed to differing slags also appeared similar, indicating that coal slag chemistry has little influence during these short (200-h) exposures. During the CERF exposure conducted with Pittsburgh coal, the specimen exhibited a thin layer of deposit after ≈100 h of testing. X-ray diffraction analysis of the deposit indicated predominantly mullite ($3Al_2O_3{\cdot}2SiO_2$), with some ordered albite ($[Na,Ca]Al[Si,Al]_3O_8$) and traces of hematite. No significant degradation of the sample was observed by SEM and EDX analysis. During the CERF exposure conducted with Alaskan/Russian coal, the dominant phases were anorthite ($CaO{\cdot}Al_2O_3{\cdot}2SiO_2$), calcium aluminum silicate ($CaO{\cdot}Al_2O_3{\cdot}SiO_2$), and ordered sodium anorthite $(Ca,Na)(Al,Si)_2Si_2O_8$. The melting temperatures of these calcium-rich silicates are also >1400°C, and reactions between the coal ash deposit and the ceramics occur predominantly in the solid state. The experimental results also indicate that Na_2O activities in the deposits (with combustion of coals that contain Fe_2O_3 and CaO) are sufficiently low to form liquid sodium silicates of various types in coal-fired systems.

Tests were also conducted at 1200°C to evaluate the combined effect of slag and simulated combustion gas with water vapor on corrosion of the materials. Analysis of cross sections of exposed specimens showed similar scale morphologies; the oxide layer thickness was slightly greater for the specimen exposed in a

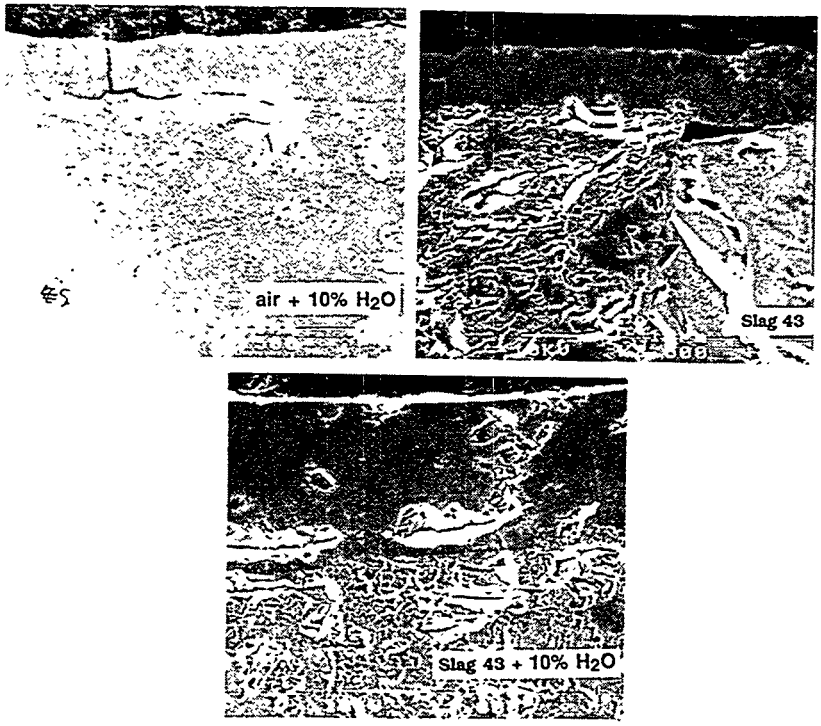

Figure 4. Scanning electron photomicrographs of cross sections of SiC in Si matrix material after 200-h exposure at 1200°C in environments of air with 10% water vapor and slag 43 with and without 10% water vapor

combined environment of slag and 10 vol.% water vapor than those obtained in either of them alone (see Fig. 4 for a specimen of SiC in a silicon matrix). At present, data are not adequate to quantify the relative effects of water vapor and slag on the scaling kinetics of these materials.

Four-Point Bend Test Data

Four-point bend tests were conducted on all of the materials at 1000, 1200, and 1400°C. The load that was necessary to cause fracture in the test was used in the following expression to calculate the flexural strength of the materials:

$$\sigma = \frac{3(L_1 - L_2)P}{2\,t^2\,w},$$

where σ is flexural strength in MPa; L_1 and L_2 are distances between support points and load points, respectively; P is load; and t and w are thickness and width of the specimen, respectively. Data obtained on the flexural strength of the materials and energy absorbed by the materials during fracture were reported earlier.[4,5]

To examine the role of exposure environment on mechanical properties, several specimens of the ceramic materials were preexposed for 200 h at 1200°C to dry air with and without water vapor, to three coal slags, identified as 43, 47, and XX, and to simulated combustion gas with and without water vapor. After exposure, the specimens were mechanically tested in vacuum at 1200°C. During these tests, the specimen surfaces exposed to the slag environments were on the support side of the fixture, ensuring a tensile mode of loading for the surfaces exposed to corrosive environments.

Figure 5 shows the flexural strength of the four materials in as-received condition and after exposure to dry air with and without water vapor. It is evident that exposures of 500 h in differing environments had little influence on the strength of all but the fiber-reinforced composite material. Analysis of fracture surfaces of exposed specimens showed formation of thin layers of silica during exposure to air. Figure 6 shows the flexural strength of the four materials after 200 h of exposure to three slags with and without water vapor. The results show that the strength of the alpha SiC and SiC in silicon-matrix materials with almost no porosity differed negligibly after exposure to environments with and without water vapor. This finding also indicates that the flexural strength of the material with a free silicon content of 47% is inherently lower and oxidation/corrosion is not of concern, based on these short exposure tests. Siliconized SiC (with 8% free Si and 2% porosity) and SiC(p) in alumina (with 10% Al and 1% porosity) showed substantial increase in flexural strength in the presence of water vapor when compared with strength of specimens exposed to an environment without water vapor. The bend-tested specimens are currently being analyzed to examine the oxidation/corrosion-product phases and to determine the cause of the noted increase in strength.

SUMMARY

Several monolithic and composite ceramic materials have been evaluated for their corrosion resistance in environments of interest in advanced combustion systems. Oxidation of these materials in air is in "passive" mode and leads to formation of silica only. Water vapor contents up to 30 vol.% in air had minimal effect on the oxidation rate of these materials at 1200°C and exposure to slag environments at 1200°C showed minimal attack, primarily due to the absence of liquid corrosive products. Exposure of these

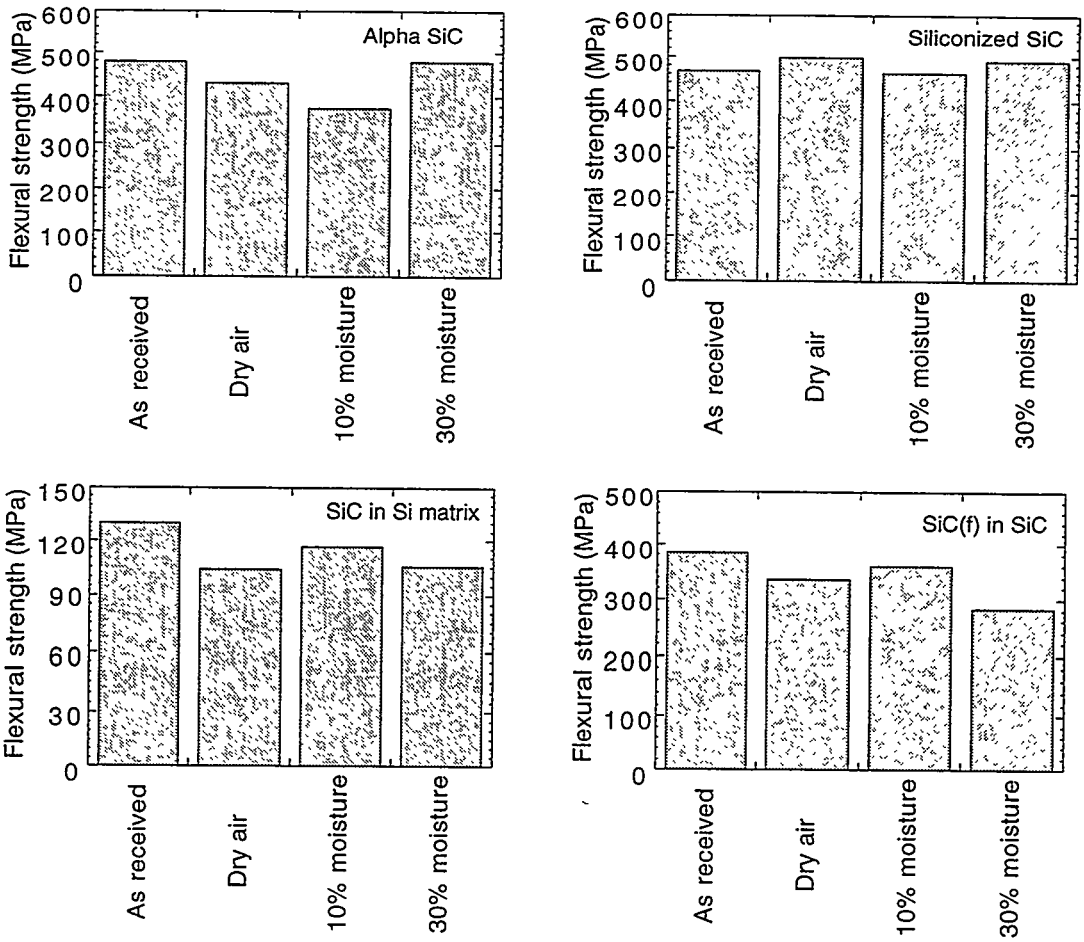

Figure 5. Effect of 500-h exposure in differing environments at 1200°C on flexural strength of several SiC-based materials

materials in coal-fired combustor experiments showed deposits rich in mullite (silica-alumina phase) and anorthite (calcia-silica-alumina phase), both of which have melting temperatures >1400°C.

Four-point bend test data showed that air oxidation up to 500 h at 1200°C had minimal effect on strength properties; tests showed minimal effect of water vapor on strength of alpha-SiC and siliconized SiC. Some strength reduction was evident in the SiC(f)/SiC matrix material; this may be due to a greater porosity of this material. Free carbon detected on the fracture surface may be deleterious over the long term. Exposure to any of the three slags had a negligible effect on the flexural strength of the materials; in the presence of slag and simulated combustion gas that contained water vapor, porous materials such as siliconized SiC and SiC(p) in Al_2O_3 showed improvement in flexure strength.

ACKNOWLEDGMENTS

This work was supported by the U.S. Department of Energy, Office of Fossil Energy, Advanced Research and Special Technologies Materials Program. The assistance of M. Mathur and M. Freeman of the

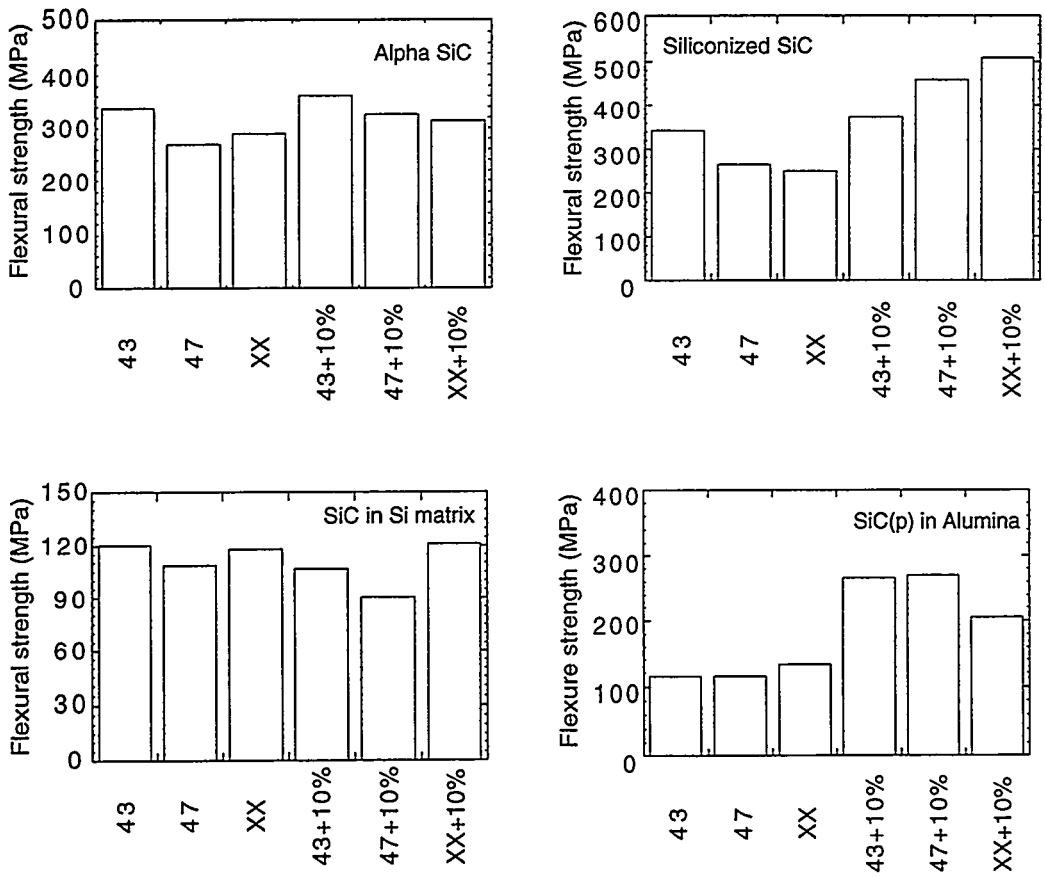

Figure 6. Effect of 200-h exposure in various slag-containing environments at 1200°C on flexural strength of several ceramic materials

Federal Energy Technology Center in the conduct of exposures in CERF is gratefully acknowledged. D. L. Rink assisted in the corrosion and four-point bend tests and microstructural analysis of exposed specimens.

REFERENCES

1. L. A. Ruth, "Combustion 2000," PETC Review, Issue 4, p. 4, Fall 1991.

2. K. Natesan, M. Yanez-Herrero, and C. Fornasieri, "Corrosion Performance of Materials for Advanced Combustion Systems," Argonne National Laboratory Report ANL/FE-93/1, 1993.

3. K. Natesan, M. Freeman, and M. Mathur, "Corrosion Performance of Materials for Advanced Combustion Systems," Proc. 9th Annual Conference on Fossil Energy Materials, ORNL/FMP-95/1, p. 71, 1995.

4. K. Natesan, "Corrosion and Its Effect on mechanical properties of Materials for Advanced Combustion Systems," Proc. 10th Annual Conference on Fossil Energy Materials, ORNL/FMP-96/1, p. 63, 1996.

5. K. Natesan, "Corrosion Performance of Ceramic Materials in Slagging Environments," NACE CORROSION/97 Conference, New Orleans, LA, March 9-14, Paper #143, 1997.

EVALUATION OF AN ALL-CERAMIC TUBESHEET ASSEMBLY FOR A HOT GAS FILTER

J. L. Bitner

Mallett Technology, Inc.
121 Hillpointe Dr., Suite 300
Canonsburg, PA 15317-9502

R. H. Mallett

Mallett Technology, Inc.
P. O. Box 14407
Research Triangle Park, NC 27709-4407

P. M. Eggerstedt

Industrial Filter & Pump Mfg. Co.
5900 Ogden Avenue
Cicero, IL 60650-3888

R. W. Swindeman

Oak Ridge National Laboratory
P.O. Box 2008
Oak Ridge, TN 37831-6084

ABSTRACT

A 10-inch thick, all-ceramic tubesheet design is evaluated for differential pressure and thermal conditions. Primary stresses from differential pressure are well within a safe allowable. The calculated peak thermal stresses at local discontinuities approach the modules of rupture for the ceramic material. Kiln tests were performed to demonstrate differential temperatures between hot center and cooler rim do not cause failures or visible tensile cracks. There appear to be mitigating mechanisms and design features in the Industrial Filter & Pump (IF&P) Mfg. Co. all-ceramic tubesheet design concept that add forgiveness in accommodating differential pressure and thermal loading stresses. A material characterization program on the ceramic materials is recommended.

INTRODUCTION

An all-ceramic tubesheet for the IF&P hot-gas filter is evaluated for thermal and structural conditions defined for the transport combustor demonstration plant at the Southern Company Services facility in Wilsonville, Alabama.[1] The all-ceramic tubesheet assembly provides support for the primary and safety ceramic candle filters that are used to remove the ash particulate from the hot gas, separates the filtered gas chamber from the unfiltered chamber and reacts the differential pressure caused by pressure drop through the filtering assembly. To simplify the analysis, bounding evaluations are performed in accordance with the IF&P design specification for the tubesheet assemblies.[2] The deterministic evaluations are based upon thermal and structural finite element analyses performed using the ANSYS® computer program.

GEOMETRY AND MATERIAL PROPERTIES

The geometry used in this all-ceramic tubesheet evaluation is from drawings given in the analysis specification for the IF&P filter design.[2]

The typical Fibroplate™ 2600 II ceramic material properties used in this evaluation are:

Modulus of Elasticity (E)	=	2×10^6 psi
Poisson's Ratio (ν)	=	0.13
Coefficient of Thermal Expansion (α)	=	3.3×10^{-6} in/in-°F
Mass Density (ρ)	=	0.144 lb-hr^2/in^4
Thermal Conductivity (k)	=	0.0939 Btu/hr-in-°F
Specific Heat (c)	=	0.13×10^{10} Btu-in/lb-hr^2-°F

As specified in the design analysis specification, temperature dependence for these properties is considered in the evaluation. The source of the properties is defined in the design analysis specification.[2]

ANALYTICAL MODELS

Three separate analysis models are used in the evaluation. The first model is an axisymmetric model shown in Figures 1 and 2. Figure 1 shows both the structural and insulation materials. Figure 2 shows only the structural components and the finite element grid.

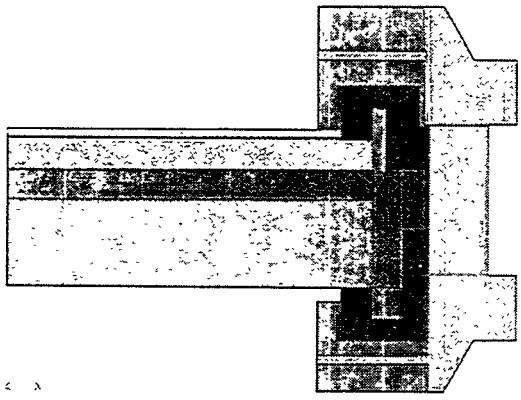

Figure 1 — Axisymmetric Model - All Materials

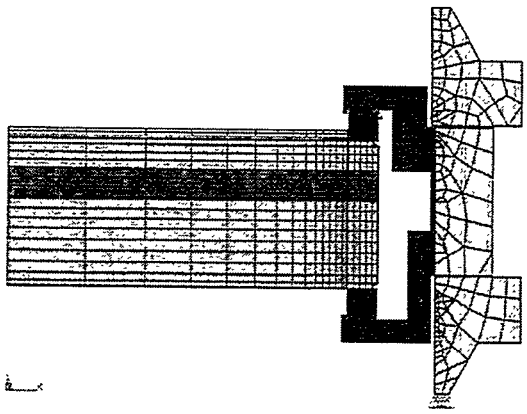

Figure 2 — Axisymmetric Model - Structural

This model is by far the most valuable in evaluating the design of the ceramic layers of the tubesheet assemblies. Other models are needed to address the tubesheet segmented support components and candle hole discontinuities. The temperatures predicted using this axisymmetric model are applicable to all components

of the assembly including the tubesheet supports and the pressure vessel. The stresses predicted for the tubesheet assemblies are also applicable except in the vicinity of local geometric effects where appropriate stress concentration factors must be applied.

The second analysis model used in the evaluation is a sector model shown in Figure 3. The purpose of the sector is to examine the effects of segmenting the metallic support ring and hold down rings. The axisymmetric model includes an artificial hoop stress in the segmented rings which is not present in this sector analysis model.

The third analysis model shown in Figure 4 is used in the evaluation to determine the stress concentration effects of the hole pattern for the filter candles. The model encompasses a typical hole pattern in a ceramic plate. Stress concentration factors are determined under differential pressure loading and rim pressure loading. These stress concentration factors are applied to the stresses obtained using the axisymmetric model for predicting the stresses in the vicinity of the holes.

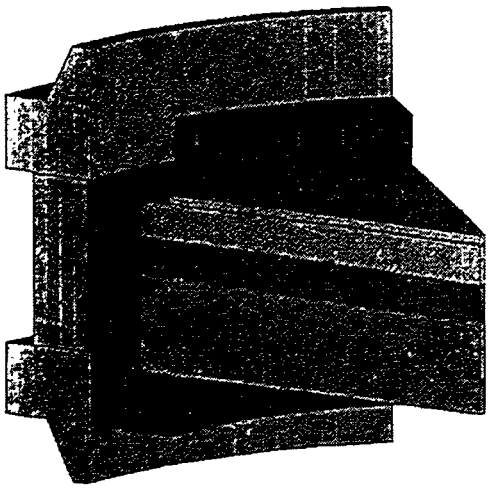

Figure 3 — Sector Model - Structural

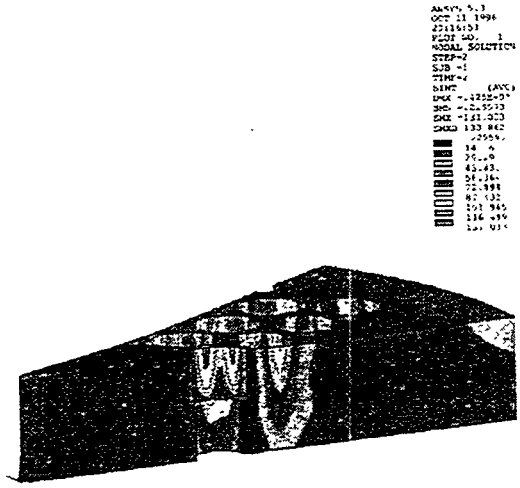

Figure 4 — Plate Model - With Holes
Rim Pressure - Stress Intensity

LOADING CONDITIONS

The loading conditions that are used in the evaluation are defined in the design analysis specification.[2] To keep the specific analysis cases to a manageable number, bounding cases are used. The two main bounding design conditions evaluated are the design differential pressure of 15 psi and design steady state temperature of 1,800 °F. Both of these values are extremely conservative since the normal operating pressure is expected to be 2 or 3 psi at a temperature between 1,200 - 1,400 °F,

ANALYSIS PROCEDURE

The finite element analysis method is used in this investigation. Calculations are performed using the ANSYS® computer program and the analytical models defined in the preceding section.[3] Quadratic finite elements with mid-side nodes are used for all models for both thermal and structural analyses. Refinement is set to obtain accurate results commensurate with features of the component being examined.

The challenges of the analysis models lie in determining the local effects within an overall model and in representing the interactions among the several components. The challenge of local effects is addressed by using several different models. The axisymmetric model is used to determine the response of the tubesheet with a simplified support structure model. The sector model is used to determine the response of the support structure with a simplified tubesheet model.

The challenge of addressing interaction effects between components is met by using alternative assumptions. For example, the tubesheet is not only analyzed as a single integral component but also as two disconnected components including the effects of contact between the components. The support rings are analyzed as being completely connected and as being loosely connected.

The thermal analysis procedures are nonlinear because of the dependence of material properties upon temperature. The structural analyses are nonlinear because the footprint of contact between parts is not known apriori. These nonlinearities require iterations which increase the calculation effort beyond that needed for linear analysis.

The greatest uncertainties in the tubesheet analysis are in the material properties needed to predict behavior and those needed to evaluate the structural integrity based upon the predicted behavior. The approximations in the analysis models and analysis procedures are judged to be acceptable considering the uncertainties in material properties and applied loading. After reviewing the design geometry, material properties and loading conditions in relation to the analysis results, more refined analyses that focus on localized strains and operational thermal transients may be appropriate to build confidence in the integrity of the design.

RESULTS

Axisymmetric Model

Thermal — The predicted steady state temperature distribution is shown in the temperature contour plot of Figure 5. The temperature of the ceramic tubesheet is nearly equal to the hot gas temperature of 1,800 °F.

The maximum temperature of the outside surface of the vessel in the vicinity of the insert ring is less than 200 °F for an ambient temperature of 70 °F. The minimum surface temperature in the flange region is 158 °F.

There is a cutout in the insulation at the bottom of the tubesheet which permits exposure of hot gas to the inside diameter of the Marinite™ ring. The top Marinite™ ring is embedded in the insulation. This difference in insulation leads to a difference in temperature of the upper and lower corners of the tubesheet components. Based upon this difference, a higher thermal stress in the upper corner is anticipated during normal operation. The main temperature gradient occurs across the segmented Marinite™ rings. The lower Marinite™ ring ranges from 1,734 °F to 693 °F. The upper Marinite™ ring ranges from 1,310 °F to 483 °F.

The key indication of thermal stress in the tubesheet of Figure 6 is the differential temperature between the hot interior and the cooler rim of the tubesheet. Below the flow block interface (to the right in Figure 6), the minimum temperature at the rim of the tubesheet is 1,450 °F. Above the flow block interface the minimum temperature at the rim of the tubesheet is 1,227 °F.

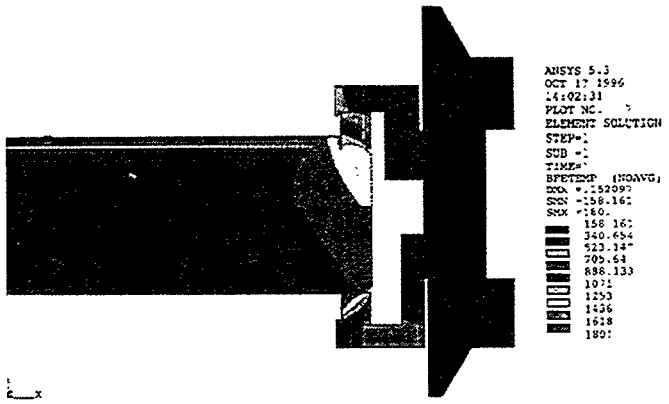

Figure 5 — Axisymmetric Model - Temperature

Figure 6 — Axisymmetric Model - Tubesheet - Temperature

Stress — For evaluating stresses two cases were examined. Analysis Case A1 specifies an integral connection across the flow block interface. This assumes that the bolts which connect the layers of the tubesheet are fully effective in making the two tubesheet assemblies respond as a single layer. Analysis Case A2 assumes the bolts are ineffective and the two tubesheet assemblies respond independently.

Case A1 shows high hoop tension exists in the relatively cool rim of the tubesheet. The maximum value in the upper tubesheet assembly is 3,350 psi. The maximum hoop tension in the lower tubesheet assembly is 2,181 psi. The compressive stress in the central region of the tubesheet reaches -618 psi. The maximum hoop stresses are approximately the same for Case A2; but, the compression in the central region reaches -847 psi. For Case A1, the maximum through-thickness axial compressive stress is -916 psi in the tubesheet caused by

the squeeze between the support rings and by the 15 psi differential pressure. For the combined steady state thermal and differential pressure loading, the maximum stress is 4,064 psi. The hoop stress is the dominant stress component. Similar results are obtained for Case A2.

For the 15 psi upward differential pressure only, the important stress values are the hoop stresses on the top and bottom in the central region. The maximum compressive stress on the bottom is 95 psi. The maximum tensile stress in the central region of the top is about the same.

The Case A2 structural results for the thermal-plus-structural loading are essentially the same as for Case A1. The tubesheet results for only pressure loading are quite different. The key results of Case A2 are the hoop stress distributions shown in Figure 7. The lower tubesheet assembly has hoop stress in the central region which varies from -148 psi to +119 psi. The upper tubesheet assembly has hoop stress that varies in the central region from -147 psi to 153 psi.

Sector Model

Thermal — The thermal results for the sector model are essentially the same as for the axisymmetric model. The overall temperature distribution at steady state conditions is shown in Figure 8.

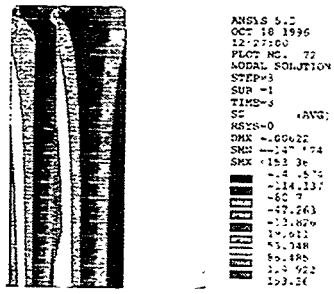

Figure 7 — Axisymmetric Model - Tubesheet - Pressure - Hoop Stress

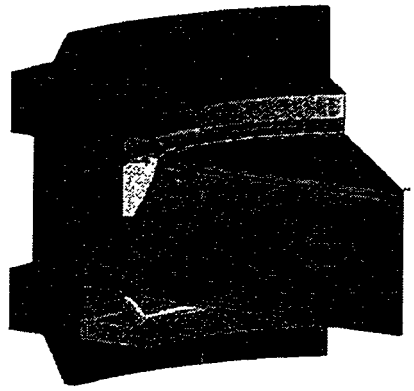

Figure 8 — Sector Model - Steady State Temperature

Stress — Two analysis cases are addressed. Case S1 is comparable to Case A1 except that the components of the support structure are segmented appropriately in Case S1. In Case A1, all components are considered to be full 360° axisymmetric rings. In Case S1, the segmented ring components are assumed to be integrally connected by the bolts and to act as a single unit. An additional Case S2 was constructed to obtain results corresponding to loosely connected ring segments.

The results for Cases S1 and S2 are for steady state thermal loading plus 15 psi differential pressure. The thermal effects are dominant. Figure 9 shows the hoop stress distribution on the symmetry plane for Case S2.

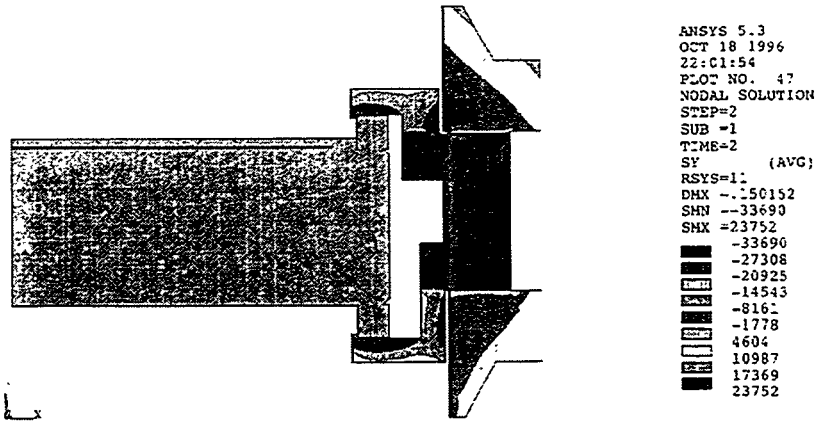

Figure 9 — Case S2 Symmetry Plane Sector Model
- Temperature + Pressure Hoop Stress

The hoop stress in the lower support ring for Case S1 shows strong bending from inside (-74,995 psi) to outside (+8,472 psi). When changed from integral to loose connection, the results show greater bending from top (-22,589 psi) to bottom (+11,955 psi) along the support platform. The maximum stress intensity of 22,445 psi indicates that hoop stress is the dominant stress component.

The hoop stress in the hold down ring segment for Case S1 shows strong bending from inside (-24,670 psi) to outside (-7,554 psi). The hot tip creates a force which bends the back plane. When changed from integral to loose connection, the results show bending from bottom (-13,767 psi) to top (7,878 psi) along the hold down platform. The maximum stress intensity of (13,763 psi) again shows that hoop stress is the dominant stress component.

Ligament Model

The overall distribution of stress intensity in the ligament model from a 15 psi pressure over the bottom surface is shown in Figure 4. These intensified results are compared to the corresponding results for the case of a tubesheet without holes to obtain a stress intensification factor. The maximum stress intensity in the tubesheet with holes is 1,232 psi at a radius of 10 inches. The stress at this location without holes is 285 psi. The stress intensity factor (sif) caused by the candle filter holes is k_p = 1,232/285 = 4.3 at the maximum stress location under differential pressure.

The overall distribution of stress intensity in the ligament model due to a 15 psi radial pressure over the outer radial surface is also determined and compared to the corresponding results for the case of a tubesheet without holes for the filter candle such as was used in the axisymmetric model of the tubesheet. The maximum stress intensity in the tubesheet with holes is 131 psi at a radius of 10 inches. The stress intensity in this location without holes is 15 psi. The stress intensity factor (sif) caused by the candle filter holes is $k_t = 131/15 = 8.7$ at the maximum stress location under radial rim pressure.

The results of the finite element analysis for the ceramic tubesheet are summarized in Table 1 in terms of hoop stress component which dominates and is nearly equal to the stress intensity. In the absence of thermal stresses, the design of the ceramic tubesheet is clearly satisfactory especially considering the normal operational differential pressure is not expected to exceed 2 or 3 psi.

Table 1 — Hoop Stress Summary

Tubesheet Assembly	Loading	Temperature °F	Max Hoop Stress (psi)		Allowable (From Spec[2])
			Nominal	Total	
Lower (bottom surface at center)	15 psi (Δp)	72	-148	636 w/ sif of 4.3	900
Upper (top surface at center)	15 psi (Δp)	72	+153	658 w/ sif of 4.3	900
Lower (outer rim)	Steady State Design Temp. of 1800 °F plus 15 psi (Δp)	1,450	--	2,181	900
Upper (outer rim)	Steady State Design Temp. of 1800 °F plus 15 psi (Δp)	1,227	--	3,350	900

For the 1,800 °F thermal loading, the structural evaluation indicates the need to refine the thermal design to raise the rim temperature of the tubesheet. However, the extent of the refinement indicated in Table 1 may be exaggerated as explained below. One of the conservatism in these results is the conservatism in the specification of a 15 psi differential pressure. Another significant conservatism in these results may be the specification of an 1,800 °F operating temperature which is greater than the expected operating temperature.

The greatest uncertainty in the structural evaluation of Table 1 is in the allowable stress. This uncertainty spans two issues. The first is the need to test material from the same process and batch as the tubesheets.

These tests need to be sufficient in number to build confidence in the material strength. The second issue concerns the extent to which the material can accommodate localized strain without failure. Thermal stresses are strain-controlled so that small strains in the local high stress region of the tubesheet may reduce the linearly-predicted stresses in Table 1 to acceptable values. This determination can only be made by testing.

FEATURE TESTS

It is important to note that a hot center with a cooler rim condition is evaluated experimentally by IF&P. The test setup for evaluating this prototypic condition is shown in Figure 10. As shown in this figure, a three-inch thick, 21.5 inch diameter test specimen plate (Fibroplate 2600 II) with 13 holes for filter candles is "sandwiched" between the upper and lower halves of a kiln. The bottom of the kiln contains the heating elements. The top of the kiln has a small vent for hot air to escape.

As shown in Figure 11, the bottom of the tubesheet is heated to 500 °F in one hour and held at 500 °F for about 1.5 hours. The temperature of the vent is 420° F and the outer edge of the tubesheet was "touchable" (perhaps < 140 °F). The temperature of the lower section is increased to 800 °F and held at 800 °F for more than an hour. At the 800 °F temperature condition, the temperature of the outer edge of the tubesheet is 205 °F as measured by a pyrometer. The kiln, with the tubesheet installed, is cooled to room temperature. A visual inspection did not reveal any cracks.

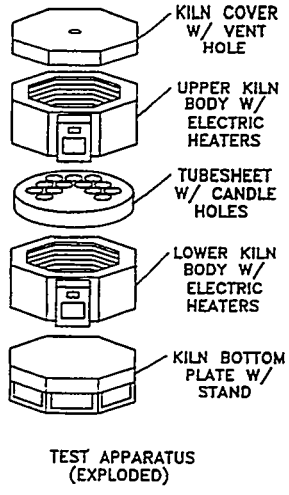

Figure 10 — Test Setup

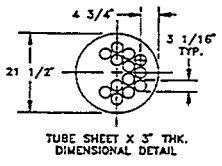

Test Specimen

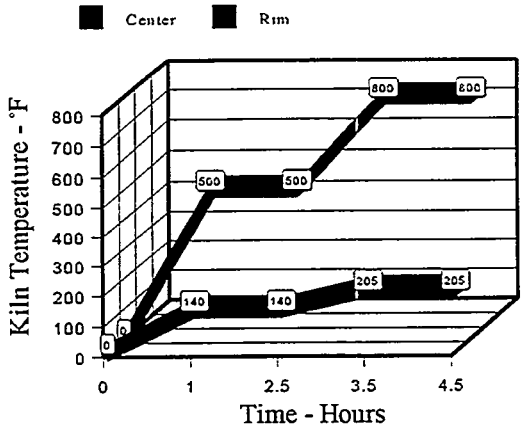

Figure 11 — Heating Histogram

In terms of a differential temperature, ΔT, between the gas and the outside diameter of the plate, this feature test is more severe (ΔT = 595 °F) than the maximum ΔT of 573 °F from the finite element analyses. From

this observation, it would indicate that there may be crack resistive features or micro-crack type stress relieving mechanisms in the Fibroplate™ 2600 II ceramic material that have not been completely characterized in the material testing of coupon specimens. Coupon test specimens are used to establish the modulus of rupture and allowable stress limits for the material.

CONCLUSIONS

There is a need to refine the local insulation around the rim of the tubesheet examined in this investigation. The objective is to reduce the rim differential temperature down toward 110 °F.

It is important to perform feature testing of the ceramic tubesheet material such as performed by IF&P to establish the extent to which the material can accommodate localized stresses at the rim corners and at the ligaments between holes in the tubesheet.

The final design of a ceramic tubesheet should be confirmed by additional analysis of temperature transients to obtain guidance for operating limits.

A comprehensive material characterization program is needed for the Fibroplate™ 2600 II to establish the basic temperature dependent material properties needed in the finite element analysis and to establish a rational design criteria for this ceramic material.

The finite element analysis technology used in this investigation provides a powerful virtual prototyping capability to minimize the need for manufacturing actual components.

REFERENCES

1. ORNL/Sub/94-SR776V/01, "Thermal and Structural Design Analysis of a Ceramic Tubesheet", November 22, 1996.

2. IF&P TR-001 "Ceramic Tubesheet Assembly Design Analysis Specification for the Power Systems Development Facility (PSDF) IF&P Filter Vessel", November 22, 1996.

3. Khonke, Peter, "ANSYS User's Manual, Theory Reference, Release 5.3", Report Number 000656, Seventh Edition, ANSYS, Inc., Houston, Pennsylvania, June 1996.

DEVELOPMENT OF NONDESTRUCTIVE EVALUATION METHODS FOR STRUCTURAL CERAMICS

W. A. Ellingson, R. D. Koehl, H. P. Engel,*
J. B. Stuckey, J. G. Sun, and R. G. Smith+
Argonne National Laboratory
*Heaviside Science, Inc.
+3M Corporation

ABSTRACT

Development of nondestructive evaluation (NDE) methods for application to fossil energy systems continues in three areas: (a) mapping axial and radial density gradients in hot-gas filters, (b) characterization of the quality of continuous-fiber ceramic matrix composite (CFCC) joints and (c) characterization and detection of defects in thermal-barrier coatings. In our work, X-ray computed tomographic imaging was further developed and used to map variations in the axial and radial density of two full-length (2.3-m) hot-gas filters. The two filters differed in through-wall density because of the thickness of the coating on the continuous fibers. Differences in axial and through-wall density were clearly detected.

Through-transmission infrared imaging with a highly sensitivity focal-plane array camera was used to assess joint quality in two sets of SiC/SiC CFCC joints. High-frame-rate data-capture suggests that our infrared imaging method holds potential for the characterization of CFCC joints.

Work to develop NDE methods that can be used to evaluate electron-beam physical-vapor-deposited coatings with platinum-aluminide (Pt-Al) bonds was undertaken. Coatings of Zirconia with thicknesses of 125 μm (0.005 in.), 190 μm (0.0075 in.), and 254 μm (0.010 in.) with a Pt-Al bond coat on René N5 Ni-based superalloy were studied by infrared imaging. Currently, it appears that thickness variation, as well as thermal properties, can be assessed by infrared technology.

INTRODUCTION

Nondestructive evaluation (NDE) technology is being developed to advance the reliable application of ceramic materials to fossil energy systems for improved efficiency and better environmental control. Advanced materials systems under development for fossil energy applications include continuous-fiber ceramic matrix composites (CFCCs) for hot-gas filters and heat exchangers, and thermal-barrier coatings (TBCs) for high gas-firing-temperature turbines.

Detection and measurement of variations in the axial and radial density of hot-gas filters are important, because change in density can be used as a process control parameter during fabrication and because density measurements can be used to study the efficiency of back-purging during cleaning.

Ceramic-to-ceramic joining is usually necessary both for shop fabrication of parts with complex shapes and for field repair. Many processes are under development to join CFCC materials. Researchers at the Idaho National Engineeering Laboratory (INEL)joined one set of

specimens with a lapjoint. A second set, also joined with a lap joint, was produced by Dow-Corning.

While focusing on monolithic SiC and CFCC's with SiC/SiC, Rabin[1] and Rabin and Moore[2] of INEL clamp tape cast sheets of SiC + C precursor between parts that are to be bonded, and then infiltrate molten Si to form a reaction-bonded silicon carbide (RBSC) joint interlayer. Regardless of the method used for joining, NDE methods must be developed to establish the completeness and quality of the joint.

Thermal-barrier coatings are key material elements that allow higher gas-firing temperatures in gas turbines with low emissions. The integrity and properties (thermal and physical) of these TBC's depends on a reliable bond coat and careful process control.

For fossil energy applications, e.g., coal-gas-fired turbines, where the turbine duty cycle is much different from a typical aircraft engine, long-term, high-temperature exposure and high-cycle fatigue can be an issue, and the likelihood of spallation is increased. Answers to questions such as; What is the status of the coating? If damaged, should the blade be repaired? replaced? become matters of concern.

Work on the NDE of TBCs is initially concentrating on two methods: a) noncontact, noninvasive time-resolved-infrared-radiometry (TRIR)[3,4] for thermal characterization and b) elastic optical scatter[5] for crack detection and disbonds. In the TRIR method a thermal excitation source and a highly sensitive, high-frame rate (up to 1900 frames/sec) infrared camera are placed on one side of the TBC. The thermal excitation source can be a high- energy flash lamp or a laser. Thermal images are acquired in time sequence and analyzed.

METHODS AND RESULTS

Hot-Gas Filters

The use of high-spatial-resolution X-ray computed tomographic (XCT) methods for the study of hot-gas filters and heat exchangers has been explored previously.[3,6-8] In the work described here, two 2.3-meter-long, 3.8-mm-O.D. Nextel 611 fiber/SiC matrix hot-gas filters, supplied by 3M Corporation, were examined by XCT imaging densitometry. One of the filters was heavly coated, whereas the other was lightly coated. Figure 1, a schematic diagram of a typical filter, shows the location of the coating.

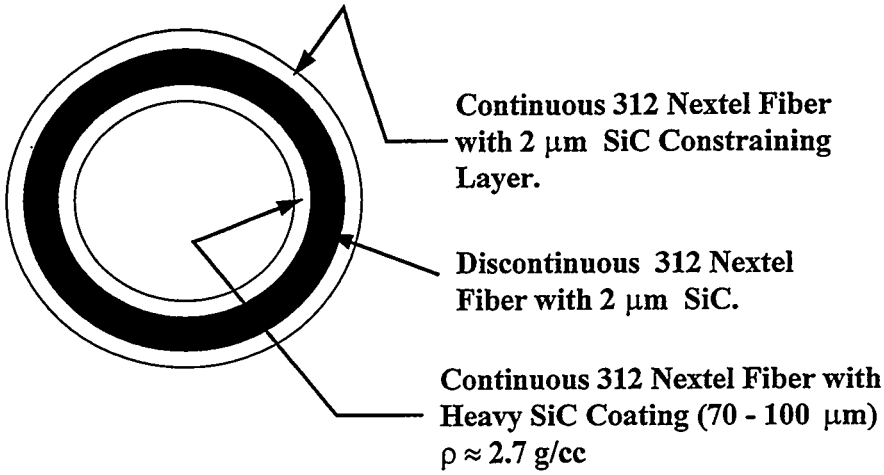

Fig. 1. Schematic diagram of cross section of 3M hot-gas filter

The XCT images were acquired every 50 mm along the length of the filters, as shown in Fig. 2, which is a projection X-ray digital radiograph (XDR). (Note that a holder is shown at the bottom of the XDR. This holder incorporates the flanges for mounting the hot-gas filters.)

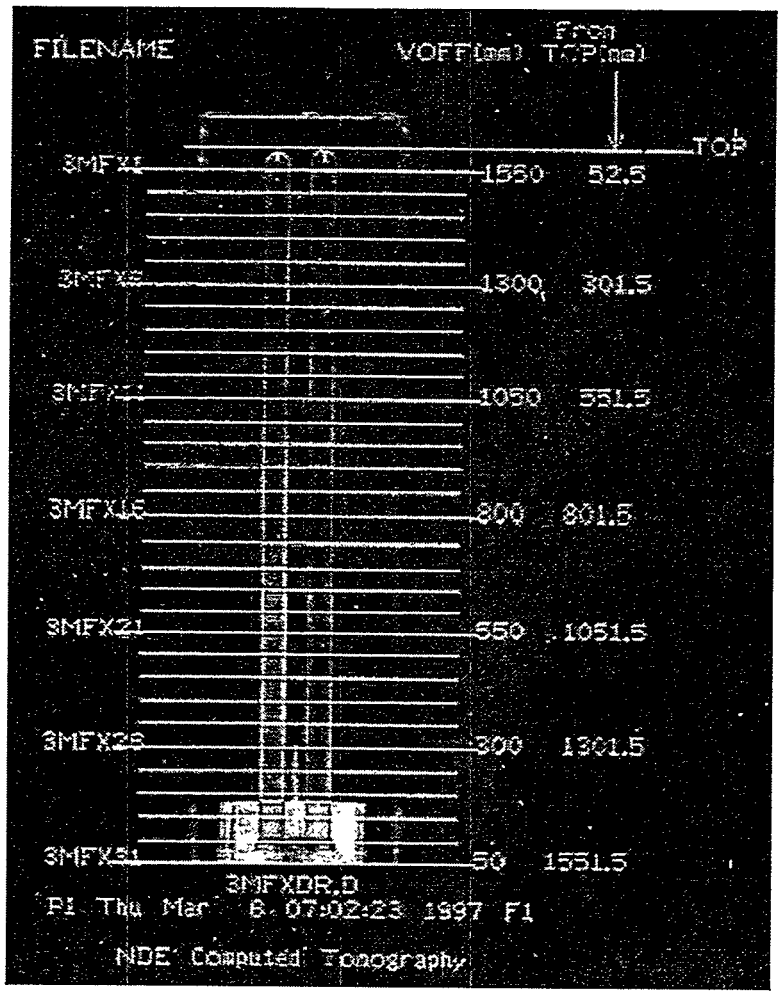

Fig. 2. X-Ray projection digital radiograph showing axial locations of X-ray tomographic images used for densitometry

The acquired XCT data clearly delineate differences between heavy and light coatings, as indicated in Fig. 3, which shows typical XCT images of the two hot-gas filters. By using digital image processing and determining the average density of each XCT image, one can plot relative density as a function of axial position. The variations in relative axial density that were obtained in this manner are shown in Fig. 4.

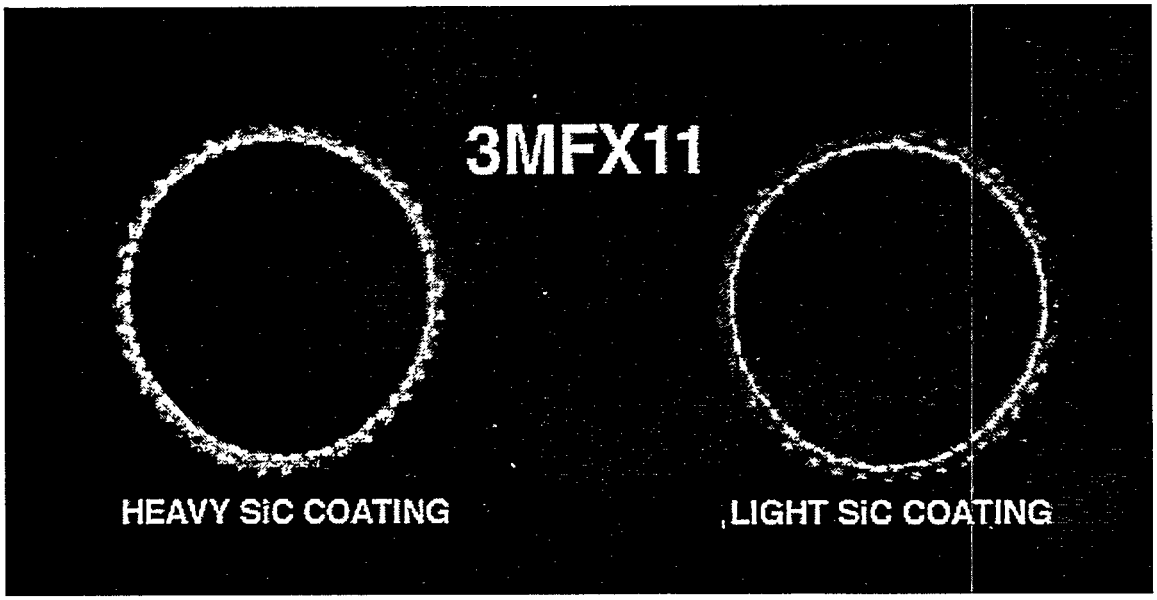

Fig. 3. Typical X-ray computed tomographic images of the 3M hot-gas filters; (a) heavy SiC coating, and (b) light SiC coating

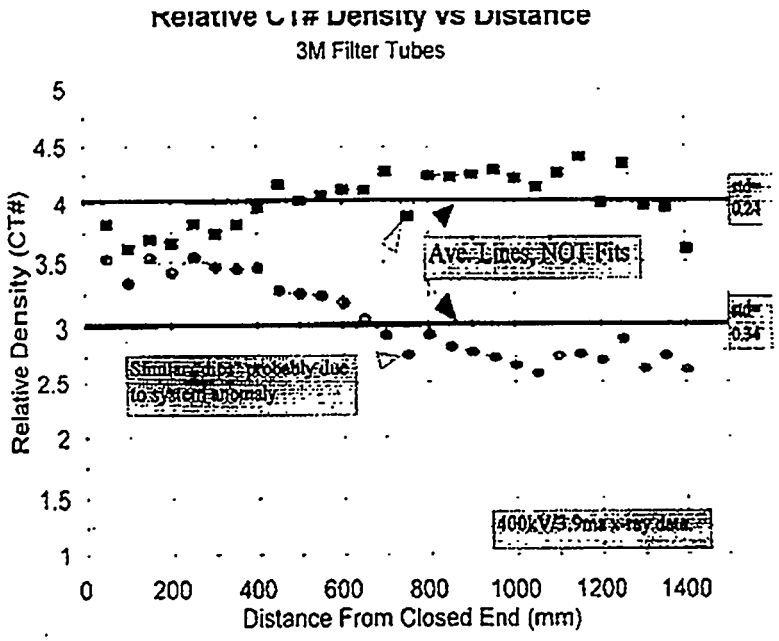

Fig. 4. Variations in relative axial density of two 3M hot-gas filters

Joints

To study the NDE of ceramic-to-ceramic joints, we used a butt-joint monolithic 15-cm-diameter SiC tube that was joined for use in a corrosion test facility at Oak Ridge National Laboratory. The tube (Fig.5) was studied by two NDE methods: XCT and impact acoustic resonance (IAR).[9] The XCT method was used to determine if large voids existed at the joint and IAR was used to the joint establish if the joint was solid, which perhaps could be considered a function of the elastic properties.

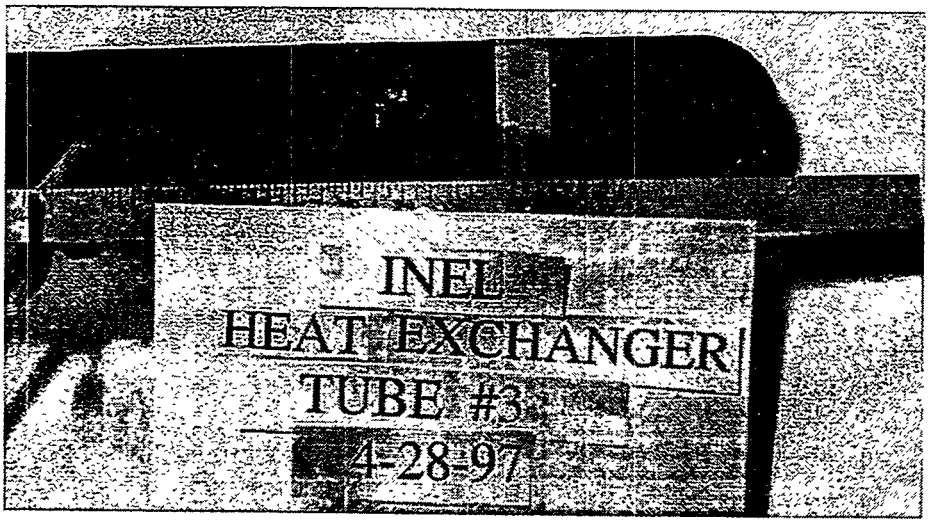

Fig. 5. Photograph of 15-cm-diameter SiC/SiC butt-joined tube

A 450 KVp XCT system was used to obtain a set of XCT images through the joint region. The XCT "slices", which were 500 μm thick, were taken sequentially, with 300-μm off-sets. Three XCT images of the joint are shown in Fig. 6, which reveals several features,

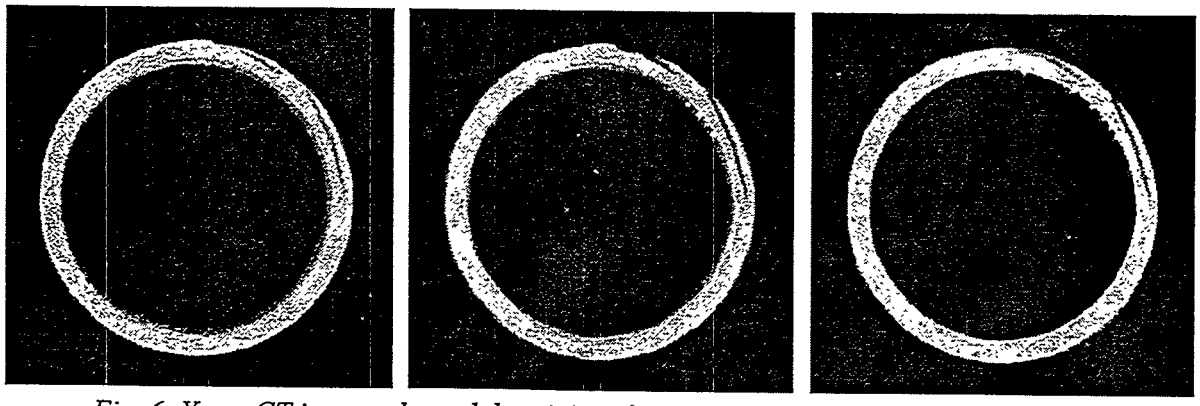

Fig. 6. X-ray CT images through butt joint of 15cm SiC/SiC tube;

(a) open unjoined areas, (b) less dense regions, and (c) so-called drop-through or regions where the "weld" material dropped to the inside. This suggests that XCT can be used to detect regions that lack penetration and, perhaps, density variations in the joint.

In the IAR method, the specimen is struck with an instrumented hammer and the resultant acoustic signal is detected by a microphone. Both the signal and the instrumented hammer are digitized in a 100-Mhz dual-channel digitizer. Impact excitations are used at uniform distances around the tube on both sides of the buttjoint. The collected data are then analyzed for changes. Results to date correlate with the voids detected by XCT, in that poorly joined regions show significantly differing frequency peaks.

Thermal-Barrier Coatings

For the work on TBCs, nine 20-mm-diameter specimens were coated with René N5 substrate, PtAl bond coat, and ZrO_2 by electron-beam physical vapor deposition. Coatings of three thicknesses, 125 μm, 190 μm, and 254 μm , were applied. In addition, two full-scale aeroderivative turbine blades that had been coated were also studied.

An area of technical interest is uniformity of coating thickness. One-sided flash thermal imaging was used to study the three coating thicknesses and the turbine blades. Sensitivity to thickness can be attaineb by obtaining time-dependent images and using digital image processing. Figure 7 shows data for each specimen and both turbine blades. These data suggest that the blades are covered with have 125-μm TBCs.

While not verified destructively, it has been suggested by the suppliers that, indeed, the typical coating thickness would be expected to be in the range of 125 μm. Thus, there is reason to believe that the thermal-flash method a reasonably be used for full field thickness measurement.

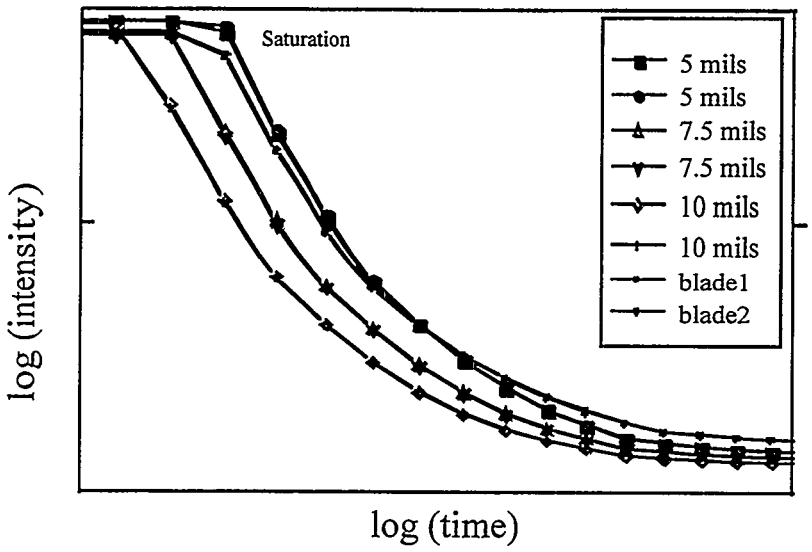

Fig. 7. Sensitivity of flash infrared imaging to EB-PVD thickness of coating applied by (Substrate is René N5 and bond coat is Pt Al)

ACKNOWLEDGMENTS

This research was sponsored by the Office of Fossil energy, Advanced Research and Technology Development materials Program [DOE/FE AA 15 10 10 0, Work Breakdoen Structure Element ANL-1], U.S. Department of Energy, under Contract W-31-109-Eng-38. B. Rabin of INEL provided joined SiC/SiC specimens, R. Bruce of GE Aircraft Engines, R. Orenstein of GE Power Generation, and B. Seth of Westinghouse Power Systems provided thermal barrier coating specimens

REFERENCES

1. B. H. Rabin, *Joining of SiC Ceramics and SiC/SiC Composites*, in Proc. of the 9th Annual Conf. on Fossil Energy Materials, Oak Ridge National Laboratory Report, ORNL/FMP-95/1, 1995, pp. 41-44.

2. B. H. Rabin and G. A. Moore, *Joining of SiC Ceramics and SiC/SiC Composites*, in Proc. of the 7th Annual Conf. on Fossil Energy Materials, Oak Ridge National Laboratory Report ORNL/FMP-93/1, 1993, pp. 33-42.

3. W. A. Ellingson, E. R. Koehl, H. P. Engel, J. A. Wilson, and J. B. Stuckey, *Development of Nondestructive Evaluation Methods for Structural Ceramics,* in Proc. of the 10th Annual Conference on Fossil Energy Materials, Oak Ridge National Laboratory Report, ORNL/FMP/-96-1, Conf. 9605167, August 1996, pp. 27-37.

4. J. B. Stuckey, Development of Non-Contact Thermal Imaging Methods for Characterizing Advanced Ceramics, Masters Thesis submitted to Northwestern University (May 1997).

5. J. G. Sun, W. A. Ellingson, J. S. Steckenrider, and S. Ahuja, *Application of Optical 'Scattering Methods to Detect Damage in Ceramics,* Chapter 5 in Machining of Ceramics and Composites, Part IV, (to be published 1997)

. Private communication, B. F. Goodrich-Supertemp, January 1996.

6. W. A. Ellingson, M. W. Vannier, and D. P. Stinton, *Application of X-ray Computed Tomography to Ceramic/Ceramic Composites*, in Characterization of Advanced Materials, E. Henneke, ed., Plenum Press, N.Y., 1991, pp. 9-25.

7. E. A. Sivers, P. A. Holloway, and W. A. Ellingson, *Obtaining High-Resolution Images of Ceramics from 3D X-ray Microtomography by Region-of-Interest Reconstruction*, in Ceramic Engineering and Science Proceedings, Vol. 14, No. 17-18, 1993, pp. 463-472.

8. E. A. Sivers, *Use of Multiple CT Scans to Accommodate Large Objects and Stretch Dynamic Range of Detectability* , in Nuclear Instruments and Methods, Phy. Res. B., Vol. 99, 1995, pp. 761-764.

9. P. R. Raju, J. R. Patel, and U. K. Vaidya, *Characterization of Defects in Graphite-Fiber Based Composite Structures Using the Acoustic Impact Technique (AIT),* J. Test Vib., Vol. 21, No. 5, 1993, pp. 377-395.

SOLID STATE ELECTROLYTE SYSTEMS

L. R. Pederson, B. L. Armstrong, T. R. Armstrong, J. L. Bates, G. W. Coffey, G. H. Hsieh, J. Li, T. O. Mason*, A. S. Rupaal**, J. W. Stevenson, and W. J. Weber

Pacific Northwest National Laboratory
P.O. Box 999
Richland, WA 99352

*Northwestern University
Evanston, IL 60208

** Western Washington University
Bellingham, WA 98225

ABSTRACT

Lanthanum gallates are a new family of solid electrolytes that exhibit high ionic conductivity and are stable to high temperatures. Compositions have been developed that are as much as a factor of two more conductive than yttria-stabilized zirconia at a given temperature, through partial replacement of lanthanum by calcium, strontium, and/or barium and through partial replacement of gallium by magnesium. Oxide powders were prepared using combustion synthesis techniques developed in this laboratory; these were sintered to >95% of theoretical density and consisted of a single crystalline phase. Electrical conductivities, electron and ion transference numbers, thermal expansion, and phase behavior were evaluated as a function of temperature and oxygen partial pressure. A key advantage of the use of lanthanum gallate electrolytes in solid oxide fuel cells is that the temperature of operation may be lowered to perhaps 800°C, yet provide approximately the same power density as zirconia-based cells operating at 1000°C.

Ceramic electrolytes that conduct both oxygen ions and electrons are potentially useful to passively separate pure oxygen from an air source at low cost. In such materials, an oxygen ion flux in one direction is charge-compensated by an opposing electron flux. We have examined a wide range of mixed ion and electron conducting perovskite ceramics in the system $La_{1-x}M_xCo_{1-y-z}Fe_yN_zO_{3-\delta}$, where M=Sr,Ca, and Ba, and N=Pr, Mn, Ni, Cu, Ti, and Al, as well as mixed conducting brownmillerite ceramics, and have characterized oxygen permeation behavior, defect chemistry, structural and phase stability, and performance as cathodes.

INTRODUCTION

Two principal glasses of oxygen ion conductors are being developed: (1) ceramics that predominantly conduct oxygen ions, and (2) ceramics that conduct both electrons and oxygen ions. The first type find application as the electrolyte in solid oxide fuel cells, as oxygen sensors, and as oxygen separation membranes. The second type are useful as

passive oxygen separation membranes, as the membrane in a catalytic reactor to partially oxidize hydrocarbons or to produce synthesis gas, and as the electrode in a fuel cell.

Lanthanum gallate ceramics comprise a new class of solid electrolytes of the first type, with high electrical conductivities and excellent stabilities at high temperatures.[1-5] Some compositions give electrical conductivities a factor of two to three greater than found for yttria-stabilized zirconia, the most widely utilized solid electrolyte.[3-5] Lanthanum gallates exhibit an ABO_3-type perovskite structure, one that is quite amenable to cation substitution. By substituting strontium, calcium, and/or barium for lanthanum and by substituting magnesium for gallium in this structure, oxygen vacancy populations can be adjusted and electrical conductivities altered.

Compositions in the (La,M)(Co, Fe)O_{3-x} system, where M = Sr, Ca, Ba, and Pr, also are ABO_3-type perovskites whose properties can be tailored through compositional variations. These ceramics exhibit mixed oxygen ion and electron conductivity.[6-8] Although the oxygen ion current is usually less than one percent of the overall current, the oxygen ion conductivity often exceeds that of yttria-stabilized zirconia by a significant margin. Partial substitution of divalent cations for lanthanum on the A-site and substitution of cobalt for iron enhances oxygen ion conductivity, generally at the expense of structural stability. Similar in structure to perovskites, certain brownmillerites are mixed conducting ceramics showing good stability under conditions necessary for the production of synthesis gas.[9,10]

LANTHANUM GALLATE ELECTROLYTES

Lanthanum gallate powders were prepared using the glycine-metal nitrate combustion synthesis method, which is particularly well-suited to make homogeneous, multicomponent metal oxide products.[11] Samples were calcined in air at 650°C to remove any residual carbon, isostatically dry pressed at ≈140 MPa, and then sintered at temperatures up to 1500°C. Phase purity was determined by x-ray diffraction, thermal expansion behavior evaluated using vertical dilatometry, electrical conductivity determined using 4-probe pulsed dc methods, and transference numbers determined as a function of oxygen partial pressure using the voltage step method.

Using stoichiometric mixes of the metal nitrates and glycine in the precursor solution, approximately 90 percent by weight of lanthanum strontium gallium magnesium oxide compositions were converted to the desired perovskite phase following calcination for a

half hour at 650°C. That amount increased to 94, 97, and 99 weight percent, respectively, after calcination to 1000, 1200, and 1400°C. High A-site substitution resulted in larger fractions of non-perovskite phases being present in the powders. Appropriately calcined powders sintered densities of greater than 97 percent of the theoretical value when heated from 1400 to 1500°C. When heated at temperatures greater than 1550°C, sintered densities actually were diminished. This was shown to be due to the formation of a suboxide of gallium, Ga_2O, which forms pressurized gas pockets within the sample.

Thermal expansion behavior was evaluated in the temperature range of 20 to 1200°C. In general, thermal expansion coefficients (TEC) were similar to that obtained for yttria-stabilized zirconia (≈10.4 x 10^{-6} cm/cm-°C). Values ranged from 11.3 x 10^{-6} cm/cm-°C for $La_{0.9}Ca_{0.1}Ga_{0.8}Mg_{0.2}O_{3-\delta}$ to 12.1 x 10^{-6} cm/cm-°C for $La_{0.8}Sr_{0.2}Ga_{0.8}Mg_{0.2}O_{3-\delta}$. Thermal expansion coefficients increased with increased acceptor content, expected since the dopants strontium and magnesium have larger ionic radii than the ions they replace in the structure.

The electrical conductivity of strontium-substituted lanthanum gallate electrolytes were typically two or more times higher than yttria-stabilized zirconia, particularly at lower temperatures. Electrical conductivities of several substituted lanthanum gallate compositions are given in Figure 1. The designation "1020" refers to 10% Sr substitution for La and 20% Mg substitution for Ga. A comparison of electrical conductivities for various lanthanum gallates are also given in Table 1. Within the composition range studied, electrical conductivity increased with increased acceptor

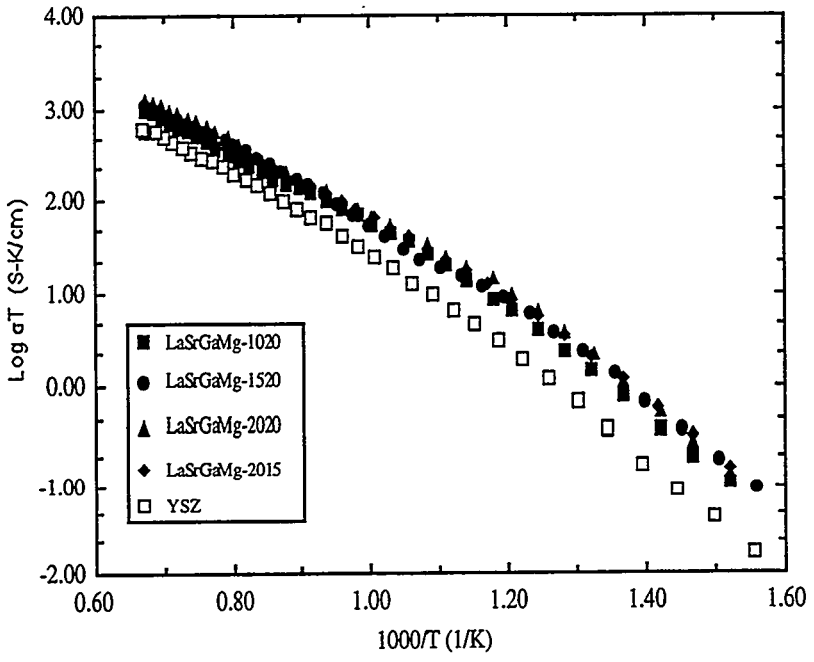

Figure 1. Electrical conductivity of lanthanum gallate compositions versus reciprocal temperature.

content (Sr and Mg substitution), the result of a concomitant increase in the concentration of oxygen vacancies. Calcium and barium-substituted lanthanum gallates were also studied. Barium-substituted compositions behaved similarly to the strontium-substituted analogs; calcium-substituted analogs were less conductive.

Table 1. Comparison of electrical conductivity of lanthanum gallate with yttria-stabilized zirconia at 600 and 1000°C

Composition	σ, 600°C	σ/σ_{YSZ}, 600°C	σ, 1000°C	σ/σ_{YSZ}, 1000°C
10% Sr, 20% Mg	$1.5x10^{-2}$	2..5	$1.5x10^{-2}$	1.4
15% Sr, 20% Mg	$1.5x10^{-2}$	2.5	$1.5x10^{-2}$	2.0
20% Sr, 15% Mg	$1.8x10^{-2}$	3.0	$1.5x10^{-2}$	1.7
20% Sr, 20% Mg	$2.0x10^{-2}$	3.3	$1.5x10^{-2}$	2.2
10% Ca, 20% Mg	$0.1x10^{-2}$	0.17	$1.5x10^{-2}$	0.33
20% Ca, 20% Mg	$0.4x10^{-2}$	0.67	$1.5x10^{-2}$	0.67
10% Ba, 20% Mg	$1.8x10^{-2}$	3.0	$1.5x10^{-2}$	1.7
yttria-zirconia	$0.6x10^{-2}$	1	$1.5x10^{-2}$	1

The lanthanum gallates are predominantly oxygen ion conductors, but not exclusively so. Transference numbers were determined for lanthanum gallate electrolytes using the voltage step method as a function of temperature and oxygen partial pressure. Platinum or gold blocking electrodes were applied to prevent the passage of a steady-state oxygen ion current. Electronic transference number results for $(La_{0.9}Sr_{0.1})_{0.95}Ga_{0.8}Mg_{0.2}O_{3-\delta}$, an A-site deficient composition, are given in Figure 2. These electrolytes are unusual in that the electronic contribution to overall conductivity first rose and then fell with decreased oxygen partial pressure.

Partial reduction of gallium from a formal +3 state to a +2 state is believed responsible for trends shown in Figure 2. Ga(III) has a $4s^0$ electron configuration, while Ga(II) has a $4s^1$ configuration. The highest possible electronic conductivity via small polaron hopping will occur when there are equal populations of Ga(II) and Ga(III), since Ga(II) provides electrons for conduction while Ga(III) provides holes. Conduction from one Ga(II) site to another Ga(II) site is less favored, since spin pairing of electrons would be required.

In summary, lanthanum gallate electrolytes hold promise for use as the electrolyte in a

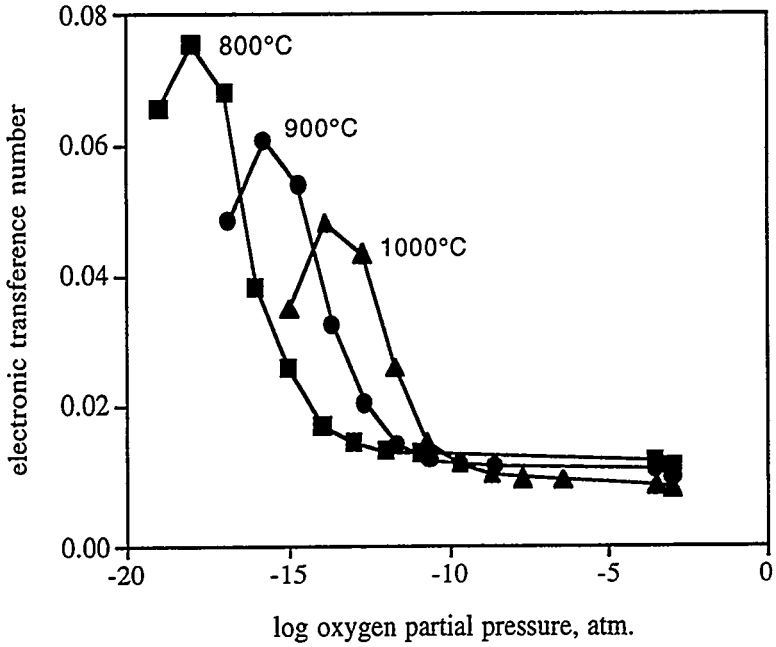

Figure 2. Electronic transference numbers for a non-stoichiometric lanthanum gallate composition, $(La_{0.9}Sr_{0.1})_{0.95}Ga_{0.8}Mg_{0.2}O_{3-\delta}$, as a function of oxygen partial pressure.

solid oxide fuel cell operating at low temperatures, among other applications. Some compositions are more conductive than yttria stabilized zirconia, particularly at low temperatures. They show predominantly ionic conduction and are relatively stable to very low oxygen partial pressures.

MIXED CONDUCTING COBALT IRON OXIDE CERAMICS

A wide range of perovskite compositions in the system $La_{1-x}M_xCo_{1-y-z}Fe_yN_zO_{3-\delta}$, where M=Sr,Ca, and Ba, and N=Pr, Mn, Ni, Cu, Ti, and Al, and a brownmillerite ceramic, $SrFeCo_{0.5}O_{2.5-\delta}$, have been prepared and have been characterized with respect to oxygen permeation behavior, defect chemistry, structural and phase stability, and performance as cathodes. Ceramic powders were synthesized using glycine-nitrate combustion methods. Compacts were uniaxially and then isostatically pressed to 140 MPa, followed by sintering at 1150 to 1250°C. Sintered densities were >95% of theoretical.

In the $La_{1-x}M_xCo_{1-y-z}Fe_yN_zO_{3-\delta}$ perovskite system, electronic conductivities at a given temperature were much higher than the corresponding ionic conductivities, as shown in Table 2. Despite oxygen ions being a minority carrier in these ceramics, the oxygen ion conductivity exceeded that of yttria-stabilized zirconia for many compositions. Compositions most highly substituted with strontium gave oxygen ion conductivities nearly a factor of ten higher than zirconia at the same temperature.

Table 2. Ionic and electronic conductivities for mixed conducting ceramics at 900°C.

Composition	Ionic Conductivity (S/cm)	Electronic Conductivity (S/cm)	Oxygen Ion Transference Number
LaSrCoFe-6428	0.23	252	9×10^{-4}
LaSrCoFe-4628	0.40	219	2×10^{-3}
LaSrCoFe-2828	0.62	120	5×10^{-3}
LaSrCoFe-2882	0.87	310	3×10^{-3}
LaCaCoFe-4628	0.03	52	6×10^{-4}
LaCaCoFe-4682	0.01	296	3×10^{-5}
LaBaCoFe-6428	0.01	123	8×10^{-5}
LaBaCoFe-4628	0.33	57	6×10^{-3}
LaBaCoFe-2828	0.37	19	2×10^{-2}

From the temperature dependence of oxygen permeation, oxygen partial pressure gradient, and sample dimensions, activation energies for ionic conduction were calculated. These are given in Table 3 for a number of different perovskite compositions. Unlike yttria stabilized zirconia or lanthanum gallate electrolytes, the derived activation energy for ionic conduction in the mixed conducting perovskites contains a contribution due to oxygen vacancy formation as temperature is increased. The ionic conductivity in any solid electrolyte is the product of three terms: carrier concentration, carrier charge, and carrier mobility. Carrier concentrations were deduced independently from a combination of thermogravimetric analyses (oxygen weight loss) as a function of temperature and iodometric titration. This enabled carrier mobilities to be deduced and activation energies associated with oxygen vacancy mobility to be calculated. Expressions for vacancy mobility and the diffusion coefficient are also included in Table 3. All but a barium-substituted composition gave activation energies associated with ion mobility in the range of 0.55 to 0.80 eV, which appear in the exponential terms given for mobility and diffusion coefficients in Table 3. Clearly, a significant portion of the apparent activation energy for oxygen permeation derives from the formation of additional oxygen vacancies.

A brownmillerite ceramic, $SrFeCo_{0.5}O_{3.25-\delta}$, has been studied for possible use as the membrane in a reactor to prepare synthesis gas (carbon monoxide and hydrogen) from the reaction of natural gas with oxygen.[10] This particular composition shows relatively good

Table 3. Conduction parameters for mixed ion and electron-conducting electrolytes

Composition	Activation Energy for Ion Conduction (eV)	Mobility (cm^2/V-s)	Diffusion Coefficient (cm^2/s)
LaSrCoFe-6428	1.30	(209/T) exp (-0.55/kT)	0.009 exp (-0.55/kT)
LaSrCoFe-4628	0.95	(269/T) exp (-0.63/kT)	0.012 exp (-0.63/kT)
LaSrCoFe-2828	0.85	(436/T) exp (-0.69/kT)	0.020 exp (-0.69/kT)
LaSrCoFe-2882	0.66	(129/T) exp (-0.56/kT)	0.005 exp (-0.56/kT)
LaBaCoFe-6428	1.64	(10700/T) exp (-1.36/kT)	0.462 exp (-1.36/kT)
LaBaCoFe-4628	0.90	(551/T) exp (-0.77/kT)	0.024 exp (-0.77/kT)
LaBaCoFe-2828	0.65	(78/T) exp (-0.59/kT)	0.003 exp (-0.59/kT)

stability at high temperatures even in the reducing conditions that exist on the natural gas side of the membrane. Transport properties for this ceramic have not been well established previously, particularly in reducing environments; such information is needed to model membrane performance. For that reason, transference numbers for as a function of oxygen partial pressure and temperature were evaluated using the voltage step polarization method. Gas buffer mixtures of hydrogen and carbon dioxide were used to control the oxygen partial pressure to as low as 10^{-20} atmospheres.

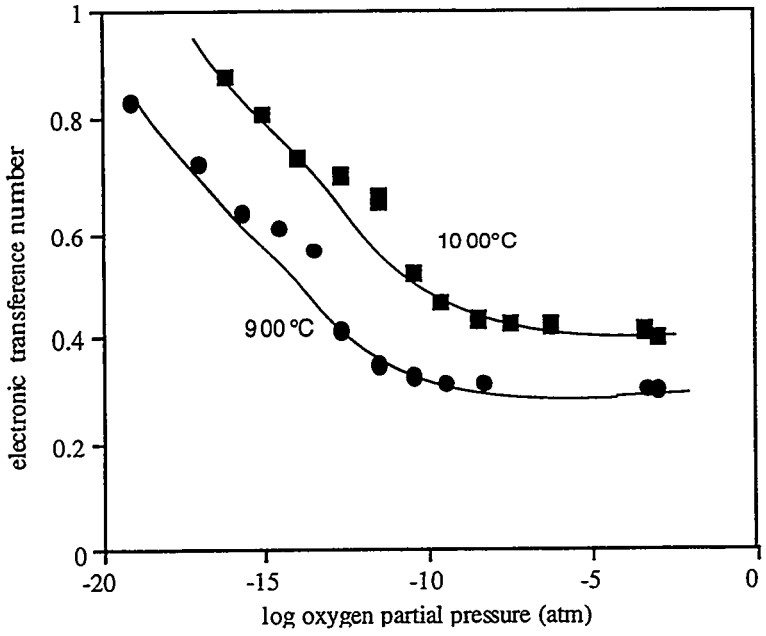

Figure 3. Electronic contribution to the overall conductivity for the ceramic $SrFeCo_{0.5}O_{3.25-\delta}$ versus oxygen partial pressure.

Ionic and electronic contributions to the overall electrical conductivity of the composition $SrFeCo_{0.5}O_{3.25-\delta}$ were similar for oxygen partial pressures greater than 10^{-10} atm, as is shown in Figure 3. The electronic contribution increased substantially for oxygen

partial pressures smaller than 10^{-10} atm, typical of an n-type semiconductor. Enhanced electronic conductivity in an environment of low oxygen partial pressure is due to the partial reduction of iron and cobalt from trivalent to divalent states.

Because electronic conduction could well be the limiting factor in determining passive oxygen flux for the brownmillerite ceramic $SrFeCo_{0.5}O_{3.25-\delta}$, this ceramic would be less effective than the mixed conducting perovskite compositions discussed above for the separation of oxygen from air. In configurations needed to prepare synthesis gas from methane, electronic conduction will not limit oxygen fluxes through the brownmillerite membrane, however, as is clear from Figure 3. In the preparation of synthesis gas, stability under reducing environments becomes an important factor, not just oxygen ion conductivity.

REFERENCES

1. T. Ishihara, H. Matsuda, Y. Mizuhara, and Y. Takita, Solid State Ionics, 70/71, 234 (1994).

2. T. Ishihara, H. Matsuda, and Y. Takita, Solid State Ionics, 79, 147 (1995).

3. M. Feng and J. B. Goodenough, Eur. J. Solid State Inorg. Chem. 31, 663 (1994).

4. P. Huang and A. Petrick, J. Electrochem. Soc. 143, 1644 (1996).

5. J. W. Stevenson, T. R. Armstrong, L. R. Pederson, and W. J. Weber, J. Electrochem. Soc. (1997, submitted).

6. Y. Taraoka, T. Nobunaga, K. Okamoto, N. Miura, and N. Yamazoe, Solid State Ionics 48, 207 (1991).

7. H. Bouwmeester, H. Kruidhof, and A. Burggraff, Solid State Ionics 72, 185 (1994).

8. J. W. Stevenson, T. R. Armstrong, R. D. Carneim, L. R. Pederson, and W. J. Weber, J. Electrochem. Soc. 143, 2722 (1996).

9. U. Balachandran, J. T. Dusek, S. Sweeney, R. Poeppel, R. L. Mieville, P. Maiya, M. Kleefisch, S. Pei, T. Kobylinski, C. A. Udovich, and A. Bose, Am. Ceram. Soc. Bull. 74, 71 (1995).

10. C. A. Udovich, M.S. Kleefisch, A. Bhattacharrya, S. Pei, U. Balachandran, J. T. Dusek, and R. L. Mieville, Proc. 1997 Spring Nat. AIChE Meeting, Houston, TX (1997).

11. L. A. Chick, L. R. Pederson, G. D. Maupin, J. L. Bates, L. E. Thomas, and G. J. Exarhos, Materials Lett. 10, 6 (1990).

ACTIVATION AND MICROPORE STRUCTURE OF CARBON-FIBER COMPOSITES

M. Jagtoyen, F. Derbyshire and G. Kimber
University of Kentucky Center for Applied Energy Research,
3572 Iron Works Pike, Lexington KY 40511-8433, USA.

INTRODUCTION

Rigid, high surface area activated carbon fiber composites have been produced with high permeabilities for environmental applications in gas and water purification. The project involves a collaboration between the Oak Ridge National Laboratory (ORNL) and the Center for Applied Energy Research (CAER), University of Kentucky[1,2]. The main focus of recent work has been to find a satisfactory means to uniformly activate large samples of carbon fiber composites to produce controlled pore structures. Processes have been developed using activation in steam and CO_2, and a less conventional method involving oxygen chemisorption and subsequent heat treatment. Another objective has been to explore applications for the activated composites in environmental applications related to fossil energy production.

Activation

Activation in steam and CO_2 has been conducted under different conditions to produce small samples that are activated relatively uniformly throughout the structure of the artefact. However, with large composites there are constraints on the use of a reactive gas in attaining a uniform partial pressure and temperature through the body of the composite. To surmount this problem, different reactor configurations were investigated. In the more successful arrangement, steam or CO_2 is introduced at several points along the length of the composite to provide a uniform flow of activating agent.

A less conventional method of oxygen chemisorption/heat treatment was selected as an alternative activation technique. This method was first described by Nandi et al[3] and more recently has been the subject of a patent by Quinn et al[4]. The procedure involves the chemisorption of oxygen at low temperatures (e.g<250°C) followed by heat treatment in nitrogen or other inert gas at temperatures up to about 900°C. It appears that slow oxygen chemisorption can produce a uniform distribution of surface oxygen groups that

are then thermally decomposed to remove carbon as CO and CO_2. Because of the limited oxygen uptake at low temperatures it is necessary to complete several cycles before there is appreciable surface area development. The results will show that very uniform BET surface areas are developed throughout the composite.

Applications

The application of the activated composites to water treatment was studied last year[5]. More recent work has focused on their possible application in evaporative loss control devices. The Amendments to the Clean Air Act of 1998 have enforced the use of more efficient carbon canisters in US automobiles to recover evaporated gasoline. The standard evaluation method for this application is the butane working capacity test which is a carbon's ability to adsorb and desorb gasoline light ends. The two most important criteria for high butane working capacity carbons are high density and a large proportion of pores in the small mesopore range (from 20-50 A). Several other practical applications of activated carbons also require wide pores, such as cyclic adsorption and desorption of volatile organic compounds (VOCs). Pitch-based carbon fibers tend to have narrow micropores and are therefore not normally useful for such applications. Hence, attempts have been made to examine the possibility of producing fibers with wider pores through varying activation conditions and fiber precursors.

EXPERIMENTAL

Composite Preparation

Carbon fiber composites are prepared at ORNL [1] by vacuum molding from water slurries containing powdered phenolic resin and chopped isotropic petroleum pitch fibers, (P-200, ~ 17.5 μm diameter, average length 380μm, supplied by courtesy of Ashland Carbon Fibers Division, Ashland Inc.). The slurry is vacuum molded into tubular, plate or rod configuration, followed by drying, curing, and carbonization to about 650°C. The carbon fiber composites are supplied to the CAER in the form of plates (28x12x1.5cm), rectangular or cylindrical shapes[5].

Activation

In attempting to uniformly activate relatively large composite samples (4.5" diameter, 6" long) in steam or CO_2, different reactor configurations and conditions have been investigated. Originally a Lindberg Blue M laboratory box furnace was used, in which the specimen was contained in a sealed stainless steel cylindrical chamber of diameter 6", and height 6". Water was pumped into the reaction chamber and vaporized at the bottom when steam flowed upwards through a perforated stainless steel plate, and was distributed around the composite.

In a more successful arrangement, steam is introduced at several points along the length of the composite. A 4900 W Lindberg furnace was acquired with an inconel chamber of dimensions 6"x 4" x 12". The activating agent, steam or CO_2 was supplied through 4 connected stainless steel distributor tubes that run along the four long corners of the furnace, Figure 1. The distributors are drilled with holes 2 mm in diameter and spaced about 1" apart along their length. The end result is to create a uniform flow of the activating agent in the chamber and around the sample. The design was developed from previous experience, where uniform activation was achieved with small samples by introducing the steam at different points around the sample. By this configuration concentration gradients in the activating gas are minimized.

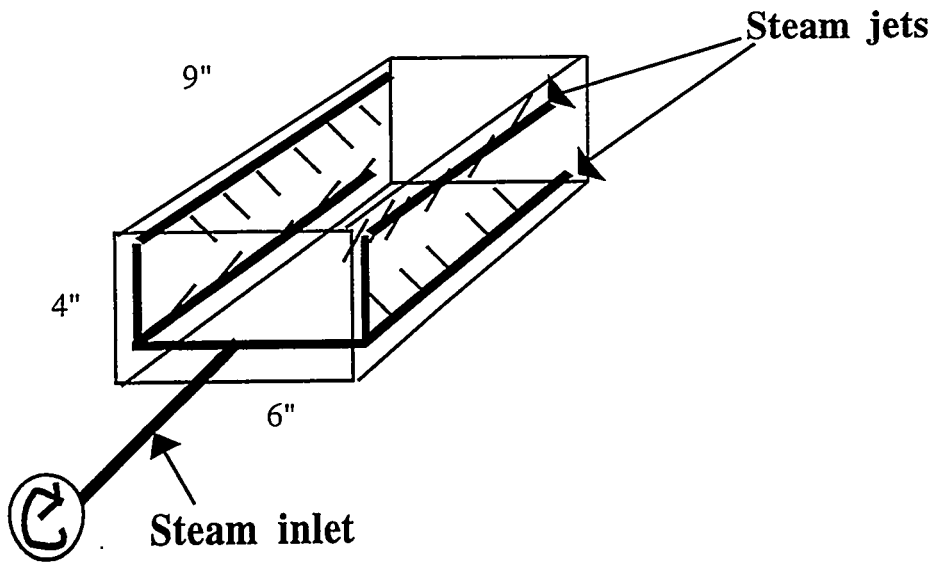

Figure 1: Configuration of steam supply in activation furnace.

Steam activation was carried out at temperatures from 800-900°C for reaction times of 0.5-3 hrs. The flow rate of water was 50-140cc/hr and of nitrogen, 2-3 lpm. Activation in CO_2 was carried out at temperatures from 850-950°C, for reaction times of 1-3 hours. The flow rate of pure CO_2 was varied from 2-3 l/min with the same multiple point gas introduction configuration.

A third method of activation involved a combination of oxygen chemisorption and carbonization. The samples were exposed to an atmosphere of 50% O_2 in N_2 at temperatures ranging from 170-240°C for periods of 1-6 hours. They were subsequently heat treated in nitrogen to 850-925°C, for 1-3 hours. The removal of carbon as carbon oxides should lead to a uniform surface area development. It is known that CO_2 is released at temperatures from 300-800°C with a maximum at about 350°C while CO is released at temperatures from 500-900°C with a maximum at 700°C.

Characterization

Porosity Surface area and pore size distributions were measured on a 10 port automated surface area analyzer, OMNISORB 610. The high efficiency of the instrument allows the measurement of surface areas, as well as the characterization of pore sizes down to 4 A, using nitrogen at 77K as the adsorbate. Surface areas were determined from the isotherms by the BET method, and pore volumes by the D-R method (micropores) and the BJH method (mesopores)[6].

Butane Working Capacity Test The butane working capacity (BWC) was developed as a measure of the effectiveness of activated carbons that are used to trap hydrocarbons released by evaporative losses from vehicle fuel systems (used in evaporative loss control devices, or ELCDs). It is also a useful indication of the properties of activated carbons with respect to other applications. Essentially, the BWC is the difference between the saturation adsorptive capacity of butane, and the amount retained upon the carbon after purging under specified conditions. The retained butane is too strongly adsorbed to allow facile desorption. The tests were performed according to ASTM method D5228-92.

DISCUSSION OF CURRENT ACTIVITIES

Uniform Activation by Steam

Sample SM12, a cylinder of carbon fiber composite produced at ORNL of diameter 11.4 cm and length 21 cm was divided into three sections each 6.9-7.8 cm long with 11.4 cm diameter. The sections weighed 140-180 grams depending on their length. In order to try to achieve uniform activation it was decided to progressively lower the normal steam activation temperature of 875°C by steps of 25°C down to 800 °C. The samples were all activated to a burnoff of 24-28% under the conditions given in Table 1. The surface area distributions through the three samples are given in Figures 2a-c.

The activation is most uniform under conditions of low temperature(800°C) and long reaction times (14 hrs), which is attributed to the low reaction rate that allows the steam to diffuse to the center of the sample before reacting. Hence, the center of the sample is activated to nearly the same extent as the periphery. The mean rate of activation (burnoff/g sample/ minute) is shown in Table 1. The reaction rate increases 27% upon increasing the temperature from 800 to 825°C and by another 50 % upon increasing temperature from 825 to 850°C. The samples do not exhibit stress cracks when activated at 800°C while at 850°C, stress cracks occur. The activation energy for steam activation was determined to be 126kJ/mol by plotting the rate of carbon burnoff in an Arrhenius plot. This is consistent with data in the literature. The activation energy is slightly higher than for the activation of coal and wood based carbons but lower than the activation energy for the activation of carbon fibers[7]. The activation energy for steam activation will be compared to that of CO_2 activation in future work. Further studies will concentrate on reducing activation time and achieving lower standard deviations in surface area distribution by further changing furnace configurations and conditions, and by the application of other techniques that are not discussed here.

Table 1: Conditions and results of steam activation at different HTT.

ID	HTT (°C)	time (hr)	start wt (g)	burnoff(B.O.) (%)	rate of B.O. (g/g.hr)	St dev BET(%)
OR267	800	14	172	26.7	0.019	17
OR 272	825	10	189	24.2	0.024	20
OR 267	850	8	133	28.7	0.036	23

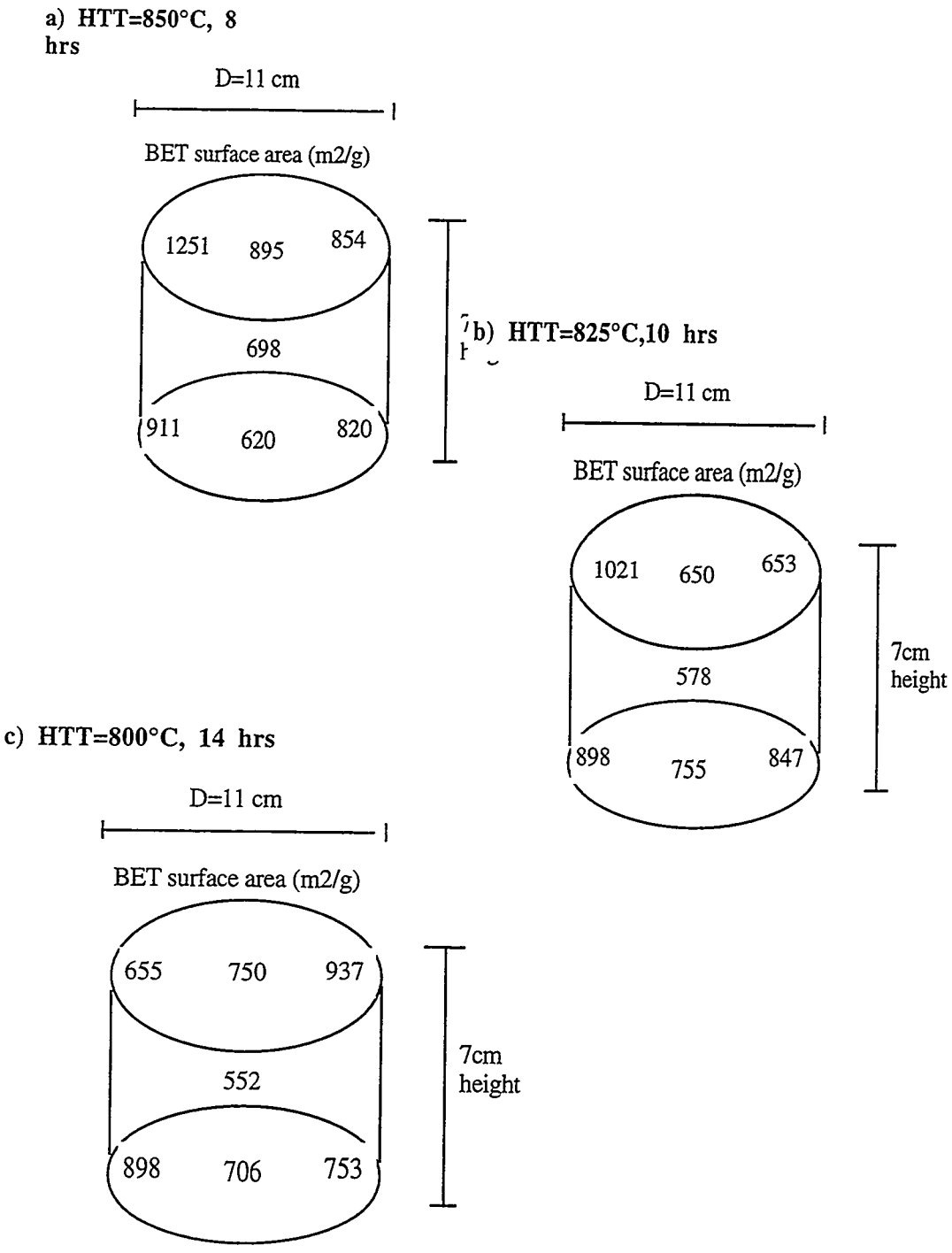

Figure 2 a-c: Distribution of BET surface area in samples activated at three different temperatures.

Uniform Activation by Chemisorption

The chemisorption of oxygen coupled with carbonization has been investigated as an activation technique for achieving uniform activation and a narrow pore size distribution. Since chemisorption is performed at temperatures where there is no carbon burn-off, the amount of oxygen uptake will reach a limiting value. As long as sufficient time is allowed for the oxygen to diffuse to all of the available surface, the extent of chemisorption should be uniform throughout the sample. Similarly, upon heat treatment, the removal of carbon as CO_x should also be uniform.

The chemisorption temperature was varied from 160-250°C. Increasing the chemisorption temperature from 225 to 250°C gave sufficient uptake of oxygen to triple the BET surface area upon heat treatment to 900°C, Table 2. The carbonization temperature was varied from 850-925°C. Heat treatment to 850°C is not sufficient to achieve significant microporosity, and heat treatment to 925°C also gives low surface area. The optimum upper temperature for maximizing the production of narrow micropores appears to be around 900°C. The surface area development in the composites was very uniform with deviation in surface area within the samples of only 3-6% for a chemisorption temperature of 250 and carbonization temperature of 900 or 925°C, Table 2.

In order to increase the surface area further, the cycles of oxygen adsorption and heat treatment were repeated several times. The surface area increased slightly with each step, to a maximum of about 440 m^2/g after a total burnoff of 9%, Figure 3. For each cycle of activation, new narrow micropores are opened. It is also found that the average pore width is reduced as the burnoff is increased, contrary to the case with steam activation. The standard deviation in surface area distribution is very small and close to the experimental reproducibility. A disadvantage when compared to steam activation is the extended processing time required

Table 2: Uniformity of activation of CFCMS by oxygen chemisorption/carbonization.

Sample#	Oxidation		Carboniz.		Burnoff	Surface area	stdev	pore volume (cc/g)	
	T(°C)	t(hr)	T(°C)	t(hr)	(wt%)	(m^2/g)	(%)	micro	meso
221	225	3	900	2	4	134	32	0.07	0.03
216	250	3	850	2	5	315	19	0.15	0.07
218	250	3	900	2	6	387	6	0.20	0.0
219	250	3	925	2	6	230	3	0.13	0.03

to achieve a certain burnoff. Activation times to achieve a 9 % burnoff are shown in Figure 4 for steam activation at different temperatures and oxygen chemisorption/carbonization. As can be seen from the Figure, a far longer processing time is needed to achieve the same burnoff for the chemisorption technique.

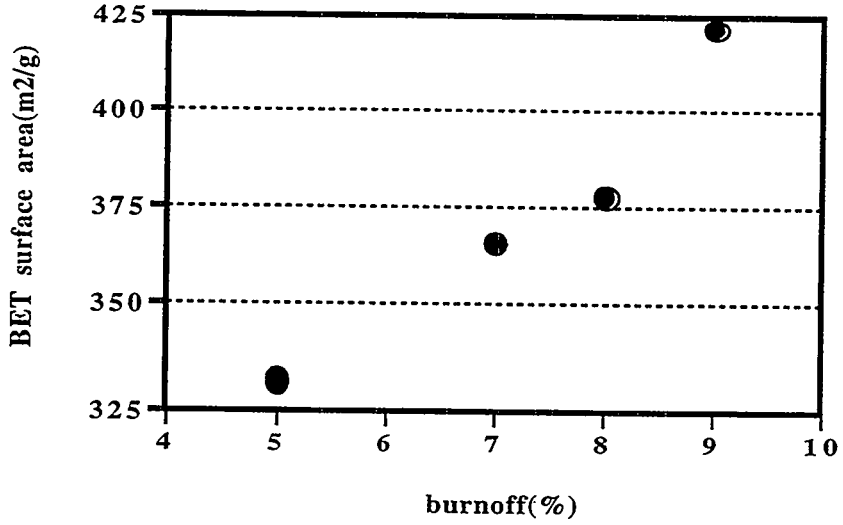

Figure 3: Increase in surface area for each cycle of oxygen chemisorption/carbonization. (Each data point shows a new cycle).

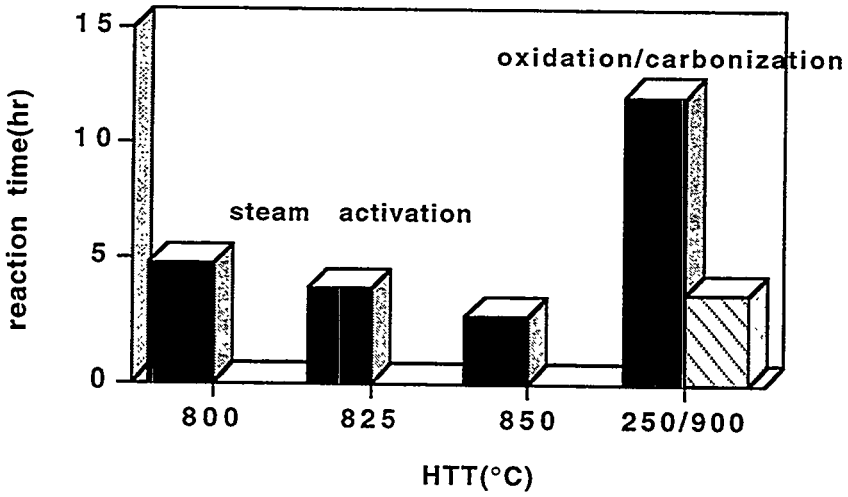

Figure 4: Reaction times for activation to 9% burnoff by steam activation at different HTT and oxygen chemisorption/carbonization.

Butane Working Capacity

Carbons for automobile evaporative control devices are required to have high BWC, as mentioned earlier. Pitch-based carbon fibers have narrow micropores and are therefore not normally useful for such applications. Because of this, carbon fiber composites were activated to high burnoffs in order to attempt to create wide porosity, Table 3. The surface area is high, up to 1800 m^2/g, but the composites still have a low proportion of mesopores. Another problem associated with activation to burnoffs higher than ~40% is that cracking and delamination of the composites occurs. A second obstacle to producing the performance expected of evaporative loss control device is the low density of the composites. The density of the standard composites as received from Oak Ridge is about 0.23 g/cc. In order to compete with the BWC of commercial carbons the density must be increased to around 0.35 - 0.4 g/cc. In the research reported here, samples SA 222 and SA 256 were ground and packed like a powdered bed to a density of 0.39 and 0.36 cc/g respectively. The results of the BWC tests are shown in Table 3. Both samples have butane adsorption capacities within the commercial range of evaporative loss control devices for automobiles, 9.7 and 8.6 g/100 ml. However, these composites also retain ~1.9 g butane per 100 ml of carbon, while wood based carbons show practically no retention.

In an attempt to improve the performance of the composites, an electrical current was applied to two of the composites during the air desorption stage to increase the sample temperature and aid desorption. A current of 4 A was applied for 25 seconds to give a temperature increase of about 50 °C. As can be seen in Table 3, the butane retentivity for sample OR 260 decreased from 1.8 g/100 ml to 0.8 g/100 ml when the current was applied. However, the BWC is still only 4.1 g/100 ml and highest BWC obtained on an activated composite was 5.5 g/100 ml which is still very low.

Even with the application of an electric current during the desorption stage, it does not seem feasible to produce a pitch-based carbon fiber composite with high performance for butane adsorption. The focus of future work will be to identify different precursor fibers that will give composites with higher butane working capacities.

Table 3: Butane Working Capacity (BWC) of activated carbon fiber composites

ID	SA222	SA 222B*	SA256*OR	263**OR	260O	260**	Wood^^
BET surface area (m^2/g)	1380	1380	1057	1728	1126	1126	1798
density (g/cc)	0.25	0.39	0.36	0.25	0.21	0.21	0.28
BWC [W/V] (g/100 ml)	**5.5**	**9.7**	**8.6**	**4.6**	**3.1**	**4.1**	**14.5**
butane activity [W/V] (g/100ml)	10.0	11.6	10.2	6.9	4.9	4.9	14.5
butane retentivity[W/V](g/100 ml)	4.5	1.9	1.6	2.3	1.8	0.8	0

* composite ground and packed to high density; ** current applied to composite to desorb butane, 4 A for 25 seconds, temperature increase ~ 50°C; ^^Wood-wood based commercial carbon

REFERENCES

1) T. D. BURCHELL, F. DERBYSHIRE, Y.Q. FEI AND M. JAGTOYEN, C. E. WEAVER, Proceedings of Eighth Cimtec World Ceramics Conference, 6/28, Florence, Italy (1994) 120.
2) M. JAGTOYEN, F. DERBYSHIRE, N, CUSTER, T. BURCHELL, 1994 Spring Meeting, Materials Research Society, San Francisco, April 4-8, 1994,Symposium Proceedings, 344, (1994) 77.
3) S. P NANDI and P. L. WALKER Jr. , FUEL, 1975, **54**, 169.
4) D. F. QUINN, J. A. HOLLAND, US Patent 5,071,820, 1991.
5) M. JAGTOYEN, F. DERBYSHIRE, G. KIMBER, Y. Q. FEI, Proceedings of the Tenth Annual Conference on Fossil Energy Materials, Fossil Energy AR&TD Materials Program, for USDOE,Oak Ridge National Laboratory, May 14-16(1996) 291.
6) GREGG, S.J., SING, K.S.W, in *"Adsorption, Surface Area and Porosity"*, 2nd ed., Academic, London , 1982, 94-100.
7) Y.Q. Fei and F. DERBYSHIRE, Proceedings, 22nd Bien. Conf. on Carbon,16-22 July,1995, 512.

ACKNOWLEDGEMENTS

The authors wish to acknowledge D. Turner and C. Lafferty of the CAER, the Commonwealth of KY and Rod Judkins of the ORNL for financial support of this work. This work is sponsored by the Fossil Energy AR&TD Materials Program, US Department of Energy, under contract no.SC19X-SN719C.

CARBON FIBER COMPOSITE MOLECULAR SIEVES

T. D. Burchell and M. R. Rogers

INTRODUCTION

Monolithic adsorbents based on isotropic pitch fibers have been developed jointly by ORNL and the University of Kentucky, Center for Applied Energy Research. Our monoliths are attractive for gas separation and storage applications because of their unique combination of physical properties and microporous structure. At ORNL we currently produce the monoliths in billets that are 10 cm in diameter and 25 cm in length. The monolithic adsorbent material is being considered for guard bed applications on a natural gas (NG) powered device. In order for the material to be successful in this application, we must attain a uniform activation to modest micropore volumes throughout the large monoliths currently being produced. Here we report the results of a study directed toward attaining uniform activation in these billets.

EXPERIMENTAL

The manufacturing process for our carbon fiber composite molecular sieve (CFCMS) materials has been reported elsewhere [1,2]. Activation was performed in a three-zone Lindburgh furnace fitted with an 20-cm diameter Inconel retort. The CFCMS samples were dried in vacuum at 300°C, heated to 850°C under He for one hour, cooled to 200°C for a chemisorption treatment in flowing O_2, and then heated again to 850°C in He. The chemisorption and activation steps were repeated until the desired total burn-off (weight loss) was attained. Micropore structure characterization was performed using a Quantichrome Autosorb-1 apparatus.

RESULTS AND DISCUSSION

A total of five billets were subjected to two cycles each of O_2 chemisorption/activation. The burn-off attained ranged from 8.5 to 13.4%, with an average burn-off of 10.4%. A typical (Type I) N_2 isotherm (77K) for sample SMW-8A is shown in Fig. 1. The Dubinin-Redushkevich (DR) micropore volume; Brunauer, Emmett, and Teller (BET) surface area; and Dubinin-Astakhov

(DA) micropore width for four SMW billets are reported in Table 1. The designations A and B indicate samples taken from opposite ends of the 25-cm long billets.

Table 1. Micropore volume, micropore size, and surface area data for CFCMS billets

Billet Number	BET Surface Area (m^2/g)	DR Micropore Volume (cm^3/g)	DA Micropore Diameter [mode] (nm)
SMW1-A	567	0.27	1.54
SMW1-B	425	0.16	1.64
SMW3-A	607	0.23	1.44
SMW3-B	448	0.17	1.48
SMW4-A	940	0.34	1.56
SMW4-B	488	0.19	1.54
SMW8-A	707	0.27	1.48
SMW8-B	441	0.16	1.54

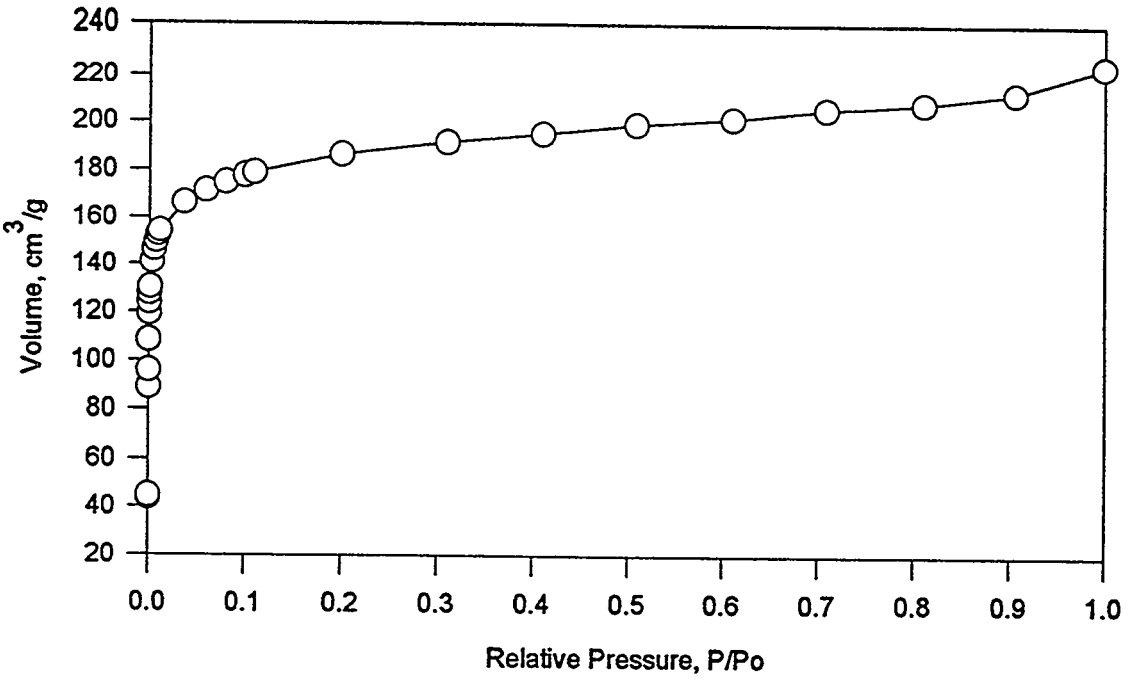

Figure 1. Typical 77K N_2 isotherm for sample SMW8A

The micropore volumes varied from 0.16 to 0.34 cm^3/g and the BET surface areas range from 425 to 940 m^2/g. Billet SM-15 was subjected to a more detailed examination to determine the uniformity of activation throughout the billet. Samples were taken at several radial locations across slices cut periodically along the billet length (Fig. 2). The BET surface area, DR micropore volume, and DA micropore size distribution were determined from the N_2 adsorption isotherm measured for each sample, and are shown in the 3D plots in Figs. 3-5. The BET surface area varied from 944 to 312 m^2/g and the DA pore diameter varied from 14 to 19.2 nm. Figure 6 shows the variation of DR micropore volume throughout billet SM-15, plotted as a function of diametral position for the five axial sampling positions. The DR volume varied from 0.12 to 0.35 cm^3/g, but there was no systematic radial or axial variation.

Figure 7 shows a breakthrough plot for an $Ar/H_2S/H_2$ mixture flowing through a sample of our CFCMS material. The H_2S was adsorbed, and breakthrough occurs some 18 minutes into the experiment. The H_2 and Ar were not adsorbed. Upon total breakthrough, the feed gas mixture flow was terminated and the desorption of the adsorbed H_2S was achieved by applying an electric current (4.5A @ 1V). Desorption occurred rapidly, as indicated by the increased concentration of H_2S in the exhaust gas stream. Regeneration of the CFCMS was thus achieved by direct electrical heating of the CFCMS. The ability of the material to readily adsorb H_2S suggests the removal of natural gas (NG) odorant additives might be achieved with a guard bed containing a billet of activated CFCMS. Consequently, a three-bed guard system was constructed and is depicted schematically in Fig. 8. The device contains three monolithic adsorbent pieces with approximate dimensions of 4.25-inches (10.8-cm) diameter and 10.0-inches (254-cm) length. Pressure drop data for He flow through an activated billet are shown in Fig.9. The measured pressure drop is slightly greater than for a packed bed of granular carbon. CFCMS is currently being evaluated as a guard-bed material for a NG fueled device.

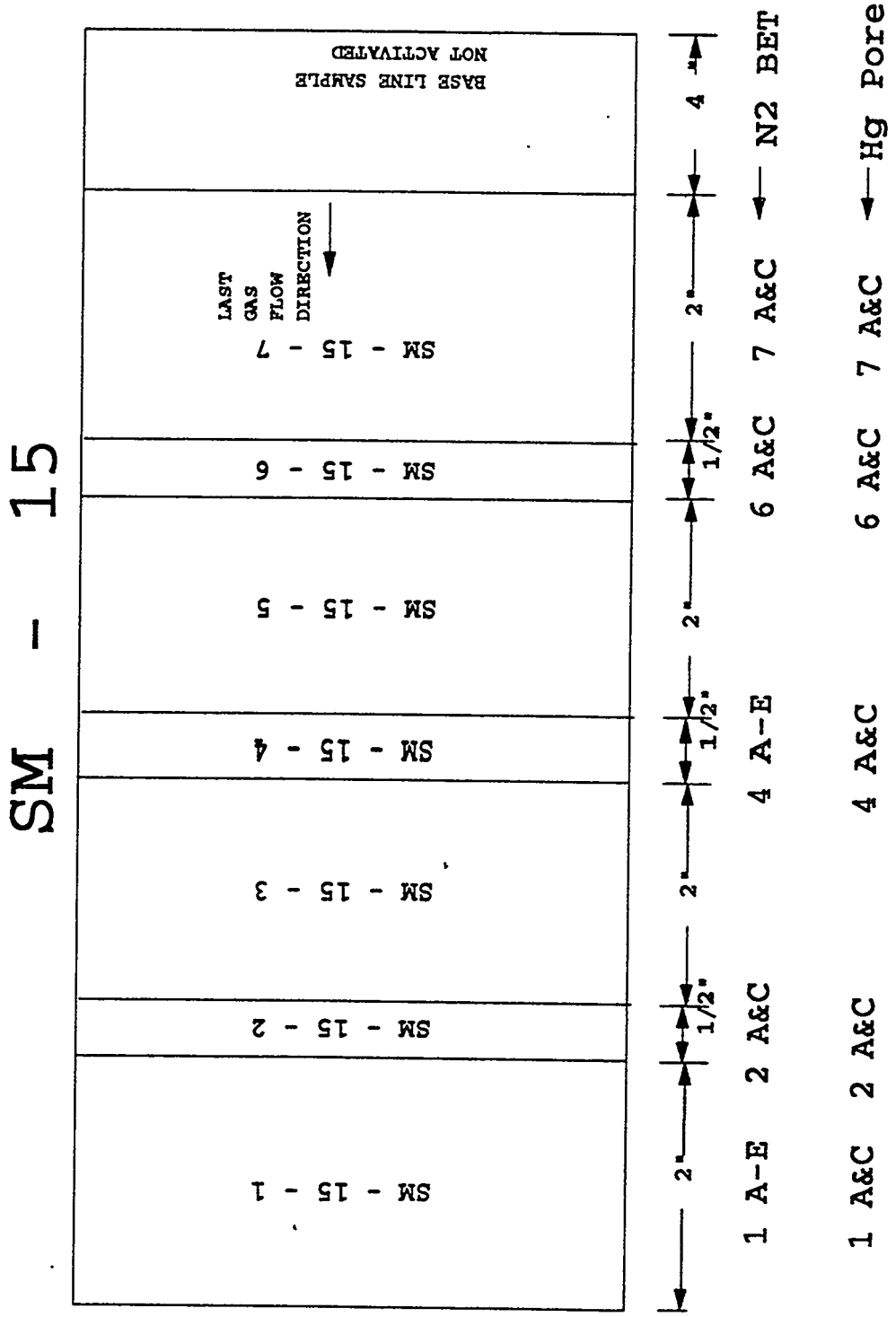

Figure 2. Sample locations in CFCMS billet SM-15

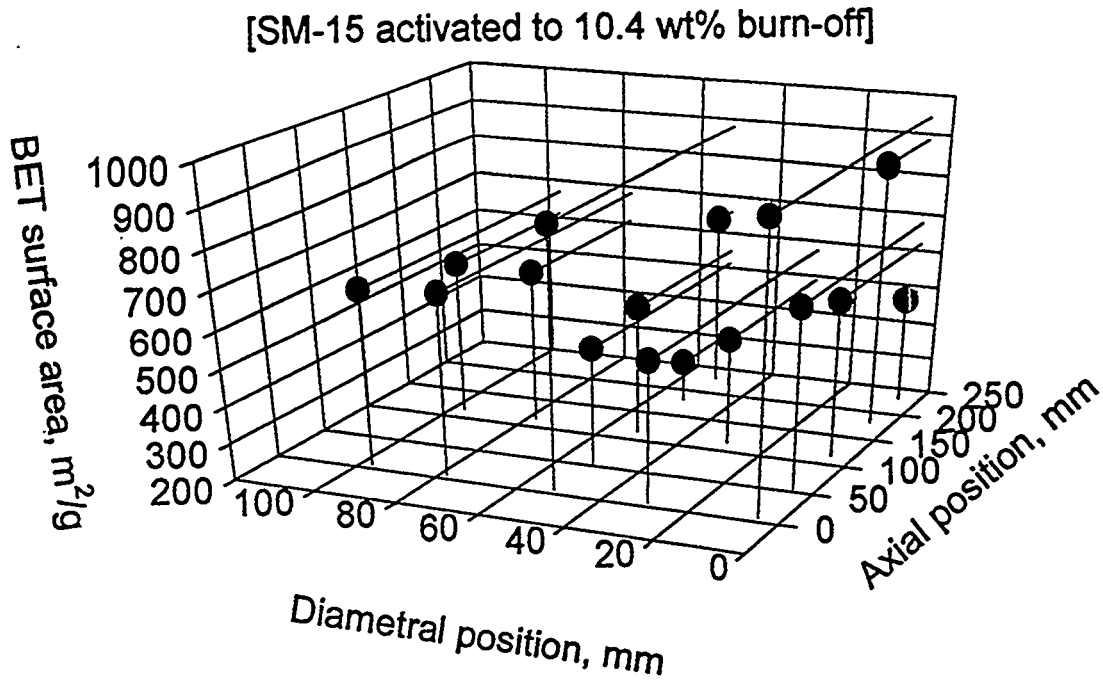

Figure 3. BET surface area as a function of position in billet SM-15

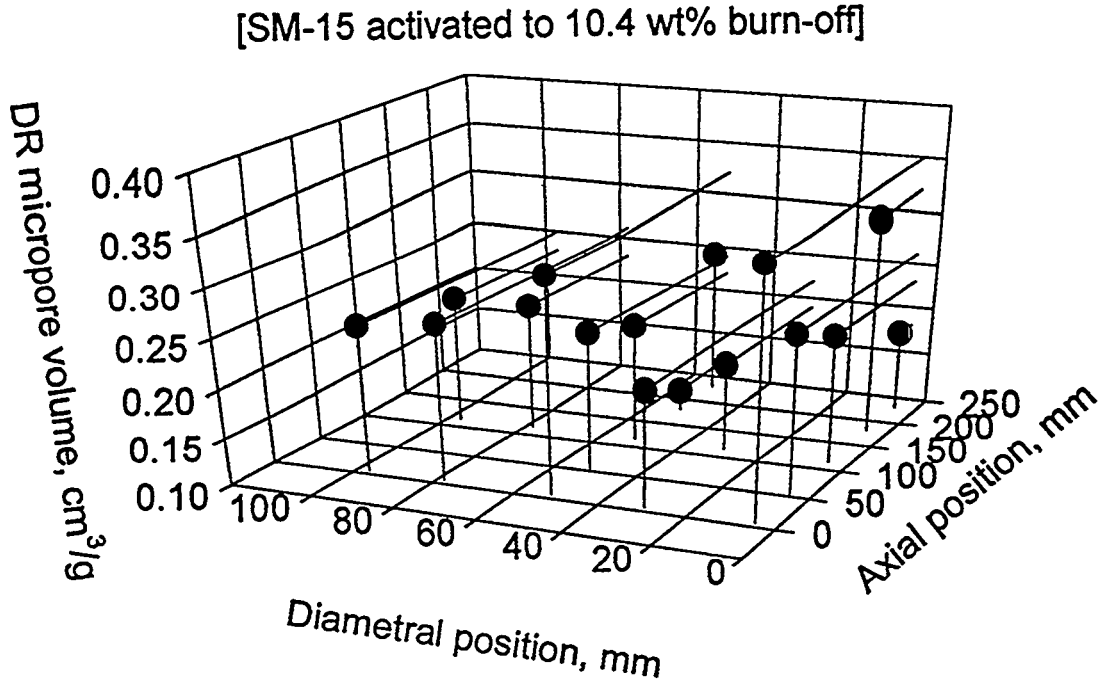

Figure 4. DR micropore volume as a function of position in billet SM-15

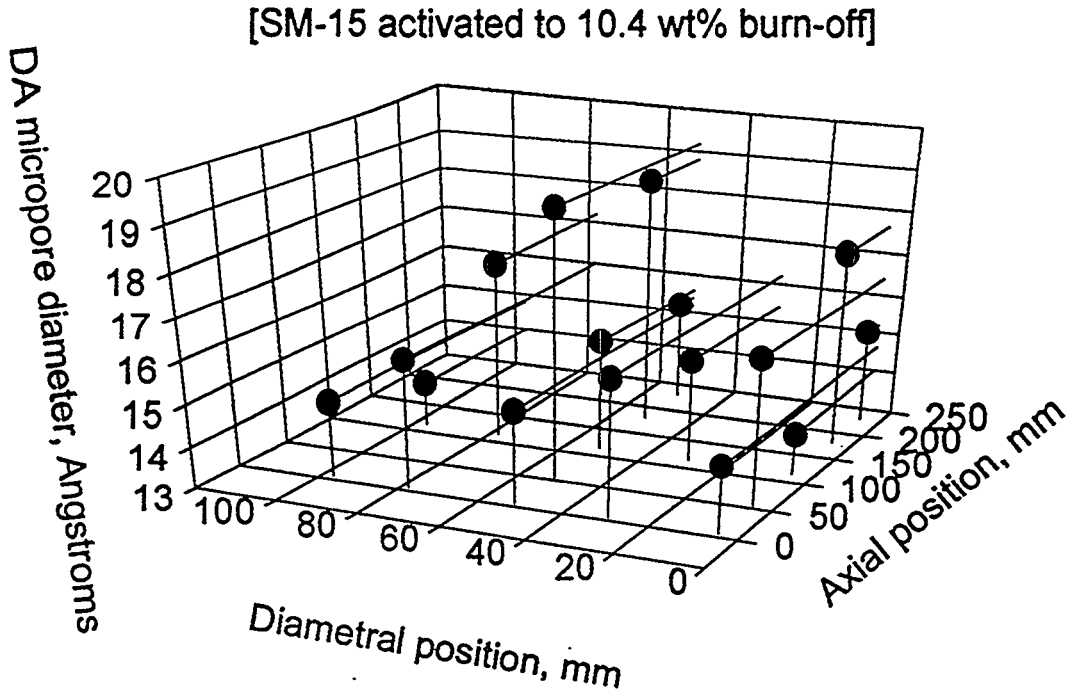

Figure 5. DA micropore diameter as a function of position in billet SM-15

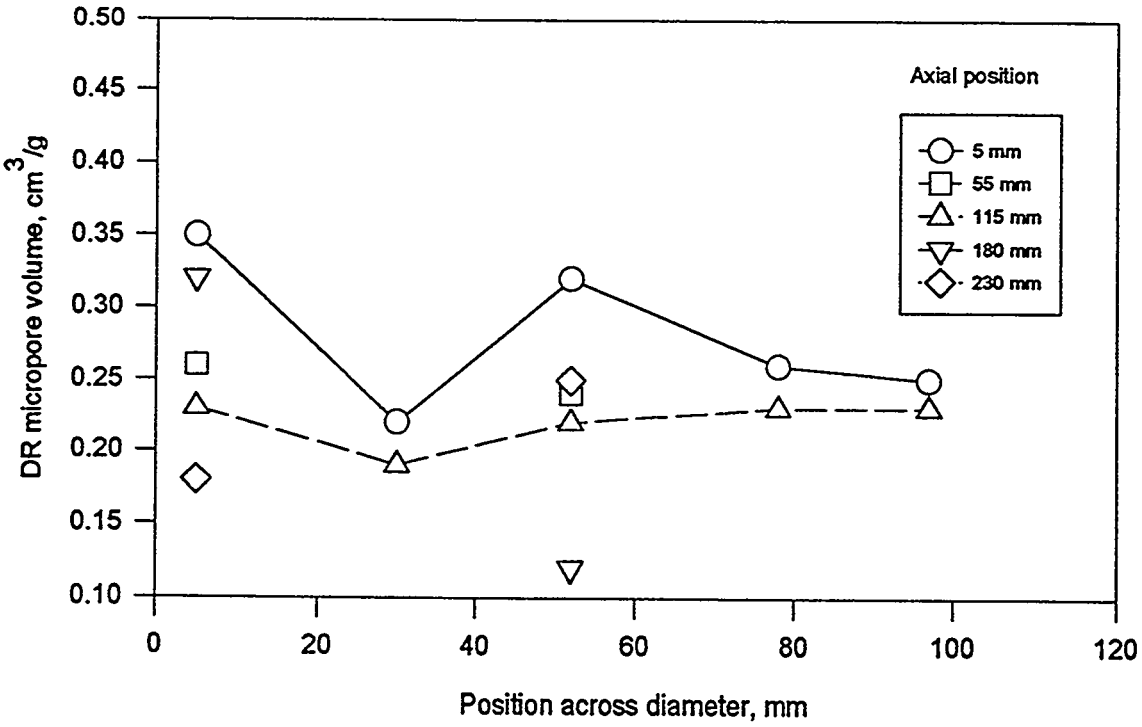

Figure 6. Variation of DR micropore volume in a CFCMS billet SM-15

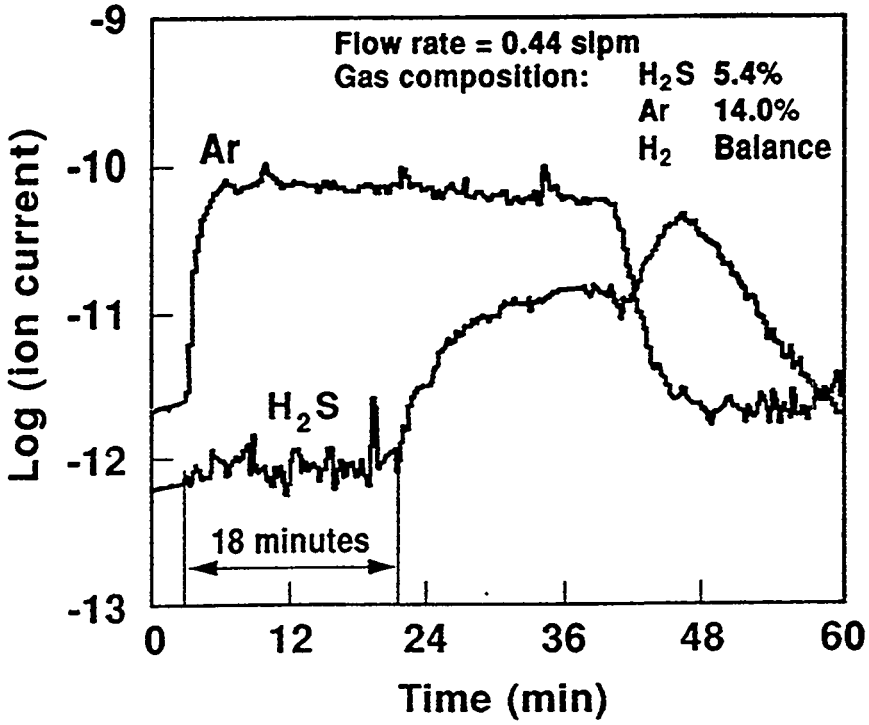

Figure 7. H_2S breakthrough plot for activated CFCMS showing the electrical desorption of the H_2S

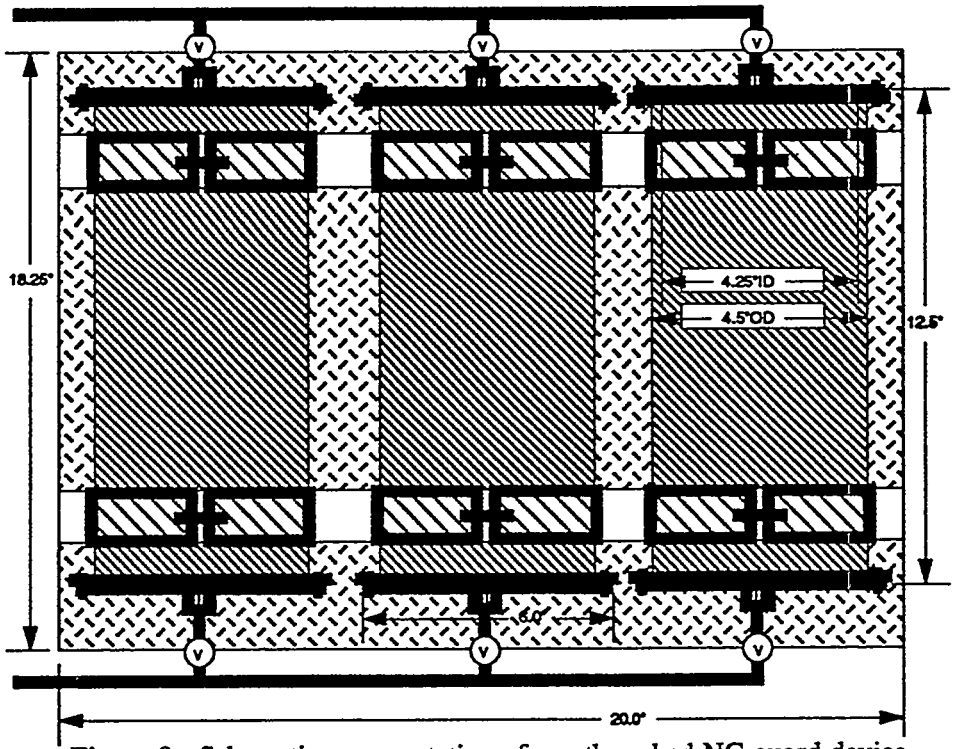

Figure 8. Schematic representation of our three-bed NG guard device containing CFCMS monoliths

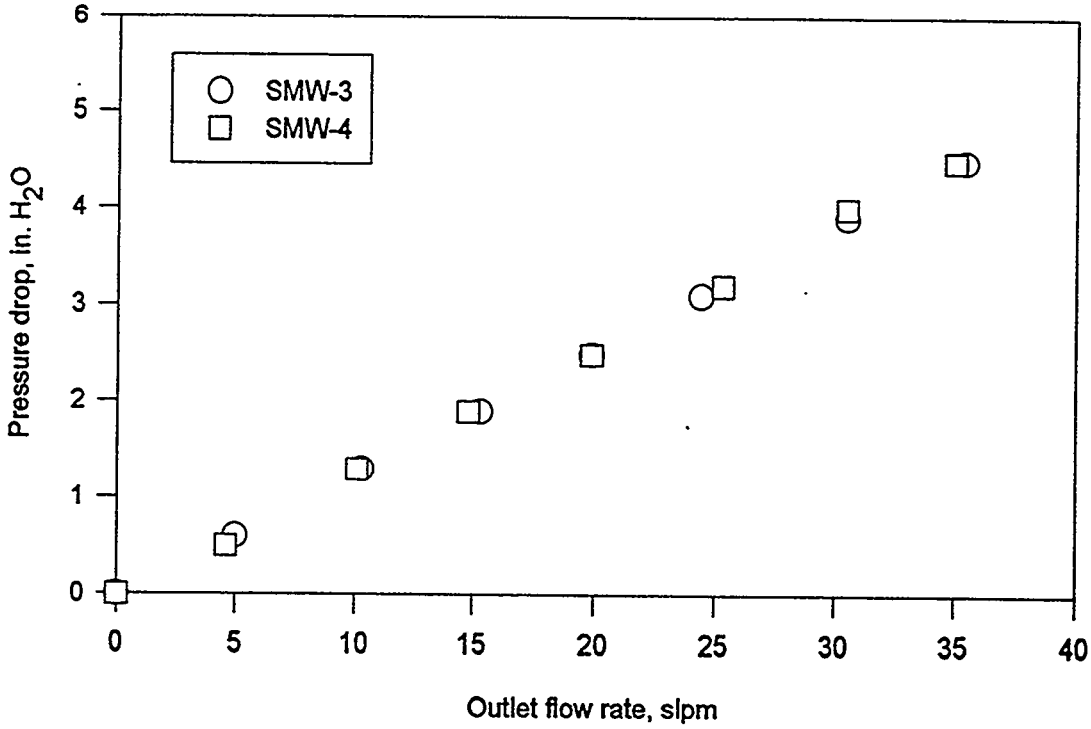

Figure 9. Pressure drop through a large monolith as a function of the He flow rate

CONCLUSIONS

Reasonably uniform activation was achieved in our CFCMS materials. Micropore volumes of 0.12 to 0.35 cm^3/g were attained. The ability of the materials to adsorb H_2S, the acceptable pressure drop, and its electrical heating capability suggests that CFCMS will make an ideal guard-bed material. Our three bed NG guard device is currently undergoing field trials.

REFERENCES

1. Burchell, T. D., Judkins, R. R., Rogers, M. R. and Williams A. M., *Carbon* **35** (1997) in press.
2. Burchell, T. D. in. *Proc. 8th Ann. Conf. on Fossil Energy Materials, CONF-9405143, ORNL/FMP-94/1*, pub. Oak Ridge National Laboratory, Aug. 1994, pp. 63-70.

SESSION II

CERAMICS, NEW ALLOYS, AND FUNCTIONAL MATERIALS

MECHANICAL PERFORMANCE OF HI-NICALON/CVI-SiC COMPOSITES WITH MULTILAYER SiC/C INTERFACES

H. G. Halverson, R. H. Carter, and W. A. Curtin

Department of Engineering Science and Mechanics
Virginia Polytechnic Institute and State University, Blacksburg, VA 24061

ABSTRACT

The mechanical properties and interfacial characteristics of new SiC/SiC ceramic composites, composed of Hi-Nicalon fibers in a CVI-SiC matrix and having a variety of multilayer SiC/C coatings between the fibers and the matrix, are studied in detail to elucidate the roles of the coatings and fibers. Axial tension tests and unload/reload hysteresis loop measurements are performed to determine mechanical performance. All materials exhibit the strong and tough behavior characteristic of good ceramic composites, with all multilayer variants performing quite similarly. SEM microscopy demonstrates that matrix cracks penetrate through the multilayers and debond at the fiber/inner-coating interface. Analysis of the hysteretic behavior leads to values for interfacial sliding resistance $\tau \approx 11$ ksi and interfacial toughness $\Gamma_i \approx 2$ J/m^2 that are nearly independent of multilayer structure, and are similar to values obtained for standard pyrolitic carbon interfaces. These results all indicate debonding at the fiber surface for all coating structures, which provides a common roughness, τ, and Γ_i. Analysis of fiber fracture mirrors provides an estimate of the in-situ strength of the fibers and demonstrates the high strength retention of the Hi-Nicalon fibers. The in-situ fiber strengths are combined with the measured pullout lengths to obtain an independent determination of τ=8.5 ksi that agrees well with the value found from the hysteretic behavior. Predictions of composite strength using the derived fiber strengths agree well with the measured value although the predicted failure strain is too large. This study demonstrates that Hi-Nicalon fiber/CVI-SiC composites perform well for a wide range of multilayer interface structures and that the interfaces present relatively high values of τ and Γ_i, both of which are beneficial to strength and toughness. The small carbon layer thicknesses in these multilayer coatings may allow for improved mechanical performance at elevated temperatures, in radiation environments, and possibly oxidizing environments.

INTRODUCTION

Here we report on a broad spectrum of experimental measurements and characterization performed on new Hi-Nicalon/CVI-SiC ceramic composites with multilayer SiC/C interfaces. These

materials were fabricated and supplied by Hyper-Therm Inc.[1] The purposes of this effort are several. First, we want to obtain the basic macroscopic mechanical performance in these systems, and assess differences between different multilayer variants. Second, we want to carefully characterize the interface sliding and interface toughness in these systems, and again correlate properties with coating structure. Third, we want to perform optical and SEM microscopy to examine the crack path selection and crack density in these materials. Fourth, we want to assess the as-processed Hi-Nicalon fiber strengths and to determine if existing theories of composite strength, validated on a wide variety of other CMC systems, can successfully predict the observed strengths of these materials. In total, this effort assesses the efficacy of both multilayer coatings and Hi-Nicalon fibers in creating high-quality composite materials for various energy applications.

MECHANICAL PROPERTIES

The materials studied here consist of Hi-Nicalon fibers in a CVI-SiC matrix with a variety of SiC/C multilayer coatings. Both the individual SiC layer thicknesses and the number of such layers were varied. The layer thicknesses were characterized as "Thin", Medium" and "Thick", and the number of layers ranged from 2 to 8. Based on SEM, the thin SiC layers are approximately 0.06-0.10 μ in thickness, the medium layers are 0.10 –0.12 μ, and the thick layers are 0.15 μ. The carbon layers ranged from 0.01-0.03 μ. Two straight-sided samples of each type were supplied. Each sample was designated by the number of layers, the thickness, and the sample number (e.g. 2M-2 is the 2-layer, Medium thickness, 2nd sample).

The stress-strain curves for these materials are all quite similar, exhibiting an initial linear response, a subsequent non-linear response due to matrix cracking, and a final failure after extensive non-linear deformation (Figure 1). The elastic modulus, onset of non-linear behavior, strength, and failure strain are all larger than similar materials having CG-Nicalon fibers, which is attributable to the improved properties of the Hi-Nicalon fibers. Table I presents the benchmark values of the mechanical behavior for each of these materials. The elastic modulus is the same for all samples, as expected for well-controlled fiber volume fraction and matrix porosity, and is independent of interface type.

The onset of matrix cracking is determined using an 0.005% offset stress and the measured elastic modulus; the values range from 13-17 ksi, with no strong dependence on interface type although the 2M samples show slightly higher values than most. The hysteresis loop widths (not shown) are essentially zero for all speciments at and below 15 ksi, indicating no sliding behavior; this suggests that the longitudinal fiber tows are not cracked/debonded until stresses larger than 15 ksi. The ultimate tensile strengths, although most are grip failures, show very little difference among almost all specimens, except for the 2M material. The stronger 2M specimen actually survived 50 ksi and failed on reloading. There

is a slight trend toward decreasing strength with increasing layer thickness (2M excepted), but the strengths for the 8K specimens could be low due to slight misalignment during sectioning. The failure strains are more variable, and the 2M samples exhibit quite high failures strains – values approaching those measured in CG-Nicalon/glass-matrix systems. The level of acoustic emission activity is superimposed on the stress-strain data in Figure 1 and shows a peak in number of events versus stress around 20-25 ksi, typical of all materials. The average number of acoustic events versus stress for all interface types (not shown) suggests that there is slightly more activity for 2 layer specimens and thin layer specimens, with the thick layer specimens generally having the lowest numbers of hits. Much of acoustic activity is at stresses larger than the regime of strong non-linearity in the stress-strain curves between 15-20 ksi, suggesting that initial transverse cracking occurs in the 90° tows below 15-20 ksi followed by further cracking in the 0° tows at higher loads. Acoustic emission declines substantially above 30-35 ksi. There were no identifiable correlations between features in the acoustic emission signal (amplitude, duration, energy, rise time) and stress.

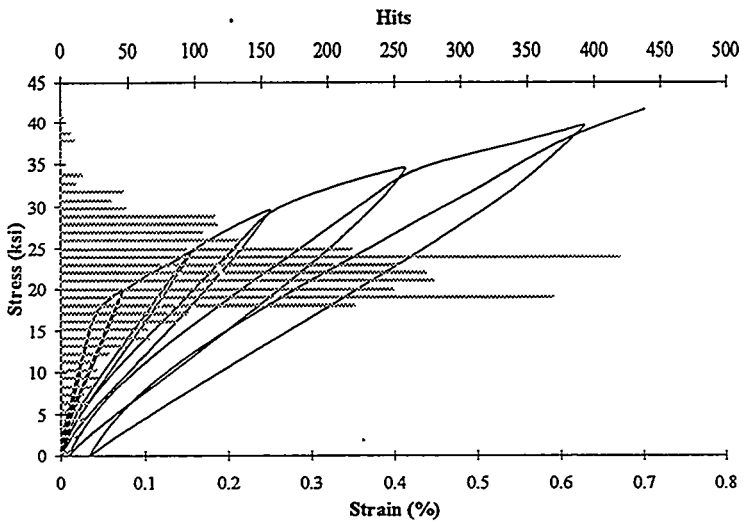

Figure 1: Sample Stress-Strain Curve

Table I: Mechanical Properties of Multi-layer SiC/SiC Materials

Specimen	Elastic Modulus (msi)	Tensile Strength (ksi)	Failure Strain (%)	0.05% Offset Stress (ksi)
2T	42.79	39.56	0.540	12.77
2M	42.10	45.90	0.741	16.88
2K	41.97	37.90	0.695	14.78
4T	45.22	37.94	0.428	15.15
4M	40.50	35.57	0.563	14.05
4K	42.46	33.80	0.614	14.50
8T	44.09	39.35	0.549	12.95
8M	40.38	36.70	0.655	15.42
8K	46.66	33.04	0.517	15.92

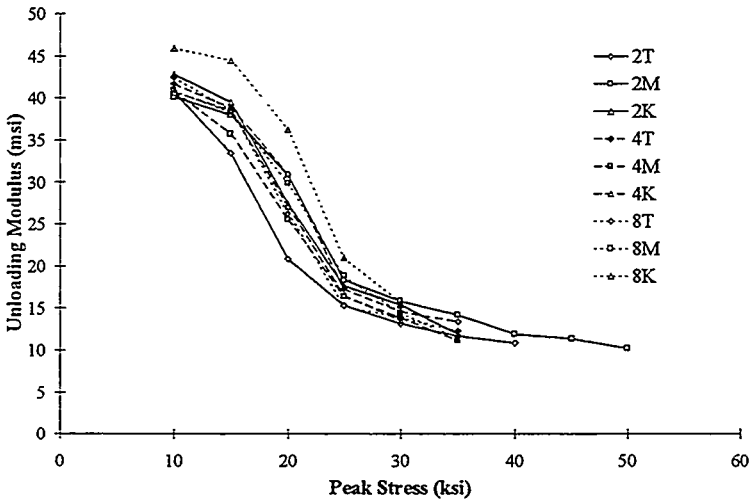

Figure 2: Unloading Modulus

The initial unloading modulus upon just unloading slightly versus the peak applied load is shown in Figure 2, and also indicates essentially no correlations among either different thickness or different numbers of layers. This shows that the crack densities are essentially identical in all materials.

MICROSCOPY OBSERVATIONS

We have performed both Optical and SEM microscopy to observe the crack behavior in these multilayer systems, and to attempt to correlate the physical cracking with the measured mechanical properties. The 2M samples were most carefully studied. Optical microscopy (not shown) under polarized light was generally successful for observing large scale cracking of matrix rich regions, transverse fiber tows, and the impingment of cracks into the 0° infiltrated fiber tows. All samples exhibited transverse cracking along the entire gauge section, with typical crack spacings d=250μm.

Of great importance to the stress-strain behavior, strength, and failure strain, is the cracking within the 0° fiber tows. It is this finer-scale cracking, rather than the larger-scale cracking in the 90° tows, that controls the major non-linear behavior of the composite and the hysteretic behavior, since frictional sliding occurs at the interfaces of the 0° fibers. To search for cracking in the 0° tow regions, we have performed SEM studies, although the microscopy is difficult because of the topography of the woven fiber surface even after careful polishing. Generally, we are unable to observe cracks that are entirely confined to the 0° tows; most of the cracks observed in the longitudinal tows are connected to the larger through-cracks. Occasionally, however, a fine crack is visible which is only 30 μm or so from another crack. The microscopy is thus, at present, inconclusive as to the presence of finer-scale cracks. We argue below that such cracks must exist, and are preparing samples to further investigate this cracking.

Figure 3 shows the efficacy of the multilayer fiber coatings. In the backscattered images, the thin carbon interlayers appear has faint dark lines and are visible near the surfaces of many fibers. *The*

cracks impinging on the fibers in the 0° tows almost always penetrate through the coatings and terminate at the fiber/inner coating interface. We have not observed any cracks terminating at the outer layers. Cracks impinging on the transverse fibers exhibit varying behavior depending on the angle of impingement. Cracks approaching nearly perpendicular to an interface penetrates to the fiber surface and then debond. Cracks approaching more obliquely can debond at one or more of the multilayer interfaces. Thus, the C layers are "weak" layers which can act to deflect cracks but it appears that some component of opening, rather than shear, is required.

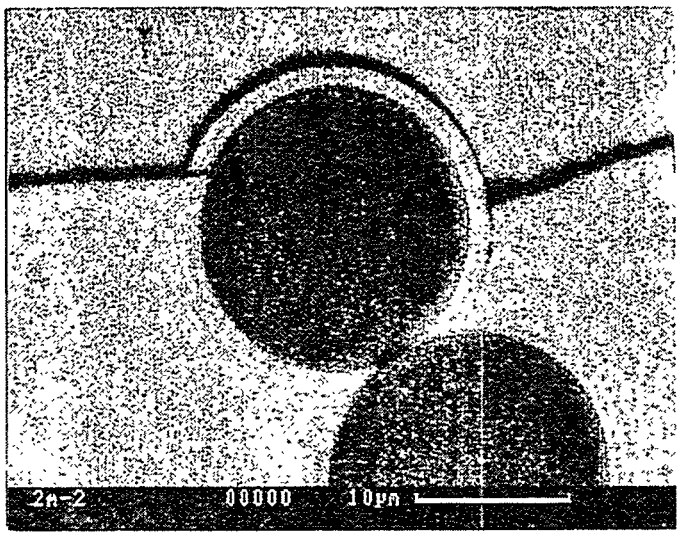

Figure 3: Oblique Crack Deflection

Although not all the different materials have been investigated in such detail, we have no evidence that the interfaces in any of the materials behave differently than discussed here. All cracks appear to penetrate the multilayer coatings when approaching at high angles. This conclusion is consistent with the measured mechanical responses showing that all materials have very similar overall deformation behavior and strength.

INTERFACIAL DEBONDING AND SLIDING

Here we analyze the measured hysteretic behavior in much more detail to elucidate differences in the interface-specific quantities: the interface frictional stress (τ) and the interface Mode II toughness (Γ_i). Debonding and sliding affect the stress-strain relation of a material, but in a standard quasi-static tensile test it is difficult to separate the various effects of the formation of new cracks, the extension of the fiber/matrix debond, and other damage events from one other. As a result, careful analysis of unloading/reloading hysteresis is used. During an unload/reload curve, no additional damage occurs in the material, and it is possible to directly relate the non-linearities in the stress-strain response to the interface properties. A typical hysteresis loop (Figure 4; inset), shows two regions, a quadratic region of increasing slip length, and a linear region where the slip zone extends over the entire debond region. Figure 4 shows the inverse of the hysteresis curve slope, the so-called Inverse Tangent Modulus (ITM), for the reloading curve for a series of peak stresses.

A method of determining Γ_i and τ from the ITM for unidirectional materials has recently been published[3]. For cross-ply materials with distinct matrix cracks in both the 90° and 0° plies, the analysis is not well-defined. Here, we will assume either (i) the only cracks are those observed in the microscopy or (ii) the existence fine-scale 0° fiber tow cracks not been observed in the microscopy. In both cases, the material can then be treated as effectively unidirectional; in case (ii) this is so only after the large through cracks have been formed, which occurs below/around 15 ksi. The constant slope region of the ITM (Figure 4) is related to τ and crack spacing d by the relationship

$$Slope = \frac{b_2(1-a_1 f)r}{2\pi d E_m f^2} \quad (1)$$

where b_2 and a_1 are known combinations of elastic properties of the fiber and matrix, f is the fiber volume fraction, r is the fiber radius, and E_m is the matrix elastic modulus.

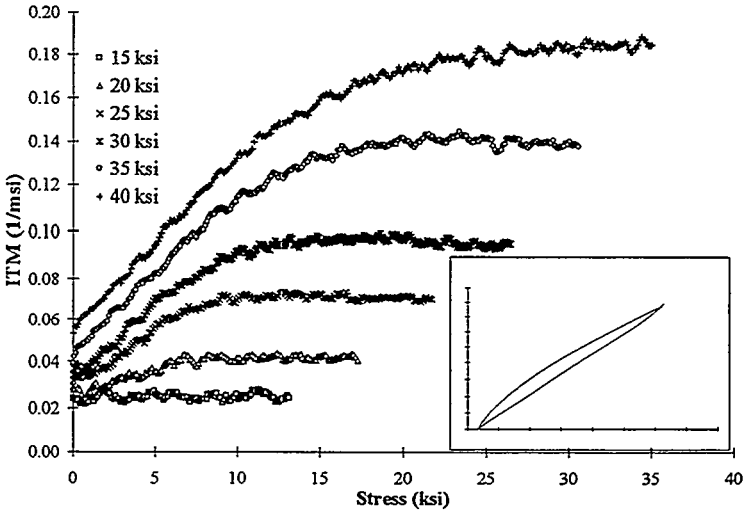

Figure 4: Inverse Tangent Modulus Plot

From our microscopy, it *appears* that the crack spacing is d≈250μ. Let us take the 250μm crack spacing to exist at 30 ksi, above which the acoustic emission (Figure 1) is decreasing rapidly and the unloading modulus (Figure 2) begins to saturate. Then, from the measured slope of the ITM at the 30 ksi peak load we can derive τ for each specimen. The typical values are around 1.2 ksi, which is very low. *In fact, we believe this analysis using the observed crack spacing must be incorrect and that this τ value is much too small.* Arguments and analysis supporting this claim are discussed below.

We now discuss an alternative method of determining the crack spacing indirectly from the mechanical test data. The mechanical data show that hysteresis does not exist at or below 15 ksi, and that significant acoustic emission ceases after 30 ksi. We thus believe that 0° tow cracking, which causes hysteresis, begins at around 15 ksi and has ended at 30 ksi. Now consider the very instant that unloading begins: the reverse slip zone has zero length and since no slip occurs the deformation must be completely elastic. Therefore, the initial unloading modulus E* is dependent only on the elastic properties of the material and the crack spacing, and the relationship is

$$\frac{E^*}{E_c} = \left(1 + \frac{D_1^0 r}{d}\right)^{-1} \quad (2)$$

where D_1^0 is a parameter found by a finite element solution[4]. For f≈32% in a 0° tow and the known elastic properties, D_1^0=2.4. Applying this to the woven structure, we assume that the modulus measured at 15 ksi reflects the modulus of the material with cracked 90° regions, and so is the "initial" value E_c to be used in Eq. (2). Then, we can use the measured initial unloading modulus (Figure 2) with Eq. (2), to derive the crack spacing d versus peak load. At 30 ksi, the crack spacing derived is 25-35 μm. A crack spacing of 30 μm was observed by Evans and coworkers on a CG-Nicalon/SiC material with a pyrolitic C interface. Our microscopy also shows the occasional crack spacing of about 30 μm in the 0 tows. Thus, our derivation of this final crack spacing is consistent with related results. In contrast, if one insists that the only cracks are those observed, with d=250 μm, then at the end of the test the unloading modulus would drop by only 7%. This is at odds with the measurements, suggesting the existence of many more cracks.

With the values of d determined above versus peak load, we now use the ITM data to derive τ. The results for τ are nearly constant versus peak load and the values obtained at 30 ksi peak stress are shown in Table II. The results for individual specimens vary from 8.7 ksi to 14.8 ksi with an average value of 11.8 ksi. We will further corroborate this value through independent measurements of fiber pullout as described in the next section.

The interface toughness, Γ_i, controls the extent of the debond and can be determined by the stress at which the transition from the frictional sliding region (constant slope of ITM) to elastic reloading region (constant ITM) occurs. This relationship is given by

$$\Gamma_i = \frac{r\sigma_p^2 c_1^2}{E_m}\left(1-\frac{\sigma_{tr}}{2\sigma_p}\right)^2 \qquad (3)$$

where σ_p is the peak applied stress of the hysteresis loop, σ_{tr} is the transition stress, and c_1 is a combination of elastic constants. The values at peak stress 20 ksi are listed in Table II, with a typical value of 2.3 J/m^2 that is similar to that obtained in standard SiC/SiC.

Analysis of the hysteretic behavior of the multilayer materials thus leads to the following conclusions: (i) the crack spacing in the 0° fiber tows is ≈30μm at the end of the matrix cracking; (ii) τ≈11 ksi; and (iii) Γ_i≈2.3 J/m^2, for all materials studied here. These properties are comparable to values obtained in the standard pyrolitic carbon interface materials with CG-Nicalon fibers. Coupled with the microscopy, which shows debonding at the fiber/inner-coating interface, this result is not too surprising: the roughness and interface toughness are controlled by properties of the fiber/inner-coating interface in both thick Carbon and multilayer materials. Of some interest is the nearly complete insensitivity to the total carbon thickness in the multilayer materials. The thermal clamping stresses must depend quite sensitively on the carbon thickness, as is well established, so we conclude that in the present materials the clamping is mainly governed by roughness of the sliding interface, which would not be controlled by the carbon thickness. The insensitivity to total C thickness also suggests that the reduced radial compliance

Table II: Interface Properties of Multi-layer SiC/SiC Materials

Specimen	Interface Frictional Stress (ksi)	Interface Toughness (J/m^2)
2T	8.67	2.58
2M	10.30	2.49
2K	11.74	2.24
4T	12.85	2.17
4M	11.64	2.42
4K	12.82	2.32
8T	11.29	2.65
8M	12.88	1.92
8K	12.66	2.23

associated with increasing total carbon thickness is not an important factor in establishing the sliding resistance.

FRACTURE MIRRORS, FIBER PULLOUT, PREDICTED STRENGTH, AND τ

The fracture surfaces of failed composites can provide a wealth of supplementary data useful for understanding the origins of the failure and the interfacial behavior. Specifically, fracture mirrors on the fracture surfaces of the pulled out fibers can be related to the as-processed fiber strength distribution (characteristic strength σ_c and Weibull modulus m) at the critical in-situ gauge length that controls the tensile strength and failure strain. The fiber pullout lengths are governed by a combination of the fiber strength (σ_c, m) and the interfacial sliding resistance τ by the relationship

$$\langle L \rangle = 0.25\,\lambda(m)\, r\sigma_c/\tau \qquad (4)$$

where λ is a known parameter around unity[2]. Therefore, measurements of both fracture mirrors and pullout lengths can be combined to quantitatively estimate τ. Moreover, the in-situ fiber strengths can be utilized to predict tensile strength as[2]

$$\sigma_{uts} = f\phi(m)\left(\frac{m}{2}\right)^{\frac{m}{m+1}}\left(1-e^{-2/m}\right)\sigma_c \qquad (5)$$

where ϕ is another known parameter.

Micrographs of the pullout from the 4T-2 specimen (gauge failure) and a typical fracture mirror are shown in

Figure 5a and b. The average pullout length is 93μm. The radius of a mirror is related to the fiber strength. Measuring a number of fracture mirrors allows for the creation of the statistical distribution of strengths {S} which are related to the desired quantities σ_c and m describing the true in-situ fiber strength

distribution. In measuring fracture mirrors for the 4T-2 specimen, only about 30% of the fibers exhibit measurable mirrors; 42% are too large and 38% are too small to assess reliably. This limits the accuracy of the determinations of the fiber strengths and, in particular, the Weibull modulus m of the fibers. Continuing nonetheless, we obtain σ_c= 388 ksi; m≈2. With the value λ=1.03 at m=2, we invert Eq. (4) to derive a value for τ of 8.1 ksi. This independent estimate is in reasonable agreement with the value of 12.5 ksi obtained from the hysteresis measurements. With the understanding that the fracture mirror data is not extremely accurate in this case, we nonetheless find that the two different methods for deriving τ are in the same range. In contrast, the estimate made using the observed 250μm crack spacing was only about 1.2 ksi – a factor of 10 difference; such a value of τ would lead to a predicted pullout of 625μm.

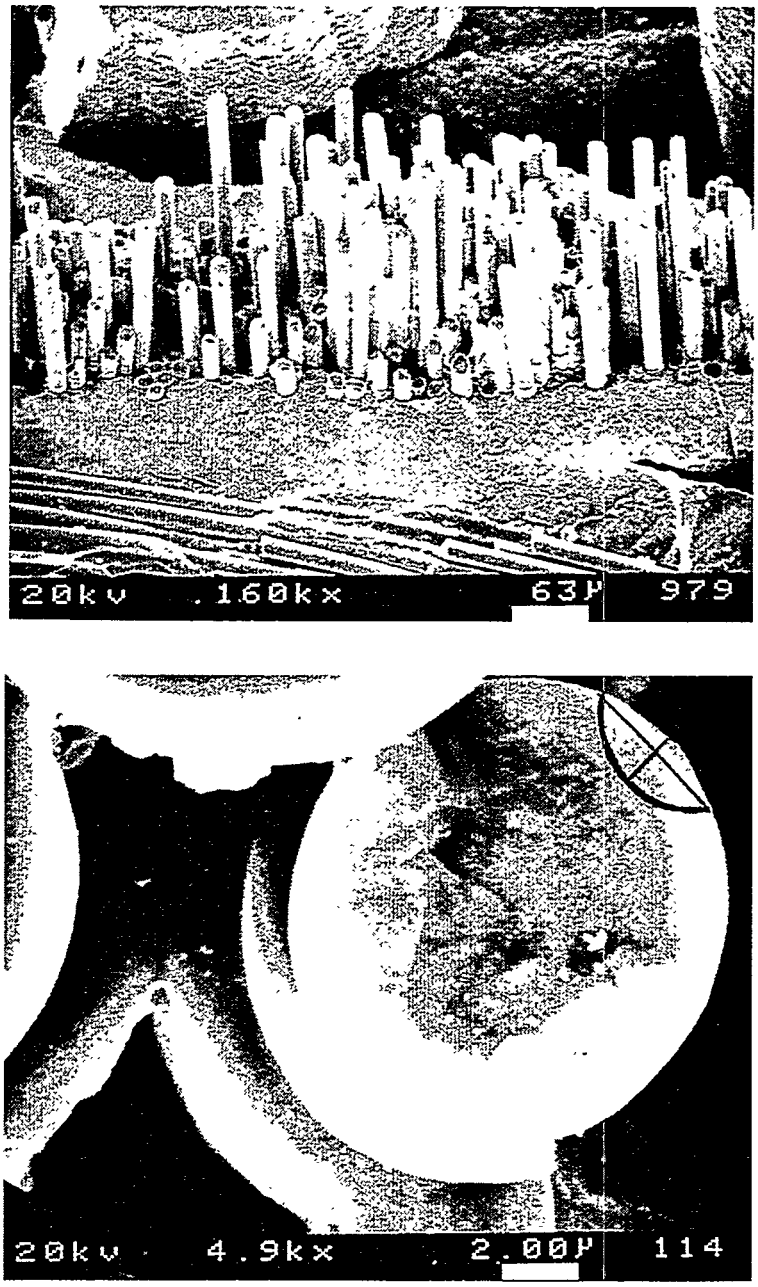

Figure 5a,b: Pullout and Fracture Mirror Photomicrographs

Using the derived values for σ_c and m, and f, the predicted composite strength is σ_{uts} = 39.2 ksi, which agrees well with the measured value of 36.7 ksi. The predicted failure strain is

$$\varepsilon_f = \left(\frac{\sigma_c}{E_f}\right)\left(\frac{2}{m}\right)^{\frac{1}{m+1}} = 0.89\%, \qquad (6)$$

which is larger than the measured value of 0.42%. Some of this deviation could be due to residual stress or flatness in the stress-strain. However, some materials exhibited much higher failure strains (see Table I), suggesting that such strains are indeed possible here.

SUMMARY

The main results of our experimental investigations on the current generation of Hyper-Therm multilayer SiC coated composites are as follows. We find that all of the materials examined show tough composite-like behavior, with large non-linearity and strain-to-failure. However, there are no significant differences among materials having different interface layer thicknesses or numbers of layers. Detailed analysis of the interfacial characteristics show all the materials to have similar interfacial sliding resistances. Microscopy on these materials shows that cracks penetrate the multilayers and tend to debond at the fiber/inner-coating interface. These observations are completely consistent with the common mechanical behavior observed. Analysis of the fracture mirrors and pullout on one specimen corroborates the interfacial sliding resistance measured using the hysteretic behavior, and indicates that the Hi-Nicalon fibers retain strength quite well after processing, in contrast to CG-Nicalon fibers. Performance of these and similar materials at elevated temperatures and under fatigue loadings will be the subject of future work. However, considerable opportunity exists for tailoring of the interface layer structure, carbon distribution, and layer roughnesses, to obtain even better materials.

Acknowledgements: Portions of this work were supported by the Department of Energy through a Phase II SBIR award to Hyper-Therm High Temperature Composites.

REFERENCES

1 Hyper-Therm, Inc., Huntington Beach, California

2 Curtin, W.A., "Theory of Mechanical Properties of Ceramic-Matrix Composites", *J. Amer. Ceram. Soc.*, Vol. 74, pp. 2837-2845, (1991).

3 Vagaggini, E., Domergue, J.-M., Evans, A.G., "Relationships between Hysteresis Measurements and the Constituent Properties of Ceramic Matrix Composites: I, Theory", *J. Amer. Ceram. Soc.*, Vol., 78, pp. 2709-2720, (1995).

4 He, M.Y., We, B.-X., Evans, A.G., Hutchinson, J.W., "Inelastic Strains due to Matrix Cracking in Unidirectional Fiber-Reinforced Composites", *Mech. Matl.*, Vol. 18, pp. 213-229, (1994).

HEAT TREATMENT EFFECTS FOR IMPROVED CREEP-RUPTURE RESISTANCE OF A Fe_3Al-BASED ALLOY

C. G. McKamey and P. J. Maziasz

Metals and Ceramics Division
Oak Ridge National Laboratory
Oak Ridge, TN 37831-6115

ABSTRACT

The iron-aluminide alloy FA-180, an Fe_3Al-based alloy with a composition of Fe-28Al-5Cr-0.5Nb-0.8Mo-0.025Zr-0.05C-0.005B (at.%), is of interest because of its improved creep-rupture resistance when compared to other Fe_3Al and FeAl-based alloys. Creep-rupture testing at 593°C and 207 MPa shows that FA-180 has a rupture life of about 100 h in the warm-rolled and stress relieved (1 h at 700-750°C) condition as compared to about 20 h for the FA-129 base alloy (Fe-28Al-5Cr-0.5Nb-0.2C). This report summarizes studies conducted in the last several years to determine the creep-rupture resistance of FA-180 as a function of the microstructures produced by varying the heat treatment temperature and cooling procedures. Solution-annealing for 1 h at 1150°C (air cooled) dramatically improved the creep-rupture life of FA-180 to about 2000 h. Transmission electron microscopy analysis showed that this strengthening was due to the precipitation of fine ZrC in the matrix and along grain boundaries. A further improvement in creep-rupture life to over 6000 h resulted from increasing the cooling rate (by quenching in oil or water) after solution annealing at 1150°C. The microstructure of the quenched specimen contained many fine dislocation loops instead of precipitates. During creep testing, these small loops evolved into a structure of larger dislocation loops and networks, resulting in significant strengthening at temperatures of 593-700°C.

INTRODUCTION

Past studies have shown that binary Fe_3Al possesses low creep-rupture strength compared to many other alloys, with creep-rupture lives of less than 5 h being reported for tests conducted at 593°C and 207 MPa.[1,2] The combination of poor creep resistance and low room-temperature tensile ductility due to a susceptibility to environmentally-induced dynamic hydrogen embrittlement[3-5] have limited use of these alloys for structural applications despite their generally excellent corrosion behavior.[6] With regard to the ductility problem, alloy development efforts have produced significant improvements, with ductilities of 10-20% and tensile yield strengths as high as 500 MPa being reported.[7,8] Initial improvements in creep resistance have been realized through small additions of B, C, Mo, Nb, and Zr.[1,9-13] Control of the amounts of these additions was also found to be important for producing improved weldability in these alloys.[12]

In recent years, further creep strengthening has been produced by using heat treatments to control the microstructure.[14,15] This paper summarizes work performed during the last three years to determine the effect of annealing temperature and the post-anneal cooling rate on creep-rupture properties and microstructural behavior.

EXPERIMENTAL PROCEDURES

The alloy composition used in this study was Fe-28Al-5Cr (at.%) with 0.5% Nb, 0.8% Mo, 0.025% Zr, 0.05% C, and 0.005% B (Oak Ridge National Laboratory designation FA-180). A 7-kg ingot was prepared by arc-melting and drop-casting into a chilled copper mold. Fabrication to an 0.8-mm-thick sheet was accomplished by hot-rolling, beginning at 1000°C and finishing at 600-650°C. After stress relieving for 1 h at 700°C, flat tensile specimens (0.8x3.18x12.7 mm) were mechanically punched from the rolled sheet. Before creep-rupture testing, specimens were annealed in air for 1 h at 1150°C and then were either air cooled to room temperature (slow cool) or were quenched in oil or water (faster cooling rate).

Creep-rupture tests were performed in air at temperatures from 593 and 750°C under stresses of 138 to 310 MPa (20-45 ksi). In order to obtain creep exponents and activation energies, minimum creep rates (MCR) were measured as the slope of the linear portion of the test curve and the data were plotted to a power-law equation. Tensile tests were also conducted at room temperature at a strain rate of 3.3×10^{-3}/s.

Scanning electron microscopy (SEM) using a Hitachi S-4100 (field emission gun) and optical metallography were used to study the microstructures and fracture modes. Analytical electron microscopy (AEM) using either a Philips CM30 (300 kV) or a CM12 [120 kV, with ultra-thin-window x-ray energy dispersive spectrometry (XEDS) detector] electron microscope was performed on samples cut from the gage portion of selected test specimens.

RESULTS AND DISCUSSION

As shown in Fig. 1, a 1-h heat treatment at 1150°C followed by air cooling to room temperature produced creep lives of over 2000 h for tests conducted at 593°C and 207 MPa. This is a significant improvement over the 100-h life observed for specimens of FA-180 heat treated at 750°C (signified by the horizontal line in Fig. 1). Especially interesting in Fig. 1 is the sharp dependence of creep strength on heat treating temperature. Transmission electron microscropy (TEM) of as-heat-treated specimens revealed the presence of a very fine DO_3 ordered structure within coarser B2 ordered domains (see Fig. 2). Also present in the matrix of specimens annealed at 1150°C was a fine dispersion of Zr-based precipitates (Fig. 2). These precipitates appeared to pin dislocations during creep, as shown in Fig. 3 for a specimen creep tested at 593°C.[14] This, together with an activation energy for creep of approximately 150 kcal/mole (a value which is about twice that obtained earlier[1] for the binary alloy heat treated at 750°C) and high creep exponents of 7-12 (ref. 15), indicated that the observed strengthening was being produced by a precipitation mechanism. The general conclusion was that the 1150°C heat treatment resulted in the dissolution of some of the coarse particles remaining from the melting and casting process. The finer Zr-based precipitates then formed during cooling or during the early stages of creep.

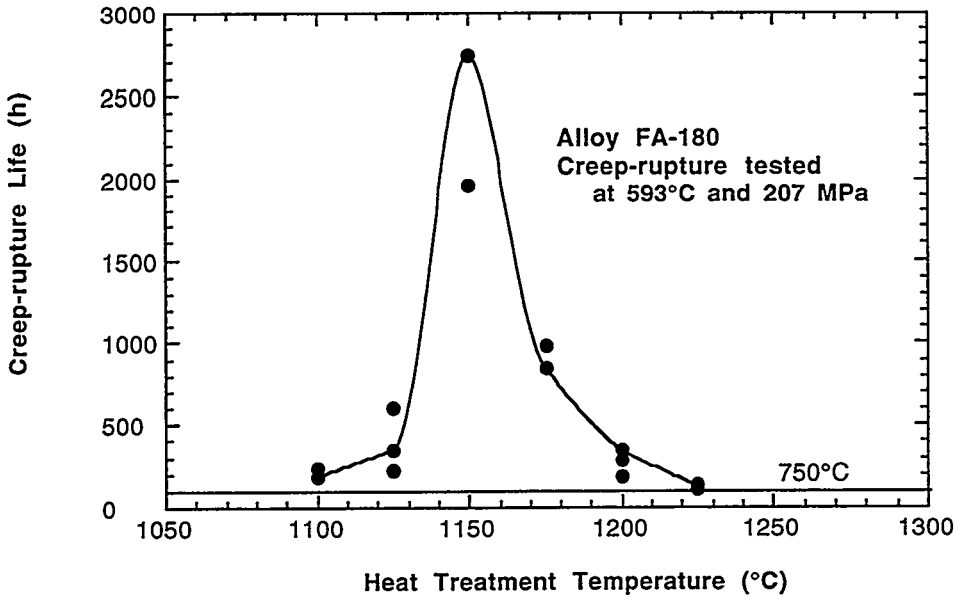

Fig. 1. Creep-rupture life as a function of heat treatment temperature for tests conducted on alloy FA-180 at 593°C and a stress of 207 MPa. The horizontal line at a life of 100 h represents the test of a FA-180 specimen heat treated for 1 h at 750°C.

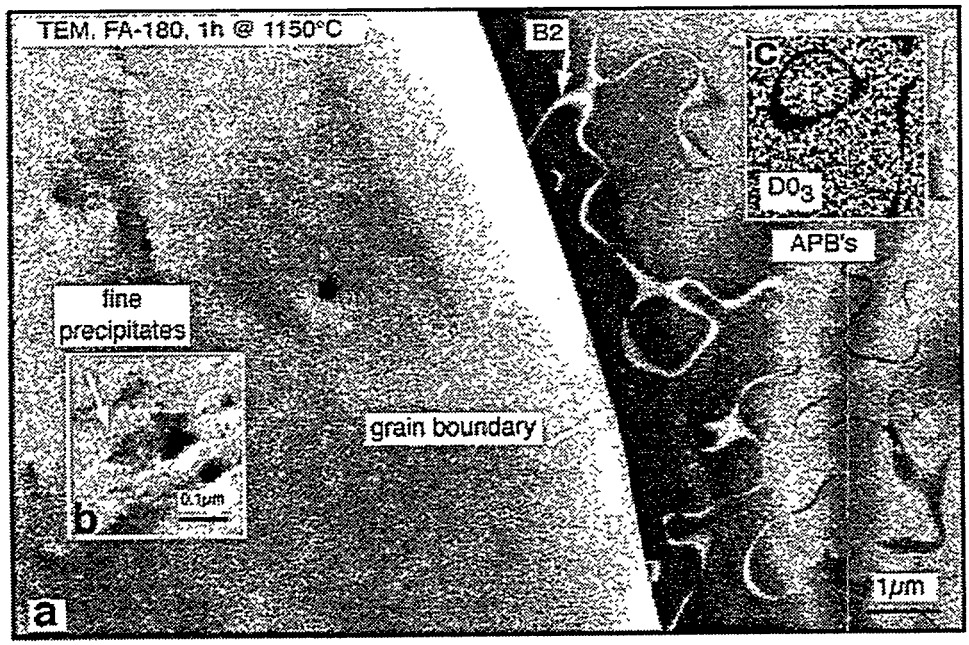

Fig. 2. Electron micrographs showing microstructural features of FA-180 as-heat-treated at 1150°C: (a) clean grain boundaries and low density of matrix dislocations, (b) fine matrix precipitates, and (c) the ordered structures produced by air cooling from 1150°C; fine DO_3 structure within coarse B2 structure.

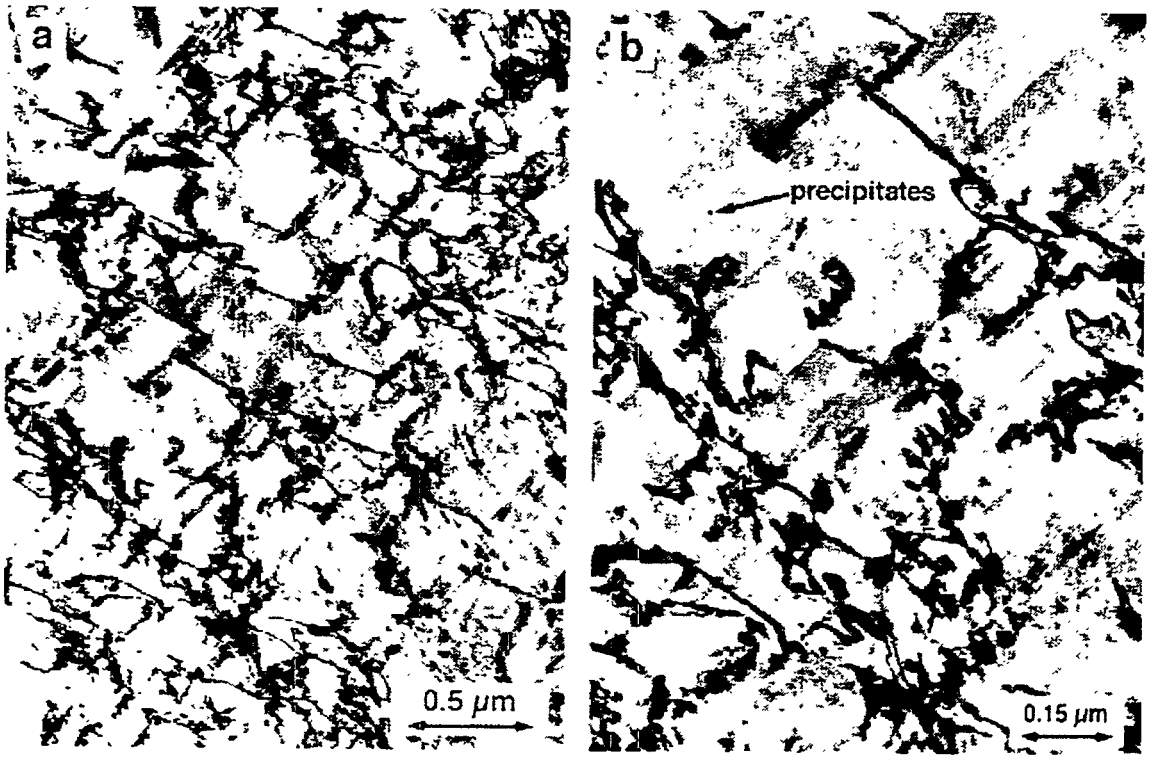

Fig. 3. Transmission electron micrographs showing (a) dislocation tangles and (b) fine matrix precipitates in alloy FA-180 air cooled from a heat treatment at 1150°C and creep tested at 593°C.

Creep-rupture tests were conducted on specimens cooled by different methods from the 1150°C heat treatment temperature and the data are presented in Table I. The more rapidly cooled specimens (oil or water quenched) exhibited the best resistance to creep. Even though the air-cooled specimen exhibited a very good rupture life of approximately 1959 h when tested at 593°C and 207 MPa, a specimen that had been quenched in oil showed no signs of rupturing (no increase in the very low, steady-state creep rate) after 6480 h, at which time the test was stopped. At more severe test conditions (650°C and 241 MPa), the ability of air-cooled specimens to resist creep was lost and failure occurred after an average of only 3 h, while an oil quenched specimen retained its resistance to rupture for over 240 h. Additionally, a water quenched specimen lasted 1637 h at 650°C and 241 MPa before rupture. In each case the fracture mode was observed to be ductile-dimpled rupture. This data suggest that there are fundamental differences in the strengthening mechanism for the quenched versus air cooled specimens.

The strengthening effect produced by quenching from 1150°C was also evident in room temperature tensile data (shown in Table II). The data in this table shows that quenching in oil resulted in hardening with an increase in yield strength from 255 to 481 MPa, even though the grain size was approximately 150 μm for both conditions. The hardening was also evident in the elongation to fracture. For all annealing conditions listed in Table II, the fracture mode was predominantly transgranular cleavage. These

Table I. Creep-Rupture Data for Alloy FA-180 as a Function of the Method Used for Cooling from the 1150°C Heat Treatment

Test Temp. (° C) Stress (MPa)	Air Cooled			Oil Quenched		
	Life (h)	Elong. (%)	MCR (/s)	Life (h)	Elong. (%)	MCR (/s)
593, 207	1959	10	8.3×10^{-7}	>6480[a]	>5	2.7×10^{-8}
650, 207	1059	11	5.5×10^{-7}	2180	14.4	8.3×10^{-8}
675, 207	2	32	1.8×10^{-3}	467	12	6.9×10^{-7}
700, 207	1	29	3.9×10^{-3}	104	11	5.5×10^{-6}
650, 241	3	42	2.2×10^{-3}	242	15	1.9×10^{-6}
650, 241				1637[b]	9[b]	2.2×10^{-7}
650, 241				86[c]	13[c]	2.6×10^{-6}

[a]Test stopped before rupture.
[b]Water-quenched from 1150° C.
[c]Oil quenched from 1150° C, then reannealed for 1 h at 750° C and air-cooled before creep testing.

Table II. Effect of Heat Treatment on Room Temperature Tensile Properties of Alloy FA-180

Heat treatment	Cooling medium	Yield strength (MPa)	Ultimate tensile strength (MPa)	Elongation (%)
1h/1150° C	air	255	347	2.7
1h/1150° C	oil	481	538	1.0
1h/1150° C+1h/750° C	oil/air	293	384	2.4

results are consistent with strengthening produced by quenched in defects, as has already been well established.[16-18] The reduced creep-rupture resistance and tensile yield strength of oil-quenched specimens that were reannealed at 750°C and air cooled (see data in Tables I and II) support this assumption.

Creep tests were conducted as a function of temperature (T) and stress (σ), and the data were fitted to a power-law creep equation of the form $\varepsilon = A\sigma^n(e^{-Q/RT})$ (ref. 19) in order to determine if the appparent activation energies for creep (Q) and the creep exponents (n) were the same in both the air-cooled and oil-quenched conditions (ε is the minimum creep rate, A is a constant, R is the gas constant). The results are shown in Figs. 4 and 5, respectively. At a stress of 207 MPa (30 ksi), the apparent Q for creep in the oil-quenched specimens was determined to be 84 kcal/mol, compared to a Q of 141 kcal/mol for air-cooled specimens. (The values of Q reported here are slightly different from those reported earlier[15,20] because more recent data have been included.) The large creep exponents shown in Fig. 5 for both the air-cooled and oil-quenched specimens are indicative of alloys which have been strengthened through some kind of

dislocation-pinning mechanism,[21-24] although the much larger slope for the oil-quenched specimens suggests a difference compared to the air-cooled specimens. For the oil-quenched specimens, a distinct change was observed in the slope of the minimum creep rate versus stress curve in Fig. 5. The break occurred at approximately 200-250 MPa, with the creep exponent decreasing from nearly 20 at the higher stresses to less than 1 at the lower stresses. Data for the air-cooled specimens also suggest the possibility of a change in slope at stresses below 100 MPa. At this point in the research, the reason for this change in slope is unknown, but it could relate to a change in the creep mechanism with stress level.

In order to better determine the stability of the microstructures produced by quenching from 1150°C, creep tests of oil-quenched specimens were conducted as a function of temperature at a constant stress of 207 MPa (30 ksi), and the data are included in Table I. The data indicate that a more efficient and stable strengthening mechanism is operative in the oil-quenched specimens. The air-cooled specimens showed good creep strengths at temperatures as high as 650°C. Above this temperature, however, the specimens quickly became severely weakened, resulting in dramatically reduced creep lives and large elongations to failure at 675°C and above. The oil quenched specimens, on the other hand, exhibited excellent creep strength at temperatures up to and including 650°C and a creep life of over 100 h at 700°C. This data supports the idea that the dislocation pinning mechanism operating in the oil-quenched specimens is more stable than that in the air-cooled specimens, in that it provides strengthening to higher temperatures and loses its effectiveness more gradually as the temperature is increased. This could mean that either more

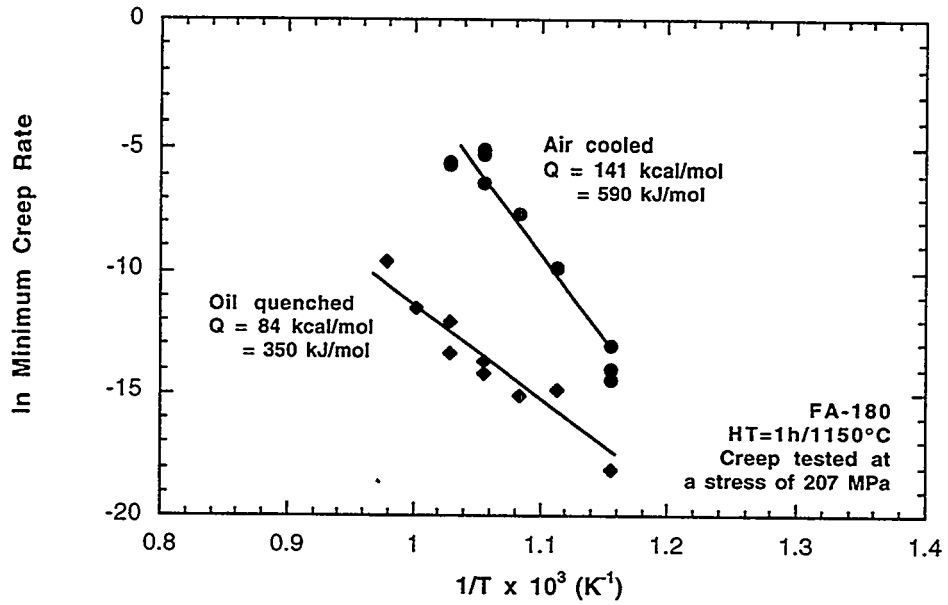

Fig. 4. Determination of creep activation energies for alloy FA-180 after either air cooling or oil quenching from a heat treatment at 1150°C.

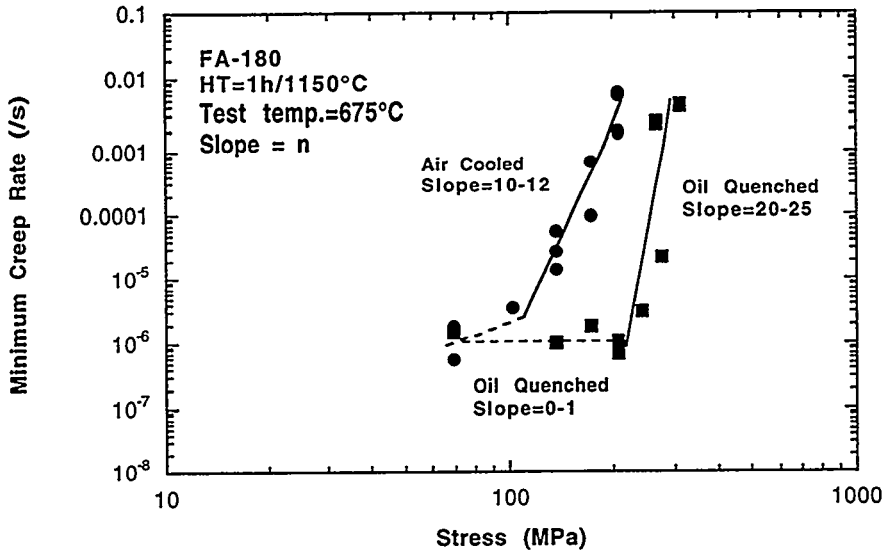

Fig. 5. Determination of creep exponents at a test temperature of 675°C for air cooled or oil quenched FA-180 heat treated at 1150°C.

and/or finer precipitates (identified previously as the strengthening mechanism in the air-cooled specimens[14]) are present in the oil-quenched specimens, or a more stable kind of pinning mechanism is active.

TEM examination of a control specimen oil quenched from 1150°C showed the presence of coarse B2 domains (Fig. 6) enclosing much smaller DO_3 domains, similar to the structure for the air cooled specimen shown in Fig. 2. In this as-heat-treated condition, the specimen also contained only a sparse distribution of dislocations. However, instead of a dispersion of precipitates, the oil-quenched specimen contained ultrafine (<10 nm) defects that were visible as black-white lobed images using g=011[B2] (see Fig. 6). These tiny defects exhibited a sharp line separating the black and white lobes that did not rotate with changes in g, consistent with the established contrast behavior of small edge loops.[25] Similar image analysis performed on the air-cooled specimen showed that those black-white strain contrast images did rotate with changes in g, consistent with their defect nature as 3-dimensional precipitates instead of 2-dimensional edge loops. Although loop nature (vacancy/interstitial) remains to be determined, many investigators observe higher vacancy concentrations in quenched FeAl type alloys,[16,17] and the likelihood of self-interstitial defects without irradiation is remote; therefore, it is reasonable to assume these are vacancy-type loops.

A TEM micrograph of the creep-induced microstructure in the gage of an oil-quenched specimen creep-tested at 593°C and 207 MPa for 6480 h without rupture is shown in Fig. 7. This microstructure clearly shows many large (>0.2 μm) loops uniformly dispersed throughout the matrix, accompanied by long pairs of 2-fold superdislocations. The growth of loops during creep from the "black dots" observed in

Fig. 6. TEM micrograph of alloy FA-180 showing B2 domains and fine dislocation loops (black dots) produced by oil-quenching from 1150°C (g=011 [B2], s=0).

the oil-quenched control specimen in Fig. 6 to the large loops observed in the creep-tested specimen is consistent with a vacancy nature. The loops observed in Fig. 7 have a basic square or rectangular shape, but with many kinks and jogs that would indicate intersections with network dislocations during creep. They appear to be distributed on orthogonal habit planes [either (110) or (100) types], and their contrast behavior (completely visible or invisible with g=011) is consistent with the behavior of edge loops.

The conclusion from TEM and the Q and n analyses is that vacancy loops, rather than fine precipitates, are the obstacles to dislocation motion in the oil-quenched material. The very low creep-rates and extended secondary creep regimes at 593°C and 650°C relative to the air-cooled material indicate that the vacancy loops are more effective barriers to dislocation climb despite their coarseness relative to the ultrafine precipitates observed in the air-cooled material. Their growth by vacancy absorption from the matrix and their direct interaction with intersecting network dislocations are likely factors making dislocation climb and glide through this loop structure more difficult than the ultrafine precipitate structure, consistent with the data in Table I. Although the general description of a mechanism which could produce creep-rupture strengthening through the pinning of dislocations on point defects would be similar for both precipitates and vacancies, fundamental differences (such as size of the defect, interfacial strength, coherency, stability as a function of temperature, etc.) could be responsible for the differences in Q and n shown in Figs. 4 and 5. The analysis of this data using a model for dispersion-strengthened materials[26] would probably be helpful in understanding the differences in the strengthening mechanisms involved.

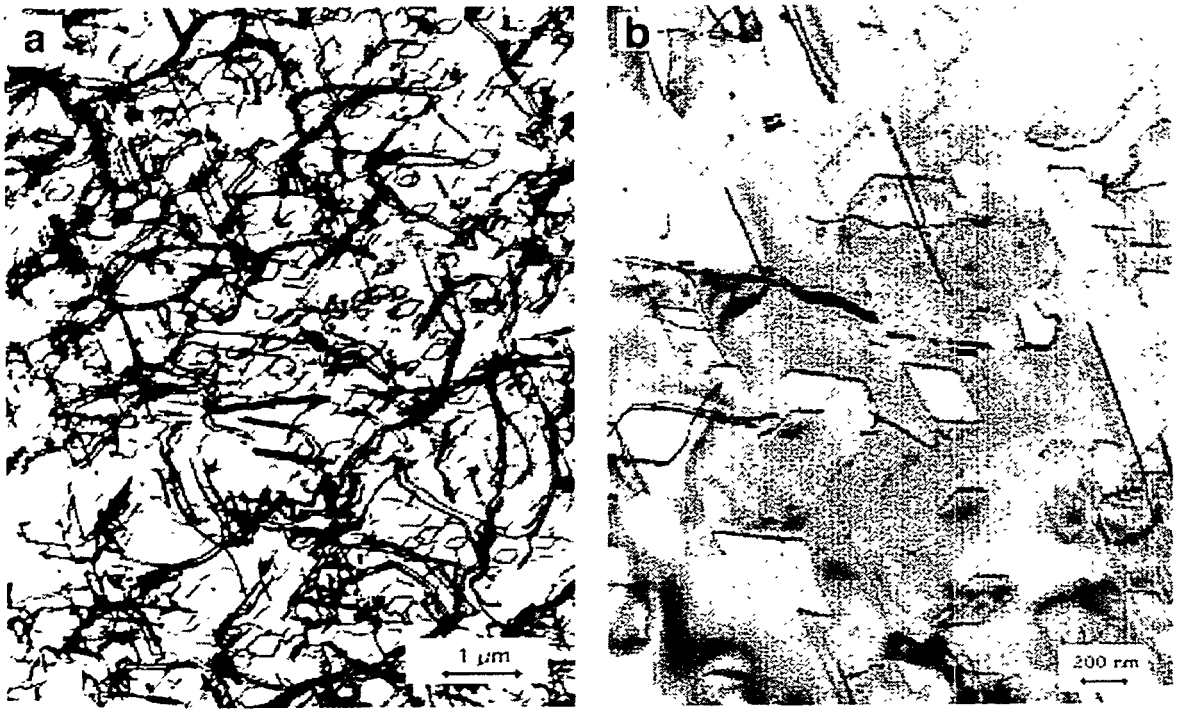

Fig. 7. TEM microstructure of a FA-180 (1150°C/oil quenched) specimen creep tested at 593°C/207 MPa for 6480 h without rupture (gage section), showing a) creep-induced dislocation network structure together with a dense dispersion of dislocation loops, and b) higher magnification showing several individual loops containing kinks and jogs, present on orthogonal habit planes (g=011[B2]).

CONCLUSIONS

The improved creep-rupture strength of an Fe_3Al-based alloy, FA-180 (Fe-28Al-5Cr-0.5Nb-0.8Mo-0.025Zr-0.05C-0.005B, at.%), was shown to be dependent on processing-induced microstructure. The creep-rupture resistance of this alloy was significantly improved by a solution-annealing heat treatment of 1 h at 1150°C. In specimens air-cooled from 1150°C, microstructural analysis revealed that strengthening was due to a fine dispersion of ZrC precipitates in the matrix and along grain boundaries. These precipi-tates were not observed in specimens annealed at higher or lower temperatures. Their presence was attributed to the dissolution of coarser ZrC particles (formed during the melting and casting process) during solution annealing, followed by reprecipitation during cooling or creep testing. Specimens solution-annealed at 1150°C and quenched to suppress the ZrC precipitation were found to be hardened by a dispersion of quenched-in loops that grew and evolved during creep testing at temperatures of 593-750°C and significantly delayed the onset of tertiary creep. Microstructural and creep activation/exponent analyses suggested that these were vacancy loops that acted as barriers to dislocation climb, resulting in the observed improvement in creep resistance.

ACKNOWLEDGEMENTS

This research was sponsored by the U.S. Department of Energy, Office of Fossil Energy, Advanced Research and Technology Development Materials Program, and by the Assistant Secretary for Energy Efficiency and Renewable Energy, Office for Industrial Technologies, Advanced Industrial Materials Program, under contract DE-AC05-96OR22464 with Lockheed Martin Energy Research Corp.

REFERENCES

1. C. G. McKamey, P. J. Maziasz, and J. W. Jones, *J. Mater. Res.*, **7(8)** (1992), 20892106.
2. C. G. McKamey, J. H. DeVan, P. F. Tortorelli, and V. K. Sikka, *J. Mater. Res.*, **6(8)** (1991), pp. 1779-1805.
3. C. T. Liu, C. G. McKamey, and E. H. Lee, *Scripta Metall. Mater.*, **24(2)** (1990), 385-90.
4. C. T. Liu and C. G. McKamey, in *High Temperature Aluminides and Intermetallics*, eds. S. H. Whang, C. T. Liu, D. P. Pope, and J. 0. Stiegler, (TMS, Warrendale, PA, 1990), pp. 133-151.
5. C. G. McKamey and C. T. Liu, in *Proceedings of ADVMAT/91, First International Symposium on Environmental Effects on Advanced Materials*, eds. R. D. Kane, (Houston, TX: NACE, 1992), paper no. 17-1.
6. P. F. Tortorelli and J. H. DeVan, in *Processing, Properties, and Applications of Iron Aluminides*, eds. J. H. Schneibel and M. A. Crimp (TMS, Warrendale, PA, 1994), pp. 257-70.
7. V. K. Sikka, *SAMPE Quart.*, **22(4)** (1991), 2-10.
8. V. K. Sikka, S. Viswanathan, and C. G. McKamey, *Structural Intermetallics*, eds. R. Darolia, J. J. Lewandowski, C. T. Liu, P. L. Martin, D. B. Miracle, and M. V. Nathal, (Warrendale, PA: The Metallurgical Society, 1993), 483-91.
9. P. J. Maziasz and C. G. McKamey, *Mater. Sci. & Eng.*, **A152** (1992), 322-34.
10. D. M. Dimiduk, M. G. Mendiratta, D. Banerjee, and H. A. Lipsitt, *Acta Metall.*, **36** (1988), 2947-58.
11. P. J. Maziasz, C. G. McKamey, and C. R. Hubbard, in *Alloy Phase Stability and Design*, eds. G. M. Stocks, D. P. Pope, and A. F. Giamei (MRS, Pittsburgh, PA, 1990), pp. 349-55.
12. C. G. McKamey, P. J. Maziasz, G. M. Goodwin, and T. Zacharia, *Mat. Sci. & Eng.*, **A174** (1994), 59-70.
13. D. G. Morris, M. Nazmy, and C. Noseda, *Scripta Metall. Mater.* **31**, 173 (1994).
14. C. G. McKamey and P. J. Maziasz, in *Processing, Properties, and Applications of Iron Aluminides*, eds. J. H. Schneibel and M. A. Crimp (TMS, Warrendale, PA, 1994), pp. 147-58.
15. C. G. McKamey, Y. Marrero-Santos, and P. J. Maziasz, in *High Temperature Ordered Intermetallic Alloys VI*, eds. J. A. Horton, I. Baker, S. Hanada, R. D. Noebe, and D. S. Schwartz (MRS, Pittsburgh, 1995), pp. 249-254.
16. P. Nagpal and I. Baker, *Metall. Trans.* **21A**, 2281 (1990).
17. A. Ball and R. E. Smallman, *Acta Metall.* **16**, 233 (1968).
18. D. J. Gaydosh and M. V. Nathal, *Scripta Metall. Mater.* 24, 1281 (1990).
19. O. D. Sherby and P. M. Burke, *Prog. Mat. Sci.* 13, 325 (1968).
20. C. G. McKamey and P. J. Maziasz, in *Proceedings of the Tenth Annual Conference on Fossil Energy Materials*, compiled by N. C. Cole and R. R. Judkins, ORNL/FMP-96/1, Aug. 1996, pp. 215-23.
21. O. D. Sherby and P. M. Burke, *Prog. Mater. Sci.* **13**, 325 (1968).
22. R. Lagneborg and B. Bergman, *Met. Sci. J.* **10**, 20 (1976).
23. K. Sadananda, H. Jones, C. R. Feng, and A. K. Vasudevan, in *High Temperature Ordered Intermetallic Alloys IV*, eds. L. A. Johnson, D. P. Pope, and J. O. Stiegler (MRS, Pittsburgh, 1991), pp. 1019-25.
24. I. Jung, M. Rudy, and G. Sauthoff, in *High Temperature Ordered Intermetallic Alloys II*, eds. N. S. Stoloff, C. C. Koch, C. T. Liu, and O. Izumi (MRS, Pittsburgh, 1987), pp. 263-74.
25. J.W. Edington, *Interpretation of Transmission Electron Micrographs*, Monograph 3 in Practical Electron Microscopy in Materials Science, N.V. Philips, Eindhoven, Netherlands, 1975.
26. J. Rösler and E. Arzt, *Acta Metal. Mater.* 38(4), 671 (1990).

THE EFFECTS OF COMPOSITION ON THE ENVIRONMENTAL EMBRITTLEMENT OF Fe_3Al Alloys

D. A. Alven and N. S. Stoloff

Rensselaer Polytechnic Institute
Troy, New York 12180-3590

Fe - 28 Al - 5Cr

ABSTRACT

This paper reviews recent research on embrittlement of iron aluminides at room temperature brought about by exposure to moisture or hydrogen. The tensile and fatigue crack growth behavior of several Fe28-Al-5Cr alloys with small additions of Zr and C are described. It will be shown that fatigue crack growth behavior is dependent on composition, environment, humidity level, and frequency. Environments studied include vacuum, oxygen, hydrogen gas, and moist air. All cases of embrittlement are ultimately traceable to the interaction of hydrogen with the crack tip.

INTRODUCTION

This paper is concerned with the embrittlement of Fe28-Al-5Cr alloys containing various levels of Zr and C by moisture and by water vapor. The iron aluminides have been considered to be brittle when tested in air at room temperature, failing by transgranular cleavage or by intergranular cracking at elongations of 5% or less. However, when tested in dry environments, ductilities of up to 25% are observed [1 - 3]. It is generally agreed that moisture in air, in contact with aluminum-rich alloys, is broken down into hydrogen and oxygen; embrittlement actually results from the penetration of hydrogen into the lattice [1 - 4].

Several techniques have been devised to avoid embrittlement or to reduce its severity. These include use of dry oxygen or high vacuum environments. However, even when tested in air the ductility of the aluminides is markedly influenced by aluminum content, presence of solutes and control of the microstructure. Alloys with 28a%Al display the highest ductility in the Fe_3Al group, and Cr is the most effective solute to further increase ductility in the presence of moisture [2]. Other techniques to improve ductility include control of grain size and shape, changes in the type and decreases in the degree of long range order, and the addition of microalloying elements [4].

This paper will discuss the rate-limiting mechanism for fatigue crack growth behavior of several Fe-28Al-5Cr alloys containing Zr and C in moist air, oxygen, vacuum and hydrogen gas environments.

Under cyclic loading, crack growth rates have been shown to vary by orders of magnitude between wet and inert (dry) environments [3, 5 - 7]. The results of our crack growth experiments will be discussed in the context of dislocation-assisted transport of hydrogen to crack tips.

Experimental Alloys and Procedure

The alloys studied, all of which were supplied by Oak Ridge National Laboratory (ORNL), are listed in Table 1. Note that the Zr and C containing alloys are partially recrystallized; their processing was governed by recommendations from ORNL to maximize tensile ductility. All alloys were tested in the partial ordered B2 state. All tensile tests were run at a strain rate of $3x10^{-4}$ s^{-1} on cylindrical specimens with a 12.7mm long by 5.7mm diameter gauge length. Fatigue crack growth experiments were performed on all alloys in air, oxygen gas(1.3 atm), and hydrogen gas(1.3 atm), as well as in vacuum. All gases used in this study were of ultra high purity grade, with a maximum water vapor content of 3 ppm Fatigue crack growth tests were run at a frequency of 20Hz and an R ratio (σ_{min}/k_{max}) = 0.5, except where noted. Compact tension specimens were used for all fatigue tests which were 31.7mm x 30.5mm x 4.8mm thick.

TABLE 1. Composition of Iron Aluminide Alloys (Atomic %)

	Ternary	1%Zr-C	0.5%Zr-C	0.5%Zr
Fe	67.0	65.95	66.45	66.5
Al-	28.0	28.0	28.0	28.0
Cr	5.0	5.0	5.0	5.0
Zr	-	1.0	0.5	0.5
C	-	0.05	0.05	-
g-size	180μm	*	*	*

*-partially recrystallized

Experimental Results

Effect of Composition

A summary of fatigue crack growth data in air for all alloys studied to date appears in Fig. 1. The fatigue crack growth data illustrate the effect of order and microstructure on the embrittlement of iron aluminides. The highest crack growth rate is found in the disordered, low aluminum content

FAP-Y alloy, while the lowest rate is found in the B2 ordered 0.5%Zr-C alloy. For Fe_3Al alloys the imperfect ordered B2 state has a lower crack growth rate than the highly ordered DO_3 state [3, 6].

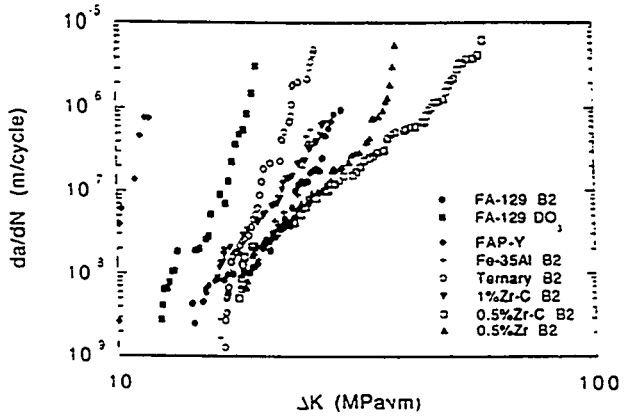

Fig. 1 Fatigue crack growth of iron aluminides in air at 25°C

The influence of environment on fatigue crack growth data for the Zr-containing alloys has been reported previously[5]. A summary of threshold stress intensities and critical stress intensities for the four alloys are shown in Fig. 2a) and b). Zr has its major effect in the high ΔK region (above the threshold region) and that 1 at% Zr is less effective than is 0.5 at% Zr. The presence or absence of carbon seems to have little influence, perhaps because of the high Zr/C ratios used in this work (see Table 1). No evidence of carbides or oxides were seen by TEM.

Fibrous tearing was predominant in all environments for the Zr-containing alloys except for 0.5%Zr and 1%Zr-C in hydrogen [5]. By contrast, FA-129 and the ternary alloy show predominantly cleavage in all environments [3, 6]. Dimpled rupture was only evident in FA-129 in the inert O_2 environment.

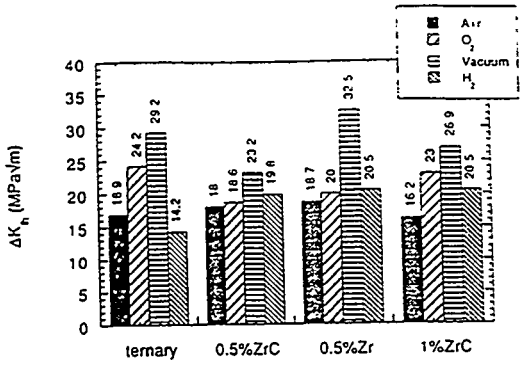

Fig. 2. (a) Threshold stress intensities in iron aluminides fatigued at 25°C. Frequency = 20Hz, R = 0.5.

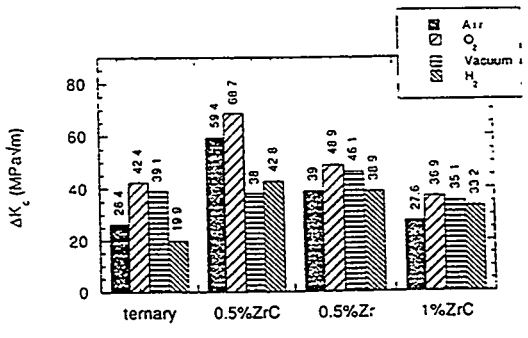

(b) Critical stress intensities in iron aluminides fatigued at 25°C. Frequency = 20Hz, R = 0.5.

Effect of Humidity

The effect of increased humidity on the FCG resistance in 0.5%Zr-C is shown in Fig. 3. Similar data were obtained for the 0.5%Zr and 1%Zr-C alloys. The fatigue test conducted in oxygen is also shown in Fig. 3, as it is considered the inert reference environment.

An increase in humidity level had no effect on ΔK_{th} in 0.5%Zr-C. $\Delta K(10^{-7})$ was reduced 16% from 29.0 MPa$\sqrt{m}$ in 21%rH air to 24.3 MPa$\sqrt{m}$ in 81%rH. The embrittling effect of increased humidity was evident in 0.5% Zr-C, since ΔK_c was reduced from 59.4 MPa$\sqrt{m}$ to 37.2 MPa$\sqrt{m}$.

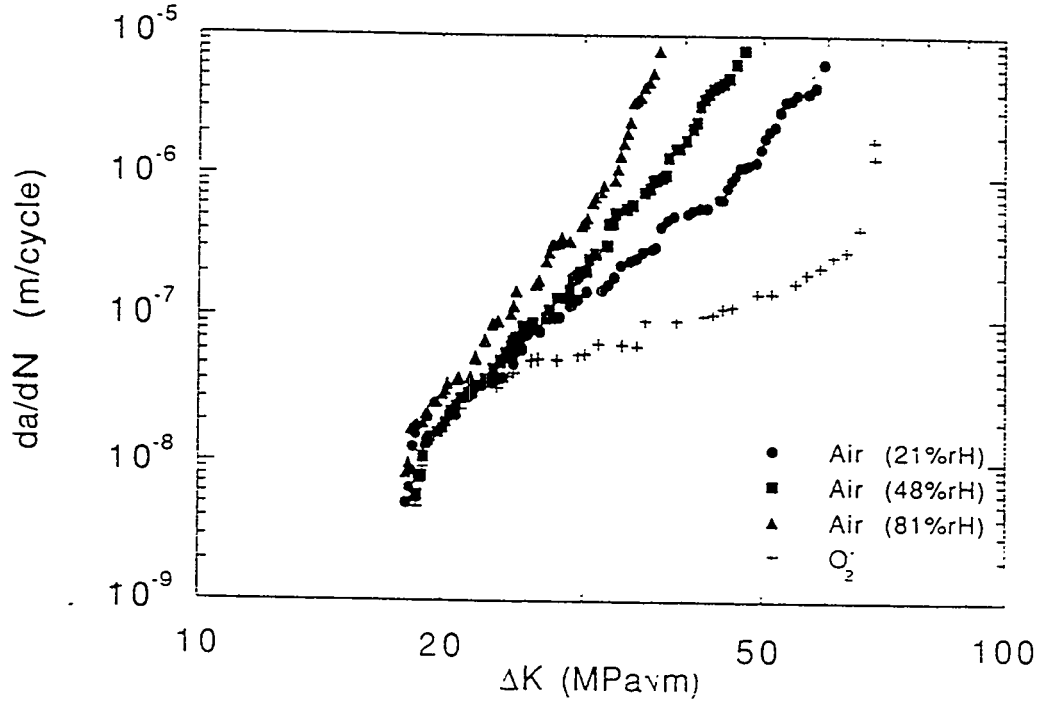

Fig. 3. Influence of humidity on fatigue crack growth of the 0.5%Zr-C alloy at 25°C.

Effect of Frequency

The effect of decreasing the test frequency for the 0.5%Zr-C alloy is shown in Fig. 4. All tests were run at a constant humidity level of 21%rH. Also shown is the fatigue test conducted in oxygen.

As can be seen in Fig. 4, the lower frequencies increased the rate of fatigue crack growth, and had a significant effect on both the threshold and critical stress intensities. The largest decrease in FCG resistance was seen between 20Hz and 2Hz, with the curves for 2Hz, 0.2Hz and 0.08Hz falling close together. While the FCG resistance and ΔK_c decreased as the frequency was lowered, ΔK_{th} increased, although the effect was small.

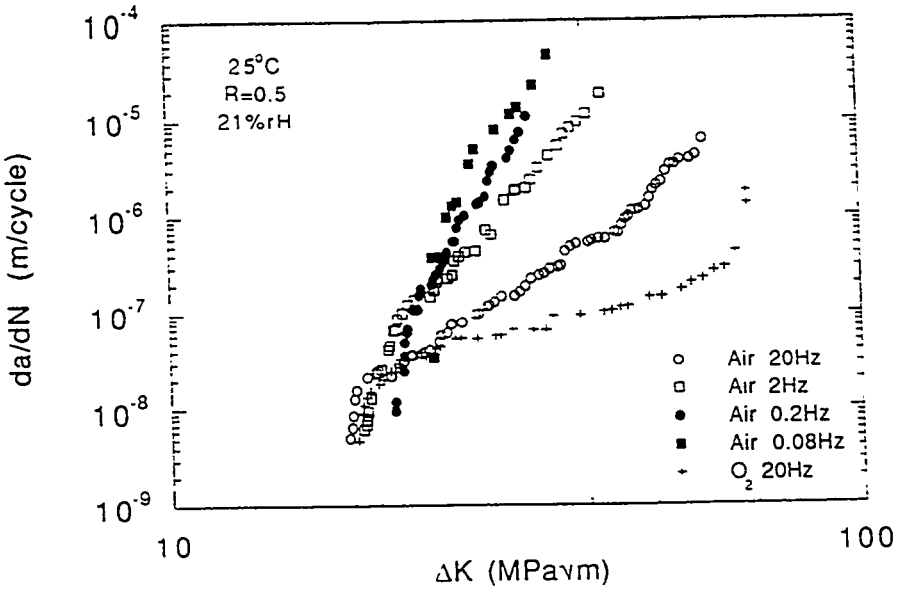

Fig. 4. Effect of frequency on 0.5%Zr-C fatigued in 21%rH air at 25°C. R = 0.5.

DISCUSSION

In terms of alloying, the addition of 0.5% Zr to Fe-28Al-5Cr results in an increase in tensile ductility and a decrease in the crack growth rate as compared with the other alloys. Carbon additions have been found to increase the critical stress intensity with little effect on the crack growth rate. There exists a limit to the beneficial effects of alloying with Zr, as the 1% Zr alloy has a higher crack growth rate than either of the 0.5% Zr alloys. Sikka [8] has previously shown that additions of 0.1 at% Zr + 0.01 at% C and 0.2 at% Zr +0.02 at% C give higher ductilities than 1 or 2 at% Zr. This suggests that the optimum Zr content for high ductility is between 0.1 and 0.5 at% Zr.

Fractographic evidence indicates two mechanisms by which the zirconium additions affect the crack growth rates in the Fe_3Al, Cr alloys. First, all the Zr-containing alloys exhibited a fibrous, transgranular surface when fatigued in oxygen (Fig. 5(b)). This is typical of ductile materials. Only the ternary alloy exhibited a characteristically brittle fracture surface in oxygen, which consisted of mixed transgranular and intergranular failure. The indications from the shift in fracture mode of the Zr-containing alloys when compared to the ternary alloy is that the addition of zirconium strengthens the grain boundaries. Previous research [9] has shown that the addition of B and Zr shifted the fracture path of several iron aluminides from intergranular to transgranular, but it was believed that the boron addition had caused the grain boundary strengthening. In this study, the addition of 0.5 at.% Zr resulted in a shift of fracture mode which indicates that zirconium also strengthens grain boundaries in Fe_3Al.

Second was the observation of some intergranular failure in 0.5%Zr and 1%Zr-C in hydrogen-

containing environments. These results are interesting as most studies on iron aluminides have shown no effect on the fracture path in alloys of less than 35% Al. Previous work supports the view that a dislocation-transport mechanism in iron aluminides is responsible for embrittlement [6, 10] . Such a mechanism would allow for increased hydrogen contents at the grain boundaries where the dislocations pile-up. Trapping of the hydrogen by precipitates along the grain boundaries could lead to premature failure, when compared to the bulk, due to localized embrittlement. The appearance of the intergranular facets in 0.5%Zr and 1%Zr-C in hydrogen bearing environments, as compared to fibrous tearing fracture in an inert environment, indicates that excess hydrogen is being delivered to, or trapped, at the grain boundaries.

An increase in the amount of intergranular facets with increased Zr content was noticed. This may also be indicative of hydrogen trapping by zirconium-containing precipitates observed by TEM. Several studies [11, 12] have noted that increased precipitation of high binding energy and high saturability traps, with respect to hydrogen, decreases the resistance to hydrogen embrittlement.

A third explanation for the increased resistance to embrittlement might lie in effects of zirconium on the oxidation behavior of these alloys. The amount of reactive elements needed has been shown to be between 0.1 and 0.2 at%-, deterioration of scale adhesion was noted with additions of over 1 at%[13-15]. While it has not been shown that this same effect is operable at room temperature, it is possible that zirconium could influence the Al_2O_3 layer which, in turn, could influence the hydrogen-metal reactions.

Previous research has shown that dislocation-assisted diffusion is the rate limiting process in hydrogen embrittlement during fatigue crack growth of iron aluminides [10]. This phenomenon has been observed in a number of materials and is responsible for increased penetration depths of hydrogen over that caused by volume diffusion [16-19]. In this section, the model proposed by Castagna [10] will be applied to 0.5%Zr-C.

In dislocation-assisted diffusion, an atmosphere of hydrogen develops about a dislocation generated near the crack tip. As the dislocation travels away from the tip, the hydrogen is dragged with it through the lattice. The penetration depth of hydrogen ahead of the crack tip is equal to the dislocation velocity times the time available per cycle, that is V/2f where V is the dislocation velocity and f the test frequency. In the model proposed by Tien and Richards [18], the predicted maximum dislocation velocity that can be achieved before the hydrogen atmosphere is stripped away from the dislocation is used to determine the maximum penetration depth for dislocation assisted transport. Calculations based on this model for the 0.5%Zr-C alloy tested at frequencies ranging from 0.08Hz to 20Hz showed that the penetration depth increased by over 200 times, from 1.29×10^{-8}m to 3.24×10^{-6}m as the frequency decreased from 20Hz to 0.08Hz.

Castagna[10] proposed that the corrosion-fatigue expression for crack growth contains both a stress intensity and frequency dependence:

$$\left(\frac{da}{dN}\right)_{cf} = A\,\Delta K^{m} r^{n} \qquad \text{Eq. 1}$$

In Eq. 1, r is the penetration depth of hydrogen ahead of the crack tip, and A is a constant. Eq. 1 indicates that there is no embrittlement if either the applied stress intensity is zero or the internal hydrogen concentration is zero and the frequency effect is reflected in the penetration depth term as the depth will increase over one cycle as the frequency decreases. If it is assumed that the mechanical component of Eq. 1 is independent of frequency and that the stress corrosion component is zero, the total crack growth rate in an embrittling environment, (da/dN), can then be expressed as a superposition of the response in the inert environment, $(da/dN)_i$, and the corrosion fatigue term as:

$$\left(\frac{da}{dN}\right) = \left(\frac{da}{dN}\right)_{i} + \left(\frac{da}{dN}\right)_{ct} \qquad \text{Eq. 2}$$

In order to verify the validity of Eq. 1, it can be rearranged as:

$$\mathrm{Log}\left(\frac{da}{dN}\right)_{ct} = \mathrm{Log}(A) + m\,\mathrm{Log}(\Delta K) + n\,\mathrm{Log}(r) \qquad \text{Eq. 3}$$

and a plot of $\mathrm{Log}(da/dN)_{cf}$ vs. $\mathrm{Log}(r_{max})$ at constant ΔK should yield a straight line with a slope of n and an intercept of $\mathrm{Log}(A) + m\mathrm{Log}(\Delta K)$. In order to create this plot, the corrosion-fatigue term must be determined from Eq. 3. This is done assuming that $(da/dN)_i$ can be taken as the response in the inert oxygen environment. The crack growth data for 0.5%Zr-C in air have been broken down into the purely mechanical component and the corrosion-fatigue component, $(da/dN)_{cf}$ at the frequencies of 20 to 0.08 Hz. The plots of Eq. 3 are shown in Fig. 7 for ΔK = 27, 29, and 31 MPa$\sqrt{m}$.

As can be seen in Fig. 5, the correlation is excellent, and from the least squares fit the exponent n in Eq. 1 is 0.74. To find the values of A and m in Eq. 1, the latter is rearranged into:

$$\mathrm{Log}\left[\frac{\left(\frac{da}{dN}\right)_{cf}}{r_{max}^{0.74}}\right] = \mathrm{Log}(A) + m\,\mathrm{Log}(\Delta K) \qquad \text{Eq. 4}$$

Plotting Eq. 4 for all values of ΔK and frequencies yields a single frequency-modified curve and from a least squares fit the values of A and m are 4.9×10^{-19} and 11.7, respectively.

As a final check, a plot of $(da/dN)_{cf}$ vs. $(r_{max})^{0.74}$ should result in a straight line for each applied stress intensity. Once again the correlation was excellent and showed that in fatigued 0.5%Zr-C hydrogen moves into the lattice ahead of the crack tip by a dislocation-assisted transport mechanism.

It should be noted that even though the degree of embrittlement increased dramatically with decreased frequency the exponent, n, was unchanged. This indicates that the embrittlement does little to

change the mobility, ease of generation , or hydrogen-carrying capacity of the dislocations in 0.5%Zr-C. Due to this observation, any hydrogen-metal interaction which involves a change in dislocation mobility, such as hydrogen enhanced plasticity or inhibited dislocation motion in the presence of hydrogen, can be ruled out.

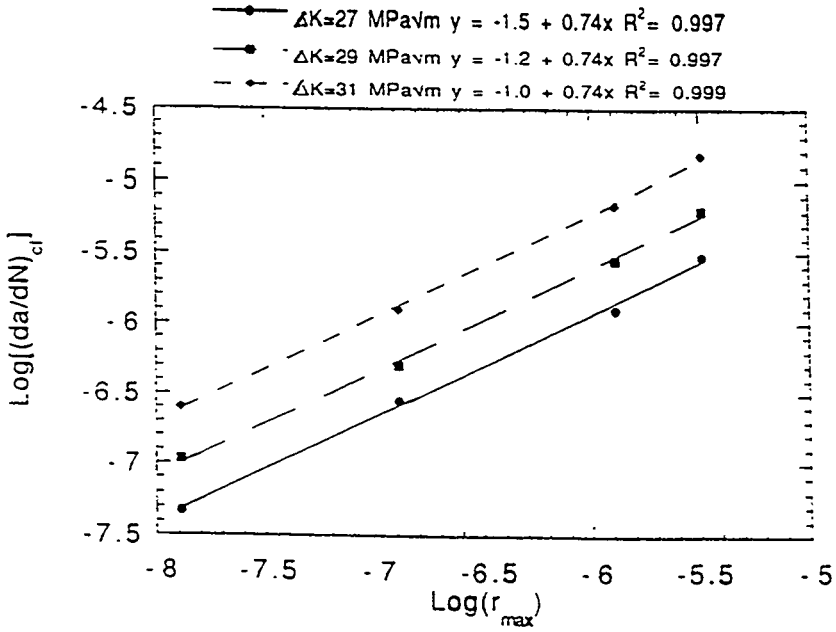

Fig. 5 Log-log plot of $(da/dN)_{cf}$ vs. maximum hydrogen penetration depth due to dislocation transport in 0.5%Zr-C fatigued in 21%rH air.

TABLE 2. Comparison of Constants in Eq.4 for 0.5%Zr-C and FA-129

Values	0.5%Zr-C	FA-129
n	0.74	0.52
m	11.7	10.3
A	4.9×10^{-19}	3.8×10^{-18}

The physical meaning of the exponent, n, in Eq. 1 has been described as either related to the quantity of hydrogen dislocations can carry into the plastic zone and the concentration of hydrogen required to enhance crack growth, or related to the distribution of penetration depths of the hydrogen-bearing dislocations [10]. Table 2 lists the calculated constants found for the two alloys analyzed. 0.5%Zr-C is found to have higher exponents and a lower pre-exponential constant than FA-129. As shown in Fig. 1, 0.5%Zr-C also displays a higher fatigue crack growth resistance than does FA-129.

SUMMARY

The susceptibility to moisture-induced hydrogen embrittlement in Fe_3Al,Cr alloys is reduced by the addition of zirconium. The beneficial effects of zirconium on the ductility and fatigue crack growth resistance of Fe_3Al,Cr alloys are limited to below 1 at.%. Zr. Fatigue crack growth resistance was seen to decrease with increased humidity level in air. The possible mechanisms for increased resistance to moisture-induced hydrogen embrittlement due to the addition of zirconium are; a) increased grain boundary strength, b) trapping of hydrogen by zirconium rich precipitates, and c) effects on the oxidation behavior. The zirconium to carbon ratio greatly influences the ductility, as proposed by Sikka [8] , and fatigue crack growth behavior in iron aluminides. Dislocation-assisted transport is responsible for the motion of hydrogen atoms released from water vapor through the lattice of 0.5%Zr-C, and this process is the rate limiting step in the hydrogen embrittlement that occurs during fatigue crack growth. 0.5%Zr-C exhibits the highest fatigue crack growth resistance in both inert and embrittling environments compared to the ternary alloy, 0.5%Zr, 1%Zr-C and to all other Fe_3Al alloys previously tested in this laboratory.

Acknowledgment

Research supported by the US Department of Energy, Fossil Energy Program, under Martin Marietta Energy Subcontract No. 19X-SF521C

REFERENCES

1. C. T. Liu, E. H. Lee and C. G. McKamey, Scr. Metall., vol. 23, pp. 875-880 (1989).

2. C. G. McKamey, J. A. Horton and C. T. Liu, J. Mater. Res., vol. 4, pp. 1156-1163 (1989).

3. A. Castagna, P. J. Maziasz and N. S. Stoloff, Influence of Environment on Crack Growth Resistance of an Fe_3Al,Cr Alloy, I. Baker, R. Darolia, J. D. Whittenberger, M. H. Yoo, Eds., High Temperature Ordered Intermetallic Alloys V (MRS Symp. Proc., Pittsburgh, 1993), vol. 288, pp. 1043-1048.

4. N. S. Stoloff and C. T. Liu, Intermet., vol. 2, pp. 75-87 (1994).

5. D. A. Alven and N. S. Stoloff in Proc. Tenth Annual Conf. on Fossil Energy Materials, ORNL/FMP-96/1, May 1996, pp. 225-235.

6. A. Castagna and N. S. Stoloff, Mater. and Design, vol. 14, pp. 73-75 (1993).

7. D. A. Alven and N. S. Stoloff, Scr. Metall., vol. 34, pp. 1937-1942 (1996).

8. V. K. Sikka, Oak Ridge National Laboratory, unpublished work, (1996).

9. C. G. McKamey, P. J. Maziasz, G. M. Goodwin and T. Zacharia, Mater. Sci. Eng., vol. 174, pp. 59-70 (1994).

10. A. Castagna, Ph.D. Thesis, Rensselaer Polytechnic Institute (1995).

11. B. G. Pound, Acta Metall. Mater., vol. 38, pp. 2373-2381 (1990).

12. B. G. Pound, Acta Metall. Mater., vol. 42, pp. 1551-1559 (1994).

13. P. Y. Hou and J. Stringer, Mater. Sci. Eng., vol. 202, pp. 1-10 (1995).

14. A. M. Huntz, Mat. Sci. Eng., vol. 87, pp. 251-260 (1987).

15. J. Stringer, Mater. Sci. Eng., vol. 120, pp. 129-137 (1989).

16. J. Albrecht, I. M. Bernstein and A. W. Thompson, Met. Trans. A, vol. 13A, pp. 811-820 (1982).

17. M. R. Louthan, G. R. Caskey, J. A. Donovan and D. E. Rawl, Mat. Sci. Eng., vol. 10, pp. 357 (1972).

18. J. K. Tien and R. J. Richards, Scripta Metall., vol. 9, pp. 1097-1101 (1975).

19. J. K. Tien, A. W. Thompson, I. M. Bernstein and R. J. Richards, Metall. Trans. A, vol. 7A, pp. 821-829 (1976).

EFFECTS OF TITANIUM AND ZIRCONIUM ON IRON ALUMINIDE WELDMENTS

B.L. Mulac*, R.P. Burt**, G.R. Edwards*, and S.A. David†

*Center for Welding, Joining, and Coatings Research
Colorado School of Mines
Golden, CO 80401

**Alumax Technical Center
Golden, CO 80401

†Oak Ridge National Laboratory
Metals and Ceramics Division
Oak Ridge, TN 37831

ABSTRACT

When gas-tungsten arc welded, iron aluminides form a coarse fusion zone microstructure which is susceptible to hydrogen embrittlement. Titanium inoculation effectively refined the fusion zone microstructure in iron aluminide weldments, but the inoculated weldments had a reduced fracture strength despite the presence of a finer microstructure. The weldments fractured by transgranular cleavage which nucleated at cracked second phase particles. With titanium inoculation, second phase particles in the fusion zone changed shape and also became more concentrated at the grain boundaries, which increased the particle spacing in the fusion zone. The observed decrease in fracture strength with titanium inoculation was attributed to increased spacing of second phase particles in the fusion zone.

Current research has focused on the weldability of zirconium- and carbon-alloyed iron aluminides. Preliminary work performed at Oak Ridge National Laboratory has shown that zirconium and carbon additions affect the weldability of the alloy as well as the mechanical properties and fracture behavior of the weldments. A sigmajig hot cracking test apparatus has been constructed and tested at Colorado School of Mines. Preliminary characterization of hot cracking of three zirconium- and carbon-alloyed iron aluminides, each containing a different total concentration of zirconium at a constant zirconium/carbon ratio of ten, is in progress. Future testing will include low zirconium alloys at zirconium/carbon ratios of five and one, as well as high zirconium alloys (1.5 to 2.0 atomic percent) at zirconium/carbon ratios of ten to forty.

TITANIUM INOCULATION

The superior oxidation and sulfidation resistance and good high temperature strength (up to 600°C) of iron aluminides make these materials attractive alternatives to stainless steels for structural applications in the fossil energy industry [1]. Iron aluminides also conserve strategic elements, such as chromium, and have the potential to be relatively low cost materials. However, the low room temperature ductility (less than 5 percent) observed in Fe_3Al-based alloys has hindered the implementation of iron aluminides for industrial applications.

Liu et al. [2, 3] improved the room temperature ductility of Fe_3Al-based alloys by changing the environment in which tensile testing was performed. The measured elongation improved from 2.2% in air, to 5.4 and 11.3% when tested in vacuum and dry oxygen, respectively. Liu et at. concluded that iron aluminides were intrinsically ductile and that the observed brittle behavior was the result of an extrinsic effect, namely hydrogen embrittlement. Recent research performed on iron aluminides at Oak Ridge National Laboratory has shown that an acceptable degree of room temperature ductility can be achieved in the presence of water vapor through alloying and thermomechanical processing [4, 5, 6, 7].

Although the properties of wrought iron aluminides have been improved, the weldability of Fe_3Al-based alloys remains an issue. Gas-tungsten arc welded iron aluminides form a coarse fusion zone microstructure which is susceptible to hydrogen cracking when water vapor is present in the welding atmosphere. Fasching et al. [8] refined the fusion zone microstructure in iron aluminide weldments with magnetic arc oscillation and observed that the refined fusion zone microstructure was more resistant to cold cracking in the presence of water vapor. However, the magnetic arc oscillation process was determined to be acceptable only for very precisely controlled applications, because the technique was extremely sensitive to changes in the concentration of water vapor in the welding atmosphere.

Titanium inoculation of iron aluminide weldments has also been shown to be an effective fusion zone refinement method [9]. With optimal welding parameters and titanium concentration, a fine, equiaxed fusion zone microstructure was achieved with weld pool inoculation.

EXPERIMENTAL PROCEDURE

Gas-tungsten arc welding was performed on 0.76mm iron aluminide alloy FA-129 (Fe - 28.0 at. pct. Al - 5.00 at. pct. Cr - 0.50 at. pct. Nb - 0.20 at. pct. C) sheet in a dry argon atmosphere. The fusion zone was inoculated by welding over a groove (machined into the welding coupon) which was filled with titanium powder (99.5%, <44μm) and encapsulated with a thin strip of alloy FA-129. All welding was performed at a travel speed of 2mm/s and a heat input of 142J/mm. Welding with two titanium concentrations (0.8 and 1.2 wt. pct.), plus welding without titanium inoculation, produced three unique fusion zone microstructures for slow strain rate tensile testing. The welding procedure, as well as the effect of welding parameters and titanium concentration on the fusion zone microstructure, have been published in greater detail elsewhere [9].

To produce samples for tensile testing, the original welding coupons (75mm x 50mm) were sheared to a width of 25 millimeters. A reduced section was then ground into the sample at the fusion

zone, and the weld bead was ground to a uniform thickness to promote fracture within the fusion zone. Only those tests in which fracture occurred within the fusion zone were considered successful.

Slow strain rate ($2.8 \times 10^{-6} s^{-1}$) tensile testing was performed on an 810 MTS system fitted with a Plexiglas chamber to control the concentration of water vapor in the testing atmosphere. Strain rate control testing was performed in atmospheres of 300 to 9000ppm water vapor as measured by a Nyad Series 300 moisture/oxygen analyzer. For tests in water vapor atmospheres, argon was bubbled through distilled water and routed through the testing chamber until the desired water vapor concentration was achieved. The lowest water vapor concentration (approximately 300ppm) was achieved by continuously routing grade 5 argon through the chamber during the duration of the test.

Metallographic samples were prepared using standard techniques. An etchant of 60ml methanol, 40ml nitric acid, and 20ml hydrofluoric acid was used to observe the grain structure, and the etchant used to contrast the fusion zone second phase particles consisted of 96ml water, 2ml nitric acid, and 2ml hydrofluoric acid.

Second phase particles within the fusion zone were analyzed on a scanning electron microscope with energy dispersive spectroscopy (EDS) and image analysis capabilities. Additional identification analysis of the particles was performed on a scanning transmission electron microscope (STEM) capable of EDS as well.

RESULTS AND DISCUSSION

As previously reported, extensive fusion zone grain refinement was achieved by titanium inoculation. The addition of 0.8 and 1.2 weight percent titanium reduced the fusion zone grain size from 530μm to 370μm and 70μm, respectively. With the significant fusion zone refinement accomplished, it was expected that slow strain rate tensile tests would show improved weldment properties similar to the results of the magnetic arc oscillation study by Fasching et al. [8]. However, with an increased titanium concentration, the fracture strength of the weldment decreased. For each titanium concentration, fracture strength also decreased with increasing water vapor concentration.

The reduced fracture strength was not the result of a change in fracture mode. With titanium inoculation, the fraction of second phase particles at the grain boundaries increased from 15 to approximately 50 percent. With the increased concentration of second phase particles at the grain boundaries, the decrease in fracture strength was originally suspected to have been caused by a change to intergranular fracture. However, all fractures occurred by transgranular cleavage, as was observed by Fasching et al. In other research performed on an Fe_3Al-based alloy, alloying with carbon caused the perovskite phase, Fe_3AlC, to be preferentially precipitated out at the grain boundaries, which reduced the

ductility [10]. The presence of the perovskite phase at the grain boundaries, however, did not change the fracture mode. When the same material was decarburized, the precipitates did not form and ductility was recovered. The presence of second phase particles at the grain boundaries can change the mechanical properties of iron aluminides without changing the fracture mode. Given the normally brittle behavior of iron aluminides, fracture initiation, not propagation, is the key concern.

The initial proposal of this research was that the hydrogen cracking susceptibility of weldments could be decreased by refining the fusion zone microstructure, as demonstrated. Fasching et al. [8] showed that the fracture strength of iron aluminide weldments refined by magnetic arc oscillation could be predicted using a Hall-Petch type model, indicating that the fracture strength was controlled by the length of the dislocation pileups at the grain boundaries. The coarse fusion zone microstructure in iron aluminide weldments accommodates relatively long dislocation pileups, generating an area of high stress concentration at the tip of each pileup. A relatively low applied stress is required to initiate fracture at the tip of a long dislocation pileup. The coarse fusion zone microstructure also provides easy crack propagation paths, further decreasing the properties of the weldment. Finer-grained materials exhibit improved mechanical properties because the average slip length is shorter, which reduces the stress at the tip of a dislocation pileup. A higher stress must therefore be applied to initiate cleavage fracture. A finer microstructure also results in a more torturous path for crack propagation. However, the finer fusion zone microstructure in inoculated weldments failed to improve the mechanical properties.

Grain boundaries are not the only microstructural features which can act to pin dislocations. Dislocations moving on a slip plane can be blocked by a second phase particle, and assuming that conditions are such that climb is difficult, a pileup can be formed at the particle. The space between particles then controls the length of the pileup.

Liu and Gurland [11] proposed a model for higher-carbon steels which related the fracture strength to the maximum slip distance as defined by the average particle spacing. The model proposed by Liu and Gurland is:

$$\sigma = \sigma_o + \frac{\sigma_c}{2}\sqrt{\rho/\Lambda} \qquad (1)$$

where:
σ = applied stress
σ_o = friction stress
σ_c = critical fracture stress of matrix
ρ = radius of curvature at crack tip
Λ = available slip distance

A linear relationship between the inverse square root of the mean particle intercept length and the fracture strength was found to exist for high carbon steels, similar to a Hall-Petch plot. Similar results were later obtained by Curry and Knott [12] for quenched and tempered steels.

With titanium inoculation, the second phase particle spacing in iron aluminide weldments was observed to be dependent upon the concentration of titanium in the fusion zone. With increased titanium concentration, the mean particle intercept length increased in the fusion zone. The fracture strength of both inoculated and non-inoculated weldments are plotted against the mean particle intercept length in Figure 1. The measured fracture strengths corresponded well to the mean intercept length, implying that the fracture strength of FA-129 weldments was controlled by the second phase particle spacing.

Because second phase particles provide cleavage nucleation sites, attributes other than the spacing of the particles can affect the mechanical properties of a material. Cleavage fracture has been proposed to initiate by three general mechanisms: slip bands blocked by barriers, mechanical twin intersections, and cracking of brittle second phase particles [13]. Cracking of second phase particles appears to be the most likely mechanism for the initiation of transgranular cleavage in iron aluminides.

Both fractured second phase particles and fractured particle/matrix interfaces were observed in inoculated FA-129 weldments after tensile testing (Figure 2). Liu and Gurland [11] observed both fracture types in steels, and concluded that, although both

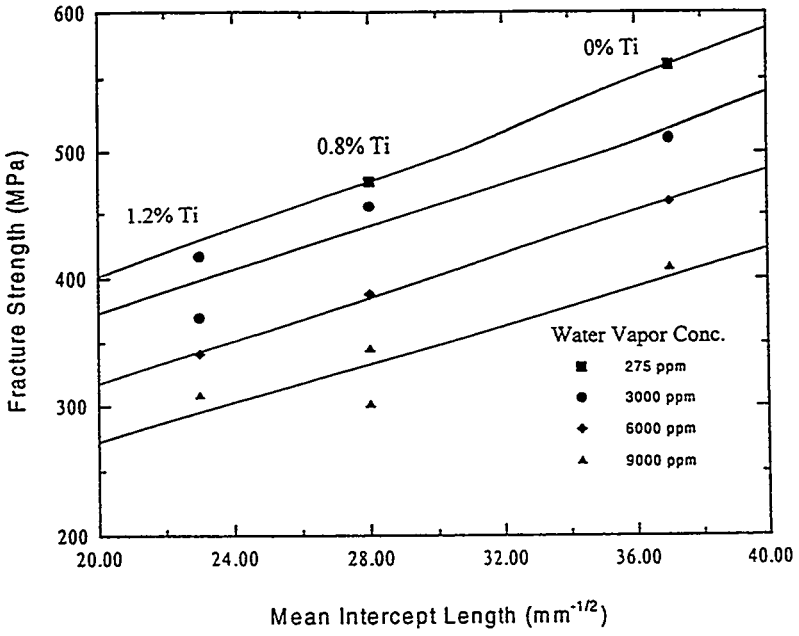

Figure 1. Effect of second phase particle spacing on the fracture strength of FA-129 weldments.

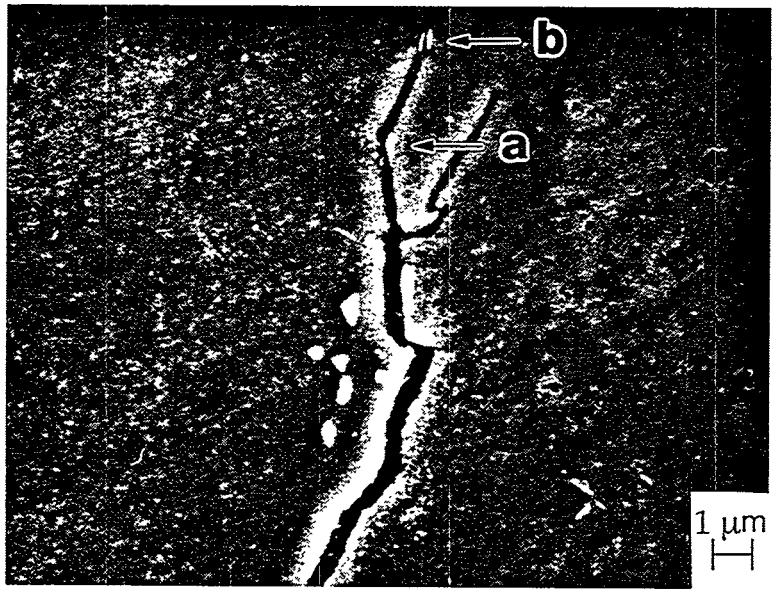

Figure 2. Fusion zone second phase particles associated with fracture in inoculated weldment. a) Failed interface b) Fractured particle.

defect types could initiate void formation, only carbide fracture could initiate cleavage nucleation. Given the hydrogen cracking susceptibility of iron aluminides, once a microcrack is initiated at a second phase particle and the Griffith crack propagation criteria is satisfied, the crack will propagate in an unstable manner. It is assumed then, that the stress required to fracture the second phase particles in the iron aluminide weldments influenced the fracture strength measured for the titanium inoculated weldments. The stress required to fracture a second phase particle is a function of the type, size, and shape of the second phase particles.

The type of second phase particle is critical because its fracture strength is dependent upon composition and crystal structure. In the present study, niobium carbides were observed in the non-inoculated welds. With titanium inoculation, the fusion zone second phase particles were observed to have a different composition. The particles consisted of niobium, titanium, and carbon. Selected area diffraction (SAD) analysis also revealed that the structure of the particles was face-centered cubic. The exact phase formed in the inoculated fusion zone was not determined. However, both niobium and titanium carbides are face-centered cubic, so the phase was most likely a complex titanium and niobium bearing carbide.

Although both carbides precipitated were face-centered cubic, they may have different fracture strengths, which are unknown. The change in particle composition and location (at the grain boundary) would have changed the stress required to initiate fracture, but the impact on weldment properties was not clear and was assumed to be a secondary effect.

With the addition of titanium to the weld metal, the second phase particles not only changed in composition, but were also observed to change in size and shape. Table 1 summarizes the fusion zone second phase particle characteristics. As titanium concentration increased, the second phase particles became more elongated and less spherical.

Table 1. Size and Shape of Fusion Zone Second Phase Particles

Weight Percent Titanium	Avg. Particle Diameter (μm)	Aspect Ratio (length/width)
0	0.51±0.24	1.7
0.8	0.44±0.16	2.7
1.2	0.52±0.16	2.6

The shape of the carbide impacts the fracture strength of a material by changing the type of crack formed when the particle is fractured. When spherical particles are fractured, a penny-shaped crack is formed. The Griffith crack propagation criteria for a penny-shaped crack is:

$$\sigma_f = \left(\frac{\pi E \gamma_p}{2(1-\upsilon^2) r} \right)^{1/2} \qquad (2)$$

where: γ_p = effective surface energy
υ = Poisson's ratio
r = particle radius

A cracked grain boundary carbide is characterized as a through-thickness nucleus. The Griffith crack criteria for a through-thickness nucleus is:

$$\sigma_f = \left(\frac{2E\gamma_p}{\pi(1-\upsilon^2) r} \right)^{1/2} \qquad (3)$$

Note that the change from a penny-shaped nucleus (spherical particle) to a through-thickness nucleus (grain boundary particle) reduces the material fracture strength by a factor of $\pi/2$. Curry and Knott [14] confirmed the dependence of the fracture strength on the size and shape of carbides in tool steels. Fracture strength was observed to decrease as carbides became larger and more elongated.

As previously noted, when titanium was added to the FA-129 fusion zones, the second phase particles were concentrated at the grain boundaries. These grain boundary particles were much more elongated than the majority of the particles in the non-inoculated fusion zones (Table 1). Therefore, the decreased fracture strength observed with titanium inoculation could have been a result of the changed shape of the cleavage nucleation sites as the particles became less spherical. However, if the fracture strength was dependent upon the second phase particle shape, the relationship between the fracture strength and particle spacing would not have been linear as was shown (Figure 1).

The addition of 0.8 weight percent titanium to the fusion zone caused the second phase particles to become more elongated. Assuming that the particle shape was critical, the decrease in fracture strength measured with the 0.8 weight percent titanium addition would have consisted of two components, a decrease caused by the increased particle spacing and a decrease caused by the particle shape change. The highest titanium addition, 1.2 weight percent, further decreased the fracture strength, but the addition did not cause any further second phase particle shape change (Table 1). The decreased fracture strength measured, therefore, could only be attributed to the increased particle spacing, and a linear relationship would not have existed between the fracture strengths and the three second phase particle spacings. Since the relationship was linear, the fracture strength could not have been dependent upon the second phase particle shape over the range of shapes observed in this study.

CONCLUSIONS

Although titanium inoculation effectively refined the fusion zone microstructure in iron aluminide weldments, the fracture strength was deteriorated by the addition of titanium. With titanium inoculation, second phase particles in the fusion zone concentrated at the grain boundaries. The higher frequency of grain boundary particles increased the spacing of the fusion zone second phase particles as well as the average aspect ratio of the particles. Transgranular cleavage was more easily initiated in weldments with the highly spaced, elongated second phase particles. Given the cracking susceptibility of iron aluminides in the presence of water vapor, a more facile fracture initiation decreased the fracture strength of the weldments.

ZIRCONIUM- AND CARBON-ALLOYED IRON ALUMINIDES

Current work has focused on the weldability of zirconium- and carbon-alloyed iron aluminides. Work performed at Oak Ridge National Laboratory has shown that additions of zirconium and carbon greatly affect the mechanical properties of iron aluminides. Studies have shown that carbides of zirconium have a beneficial effect on creep resistance and additions of 0.1% to 0.5% zirconium improve tensile and fatigue properties [17]. Small amounts of zirconium are beneficial for oxidation resistance as well. Zirconium changes the morphology of the oxides formed at high temperature and retards oxide spalling [18].

However, a major concern with zirconium-containing alloys is weldability. Hot cracking has been observed more frequently in zirconium-containing alloys than was seen with alloy FA-129 or other ternary alloys. Zirconium lowers the liquidus temperature of the alloy, which results in an increase in the amount of liquid present during weld solidification. Two techniques have been identified as possible solutions to the hot cracking problems: 1) reduce the amount of liquid present during weld solidification, and 2) increase the amount of liquid present during weld solidification. The first technique would involve decreasing the amount of zirconium present during the time of solidification either by decreasing the total concentration of zirconium in the alloy, or by adding sufficient carbon to tie the zirconium up as zirconium carbides prior to final solidification. The second technique looks at increasing the amount of zirconium concentration in the alloy to provide enough liquid to back fill a forming hot crack and "heal" it. Future research on this program will be focused on characterizing the effects of zirconium and carbon on the hot cracking resistance of iron aluminides.

PRELIMINARY TESTING AND RESULTS

Testing of hot cracking resistance is in progress on three iron aluminide alloys containing zirconium and carbon. Compositions are shown in Table 2. The alloys contain different total concentrations of zirconium at the same zirconium/carbon ratio of ten. Alloy specimens are cut from 0.76mm sheet into 50x50mm coupons, heat treated at 650°C for two hours, and then pickled to remove any oxide. Gas tungsten arc welding and determination of the critical cracking stress in a sigmajig apparatus constitutes the testing procedure.

Table 2. Compositions of Zirconium-Containing Alloys

Alloy	Fe (at%)	Al (at%)	Cr (at%)	Zr (at%)	C (at%)
A	Bal.	28	5	0.2	0.02
B	Bal.	28	5	0.35	0.035
C	Bal.	28	5	0.5	0.05

The threshold hot cracking stress of alloys A and C have been determined to be 10 KSI and 8 KSI, respectively. The results indicate that increasing zirconium content decreases the hot cracking resistance of iron aluminides. When compared with other iron aluminide alloys (see Table 3 for compositions), the hot cracking resistance of the zirconium/carbon alloys is inferior, as shown in Figure 3.

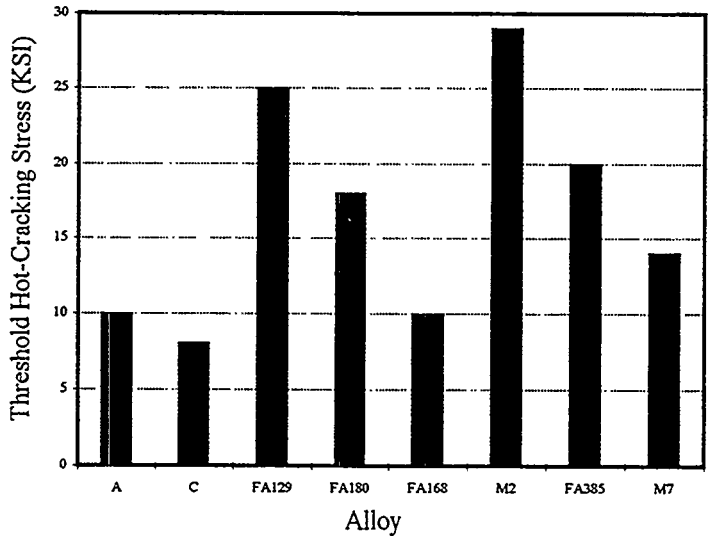

Figure 3. Comparison of threshold stress of zirconium-containing alloys to other iron aluminides.

Table 3. Compositions of Other Iron Aluminides.

Alloy	Al (wt%)	Mo (wt%)	Zr (wt%)	B (ppm)	Cr (wt%)	Nb (wt%)	C (wt%)
FA129	16	-	-	-	5.4	1.0	0.04
FA180	16	1.6	0.05	10	5.4	1.0	0.01
FA168	16	1.6	0.1	10	5.4	1.0	0.007
M2	21.2	0.42	0.1	50	-	-	0.03
FA385	21.2	0.42	0.1	-	-	-	0.03
M7	21.2	0.42	0.2	-	2.3	1.0	0.06

FUTURE WORK

Five alloys containing zirconium ranging from 0.05 to 0.5 atomic percent and possessing a zirconium/carbon ratio of ten will be characterized. The effects of carbon on hot cracking resistance will also be studied by varying the zirconium/carbon ration from ten to five and then one, while holding the zirconium concentration at 0.1 atomic percent. These compositions should contain less low melting point liquid during solidification and thus manifest better hot cracking resistance. High zirconium alloys (1.5 to 2.0 atomic percent or with a ratio of 30 to 40) will also be evaluated to determine the amount of zirconium necessary to eliminate hot cracking by liquid backfilling. Limited characterization of slow strain rate tensile properties of selected alloys at varying water vapor concentrations also will be performed.

Acknowledgments

This research was sponsored by the U.S. Department of Energy, Fossil Energy AR&TD Materials Program under subcontract 19X-27421C. Dr. Gene Goodwin's assistance with hot cracking equipment construction and advice was greatly appreciated. The authors also acknowledge Dr. Vinod Sikka and the Materials Processing Group at ORNL, who provided the material used in this research.

References

1. McKamey, C. G., J. H., Tortorelli, P. F., and Sikka, V. K. 1991. J. of Mat. Sci. Res. 6: 1779.

2. Liu, C. T., Lee, E. H., and McKamey, C. G. 1989. Scripta Met. 23: 875.

3. Liu, C. T., McKamey, C. G., and Lee, E. H. 1990. Scripta Met. 24: 385.

4. McKamey, C. G., Horton, J. A., and Liu, C. T. 1988. Scripta Met. 22: 1679.

5. McKamey, C. G., Horton, J. A., and Liu, C. T. 1989. J. Mat. Res. 4: 1156.

6. McKamey, C. G. and Liu, C. T. 1990. Scripta Met. 24: 2119.

7. Sanders, P. G., Sikka, V. K., Howell, C. R., and Baldwin, R. H. 1991. Scripta Met. 25: 2365.

8. Fasching, A. A., Edwards, G. R., and David, S. A. To be published. Sci. and Tech. of Welding and Joining.

9. Burt, R. P., Edwards, G. R., and David, S. A. 1996. To be published. Proc. and Fab. of Adv. Mat.-V. Proceedings of 1996 TMS Fall Meeting.

10. Kerr, W. R. 1986. Met. Trans. 17A: 2298.

11. Liu, C. T. and Gurland, J. 1968. Trans. ASM. 61: 156.

12. Curry, D. A. and Knott, J. F. 1979. Met. Sci. (June): 341.

13. McMahon, C. J. and Cohen, M. 1965. Acta Met. 13: 591.

14. Curry, D. A. and Knott, J. F. 1978. Met. Sci. (Nov.): 511.

15. Evans, A. G. 1983. Met. Trans. 14A: 1349.

16. Wallin, K., Saario, T., and Törrönen, K. 1984. Met. Sci. 18: 13.

17. Alven, D.A. and Stoloff, N.S. 1996. Proceedings of the Tenth Annual Conference on Fossil Energy Materials. Conf-9605167: 225.

18. June, M. PALL Corporation. Verbal communication.

EFFECTS OF 1000 °C OXIDE SURFACES ON ROOM TEMPERATURE AQUEOUS CORROSION AND ENVIRONMENTAL EMBRITTLEMENT OF IRON ALUMINIDES

R. A. Buchanan and R. L. Perrin

Dept. of Materials Science and Engineering
University of Tennessee
Knoxville, TN 37996-2200

ABSTRACT

Results of electrochemical aqueous-corrosion studies at room temperature indicate that retained in-service-type high-temperature surface oxides (1000 °C in air for 24 hours) on FA-129, FAL and FAL-Mo iron aluminides cause major reductions in pitting corrosion resistance in a mild acid-chloride solution designed to simulate aggressive atmospheric corrosion. Removal of the oxides by mechanical grinding restores the corrosion resistance. In a more aggressive sodium tetrathionate solution, designed to simulate an aqueous environment contaminated by sulfur-bearing combustion products, only active corrosion occurs for both the 1000 °C oxide and mechanically cleaned surfaces of FAL. Results of slow-strain-rate stress-corrosion-cracking tests on FA-129, FAL and FAL-Mo at free-corrosion and hydrogen-charging potentials in the mild acid chloride solution indicate somewhat higher ductilities (on the order of 50 %) for the 1000 °C oxide surfaces as compared to the mechanically cleaned surfaces. These results suggest that the 1000 °C oxides retard the penetration of hydrogen into the metal substrates and, consequently, are beneficial in terms of improving resistance to environmental embrittlement. In the aggressive sodium tetrathionate solution, no differences are observed in the ductilities produced by the 1000 °C oxide and mechanically cleaned surfaces for FAL.

INTRODUCTION

The overall objective was to study the effects of in-service-type high-temperature oxides on the room-temperature aqueous corrosion and environmental embrittlement properties of iron aluminides. The study was designed to be consistent with past and on-going research by Tortorelli and DeVan at the Oak Ridge National Laboratory (ORNL), who have evaluated the high-temperature oxidation resistances of Fe_3Al-based iron aluminides (FA-129 and FAL) in air to simulate combustion products.[1] Equally importantly, Tortorelli and Alexander are conducting studies to characterize the chemical, morphological, and mechanical properties of the oxide scales created by these exposures after cool-down to room temperature.[2] The characteristics of these

scales, and in particular the cracking/spallation characteristics, will have a strong influence on the aqueous-corrosion and hydrogen-embrittlement behaviors of the iron aluminides during shut-down periods at room temperature.

EXPERIMENTAL PROCEDURES

FA-129 and FAL iron aluminides were selected for investigation to be consistent with the work by Tortorelli and DeVan.[1] In addition, the iron aluminide FAL-Mo was included. The chemical compositions are given in Table 1. FAL-Mo is very similar to FAL, but with the addition of 1.0 % Mo. Due to the Mo addition, it has been shown to have superior aqueous-corrosion resistance in acid-chloride and sulfur-bearing electrolytes.[3-5]

Table 1. Chemical compositions of iron aluminides (atomic percent).

Alloy	Fe	Al	Cr	Mo	B	Zr	Nb	C	Y
FA-129	66.3	28.0	5.0	-	-	-	0.5	0.2	-
FAL	66.9	28.0	5.0	-	-	0.1	-	-	-
FAL-Mo	65.9	28.0	5.0	1.0	0.04	0.08	-	-	-

To produce the in-service-type high-temperature oxide scales, specimens of all alloys were exposed to air at 1000 °C for 24 hours, then furnace cooled (based on recommendations by Dr. Peter Tortorelli at ORNL). Aqueous corrosion and environmental embrittlement tests were conducted on specimens with, and for comparison, without the 1000 °C oxide. The 1000 °C oxide specimens were first ground through 600-grit SiC, then exposed to the 1000 °C heat treatment. The specimens without the 1000 °C oxide, i.e., the mechanically cleaned specimens, were first ground through 600-grit SiC, then exposed to the 1000 °C heat treatment, then ground again through 600-grit SiC to remove the high-temperature oxides. Specimens were contained in alumina crucibles during all heat treatments.

The principal electrolyte employed in this study was a mild acid-chloride solution [pH = 4 (H_2SO_4), 200 ppm Cl^- (NaCl)]. In this solution, the alloys evaluated are susceptible, to varying degrees, to pitting corrosion. An excellent method for evaluating the relative pitting corrosion

susceptibility involves producing and analyzing cyclic anodic polarization curves. A schematic illustration of a cyclic anodic polarization curve is shown in Figure 1, where certain electrochemical parameters are identified.

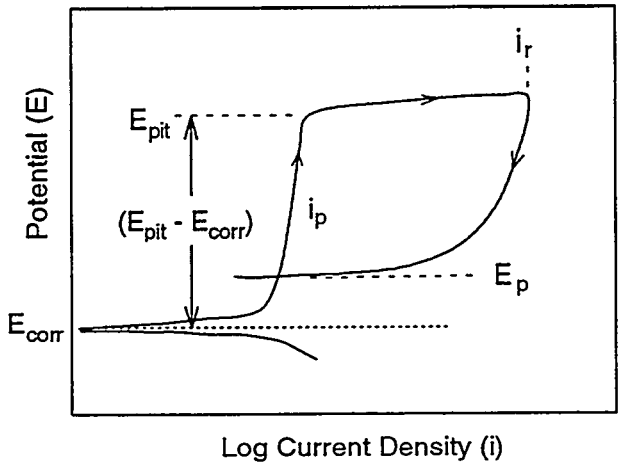

Fig. 1. Schematic illustration of cyclic anodic polarization behavior.

E_{corr} is the steady-state, open-circuit, free corrosion potential; i_p is the passive current density, reflective of passivation wherein the material develops a thin, protective, oxide/hydroxide passive film, and, therefore, corrodes at a very low rate; E_{pit} is the critical pitting potential at which pitting corrosion initiates; i_r is the reversing current density; and E_p is the protection (or repassivation) potential. A parameter often used to characterize the relative resistance to pitting corrosion is the difference between E_{pit} and E_{corr}, i.e., $(E_{pit} - E_{corr})$, with higher values corresponding to greater pitting resistance.

In the present study, room-temperature cyclic anodic polarization tests were conducted utilizing a standard polarization cell and an EG&G Model 273 potentiostat. Stabilization of each specimen was allowed to occur for at least one hour, after which E_{corr} was measured. The cyclic polarization curve was then generated at a scan rate of 600 mV/h. The reversing current density was 1000 $\mu A/cm^2$. Polarization tests were conducted on FA-129, FAL and FAL-Mo in the mild acid-chloride solution [pH = 4 (H_2SO_4), 200 ppm Cl^- (NaCl)] to simulate aggressive atmospheric corrosion. In addition, tests were conducted on FAL in 0.001 M sodium tetrathionate solution ($Na_2S_4O_6$) to simulate an aqueous solution contaminated by sulfur-bearing combustion products.

The environmental embrittlement characterizations involved room-temperature slow-strain-rate tests (SSRTs) in the mild acid-chloride solution (FA-129, FAL and FAL-Mo) and the sodium tetrathionate solution (FAL). In these tests, the specimens were continuously strained in tension at a very slow rate to enhance corrosion and hydrogen-embrittlement effects. The tests were conducted at a strain rate of 1.2×10^{-6} s^{-1} in a load frame which contained the corrosion cell. Tests were conducted at the free corrosion potential, E_{corr}, and at a cathodic hydrogen-charging potential of -1500 mV(SHE).

RESULTS AND DISCUSSION

The cyclic anodic polarization behaviors of FA-129 (28Al-5Cr), FAL (28Al-5Cr-0.1Zr) and FAL-Mo (28Al-5Cr-1Mo-0.08Zr), in the 1000 °C oxide and mechanically cleaned conditions and in the mild acid chloride solution, are shown in Figures 2, 3 and 4, respectively. The polarization results are summarized in Figure 5, where the resistance to localized corrosion (in terms of the measured parameter (E_{pit} - E_{corr})) is shown for all materials in both surface conditions. In cases where passivation was not obvious, E_{pit} was taken as the potential corresponding to a current density of 10 $\mu A/cm^2$. It is apparent that the mechanically cleaned surfaces for all materials demonstrated superior localized corrosion resistance relative to the 1000 °C oxide surfaces.

The polarization results for FAL-Mo in the 0.001 M sodium tetrathionate solution are shown in Figure 6. This solution proved to be very aggressive toward both the 1000°C oxide and mechanically cleaned conditions. Passivation did not occur for either surface condition.

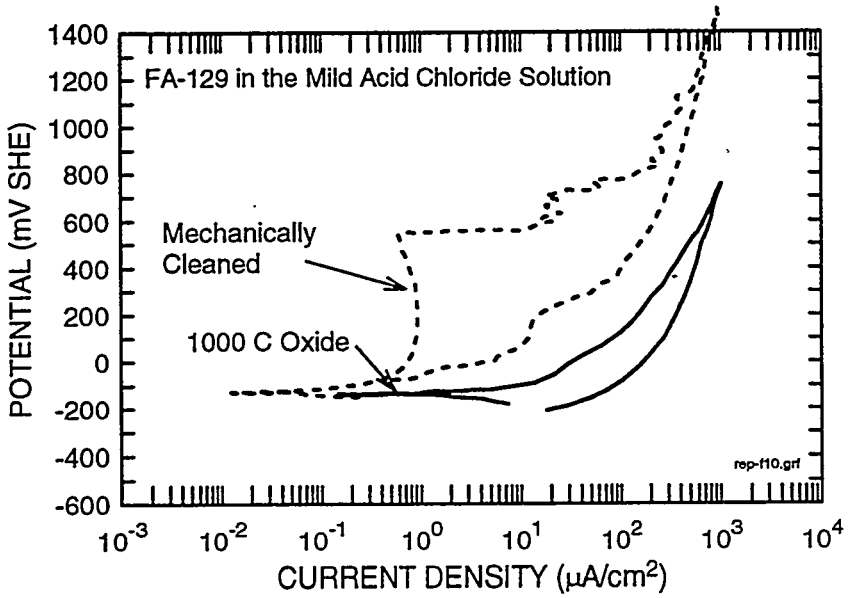

Fig. 2. Cyclic anodic polarization behaviors of FA-129 with 1000 °C oxide and mechanically-cleaned surfaces in the mild acid chloride solution.

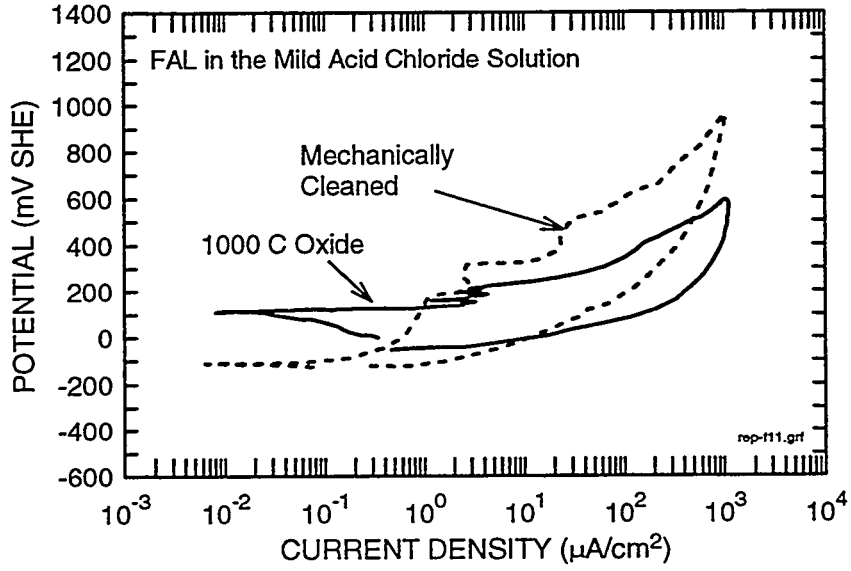

Fig. 3. Cyclic anodic polarization behaviors of FAL with 1000 °C oxide and mechanically-cleaned surfaces in the mild acid chloride solution.

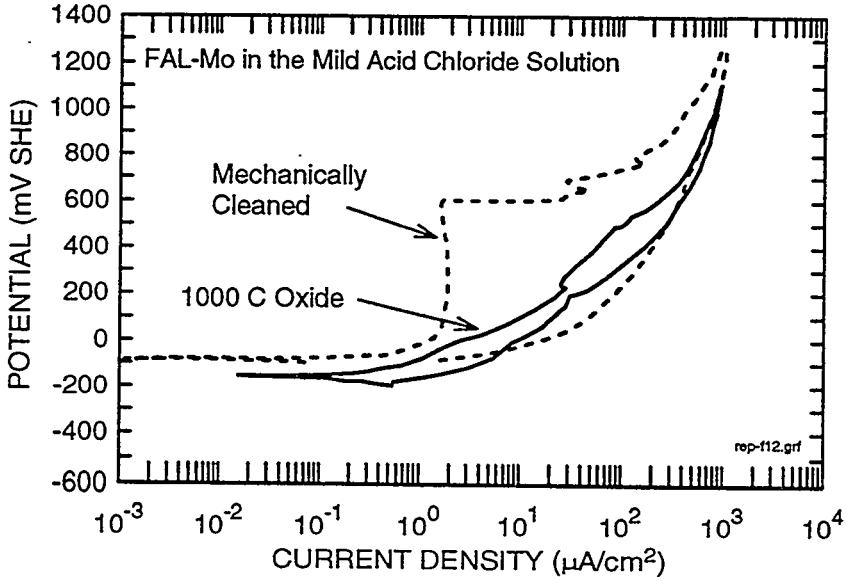

Fig. 4. Cyclic anodic polarization behaviors of FAL-Mo with 1000 °C oxide and mechanically-cleaned surfaces in the mild acid chloride solution.

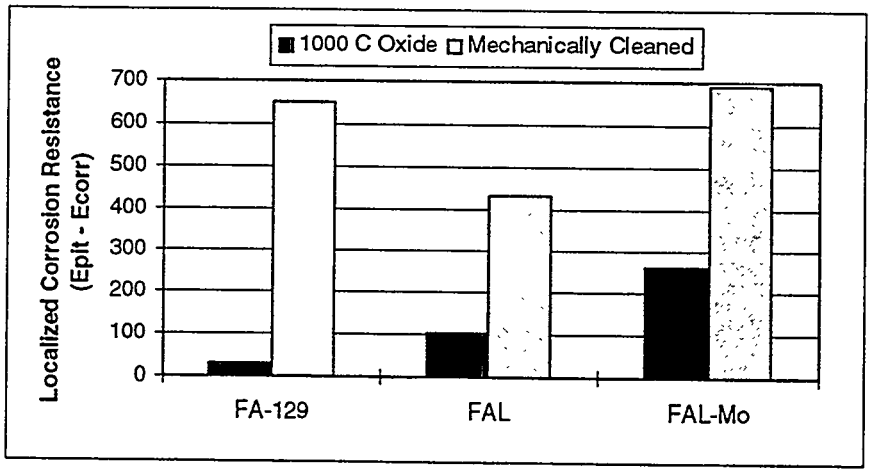

Fig. 5. Effects of 1000 °C oxide and mechanically cleaned surfaces on localized corrosion resistance in the mild acid chloride solution.

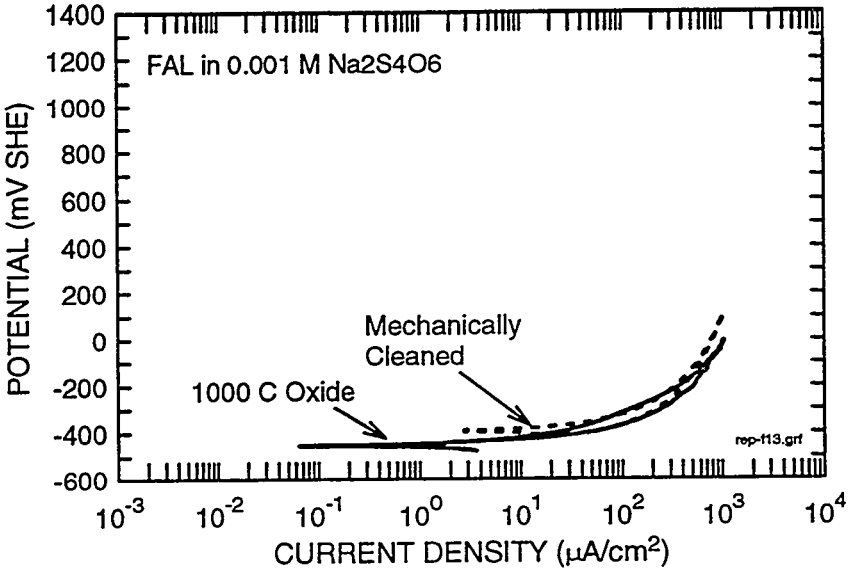

Fig. 6. Cyclic anodic polarization behaviors of FAL with 1000 °C oxide and mechanically-cleaned surfaces in the 0.001 M sodium tetrathionate solution.

The slow-strain-rate test results for replicate specimens of FA-129, FAL and FAL-Mo in the mild acid chloride solution, in terms of the average percent-total-plastic-elongation at the free corrosion potential, E_{corr}, and at the hydrogen-charging potential, -1500 mV(SHE), are given in Figure 7(a) and (b), respectively. It is seen that the 1000 °C oxide surfaces produced higher ductilities than the mechanically cleaned surfaces for all materials at both potentials. At E_{corr}, the average increase in ductility was 39 %, and at -1500 mV(SHE), 52 %. At the hydrogen-charging potential, the FAL and FAL-Mo 1000 °C oxides were noticeably more effective than the FA-129 1000 °C oxide in improving the ductilities. These results imply that the 1000 °C oxides retard hydrogen penetration into the metal substrates and, therefore, improve the resistances of the materials to environmental embrittlement. Under the conditions of this study, the 1000 °C oxides produced beneficial effects, but not dramatically beneficial effects.

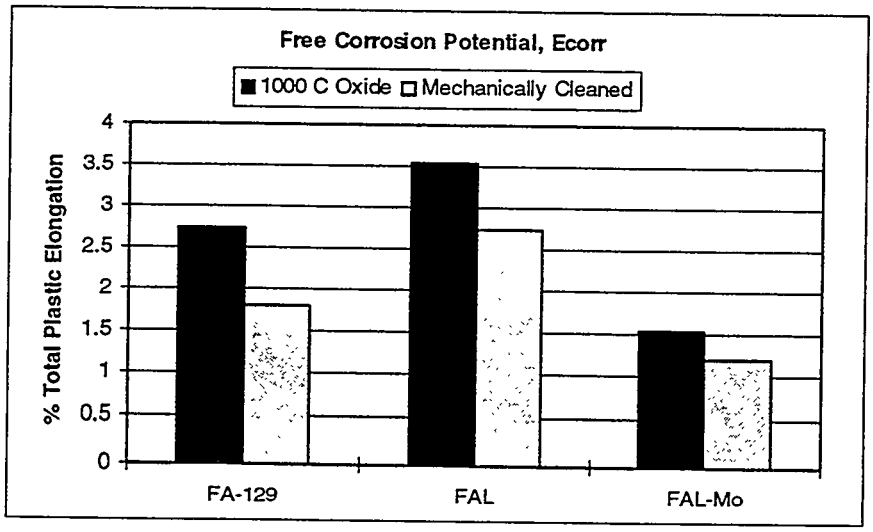

(a)

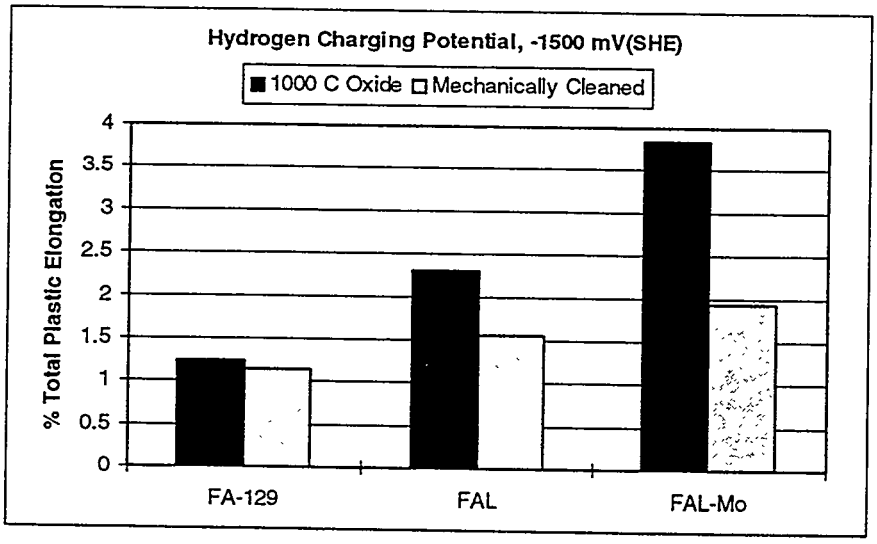

(b)

Fig. 7. Slow-strain-rate test results for iron aluminides in the mild acid chloride solution at (a) the free corrosion potential, E_{corr}, and (b) the hydrogen-charging potential, -1500 mV(SHE).

The slow-strain-rate test results for FAL in the 0.001 M sodium tetrathionate solution, in terms of percent total plastic elongation and fracture stress values, are presented in Table 3. It is seen that the 1000 °C oxide and mechanically cleaned surfaces produced approximately equal ductilities at each of the potentials. Therefore, in this solution, which was considerably more aggressive than the mild acid chloride solution, no beneficial effects were observed for the 1000 °C oxide surfaces in terms of resistance to environmental embrittlement.

Table 3. Results of slow strain-rate tests on FAL iron aluminide in 0.001 M sodium tetrathionate solution.

Material	Potential	Surface Condition	Fracture Stress (ksi)	(MPa)	Percent Total Plastic Elongation
FAL	E_{corr}	Mechanically Cleaned	23	158	1.2
		1000°C Oxide	23	158	1.2
	-1500 mV SHE	Mechanically Cleaned	32	220	1.4
		1000°C Oxide	26	179	1.6

CONCLUSIONS

In terms of room-temperature aqueous corrosion behavior in the mild acid chloride solution, designed to simulate aggressive atmospheric corrosion, the retained 1000 °C oxides (reflective of in-service oxidation) consistently produced major, detrimental results relative to the mechanically cleaned surfaces. Specifically, the pitting corrosion resistances were much lower for the 1000 °C surfaces, relative to the cleaned surfaces, for FA-129, FAL and FAL-Mo Fe_3Al-based iron aluminides. It is believed that the detrimental corrosion effects associated with the high-temperature oxides are related to flaws in the oxides which serve as crevice corrosion sites, thus increasing the susceptibility to localized corrosion.

In terms of room-temperature environmental embrittlement behavior in the mild acid chloride solution, the retained 1000 °C surface oxides consistently produced marginally beneficial results relative to the mechanically cleaned surfaces. Specifically, slow-strain-rate tests of FA-129, FAL and FAL-Mo at free-corrosion and cathodic-hydrogen-charging potentials showed consistently higher ductilities (≈ 50 % higher) for the 1000 °C oxide surfaces as compared to the cleaned

surfaces. It is believed that the beneficial effects associated with the high-temperature oxides, i.e., greater resistance to environmental embrittlement, are due to the oxides serving as barriers to hydrogen penetration of the metal substrates in those surface regions where the oxides maintain adherency with the substrates.

More detailed information on this study is available in Reference 6.

REFERENCES

1. J. H. DeVan and P. F. Tortorelli, "Environmental Effects on Iron Aluminides," Proceedings of the Eighth Annual Conference on Fossil Energy Materials, ORNL/FMP-94/1, 309-320, Oak Ridge National Laboratory, Oak Ridge, TN (1993).

2. P. F. Tortorelli and K. B. Alexander, "Mechanically Reliable Scales and Coatings," pp. 247-56 in Proceedings of the Ninth Annual Conference on Fossil Energy Materials, N. C. Cole and R. R. Judkins (comp.), U. S. Department of Energy, August 1995.

3. R. A. Buchanan and J. G. Kim, "Fe_3Al-Type Iron Aluminides: Aqueous Corrosion Properties in a Range of Electrolytes and Slow-Strain-Rate Ductilities During Aqueous Corrosion," Final Report, U. S. Dept. of Energy, Fossil Energy AR & TD Materials Program, ORNL/Sub/88-07685CT92/02, National Technical Information Service, Springfield, VA, August, 1992.

4. J. G. Kim and R. A. Buchanan, "Aqueous Corrosion Properties and Slow-Strain-Rate Ductilities of Fe_3Al-Based and Lean-Aluminum Iron Aluminides," Final Report, U. S. Dept. of Energy, Fossil Energy AR & TD Materials Program, ORNL/Sub/88-07685CT92/03, National Technical Information Service, Springfield, VA, August, 1993.

5. J. G. Kim and R. A. Buchanan, "Pitting and Crevice Corrosion of Iron Aluminides in a Mild Acid-Chloride Solution," Corrosion, Vol. 50, No. 9, pp. 658-668, Sept., 1994.

6. R. A. Buchanan and R. L. Perrin, "Effects of High Temperature Surface Oxides on Room Temperature Aqueous Corrosion and Environmental Embrittlement of Iron Aluminides," Final Report, U. S. Dept. of Energy, Fossil Energy AR & TD Materials Program, ORNL/Sub/88-07685CT92/05, National Technical Information Service, Springfield, VA, September, 1996.

THE INFLUENCE OF PROCESSING ON MICROSTRUCTURE AND PROPERTIES OF IRON ALUMINIDES

R. N. Wright, J. K. Wright, and M. T. Anderson

Idaho National Engineering and Environmental Laboratory
Lockheed Martin Idaho Technologies Company
Idaho Falls, ID 83415-2218

ABSTRACT

Oxide dispersion strengthened (ODS) iron aluminide alloys based on Fe3Al have been formed by reaction synthesis from elemental powders followed by hot extrusion. The resulting alloys have approximately 2.5% by volume Al_2O_3 particles dispersed throughout the material. A proper combination of extrusion temperature, extrusion ratio, and post-consolidation heat treatment results in a secondary recrystallized microstructure with grain sizes greater than 25mm. ODS material with 5% Cr addition exhibits approximately an order of magnitude increase in time to failure at 650°C compared to a similar alloy without the oxide dispersion. Addition of Nb and Mo along with Cr results in decreased minimum creep rates, however, the time to rupture is greatly reduced due to fracture at low strains initiated at large Nb particles that were not put into solution. The activation energy for creep in the 5% Cr ODS material is on the order of 210kJ/mole and the power law creep exponent is 9-9.5. Transmission electron microscopy examination of the substructure of deformed samples indicates some formation of low angle dislocation boundaries, however, most of the dislocations are pinned at particles. The TEM observations and the value of the creep exponent are indicative of dislocation breakaway from particles as the rate controlling deformation mechanism. The TEM results indicate that particles smaller than about 100nm and larger than about 500nm do not contribute significantly to dislocation pinning.

INTRODUCTION

Iron aluminides near the composition Fe_3Al display outstanding resistance to sulfidation and are attractive for possible applications in fossil fired plants.[1] Although these alloys were investigated

extensively in the 1960's, brittle room temperature behavior resulted in little industrial interest. More recent studies have identified the brittle behavior as a result of a hydrogen effect associated with water vapor. In the absence of water vapor, Fe_3Al has reasonable tensile ductility at room temperature.[2] More significantly from an applications point of view, it has been found that room temperature tensile elongation of greater than 20% can be achieved under ambient conditions through alloying with 2-5% Cr and control of the microstructure to retain the maximum amount of B2 order.

Despite major advances in increasing the ambient temperature ductility, relatively poor elevated temperature properties is still a limitation for applications of iron aluminides.[3] It has been suggested that as a result, iron aluminide coatings on high strength ferrous alloys may be an attractive alternative.[4] In addition a number of strategies for increasing the creep resistance of alloys based on Fe_3Al have been suggested. Alloying with refractory metal additions, principally Mo, Nb and Zr, has been shown to be effective, particularly if fine refractory carbides can be formed.[5] Experience with oxide dispersion strengthened nickel based and FeCrAl based alloys has suggested that the creep resistance of Fe_3Al can be dramatically improved by dispersion of fine stable oxide particles. The most common approach to oxide dispersion strengthening is through high energy ball milling of prealloyed powders with a rare earth oxide, followed by hot consolidation. An alternative approach, reported here, is to use the natural tendency of reaction synthesis from elemental powders to result in a finely distributed oxide to improve the creep resistance of Fe_3Al + 5%Cr.[6]

DISCUSSION OF CURRENT ACTIVITIES

Experimental Procedure

Reaction synthesized material was made using carbonyl iron (8μm diameter), helium gas atomized aluminum (10μm diameter) and chromium (1-5μM diameter) powders, mixed in proper proportions to yield Fe-28Al-5Cr (all compositions are given in this paper in atomic percent). Reaction between the elemental iron and aluminum, and solution of the chromium in the iron aluminide, occurred during a two hour thermal treatment at 1100°C under flowing argon. This process resulted in porous pre-forms that were subsequently sealed in steel cans and extruded in a 16:1 reduction in area ratio at 900°C. Test specimens were machined from the extruded material and heat treated at 1200°C to form large (>25mm

in length) grains elongated in the test direction, by secondary recrystallization. Appropriate extrusion ratio, extrusion temperature, and grain growth temperature were selected based on previous work.[7]

Creep tests were performed in laboratory air in constant load testing frames with applied stresses from 50 to 135MPa, and temperatures from 600 to 800°C. Many of the tests were carried out to failure to obtain creep rupture data. A few tests were interrupted to obtain specimens for examination using transmission electron microscopy. Those samples were held under the applied stress while the furnace was turned off and the specimen allowed to cool to room temperature to prevent relaxation of the dislocation structure. In order to determine the power law creep exponent, additional tests were conducted by allowing steady state creep to be attained and subsequently jumping the stress to higher values while maintaining constant temperature. For these tests to be valid it is assumed that the sample remains isostructural; given the relatively small creep strains observed in these tests and the small jumps in stress, this condition is valid for the values reported below.

Results and Discussion

Creep data for the dispersion strengthened material and conventional powder metallurgy processed (P/M) material of the same composition are given in Table 1. Larson-Miller plots for conventional P/M Fe_3Al and the dispersion strengthened material are shown in Figure 1. The increased time to rupture is clearly evident from this plot. Note that the P/M alloy considered in the Larson-Miller plot contains only 2% Cr, rather than the 5% in the dispersion strengthened material. We have shown previously the increasing the Cr from 2 to 5% reduces the creep rupture life, however, since the dispersion strengthened material has poor room temperature ductility, 5% Cr was used to obtain maximum tensile properties.

Assuming that the dispersion strengthened material follows conventional power law creep behavior, the apparent activation energy for creep can be determined from the data as plotted in Figure 2. The value determined in this study is 210kJ/mole ±20 kJ/mole. This value compares reasonably well with values determined for binary Fe_3Al, 280kJ/mole.[8] Although this value is in agreement with the self-diffusion activation energy for iron in Fe_3Al, 204kj/mol, the apparent value determined from the plot should be corrected somewhat for the threshold stress associated with particle pinning.[9] The corrected value has not yet been determined because an accurate temperature dependent shear modulus is not available. The apparent activation energy reported here is more than an order of magnitude larger than the value reported by McKamey for carbide strengthened Fe_3Al.[10] The reason for this large difference is not yet known.

The power law stress exponent can be determined from the data plotted in Figure 3. The slope of the plots yields an approximate average value of 9.5. This value is much greater than commonly observed for metals and alloys (4-5), however, large stress exponents have been reported for a number of dispersion strengthened materials.[11] Arzt et al., found values of >50 for particle strengthened Al alloys and on the order of 13 for NiAl containing several different dispersions.[12-13] It has also been reported that values of 13-14 are found in high energy ball milled FeAl alloys.[14] The value determined here is also in reasonable agreement with the value of 10 reported for carbide strengthened Fe_3Al by McKamey et al.[10]

Table 1. Creep properties of conventional P/M and oxide dispersion strengthened materials.

Material	Heat Treatment (°C-time)	Test Temp. (°C)	Applied Stress (MPa)	Creep Rate (s^{-1})	Time to Rupture (hrs)
P/M	N/A	500	137.9	4.72E-09	3398
P/M	N/A	500	275	7.32E-08	125
P/M	N/A	600	76	138	418
P/M	N/A	600	103	275	72
P/M	N/A	600	138	2.08E-06	15
P/M	N/A	650	34	2.36E-08	1464
P/M	N/A	650	76	5.99E-07	47
ODS	1200-1 hr	650	75.8	4.97E-09	512.8
ODS	1200-1 hr	675	78.5	4.82E-08	62
ODS	1200-1 hr	700	50	4.86E-09	255.8
ODS	1200-1 hr	800	50	1.33E-08	15
ODS	1200-1 hr	600	50	8.33E-11	>4400
ODS	1200-1 hr	600	75.8	2.08E-09	2527.4
ODS	1200-1 hr	650	50	2.5E-10	>2100
ODS	1200-1 hr	675	50	9.17E-10	856.3
ODS	1200-1 hr	625	50	6.94E-9	N/A
ODS	1200-1 hr	625	60	1.67E-09	N/A
ODS	1200-1 hr	625	110	1.02E-06	N/A
ODS	1200-1 hr	625	75.8	8.64E-09	N/A
ODS	1200-1 hr	625	100	4.42E-07	N/A
ODS	1200-1 hr	650	60	3.22E-09	N/A
ODS	1200-1 hr	650	100	9.03E-07	N/A
ODS	1200-1 hr	675	60	8.75E-09	N/A
ODS	1200-1 hr	675	85	7.0E-07	N/A

Dislocation structures were examined in several samples deformed in creep to different total strains. There was some evidence of recovery of dislocation structures into low angle boundaries, Figure 4, however, the majority of dislocations were found to be uniformly distributed throughout the

microstructure. A representative region of a sample deformed to about 10% plastic strain and cooled under load to pin the dislocations is shown in Figure 5. Note in the figure that the majority of dislocations are pinned at particles that are on the order of 100nm in diameter or greater.

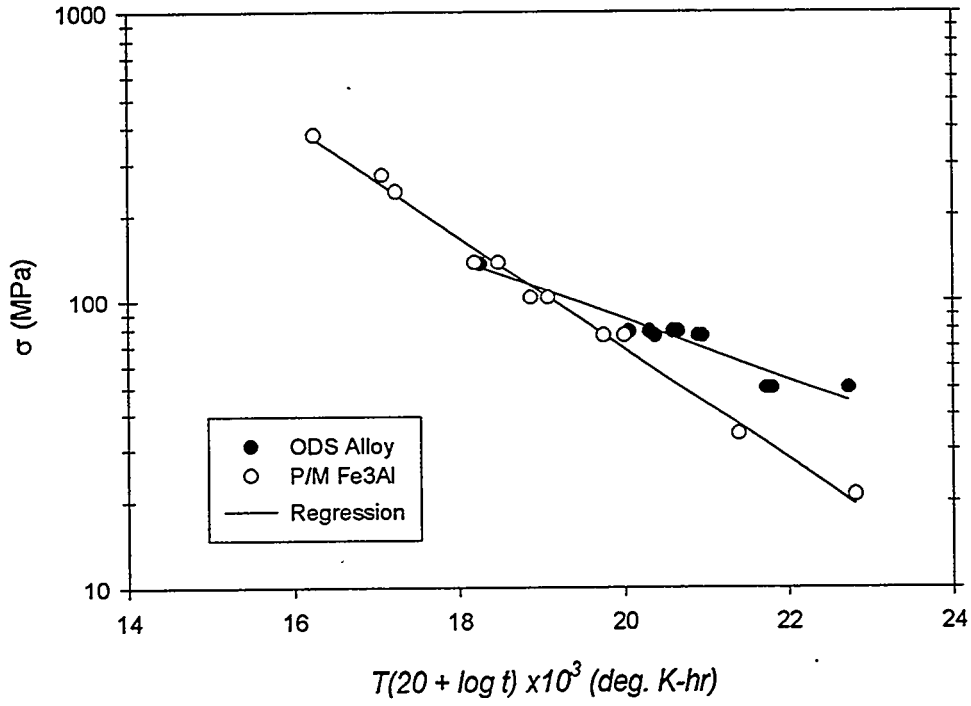

Figure 1. Larson-Miller plots for powder metallurgy and dispersion strengthened materials.

The Burgers vector of dislocations active in Fe_3Al during creep deformation is somewhat controversial. It has been reported that <111> superdislocations and <100> dislocations that are perfect in the B2 structure are both mobile under creep conditions.[6] A Burgers vector analysis was carried out in the current study, however, with the zone axes that could be accessed in the heavily textured material the results could not differentiate unambiguously between the two types of dislocation. It does appear that many of the dislocations observed in the dispersion strengthened material deformed in creep above 600°C were superdislocations, suggesting at least some fraction of the pinned dislocations were of the <111> type.

It is clear form the TEM results that the interaction between the particles and dislocations was attractive, rather than repulsion from strain fields associated with dislocations, for example. The unit

process responsible for improved creep resistance in these materials therefore appears to be dislocation climb and breakaway from pinning particles. This particle pinning mechanism is consistent with the relatively high value of the power law creep exponent (≈9) that was determined for these alloys. There was no evidence of dislocation loop formation around particles that might suggest that an alternative, Orowan looping, process was active.

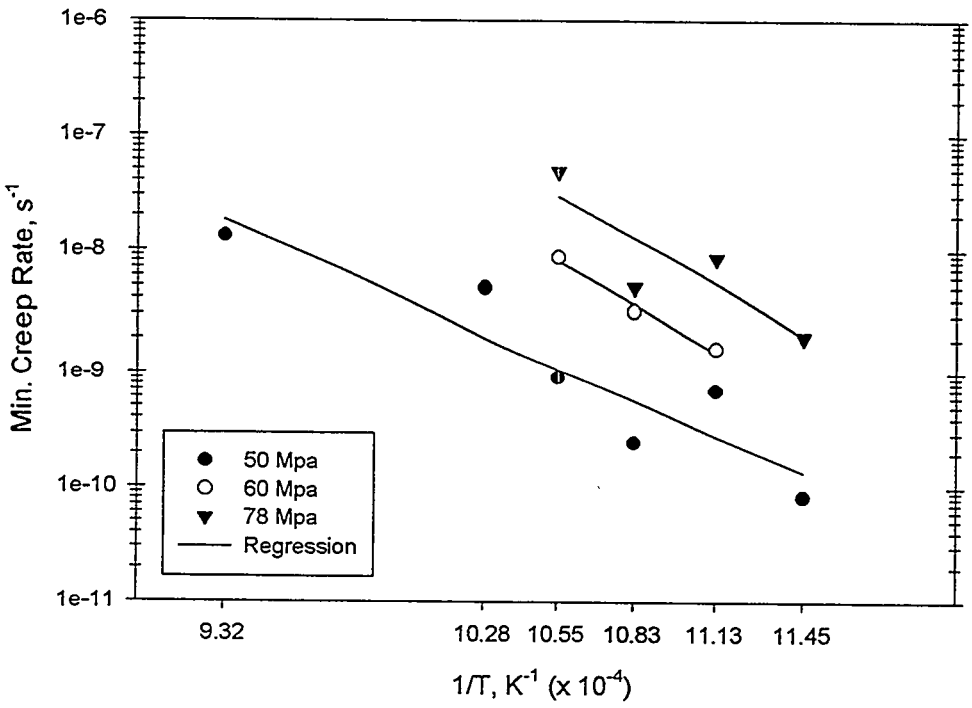

Figure 2 Minimum creep rate as a function of reciprocal temperature for three stress levels.

Additions of refractory metals to the Fe_3Al based alloys have been shown to increase the resistance to creep.[10] This effect can occur due to increasing the critical temperature or solution strengthening, however, the most significant increase in time to rupture appears to be as a result of precipitation of fine carbides. Since transition metal carbides are probably not stable with respect to coarsening at temperatures above about 800°C no effort was made in this study to incorporate their effect. An attempt was made to improve the creep resistance of the matrix material by additions of about 2% Mo and Nb. An improvement in minimum creep rate was observed in some cases compared to the dispersion strengthened material with only Cr additions, however, large elemental Nb particles remained undisolved in the matrix

which initiated fracture, resulting in short time to rupture values. Additional alloys have been processed with additions of very fine particle sizes of Mo and Nb which are expected to result in complete dissolution of the alloying elements, testing of these alloys has recently begun.

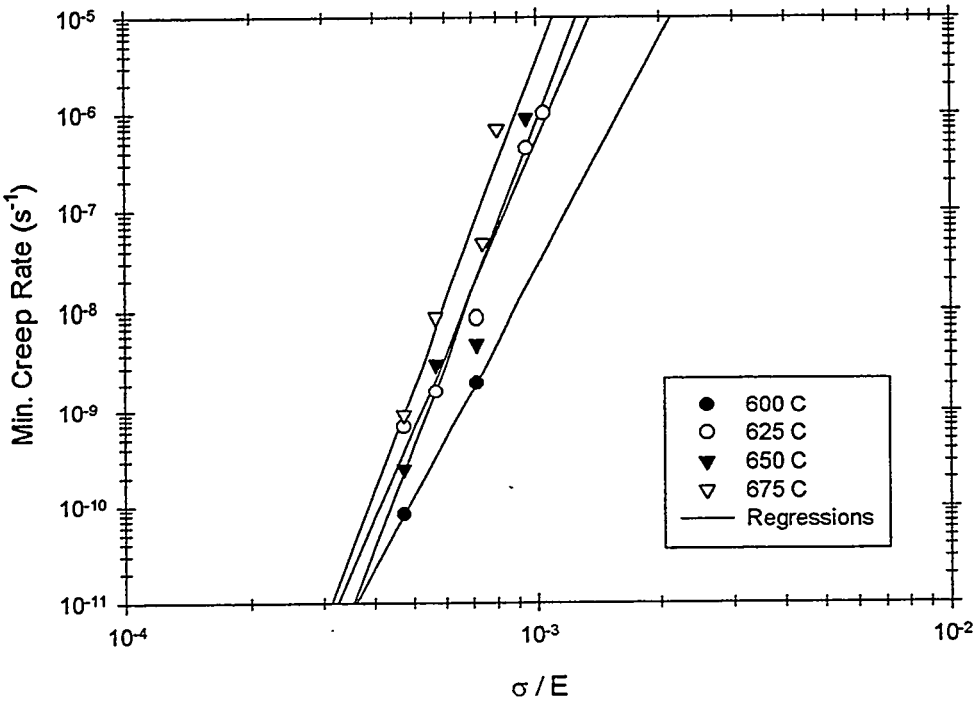

Figure 3. Minimum creep rate plotted as a function of the applied stress normalized to Youngs modulus.

Conclusions

A dispersion of fine oxides from reaction synthesis of Fe_3Al from elemental powders significantly increases the time to rupture of the material compared to conventional powder metallurgy processing. Increased creep lifetime is a result of reduced minimum, or steady state, creep rates. The elongation to failure is reduced in the dispersion strengthened material compared to conventional powder metallurgy alloy. The TEM results show that here is an attractive interaction between the oxide particles and dislocations, which results in a power law creep exponent of ≈9. This value is about twice that normally found for metals and alloys, and is indicative of particle strengthening. The activation energy for creep

was determined to be 210kj/mole, a value that is approximately the same as Fe_3Al without the particle dispersion and roughly equal to the activation energy for self-diffusion of iron in the intermetallic.

Figure 5. Dislocation structure in a sample deformed to 5% plastic strain at 675°C and a stress of 78MPa.

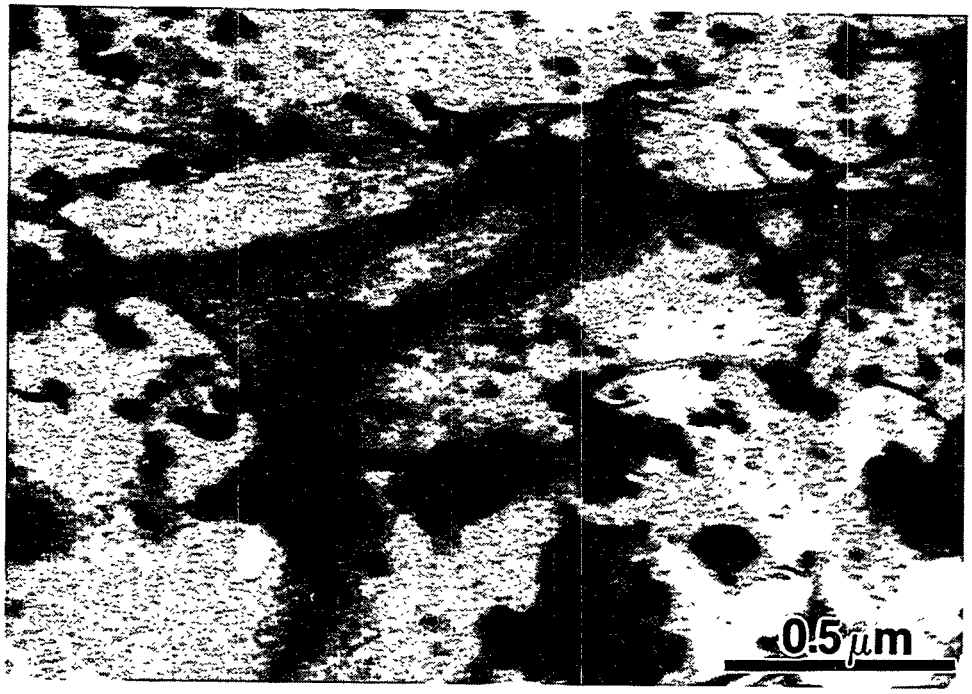

Figure 6. Dislocation structure in a sample deformed to 10% plastic strain at 675°C and a stress of 50MPa.

REFERENCES

1. C. G. McKamey, J. H. DeVan, P. F.Tortorelli, and V. K. Sikka, "A Review of Recent Developments in Fe_3Al Based Alloys", J. Mater Res., Vol. 6, 1991, pp. 1779-1804.
2. C. T. Liu, C. G. McKamey and E. H. Lee, "Environmental Effects on Room Temperature Ductility and Fracture in Fe_3Al", Scripta Metall. Et Mater., Vol. 24, 1990, pp. 385-390.
3. C. R. Clark, R. N. Wright, J. K. Wright and B. H. Rabin, "Elevated Temperature Mechanical Properties of Reaction Synthesized Fe_3Al". Scripta Metall. Et Mater., Vol. 32, 1995, pp. 1883-1887.
4. R. N. Wright, J.R. Fincke, W. D. Swank, D. C. Haggard and C. R. Clark, "The Influence of Process Parameters on the Microstructure and Properties of Fe_3Al Based Coatings", Elevated Temperature Coatings: Science and Technology, N. B. Dahotre, et al., eds., TMS, 1995, pp. 157-166.
5. R. N. Wright and J. K. Wright, "The Influence of Processing on the Microstructure and Properties of Iron Aluminides", Proc. 10th Conf. On Fossil Energy Materials, ORNL, 1996, pp. 373-380.
6. D. G. Morris, M. Nazmy and C. Noseda, "Creep Resistance of a New Alloy Based on Fe_3Al", Scripta Metall et Mater., Vol. 31, 1994, pp. 173-178.
7. T. M. Lillo, R. N. Wright, B. H. Rabin and J. K. Wright, "Microstructure and Properties of Reaction Synthesized Iron Aluminides", Inter. Conf. On Heat Resistant Alloys II, K. Natesan, et al., eds., ASM International, 1995, pp. 579-587.
8. J. A. Jimenez and G. Frommeyer, "Creep Behavior of Intermetallic Fe-Al and Fe-Al-Cr Alloys, Mater. Sci. Eng., Vol. A220, 1996, pp. 93-99.
9. Z. S. Tokei, J. Bernardini, P. Gas and D. L. Beke, "Volume Diffusion of Iron in Fe_3Al: Influence of Ordering", Acta Metall. Et Mater., Vol. 45, 1997, pp. 541-546.
10. C. G. McKamey and P. J. Maziasz, "Effect of Heat Treatment at 1150°C on Creep Properties of Alloy FA-180", Proc. 10th Conf. On Fossil Energy Materials, ORNL, 1996, pp. 215-221.
11. A. M. Brown and M. F. Ashby, "On the Power Law Creep Equation", Scripta Meatll., Vol. 14, 1980, pp. 1297-1302.
12. E. Arzt, E. Gohring and P. Grahle, "Dispersion Strengthened Intermetallics by Mechanical Alloying: Creep Results and Dislocation Mechanisms", Mater. Res. Soc. Proc. Vol. 288, 1993, pp. 861-866.
13. J. Rrosler, R. Joos and E. Arzt, "Microstructure and Creep Properties of Dispersion-Strengthened Aluminum Alloys", Metall. Trans., Vol. 23A, 1992, pp. 1521-1314.
14. K. Wolski, F. Thevenot and J. Le Coze, "Influence of Nanometric Oxide Dispersion on Creep Resistance of ODS FeAl Prepared from Prealloyed Powders", Scripta Meatll. Et Mater., Vol 34, 1996, pp. 815-823.

MECHANISMS OF DEFECT COMPLEX FORMATION AND ENVIRONMENTAL-ASSISTED FRACTURE BEHAVIOR OF IRON ALUMINIDES

B. R. Cooper[1], L.S. Muratov[1], B.S.-J. Kang[2], and K.Z. Li[2]

[1] Physics Department

[2] Mechanical and Aerospace Engr. Dept.

West Virginia University

Morgantown, WV 26506

ABSTRACT

Iron aluminide has excellent corrosion resistance in high-temperature oxidizing-sulfidizing environments; however, there are problems at room and medium temperature with hydrogen embrittlement as related to exposure to moisture. In this research, a coordinated computational modeling/experimental study of mechanisms related to environmental-assisted fracture behavior of selected iron aluminides is being undertaken. The modeling and the experimental work will connect at the level of coordinated understanding of the mechanisms for hydrogen penetration and for loss of strength and susceptibility to fracture. The focus of the modeling component at this point is on the challenging question of accurately predicting the iron vacancy formation energy in $Fe_3A\ell$ and the subsequent tendency, if present, for vacancy clustering. We have successfully performed, on an *ab initio* basis, the first calculation of the vacancy formation energy in $Fe_3A\ell$. These calculations include lattice relaxation effects which are quite large. This has significant implications for vacancy clustering effects with consequences to be explored for hydrogen diffusion. The experimental work at this stage has focused on the relationship of the choice and concentration of additives to the improvement of resistance to hydrogen embrittlement and hence to the fracture behavior. For this reason, comparative crack growth tests of FA-186, FA-187, and FA-189 iron aluminides (all with basic composition of Fe-28Aℓ-5Cr, at % with micro-alloying additives of Zr, C or B) under, air, oxygen, or water environment have been performed. These tests showed that the alloys are susceptible to room temperature hydrogen embrittlement in both B2 and DO_3 conditions. Test results indicated that FA-187, and FA-189 are intrinsically more brittle than FA-186.

INTRODUCTION

Because of their excellent corrosion resistance in high temperature oxidizing-sulfidizing environments in combination with low cost and other advantages, iron aluminides are of great potential use in fossil energy technology, however, there are problems at room and medium temperatures with hydrogen embrittlement as related to exposure to moisture.[1,2] In this research, a coordinated computational modeling/ experimental study of mechanisms related to environmental-assisted fracture behavior of selected iron aluminides is being undertaken. The modeling and the experimental work will connect at the level of coordinated understanding of the mechanisms for hydrogen penetration and for loss of strength and susceptibility to fracture.

The vacancy formation behavior and the likelihood of the vacancies clustering and/or forming complexes with additives (or impurities) or other defects will play a central role in determining susceptibility to fracture, both directly and indirectly via the effects on crucial diffusion processes. Therefore the focus of the modeling component at this point is on the challenging question of accurately predicting the iron vacancy formation energy in $Fe_3A\ell$ and the subsequent tendency, if present, for vacancy clustering. We have successfully performed, on an *ab initio* basis, the first calculation of the vacancy formation energy[3] in $Fe_3A\ell$. These calculations include lattice relaxation effects. Interestingly, there are two types of iron sites and hence two rather different vacancy formation energies. Both types of vacancy site involve quite large atomic movements, of the order 13-15% of the unrelaxed relative position, for the nearest neighbors.

For the experimental component, environmental-assisted fracture behavior of three iron aluminides (designated as FA-186, FA-187, and FA-189, all with various alloy additives such as Zr, C,or B) were investigated to study the effect of alloy additives on fracture behavior, in particular, resistance to hydrogen embrittlement. Crack growth tests of the iron aluminides subjected to constant tensile loading in air, oxygen or water environment were conducted. Moire interferometry was applied to obtain full-field crack-tip displacements, from which crack extension, crack growth rate, and the stress intensity factor were evaluated. Evidence of moisture embrittlement for the three iron aluminides was observed. We found that the presence of a small amount of moisture is sufficient to cause embrittlement. The comparative tests also showed that specimens in B2 condition have slightly better crack resistance than those in DO_3 condition. Test results indicated that FA-187 and FA-189 are intrinsically more brittle than FA-186 in both B2 and DO_3 conditions. SEM fractographic and optical microstructural analyses relevant to failure analysis of the iron aluminides was also performed and is discussed below.

COMPUTATIONAL MODELING

Atomistic computational modeling is being undertaken to find the preferred geometries and the formation energies of iron vacancies and vacancy pairs (Fe-Fe) for FeAℓ and Fe3Aℓ. An indication of vacancy clustering in Fe3Aℓ, with consequences for dislocation behavior, may be important for understanding the role of dislocation-assisted diffusion in the hydrogen embrittlement mechanism.

A fully quantum mechanical full-potential LMTO technique, including force calculations, is being applied to find the formation energies of iron vacancies and vacancy pairs (Fe-Fe) in FeA$\ell$and Fe3Aℓ. The method being used is our well established fully quantum mechanical full potential linear combination of muffin-tin-orbitals (LMTO) technique.[4,5] This is an *ab initio* all-electron technique with full relativistic corrections included. To assure high accuracy we have implemented an augmented basis through use of multiple κ's and energy windows.[5,6] Initially we have found the preferred unrelaxed geometry through use of total energy minimization. To treat relaxation effects for this transition metal system, we have implemented a force methodology based on our full-potential LMT total energy technique and have applied this to vacancy formation energies in both FeAℓ and Fe3Aℓ. We will next calculate the divacancy binding energy (or the absence thereof).

The vacancy energy is calculated by first calculating the total energy of the initial perfect (without vacancy) supercell. We then subtract from that the energy the sum of the total energy of the supercell with a vacancy plus the energy contribution of the removed atom. The atomic energy contribution is taken from the bulk energy of the element (iron) scaled to reproduce the total energy of the intermetallic compound.

In Fe3Aℓ there are two types of iron site. Type A has eight iron nearest neighbors at a distance of $\sqrt{3}\,a/4$; while type B has four iron and four aluminum nearest neighbors. This then leads to there being two types of vacancy and the possibility of three types of divacancy (AA, AB, BB). We have carefully examined the density of states for the two types of iron site (see Fig. 1), and they are quite different.

In order to have sufficient degrees of freedom to fully investigate the effects of lattice relaxation, we have used a 32-atom supercell (eight formula units of Fe3Aℓ). For the type A iron sites, the unrelaxed vacancy formation energy is 3.8 eV, and there is an energy lowering of 0.8 eV caused by lattice relaxation. This gives a net vacancy formation energy of 3.0 eV. Interestingly, the changes in bond lengths are quite large, up to 13% of the nearest neighbor distance. For the type B sites, the unrelaxed vacancy formation energy is 2.8 eV, and there is an energy lowering of 1.01 eV associated with lattice relaxation. For B sites, this gives a net vacancy formation energy of 1.79 eV. Again, the changes in bond lengths are quite large, up to 15% of the nearest neighbor distance.

Significantly for the possibility of vacancy clustering, our preliminary calculations in the 32-atom supercell indicate a strong interaction between vacancies of about 0.3 eV. During the coming year we will refine this estimate by performing the divacancy calculations for much larger supercells.

EXPERIMENTAL PROGRAM

Materials

Alloys used in this study were fabricated at Oak Ridge National Laboratory (ORNL) by vacuum induction melting and casting into graphite molds. The ingots were then hot forged (two passes, 25% per pass) at 1000^{o}C followed by hot rolled at 800^{o}C for seven passes (15% per pass) to produce finished plate thickness of 6.35 mm. The finished plates were either heat treated at 900^{o}C for one hour then air quenched to produce partially ordered B2 structure or heat treated at 900^{o}C for one hour followed by 550^{o}C for 72 hours then air quenched to produce DO_3 structure. Table 1 shows the alloy composition of FA-186, FA-187 and FA-189.

Single-edge-notched (SEN) specimens were cut from the plates using an EDM machine and specimen surfaces were hand-polished with fine grid sandpapers followed by thorough solution cleaning. Figure 2 shows the test specimen geometry. The notch of each specimen was cut using 0.1 mm diameter EDM wire with notch direction parallel to the rolling direction.

Test Apparatus

An environmental materials testing chamber was constructed to conduct crack growth tests of iron aluminides using moire interferometry under controlled gas content (air, argon, hydrogen gas or dry oxygen) environments. The chamber can also be filled with water to conduct crack growth test in water. Figure 3 shows a schematic drawing of the environmental test chamber. For crack growth tests under oxygen environment, the chamber was first pumped down to about 10^{-2} torr, and oxygen with research purity of 99.999% was filled in the chamber at a pressure of 1.2 atm. The pumping and filling cycle was done 4 or 5 times before the crack growth test. Additionally, a moisture trap with absorption capacity of 25 grams H_2O was put inside the chamber to reduce the residual moisture in the test environment. It should be noted that unless the chamber is pumping down to a high vacuum state (say 10^{-8} torr), some amount of residual moisture is still present in the chamber, particularly, near the EDM-cut crack tip region. We did a preliminary residual gas measurement of the chamber under the above mentioned "oxygen" environment using RGA and estimate that the partial pressure of residual moisture and hydrogen is about 0.25-0.04 and 0.06-0.05 times of the atmospheric air, respectively.

Moire interferometry is capable of high sensitivity full-field surface deformation measurement[7]. At WVU, we have demonstrated that moire interferometry can be applied to study environmental assisted cracking problems.[8,9] Figure 4 shows a schematic drawing of the optical setup for moire interferometry test with the environmental chamber mounted on the optical bench.

Crack Growth Tests

Table 2 shows the test matrix. As shown, a total of sixteen comparative crack growth tests under various environments were conducted. Figure 5 shows representative moire fringe patterns of FA-189 under air environment. Figure 6 shows representative SEM fractographs of alloys tested in air environment. Figure 7 shows the measured crack extension versus time data, and Figure 8 shows the measured crack growth rate versus applied stress intensity factor.

For alloy FA-186 tested in air or oxygen condition, multiple cracks were formed as soon as the initial crack started to grow. The extension of these multiple microcracks formed an expanding damage zone which grew stably leading to final failure. This feature of extensive multiple microcracking was not found for alloys FA-187 and FA-189. Instead, a clear single crack growth pattern was observed (e.g. Figure 5).

As shown in Table 2, for alloys FA-186, FA-187, and FA-189 tested in water environment, accelerated effect of hydrogen embrittlement was observed and resulted in lower fracture toughness and fast fracture behavior, i.e. no slow stable crack growth was observed comparing to the specimens tested in air or oxygen environment. Test results in Table 2 also showed that with the same applied stress intensity factor, specimens tested in oxygen lasted 3 to 9 times longer than those tested in air, indicating the effect of moisture embrittlement for all three iron aluminides. Also, specimens with partially ordered B2 condition have slightly better fracture resistance than those in DO_3 condition for all three alloys. However, the susceptibility of hydrogen embrittlement varies among the test alloys. As shown in Figures 7 and 8, crack growth tests of the ternary alloy FA-186 tested in air showed some small amount of increased crack growth rate compared to those tested in oxygen; only crack growth test in water showed significant effect of hydrogen embrittlement for FA-186. This is not the case for alloys FA-187 and FA-189, which showed substantial faster crack growth rate in air than when tested in oxygen.

Overall, our test results indicate that among the three alloys, the ternary alloy FA-186 has the best fracture resistance, highest fracture toughness and least sensitivity to hydrogen embrittlement (Table 2). This finding is quite surprising since the purpose of micro-alloying addition to the ternary alloy (0.5% Zr0.05%C (FA-187) or 0.5% Zr0.05%C0.005%B (FA-189)) is to enhance its resistance to hydrogen embrittlement. It should be noted that recently Alven and Stoloff[10] conducted fatigue crack growth tests of several iron aluminides including FA-186 and FA-187 under air, oxygen, vacuum or 1.3 atm hydrogen environment. Their results, in contrast, showed that FA-187 has lower fatigue crack growth rate than that of FA-186. Since hydrogen embrittlement is a diffusion-controlled process and past studies have indicated that low strain rate loading can promote hydrogen embrittlement[1], the 0.5%Zr0.05%C addition (FA-187) may provide stronger grain boundary bonding for better fatigue resistance than the base ternary alloy (FA-186), but under constant static loading condition and with its smaller grain size, at the high-stress crack tip region, initial intergranular microcracks may assist the diffusion of atomic hydrogen (which is generated

due to the chemical reaction of the aluminum atoms in the aluminides react with moisture, $2Al+3H_2O - Al_2O_3+6H$) along crack-tip grain boundaries which subsequently caused accelerated dislocation motion at cleavage plans that resulted in brittle cleavage fracture. Further research is needed to clarify or validate the above assertion.

Failure characteristics of the tested alloys are tabulated in Table 3. We roughly divided the fractured surface into three areas corresponding to the changes of failure mode. For alloys FA-187 and FA-189, initial crack growth always started with intergranular mode (e.g. Figure 6) then shifted to mixed intergranular/transgranular cleavage mode and finally to transgranular failure. As the moisture content is increased in the test environment (i.e. from oxygen to air to water), we observed an increased intergranular failure pattern in area 2.

For ternary alloy FA-186, except for the sample tested in water which showed intergranular mode in area 1, transgranular cleavage is the dominate failure mode. However, the sample tested in air had rougher cleavage facets (i.e. more tilt and twist boundaries). In hydrogen-free environment cleavage generally takes place along crystallographic planes with the lowest packing density, and thus resulted in larger cleavage facets (Figure 6). While in hydrogen-containing environment, hydrogen embrittlement is proposed to be associated with dislocation transport of hydrogen[2], which occurred along crystallographic planes with the highest packing density, i.e. more rougher cleavage facets as we observed in the fractographic analyses.

Our test results indicated that FA-187 and FA-189 are intrinsically more brittle than FA-186. As discussed in ref. 11, the level of zirconium addition needs to be carefully controlled. Some amount of zirconium addition (say about 0.1%) is beneficial to promote scale adhesion for protection against corrosion in harsh environment; however, too much zirconium addition (such as 0.5% Zr in FA-187) may produce intrinsically brittle iron aluminide alloy.

The purpose of adding a small amount of boron in FA-189 was to improve the strength of grain boundaries so that intergranular failure can be minimized. However, our test results indicate just the opposite. This may be related to the composition of the alloy. In a similar system, $Ni_3A\ell$, where the stoichiometric proportion of binary alloy is 25%Aℓ, it has been reported[12-14] that when boron is introduced to $Ni_3A\ell$ alloy, aluminum has to be reduced to 23-24% in order to strengthen grain boundaries and to optimize ductility. Similar modifications of stoichiometric proportion may be necessary for FA-189. Systematic experiments are needed to determine the best stoichiometric proportion of $Fe_3A\ell$ when boron is added to the material system.

CONCLUSIONS

Interestingly, there are two types of iron sites and hence two rather different vacancy formation energies. Both types of vacancy site involve quite large atomic movements, of the order 13-15% of the unrelaxed relative position, for the nearest neighbors. Significantly for the possibility of vacancy clustering, our preliminary calculations in the 32-atom supercell indicate a strong interaction between vacancies of about 0.3 eV. During the coming year we will refine this estimate by performing the divacancy calculations for much larger supercells.

Comparative crack growth tests of FA-186, FA-187 and FA-189 iron aluminides under air, oxygen or air environment were conducted and results showed substantial difference of crack-tip deformation profile and crack growth rate among the alloys. Test results also showed that with the same applied stress intensity factor, specimens tested in oxygen lasted 3 to 9 times longer than those tested in air, indicating the effect of moisture embrittlement for all three iron aluminides. Alloys with partially ordered B2 structure have slightly better fracture resistance than those in DO_3 structure. Finally, our test results indicated that FA-187 and FA-189 are intrinsically more brittle than FA-186.

ACKNOWLEDGMENTS

This research is sponsored by the U.S. Department of Energy, Office of Fossil Energy, Advanced Research and Technology Development (AR&TD) Materials Program at the Oak Ridge National Laboratory under contract no. SUB-19X-ST547C with Lockheed Martin Energy Systems, Inc. Additional support from the WVU NRCCE is also acknowledged. Technical assistance from Dr. C.T. Liu from ORNL is greatly appreciated.

REFERENCES

1. N.S. Stoloff and C.T. Liu,"Environmental Embrittlement of Iron Aluminides - Review," Intermetallics, 2, pp.75-87, (1994).
2. A. Castagna, D.A. Alven and N.S. Stoloff, "Environmental Embrittlement of Iron Aluminides under Cyclic Loading Condition," Proceedings of the Ninth Annual Conference on Fossil Energy Materials, Oak Ridge, TN, pp. 377-386, May 16-18 (1995).
3. L.S. Muratov and B.R. Cooper, Bull. Am. Phys. Soc. 42, 737 (1997).
4. D.L. Price and B.R. Cooper, Phys. Rev. B 39, 4945 (1989).
5. D.L. Price, B.R. Cooper and J.M. Wills, Phys. Rev. B 46, 11368 (1992).
6. D.L. Price, J.M. Wills and B.R. Cooper, Phys. Rev. B 48, 15301 (1993).
7. D. Post, Moire interferometry, Chapter 7 in SEM, Handbook on Experimental Mechanics, ed. A.S. Kobayashi. Prentice-Hall, Englewood Cliffs, NJ, pp.314-387, (1987).
8. F.X. Wang and B.S.-J. Kang, "Moire Interferometry in Liquid Medium," SEM, Proceeding of the VII International Congress on Experimental Mechanics, PP.1711-1716, Las Vegas, NA, June 8-11 (1992).

9. B.S.-J. Kang, G. Zhang, P. Liu and M. Ellathur, "Stress Accelerated Grain Boundary Oxygen Embrittlement on Creep Crack Growth of Ni-base Superalloys", 1995 ASME Winter Conference, San Francisco, CA, November, 20-24 (1995).
10. D.A. Alven and N.S. Stoloff, "The Influence of Composition on Environmental Embrittlement of Iron Aluminides," Proceedings of the Tenth Annual Conference on Fossil Energy Materials, Oak Ridge, TN, pp. 225-235, May 14-16 (1996).
11. C.G. McKamey, P.J. Maziasz and Y. Marrero-Santos, "Effects of Composition and Heat Treatment at 1150^0C on Creep-Rupture Properties of Fe_3Al-based Alloys," Proceedings of the Ninth Annual Conference on Fossil Energy Materials, Oak Ridge, TN, pp. 369-376, May 16-18 (1995).
12. J.T. Guo, C. Sum, H. Li, Z.Y. Zhang, Y.J. Tang, and Z.Q. Hu, Mater. Res. Soc. Symp. Proc. Vol.213, pp.655-659, (1991).
13. J.A. Horton and M.K. Miller, Mater. Res. Soc. Symp. Proc. Vol.81, pp.105-110, (1987).
14. H.P. Karnthaler, R. Kozubski, W. Pfeiler, and C. Renteberger, Mater. Res. Soc. Symp. Proc. Vol.364, pp.309-314, (1995).

Table 1 Chemical Composition of Iron Aluminides (at %)

Alloy	Fe	Aℓ	Cr	Zr	C	B
FA-186	balance	28	5			
FA-187	balance	28	5	0.5	0.05	
FA-189	balance	28	2	0.5	0.05	0.005

Table 2 Test Matrix

Iron aluminide	Specimen	Structure Condition	Initial Crack	Environment	Initial K $MPa\sqrt{m}$	Lasting Time
FA-186	86-1	B2	FP	Air	36.9	7 min
	86-5	B2	FP	Dry Oxygen	36.8	21 min
	86-10	DO_3	EDM	Air	25 28.3	94 min[c] 1 min
	86-9	DO_3	EDM	Dry Oxygen	25 28.7	19 hr[d] 21 min
	86-w1	DO_3	EDM	Water	13.35 22.12	2 hr[d] 8 second
FA-187	87-1	B2	EDM	Air	25	3.5 min
	87-5	B2	EDM	Dry Oxygen	25	15 min
	87-8	DO_3	EDM	Air	25	2 min
	87-7	DO_3	EDM	Dry Oxygen	25	18 min
	87-w1	DO_3	EDM	Water	15.43	46 second
FA-189	89-2	B2	EDM	Air	17.36	7 min
	89-1	B2	EDM	Dry Oxygen	17.36	20 min
	89-7	DO_3	EDM	Air	17.36	3 min
	89-6	DO_3	EDM	Dry Oxygen	17.36	12 min
	89-w1	DO_3	EDM	Water	13.1	60 second
	89-w2	DO_3	EDM	Water	20.76	8 second

[a] All tests were conducted at room temperature;
[b] FP: Fatigue Pre-cracked; EDM: Electron-Discharge Machining;
[c] Slow crack growth;
[d] Almost no crack growth.

Table 3. Failure mode and illustration of the fractured surfaces studied

Alloy	Specimen	Environment	Area 1	Area 2	Area 3
FA-186	86-1	Air	mixed	mixed	transgranular
	86-5	Dry Oxygen	mixed	transgranular	transgranular
	86-10	Air	mixed	mixed	transgranular
	86-9	Dry Oxygen	mixed	transgranular	transgranular
	86-w1	Water	intergranular	mixed	transgranular
FA-187	87-1	Air	intergranular	mixed	mixed
	87-5	Dry Oxygen	intergranular	mixed	transgranular
	87-8	Air	intergranular	mixed	transgranular
	87-w1	water	intergranular	intergranular	mixed
	87-7	Dry Oxygen	intergranular	transgranular	transgranular
FA-189	89-2	Air	intergranular	mixed	transgranular
	89-1	Dry Oxygen	intergranular	transgranular	transgranular
	89-7	Air	intergranular	mixed	transgranular
	89-6	Dry Oxygen	intergranular	transgranular	transgranular
	89-w2	water	intergranular	intergranular	mixed

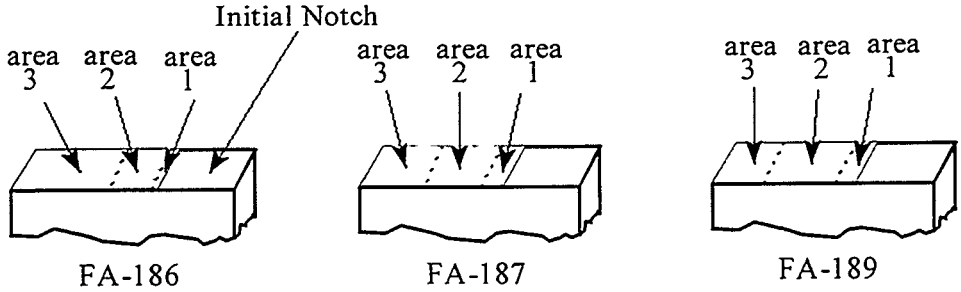

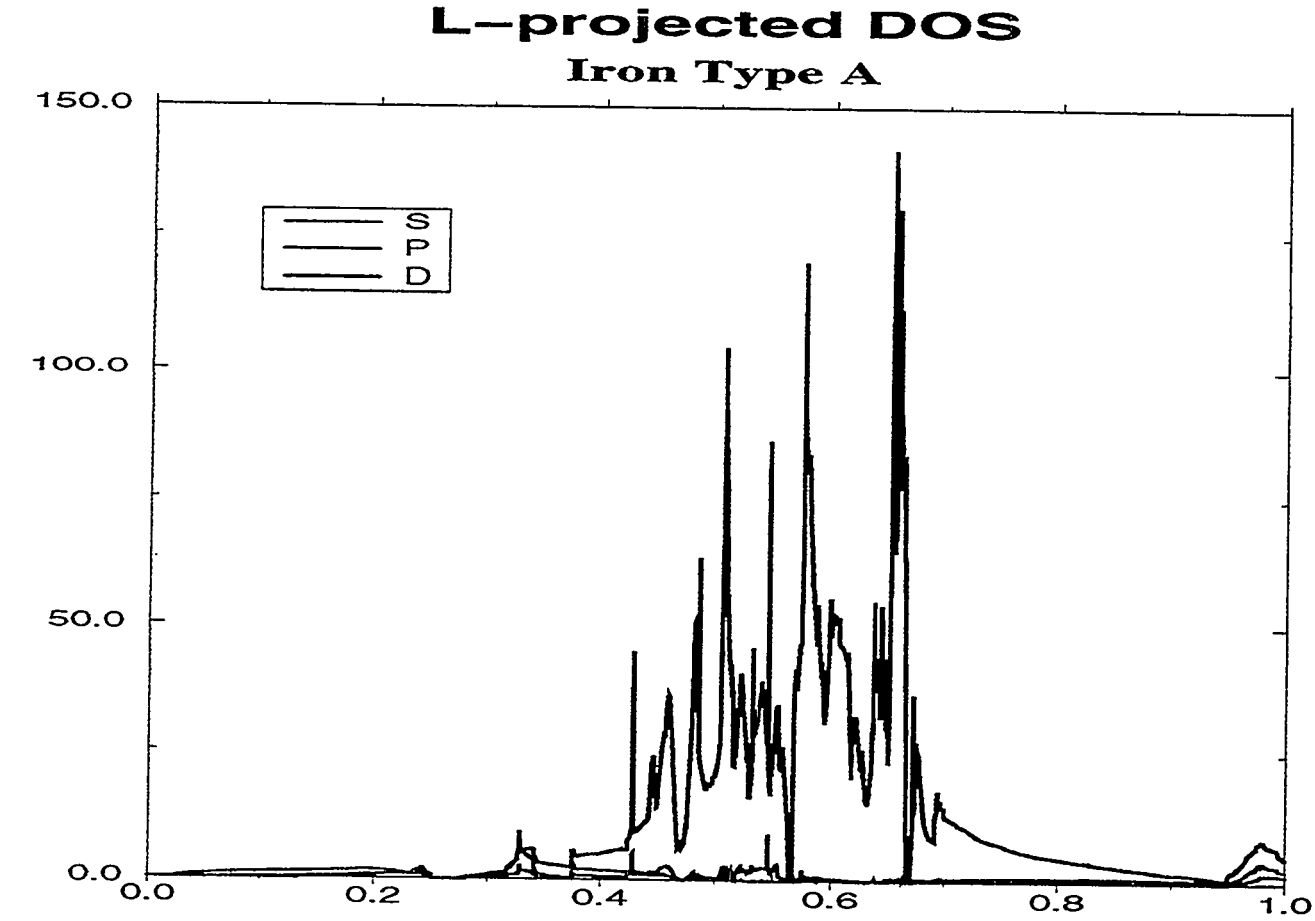
L–projected DOS
Iron Type A
150.0
100.0
50.0
0.0
S
P
D
0.0
0.2
0.4
0.6
0.8
1.0

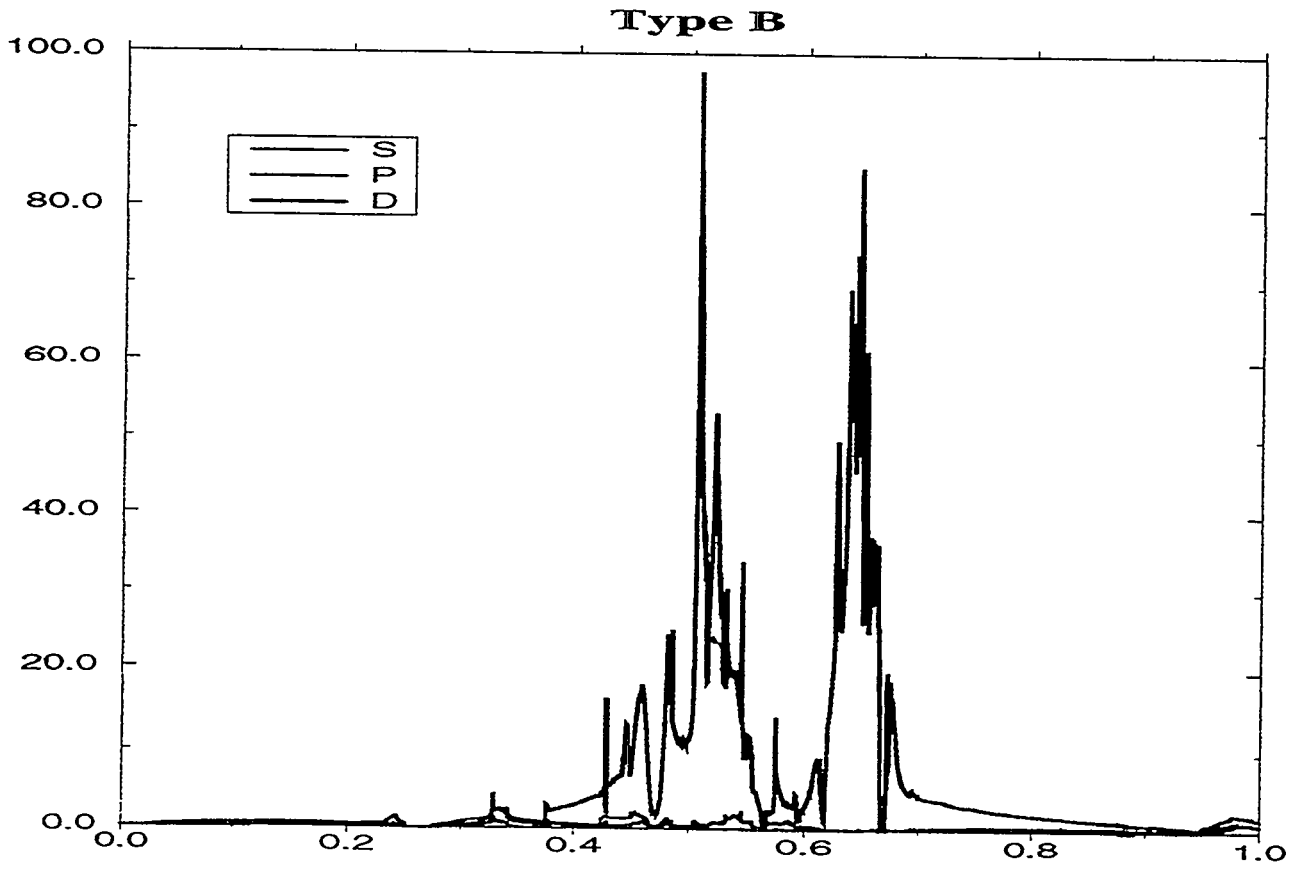
Type B
100.0
80.0
60.0
40.0
20.0
0.0
S
P
D
0.0
0.2
0.4
0.6
0.8
1.0

Fig. 1

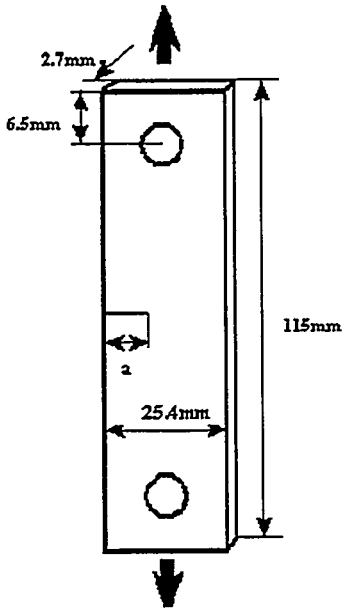

Fig.2 Single-edge-notched specimen

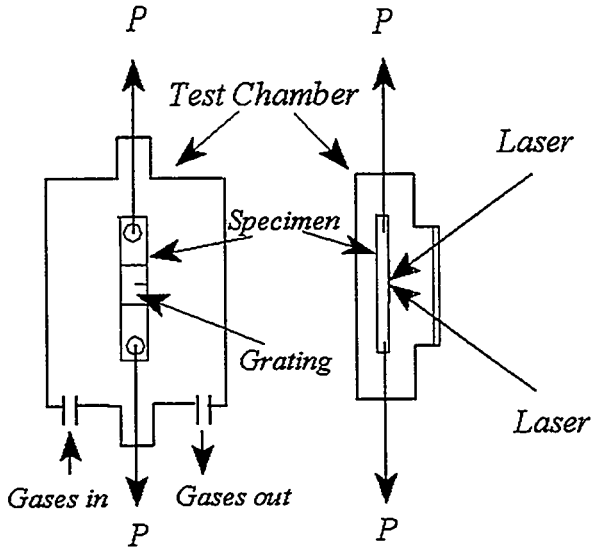

Fig.3 Schematic drawing of the enviromental testing chamber

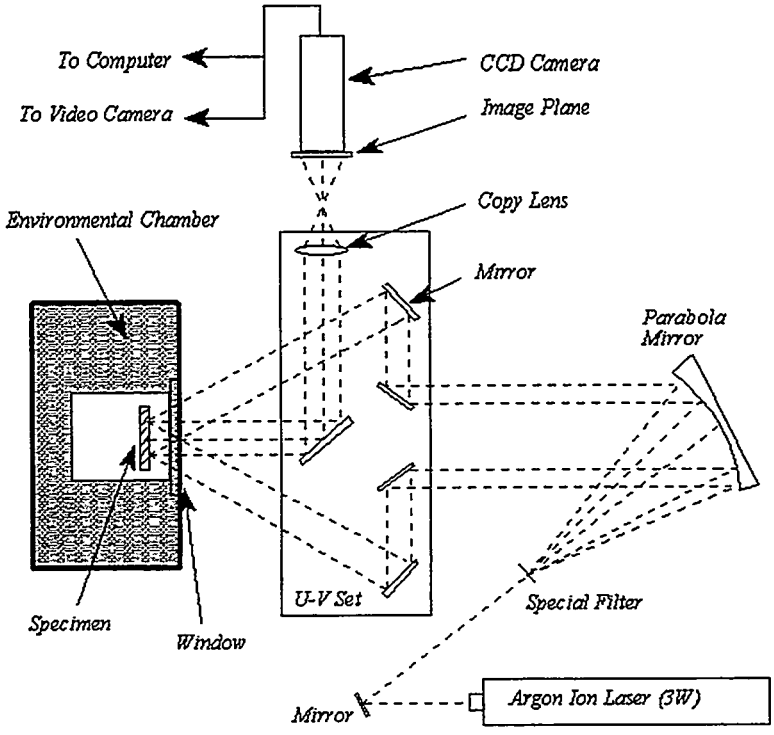

Fig.4 Optical setup for moire interferometry test

Alloy FA-189
Room Temp, Air K=17.06 $MPa\sqrt{m}$

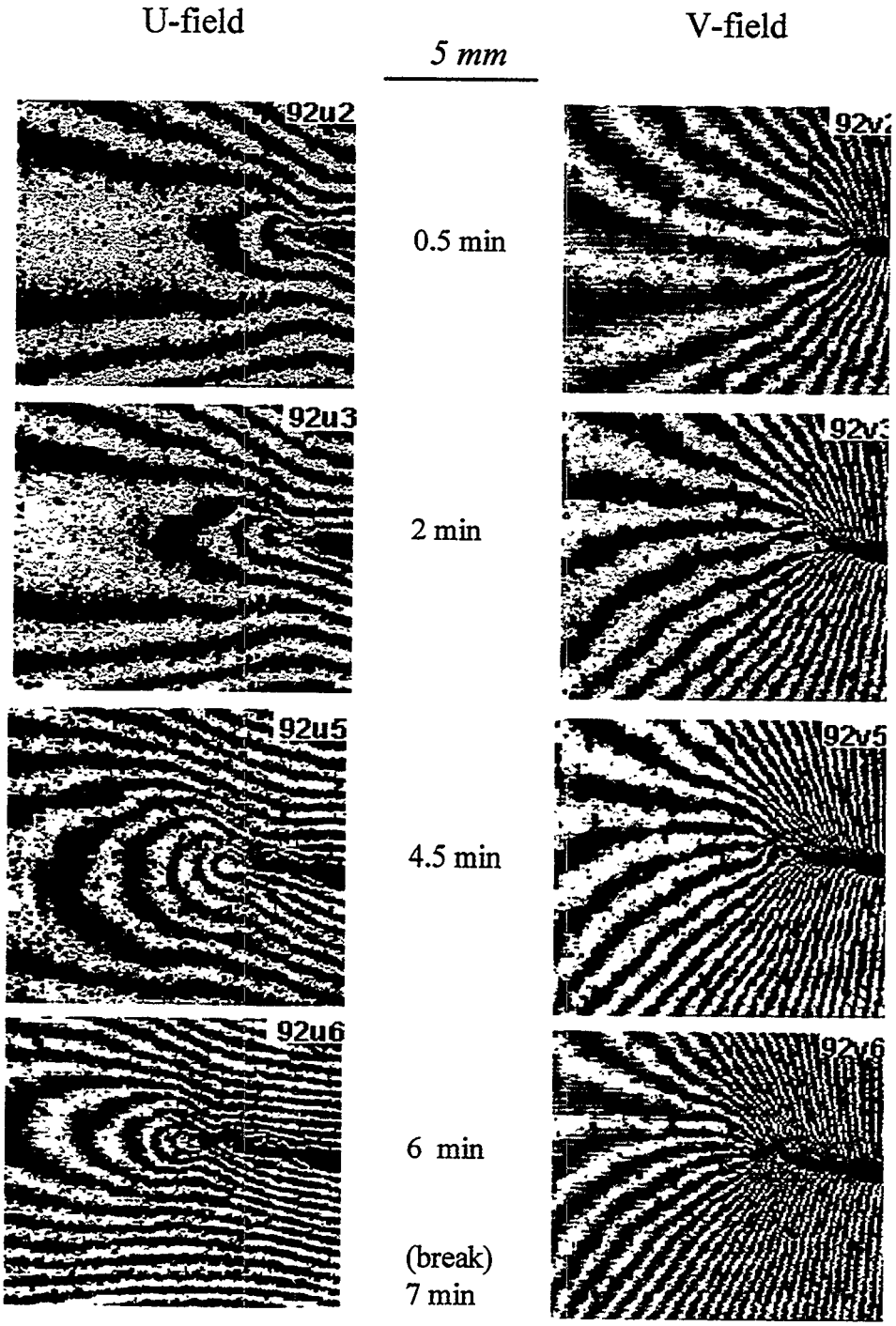

Fig. 5 u- and v- displacement fields of alloy FA-189 SEN specimen tested in air

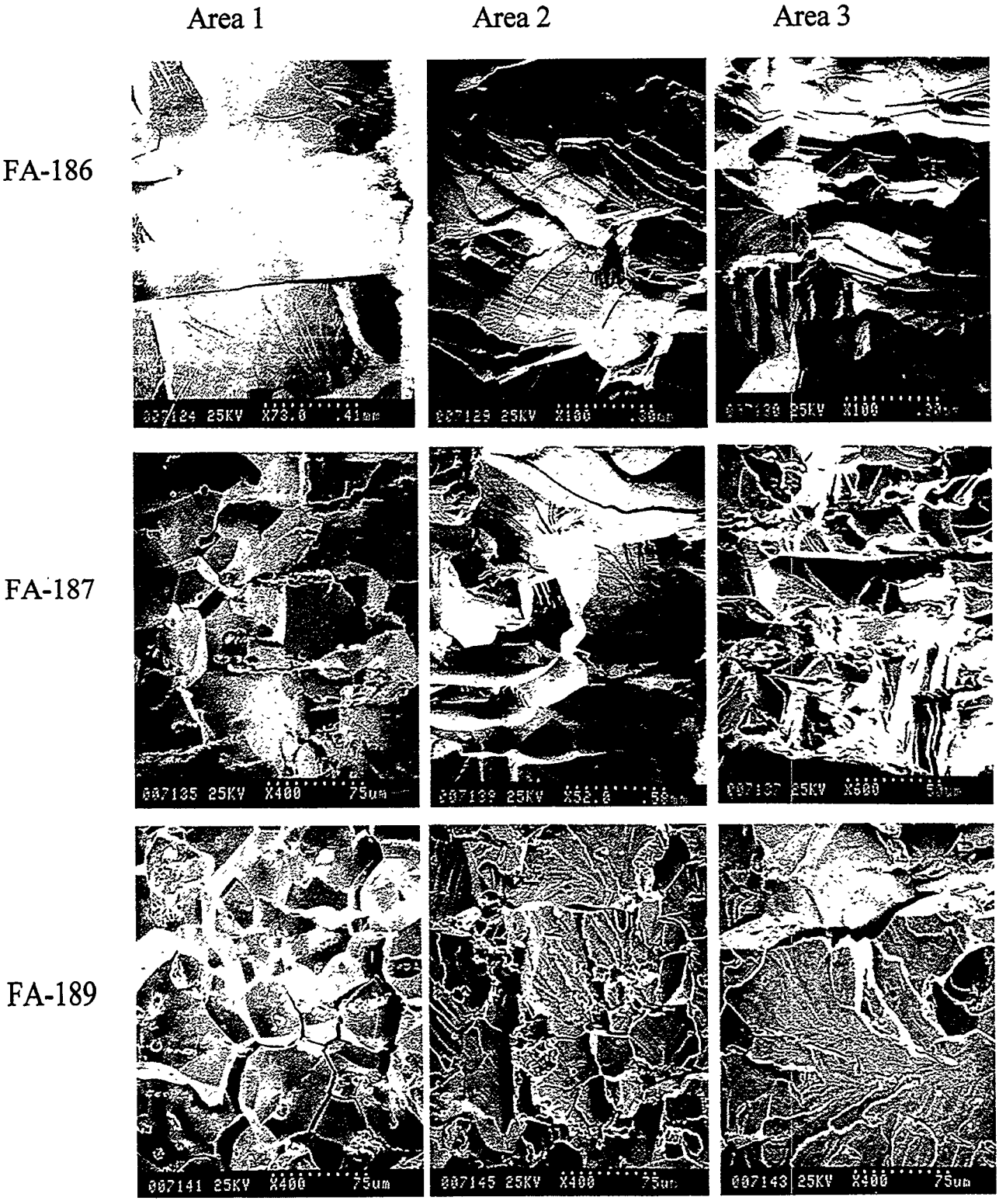

Fig.6 Representive fractographies for FA-186, FA-187 and FA-189 tested in the air environment

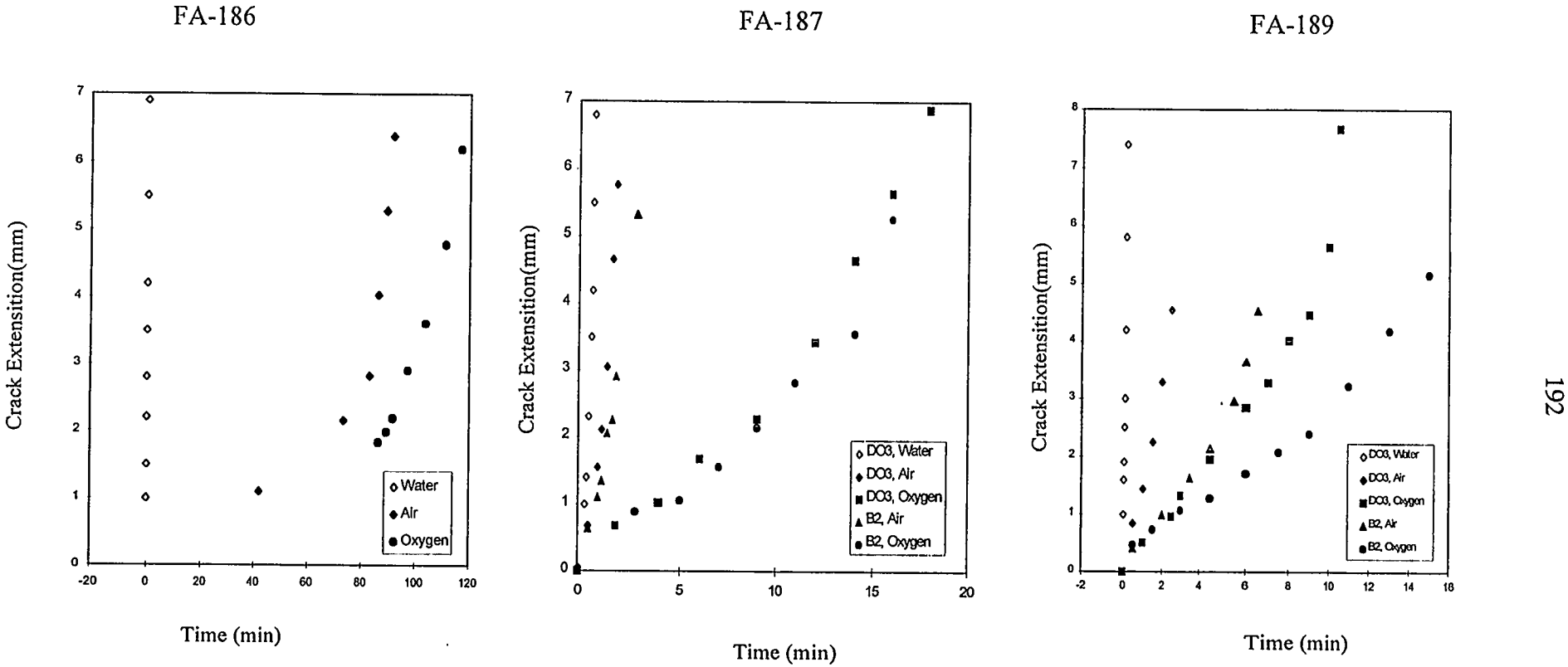

Fig.7 Crack ExtensionVesus Time

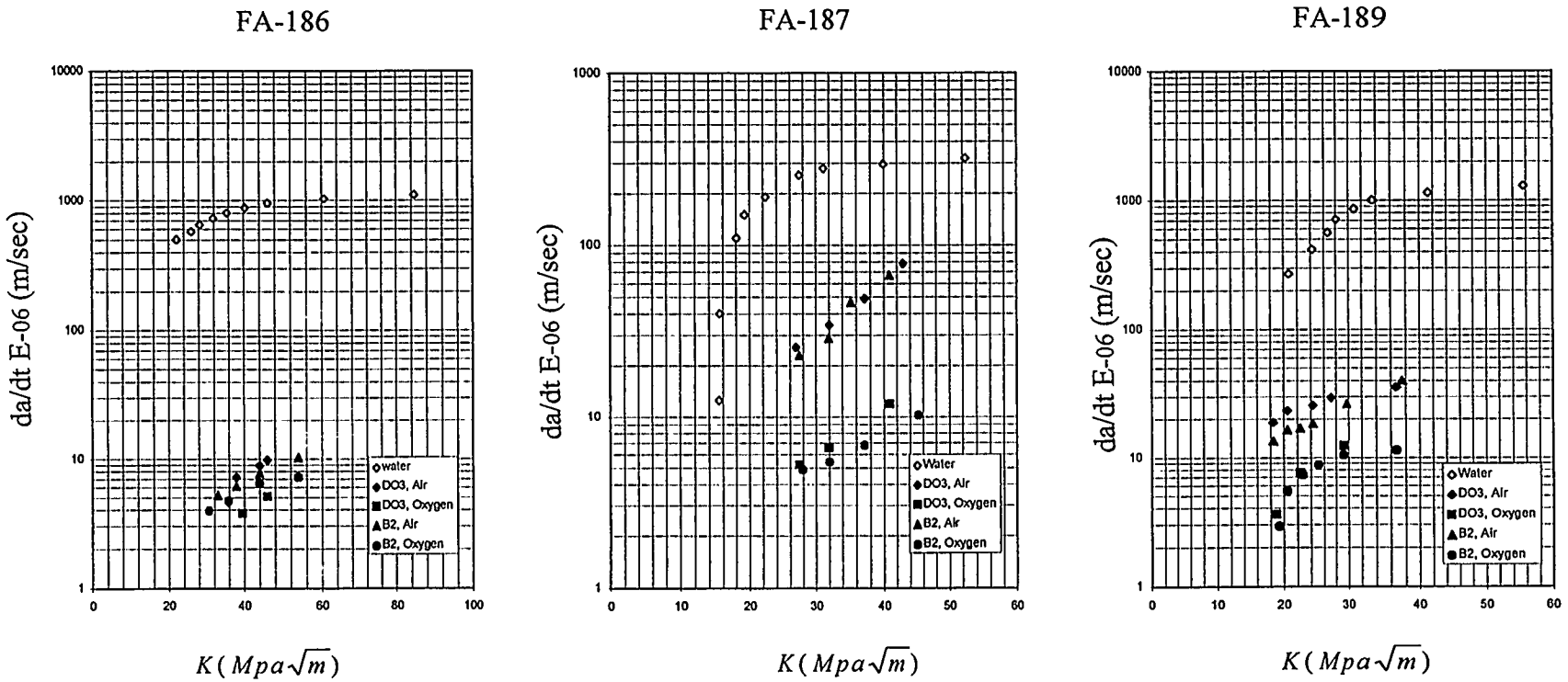

Fig.8 Environmental crack growth rate for FA-186, FA-187 and FA-189

ULTRAHIGH TEMPERATURE INTERMETALLIC ALLOYS

M. P. Brady, J.H. Zhu, C. T. Liu, P. F. Tortorelli, J.L. Wright, C.A. Carmichael, and L.R. Walker

Metals and Ceramics Division
Oak Ridge National Laboratory
Oak Ridge, Tennessee, U. S. A.

ABSTRACT

A new family of Cr-Cr_2X based alloys with fabricability, mechanical properties, and oxidation resistance superior to previously developed Cr-Cr_2Nb and Cr-Cr_2Zr based alloys has been identified. The new alloys can be arc-melted/cast without cracking, and exhibit excellent room temperature and high-temperature tensile strengths. Preliminary evaluation of oxidation behavior at 1100°C in air indicates that the new Cr-Cr_2X based alloys form an adherent chromia-based scale. Under similar conditions, Cr-Cr_2Nb and Cr-Cr_2Zr based alloys suffer from extensive scale spallation.

INTRODUCTION

The objective of this work is to develop a new generation of structural materials based on intermetallic alloys for use at high-temperatures in advanced fossil energy conversion systems. Target applications of such ultrahigh strength alloys include hot components (for example, air heat exchangers) in advanced energy conversion systems and heat engines. However, these materials may also find use as wear-resistant parts in coal handling systems (for example, nozzles), drill bits for oil/gas wells, and valve guides in diesel engines.

The developmental effort to date has focused on the Cr_2Nb and Cr_2Zr Laves phases[1-6]. Such Laves phases possess high melting points[7-9] and offer the potential for exceptional high-temperature strength[1-5]. However, they are extremely brittle at ambient temperatures[1-5,8]. In order to improve ambient temperature mechanical properties, two-phase "CN" alloys based on a soft Cr-rich solid solution phase reinforced with the hard Cr_2Nb or Cr_2Zr Laves phases have been developed[1-5].

For some Cr-Cr_2Nb based alloys, very high strengths at temperatures of 1200°C have been obtained[1,2]. However, improvements in ambient-temperature toughness and ductility have been modest[1,2]. This is thought to be due in part to thermal expansion mismatch between the Cr solid solution phase and the Cr_2Nb Laves phase, which leads to defects during fabrication, and extensive precipitation of the Cr_2Nb phase in the Cr solid solution phase[1].

The Cr-Cr_2Zr system shows better fabricability and crack resistance than the Cr-Cr_2Nb system, possibly due to a smaller mismatch of the coefficients of thermal expansion of the Cr solid solution and Laves phases[1]. The solubility of Zr in Cr is also much lower than that of niobium[9], which prevents extensive Cr_2Zr Laves phase preciptation in the Cr solid solution phase. However, the Cr-Cr_2Zr based alloys have poor oxidation resistance, and generally tend to be weaker at high-temperatures than the Cr-Cr_2Nb based alloys[1]. Significant property improvements in the Cr-Cr_2Zr based alloys beyond those already achieved appear unlikely.

The metallurgical insights gained from the study of the Cr-Cr_2Nb and Cr-Cr_2Zr systems have provided the basis for the selection of a promising new Cr-Cr_2X system with superior properties. Current efforts are focused on compositional optimization of alloys based on this new system. This report presents an overview of microstructural characterization, mechanical properties, and oxidation behavior for a near-optimized Cr-Cr_2Zr based alloy and several promising new Cr-Cr_2X based alloys.

ALLOY PREPARATION AND PROCESSING

CN alloys based on the Cr-Cr_2Zr and Cr-Cr_2X systems weighing 400-500 g were prepared by arc melting and drop casting in a copper mold (2.5 cm diam x 7.6 cm long) preheated to 200°C. Small 40 g castings of Cr-Cr_2X based alloys were also prepared by arc melting and drop casting in a chilled copper mold. High-purity chromium and other metal chips were used as charge materials. In particular, the Cr-Cr_2X based alloys were easily cast and showed no evidence of cracking. After heat treatment, the large 400-500 g alloy ingots were clad inside Mo billets and hot extruded at 1480°C and an extrusion ratio of 4:1. The hot-extruded material was then heat treated and used for tensile specimens. The small 40 g castings were used as-cast to provide specimens for oxidation exposures.

MICROSTRUCTURAL ANALYSIS

Figure 1 shows optical and scanning electron micrographs of hot-extruded CN129, which is a near-optimized Cr-Cr_2Zr based alloy containing four alloying additions (see Table 1). The microstructure consists of patches of the Cr solid solution phase surrounded by interconnected Cr_2Zr Laves phase. It is important to note that, unlike the Cr-Cr2Nb system[1], no precipitation of Cr2Zr particles was found in the primary Cr-rich patches (by scanning electron microscopy). Wavelength dispersive electron probe microanalysis (pure element standards) of the Cr solid solution and Laves phases in CN129 are shown in Table 1.

a)

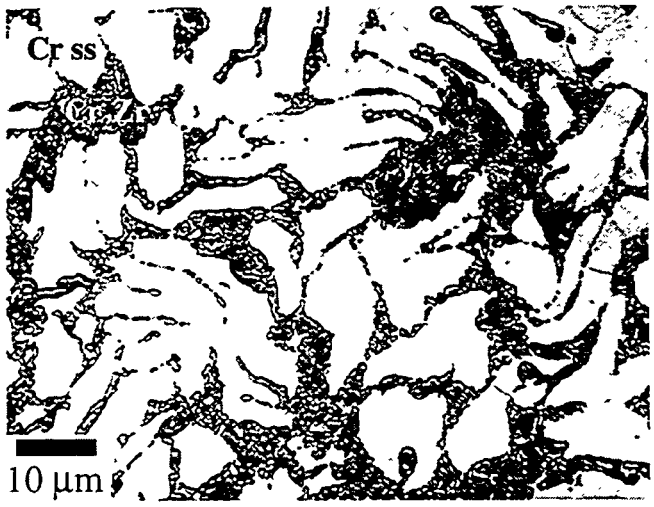

b)

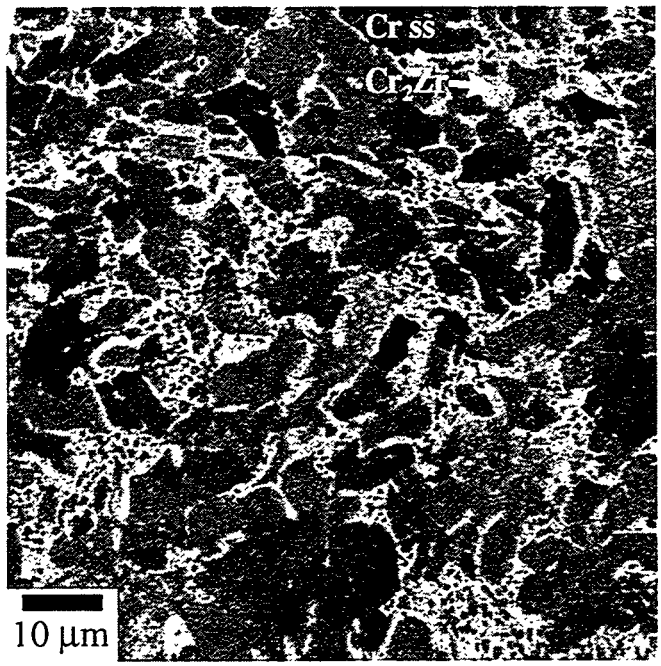

Fig. 1- Microstructure of hot-extruded CN129. a) Optical (light microscopy): Cr solid solution (Cr ss) light, Cr_2Zr Laves dark b) Scanning Electron (secondary): Cr ss dark, Cr_2Zr Laves light.

Table 1- Electron probe microanalysis of hot-extruded CN129 (at.%). An average of 3-6 measurements for each phase is reported. The data is estimated to be accurate within ± 1-2 at.%.

CN129	Cr	Zr	X1	X2	X3	X5
Cr solid solution	93.04	0.02	4.99	0.53	1.27	0.16
Laves	49.12	26.08	6.37	11.19	3.30	3.94
Nominal	84	5	5	3	2	1

Figure 2 shows optical and scanning electron micrographs of hot-extruded CN130, which was one of the first Cr-Cr_2X based alloys to be studied. The microstructure consists of a fine dispersion of spherodized Cr_2X Laves phase particles dispersed in a Cr solid solution matrix. Such a microstructure is expected to be nearly ideal for achieving optimum mechanical properties. Electron microprobe analysis of CN130 is shown in Table 2.

TENSILE PROPERTIES

Button-type tensile specimens with gage dimensions 0.31 cm diam x 0.95 cm long were machined by electro-discharge machining from hot-extruded material, followed by grinding and polishing with "0" Emery paper. The tensile specimens were tested in an Instron Testing Machine at room temperature, 800°C, and 1000°C in air, and at 1200°C in vacuum (crosshead speed of approximately 0.25 cm/minute).

Table 3 summarizes the tensile properties of two near-optimized Cr-Cr_2Zr based alloys, CN128 and CN129. No macroscopic yielding prior to fracture was observed. However, room-temperature fracture strengths of greater than 80 ksi (550 MPa) were obtained. These fracture strengths are slightly higher than that of the best Cr-Cr_2Nb based alloys[1,2].

The alloy CN129 also showed no macroscopic tensile ductility at 1000°C, but was extremely ductile at 1200°C. This suggests that the ductile to brittle transition temperature (DBTT) of Cr-Cr_2Zr based alloys is around 1100°C. At 1200°C, the alloy is very strong, with an ultimate tensile strength of greater than 58 ksi (400 MPa).

The tensile properties of the first generation of Cr-Cr_2X based alloys are summarized in Table 4. Strengths of over 100 ksi (689 MPa) were obtained at room temperature (no macroscopic yielding prior to fracture was observed). At 800°C, elongation on the order of 1% and fracture strengths in excess of 130 ksi (896 MPa) were obtained. Although not yet optimized, this first generation of Cr-Cr_2X based alloys already exhibits much better lower-temperature tensile behavior than the best Cr-Cr_2Nb and Cr-Cr_2Zr based alloys[1]. The tensile elongation increases with temperature, and reaches around 20% at 1200°C. At 1200°C, one Cr-Cr_2X based alloy exhibited an ultimate tensile strength of greater than 50 ksi (345 MPa), which is in the range of the tensile properties obtained for the Cr-Cr_2Nb and Cr-Cr_2Zr based alloys at 1200°C[1].

a)

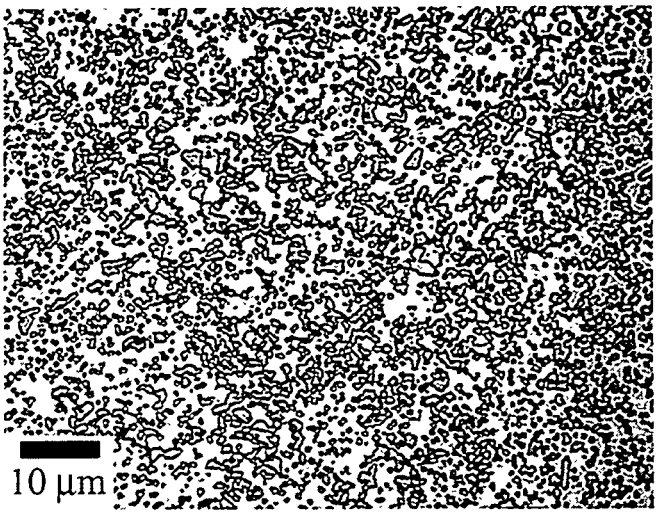

b)

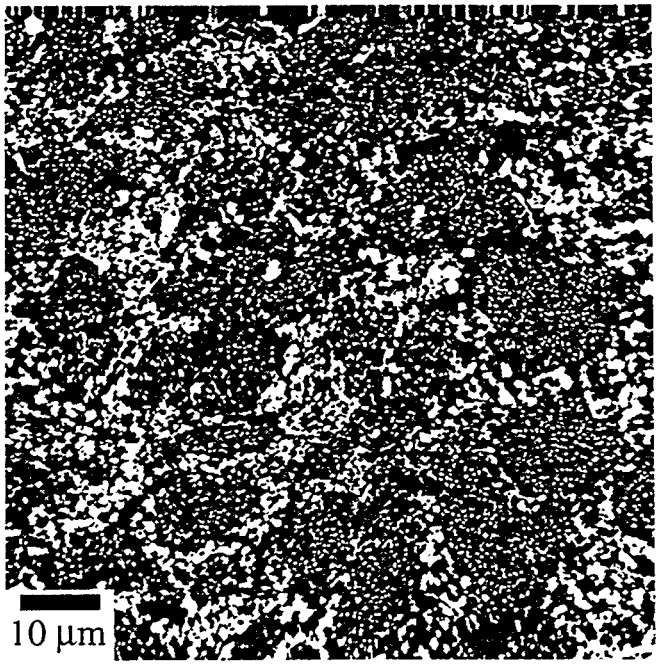

Fig. 2- Microstructure of hot-extruded CN130. a) Optical (light microscopy): Cr ss matrix, Cr_2X Laves second phase b) Scanning Electron (secondary): Cr ss dark, Cr_2X Laves light, Oxide inclusion black.

Table 2- Electron probe microanalysis of hot-extruded CN130 (at.%). An average of 3-6 measurements for each phase is reported. The data is estimated to be accurate within ± 1-2 at.%.

*CN130	Cr	X	X1	X3
Cr solid solution	93.69	0.95	5.33	0.03
Laves	68.01	27.16	4.824	0.003
Nominal	86.5	8	5	0.5

*X3-rich oxide particles and a very minor volume fraction phase of Cr-33X-8.5X1 were also observed.

Table 3- Tensile properties of hot-extruded Cr-Zr base alloys.

Alloy No.	Alloy Composition (at. %)	Yield Strength (ksi)	Fracture Strength (ksi)	Elongation (%)
	Room Temperature			
CN128	Cr-6Zr-5X1-3X2-1X3-1X5	>83.6	83.6	*
CN129	Cr-5Zr-5X1-3X2-2X3-1X5	>81.5	81.5	*
	1000°C			
CN129		>81.3	81.3	*
	1200°C			
CN129		45.1	58.6	>63+

* Fracture prior to macroscopic yielding
+ The test was stopped after straining to 63%

While it is unlikely that CN alloys will ever be able to exhibit appreciable room-temperature tensile ductility, significant room-temperature fracture toughness may be possible because of the two-phase microstructure. Quantitative measurements of room temperature fracture toughness of the Cr-Cr_2X based alloys have not yet been made. However, qualitative assessment of room-temperature toughness by simple "drop" and "hammer-impact" tests suggest that the Cr-Cr_2X based alloys possess superior toughness to the Cr-Cr_2Nb and Cr-Cr_2Zr based alloys. The best Cr-Cr_2Nb and Cr-Cr_2Zr based alloys to date exhibit room-temperature fracture toughness on the order of 7-8 MPa$\sqrt{m}$. The Cr-Cr_2X based alloys are therefore expected to have fracture toughness greater than this range.

OXIDATION BEHAVIOR

All CN alloys will require an oxidation-resistant coating at temperatures above approximately 1000°C because of chromia (Cr_2O_3) scale volatility[10]. Previous and ongoing work at The Ohio State University has demonstrated that silicide coatings applied by a pack cementation process can substantially improve the isothermal and cyclic oxidation resistance of CN alloys at temperatures above 1000°C in air[11-13]. However, in application, the CN alloys must demonstrate a degree of oxidation resistance at these high temperatures to provide for survivability in the event of coating failure. Therefore, a screening test that consisted of 1100°C exposures in room air was adopted to evaluate the high-temperature oxidation resistance of the newly developed CN alloys.

Table 4- Tensile properties of hot-extruded Cr-8X based alloys.

Alloy No.	Alloy Composition (at. %)	Yield Strength (ksi)	Fracture Strength (ksi)	Elongation (%)
	Room Temperature			
CN130	Cr-8X-5.0X1-0.5X3	>104	104	*
CN132	Cr-8X-5.0X1-3.0X2-0.5X3-0.05X6	>71	71	*
CN133	Cr-8X-2.5X1-3.0X2-0.5X3	>101	101	*
	800°C			
CN130		120	120	0.8
CN132		134	137	1.2
CN133		>69	69	*
	1000°C			
CN130		86	97	7.6
CN132		97	104	3.0
CN133		81	89	8.6
	1200°C			
CN130		37	45	16.6
CN132		42	51	18.5
CN133		30	36	22.0

*Fracture prior to macroscopic yielding.

Disk shaped oxidation specimens of 8-13 mm in diameter and 1 mm thickness were sectioned from as-cast or hot-extruded material and polished to a 600 grit finish using SiC paper. The oxidation specimens were placed in an alumina crucible and covered with an alumina lid. At intervals of 1, 4, 10, 30, 48, and 120 hours, the samples were removed from the furnace at temperature, air-cooled, weighed, and returned to the furnace at temperature. Using this interrupted weight change procedure, both isothermal and cyclic oxidation resistance may be surveyed. Volatilization of chromia occurred during the test, as evidenced by a green stain on the inside surfaces of the alumina crucible and lid.

The interrupted weight change oxidation data for Cr-10X, Cr-10Nb, and pure Cr are shown in Figure 3. Comparison data for the Cr-Cr_2Zr based alloy CN129 are also provided. Cr-10X exhibited excellent oxidation resistance for a chromia-former at this high-temperature and was the only one to survive the interrupted weight change screening intact. After 6 cycles and 120 h of exposure at 1100°C, a uniform scale with only very slight evidence of spallation at the sample edges was observed. In contrast, Cr-10Nb and pure Cr suffered from extensive scale spallation. CN129 catastrophically failed between the 10 and 30h cyclic intervals. Preliminary cross-section analysis of isothermally oxidized CN129 indicates that Zr in the

Cr_2Zr Laves phase is extensively internally oxidized. This may have led to catastrophic failure during the interrupted weight change exposure as a result of coefficient of thermal expansion mismatch between the internal zirconium oxide and the surrounding metal.

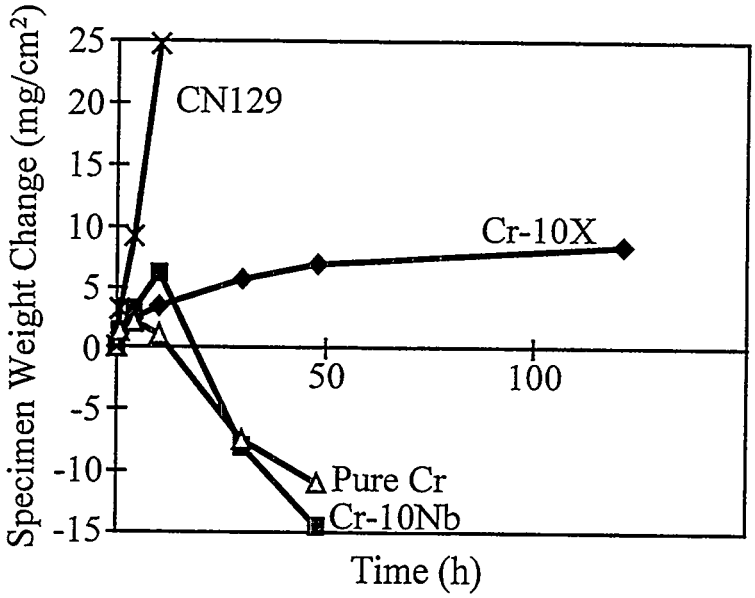

Fig. 3- Interrupted weight change data for as-cast Cr-10X, Cr-10Nb, and pure Cr at 1100°C in room air (at.%). Data for hot-extruded CN129 (Cr-5Zr-5X1-3X2-2X3-1X5 at.%) are also shown.

Cross-section scanning electron micrographs of Cr-10X, Cr-10Nb, and pure Cr after 6 cycles and 120 hours of exposure at 1100°C are shown in Figure 4. A continuous chromia scale formed on Cr-10X. Microhardness measurements in the metal beneath the metal/scale interface showed no evidence of interstitial O or N penetration (note that this technique is only sensitive to within about 5-10 microns of the metal/scale interface). The scale that formed on Cr-10Nb consisted primarily of a complex mixture of chromium and/or chromium plus niobium oxides. X-ray diffraction data from 1200°C exposed Cr-10Nb suggests the presence of Cr_2O_3 and $CrNbO_4$, in agreement with prior observation on Cr-Cr_2Nb alloys oxidized at 950°C[14]. No scale remained on pure Cr. Microhardness measurements in both Cr-10Nb and pure Cr indicate significant hardening and embrittlement in the metal beneath the metal/scale interface.

Figures 5 and 6 show 1100°C interrupted weight change data for alloying additions of X1 or X2 to a Cr-8X based alloy. Cr-8X was less oxidation resistant than Cr-10X due to a tendency to spall, but was preferred from a mechanical property standpoint. Additions of X1 to Cr-8X resulted in comparable oxidation resistance to Cr-10X (Figure 5). However, additions of X2 were deleterious to the oxidation resistance of Cr-8X (Figure 6). These results are surprising because the reverse effect had been observed

for additions of X1 and X2 to Cr-Cr_2Nb based alloys[15], although that data was obtained isothermally at lower temperatures. The reasons for these differences are under investigation.

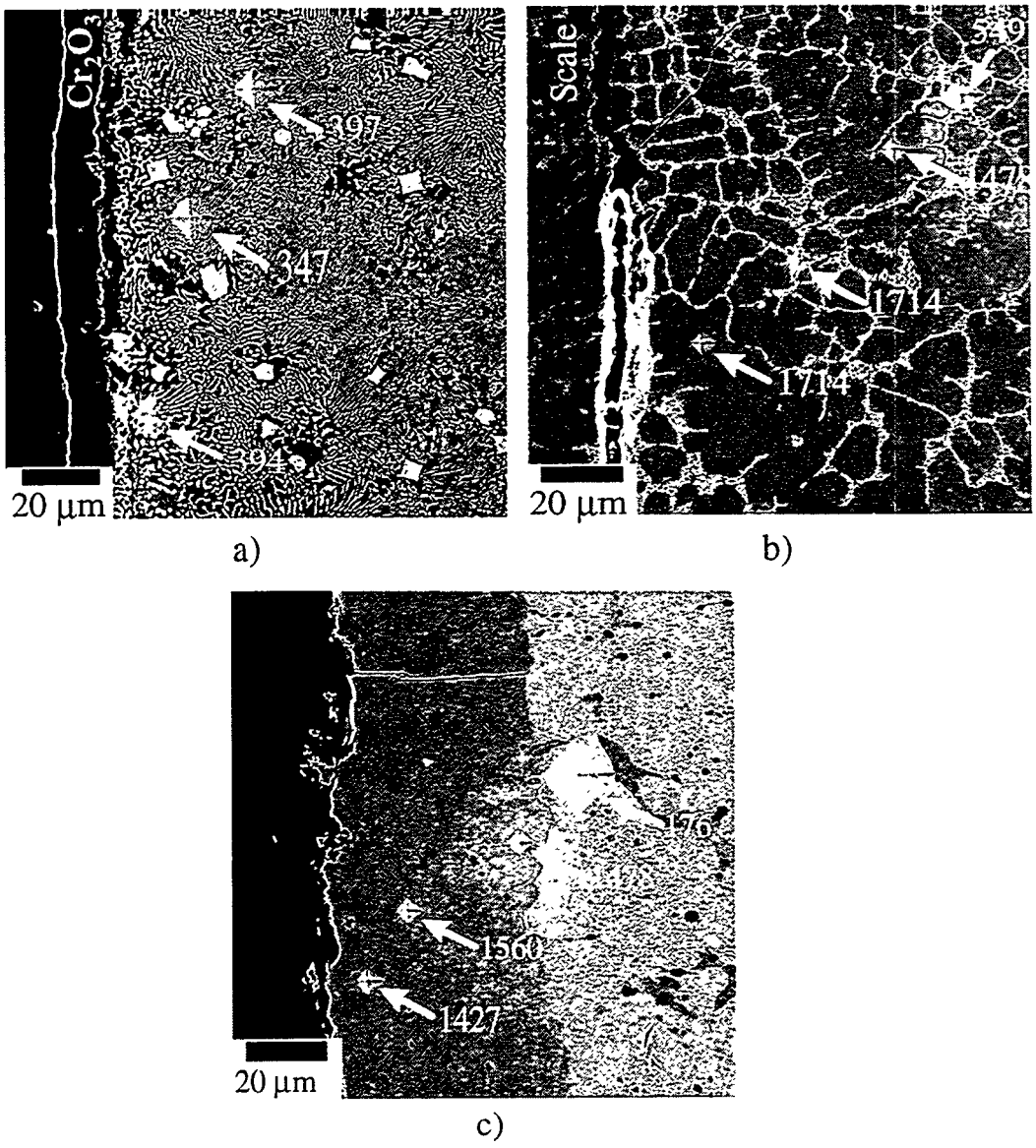

Fig. 4- Cross-section scanning electron (secondary) micrographs of as-cast (a) Cr-10X (≅ 15μm thick scale), (b) Cr-10Nb (≅ 550 μm thick scale), and (c) pure Cr (complete scale spallation) after 6 cycles and 120 h at 1100°C in room air. The Vicker's hardness indentation was performed at a load of 100 g for 15 seconds.

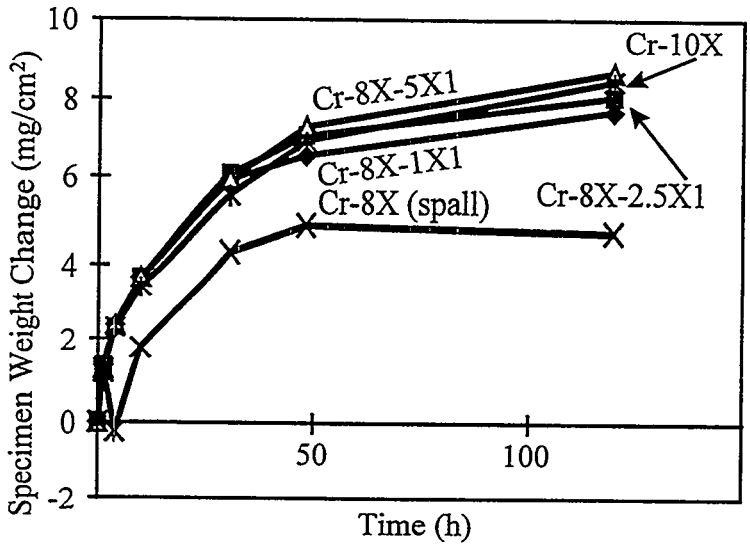

Fig. 5- Interrupted weight change data for as-cast Cr-8X-1X1, Cr-8X-2.5X1, Cr-8X-5X1, Cr-8X, and Cr-10X at 1100°C in room air (at.%).

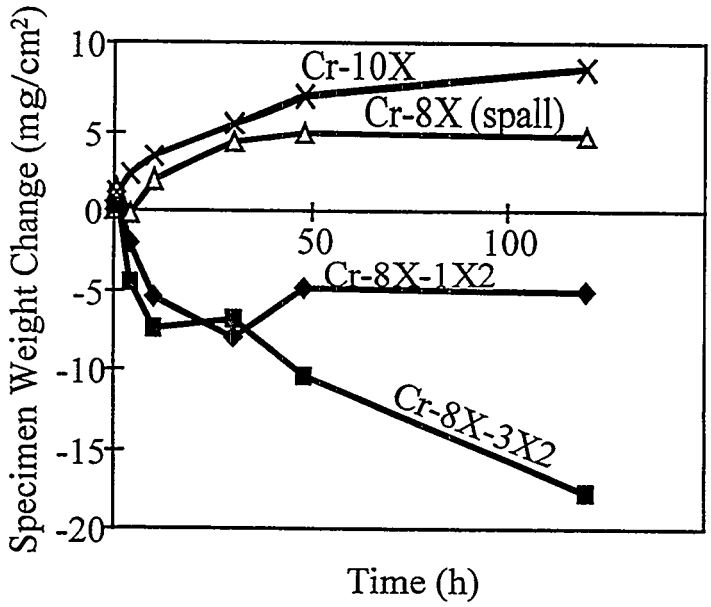

Fig. 6- Interrupted weight change data for as-cast Cr-8X-1X2, Cr-8X-3X2, Cr-8X, and Cr-10X at 1100°C in room air (at.%).

SUMMARY AND FUTURE WORK

A new family of Cr-Cr_2X based alloys has been identified, whose fabricability, mechanical properties, and oxidation resistance are dramatically better than that of previously developed Cr-Cr_2Nb and Cr-Cr_2Zr based alloys. Future work will concentrate on a more complete evaluation of mechanical properties, including room temperature fracture toughness, and compositional modification for optimum mechanical properties and oxidation resistance.

ACKNOWLEDGMENTS

The authors thank Dewey Easton for the hot extrusions, and Bruce Pint, Joachim Schneibel, and Jim Distefano for their reviews of the manuscript. This research was sponsored by the Fossil Energy Advanced Research and Technology Development (AR&TD) Materials Program, U S. Department of Energy, under contract DE-AC05-96OR22464 with Lockheed Martin Energy Research Corporation.

REFERENCES

1. C. T. Liu, P. F. Tortorelli, J. A. Horton, D. S. Easton, and L. Heatherly, pp. 477-89 in *Proc. Tenth Annual Conf. Fossil Energy Materials*, N. C. Cole and R. R. Judkins (comp.), U. S. Department of Energy, August 1996.
2. C. T. Liu, P. F. Tortorelli, J. A. Horton, D. S. Easton, J. H. Schneibel, L. Heatherly, C. A Carmichael, M. Howell, and J. L. Wright, pp. 415 - 26 in *Proc. Ninth Annual Conf. Fossil Energy Materials*, N. C. Cole and R. R. Judkins (comp.), U. S. Department of Energy, August 1995.
3. C. T. Liu, J. A. Horton, and C. A. Carmichael, pp. 377-390 in *Proc. 8th Annual Conf. on Fossil Energy Materials*, N. C. Cole and R. R. Judkins (comp.), U. S. Department of Energy, August 1994.
4. C. T. Liu, J. A. Horton, and C. A. Carmichael, pp. 297-307, in *Proc. 7th Annual Conf. on Fossil Energy Materials*, N. C. Cole and R. R. Judkins (comp.), U. S. Department of Energy, July 1993.
5. C. T. Liu, pp. 375-383 in *Proc. 6th Annual Conf. Fossil Energy Materials*, N. C. Cole and R. R. Judkins (comp.), U. S. Department of Energy, July 1992.
6. F. Laves, p. 124 in Theory of Alloy Phases, American Society for Metals, Metals Park, OH, 1956.
7. D. J. Thoma and J. H. Perepezko, Mat. Sci. and Eng. A156 (1992) 97.
8. H. J. Goldschmidt and J. A. Brand, J. Less-Common Met. 3 (1961) 44.
9. T. B. Massalski, J. L. Murray, L. H. Bennett, and H. Baker (eds.), Binary Alloy Phase Diagram, American Society for Metals, Metals Park, OH, 1986.
10. P. Kofstad, High-temperature Corrosion, Elsevier, London, 1988.
11. Y-R. He, M. Zheng, and R.A. Rapp, 465-476, in *Proc. Tenth Annual Conf. Fossil Energy Materials*, N. C. Cole and R. R. Judkins (comp.), U. S. Department of Energy, August 1996.
12. Y-R. He, R. A. Rapp, and P. F. Tortorelli, "Oxidation-Resistant Ge-Doped Silicide Coating on Cr-Cr_2Nb Alloys by Pack Cementation," pp. 109-117, *Mater. Sci. and Eng. A*, A222, 1997.
13. Y-R. He and R. A. Rapp, these proceedings.
14. P.F. Tortorelli and B.A.. Pint, pp.174-185 in Fundamental Aspects of High-Temperature Corrosion, D.A.. Shores, R.A.. Rapp, and P.Y. Hou (eds.), Proceedings Volume 96-26, The Electrochemical Society, Pennington, New Jersey, 1997.
15. P.F. Tortorelli and J.H. DeVan, pp.391 - 400 in *Proc. Eighth Annual Conf. Fossil Energy Materials*, N.C. Cole and R.R. Judkins (comp.), CONF-9405143, U. S. Department of Energy, August 1994.

STUDY OF FATIGUE AND FRACTURE BEHAVIOR OF $NbCr_2$-BASED ALLOYS: PHASE STABILITY IN Nb-Cr-Ni TERNARY SYSTEM

J. H. Zhu*, P. K. Liaw*, and C. T. Liu+

*Department of Materials Science and Engineering
The University of Tennessee, Knoxville, TN 37996

+Metals and Ceramics Division, Oak Ridge National laboratory
Oak Ridge, TN 37831-6115

ABSTRACT

Phase stability in a ternary Nb-Cr-Ni Laves phase system was studied in this paper. Our previous study in $NbCr_2$-based transition-metal Laves phases has shown that the average electron concentration factor, e/a, is the dominating factor in controlling the phase stability of $NbCr_2$-based Laves phases when the atomic size ratios are kept identical. Since Ni has ten out-shell electrons, the substitution of Ni for Cr in $NbCr_2$ will increase the average electron concentration of the alloy, thus leading to the change of the crystal structures from C15 to C14. In this paper, a number of pseudo-binary $Nb(Cr,Ni)_2$ alloys were prepared, and the crystal structures of the alloys after a long heat-treatment at 1000°C as a function of the Ni content were determined by the X-ray diffraction technique. The boundaries of the C15/C14 transition were determined and compared to our previous predictions. It was found that the electron concentration and phase stability correlation is obeyed in the Nb-Cr-Ni system. However, the e/a ratio corresponding to the C15/C14 phase transition was found to move to a higher value than the predicted one. The changes in the lattice constant, Vickers hardness and fracture toughness were also determined as a function of the Ni content, which were discussed in light of the phase stability difference of the alloys.

INTRODUCTION

Laves phases with AB_2 composition comprise the single largest class of intermetallics, yet they are the least studied, compared with the conventional intermetallics, such as B2, $L1_2$, etc. Transition-metal Laves phases are currently being considered for many practical applications, e.g., $(Hf,Zr)V_2$ as superconducting material, $Zr(Cr,Fe)_2$ as hydrogen storage material, etc.[1,2] More recently, HfV_2-, $HfCr_2$- and $NbCr_2$-based two-phase alloys[3-9] are being developed for high-temperature structural uses, because of their good retention of mechanical properties at elevated temperatures. However, their low ductility and brittle fracture characteristics at ambient temperatures are the main concerns for structural applications of these materials.

Laves phases generally crystallize into one of the three topologically close-packed structures: cubic C15 – $MgCu_2$ structure, hexagonal C14 – $MgZn_2$ structure, and dihexagonal C36 – $MgNi_2$ structure.[10] Although Laves phases are generally stabilized by the size-factor principles, the stability of each crystalline structure is also influenced by the electron concentration factor (e/a). The classic work by Laves and Witte[11,12] showed that for several quasi-binary alloy systems involving $MgCu_2$ and $MgZn_2$, with

increasing valence electron concentration, the three Laves types, $MgCu_2$, $MgNi_2$, and $MgZn_2$, exist in that order. One attractive way to improve the deformability of complex Laves phases is to control their crystalline structure in a way that stress-assisted phase transformation and/or mechanical twinning can be triggered during plastic deformation.[13,14] It is thus important to know the factors governing the phase stability in transition-metal Laves alloys.

In our previous investigation[15], a number of binary and ternary phase diagrams were surveyed, and the phase stability criteria in the $NbCr_2$-based Laves phase systems, binary X-Cr and Nb-X and ternary Nb-Cr-X, were studied. It was shown that when the atomic size ratios are kept identical, the average electron concentration factor, e/a, is the dominating factor in controlling the phase stability of $NbCr_2$-based transition-metal Laves phases. The e/a ratios for different Laves polytypes were determined as follows: with e/a < 5.76, the C15 structure is stabilized; at an e/a range of 5.88-7.53, the C14 structure is stabilized; with e/a > 7.65, the C15 structure is stabilized again. A further increase in the electron concentration factor (e/a > 8) leads to the disordering of the alloy. The results are summarized in Fig. 1.

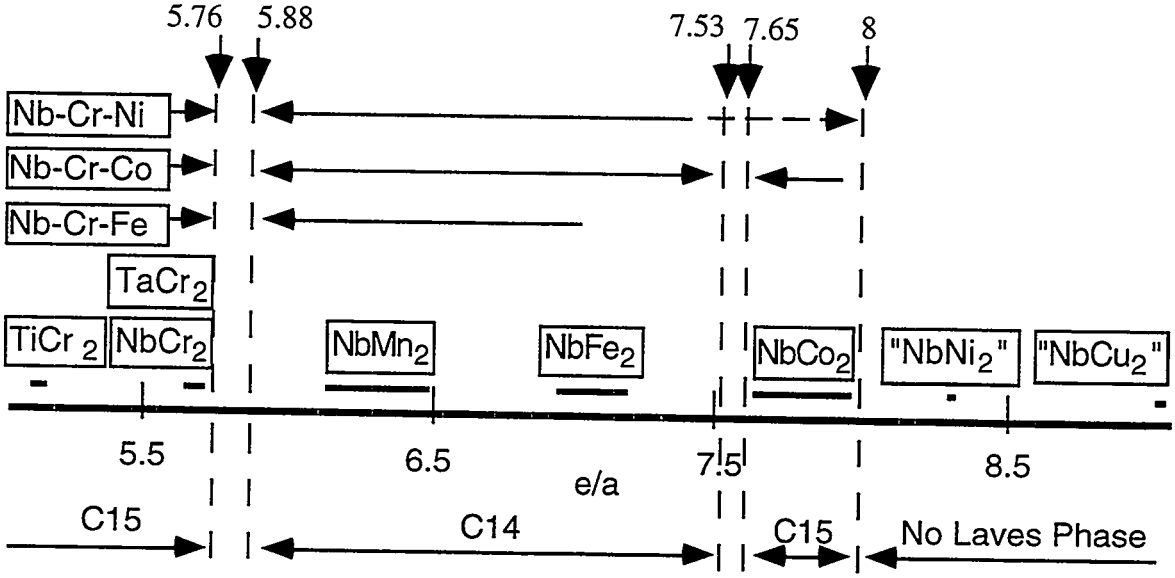

Fig. 1 Effect of average electron concentration (e/a) on phase stability in binary and ternary $NbCr_2$-based systems[15]

In this investigation, the Laves-phase stability in the ternary Nb-Cr-Ni system was studied experimentally to verify the observed e/a/phase stability correlation. Since Ni has ten outshell electrons, the addition of Ni to substitute for Cr (e/a = 6) in $NbCr_2$ is very effective in increasing the average electron concentration. By a systematic replacement of Cr with Ni, it is possible to see a whole spectrum (e.g., C15 → C14 → C15) of changes in the crystal structure of the Laves-phase based $Nb(Cr,Ni)_2$ alloys. The results reported here include the phase structures, lattice constants, hardness, and fracture toughness of the Laves phases as a function of the Ni content.

EXPERIMENTAL PROCEDURES

A series of pseudo-binary $Nb(Cr,Ni)_2$ alloys with 0, 1, 3, 5, 10, 20, 35 at % Ni were produced by replacing Cr with Ni, while keeping the percentage of Nb constant (33.3 at.%). Table 1 lists the nominal chemical compositions (at.%) and the average electron concentrations (e/a) and the predicted crystal structures (using the data shown in Fig. 1) of the alloys studied in this work. These alloys are in the C15 region, the C15/C14 transition region, and the C14 region, respectively, according to the prediction of Fig.1.

Table 1 The chemical compositions, e/a ratios, and predicted structures of pseudo-binary $Nb(Cr,Ni)_2$ alloys

Alloy No.	1	2	3	4	5	6	7
Ni Content	0	1	3	5	10	20	35
e/a Ratio	5.67	5.71	5.79	5.87	6.07	6.47	7.07
Structure	C15	C15	C15/C14	C15/C14	C14	C14	C14

All the alloys of about 50 grams were prepared by arc-melting techniques using starting materials of 99.8% Nb, 99.99% Cr, and 99.95% Ni. An excess amount (typically 1%) of Cr was added to compensate for the evaporation loss of Cr during melting. Arc-melting was carried out in a chamber which was evacuated by a mechanical pump and flushed with ultra-high purity (UHP) argon gas four or five times, and finally backfilled with UHP argon gas. A Zr sample was melted prior to melting the alloy charge each time in order to getter the oxygen in the chamber. The arc-melting was done using a thoriated tungsten electrode on a water-cooled copper hearth. Each ingot was inverted and remelted at least 7 times to ensure macroscopic compositional homogeneity. The alloys were homogeneized in vacuum at 1300°C for 90 hours, then slowly cooled in the furnace, except two alloys with 20 and 35 at% Ni, which were homogenized at 1100°C for 120 hours. Finally, all the alloys were heat treated at 1000°C for 1000 hours, then water quenched to retain the equilibrium condition at 1000°C.

X-ray diffraction measurements were made using a Scintag XD2000 diffractometer with the Cu K_a (λ = 0.15406 nm) radiation. Powdered samples were used, and the lattice parameter determination was furnished by using a Si standard for internal calibration. The microhardness was measured using a load of 500 g with a holding time of 15 seconds. For fracture toughness determination, a load of 200 g was used for indentation, and the crack lengths were measured immediately after the indentation to eliminate the possibility of slow crack propagation after removal of the indentor. The following equation was used to calculate the fracture toughness of the alloy[16,17]:

$$K_{IC} = A\left(\frac{E}{H}\right)^{n} \frac{P}{L^{3/2}} \qquad (1)$$

where K_{IC} = fracture toughness ($MPa\sqrt{m}$), E = Young's modulus (GPa), H = Vickers hardness (GPa), P = load (N), and L = average length of the 4 radial cracks from the center of the indent to the crack tip. A and n are constants, which are taken here as 0.016 and 0.5 respectively.

RESULTS AND DISCUSSIONS

X-ray diffraction results show that the Laves phase after the addition of up to 5 at.% Ni maintains its original C15 structure, while the C14 structure is stabilized for alloys with 10, 20, and 35 at% Ni. Thus,

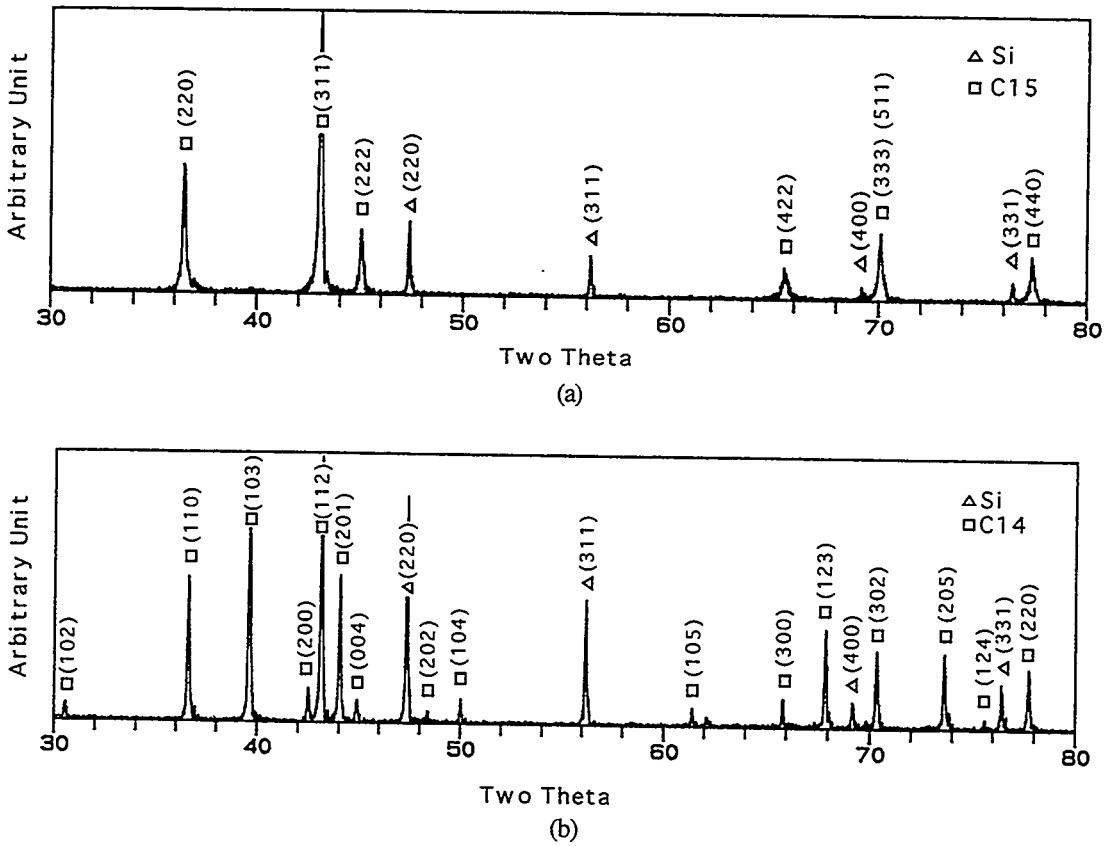

Fig. 2 X-ray diffraction patterns of $Nb(Cr, Ni)_2$ alloys with (a) 5 at.% Ni and (b) 10 at.% Ni, which were indexed as C15 and C14, respectively

the C15-->C14 phase transition is observed for the ternary system. Figure 2 shows the diffraction patterns for alloys with 5 and 10 at.% Ni, which were indexed as C15 and C14, respectively. However, the phase boundaries of the C15/C14 transition seem to move to higher electron concentration values, compared to the results predicted from Fig. 1. As an example, according to Fig. 1 and Table 1, the alloy with 5 at.% Ni

alloy should be in the transition region, i.e., either C14 and C15 two phases coexist or some intermediate structures other than C14 and C15 will be stabilized. It is still in the C15 region from the experimental data (see Fig. 2(a)). It is thus clear that the maximum electron concentration for stabilizing the C15 structure will be greater than 5.87. More alloys with the Ni contents between 5 and 10 at.% are being prepared, and the precise phase boundaries will be determined.

The crystal lattice parameters of the C15 and C14 Laves phases were measured for the pseudo-binary $Nb(Cr,Ni)_2$ alloys with various Ni contents. Figure 3 shows the graph for the dependence of the lattice constant a of the cubic C15 $Nb(Cr,Ni)_2$ alloy on the nickel content. As the Ni content increases, the lattice constant decreases linearly. Figure 4 illustrates the dependence of the lattice parameters a and c of the hexagonal C14 $Nb(Cr,Ni)_2$ alloy on the nickel content. As the Ni content increases, both a and c decrease linearly. Extrapolation of these dependence to 0 per cent Ni, i.e. to pure $NbCr_2$ gives us the lattice parameters of the high-temperature modification (C14) of the compound $NbCr_2$ (a = 4.9322 Å, c = 8.1312 Å), which were also plotted in 4. The dependence of the c/a ratio of the hexagonal C14 $Nb(Cr,Ni)_2$ alloy on nickel content is plotted in Fig. 5. As the Ni content increases, the c/a decreases linearly. It will be interesting to prepare some pseudo-binary $Nb(Cr,Ni)_2$ alloys with higher Ni contents and study the crystal structure and the lattice parameter of the alloys, since some work has indicated that the solubility of Ni in NbCr2 is less than 40 at. %. According to our prediction of the e/a correlation with phase stability, the Ni can substitute a higher percentage of Cr from the electron concentration point of view. Our work in the ternary Nb-Cr-Cu system has demonstrated that in addition to the e/a criterion, the electronegativity may also be an important factor in limiting the solubility of the solute atom in $NbCr_2$ compound.[15]

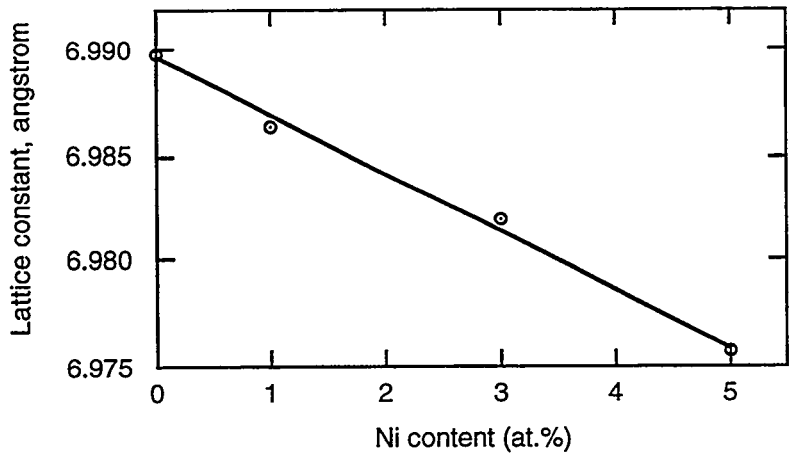

Fig. 3 Dependence of lattice constant, a, of cubic C15 phase on the nickel content

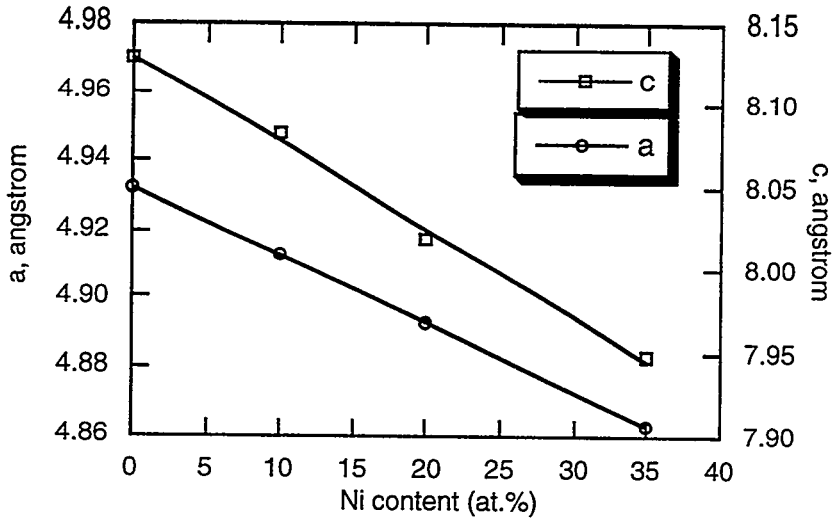

Fig. 4 Dependence of lattice parameters, a and c, of hexagonal C14 on the nickel content

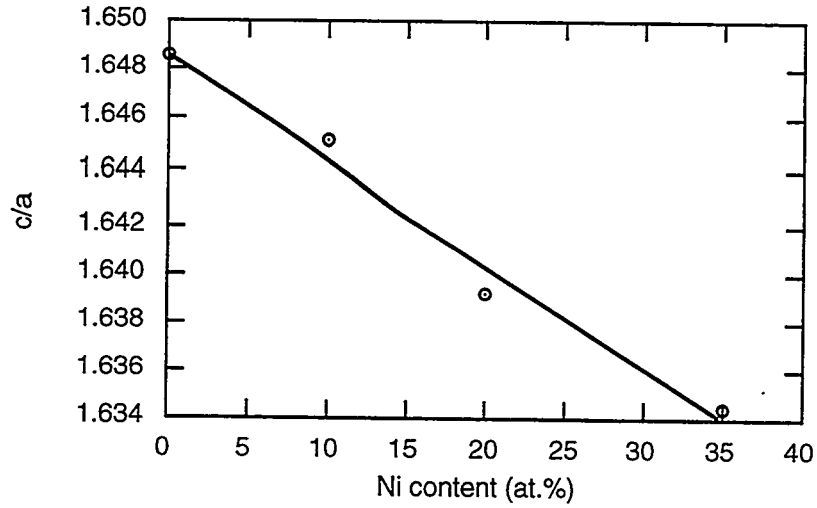

Fig. 5 Dependence of c/a of hexagonal C14 phase on the nickel content

The Vickers hardness of the pseudo-binary $Nb(Cr,Ni)_2$ alloys with various Ni contents is plotted in Fig. 6. It is clear from this figure that the addition of the nickel to substitute for Cr increases the hardness of the Laves phase. Also, the trend is that the Ni increases the hardness of the C15 structure more significantly than that of the C14 structure. The decreased lattice constants by the addition of Ni signifies the close-up of the close-packed lattice structure and an increase in the interatomic bonding. This can be used to explain the hardness increases as the Ni content in the alloy increases.

Figure 7 shows the cracking situation in the area near the indentation for a $Nb(Cr.Ni)_2$ alloy with 10 at% Ni, from which we can measure the average crack length, L. The fracture toughness calculated using Eq. (1) as a function of Ni content is shown in Fig. 8. Basically, the fracture toughness of the monolithic Laves

phase is very low, about 1 $MPa\sqrt{m}$, which is a consequence of the topologically close packing manner of the structure and the subsequent difficulty in activating dislocation sources in the material. No general trend regarding the effect of the Ni content on the fracture toughness of the Laves alloys can be deduced from this curve. The toughness value near the phase boundary may increase, due to the fact that the associated structure is metastable, and it is easy to transform from one structure to another during deformation. Unfortunately, none of the alloys used in this investigation falls in the transition region. More alloys in the transition region is being prepared, and the fracture toughness of these alloys will be determined.

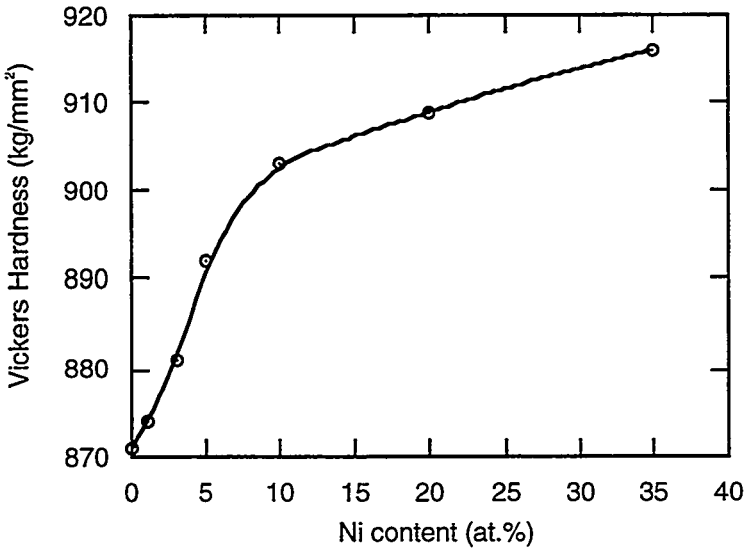

Fig. 6 The effect of Ni content on the Vickers hardness of $NbCr_2$ alloys

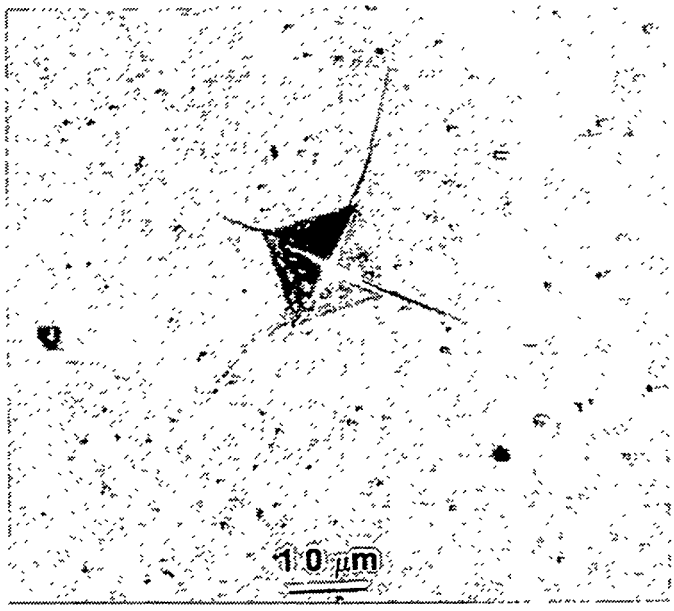

Fig. 7 Cracking phenomenon near the indented region for the alloy with 10 at.% Ni

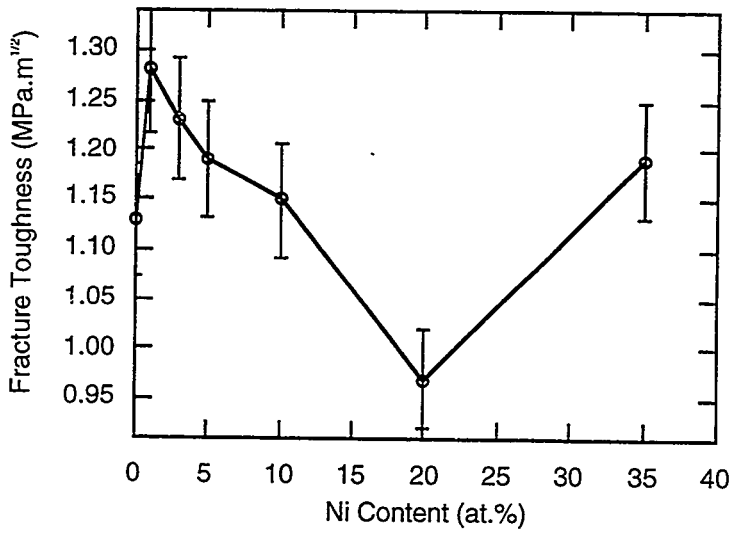

Fig. 8 Fracture toughness values of the laves phases as a function of the Ni content

CONCLUSIONS

It has been shown that the average electron concentration factor, e/a, is the dominating factor in controlling the phase stability of the ternary Nb-Cr-Ni Laves phase system. The substitution of Ni for Cr in $NbCr_2$ increases the average electron concentration of the alloy, thus leading to the change of the crystal structures from C15 to C14. X-ray diffraction results show that for the alloys with $\leq$ 5 at.% Ni, the C15 structure is stabilized and for the alloys with $\geq$ 10 at.% Ni the C14 structure is stabilized. From this result, it is clear that the e/a ratio corresponding to the C15/C14 phase transition must be at a value higher than the one previously predicted. The changes in the lattice constant, Vickers hardness, and fracture toughness were also determined as a function of the Ni content. As the Ni content increases, the lattice constants decrease for both C15 and C14 structures, while the Vickers hardness increases over the whole range of the Ni concentration investigated. The fracture toughness is low for all the alloys, and no general trend regarding the fracture toughness can be detected as the Ni content increases. Further investigation will concentrate on alloy compositions containing 5-10 at.% Ni. The phase boundaries of C15/C14 structures will be precisely determined, and the fracture toughness of the alloys near phase boundaries will be studied to see if mechanical twinning and/or stress assisted phase transformation can be triggered, and toughness can be increased for such alloys.

ACKNOWLEDGMENTS

We would like to thank Nancy Cole, Rod Judkins and Paul Carlson of the Oak Ridge National Laboratory for programmatic support, and Joe Wright, Elmer Lee and Cecil Carmichael for their technical assistance. The research was sponsored by the Fossil Energy AR & TD Materials Program, U.S. Department of Energy, under subcontract 11X-SP173V to the University of Tennessee with Lockheed Martin Energy Research Corp.

REFERENCES

1. K. Inoue and K. Tachikawa, IEEE Trans. Magnetics, vol. 15, p. 635, 1979.
2. D. Ivey and D. Northwood, J. of Less- Common Met., vol. 115, p. 23, 1986.
3. F. Chu and D.P. Pope: in High-Temperature Ordered Intermetallic Alloys V, MRS. Symp. Proc. 288, p. 561, 1993.
4. K. S. Kumar and D.B. Miracle, Intermetallics, vol. 2, p. 257, 1994.
5. M. Takeyama and C.T. Liu, Mater. Sci. & Eng. A, vol. 132, p. 61, 1991.
6. J.A. Cook, P.K. Liaw, and C.T. Liu: in Fatigue and Fracture of Ordered Intermetallics, W. O. Soboyejo, T. S. Srivatsan & R. O. Ritchie, eds., TMS, Warrendale, PA, p. 155, 1995,.
7. J.A. Cook, P.K. Liaw, C.T. Liu, and S.B. Bhaduri: in the Johannes Weertman Symposium, R. J. Arsenault et al., eds., TMS, Warrendale, PA, p. 47, 1996.
8. K.S. Chan and D.L. Davidson, JOM,, p. 62, Sept. 1996.
9. D.J. Thoma and J.H. Perepezko, Mater. Sci. & Eng. A, vol. 156, p. 97, 1992.
10. T.B. Massalski: in Physical Metallurgy Part 1, R. W. Cahn & P. Hassen, eds., North-Holland Physics Publishing, NY, p. 190, 1983.
11. F. Laves & H. Witte, Metallwirschaft, vol. 14, p. 645, 1935.
12. F. Laves & H. Witte, Metallwirschaft, vol. 15, p. 840, 1936.
13. Y. Liu, J.D. Livingston, and S.M. Allen, Metall. Tran. A, vol. 23, p. 3303, 1992.
14. M. Grujicic, S. Tangrila, O.B. Cavin, W.D. Porter, and C.R. Hubbard, Mater. Sci. & Eng. A, vol. 160, p. 37, 1993.
15. J. H. Zhu, P. K. Liaw, and C. T. Liu, "Electron Concentration and Phase Stability in $NbCr_2$-Based Laves Phase Alloys", Final Report, U. S. Dept. of Energy, Fossil Energy AR & TD Materials Program, ORNL/Sub/93-SP173/02, National Technical Information Service, Springfield, VA, May, 1997; submitted to Metall. Trans.
16. M. Sakai and R.C. Bradt, Inter, Mat. Rev., vol. 38, No.2, p. 53, 1993.

17. G.R. Anstis, P. Chantikul, B.R. Lawn, and D.B. Marshall, J. of Amer. Ceramics. Soc., vol. 64, No. 9, p. 533, 1981.

WELD OVERLAY CLADDING WITH IRON ALUMINIDES

G. M. Goodwin

ABSTRACT

We have established a range of compositions for these alloys within which hot cracking resistance is very good, and within which cold cracking can be avoided in many instances by careful control of welding conditions, particularly preheat and postweld heat treatment. For example, crack-free butt welds have been produced for the first time in 12-mm thick wrought Fe3Al plate. Cold cracking, however, still remains an issue in many cases.

We have developed a commercial source for composite weld filler metals spanning a wide range of achievable aluminum levels, and are pursuing the application of these filler metals in a variety of industrial environments. Welding techniques have been developed for both the gas tungsten arc and gas metal arc processes, and preliminary work has been done to utilize the wire arc process for coating of boiler tubes.

Clad specimens have been prepared for environmental testing in-house, and a number of components have been modified and placed in service in operating kraft recovery boilers.

In collaboration with a commercial producer of spiral weld overlay tubing, we are attempting to utilize the new filler metals for this novel application.

INTRODUCTION

To utilize the excellent properties of alloys based on the Fe3Al nominal composition, particularly resistance to high temperature oxidation and corrosion, we are continuing to develop welding filler metals, procedures, and parameters aimed at introducing these

new alloys into commercial service. Although emphasis is still placed on conventional weld overlay techniques, considerable progress has been made recently toward joining thick section monolithic materials, and applying alternative cladding techniques, including spiral weld cladding and wire arc thermal spraying.

Prior efforts (1-6) have identified the causes of hot cracking in these alloys, and, by compositional modification, essentially eliminated it. Cold cracking, however, remains an issue, although recent efforts have made progress toward minimizing it, primarily by control of composition and welding parameters, especially preheat and postweld heat treatment.

Development of filler metals, processes, and procedures is ongoing concurrent with introduction of the materials into service in a variety of industrial applications.

Filler Metal Development

Using the approach described earlier (6), we have developed and now have available a family of filler metal compositions spanning a range of aluminum content from less than 8 to greater than 26 weight percent (Table I). These composite wires are 0.0625-in (1.6mm) diameter, in spooled form, and can thus be used with automatic wire feeders in a number of welding and cladding processes. The actual deposit composition can be modified as desired by control of dilution, deposition rate, and other welding parameters.

Heat Treatment Effects

It was established earlier (4,5) that weld preheat and postweld heat treatment could be effective at avoiding cold cracking of the weld deposits. Based on extensive testing over the range of filler metal compositions, efforts to reduce preheat below 350°C, or postweld heat treatment below 750°C have consistently been unsuccessful at preventing cracking. We conclude, therefore, that these conditions are required, as a minimum, to reliably avoid cold cracking. Using these parameters, however, we have been able to use

TABLE I. COMPOSITION OF IRON ALUMINIDE ALLOY FILLER METALS

	WEIGHT %	Al	Cr	C	Zr	Mo
Stoody I	Aim, all weld metal	20.0	7.0	0.10	0.25	0.25
	Actual, all weld metal	21.8	7.3	0.06	0.40	NA[c]
	Actual, clad deposit [a]	12.6	6.0	0.08	0.20	0.44
	Actual, clad deposit [b]	15.3	12.7	0.05	0.22	0.40
Stoody II	Aim, all weld metal	20.0	--	0.10	0.25	0.25
	Actual, all weld metal	21.5	--	0.08	0.25	NA
	Actual, clad deposit [a]	12.6	--	0.10	0.12	0.40
Stoody III	Aim, all weld metal	12.0	--	0.10	0.25	0.25
	Actual, all weld metal	12.5	--	0.06	0.40	NA
	Actual, clad deposit [a]	7.6	--	0.07	0.32	0.40
Stoody IV	Aim, All weld metal	26.0	--	0.10	0.25	0.25
	Actual, all weld metal	26.5	--	0.08	0.60	NA
	Actual, clad deposit [a]	14.1	--	0.09	0.32	0.40

[a] Single layer automatic gas metal arc on 1-in. thick type 2 1/4 Cr-1Mo steel
[b] Single layer manual gas tungsten arc on 1/2-in. thick type 310 stainless steel
[c] NA - Not Analyzed

the new filler metals to join monolithic sections of plate material which had previously been considered unweldable. Figure 1 shows a metallographic cross-section of a multipass gas tungsten arc weld in 1/2-in (12.7mm) thick alloy FA-129 plate. To match the aluminum level of the base plate (16 weight %), we chose the 20 weight % weld wire (Stoody II), thus allowing for arc losses and dilution by the base plate. As is seen in figure 1.b, the weld microstructure is free of cracks and porosity, and has a narrow heat affected zone and relatively fine-grained fusion zone.

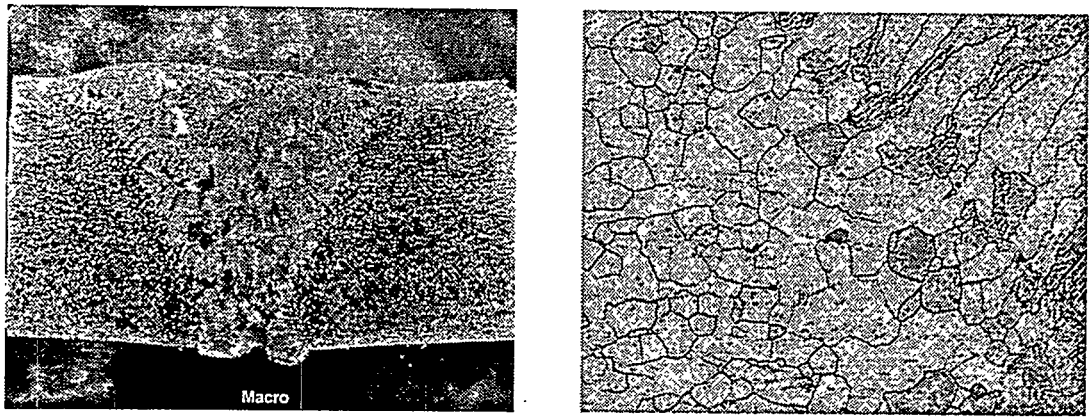

Fig. 1. Multipass Gas Tungsten Arc Weld in 12.7-mm Thick Alloy FA-129 Plate a) Macrosection, and b) Microstructure; note narrow heat affected zone, fine grained fusion zone, and absence of cracks and porosity.

Industrial Service Testing

Pursuing the tasks started earlier (6), we have prepared several additional components for in-service testing in commercial paper mill recovery boilers, and continue to monitor the condition of parts previously modified by weld overlay. As a basis for comparison, we have also prepared components using high-chromium commercial filler wires, E-Brite 26-1 and Inconel 617 with 26% and 23% chromium, respectively. These alloys would be considered the primary competition for the iron aluminides in high temperature oxidizing/sulfadizing environments.

Wire Arc Cladding*

Wire arc cladding, also known as arc spraying, is being investigated as an alternative to conventional gas tungsten arc or gas metal arc weld cladding. The process is shown schematically in figure 2, from (7). Basically, an arc is struck between two independently fed wires, and compressed gas is used to detach molten droplets from the arc zone and propel them to the substrate. It is a high velocity, high deposition rate process, with droplet temperatures high enough to assure good bond strength. Figure 3.a is an overall view and figure 3.b shows a cross-section of 3-in (76mm) OD carbon

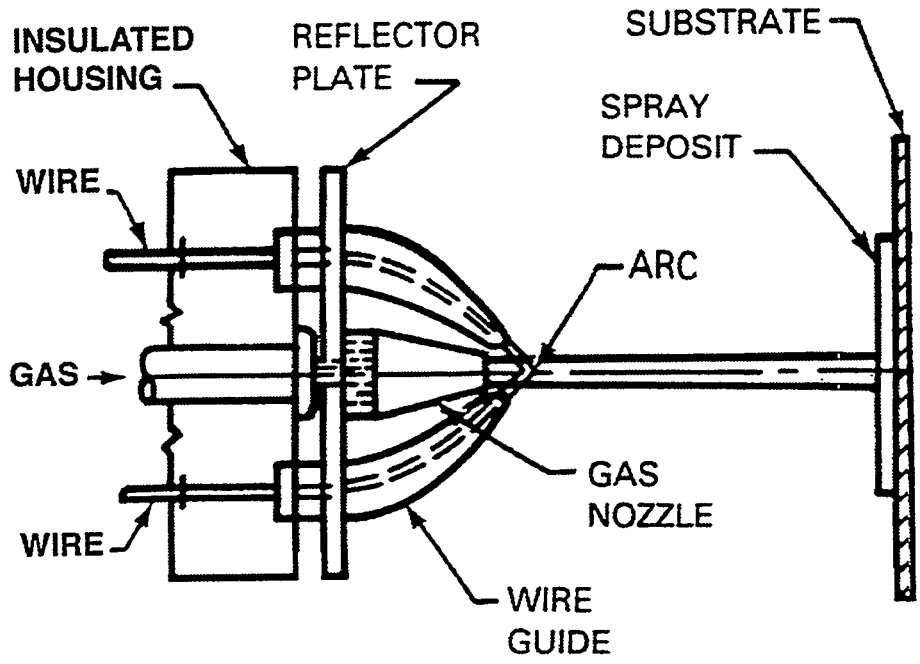

Fig. 2. Wire Arc Spray Process

steel boiler tube clad with composite filler wire. Spray parameters were 100 amperes DC, 30 volts, and 90 psi air pressure. As seen in figure 3, the coating is heterogeneous,

*This task is being performed in collaboration with E. A. Franco-Ferreira of the Engineering Technology Division.

but sound. Thermal cycling of clad specimens to 427°C in air has shown no evidence of spalling after 25 cycles. In order to control the degree of oxidation of the coating, additional specimens are being prepared using nitrogen and argon as carrier gases.

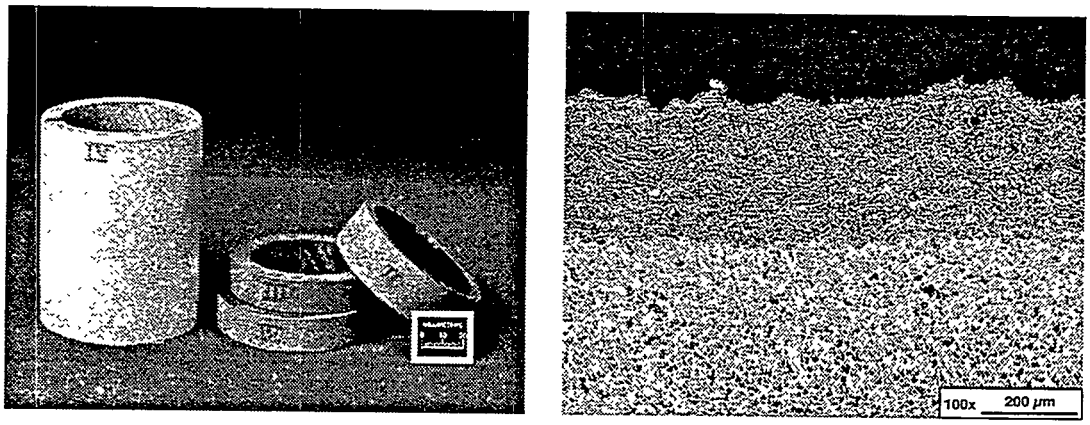

Fig. 3. Boiler Tube Coated by Wire Arc Cladding: a) Overall and b) Microstructure

Spiral Weld Cladding

The spiral weld cladding technique (figure 4 shows an example) uses a combination of gas metal arc and gas tungsten arc welding to overlay boiler tubing prior to fabrication of tube panels. In collaboration with a commercial supplier of spiral welded product, we are using the process to clad carbon steel with the Stoody I composite filler wire composition. If this approach is successful, it will provide a viable alternative to coextruded bimetallic tubing.

CONCLUSIONS

- Hot cracking has essentially been eliminated, but cold cracking still remains an issue in many cases; preheat (350°C minimum) and postweld heat treatment (750°C minimum) are required to reliably avoid it.
- We have developed and have available a family of filler metal compositions from less than 8 to greater than 26 weight % aluminum.

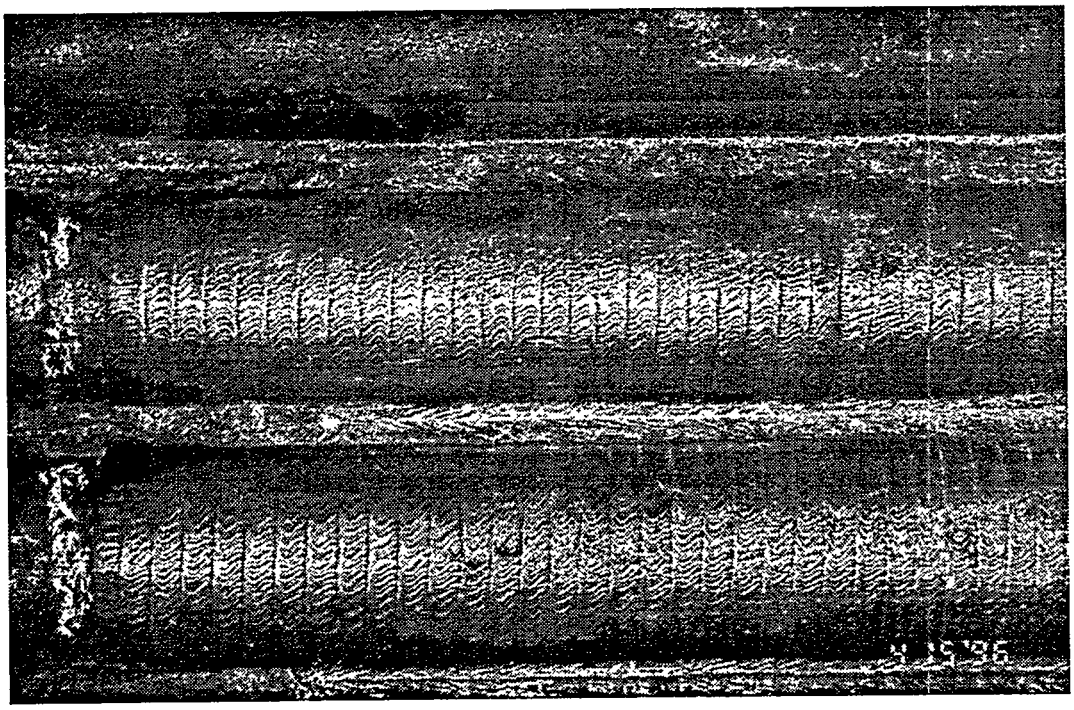

Fig. 4: Spiral Weld Clad Tubing

- Plate thicknesses can be successfully welded under proper conditions.
- Industrial service testing in recovery boilers is continuing.
- Wire arc cladding is being developed as an alternative to conventional weld overlay cladding.
- Spiral weld cladding is being investigated as a replacement for coextruded bimetallic tubing.

REFERENCES

1. T. Zacharia and S.A. David, *"Weldability of Iron Aluminides,"* proceedings of the Fifth Annual Conference on Fossil Energy Materials, ORNL/FMP-91/1, Oak Ridge National Laboratory, September 1991.

2. T. Zacharia, P.J. Maziasz, S.A. David, and C.G. McKamey, *"Weldability of Fe_3Al Based Iron Aluminide Alloys,"* proceedings of the Sixth Annual Conference on Fossil Energy Materials, ORNL/FMP-92/1, Oak Ridge National Laboratory, July 1992.

3. G.M. Goodwin, C.G. McKamey, P.J. Maziasz, and V.K. Sikka, *"Weldability of Iron Aluminides,"* proceedings of the Seventh Annual Conference on Fossil Energy Materials, ORNL/FMP-93/1, Oak Ridge National Laboratory, July 1993.

4. G.M. Goodwin, P.J. Maziasz, C.G. McKamey, J.H. Devan, and V.K. Sikka, *Weldability of Iron Aluminides,"* proceedings of the Eighth Annual Conference on Fossil Energy Materials, ORNL/FMP-94/1, Oak Ridge National Laboratory, August 1994.

5. G.M. Goodwin, *"Weld Overlay Cladding With Iron Aluminides,"* proceedings of the Ninth Annual Conference on Fossil Energy Materials, ORNL/FMP-95/1, Oak Ridge National Laboratory, August 1995.

6. G.M. Goodwin, *"Weld Overlay Cladding with Iron Aluminides,"* proceedings of the Tenth Annual Conference on Fossil Energy Materials, ORNL/FMP-96/1, Oak Ridge National Laboratory, August 1996.

7. Welding Handbook, **2**, Eighth Ed., pp. 872-74, American Welding Society, Miami, Fla., 1991.

CERAMIC MEMBRANES FOR HIGH TEMPERATURE HYDROGEN SEPARATION

K. D. Adcock, D. E. Fain, D. L. James, L. E. Powell, T. Raj,
G. E. Roettger, and T. G. Sutton

East Tennessee Technology Park
P. O. Box 2003
Oak Ridge, TN 37831-7271

ABSTRACT

The separative performance of our ceramic membranes has been determined in the past using a permeance test system that measured flows of pure gases through a membrane at temperatures up to 275°C. From these data, the separation factor was determined for a particular gas pair from the ratio of the pure gas specific flows. An important project goal this year has been to build a Mixed Gas Separation System (MGSS) for measuring the separation efficiencies of membranes at higher temperatures and using mixed gases.

The MGSS test system has been built, and initial operation has been achieved. The MGSS is capable of measuring the separation efficiency of membranes at temperatures up to 600°C and pressures up to 100 psi using a binary gas mixture such as hydrogen/methane. The mixed gas is fed into a tubular membrane at pressures up to 100 psi, and the membrane separates the feed gas mixture into a permeate stream and a raffinate stream. The test membrane is sealed in a stainless steel holder that is mounted in a split tube furnace to permit membrane separations to be evaluated at temperatures up to 600°C. The compositions of the three gas streams are measured by a gas chromatograph equipped with thermal conductivity detectors. The test system also measures the temperatures and pressures of all three gas streams as well as the flow rate of the feed stream. These data taken over a range of flows and pressures permit the separation efficiency to be determined as a function of the operating conditions. A mathematical model of the separation has been developed that permits the data to be reduced and the separation factor for the membrane to be determined.

INTRODUCTION

The primary purpose of this project is to develop methods for producing highly efficient gas separation membranes for separating hydrogen from gasified coal at temperatures of 1000°F (538°C) or higher. This work has been focused on the development of alumina membranes having extremely small pores that can separate gas molecules on the basis of molecular size, i.e., by molecular sieving. A hard sphere diffusion model was developed earlier, which provided a basis for estimating the extremely high separation factors that should be achievable (for a binary gas mixture) as the membrane mean pore size is reduced and approaches the molecular diameter of the larger gas molecule.[1] Since ceramic membranes typically have some pores that are substantially larger than the mean pore size, a more recent study modeled the effects of oversized pores on the performance of gas separation membranes and showed the importance of limiting the size and frequency of such oversized pores.[2]

In our membrane development work, alumina membranes having estimated mean pore diameters as small as 5 Angstroms have been produced and tested, and very high separation factors have been measured.[3] The separation factors of our ceramic membranes have been determined to date from pure gas flow data measured at several temperatures up to a maximum of 275°C. An important project goal for FY 1997 has been to build a new test system for measuring the separation efficiencies of membranes at much higher temperatures and using mixed gases.

DISCUSSION OF CURRENT ACTIVITIES

Mixed Gas Separation System

A Mixed Gas Separation System (MGSS) has been designed and built at the East Tennessee Technology Park to provide the capability to measure separation efficiencies of membranes with mixed gas streams of interest at temperatures up to 600°C and pressures

up to 100 psi. Construction, calibration, and startup of the MGSS have been completed. An initial membrane has been installed in the test system, and it is being tested to check out and verify overall system operations. The primary purpose of the MGSS is to evaluate the ability of membranes to separate gases. That can be done most effectively using a binary gas mixture. The test system can also be used to evaluate the functional performance of membranes with gas mixtures containing many gases.

Description of the MGSS

A diagram of the new test system is shown in Fig. 1, and a view of the completed system is shown in Fig. 2. In this test system, the membrane separates the constituents of a binary gas mixture that normally contains hydrogen as one of the constituents. A mixture of gases, such as hydrogen and methane, are supplied to the test system from compressed gas cylinders. The test gases are passed through a molecular sieve dryer to remove residual water. The test gas is then metered, and the flow rate measured, by one of four orifices that are sealed in an orifice manifold. The gas mixture flows through stainless steel tubing that passes through a preheater that heats the gas to approximately the desired test temperature. The heated gas flows immediately into a split-tube furnace (Fig. 3) where the temperature is accurately controlled at any specified temperature up to 600°C.

The membrane being tested is sealed in a stainless steel holder (Fig. 4) located at the center of the split-tube furnace. The test gas mixture, e.g., hydrogen and methane, flows into the feed end of the tubular membrane. As the gas flows axially through the membrane, the smaller gas molecules (i.e., hydrogen) preferentially pass through the ultra-small pores in the wall of the molecular sieve membrane. This provides a permeate stream containing a higher concentration of hydrogen. The raffinate stream flowing out the exit end of the tubular membrane contains a reduced concentration of hydrogen but an increased concentration of methane.

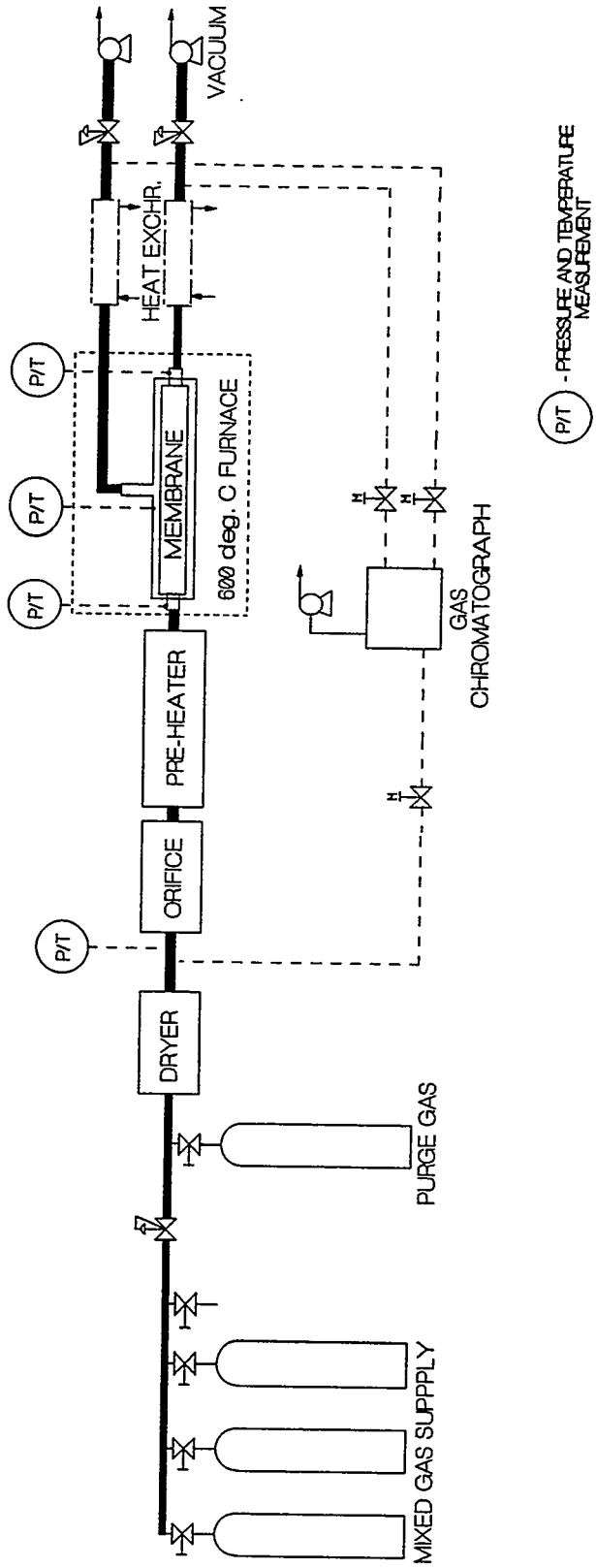

Fig. 1. Diagram of the Mixed Gas Separation System that has been built to measure the separation efficiency of membranes at temperatures up to 600 degrees C.

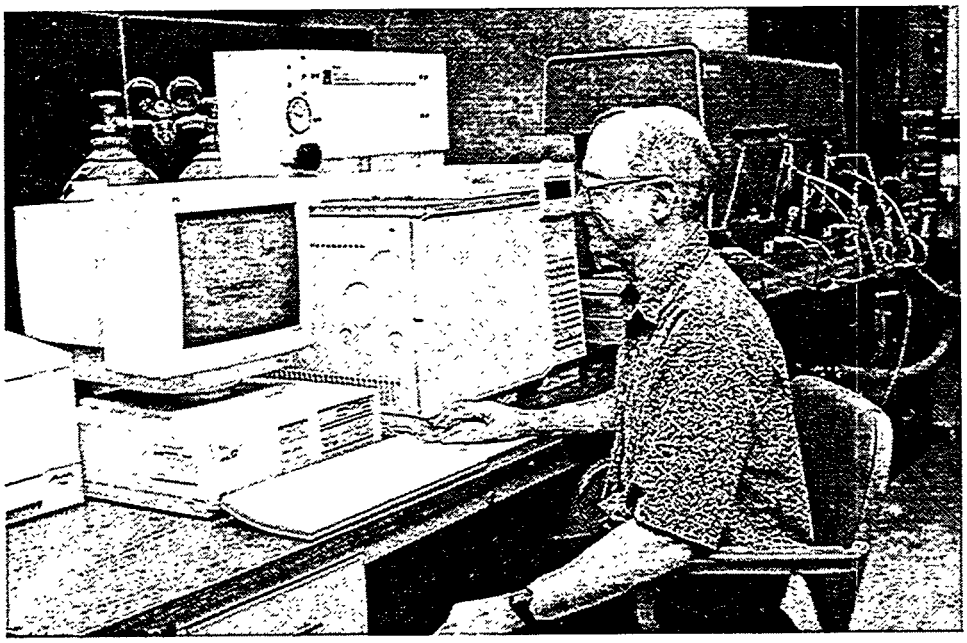

Fig. 2. Recently completed Mixed Gas Separation System.

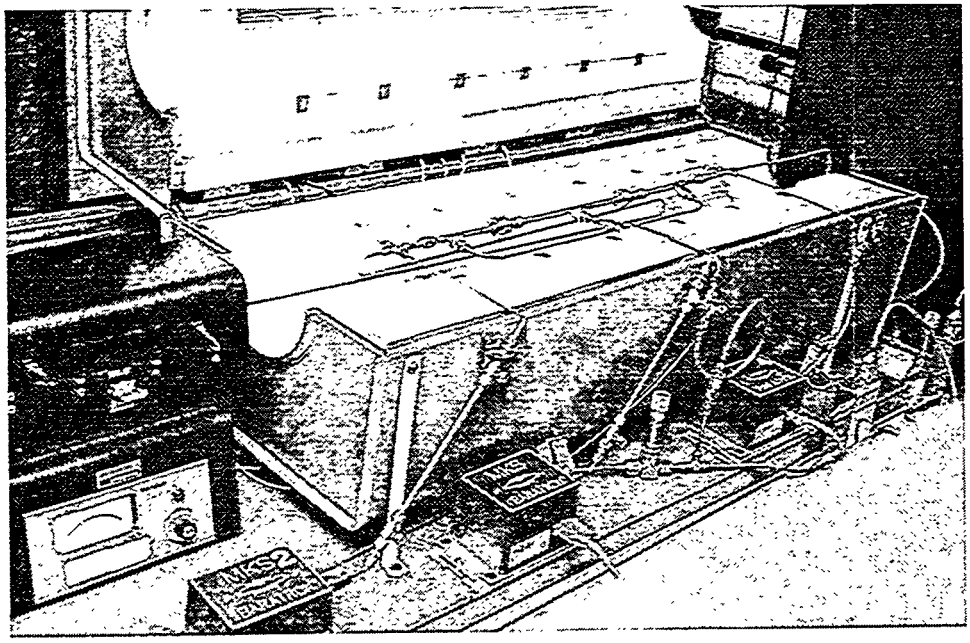

Fig. 3. Split tube furnace containing membrane holder that permits membrane separations to be evaluated at temperatures up to 600°C.

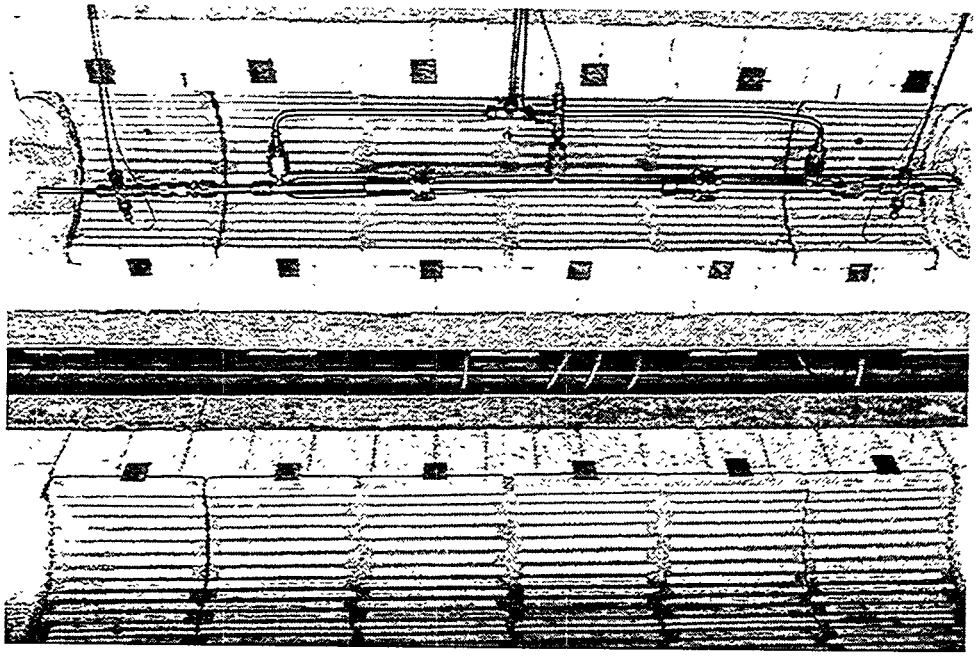

Fig. 4. Stainless steel holder containing membrane being tested in the MGSS.

The temperatures and pressures of the feed, permeate, and raffinate streams are measured by thermocouples and pressure transducers. Pressure taps and thermocouples are sealed into the tubing that connects to the two ends of the membrane holder as well as in the shell (permeate stream) of the holder as can been seen in Fig. 4. The feed, permeate, and raffinate streams are periodically sampled and analyzed by a gas chromatograph (Fig. 5) with thermal conductivity detectors (TCDs) to determine the compositions of the three gas streams. Data from all the measuring devices are collected, stored, and displayed on a dedicated computer. These data are reduced to determine the separation factor of the membrane.

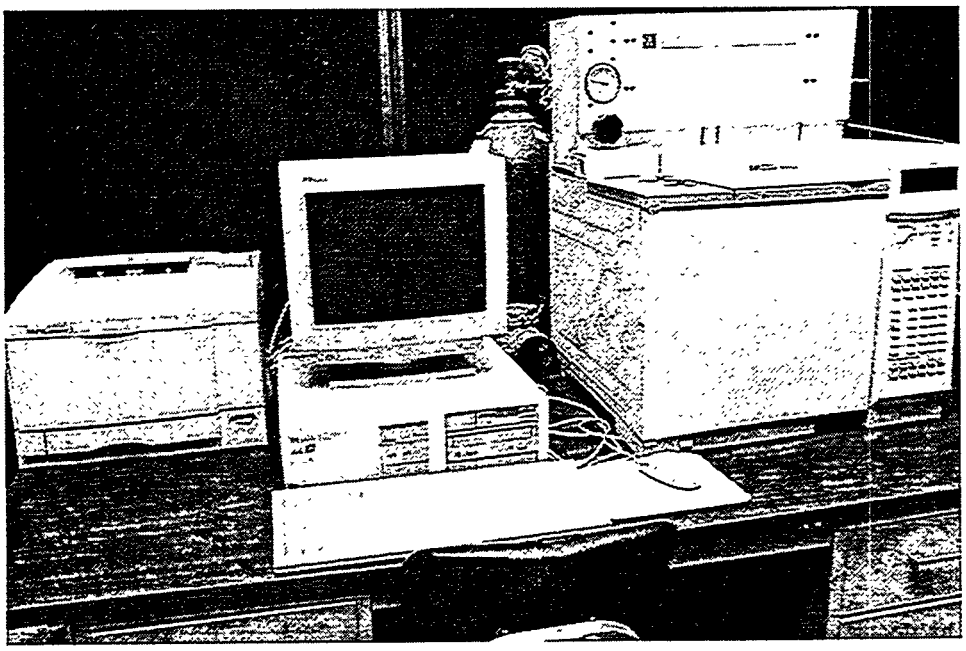

Fig. 5. Gas chromatograph used to analyze composition of feed, permeate, and raffinate streams.

Model for Data Evaluation

Introduction

The major function of our MGSS is the evaluation of fundamental characteristics of membranes. In many cases, a separation system is used to measure practical separations for evaluation of commercial applications. There are some basic differences in the design of systems for these two purposes. If the separation system is to be used only to evaluate potential commercial applications, it is a simple matter of measuring the performance of a membrane at some specified operating conditions. In this case, the mole fractions of the feed, permeate, and raffinate streams are measured directly and compared with results from other membranes or other processes.

The usual procedure to learn fundamental characteristics of membranes is to measure the flow of individual pure gases. The ideal separation factor, f*, (a fundamental membrane characteristic) is then the ratio of the specific flows [molar flow/(area x time

x pressure drop)] of the individual gases. This assumes no interaction between the different molecules. However, interaction is likely except in very special limits, therefore, it is important to actually measure the separation with mixtures of gases.

The ideal maximum difference in mole fraction between the permeate and feed streams can be expressed by the relation,

$$\Delta C^* = \frac{C_1(1 - C_1)(f^* - 1)(1 - w)}{f^*(1 - C_1) + C_1} \quad .$$

The measured value is $\Delta C = C_1 - C_0$.

A good measure of membrane performance is $\Delta C/\Delta C^*$.

In these equations, C_0 is the feed mole fraction and C_1 is the permeate mole fraction, and w is the ratio of permeate pressure to the feed pressure.

The evaluation of data from a separation system can be complicated by many factors; for example, momentum exchange between molecular species which is generally proportional to the pressure drop across the membrane. It is also related to the recovery fraction or to the ratio of permeate to feed flow rate, herein referred to as the cut. The separation can also produce concentration polarization, which reduces the effect of the membrane separation factor. Separation data must be acquired in such a way that the data can be extrapolated to meaningful results. Therefore, the MGSS was designed and constructed to allow a wide range of operating conditions to provide for a significant range in recovery or cut and pressure and temperature to allow accurate extrapolation.

Information about the membrane can be acquired by measuring the mole fractions of all three streams as a function of the cut for several appropriate pressure drop levels. For a fixed pressure drop, the ratio of the mole fraction change between the feed and the permeate streams to the change expected for an ideal separation factor is plotted against the cut and extrapolated to zero cut. An example of such an evaluation is shown in Fig. 6. In this example, it was assumed that there was no concentration polarization. The values

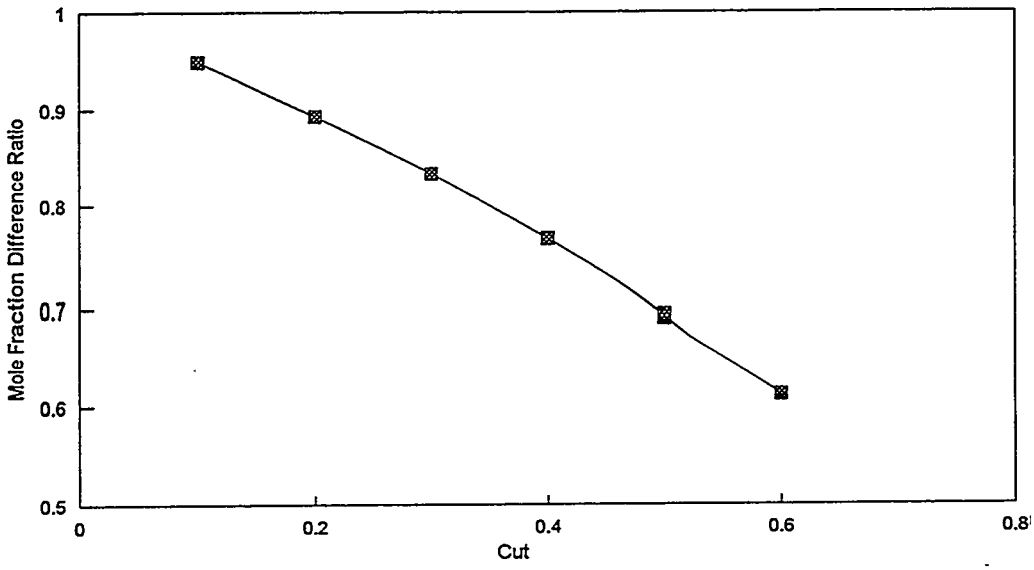

Fig. 6. An example of the membrane performance factor as a function of cut assuming no concentration polarization.

obtained at zero cut are then plotted against the pressure drop as shown in Fig. 7. The value extrapolated to zero pressure drop will be indicative of the real separation factor compared to the ideal separation factor. Such an evaluation requires a large amount of experimental data, but also provides significant information about the variation in separation factor as a function of operating parameters.

Computational Fluid Dynamic Calculations

A more explicit method is being developed to evaluate the separation factor directly. A computational fluid dynamic algorithm is being adapted to make direct calculation of the separation factor at various operating conditions. This will significantly reduce the amount of experimental data needed for the membrane evaluation and will give more insight into the dynamics of the separation process. Once perfected, it can also be used to optimize the economic operation of a membrane in a given separation system.

Boundary conditions have been established for the problem, and procedures are being developed for performing iterative calculations to determine a separation factor that will produce the measured feed, permeate, and raffinate stream mole fractions.

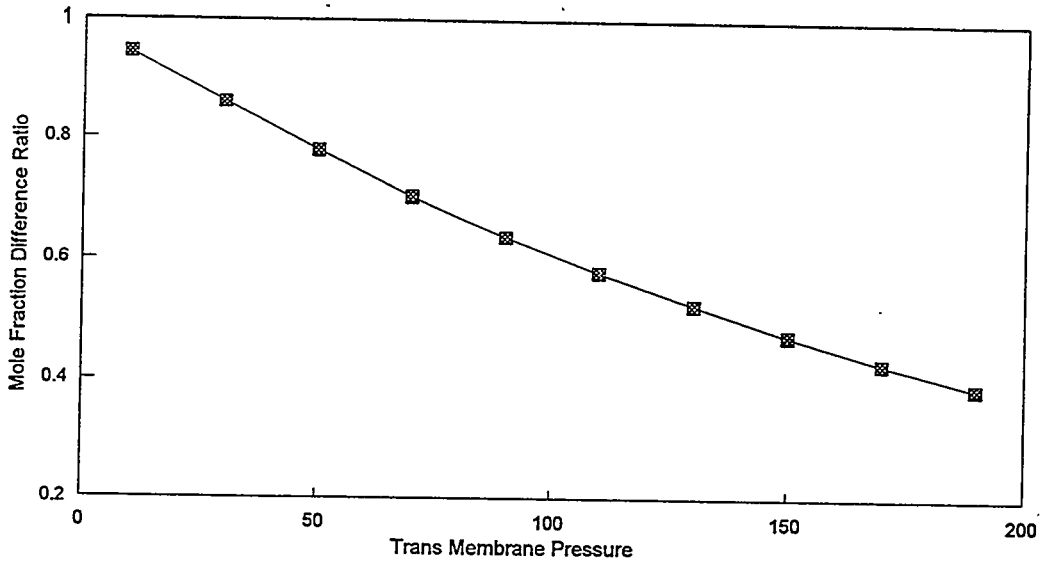

Fig. 7. An example of the membrane performance factor as a function of pressure difference across the membrane.

The current startup tests being conducted with the MGSS are providing data to check out and verify the overall system operation and provide data to use with these data reduction models.

REFERENCES

1. D. E. Fain and G. E. Roettger, "Coal Gas Cleaning and Purification with Inorganic Membranes," *Transactions of the ASME*, 115 (3), pp. 628-633 (July 1993).

2. G. E. Roettger and D. E. Fain, *Effects of Leaks on Gas Separation Performance of Nano Pore Size Membranes*, K/TSO-24, Lockheed Martin Energy Systems, Inc. Oak Ridge, K-25 Site, Oak Ridge, Tennessee, October 1996.

3. D. E. Fain and G. E. Roettger, "High Temperature Inorganic Membranes for Separating Hydrogen," in *Proceedings of the Ninth Annual Conference on Fossil Energy Materials*, Oak Ridge, Tennessee, May 16-18, 1995, pp. 185-193.

HIGH-TEMPERATURE CORROSION BEHAVIOR OF IRON-ALUMINIDE ALLOYS AND COATINGS

P. F. Tortorelli, B. A. Pint, and I. G. Wright

Oak Ridge National Laboratory
Oak Ridge, Tennessee, U. S. A.

ABSTRACT

The long-term oxidation performance of ingot- and powder-processed Fe-28 at.% Al-(2-5)% Cr alloys with minor oxygen-active element or oxide additions was characterized for exposures in air at 1000-1300°C. Additions of Zirconium or yttria substantially improved the adhesion of alumina scales grown on iron aluminides. At lower temperatures, the ingot-processed alloys performed similarly to ODS Fe_3Al alloys and other alumina-formers. However, at 1200 and 1300°C, the oxidation resistance of the ingot-processed Fe_3Al was degraded due to deformation of the substrate and some localized reaction product growth. Other oxidation experiments showed that the addition of an oxide dispersion to iron aluminides reduced the critical aluminum concentration for protective alumina scale formation. Oxide-dispersion-strengthened Fe_3Al alloys made from commercially prepared powders and an iron-aluminide coating with 21% Al and 1% Cr, prepared by a gas metal arc weld-overlay technique, showed excellent oxidation/sulfidation resistance.

INTRODUCTION

Iron aluminides containing greater than about 20-25 at.% Al have oxidation/sulfidation resistance at temperatures well above those at which these alloys have adequate mechanical strength.[1,2] In addition to alloying and processing modifications for improved creep resistance of wrought material, this strength limitation is being mitigated by development of oxide-dispersion-strengthened (ODS) iron aluminides[3,4] and by evaluation of Fe_3Al alloy compositions as coatings or claddings on higher-strength, less corrosion-resistant materials.[5-9] As part of these efforts, the high-temperature oxidation and oxidation-sulfidation behaviors of iron-aluminide weld overlays and ODS alloys are being characterized and compared to results for ingot-processed material. Other recent oxidation results for ODS Fe_3Al, as related to lifetime prediction, can be found elsewhere.[4]

OXIDATION OF Fe_3Al ALLOYS

The long-term oxidation performance of ingot- (I/M) and powder-processed (P/M) Fe-28% Al-(2-5)% Cr alloys was characterized for isothermal and cyclic exposures in air at 1000-

1300°C. (All compositions are in at.%.) The P/M alloys were prepared by mechanically blending powders of gas-atomized Fe-28% Al-2% Cr (FAS) and submicron oxides in a flowing Ar atmosphere using a high-speed attritor and stainless steel balls.[3,10] The blended powder was canned, degassed, and extruded at 1100°C. For comparison, ingot-processed Fe-28% Al-2 or 5% Cr alloys and a commercial ZrO_2-dispersed (0.06% Zr) Fe-20% Cr-10% Al composition (Kanthal alloy APM) were also oxidized. The APM alloy is used as the benchmark for oxidation resistance as it typically displays low scale-growth and spallation rates at high temperatures under both isothermal and thermally cycled conditions.[11]

As illustrated in Figs. 1-4, the I/M Fe-28% Al-2% Cr (denoted FASN in this paper) consistently showed rapid weight gain kinetics under cyclic oxidation conditions at 1000-1300°C. At 1000°C (Fig. 1) and 1100°C (Fig. 2), Fe-28% Al-5% Cr-0.1% Zr (FAL) and P/M FAS-Y_2O_3 displayed similar oxidation resistance. However, while not apparent from the gravimetric data in Fig. 2, the alumina scales that developed on FAL and FAS-Y_2O_3 at 1100°C showed different characteristics: after about 500 h, the product on the former was thicker, more convoluted, and cracked on cooling, while the oxide on the latter showed a greater spallation tendency. Nevertheless, comparison of the data for these alloys to those for FASN clearly indicates that additions of zirconium or yttria substantially improved the adhesion of alumina scales grown on iron aluminides. These results are not unexpected;[2,9,12] the present observations simply reinforce the importance of small amounts of oxygen-active elements, and oxides based on the same, in improving oxidation resistance.[13] The two iron aluminides with such dopants had oxidation rates comparable to that of ZrO_2-dispersed FeCrAl (APM) at 1000°C (Fig. 1). At 1100°C (Fig. 2), APM showed superior oxidation resistance.

While the oxidation resistance of FAL was about the same as that of the FAS-Y_2O_3 at 1000 and 1100°C, significant differences between these two alloys were noted at 1200 and 1300°C (see Figs. 3 and 4). At these temperatures, the aluminum consumption rate, as measured by the total weight gain (that of the specimen as well as any oxide that has spalled) was higher for the FAL alloy. (With respect to the data shown in Fig. 4, the FAS-Y_2O_3 specimen went into breakaway oxidation[14] before the FAL simply because it was about half the thickness of the latter and thus had a substantially smaller aluminum reservoir to continually form protective Al_2O_3.[15-17]) This difference in oxidation behavior between the FAL and FAS-Y_2O_3 alloys may be at least partially explained by some localized inward growth of alumina observed for the former specimens (see Fig. 5). These areas of accelerated reaction could possibly be related to sites of casting/forming defects.

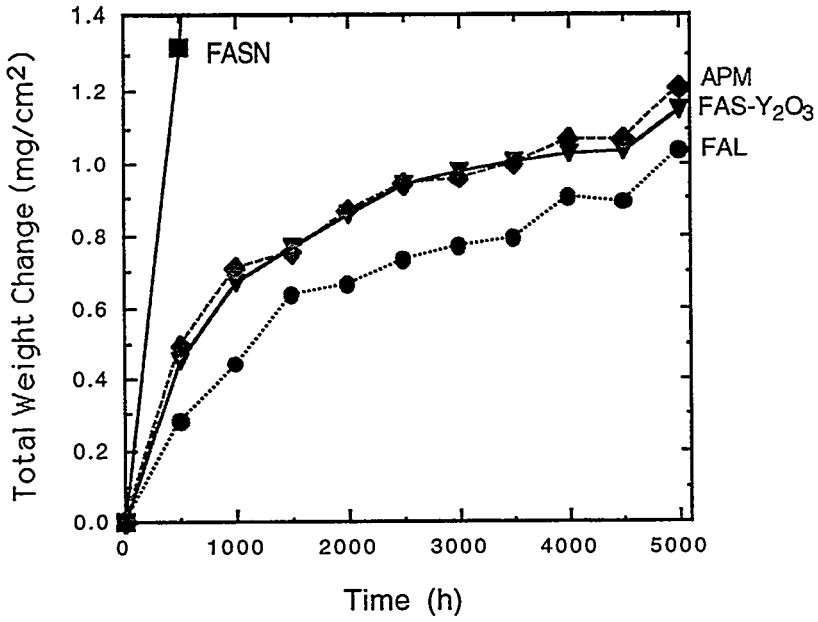

Fig 1. Total weight gain (specimen + spall) for 500-h cycles at 1000°C in laboratory air.

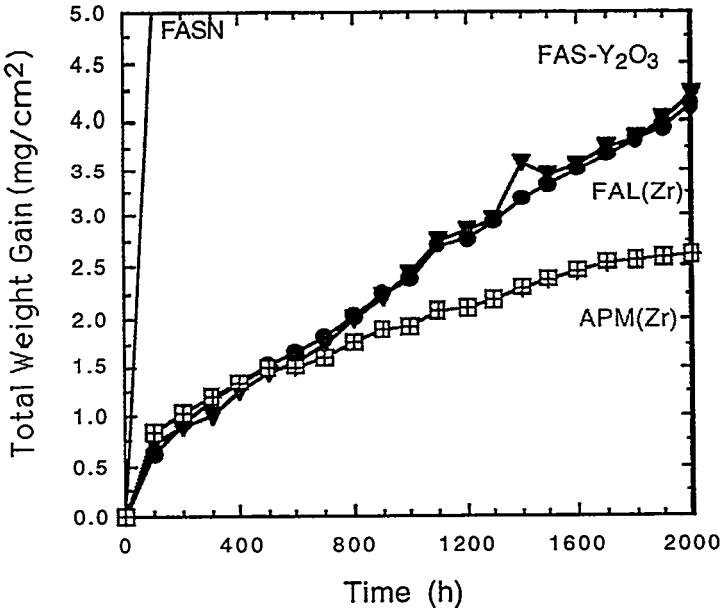

Fig. 2. Total weight gain (specimen + spall) for 100-h cycles at 1100°C in laboratory air.

A second factor contributing to the higher oxidation rate of FAL very well may be substrate strength. While the creep strengths of these alloys have not been determined, it appeared from evaluation of the as-oxidized specimens that the I/M FAL was weaker than the P/M Y_2O_3-containing FAS in that it was more easily deformed during high-temperature oxidation. Evidence for such has been shown previously for 1300°C oxidation[15,18] and from

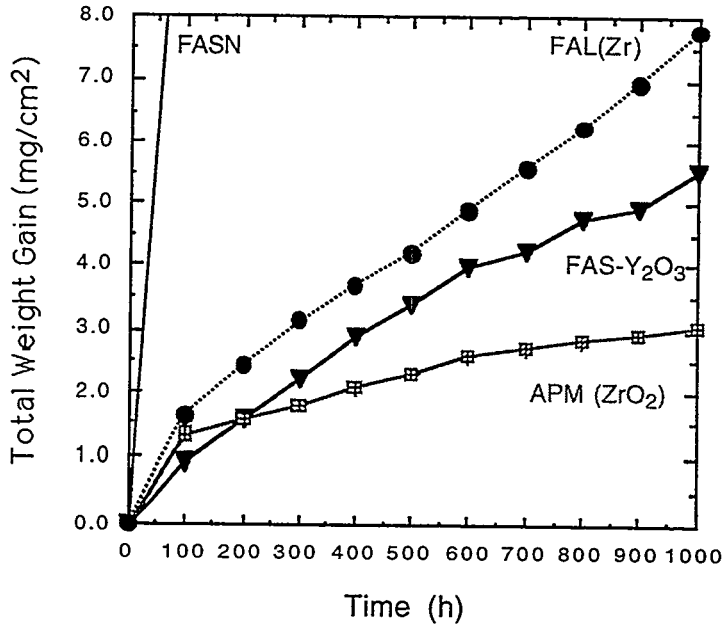

Fig. 3. Total weight gain (specimen + spall) for 100-h cycles at 1200°C in laboratory air.

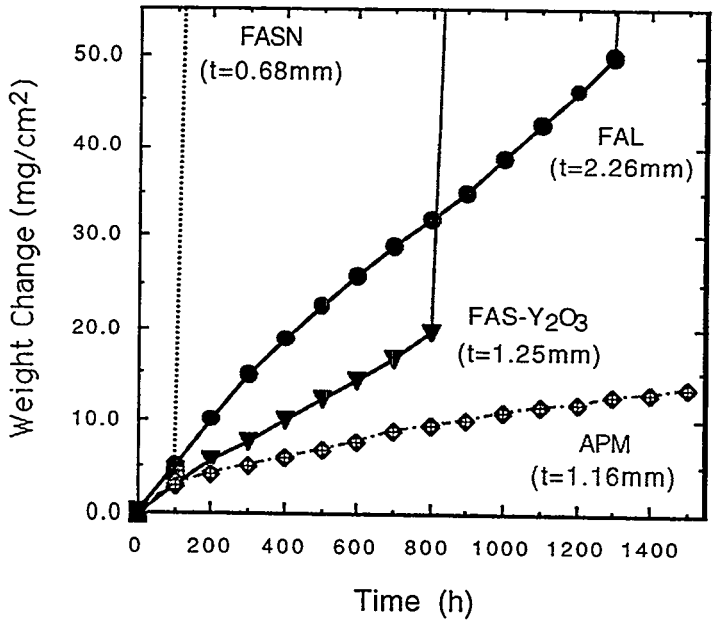

Fig. 4. Total weight gain (specimen + spall) for 100-h cycles at 1300°C in laboratory air. Starting specimen thicknesses (t) are noted.

the present experiments at this temperature. For example, Fig. 5 shows that the growth of alumina on FAL apparently significantly deformed the substrate. This ultimately results in a highly convoluted and cracked alumina scale. This deformation compromises the ability of the alumina scale formed on FAL to fully protect the substrate from reaction with the oxidizing

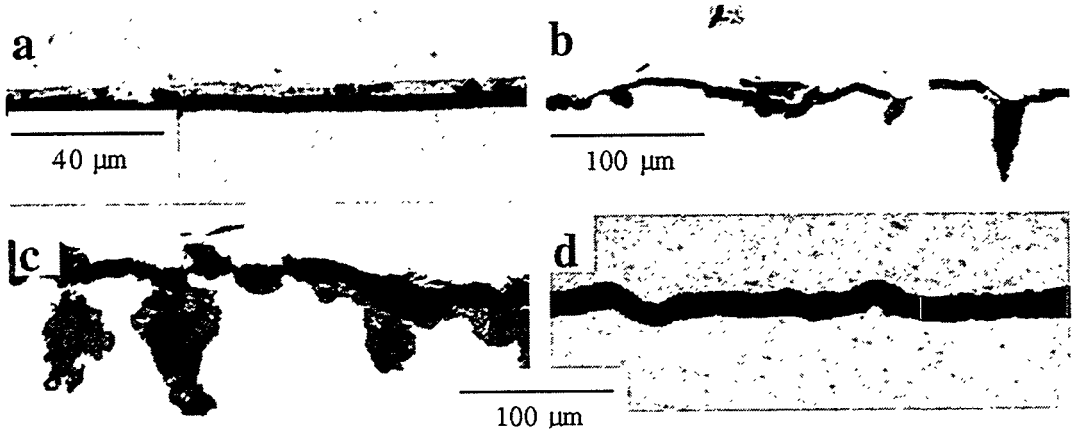

Fig. 5. Optical micrographs of cross sections of alumina-forming alloys exposed isothermally for 100 h in laboratory air (a) - (c) FAL, 1300°C; (d) APM, 1200°C. Specimens were coated with copper (upper light area) before sectioning. Comparison of (b) and (d) shows the scale grown on FAL is convoluted while the oxide on APM is relatively flat. Intermittent inward growth of alumina can be seen in (b) and (c).

species. Observations of a FAL specimen oxidized at 1200°C using 1-h cycles revealed similar scale convolutions and cracking. In contrast, the ODS iron aluminides exposed under the same conditions tended to show scale spallation due to interfacial void formation.

Although Y_2O_3 in FAS and Zr in FAL have beneficial effects on oxidation resistance, previous and present results indicate that these dopants are not as effective in the iron aluminides as when they are added to FeCrAl and β-NiAl.[18] As shown in Figs. 1-5, neither of these additions resulted in oxidation behavior as good as that of APM at 1100°C and above. The APM alloy remained relatively flat and the substrate-oxide interface was void-free (Fig. 5d). The reasons for the variations in oxidation performance between these different alumina-forming alloy systems are not known, but substrate strength and associated effects on scale buckling and void formation[18] are probably contributing factors.

As the high-temperature corrosion resistance of iron aluminides critically depends on the ability to grow and maintain a protective alumina layer, the minimum aluminum concentration necessary for formation of a continuous Al_2O_3 scale in air (c_{Al}) has been determined to be approximately 19% for I/M Fe-Al(-Cr) alloys.[19] As shown by the solid circles in Fig. 6, aluminum concentrations lower than this value lead to substantially greater weight gains for similar oxidation conditions. For 100-h exposures at 900°C, it was found that the oxidation product contained significant amounts of iron oxide and thus was not protective when weight gains were greater than about 1 mg/cm^2. Using weight gain as an indicator of alumina formation, it has been shown that c_{Al} for selected ODS (P/M) Fe_3Al alloys was lower than the value determined for I/M Fe-Al(-Cr) alloys . This shift in c_{Al} is illustrated in Fig. 6,

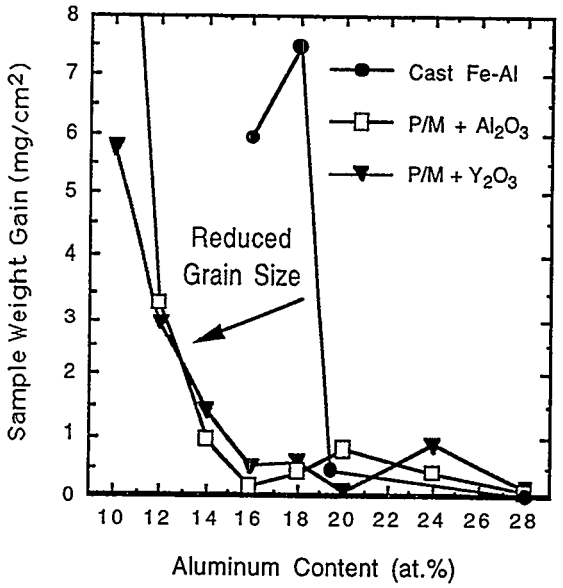

Fig. 6. Specimen weight change versus aluminum content after 100 h in air at 900°C for P/M and I/M Fe-Al alloys.

which shows that the critical aluminum concentration for the P/M alloys was ~13%. The addition of Y_2O_3 to the P/M alloy (which always contains a dispersion of Al_2O_3) did not significantly change this value. Similarities between Al_2O_3- and Y_2O_3-dispersed Fe-Al and c_{Al} values were observed from 600-1300°C.[20]

In attempting to explain the difference in c_{Al} between I/M and P/M versions of Fe_3Al alloys, the respective starting grain sizes of these materials must be considered. For the I/M alloys, average grain size is approximately 40 μm (or even larger) versus ~1 μm for the as-extruded P/M products. In addition, the oxide dispersions in the P/M alloys help to maintain the small grain size during elevated-temperature exposures. Because of this, the finer grain size of the P/M iron aluminides can promote more rapid transport of aluminum to the oxidizing surfaces. This would lower the apparent c_{Al} ,as the time to the onset of nonprotective oxide formation (breakaway) is also dependent on (proportional to) the diffusion coefficient of aluminum in the alloy.[14,16,17]

OXIDATION-SULFIDATION OF ODS Fe_3Al ALLOYS

Iron aluminides produced by conventional I/M procedures, have excellent sulfidation resistance in H_2S-containing environments.[2,19,21,22] Therefore, it has been of continuing interest to learn whether ODS iron aluminides show similar corrosion behavior. Preliminary data, obtained by exposing as-extruded P/M FAS and FAS-Y_2O_3 to 5.4% H_2S-79.4% H_2-1.6%

H_2O-13.6% Ar (by volume) showed that the oxidation/sulfidation rates of these iron aluminides were similar to that of many I/M Fe_3Al alloys.[9] Specifically, the isothermal weight gains of these P/M FAS alloys were somewhat greater than I/M FAS, but less than Fe_3Al-5% Cr produced by I/M processing. Subsequently, alloys of FAS-Y_2O_3 were produced from commercially-prepared powders.[4] These products were designated PMWY to distinguish them from the earlier ODS FAS-Y_2O_3 alloys; their detailed compositions and metallurgical characteristics are described elsewhere.[4] Specimen coupons were cut from recrystallized PMWY1 and PMWY2 (see ref. 4) and exposed to the same aggressive oxidizing/sulfidizing (H_2S-H_2-H_2O-Ar) environment at 800°C under both isothermal and thermal cycling conditions. The oxygen partial pressure, as determined by a solid-state oxygen cell, was 10^{-22} atm, and the sulfur pressure was calculated to be 10^{-6} atm. The isothermal results are shown in Fig. 7, which compares the thermogravimetric results for the PMWY alloys with similar data for I/M Fe_3Al alloys with 2 and 5% Cr and the previous as-extruded P/M FAS and FAS-Y_2O_3.[9] Note that the gravimetric curves for the PMWY alloys essentially mimic that for the benchmark I/M FAS composition. These weight gains are extremely low given the aggressiveness of the H_2S-H_2-H_2O-Ar gas. Indeed, under similar conditions, weight gains for Fe-20% Cr-10% Al alloys (such as APM) and stainless steels would be 1-3 orders of magnitude higher.[21,22] Furthermore, sulfidation resistance was maintained after a few thermal cycles; there was essentially no change in the rate of weight gain when a thermogravimetric experiment was periodically interrupted by cooling to room temperature and reheating to the exposure temperature.

The more rapid initial weight gains of the P/M FAS and FAS-Y_2O_3 specimens relative to those of the PMWY-1 and PMWY-2 in the oxidizing-sulfidizing environment may be related to grain size. It was previously hypothesized that the former alloys showed greater weight gains than the I/M FAS because their fine grain size allowed a more rapid diffusion of chromium to the reaction front and resulted in higher initial weight gains due to formation of chromium sulfides.[9] This argument may also explain the lower weight gains of the PMWY alloys shown in Fig. 7; the average grain size of the PMWY coupons was much larger than that of the as-extruded P/M FAS and FAS-Y_2O_3 specimens due to the recrystallization heat treatment.[4]

OXIDATION-SULFIDATION OF IRON-ALUMINIDE WELD OVERLAYS AT 800°C

This section contains corrosion data on weld deposits produced by gas metal arc (GMA) welding. Results for coatings produced by the gas tungsten arc (GTA) process as well as initial data for GMA overlays have been reported previously.[7,9] The development efforts associated

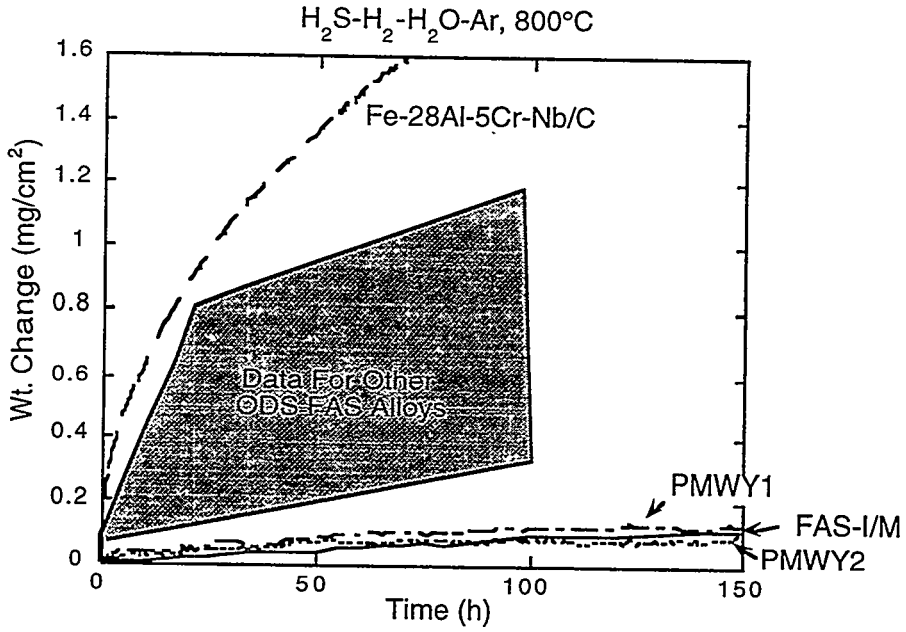

Fig. 7. Weight change versus time for specimens isothermally exposed to H_2S-H_2-H_2O-Ar at 800°C. The PMWY alloys are FAS-Y_2O_3 produced from commercially prepared powders and were exposed in the as-recrystallized condition. The specimen designated FAS-I/M was produced by ingot metallurgy processing and represents the benchmark behavior in this environment. The Fe_3Al - 5% Cr alloy was also produced by ingot metallurgy and contains 1% Nb and 0.2% C. The shaded area represents the range of data reported previously (see ref. 9) for as-extruded FAS and FAS-Y_2O_3 prepared from laboratory-produced powder mixtures.

with the GTA and GMA processes used to produce the weld overlays are described elsewhere.[5,6]

Weld overlays were deposited on Fe-2.25 Cr-1 Mo (wt%) steel substrates by GMA welding. As in previous oxidation-sulfidation studies,[7,9] coupons were prepared by cutting rectangular specimens from the overlay pad and then grinding away all the substrate material so that only weld metal (approximately 1-2 mm thick) remained. In this way, only the corrosion behavior of the weld deposit, rather than the coating/substrate system, is evaluated.[7,9] Oxidation-sulfidation behavior was characterized by use of a continuous-recording microbalance to measure the weight of these specimens during exposure at 800°C to the H_2S-H_2-H_2O-Ar mixed gas described above.

The use of welding to produce iron-aluminide coatings results in a loss of selected elements from the rod/wire by vaporization and significant mixing of the filler metal and substrate alloys (dilution) during deposition.[5,6] Because there is essentially no aluminum in the Fe-Cr substrates, the concentration of this element in the overlay is significantly less than in the weld rod/wire used to produce it. The extent of this dilution in aluminum depends on vaporization

losses during welding and the relative amount of substrate material melted. Thus, it is affected by parameters such as current, voltage, polarity, travel speed, etc. When dilution is controlled such that the aluminum content of the weld deposit exceeds about 20%, good oxidation-sulfidation resistance results.[7,9] A GMA weld overlay with 21% Al and 1% Cr (denoted, for the purposes of this paper, as S2) consistently showed gravimetric behavior equivalent to the baseline FAS composition, which serves as the benchmark by which all other alloys are judged with respect to this mixed gas environment[21] (see Fig. 8). As shown in Fig. 9, S2 specimens showed better oxidation-sulfidation resistance than a previously examined GMA weld overlay[9] with the same Al level, but a significantly higher Cr concentration (because it was produced with a different weld wire). The deleterious effect of chromium on corrosion resistance in this environment is well documented,[2,21,22] and can explain the differences between the present and prior GMA results. Interestingly, as also shown in Fig. 9, the GMA S2 weld overlay had better oxidation-sulfidation resistance than a GTA one with 37% Al. This Al level normally offsets the deleterious effect of Cr,[21] so, in this case, there may be compositional inhomogeneity in the GTA weld overlay. As discussed previously,[9] the GMA process, which involves a substantially higher energy input into the weld, may promote more complete mixing of the deposit, and therefore result in more reproducible and better corrosion resistance in this environment than overlays produced by GTA.

The present results indicate that, in combination with a low chromium concentration, the aluminum level of the S2 weld overlay appears to be sufficient to show excellent corrosion

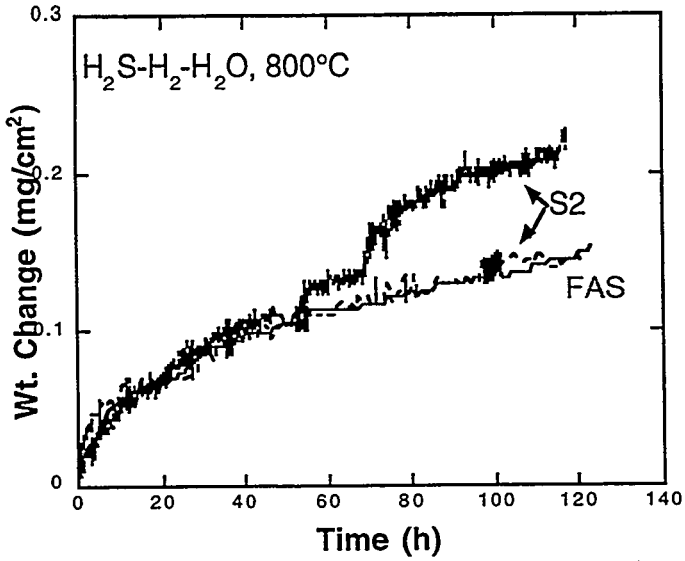

Fig. 8. Weight change versus time for I/M FAS and two specimens from a GMA weld overlay with a composition of Fe - 21% Al - 1% Cr (S2). Differences in behavior are negligible on this scale.

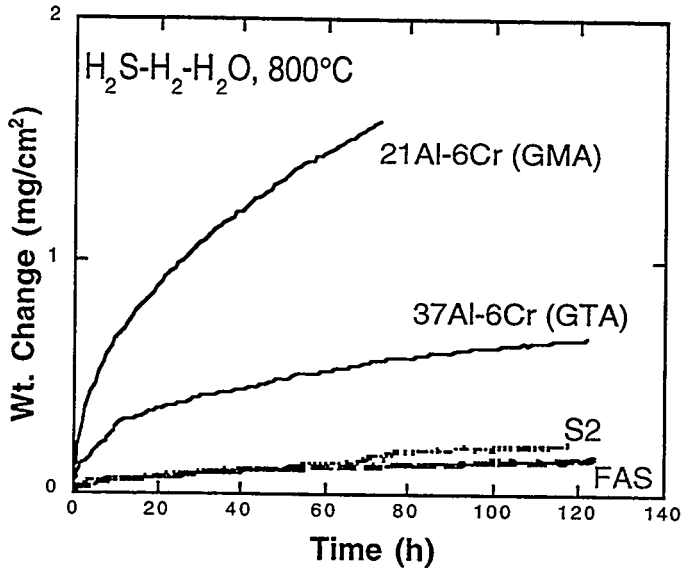

Fig. 9. Weight change versus time for I/M FAS and specimens from GMA and GTA weld overlays with compositions as shown. The curves designated S2 are the same as shown in Fig. 8 and are for a GMA weld overlay with a composition of Fe - 21% Al - 1% Cr. The FAS (I/M) curve is also the same as shown in Fig. 8.

resistance in an aggressive oxidizing/sulfidizing environment under isothermal conditions. However, aluminum concentrations of 20 - 21% are marginal with respect to maintaining low corrosion rates over extended periods of time, particularly if thermal cycling exacerbates the aluminum depletion process.[9] Weldability problems notwithstanding,[5,6] higher aluminum concentrations in the overlays would delay any onset of accelerated reaction caused by depletion of this element and improve the corrosion behavior of iron-aluminide coatings containing substrate elements, such as chromium and nickel, that are deleterious to sulfidation resistance (compare the 21Al-6Cr and 37Al-6Cr gravimetric curves in Fig. 9).[21,22]

SUMMARY AND CONCLUSIONS

The long-term oxidation performance of ingot- and powder-processed Fe-28 at.% Al-(2-5)% Cr alloys with minor oxygen-active element or oxide additions was characterized for exposures in air at 1000-1300°C. The oxidation-sulfidation behaviors of oxide-dispersion-strengthened Fe_3Al alloys and iron-aluminide weld overlays were also investigated.

Additions of zirconium or yttria substantially improved the adhesion of alumina scales grown on iron aluminides. At lower temperatures, the ingot-processed alloys performed similarly to ODS Fe_3Al alloys and other alumina-formers. However, at 1200 and 1300°C, the

oxidation resistance of the ingot-processed Fe_3Al was degraded due to deformation of the substrate and some localized reaction product growth. Other oxidation experiments showed that the addition of an oxide dispersion to iron aluminides reduced the critical aluminum concentration for protective alumina scale formation.

Alloys of Fe-28 at.% Al-2% Cr-Y_2O_3 were produced from commercially-prepared powders and exposed to an highly aggressive oxidizing/sulfidizing (H_2S-H_2-H_2O-Ar) environment at 800°C under isothermal and thermal cycling conditions. The results from these experiments showed that these alloys had excellent oxidation/sulfidation resistance that was comparable to that of the ingot-processed version of the base alloy.

Iron-aluminide coatings were prepared by a gas metal arc weld-overlay technique. Specimens cut from the weld deposits were isothermally exposed to the H_2S-H_2-H_2O-Ar environment at 800°C. Excellent corrosion resistance was observed for a weld overlay with 21% Al and 1% Cr, but higher aluminum concentrations will be necessary to assure long-term performance in this environment, particularly under thermal cycling conditions.

ACKNOWLEDGMENTS

The authors thank M. Howell for experimental support and J. R. DiStefano, G. M. Goodwin, and J. R. Keiser for their reviews of the manuscript. This research was sponsored by the Fossil Energy Advanced Research and Technology Development (AR&TD) Materials Program, U S. Department of Energy, under contract DE-AC05-96OR22464 with Lockheed Martin Energy Research Corporation.

REFERENCES

1. C. G. McKamey, J. H. DeVan, P. F. Tortorelli, and V. K. Sikka, "A Review of Recent Developments on Fe_3Al-Based Alloys," *J. Mater. Res.* 6 (1991) 1779-1805.

2. P. F. Tortorelli and J. H. DeVan, "Compositional Influences on the High-Temperature Corrosion Resistance of Iron Aluminides," pp. 257-70 in Processing, Properties, and Applications of Iron Aluminides, J. H. Schneibel and M. A. Crimp (eds.), The Minerals, Metals, and Materials Society, Warrendale, PA, 1994.

3. I. G. Wright, B. A. Pint, E. K. Ohriner, and P. F. Tortorelli, "ODS Iron Aluminides," pp. 359-71 in *Proc. Tenth Annual Conf. Fossil Energy Materials*, N. C. Cole and R. R. Judkins (comp.), U. S. Department of Energy, August 1996.

4. I. G. Wright, B. A. Pint, P. F. Tortorelli, and C. G. McKamey, "Development of ODS Fe_3Al Alloys," these proceedings.

5. G. M. Goodwin, P. J. Maziasz, C. G. McKamey, J. H. DeVan, and V. K. Sikka, "Weldability of Iron Aluminides," pp. 205-10 in *Proc. Eighth Annual Conf. Fossil Energy Materials*, N. C. Cole and R. R. Judkins (comp.), CONF-9405143, U. S. Department of Energy, August 1994.

6. G. M. Goodwin, "Weld Overlay Cladding with Iron Aluminides," pp. 381-92 in *Proc. Tenth Annual Conf. Fossil Energy Materials*, N. C. Cole and R. R. Judkins (comp.), U. S. Department of Energy, August 1996.

7. P. F. Tortorelli, J. H. DeVan, G. M. Goodwin, and M. Howell, "High-Temperature Corrosion Resistance of Weld Overlay Coatings of Iron Aluminide," pp. 203-12 in Elevated Temperature Coatings: Science and Technology I, N. B. Dahotre, J. M. Hampikian, and J. J. Stiglich (eds.), The Minerals, Metals, and Materials Society, Warrendale, PA, 1995.

8. K. Natesan and R. N. Johnson, "Corrosion Performance of Fe-Cr-Al and Fe Aluminide Alloys in Complex Gas Environments," pp. 591-99 in Heat-Resistant Materials II, K. Natesan, P. Ganesan, and G. Lai (eds.), ASM International, August 1995.

9. P. F. Tortorelli, B. A. Pint, and I. G. Wright, "High-Temperature Corrosion Behavior of Coatings and ODS Alloys Based on Fe_3Al," pp. 393-403 in *Proc. Tenth Annual Conf. Fossil Energy Materials*, N. C. Cole and R. R. Judkins (comp.), U. S. Department of Energy, August 1996

10. B. A. Pint, K. B. Alexander, and P. F. Tortorelli, "The Effect of Various Oxide Dispersions on the Oxidation Resistance of Fe_3Al," pp. 1315-20 in High-Temperature Ordered Intermetallic Alloys VI, J. A. Horton, I. Baker, S. Hanada, R. D. Noebe, and D. S. Schwartz (eds.), The Materials Research Society, Pittsburgh, PA, 1995.

11. B. A. Pint, A. J. Garratt-Reed, and L. W. Hobbs, "The Reactive Element Effect in Commercial ODS FeCrAl Alloys ," *Mater. High Temp.* 13 (1995) 3-16.

12. B. A. Pint, "Study of the Reactive Element Effect in ODS Iron-Base Alumina-Formers," submitted for publication in *Mater. Sci. Forum,* 1996.

13. B. A. Pint, "Experimental Observations in Support of the Dynamic Segregation Theory to Explain the Reactive Element Effect," *Oxid. Met.* 45 (1996) 1-37.

14. P. Kofstad, High Temperature Oxidation, 1988.

15. J. H. DeVan, P. F. Tortorelli, and M. J. Bennett, "Environmental Effects on Iron Aluminides," pp. 309 - 20 in *Proc. Eighth Annual Conf. Fossil Energy Materials*, N. C. Cole and R. R. Judkins (comp.), CONF-9405143, U. S. Department of Energy, August 1994.

16. W. J. Quaddakers and M. J. Bennett, "Oxidation Induced Lifetime Limits of Thin Walled Iron Based Alumina Forming Oxide Dispersion Strengthened Alloy Components," *Mater. Sci. Technol.*, 10 (1994) 126-31.

17. M. J. Bennett, J. H. DeVan, and P. F. Tortorelli, "The Oxidation Behavior of Iron Aluminides in Air at 1300°C," accepted for publication in *Proc. Third Int'l. Conf. on Microscopy of Oxidation*, S. B. Newcomb and J. A. Little (eds.), The Institute of Materials, London, September 1996.

18. B. A. Pint, P. F. Tortorelli, and I. G. Wright, "The Oxidation Behavior of ODS Iron Aluminides," *Werkst. Korros.* 47 (1996) 663-74.

19. J. H. DeVan and P. F. Tortorelli, "Oxidation-Sulfidation Behavior of Iron Alloys Containing 16 to 40 Atomic Percent Aluminum," *Corros. Sci.* 35 (1993) 1065-71.

20. B. A. Pint and J. Lebowitz, Oak Ridge National Laboratory, unpublished results, 1996.

21. J. H. DeVan, "Oxidation Behavior of Fe_3Al and Derivative Alloys," pp. 107-115 in Oxidation of High-Temperature Intermetallics, T. Grobstein and J. Doychak (eds.), The Minerals, Metals, and Materials Society, 1989.

22. J. H. DeVan and P. F. Tortorelli, "Oxidation/Sulfidation of Iron-Aluminum Alloys," *Mater. at High Temp.* 11 (1993) 30-35.

CORROSION-RESISTANT COATING DEVELOPMENT

D. P. Stinton, D. M. Kupp, and R. L. Martin

ABSTRACT

SiC-based heat exchangers have been identified as the prime candidate material for use as heat exchangers in advanced combined cycle power plants. Unfortunately, hot corrosion of the SiC-based materials created by alkali metal salts present in the combustion gases dictates the need for corrosion-resistant coatings. The well-documented corrosion resistance of CS-50 combined with its low (and tailorable) coefficient of thermal expansion and low modulus makes CS-50 an ideal candidate for this application. Coatings produced by gelcasting and traditional particulate processing have been evaluated.

INTRODUCTION

Gelcasting of sodium-zirconium-phosphate (NZP) based materials[1-3] has been identified as a candidate process for applying high temperature, corrosion resistant coatings on to ceramic substrates. The gelcasting process, normally most useful in producing relatively large or complex ceramic or metallic monoliths, is being considered as a technique for applying conformal coatings to SiC composite heat exchanger tubes. The corrosion resistance of the $Ca_{0.5}Sr_{0.5}Zr_4P_6O_{24}$ (CS-50) material for the prescribed application has been well documented[4,5]. This characteristic, combined with its low (and tailorable) coefficient of thermal expansion (CTE) makes CS-50 an ideal candidate for evaluation in this application. The major hurdle has been in identifying an application technique which is both technically and economically feasible. While various chemical vapor deposition (CVD) and physical vapor deposition (PVD) techniques can be used to apply desirable coatings to idealized substrates, the complex composition of the coatings and the large size of the heat exchanger tubes (up to 15 feet long) makes the use of these techniques difficult and costly. Application techniques such as plasma spraying have also been tried with varying degrees of success.

By combining the attributes of polymer chemistry with those of traditional particulate processing, gelcasting has proven itself to be a viable contender in this area. However, while gelcasting of CS-50 based monoliths has proven to be relatively straightforward, the mechanical interaction of a gelcast body with a rigid substrate throughout the various processing steps addresses some of the most fundamental (and persistent) problems in traditional particulate processing (e.g. drying/sintering shrinkage and thermal expansion).

The development of an NZP-based coating was undertaken from a product development (rather than a scientific interest) point of view in an effort to maximize the amount of applicable progress made. Experiments were conducted using multivariate, small sample sizes. Since both the gelcasting process and the NZP type materials are well understood, it made sense to directly focus upon the new application, i.e. the gelcasting of NZP materials as a coating on a SiC/SiC composite substrate.

Since the gelcasting of CS-50 was previously proven to be feasible in standard gelcasting applications (i.e. monolithic geometries), an effort to improve the basic process was undertaken. The major problems envisioned in the process (and initially addressed) included:

1. Shrinkage of the CS-50 coating during processing leading to catastrophic failure of the coating.
2. Matching of the CTE of the coating to that of the substrate without detrimentally affecting other downstream processes.
3. Selection of a stable material systems which is non-reactive with the substrate and offers maximum corrosion protection.

From a fundamental standpoint, tailoring of the CTE of the coating to match that of the substrate is straightforward. By combining the CS-50 with a material having a CTE greater than that of the substrate in the proper ratios, a material system having the appropriate CTE could be customized. By approximating the CTE of the SiC ceramic matrix composite, the CTE of CS-50 can be increased to that of the SiC substrate by the correct addition of alumina for example. Trials evaluating various coating to substrate CTE ratios must be carried out to determine the optimal coating CTE.

One of the major obstacles in the application of a particulate coating on to a substrate is the accommodation of the shrinkage of the applied coating due to such things as polymer cross linking, drying, binder removal, etc. The most direct way of reducing such shrinkage is through the optimization of the particle packing or solids loading of the powder system (i.e. slurry) being used. While many complex models exist for predicting and interpreting particle packing behavior, it is sufficient for current purposes to simply maximize the amount of solid material per quantity of slurry liquid (water and/or liquid chemicals) while still maintaining a usable slurry rheology. By maximizing the solids loading level, more particle to particle contacts are generated, reducing shrinkage through particle rearrangement and increasing green strength.

Assuming a roughly equiaxed particle morphology where random particle orientation produces a more or less homogeneous, isotropic particle array, a solids loading level can generally be maximized by using a powder with a very narrow (i.e. monosized) or very broad particle size distribution. This distribution width, S_w, can be calculated from the following:

$$S_w = \frac{2.56}{d_{90} - d_{10}} \quad \text{where}$$

d_{90} = particle diameter equivalent to 90% of the cumulative distribution

d_{10} = particle diameter equivalent to 10% of the cumulative distribution

Ideally, the distribution width should be very wide ($S_w \# 2$) or very narrow ($S_w \exists 7$) to achieve maximum particle packing density (i.e. solids loading) in a slurry or green/fired component. Since it can be difficult and expensive to produce a monosized powder in reasonable quantities, a powder with a wide particle size distribution is generally more desirable. Since the base low expansion powder will likely be amended with a relatively high CTE material to develop a suitable coating CTE, intelligent selection of the "modifier" in terms of thermomechanical properties and particle size characteristics will also enhance the particle packing and rheological behavior of the powder system.

DISCUSSION

The processability and composition of the components of the corrosion resistant coating were the two basic concerns initially addressed. Sodium-zirconium-phosphate (NZP) material ($Ca_{0.5}Sr_{0.5}Zr_4P_6O_{24}$) was selected as the primary component based on its low CTE and excellent corrosion resistance[4,5]. As previously discussed, the CTE of the NZP material (grade CS-50 from LoTEC, Inc.) was selected as the base material to be amended by another corrosion resistant material in order to tailor the coating CTE. Alumina (grade RCHP/no MgO from Reynolds) was selected as the modifying material based on previous gelcasting performance and its generally excellent corrosion resistance. This specific grade of material has a fine median particle size (<1 Φm) which would enhance the packing and rheological behavior of a CS-50/alumina mixture. Initially, gelcasting of pure CS-50 was carried out to establish a baseline procedure for the NZP family of base materials. Prior art in the gelcasting of these materials established basic formulations and procedures. The standard monomer solution (which is crosslinked in a downstream process) was a 15 wt. % aqueous solution of a 6:1 ratio of MAM (methacrylamide) to MBAM (methylene bisacrylamide). This solution served not only as the polymeric precursor but also as the fluid in which the particulate materials were ball milled and mixed. Since it was critical to maximize the solids loading of the slurry (i.e. volume % ratio of solids to liquids), solids loading levels of the slurries began at ~ 50 vol.% and were gradually increased until the desired viscosity had been reached. Eventual solids loading levels of ~60 vol. % were reached for the pure CS-50 gelcastable slurry.

Milling was carried out in HDPE jars (~750 ml.) with 6 mm. diameter zirconia media. Darvan 821A was added to the precursor solution as a dispersant. Generally, gentle milling was carried out only to disperse, homogenize and wet the powder, not necessarily to modify the particle shapes or size distributions.

Once it was determined that an optimized solids loading level had been reached, the slurry was strained through a -325 mesh screen to remove media and dried mill residue. The slurry was then de-aired using a vacuum dessicator until a bubble-free slurry resulted. At this point the slurry is suitable to begin the casting procedure. A combination of crosslinking catalysts and accelerants [TEMED(tetramethylethyl diamine) and 10% aqueous solution of APS (ammonium

persulfate)] is added to convert the monomer precursor solution to a polymeric binder. Since the kinetics of crosslinking is relatively slow (and controllable), time is available to pour the slurry into a mold before complete gelation of the binder/powder system occurs.

Since the gelcasting trials of the pure CS-50 composition were successful, preliminary efforts incorporating the CTE modifier, alumina, were started. By approximating the CTE of the SiC ceramic matrix composite to be ~ 4.5 x 10^{-6}/EC, the CTE of CS-50 (3.0 x 10^{-6}/EC) can be increased to that of the SiC substrate by the correct addition of alumina for example (CTE ~ 8.0 x 10^{-6}/EC). Using the rule of mixtures as a basis for formulation, a body comprised of 70 vol. % CS-50 / 30 vol. % Al_2O_3 (66 wt. % CS-50/34 wt. % Al_2O_3) was formulated, approximating the CTE of the SiC/SiC substrate.

A particle size analysis was completed on the CS-50 powder using a Horiba LA-700 particle size analyzer. The particle size distribution for the powder was bimodal (0.3 Φm and 20 Φm), with a mean particle size of ~ 13.4 Φm. The distribution width, S_w, is calculated to be ~1.4 (very wide). However, visually and to the touch, the powder seemed to contain a fraction of grit (i.e. large, hard agglomerates) which can be broken with moderate pressure. These agglomerates can also be disintegrated somewhat with intensive ultrasonic agitation. The mean particle size for a sample which received intensive agitation with an outboard ultrasonic horn was reduced by 17% from 13.4 Φm to 11.1 Φm with additional agitation (beyond that provided in the Horiba chamber prior to analysis). Furthermore, the percentage of particles greater than ~30 Φm decreased from 8.5 to 4.5%, likely due to the breaking up of the hard agglomerates.

After sustained, but gentle milling, the solids loading level and related rheological behavior of the CS-50 and alumina powder mix appears to be outstanding at 70 vol. % CS-50 / 30 vol. % alumina at 66 vol. % solids loading. Approximately 0.7 wt. % Darvan 821A (based on total solids) was added as a dispersant to the 70/30 slurry in the aqueous MAM/MBAM solution. Most notable from the particle size distribution is the lack of particles greater than 20 Φm in comparison to the standard and ultrasonically agitated slurries which show particle sizes for the as-received and sonicated CS-50 powder to be 60-75 Φm. It appears that the low intensity ball milling done to homogenize the powder/monomer slurry, is sufficient to break up the light aggregate suspected of existing in the as-received CS-50. Once the CS-50 powder is dispersed,

along with the addition of 30 vol. % alumina, a very wide distribution width, Sw, of 1.51 is achieved. This wide distribution combined with the deagglomerated slurry components provides the basis for a high solids loading level (>66 vol. % solids). While the particle size distribution of the as-received CS-50 powder is also very wide (Sw = 1.46), the distribution appears to be an artifact of particle agglomeration and fines, not the true, primary particle size distribution measured after mechanical deagglomeration.

Two component slurries at 60/40, 70/30, 80/20 and 90/10 vol.% CS-50/alumina were prepared and evaluated for rheological behavior and powder co-processing behavior related to slurry additives (e.g. dispersants and anti-foaming agents) and critical solids loading levels. Samples 25 mm. x 25 mm. were gelcast and dried without apparent problems. Samples were processed through thermal binder removal (1EC/min. to 600EC, hold for 1 hour) and sintered in air at 1325EC for 4 hours without physical damage. Compositional analysis was not completed on any samples.

Since the processing of a gelcast CS-50/alumina monolith was successful for each composition, the application of a similar slurry to a SiC composite substrate was tried. SiC/SiC tube sections (25 mm. diameter x 20 mm. long) were dipped into each of the CS-50/alumina slurries which had been catalyzed but had not crosslinked. Multiple dips on different samples provided a variety of coating thicknesses for analysis of adhesion and cracking behavior through drying and firing steps. Freshly dipped samples were suspended in a relatively airtight container (since contact with air inhibits gelation) until gelation had completed and residual moisture had dried. After a standard binder burnout cycle was completed, the coated samples were heat treated at 1200EC (in air) for 5 days. While the sintering temperature for CS-50 based materials (especially when "alloyed" with alumina) is >1300EC, a maximum temperature of 1200EC was used to avoid degradation of the SiC composite. Relatively long sintering times were used to promote densification of the coating at the lower firing temperature and also to evaluate the thermomechanical performance of the coating.

Two distinct phenomena were investigated; coating thickness and composition. After long term firing, samples with coating thicknesses greater than about 2 mm. exhibited severe cracking throughout the surface of the coating in the form of continuous crazing, as well as deeper fissures

appearing radially on the ends of the tube section. Other substantial cracking occurred on the circumference of the tube section, apparently as a result of the shrinkage of the particulate coating during drying and sintering. Thinner coatings (<1 mm.) did not exhibit the same cracking pattern as the thicker coatings, with only a thin crack occurring at the edge of the tube section (juncture between the tube end and outside diameter). Samples of the composition 90 vol.% CS-50 /10 vol.% alumina also showed reduced overall cracking due to proper tailoring of the CTE. In these cases, a continuous, adherent and somewhat densified coating was developed.

As a result of the improved adhesion and resistance to cracking associated with the reduced coating thickness, the gelcasting technique used to produce these coatings (and in general, much larger monolithic structures) was abandoned in favor of a much more straight forward "non-monomer" slurry approach. By utilizing a traditional aqueous slurry, the need for expensive and toxic monomer precursor materials was eliminated. Furthermore, the problem of gelation being inhibited by exposure to air is no longer an issue since the monomer crosslinking phase is no longer a requirement of the process. The air exposure limitation of gelcasting may have led to some costly and complicated engineering problems if larger tubes were ever to be coated.

As an initial characterization of the fired composite/coating sample, XRD was performed to determine the extent (if any) of the CS-50 degradation related to substrate exposure, prolonged high temperature use and/or the alloying with another material (i.e. alumina). Samples of 70 vol.% CS-50/30 vol.% alumina were prepared using a non-gelcasting slurry to dip coat SiC/SiC tube sections. Samples were dipped and dried followed by a binder burnout at 600EC./1hr. The coated tube sections were sintered at 900, 1000, 1100 and 1200EC for 48 hrs. A standard coating of pure CS-50 was also prepared identically and sintered at 1200EC for 48 hrs. XRD results (Figure 1) show the generation of an unidentified phase in the 70/30 sample at 1200EC. The intensity of this phase decreases with sintering temperature and does not exist in the pure CS-50 coating at 1200EC exposure. Furthermore, three low angle peaks (11-14E 22) which exist in the XRD trace for pure CS-50 at 1200EC decrease in intensity with increasing process temperature. While the XRD data is open to interpretation and is not fully completed, it does indicate that the addition of the alumina to the pure CS-50 as a CTE modifier reacts to form what may be an undesirable phase.

Without further analysis or actual corrosion testing to evaluate the performance of the unidentifiable phase(s), it was decided to consider modification of the CS-50 CTE with other materials such as:

1. 4% Y_2O_3 stabilized ZrO_2
2. 12% CeO stabilized ZrO_2
3. Cr_2O_3

Using established procedures and general compositions, the above materials were used to make three new slurries as follows: 90 vol.% CS-50/10 vol%. modifier at 65 vol.% solids loading. SiC composite tube sections were dip coated with each slurry and dried. Following binder burnout, the samples were heat treated at 1200EC for 4 days.

SUMMARY

Initial trials using alumina modified CS-50 indicated that a relatively thin coating of a 90 vol.% CS-50/10 vol. % alumina provided the best adhesion to the SiC tube section in addition to providing a relatively crack free, continuous coating. Corrosion tests were not performed on these samples, but x-ray diffraction indicated a possible degradation of the CS-50 or generation of a phase non-existent in the as-received raw materials. A new selection of CTE modifiers based on individual corrosion resistance replaced the alumina. Stabilized ZrO_2 and Cr_2O_3 were added to the CS-50 in the same relative volume fraction. It became apparent that it was not the matching of the coating and substrate CTEs, but the relative CTEs which were important. Therefore, as a convenient and comparable starting point, the 90/10 ratio of CS-50/CTE modifier was maintained. The ZrO_2 and Cr_2O_3 modified coatings processed well and remained intact through a 1200EC/5 day soak.

In general, the theory involving maximizing the solids loading of the slurry proved to be useful. Powder particle sizes can be modified "ad nauseum" if necessary to obtain a highly loaded slurry with desirable rheological characteristics. The viscosity of a given slurry is only important as it relates to the coating technique used to apply the slurry to the substrate. If the slurry is fluid enough to mix and/or mill and can be applied by the method of choice (e.g. dipping, painting, spraying etc.) with minimal dripping or deformation, then that is the most appropriate slurry rheology.

The deviation from gelcasting technology to more traditional particulate processing also simplifies the process tremendously. Not only are the expensive and somewhat toxic chemicals avoided, but such things as working time (until gelation) and processing techniques are streamlined as well. Preliminary XRD analysis of the CS-50 plus ZrO_2 and Cr_2O_3 coatings indicated much less degradation of CS-50 than for CS-50 plus Al_2O_3. Samples of each of the new compositions have been fabricated and are awaiting CTE determination and high temperature, flowing gas corrosion tests.

REFERENCES

(1) C.-Y. Huang, D. K. Agrawal, H. A. McKinstry, and S. Y. Limaye, "Synthesis and Thermal Expansion Behavior of $Ba_{1+x}Zr_4P_{6-2x}Si_{2x}O_{24}$ and $Sr_{1+x}Zr_4P_{6-2x}Si_{2-x}O_{24}$ Systems," *J. Mater. Res.*, **9**, 2005(1994).

(2) S. Y. Limaye and R. Nageswaran, "Development of NZP Ceramic-Based "Cast-in-Place" Diesel Engine Port Liners," Final Report, LoTEC, Inc., West Valley City, UT, November 1994.

(3) T. B. Jackson, S. Y. Limaye, and W. D. Porter, "The Effects of Thermal Cycling onthe Physical and Mechanical Properties of [NZP] Ceramics"; pp. 63-80 in Ceramics Transactions, Vol. 52, *Low-Expansion Materials*. Edited by D. P. Stinton and S. Y. Limaye, American Ceramic Society, Westerville, OH, 1995.

(4) W. Y. Lee, D. P. Stinton, and D. L. Joslin, "Interaction of Low-Expansion NZP Ceramics with Na_2SO_4 at 1000EC," *J. Am. Ceram. Soc.*, **79**, 484(1996).

(5) W. Y. Lee, K. M. Cooley, C. C. Berndt, D. L. Joslin, and D. P. Stinton, "High-Temperature Chemical Stability of Plasma-Sprayed $Ca_{0.5}Sr_{0.5}Zr_4P_6O_{24}$ Coatings on Nicalon/SiC Ceramic Matrix Composite and Ni-Based Superalloy Substrates," *J. Am. Ceram. Soc.*, **79**, 2759(1996).

SESSION III

WORKSHOP ON MATERIALS ISSUES IN LOW-EMISSION BOILERS AND HIGH EFFICIENCY COAL-FIRED CYCLES

SUMMARY OF WORKSHOP ON MATERIALS ISSUES IN LOW EMISSION BOILERS AND HIGH EFFICIENCY COAL-FIRED CYCLES

The agenda for the workshop is included in Appendix A. The purpose of the workshop was to review with experts in the field the materials issues associated with two of the primary coal power systems being developed by the DOE Office of Fossil Energy. The DOE-FE Advanced Power Systems Program includes natural gas-based and coal-based power systems. Major activities in the natural gas-based power systems area include the Advanced Turbine Systems (ATS) Program, the Fuel Cells Program, and Hybrid Cycles. The coal-based power systems projects include the Low Emissions Boiler Systems (LEBS) Program, the High-Performance Power Systems Program (HIPPS), the Integrated (Coal) Gasification Combined-Cycle Program, and the Fluidized-Bed Combustion Program. This workshop focused on the materials issues associated with the LEBS and HIPPS technologies.

The workshop was organized around presentations by DOE sponsor representatives and LEBS and HIPPS contractor representatives. The three LEBS contractors, ABB Combustion Engineering, Babcock & Wilcox (B&W), and D. B. Riley, and the two HIPPS contractors, United Technologies Research Center (UTRC) and Foster Wheeler, were represented in the workshop through presentations by personnel from the respective companies. In addition, representatives of organizations providing support to these companies in addressing materials challenges for the LEBS and HIPPS systems also made presentations. These presentations provided the stimulus for discussions on the materials issues and in establishing the direction for future activities on the AR&TD Materials Program.

The objectives of the LEBS Program are to develop, by 2000, systems that will achieve 42-45 percent net efficiencies (HHV basis) in power generation with significantly reduced emissions and costs compared to current pulverized coal-fired plants that meet New Source Performance Standards (NSPS). The LEBS Program includes three different design concepts developed by the three contractors. ABB Combustion Engineering is pursuing the Kalina cycle. This cycles uses an ammonia-water working fluid that has an extended boiling range and permits more efficient heat transfer than occurs with a single working fluid, such as water. Both B&W and D. B. Riley have adopted supercritical steam (Rankine) cycles with double reheat, operating at a steam pressure of 31.5 MPa (4500 psi) and main and reheat temperatures of 593°C (1100°F). Low-NO_x burners will be used in all of these plants.

There appeared to be consensus among the workshop participants that the critical components of the LEBS systems, particularly for the B&W and D. B. Riley concepts, included superheater tubing and headers, and high- and low- pressure reheater tubing and headers. The production of steam at 1100°F can result in metal wall temperatures of 1200°F. Critical piping in these systems are the main steam piping with an internal diameter of ten inches and wall thickness of 2 to 3 inches, high pressure reheat piping with an internal diameter of 20 inches and wall thickness of 1 to 2 inches, and low pressure reheat piping with an internal diameter of 30 inches and a wall thickness up to 1 inch. Performance criteria of the materials for these system elements are ASME certification by 2000, sufficient allowable stresses at design temperatures, that they be fabricable and manufacturable, provide a lifetime (mechanical properties, primarily creep, and corrosion resistance) of at least 20 years, and that they be available at competitive prices. The use of low-NO_x burners may result in the need for additional corrosion protection because the substoichiometric oxygen environments obtained near waterwalls has resulted in sulfidation attack not usually associated with combustion units.

The major materials issues include furnace wall sulfidation, fatigue and cracking, and superheater and reheater fuel ash corrosion. The use of new alloys will require demonstration of their long-term metallurgical stability and fabricability. There are, of course, numerous considerations in the determination and selection of the materials to use in these high-performance plants. It appears possible to build and meet the required performance criteria of these LEBS systems with commercially available materials. However, these systems have operating conditions that push the limits of performance of available materials and improvements in conventional alloys and development of new alloys are needed. A general conclusion of the workshop was that high-strength ferritic steels should be exploited to the maximum extent possible to take advantage of their performance characteristics, fabricability and availability, and attractive costs. The continued development of low-cost superalloys is appropriate. Improvements in corrosion (primarily fire-side) resistance continues to be a need. If sufficient data are developed to meet the engineering design requirements and to build needed confidence in them, oxide-dispersion-strengthened (ODS) ferritic alloys could have a major impact on future supercritical plant construction.

Based on the deliberations of the participants in this workshop, the AR&TD Materials Program appears to be properly focused on the most important of materials issues associated with advanced coal-

fired power generation systems such as LEBS. The Program activities include work on advanced ferritic and austenitic steels, fire-side corrosion in coal-fired power generation plants, and the development of ODS alloys. The Program has had ongoing for several years the development of advanced austenitic alloys that will meet the performance criteria of even more advanced plants operating at 1200°F and 5000 psi steam conditions. Based on data obtained to date, the ORNL-developed iron aluminide alloys appear to be quite capable of providing the required corrosion resistance in low-NO_x burner systems. These alloys may be used as protective surfaces, which can be applied by a variety of conventional coating techniques.

The objectives of the HIPPS Program are to develop, by 2006, a coal-based power generation system that will achieve superior emissions performance at efficiencies of 50 percent or greater and to provide electricity at a cost of at least 10 percent less that current coal-fired plants that meet New Source Performance Standards (NSPS). The HIPPS plants are indirectly-fired (coal) units that use air as the working fluid for a gas turbine and employ a steam bottoming cycle to achieve maximum efficiency. Two contractor teams, the UTRC team and the Foster Wheeler team, are taking different approaches to the development of HIPPS. The UTRC plant integrates a gas-turbine cycle into a coal-fired plant by heating clean air in a high-temperature air furnace (HITAF). Natural gas firing may be required to heat the air to the requisite turbine inlet temperature. Foster Wheeler is developing an all-coal-fired HIPPS system. A pyrolyzer converts coal to fuel gas and char. The fuel gas is delivered to the gas turbine combustor and natural gas augmentation is not required. The char is burned in the HITAF.

The most critical of the materials challenges for HIPPS was clearly determined to be the ceramics for the air heater. Several materials are being evaluated for the application including sintered α-SiC (Carborundum's Hexoloy), sintered β-SiC (Coors), siliconized SiC (Saint Gobain/Norton), SiC particulate reinforced alumina (DuPont Lanxide), and SiC fiber-reinforced SiC (DuPont). Silicon-based ceramics generally have been favored because of their superior mechanical properties and superior heat transfer characteristics. Availability at reasonable cost and reliability are outstanding issues associated with all of the ceramic candidates. These high-temperature HIPPS plants will achieve temperatures that result in slag formation. The acidity or basicity of slags can be critical to degradation of ceramic materials. Generally, an acidic slag will be more aggressive toward basic ceramics and vice

versa through an acid-base neutralization reaction. Also, formation of low-melting silicates, aluminosilicates, etc., can result in accelerated corrosion of silicon-based ceramics. A preferred, although usually not feasible, approach would be to select ceramics and coal types to ensure compatibility in the slagging environment. Numerous test activities are underway to identify the ceramic materials with the best combination of properties to minimize compromise in selection.

The AR&TD Materials Program focus on structural ceramic composites is for heat exchanger applications such as that required in the air heaters or air furnace for HIPPS. That work is directed toward continuous fiber reinforced SiC, which, as noted, is one of the prime candidates for HIPPS. The Program is comprehensive in addressing all issues associated with the use of SiC-based ceramics in these demanding applications, including fabrication/processing, mechanical properties, corrosion, nondestructive evaluation, and fracture mechanics.

SESSION IV

NEW ALLOYS

DEVELOPMENT OF ODS-Fe_3Al ALLOYS

I. G. Wright, B. A. Pint, P. F. Tortorelli, and C. G. McKamey

Oak Ridge National Laboratory
Oak Ridge, Tennessee, U.S.A.

SUMMARY

The overall goal of this program is to develop an oxide dispersion-strengthened (ODS) version of Fe_3Al that has sufficient creep strength and resistance to oxidation at temperatures in the range 1000 to 1200°C to be suitable for application as heat exchanger tubing in advanced power generation cycles. The main areas being addressed are: (a) alloy processing to achieve the desired alloy grain size and shape, and (b) optimization of the oxidation behavior to provide increased service life compared to semi-commercial ODS-FeCrAl alloys intended for the same applications. The recent studies have focused on mechanically-alloyed powder from a commercial alloy vendor. These starting alloy powders were very clean in terms of oxygen content compared to ORNL-produced powders, but contained similar levels of carbon picked up during the milling process. The specific environment used in milling the powder appears to exert a considerable influence on the post-consolidation recrystallization behavior of the alloy. A milling environment which produced powder particles having a high surface carbon content resulted in a consolidated alloy which readily recrystallized, whereas powder with a low surface carbon level after milling resulted in no recrystallization even at 1380°C. A feature of these alloys was the appearance of voids or porosity after the recrystallization anneal, as had been found with ORNL-produced alloys. Adjustment of the recrystallization parameters did not reveal any range of conditions where recrystallization could be accomplished without the formation of voids. Initial creep tests of specimens of the recrystallized alloys indicated a significant increase in creep strength compared to cast or wrought Fe_3Al, but the specimens failed prematurely by a mechanism that involved brittle fracture of one of the two grains in the test cross section, followed by ductile fracture of the remaining grain. The reasons for this behavior are not yet understood. The cyclic oxidation kinetics of ODS-Fe_3Al alloys made from commercially-produced powder indicated a decrease in the tendency for scale spallation at 1100 and 1200°C compared to equivalent ORNL-produced alloys. The overall oxidation rate at 1100°C in terms of total oxygen consumption as a function of time was essentially the same as for a semi-commercial ODS-FeCrAl alloy. Hence, this improvement indicates an increase in the oxidation-limited lifetime compared to both ODS-Fe_3Al alloys prepared at ORNL, and to the ODS-FeCrAl alloy.

INTRODUCTION

Interest in increasing the efficiency of coal-fired power plants has led to the examination of alternatives to the steam boiler-Rankine cycle systems, for which increases in efficiency have been limited by the slow progress in improving the ability to handle steam at temperatures much in excess of 565°C (1050°F). Indirect-firing of gas turbines in open or closed cycles is one approach to linking the higher efficiencies possible via the Brayton cycle with coal as the fuel. Current programs involving indirectly-fired gas turbine cycles are aimed at high cycle efficiencies, of the order of 47 percent based on the higher heating value (HHV) of the fuel, and involve open cycle systems in which air is heated to 760°C (1400°F) in a metallic heat exchanger, followed by further heating to 982°C (1800°F) in a natural gas-fired ceramic heat exchanger [1-3]. A variant of this approach is where part of the coal is pyrolyzed to produce the fuel gas used to fire the final heat exchanger or the turbine; in that case the air entering the turbine is heated to 1288°C (2350°F).

Successful implementation of indirectly-fired cycle technologies will require the development of a durable coal-fired heat exchanger capable of heating the working fluid to very high temperatures, in addition to adapting a gas turbine for this particular duty. The ferritic ODS alloys based on Fe-Cr-Al have the potential for application at higher temperatures than the modified conventionally-strengthened alloys in which the strengthening mechanisms degrade as the precipitated phases become less stable with increasing temperature. Oxide dispersion-strengthened alloys can provide creep strength up to approximately 90 percent of the alloy melting temperature (which is ≈1480°C for FeCrAls). A heat exchanger of harp design, made from 4 m long, 2.5 cm diam. ODS-FeCrAl tubes, was recently shown to be capable of heating air to 1100°C in a closed-cycle demonstration plant [4]. Compared to ODS-FeCrAl alloys, ODS-Fe_3Al has potential advantages of lower cost, lower density, and superior oxidation and sulfidation resistance, provided that similar gains in creep strength can be realized through the ODS process.

ALLOY PREPARATION

Yttria-containing Fe_3Al alloy powder was prepared by the PM-ODS Werkstoffe division of Metallwerk Plansee (PM), using high-energy ball milling, from prealloyed Fe_3Al powder made by

argon-atomization by Homogeneous Metals (HM). The chemical analysis of the starting powder is shown in Table 1; it was spherical in shape, and had a mean particle size of 75 μm (range 30 to 200 μm). The milling parameters used by PM were based on those used in the commercial production of its PM2000 alloy (Y_2O_3-dispersion-strengthened FeCrAl). The main difference was that three different milling environments (cover gas plus process control agents [PCAs]) were employed (Routes A, B, and C in Table 1). After milling, the powder particle size ranged up to 480 μm for powder from Route C, whereas the use of PCAs resulted in smaller powder particle sizes with, for instance, the powder from Route A having a maximum particle size of 200 μm.

The bulk chemical analyses of the milled powders, shown in Table 1, indicate that the powder processed by Route C had picked up a significantly lower level of oxygen than had the other two powders. In contrast, the Route A powder exhibited significantly higher levels of nitrogen, carbon, and hydrogen than the other powders. The pickup of nitrogen, hydrogen and carbon was similar for the powders from Routes B and C, with the Route C powder showing slightly lower levels.

Table 1. Chemical Analyses of Fe_3Al Powders (wt %)

Element	As-Received		Route A	Route B	Route C
	HM	PM			
Fe	Bal.	79.6			
Al	16.3	18.20 (Bal.)			
Cr	2.4	2.18			
Zr	20 ppm	26 ppm			
O (total)	60 ppm	110 ppm	1,800 ppm	1,900 ppm	1,400 ppm
O (from Y_2O_3)			1,025 ppm	1,053 ppm	1,080 ppm
O bal.			775 ppm	847 ppm	320 ppm
O pickup			*665 ppm*	*737 ppm*	*210 ppm*
N	18 ppm	7 ppm	1,264 ppm	145 ppm	88 ppm
N pickup			*1257 ppm*	*138 ppm*	*81 ppm*
H		16 ppm	115 ppm	40 ppm	29 ppm
C		24 ppm	667 ppm	360 ppm	303 ppm
C pickup			*643 ppm*	*336 ppm*	*279 ppm*
O/Al			*0.010*	*0.010*	*0.008*
Fe/Al			*4.37*	*4.37*	*4.37*
C/Fe			*0.009*	*0.0005*	*0.0004*
C/Al			*0.004*	*0.002*	*0.002*
C/O			*0.37*	*0.19*	*0.22*

Auger analysis of the surfaces of the as-milled powders indicated that the main difference was the carbon content. As shown in Table 2, the C/Fe, C/Al, and C/O ratios were greatest for powder milled by Route B. Comparison with the bulk analyses in Table 1 suggests that the

powder particle surfaces were enriched in aluminum oxide and carbon. The presence of the surface oxide was expected; the surface carbon enrichment is presumed to result largely from interaction of the powder particles with the ball surfaces during milling.

Samples of each powder were canned in mild steel, hot degassed, and consolidated into bar by extrusion (9:1 ratio) at 1050°C following preheating for 45 min. The flow stresses measured during extrusion ranged from 810 to 850 Pa. After extrusion, all the samples exhibited a sub-micron size grain structure. The microhardness values (HV10) for these structures were 486, 413,

Table 2. Auger Analyses of As-Milled Powders

Sample	Auger Analysis (%)				Relative Counts				
	C	O	Fe	Al	O/Al	Fe/Al	C/Fe	C/Al	C/O
A1	7.8	35.7	31.47	25.03	7.13	1.58	0.23	0.36	0.05
A2	9.11	36.11	31.17	23.61	7.65	1.66	0.27	0.44	0.06
B1	19.2	29.64	30.3	20.87	7.10	1.83	0.58	1.05	0.15
B2	21.2	31.49	28.19	19.1	8.25	1.86	0.68	1.27	0.15
C1	14.5	32.99	29.04	23.49	7.02	1.55	0.45	0.70	0.10
C2	12.4	31.73	29.86	26.04	6.09	1.44	0.38	0.54	0.09

and 399 kg/mm^2, for powder A, B, and C, respectively. The chemical compositions of the consolidated alloys are shown in Table 3. Compared to the composition of the starting powder, some loss of aluminum is evident, with the greatest loss observed for Powder A (PMWY-1) which also showed the largest pickup of oxygen. The oxygen levels in PMWY-2 and -3 remained essentially the same as in the as-milled powders, but PMWY-2 showed an increase in nitrogen content after consolidation of the order of 900 wppm. The carbon levels of all three alloys were essentially unchanged after consolidation.

RECRYSTALLIZATION

The initial attempt to recrystallize the consolidated alloys used the same conditions as for PM2000, which involved annealing at 1380°C for 1 hr. Two of the alloys, PMWY-1 and 2, exhibited a very large, elongated grain structure, whereas alloy PMWY-3 showed no signs of recrystallization. The recrystallized alloys also exhibited a significant amount of porosity which appeared to be associated with the recrystallization anneal, since the as-extruded alloys were pore-free, as was alloy PMWY-3 after the anneal.

Porosity similar to that observed in the alloys PMWY-1 and -2 has been observed in other ODS alloys [5-7]. The extent and size of the pores apparently depends not only on powder processing parameters, but also varies among alloys processed by the same route [8]. The source of the porosity has been attributed to gas bubbles resulting from argon adsorbed on the original powder particles, but pores were still found when hydrogen was used as the cover gas during the milling step [5]. One model discounts the effects of gas from dissolved or bonded oxygen and carbon or nitrogen, and suggests a more likely cause is void condensation from stress-induced vacancy migration, with oxide shell growth around the pore walls by reduction of entrapped water vapor by the oxygen-active elements in the alloy [6]. Another model suggests that the voids result from plastic deformation by hydrogen liberated by the reduction of adsorbed water vapor (or hydroxides) on the original powder particle surfaces [7]. The source of the adsorbed gas is the original gas atomization process and/or the milling process; the relative importance of these sources is unclear.

Based on reported observations that such porosity in ODS alloys is usually absent or is smaller at lower temperatures [7], samples of the alloys were annealed at various combinations of

Table 3. Chemical Compositions of Extruded Alloys (wt %)

Element	PMWY-1 (Powder A)	PMWY-2 (Powder B)	PMWY-3 (Powder C)
Fe	81.68	81.45	81.54
Al	14.67	15.36	15.43
Cr	2.61	2.33	2.33
Y	0.38	0.39	0.40
Zr	<100 ppm	<100 ppm	<100 ppm
O (total)	3,232 ppm	2,073 ppm	1,452 ppm
O (Y_2O_3)	1,025 ppm	1,053 ppm	1,080 ppm
O bal.	2,207 ppm	1,020 ppm	372 ppm
Overall O pickup	*2,097 ppm*	*910 ppm*	*262 ppm*
N	968 ppm	1,024 ppm	44 ppm
C	600 ppm	400 ppm	300 ppm
B	<3 ppm	<3 ppm	<3 ppm
Cu	0.01	0.01	0.01
Mn	0.04	0.03	0.02
Ni	0.05	0.03	0.03
P	0.008	0.008	0.008
Si	0.04	0.03	0.04
Ti	0.01	<0.01	<0.01
Y	0.38	0.39	0.40
(Y_2O_3	0.48	0.50	0.51)
S	22 ppm	20 ppm	16 ppm

temperature and time to observe the recrystallization behavior and tendency to develop porosity. As mentioned above, Alloy PMWY-3 did not recrystallize under any of treatments used (up to 1hr at 1380°C). Alloy PMWY-2 did not recrystallize below 1200°C, and Alloy PMWY-1 did not recrystallize below 1300°C; the fine-grained microstructure of Alloy PMWY-1after annealing at 1300°C for 2 hr. is shown in Fig. 1. The microstructures of Alloy PMWY-2 after annealing for 2 hr at 1200, 1250, and 1300°C are illustrated in Figs. 2-4 and show that, while recrystallization is essentially complete after 2 hr at 1200°C, small areas of what appeared to be unrecrystallized grains persisted, even at 1300°C. These areas appeared as elongated dark-colored streaks in longitudinal cross sections (Fig. 2a), and as dark patches in transverse sections (Fig. 2b). With increasing temperature, the number and size of these areas tended to decrease, although one or two patches were still visible in typical transverse sections after 2 hr at 1300°C (Fig. 4b). Also evident in Figs. 2-4, especially in transveres sections, is the porosity that developed upon annealing, and which increased with increasing time and temperature.

The hardness of the alloys decreased on the order of 75-100 kg/mm^2 following the recrystallization anneal, and progressively decreased with increasing annealing temperature and time.

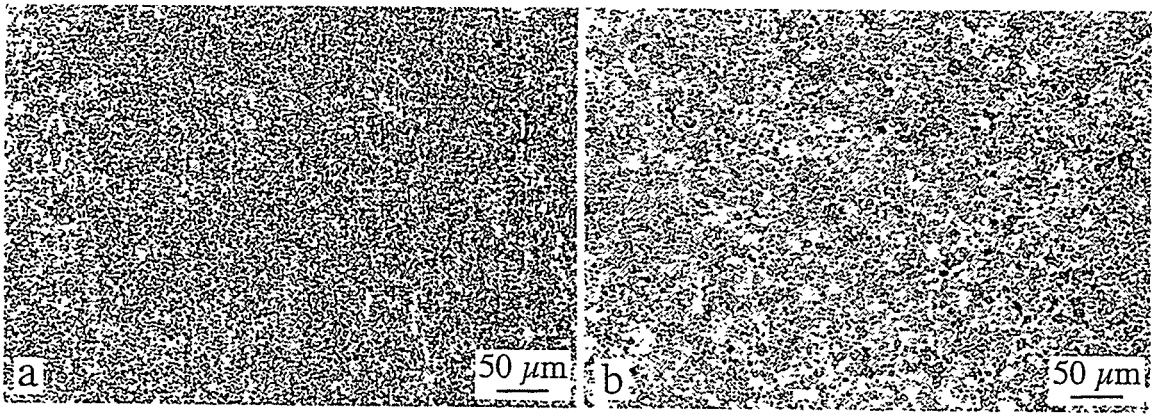

Fig. 1. Cross sections of Alloy PMWY-1 showing essentially no recrystallization after annealing for 2 hr at 1300°C: (a) longitudinal section, (b) transverse section.

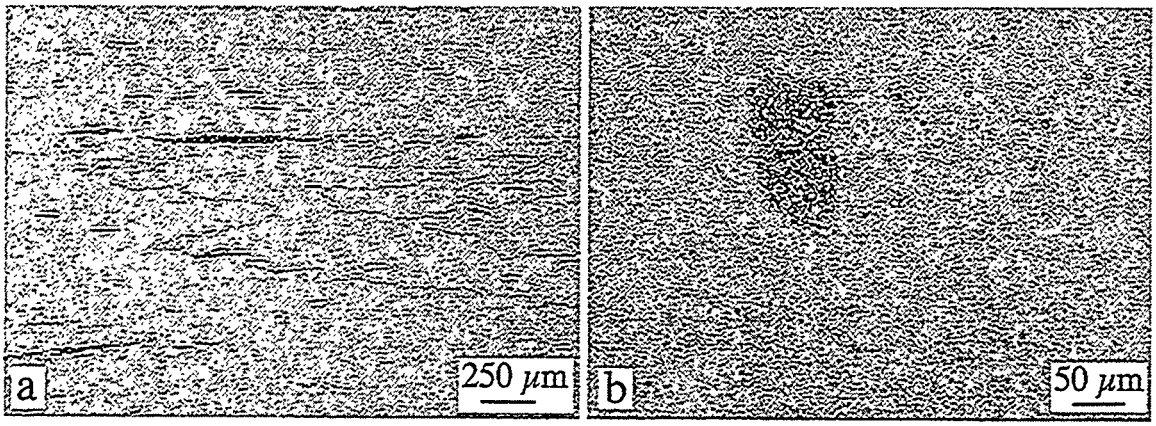

Fig. 2. Cross sections of Alloy PMWY-2 after annealing for 2 hr at 1200°C: (a) longitudinal, (b) transverse.

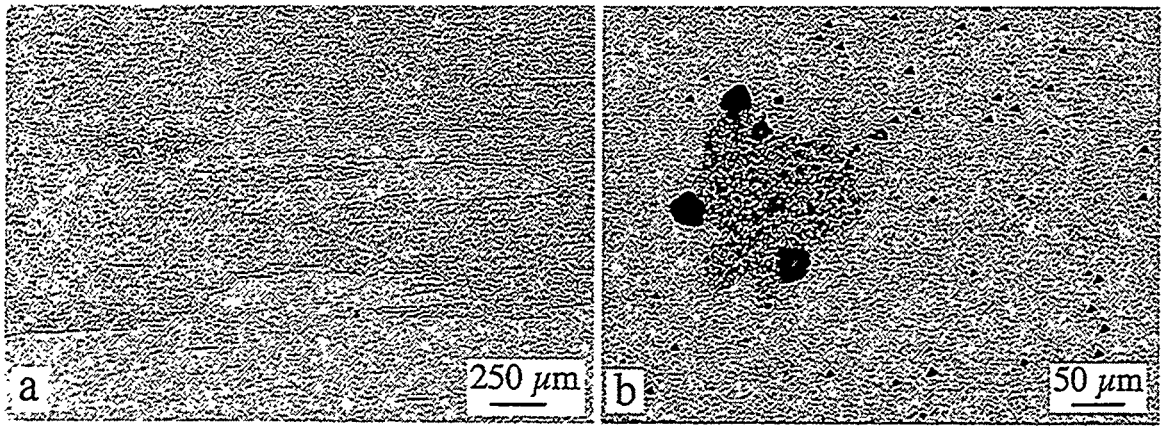

Fig. 3. Cross sections of Alloy PMWY-2 after annealing for 2 hr at 1250°C: (a) longitudinal, (b) transverse.

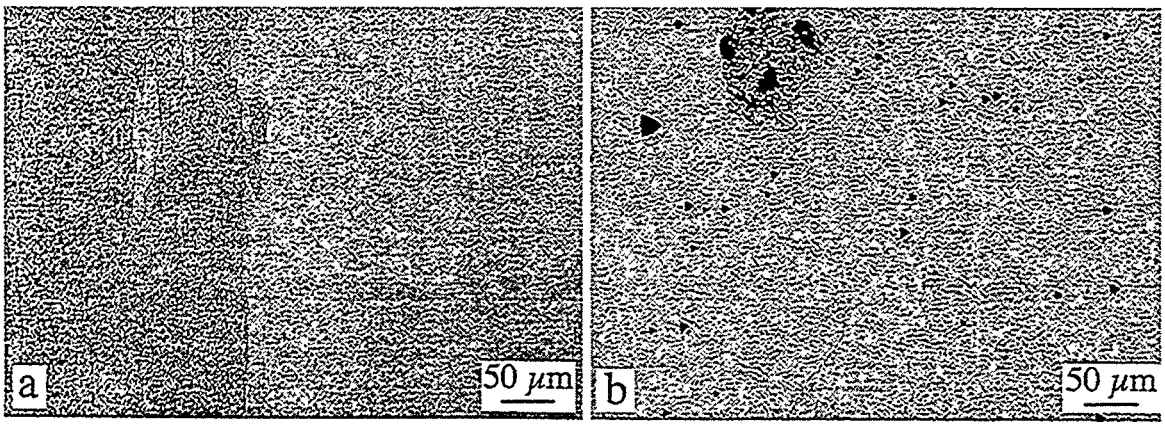

Fig. 4. Cross sections of Alloy PMWY-2 after annealing for 2 hr at 1300°C: (a) longitudinal, (b) transverse.

CREEP TESTS

Round creep-rupture specimens with a gage diameter of approximately 3 mm and a gage length of 17.8 mm were machined from bars of alloy PMWY-2 that had been recrystallized at 1300°C. Two initial creep rupture tests were performed in air. The first test, at 980°C and 48 MPa, failed in 68.35 hr with a final elongation of 1.7% and a minimum creep rate of 0.01%/hr. The next test at 1075°C at the same stress resulted in a creep-life of 8.3 hr, with a final elongation of 3.1% and a minimum creep rate of 0.04%/hr. The curves of life-versus-elongation are shown in Fig. 5. Both specimens exhibited low minimum creep rates when compared to precipitation-strengthened Fe_3Al-based alloys [9], at a higher temperature than possible with these alloys. The results of these two tests are compared with binary Fe_3Al, the precipitation-strengthened Fe_3Al-based FA-180 alloy, and two stainless steels in Fig. 6.

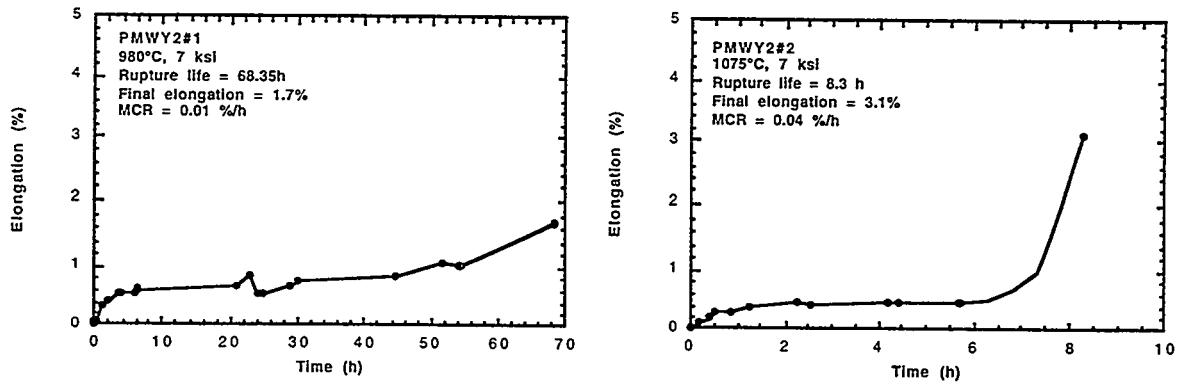

Fig. 5. Creep-rupture curves for PMWY-2 alloy tested at a stress of 48 MPa at (a) 980°C and (b) 1075°C in air.

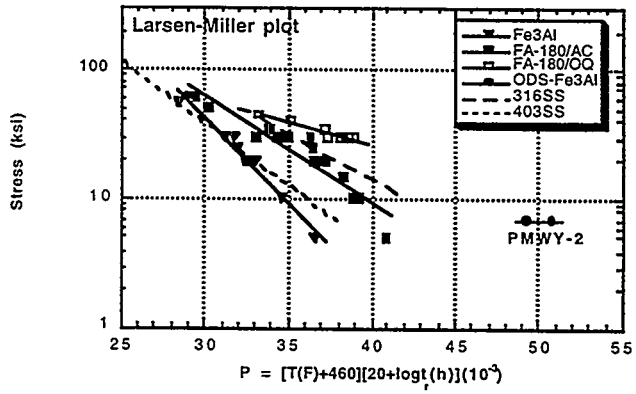

Fig. 6. Larson-Miller plot to compare creep performance of PMWY-2 with Fe_3Al, alloy FA-180 and two stainless steels.

Examination of the specimens after testing indicated that the mode of failure was not uniform, as illustrated in the scanning electron microscopy (SEM) secondary electron images in Fig. 7. Figure 8a shows that over half of the fracture surface of the 1075°C specimen exhibited had a brittle, transgranular appearance with dimples and pores characteristic of microvoid coalescence. There were also long stringer-like features which appeared more ductile and possibly contained particles (Fig. 8b). High magnification examination of the area of brittle fracture showed the presence of oxides (assumed to be the Y_2O_3 dispersion) and small pores (visible as black dots in Fig. 8c). However, there was no obvious origin of the crack in the area of either specimen that had experienced brittle fracture. Further creep testing was suspended until the cause of the brittle failure was found.

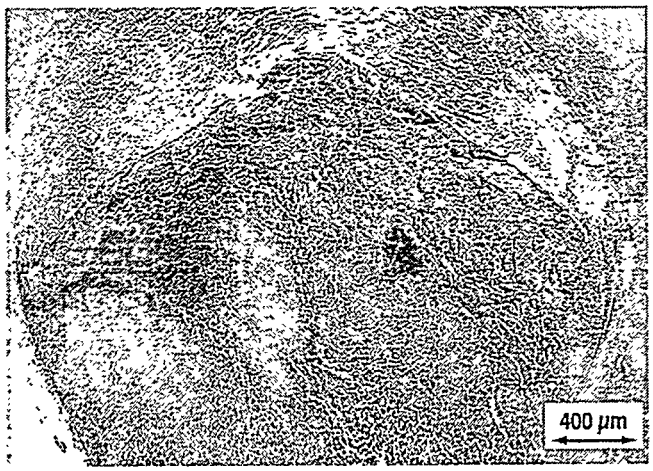

Fig. 7. SEM image of fracture face of specimen tested at 1075°C showing the non-uniform nature of the creep rupture.

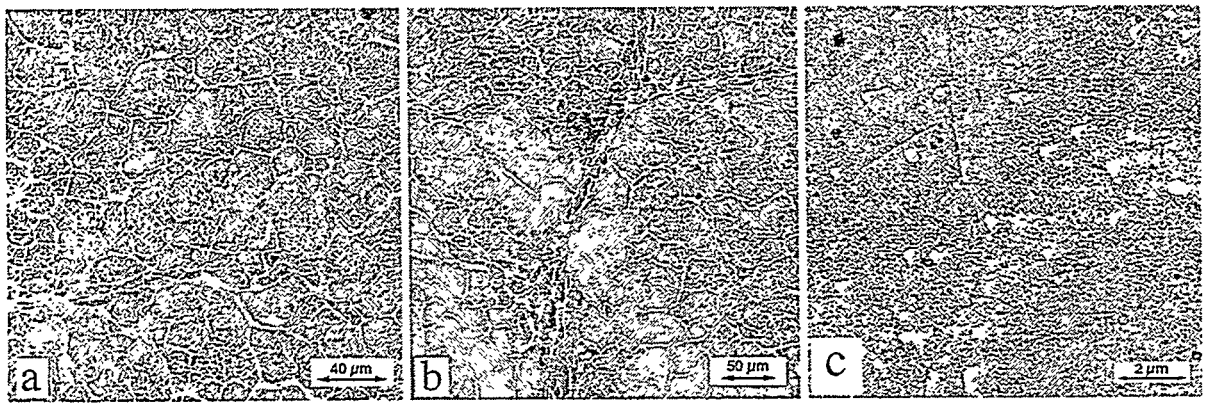

Fig. 8. SEM images showing typical features of the more brittle regions of the creep rupture surfaces of PMWY-2: (a) microvoids in specimen tested at 980°C, (b) stringer in specimen tested at 980°C, (c) cavities, oxide particles, and needle-like phase in specimen tested at 1075°C.

Figure 9 is an optical micrograph showing the creep rupture in the short-transverse direction parallel to the extrusion direction from the specimen tested at 1075°C. Approximately half of the specimen cross section that fractured transgranularly in a brittle manner apparently corresponded to one of the two grains that constituted the cross section of the gauge length (Fig. 9a), The roughly one-third of the specimen that had begun to neck down corresponded to the other main grain in the essentially bi-crystal specimen, and contained a large number of creep cavities and evidence of cavity growth and coalescence near the fracture (Fig. 9b). A light etch of the specimen indicated the possible existence of several elongated grains of up to 200 μm in width in the part of the specimen that had necked and elongated (Fig. 9b). Whereas the cross section of the gage length away from the fracture contained basically two visible grains running the length of the specimen, near the center of the section was a stringer about 3 mm long consisting of what appeared to be finer, unrecrystallized grains and inclusions; this region did not appear to play any part in the specimen failure. Also visible in the necked area of the specimens were enlarged voids (or creep cavities) which had been distorted by the necking, and a phase with a needle-like morphology characteristic of a carbide phase such as Fe_3AlC [10] visible in Fig. 8c..

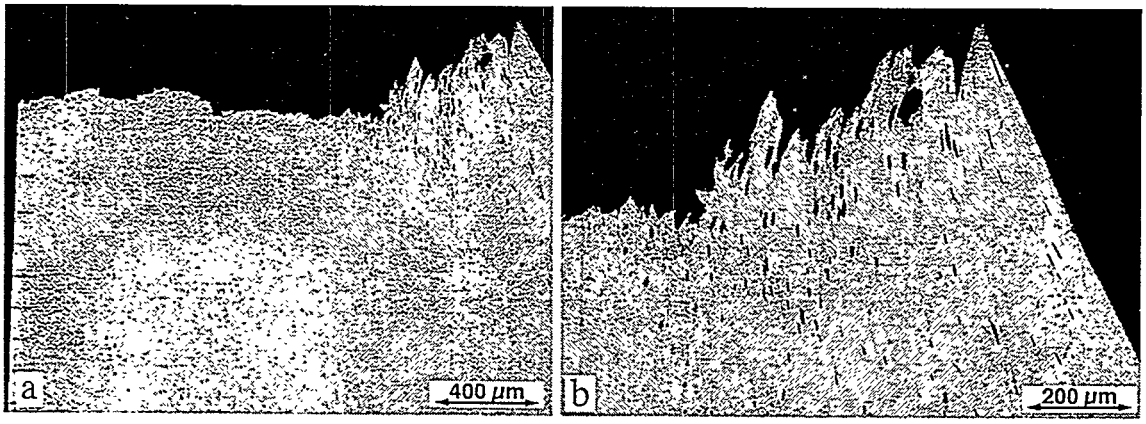

Fig. 9a. Cross section of fracture face of specimen tested at 1075°C, showing: (a) complete fracture section, and (b) enlarged view of necked region.

Reexamination of specimens used in the 1300°C recrystallization experiments indicated areas in one specimen of alloy PMWY-2 which exhibited internal cracks, as shown in Figs. 10a and b. The appearance of these cracks suggested a crystallographic preference, and that they probably occurred after the annealing treatment. No such cracks were observed in any of the specimens annealed at temperatures from 1150°C to 1250°C, or at 1380°C. This examination is continuing.

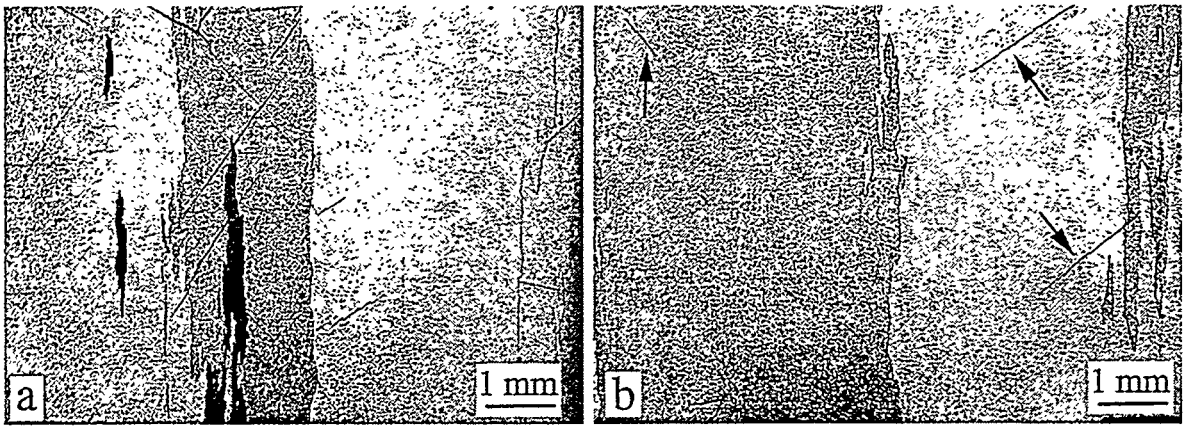

Fig. 10. Cracking in Alloy PMWY-2 annealed at 1300°C for (a) 1hr and (b) 2 hr.

OXIDATION LIFETIME TESTS

Data for use in estimating the high-temperature oxidation lifetimes of a recrystallized alloy (PMWY-2) and non-recrystallized alloy (PMWY-3) were generated by means of thermal cycling tests using specimens exposed in individual, lidded alumina crucibles in air in a muffle furnace. The exposure temperature was 1100°C, and each thermal cycle lasted for 100 hr. The specimen weight changes in this test are compared in Fig. 11a with data for an earlier version of this alloy (FAS3Y) made at ORNL [11], and for three commercial ODS FeCrAl alloys (Kanthal APM, MA956, ODM-751). The most obvious result is the large reduction in scale spallation for the PMWY alloys compared to FAS3Y, although there still appears to be a tendency to some spallation at times longer than 1,200 hr. The reasons for this improvement are not immediately clear; the PMWY specimens will be examined when the exposures are completed. Despite the tendency to some scale spallation, the overall weight change due to oxygen uptake (aluminum consumption), shown in Fig. 11a, was very similar for the PMWY alloys and the ODS-FeCrAl alloys. The fact that the kinetics for each PMWY alloy corresponded to a single near-parabolic rate suggested that any scale spallation that occurred did not affect the rate-controlling scale layer, at least within the sensitivity of the test method.

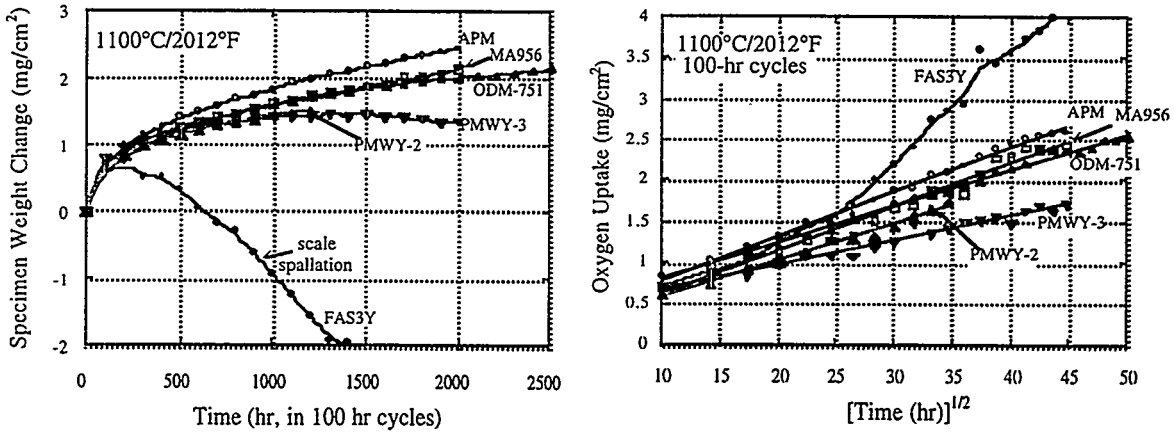

Fig. 11. Oxidation kinetics at 1100°C: (a) specimen weight gains, (b) parabolic oxidation plots

These new kinetic data were used to calculate the expected oxidation-limited lifetime of a 2.5 mm thick tube wall (following a procedure described previously [11]), with the result shown in Fig. 12. Whereas the scale spallation behavior of the FAS3Y alloy resulted in an oxidation lifetime at 1100°C equivalent to the commercial ODS-FeCrAl alloys despite its larger reservoir of aluminum (15.8 vs 4.5 to 5.5 weight percent), the reduced level of scale spallation from the PMWY alloys allowed the benefit of the larger aluminum reservoir to be realized. The projected oxidation-limited lifetime at 1100°C for the PMWY alloys ranges up to 234 x 10^6 hr, compared to 0.5 to 2.6 x 10^6 hr for the commercial ODS-FeCrAl alloys.

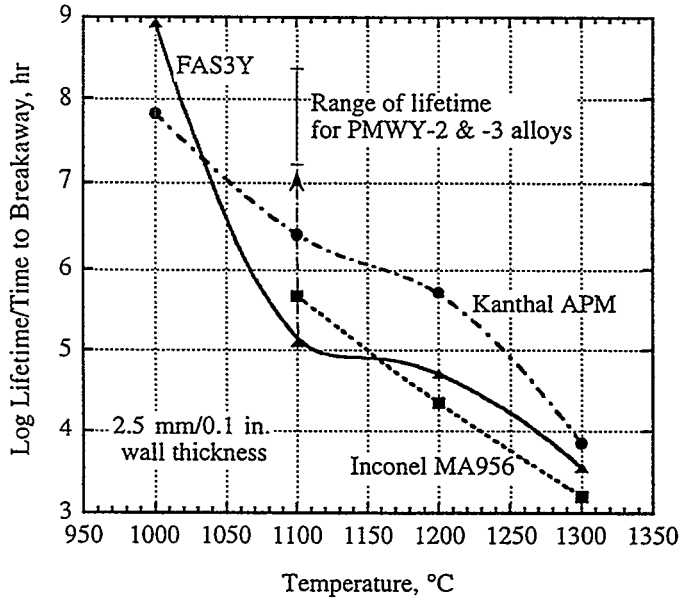

Fig. 12. Estimated oxidation-limited lifetimes for ODS alloys (2.5 mm wall thickness), with data for new ODS-Fe_3Al alloys indicated at 1100°C

CONCLUSIONS

The large, high aspect ratio grain structure desired in ODS alloys for good high-temperature creep strength has been achieved in yttria-strengthened Fe_3Al, with specimens exhibiting grains several centimeters long. The annealing treatment used to recrystallize the alloys also resulted in the formation of porosity in the alloy, which must be minimized in order to maximize the mechanical performance of the alloy. Initial creep tests at relatively high temperatures indicated good promise, but premature failure of the first specimens by a partially brittle mode prevented realization of the full potential of the grain structure. The cause of the brittle behavior is the subject of investigation, and was not obviously linked to pre-existing defects. The oxidation-limited lifetime at 1100°C in air for the alloys derived from commercially-processed alloy powder was significantly longer than for similar ORNL-processed alloys, due to a reduced tendency to scale spallation. The oxidation data for the ODS-Fe_3Al also suggest a longer life at 1100°C than competing commercial ODS-FeCrAl alloys.

ACKNOWLEDGMENTS

This research was sponsored by the Fossil Energy Advanced Research and Technology Development (AR&TD) Materials Program, U. S. Department of Energy, under contract DE-AC05-84OR21400 with Lockheed Martin Energy Research, Inc. Mr. H. F. Longmire was responsible for the metallographic preparation of the specimens, and Mr. C. A. Carmichael performed the creep tests.

REFERENCES

1. J. M. Klara,"HIPPS: beyond state-of-the-art, Part I," *Power Engineering*, 12, 37-39 (1993).
2. J. M. Klara, "HIPPS can compete with conventional PC systems: Part II," *Power Engineering*, 13, 20-23 (1994).
3. F. L. Robson, J. Ruby, and D. J. Seery, "Repowering with High-Performance Power Plant Systems (HIPPS)," Proc. Pittsburgh Coal Conf. (Sep. 1996), pp. 162-167.
4. Q. J. Mabbutt, The British Gas Closed Cycle Demonstrator-Final Year Report, British Gas Report (1995).
5. W. Lengauer, P. Ettmayer, D. Sporer, and G. Korbe, "Pore Formation in P/M Ferritic ODS Superalloys During High-Temperature Heat Treatment I. Considerations and Experimental Starting Points," Powder Metallurgy Intl., 22 (2), 19-22 (1990).

6. D. Sporer, W. Lengauer, P. Ettmayer, and G. Korbe, "Pore Formation in P/M Ferritic ODS Superalloys During High-Temperature Heat Treatment II. Thermodynamic Considerations and Conclusions," Powder Metallurgy Intl., 23 (3), 162-165 (1991).

7. B. Heine, R. Kirchheim, U. Stolz, and H. Fischmeister, "Studies on Pores Caused by Annealing ODS-Iron-Base Superalloys," Powder Metallurgy Intl., 24 (3), 158-163 (1992).

8. Q. J. Mabbutt, British Gas plc., private communication with I. G. Wright, 1996.

9. C. G. McKamey and P. J. Maziasz, "Effect of Heat Treatment Temperature on Creep-Rupture Properties of Fe_3Al-Based Alloys," Processing, Properties, and Applications of Iron Aluminides, Eds. J. H. Schneibel and M. A. Crimp, TMS, Warrendale, PA (1994), pp. 147-158.

10. M. Palm, and G. Indin, "Experimental Determination of Phase Equilibria in the Fe-Al-C System," Intermetallics, 3, 443-454 (1995).

11. I. G. Wright, B. A. Pint, E. K. Ohriner, and P. F. Tortorelli, "ODS Iron Aluminides," Proc. Tenth Ann. Conf. on Fossil Energy Materials, ORNL Report No. ORNL/FMP-96/1, CONF-9605167 (1996), pp. 359-371.(1996), pp. 359-371.

Iron Aluminide Weld Overlay Coatings for Boiler Tube Protection in Coal-Fired Low NOx Boilers

S.W. Banovic, J.N. DuPont, and A.R. Marder

Energy Research Center
Lehigh University
Bethlehem, PA 18015

ABSTRACT

Iron aluminide weld overlay coatings are currently being considered for enhanced sulfidation resistance in coal-fired low NOx boilers. The use of these materials is currently limited due to hydrogen cracking susceptibility, which generally increases with an increase in aluminum concentration of the deposit. The overall objective of this program is to attain an optimum aluminum content with good weldability and improved sulfidation resistance with respect to conventional materials presently in use. Research has been initiated using Gas Tungsten Arc Welding (GTAW) in order to achieve this end. Under different sets of GTAW parameters (wire feed speed, current), both single and multiple pass overlays were produced. Characterization of all weldments was conducted using light optical microscopy, scanning electron microscopy, and electron probe microanalysis. Resultant deposits exhibited a wide range of aluminum contents (5 - 43 wt%). It was found that the GTAW overlays with aluminum contents above ~10 wt% resulted in cracked coatings. Preliminary corrosion experiments of 5 to 10 wt% Al cast alloys in relatively simple H_2/H_2S gas mixtures exhibited corrosion rates lower than 304 stainless steel.

INTRODUCTION

To comply with clean air regulations, fossil fired boilers are being retrofitted to reduce NOx emissions[1-3]. The design principle is to delay the mixing of fuel and air to create a low temperature, fuel-rich flame which will suppress the NOx formation in a substoichiometric combustion gas[2]. In conventional burners, sulfur from the fuel is generally oxidized to form SO_2 and SO_3, which are generally non-corrosive at furnace wall temperatures. However, with newer low NOx burners, H_2S is now generated and protective oxide scales are often replaced by less protective sulfide scales. In order to protect the existing tubes from accelerated sulfidation attack, stainless steel and superalloy weld overlay coatings are typically used. These alloys are expensive and form a brittle interfacial layer which is often susceptible to cracking under thermal cycling conditions. In contrast, iron

aluminide alloys with aluminum contents above ~10 wt% Al possess excellent sulfidation resistance in very aggressive environments [6-9] and form no brittle interface between the substrate and coating. However, the aluminum content of the overlay is limited due to hydrogen cracking susceptibility, which generally increases with an increase in the aluminum concentration [10-12]. Previous research on iron aluminides utilized gases which were very aggressive and may not be indicative of low NOx boiler conditions [2-4]. Therefore, research has been initiated to evaluate weldable coatings, i.e. lower aluminum overlays, in environments more representative of low NOx boilers. The overall objective of this work is to study various iron aluminum weld overlay compositions and relate their processing and microstructure to properties which are critical in low NO_x boiler environments: weldability, sulfidation. These results will be compared with other weld overlay candidates being considered.

EXPERIMENTAL PROCEDURE

Overlay samples were produced using Gas Tungsten Arc Welding (GTAW) conducted in a fully automated welding research laboratory. The wire feed speed and current were varied to produce different aluminum concentrations within the deposits. Pre-heat and post-weld heat treatments were not conducted on the GTAW overlays, but an interpass temperature was maintained between 300-350°C for the multiple pass welds. A dye penetrant technique was used to assess cracking of the overlays.

Cast Fe-Al alloys with varying aluminum contents, based upon the preliminary GTAW weldability studies, were produced at Oak Ridge National Laboratories by arc-melting high purity components under argon and drop casting into a water cooled copper mold. Obtaining bulk specimens eliminated the timely task of removing samples from the weld material, as well as eliminating the aluminum-poor region near the substrate that could negatively influence the corrosion behavior [13].

Sulfidation corrosion behavior was characterized by use of a thermogravimetric balance that measured weight gain as a function of time. Samples with dimensions 10mm x 12mm x 3mm were cut from the cast Fe-Al alloys. Samples were ground to 600 grit with silicon carbide papers, ultrasonically cleaned, and weighed to the nearest mg before being placed in the balance. Samples were heated at a rate of 50°C/min and isothermally held at 600°C for 50 hr in a mixed gas consisting of 0.1% H_2S - 3.0% H_2 - bal Ar (by volume). The oxygen partial pressure, as determined by a solid-state oxygen cell, was 10^{-28} atm, and the sulfur partial pressure was estimated to be 10^{-9} atm. Samples were then cooled to room temperature at a rate of 20°C/min before removal from the chamber.

Samples for microstructural analysis were removed using an abrasive cut-off wheel and cross-sections mounted in cold-setting epoxy. Metallographic samples were polished through 0.04μm colloidal silica and etched with a solution of 60ml methanol, 40ml nitric acid, and 20ml hydrochloric acid. Microstructural characterization was performed with both light optical microscopy (LOM) and scanning-electron microscopy (SEM). Qualitative

and quantitative compositional information was obtained via energy dispersive spectroscopy (EDS) and wavelength dispersive spectrometry (WDS), respectively. WDS was conducted on a JEOL 733 SuperProbe using an accelerating voltage and probe current of 15kV and 15nA, respectively. K_α x-ray lines were analyzed and counts converted to weight percentages using a ϕ (ρz) correction scheme.

RESULTS and DISCUSSION

Weldability

Figure 1 shows the sample matrix of single weld pass overlays produced by GTAW. To obtain a wide range of aluminum contents in the overlay, wire feed speeds were varied between 10 and 65 mm/sec at current levels of 250, 275, and 300A. Single pass overlays were first deposited to ensure that the microstructure and compositions of the overlays were not complicated by overlapping passes. Samples were assessed as crack/no crack using a dye penetration technique. For those that were cracked, the number of cracks that occurred are located to the right of the symbols in Figure 1, with M signifying more than 15 cracks in the sample. The numbers to the left of the symbols denote the amount of aluminum in the deposit (in wt%) as measured using EPMA. Below ~10 wt% Al the overlays did not crack, while those just above this value had very few cracks. While two different types of microstructures were observed (see reference [14]), cracking was not controlled by any type of microstructural feature. Overlay compositions on either side of the crack/no crack boundary exhibited reproducible cracking tendencies.

Based upon the single pass results, a second experimental matrix was conducted to produce multiple pass weld overlays using similar parameters, Figure 2. As found for the single pass welds, the cracking results were again related to the aluminum concentration of the overlays. Due to the 50% overlap of adjacent passes, the aluminum contents of the multiple pass welds were higher than that of the corresponding single pass overlays prepared at identical processing parameters. Electron microprobe traces through the overlay, conducted parallel to the coating-substrate interface, showed that the weldement was relatively homogeneous on a macroscopic scale at these processing parameters, Figure 3. Large columnar grains were found for all samples, with cracks occurring in both intergranular and transgranular modes.

The combination of high wire feed speed and low current produced cracked overlays for both sets of deposits. This processing scheme results in high aluminum in the overlay due to the larger volume of Al being added to the system, as well as reduced mixing between the two constituents [15]. During deposition, current flowing through the arc is the main source of heat that melts the base metal and filler wire. While in the liquid state, mixing occurs to produce an alloy of the two elements with a composition dependant upon the volume of

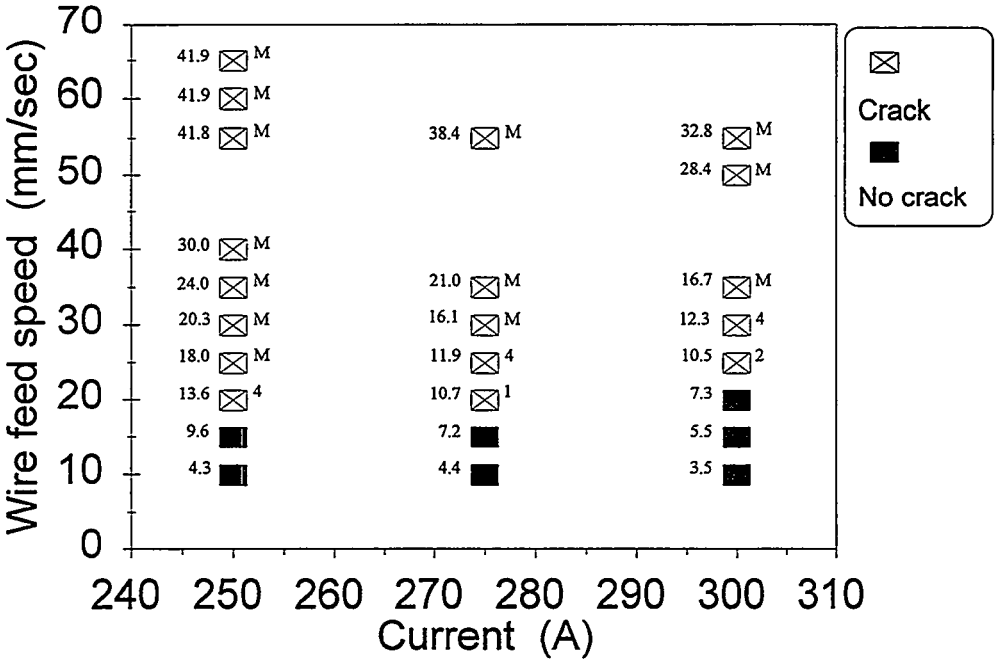

Figure 1: Sample matrix of single weld pass overlays produced by GTAW. Each box represents an overlay deposited at that processing condition and was subsequently labeled as cracked or no crack. Numbers to the right of the cracked data points signifies the number of cracks that occurred, with M being more than 15. The numbers to the left denote the wt% of aluminum in the deposit.

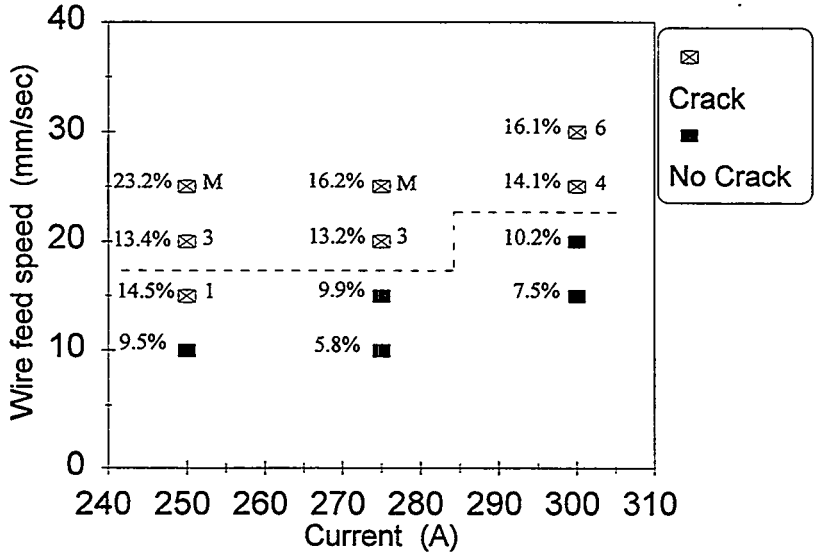

Figure 2: Sample matrix of multiple pass weld overlays. The symbols correspond to those in Figure 1. The crack/no crack boundary for the single weld pass overlays is represented by the dashed line.

each material that was melted. For a fixed wire feed speed, decreasing the current results in a smaller volume of melted substrate that can mix with the melted wire, thus leading to higher aluminum concentrations in the overlay. Conversely, for a fixed current, increasing the wire feed speed allows for more melted aluminum to mix with the base metal, again resulting in higher aluminum contents. The decrease in mixing through out the weld can be better illustrated by the electron microprobe traces, perpendicular to the coating-substrate interface, through the single weld bead and partially mixed zone (PMZ), Figure 4. It is also believed that this decrease in mixing contributed to the formation of the dendritic structure found at the higher aluminum weight percentages.

The higher aluminum content overlays have previously been found to be more susceptible to hydrogen-induced (cold) cracking [10,11]. During the welding process, stresses are formed in the substrate that place the weldement in tension after solidifying. The stresses, in addition to the available hydrogen from the atmosphere, were seen to cause cracking soon after solidification, as well as days after depositing the overlays. In order to assess the reliability of the small scale plate results, deposition of ≤ 10 wt% Al overlays onto large scale panels using the GMAW are planned in future experiments.

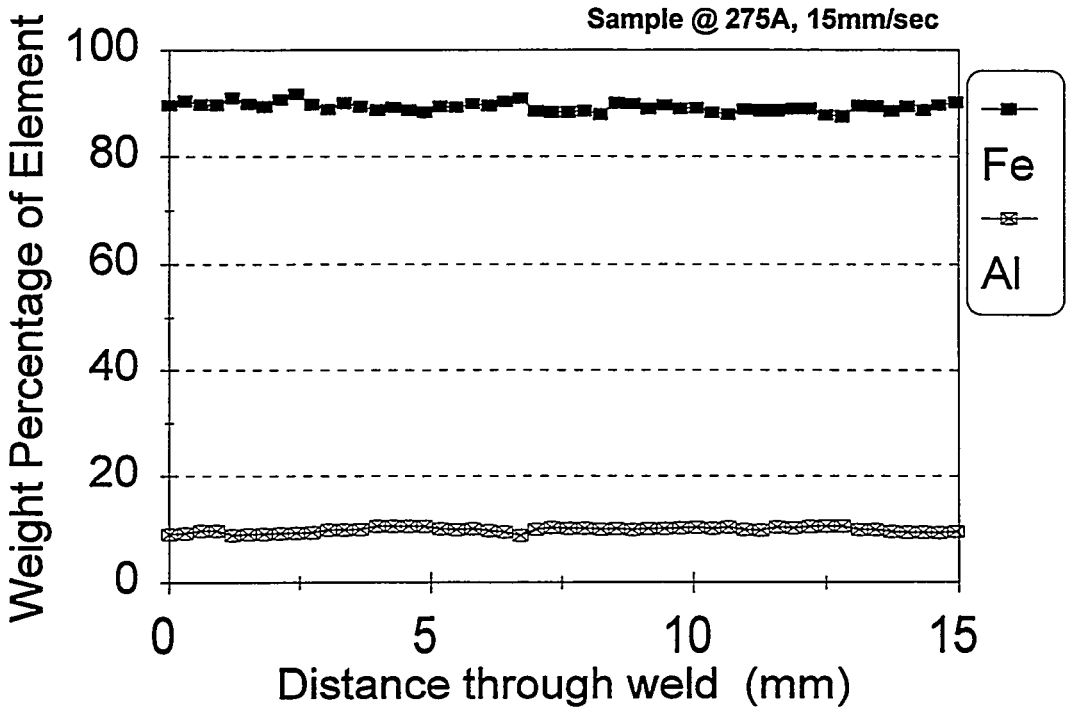

Figure 3: Electron microprobe trace parallel to the coating-substrate interface for a multiple pass weld overlay showing a relatively homogeneous composition on a macroscopic level.

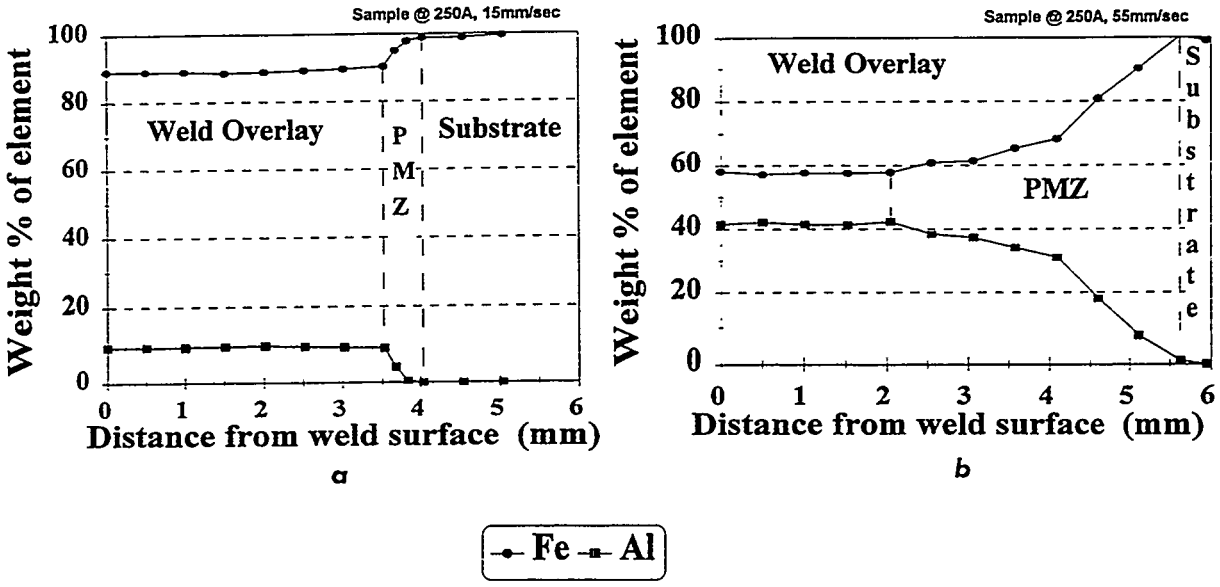

Figure 4: Electron microprobe trace perpendicular to the coating-substrate interface showing a) high level of mixing in a low aluminum content overlay and b) low level of mixing in a high aluminum content overlay.

Corrosion Resistance

The work of Tortorelli et. al [13,16] showed that the oxidation/sulfidation resistance of iron aluminide weld overlay coatings could be explained on the basis of what was known from previous studies of bulk samples of similar compositions. Therefore, cast Fe-Al alloys, with aluminum contents beneath the crack/no crack boundary of Figure 1 (5, 7.5, and 10 wt% Al), were used for preliminary corrosion studies. In addition, by using the cast alloys, the aluminum-poor region near the coating-substrate interface, as seen in Figure 4b, was eliminated. Prior research [13] demonstrated that the corrosion products more readily form on the face closer to the substrate of weld overlay corrosion samples due to the inhomogeneous composition in this area. If this Al depleted region is not throughly removed, the corrosion behavior may be negatively influenced.

The corrosion environment chosen was generally less *aggressive* than those presently found in the literature [5-9,13,16], in terms of gas composition and temperature, so as to be more representative of boiler conditions[2-4]. Previous work on binary Fe-Al alloys showed that up to ~750°C, at least 10 wt% (≥ 18 at%) is needed for good sulfidation resistance [5-8]. However, these studies had either higher temperatures or partial pressure of sulfur than the conditions selected here. The simple gas mixture for these studies should promote the formation of iron sulfide and aluminum oxide at the partial pressures and temperatures denoted [1,17]. After an understanding of the kinetics of this simple gas, multiple component gases will be used to further evaluate the corrosion resistance of the alloys.

The weight changes for the alloys tested are shown in Figure 5. The 5 wt% alloy was the only one to displayed a significant weight gain among the Fe-Al alloys, which nearly tripled that of the other two tested. The linear kinetic rate for this alloy (k_l = 3.22 x 10^{-4} mg cm^{-2} min^{-1}) was less than those previously reported [5] for similar alloys in more aggressive conditions (k_l = 7.1 x 10^{-2} mg cm^{-2} min^{-1}). The 7.5 and 10 wt% alloys had negligible weight gain, especially when compared to the 1008 and 304SS alloys.

The weight gain measurements can be collaborated with SEM micrographs of the sample surfaces, Figure 6. The decrease in corrosive product can be seen as the aluminum content increases in the alloy. The 5 wt% sample has a scale that completely covered the surface. EDS techniques detected iron and sulfur. The scale morphology, consistent with previous research [5,17], in addition to the EDS spectra, suggests this is an iron sulfide scale. An aluminum peak was not present in the spectra indicating that the iron sulfide scale is either a few microns thick, since the interaction volume is ~ 1 μm with these SEM parameters [18], or very little aluminum is present in the product. The 7.5 wt% alloy had few, large iron sulfide particles on the surface (Figure 6b), with the presence of an aluminum peak in the EDS spectra. The 10 wt% alloy was devoid of any large particles (Figure 6c) and the spectra showed all three peaks (Fe, Al, and S). Due to limitations of the EDS system, oxygen could not be detected to determine if the formation of any oxides occurred.

With the promising corrosion resistance of the low Al content alloys in the simple gas presented here, future investigation into the influence of more severe gas compositions and higher temperatures on the corrosion behavior of these alloys is planned.

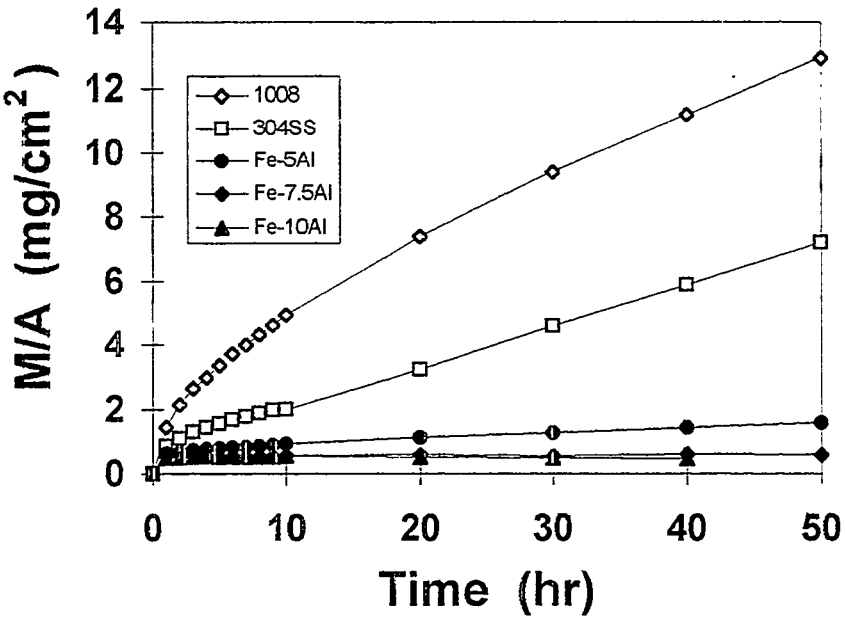

Figure 5: Weight change versus time for commercial and cast Fe-Al alloys exposed to 0.1%H2S - 3.0%H2 - bal Ar at 600°C for 50 hr.

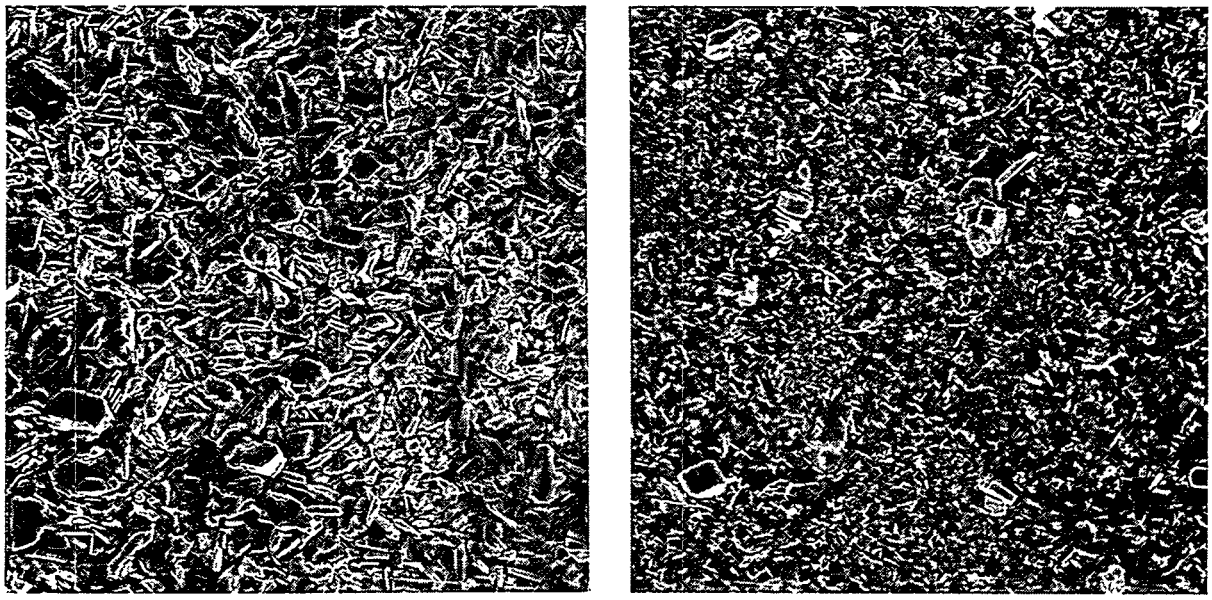

a) b)

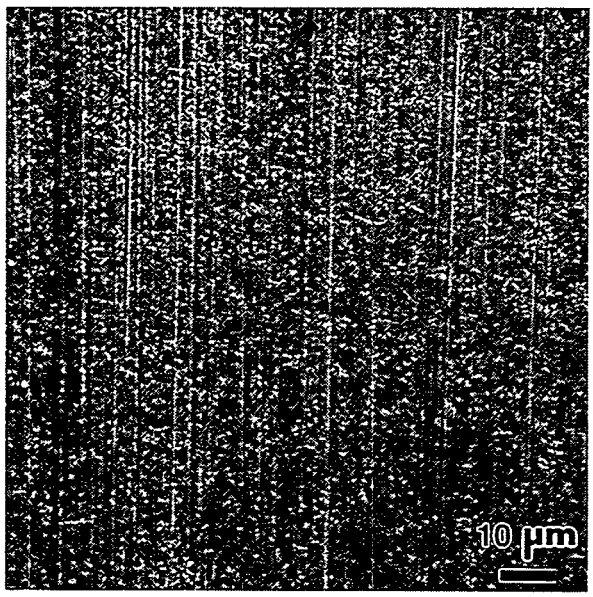

c)

Figure 6: SEM micrographs showing the corroded surface of a) the 5 wt% Al alloy, b) the 7.5 wt% Al alloy, and c) the 10 wt% Al alloy.

SUMMARY

This goal of this research is to find a compositional window in which weldable Fe-Al coatings can be deposited and perform well in environments indicative of low NOx boilers. Initial weldability studies have shown that below 10 wt% Al, sound overlays coatings can be produced without a pre- or post weld heat treatment using GTAW. Preliminary corrosion studies of alloys near this compositional boundary show promise in environments, while less aggressive than typically seen in the literature, indicative of boiler conditions.

FUTURE WORK

Future work will include installation of a co-extruded Fe-Al alloy tube, currently being prepared at ORNL, into an actual low NOx boiler to provide information on the corrosion resistance of Fe-Al alloys in real boiler environments. Weld overlays with ≤ 10 wt% Al will be deposited onto large-scale boiler tube panels using GMAW to correlate the weldability results of the small scale plates to actual large-scale panels. The influence of gas composition, aluminum content (5.0 to 12.5 wt% Al), and temperature on the corrosion behavior of Fe-Al alloys will be investigated in detail.

ACKNOWLEDGMENTS

This research was sponsored by the Fossil Energy Advanced Research and Technology Development (AR&TD) Materials Program, US Department of Energy, under contract DE-AC05-96OR22464 with Lockheed Martin Energy Research Corporation. The authors wish to thank V.K. Sikka from ORNL for the Fe-Al cast alloys used in corrosion testing.

REFERENCES

1. Stringer, J. 1990. In High Temperature Oxidation and Sulphidation Processes, ed. J.D. Embury, Pergamon Press, Toronto, Ontario, pp. 257-75.
2. Chou, S.F, Daniel, P.L., Blazewicz, A.J., and Dudek, R.F. Hydrogen Sulfide Corrosion in Low NOx Combustion Systems, presented to the Metallurgical Society of AIME, Detroit, Michigan, Sept 17-19, 1984, Babcock & Wilcox report # RDTPA 84-12.
3. Urich, J.A. and Kramer, E. Designing Solutions for Low NOx Related Waterwall Corrosion. In *1996 Internaitional Joint Power Generation Conference, Vol 1*, pp.25-9, ASME, EC-Vol. 4/FACT-Vol. 21.
4. Gabrielson, J.E. and Kramer, E.D. Measurement of Reducing Gases Formed in Low NOx Combustion. In *1996 International Joint Power Generation Conference, Vol 1*, pp.19-23, ASME, EC-Vol. 4/FACT-Vol. 21.
5. Strafford, K.N. and Manifold, R. 1969. The Scaling Behavior of an Iron-5% Aluminum Alloy in Sulfur Vapor, Oxidation of Metals, 1 (2), pp. 221-40.

6. Strafford, K.N. and Manifold, R. 1972. The Effects of Aluminum Alloying Additions on the Sulfidation Behavior of Iron, Oxidation of Metals, 5 (2), pp. 85-112.
7. Patnaik, P.C. and Smeltzer, W.W. 1985. Journal of the Electrochemical Society, 132, pp 1226-32.
8. Smith, P.J. and Smeltzer, W.W. 1987. Oxidation of Metals, 28, pp. 291-7.
9. DeVan, J.H. and Tortorelli, P.F. 1992. High Temperature Corrosion of Iron Aluminides, Corrosion 92, Paper 127.
10. Maziasz, P.J., Goodwin, G.M., Liu, C.T., and David, S.A. 1992. Effects of Minor Alloying Elements on the Welding Behavior of FeAl Alloys for Structural and Weld-Overlay Cladding Applications, Scripta Metallurgica et Materialia, 27 (12), pp. 1835-40.
11. David, S.A., Horton, J.A., McKamey, C.G. Zacharia, T., and Reed, R.W. 1989. Welding of Iron Aluminides, Welding Journal, Sept, pp. 372s-81s.
12. Fasching, A.A., Ash, D.I., Edwards, G.R., and David, S.A. 1995. Hydrogen Cracking Behavior in an Iron Aluminide Alloy Weldment, Scripta Metallurgica et Materialia, 32 (3), pp. 389-94.
13. Tortorelli, P.F., DeVan, J.H., Goodwin, G.M., and Howell, M., "High Temperature Corrosion Resistance of Weld Overlay Coatings of Iron Aluminide", pp. 203-12 in *Elevated Temperature Coatings: Science and Technology I*, Rosemont, IL, Oct 3-6, 1994, TMS, Warrendale, PA, 1994.
14. S.W. Banovic, J.N. DuPont, and A.R. Marder, *Processing and Structure of Insitu Fe-Al Alloys Produced by Gas Tungsten Arc Welding*, ORNL/Sub/95-SU604/01, Martin Marietta Energy Systems, Inc., Oak Ridge Natl. Lab., February 1997.
15. DuPont, J.N. and Marder, A.R. 1996. Dilution in Single Pass Arc Welds, Metallurgical and Materials Transactions B, 27B, pp.481-9.
16. Tortorelli, P.F., Goodwin, G.M., Howell, M., and DeVan, J.H., "Weld-Overlay Iron-Aluminide Coatings for Use in High Temperature Oxidizing/Sulfidizing Environments", pp. 585-90 in *Heat-Resistant Materials II*, Gatlinburg, TN, Sept 11-14, 1995, ASM, Materials Park, OH, 1995
17. DeVan, J.H., Hsu, H.S., and Howell, M., *Sulfidation/Oxidation Properties of Iron-Based Alloys Containing Niobium and Aluminum*, ORNL/TM-11176, Martin Marietta Energy Systems, Inc., Oak Ridge Natl. Lab., May 1989.
18. Goldstein, J.I., et. al. Scanning Electron Microscopy and X-Ray Microanalysis, 2nd Edition, pp. 87-90, Plenum Press, New York, New York, 1992.

CORROSION PERFORMANCE OF IRON ALUMINIDES IN FOSSIL ENERGY ENVIRONMENTS*

K. Natesan
Energy Technology Division
Argonne National Laboratory
Argonne, IL 60439

ABSTRACT

Corrosion of metallic structural materials in complex gas environments of coal gasification and combustion is a potential problem. The corrosion process is dictated by concentrations of two key constituents: sulfur as H_2S or SO_2 and chlorine as HCl. This paper presents a comprehensive review of the current status of the corrosion performance of alumina scales that are thermally grown on Fe-base alloys, including iron aluminides, in multicomponent gas environments of typical coal-conversion systems. Mechanisms of scale development/breakdown, performance envelopes for long-term usage of these materials, approaches to modifying the surfaces of engineering alloys by cladding or coating them with intermetallics, and in-service experience with these materials are emphasized. The results are compared with the performance of chromia-forming alloys in similar environments. The paper also discusses the available information on corrosion performance of alloys whose surfaces were enriched with Al by the electrospark deposition process or by weld overlay techniques.

INTRODUCTION

New structural materials based on Fe-Al intermetallic alloys are being developed for application in process industries and power generation systems. In the Fe-Al system, the alloys of interest are Fe_3Al and FeAl. In general, other elements are added to these alloys to improve their mechanical and/or corrosion properties in differing environments. Corrosion resistance is generally imparted to structural alloys by in-situ development of chromia, alumina, or silica scales on the alloy surface. The slower the growth rate of the oxide, the better the oxidation resistance of the alloy. In this vein, alumina scales, with inherently slower growth rates, can offer substantial advantages over chromia scales, especially in single-oxidant environments. The oxide scales also act as barriers to the transport of corrosion-accelerating reactants such as S, Cl, and alkalis, and they retard the scaling kinetics of the underlying substrate alloys when they are exposed to multioxidant environments. The oxidation resistance of iron aluminides depends on the formation of a chemically stable Al_2O_3 surface layer upon exposure to an oxidizing environment. Studies of the phase stability in the Fe-Al-O system demonstrate that Al_2O_3 will form on the Fe aluminide class of alloys even at relatively low pO_2. The Al levels present in Fe aluminides are well in excess of the critical concentration needed for the formation of a continuous alumina scale on the surface. However, at lower temperatures, transient Fe oxides will be present and the thermodynamically stable alumina can develop a continuous scale only over long exposure times.

*Work supported by the U.S. Department of Energy, Office of Fossil Energy, Advanced Research and Technology Development Materials Program, Work Breakdown Structure Element ANL–4, under Contract W–31–109–Eng–38.

CHARACTERISTICS OF ALUMINA SCALES

The only thermodynamically stable solid oxide in the Al-O system is Al_2O_3 (melting point 2072°C). Various structural forms of the oxide are possible and the stability of different oxide forms is dictated by temperature. While Cr_2O_3 normally exhibits p-type electrical behavior in which Cr is mobile, alumina exhibits more complex electrical properties whereby either Al or O may be mobile. Based on the bulk self-diffusion data in polycrystalline material depicted in Fig. 1, the rate of Cr_2O_3 scale formation would be expected to exceed the rate of Al_2O_3 scale formation by more than six orders of magnitude at temperatures <1200°C, assuming growth is controlled by cation diffusion in each case. Extrapolation of the diffusion data to lower temperatures indicates that below ≈1275°C, the rate of anion diffusion will exceed the rate of cation diffusion. Below ≈900°C, the alumina is generally formed as γ-Al_2O_3 and the corrosion protection of this alumina is not well established.[1]

A comparative analysis of growth rates of Cr_2O_3 and Al_2O_3 scales was made by Hindam and Whittle.[2] The scaling-rate constants shown in Fig. 2 as a function of temperature indicate significant scatter in the data for chromia scale formed in different alloys and less scatter for formation of alumina. However, the results show that the scaling rates for alumina are at least a few orders of magnitude lower than for chromia, especially at lower temperatures. One concern is that the alumina scaling rate is so low that transient oxides of Fe, Ni, and Cr may be present in the corrosion-product scale for a long period of exposure and thus the benefit of slow-growing alumina for corrosion protection may not be realized in practice.

Oxygen partial pressure appears to have little influence on the rate of Al_2O_3 scale formation,[3] but impurities may dope the oxide and influence its growth characteristics,[4] permit formation of spinel oxides, and play a vital role in the mechanical behavior of Al-rich oxide scale. The rate of S diffusion through Al_2O_3 can be 1 to 4 orders of magnitude greater than the rate of O diffusion, depending on oxide grain size (see Fig. 3), but may be 1.5 to 4.5 orders of magnitude lower than the rate of S diffusion through Cr_2O_3.[5] In both oxides, however, the partial pressures of S_2 and O_2 will determine whether sulfidation is induced and scale breakdown occurs.[6]

OXIDATION BEHAVIOR OF AL-CONTAINING ALLOYS

In Ni-Al, Fe-Al, and Co-Al binary alloys, an Al content in excess of 10 wt.% is normally needed to support formation of a surface Al_2O_3 scale.[7] The presence of Cr reduces the amount of Al required to form Al_2O_3 (to 3-5 wt.%).[8] Chromium minimizes internal oxidation of Al by acting as an oxygen getter,[9] but when it is present in high concentrations (>25 wt.% in Fe-Cr-Al alloys), ductility and workability of the

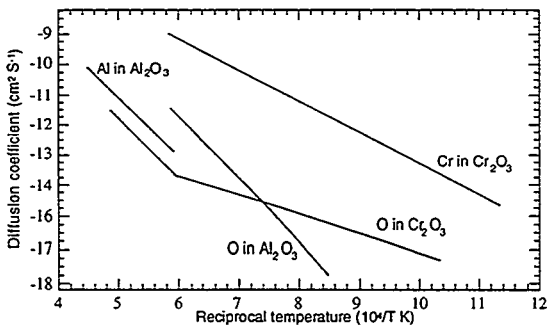

Figure 1. Self-diffusion data in chromia and alumina.

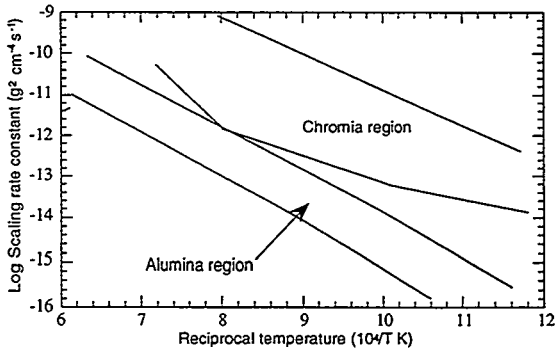

Figure 2. Rate constants for formation of alumina and chromia scales (based on data from Ref. 2)

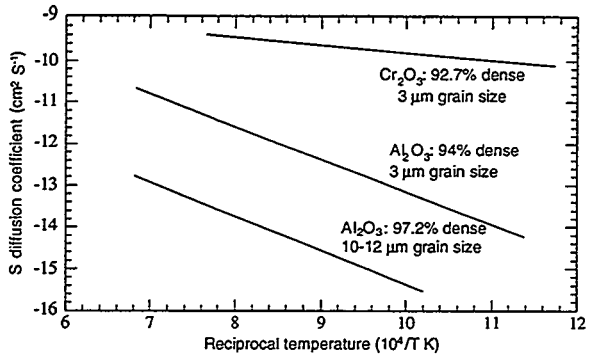

Figure 3. Rates of sulfur diffusion in alumina and chromia (based on data from Ref. 5).

alloy are impaired.[10] The commercially available structural alloys that form alumina scale generally also contain a fairly high concentration of Cr. In these alloys, the Cr-Al ratio appears to dictate the scaling kinetics and long-term mechanical integrity of the scale. A combination of good mechanical properties and oxidation resistance is generally obtained by optimizing the alloy chemistry. A Cr content of 20 wt.% or more is necessary to support alumina scale formation with only 5 wt.% Al. In the case of structural alloys, sufficient Ni in the alloy ensures austenite stability (providing creep strength), while maximizing the Fe content reduces cost. Alloy grain size is important in quaternary Fe-Cr-Ni-Al alloys in promoting alumina formation unless a second phase is present.[11]

Mechanical stability or the lack of it is a well-known problem associated with alumina scales. Scales composed of alumina commonly exhibit mechanical instability, e.g., cracking, spallation, and delamination, which poses a serious drawback in the application of Al_2O_3-forming alloys. The growth of a surface scale under isothermal or thermal-cycling conditions inevitably results in the generation of stress.[12] Compressive stresses will accumulate in a scale until some critical point is reached at which relief of stress must occur. If adhesion is poor, as it may be in many thermally grown Al_2O_3 scales, localized scale buckling may result in tensile fracture. The loss of corrosion resistance depends on the level of applied stress and also on the initial level of stress in the scale and the amount of deformation that can be accommodated. The area of metal surface exposed by scale cracking and the ability of the alloy to reform a protective scale will influence the rate of alloy degradation.

To examine the adhesion of thermally grown scales to the substrate, Natesan et al.[13] applied a tensile pull to separate the scale from the substrate. The technique they used involves attaching an epoxy-coated pin to the scale surface at a temperature sufficient to cure the epoxy. The pin is subsequently separated from the sample at room temperature by applying a tensile load. The surfaces of pulled pins are subsequently examined to assess whether the debonding occurred in the scale itself or at the scale/metal interface. The strength of the epoxy, and hence the maximum strength measurable by this procedure, was ≈71 MPa. If the applied load and pin area of contact are known, the stresses needed to pull the scale from the substrate can be calculated. The results obtained indicate a substantial scatter in the data from oxidized specimens. It is believed that for many samples (especially, for those prone to oxide spallation), voids or variations in the topography of the oxide layer result in an incomplete bond between the oxide and the epoxy-coated pin. Furthermore, in some of the samples, separation between the pin and the oxide occurred in the oxide itself rather than at the oxide/alloy interface.

Several iron aluminide alloys (see Table 1 for compositions) were used in this study. Alloy FA 186 is a ternary alloy that contains Fe, Cr, and Al and is considered a base alloy. Alloy FA 129 is designed to exhibit high ductility at room temperature while retaining its strength at high temperatures, whereas FAL is designed for improved oxidation resistance through addition of Zr. Alloy FAS is designed to resist sulfidation, and FAX is designed for improved resistance in aqueous environments by deliberate addition of Mo. Figure 4 shows the maximum stress endured by the scales on the alloys oxidized at 800, 1000, and 1200°C. The results show a peak in maximum stress value for specimens of FAS, FA 186, and FA 129 exposed at 1000°C. On the other hand, maximum stress values for FAL and FAX specimens are almost independent of exposure temperature. The adhesion test results from FAL and FAX also indicate that even with a wide variation in oxide layer thickness (resulting from oxidation for 100 h at 800-1200°C), the tensile stress needed to pull the sample from the substrate is fairly independent of oxide thickness. The difference in stress values for FAL and FAX must be due to differences in the chemistry in the scale and in the scale/alloy interface, which are directly influenced by the initial composition of the substrate alloy. The results also show that Zr (in FAL) and Nb (in FA 129) additions have a s imilar effect at 1000 and 1200°C, where α-Al_2O_3 will be the stable oxide in the scale. A comparison of the results obtained from these two alloys after 800°C oxidation indicates that addition of Zr, rather than Nb, may stabilize the alumina scale (i.e., minimize the transient oxides) on the alloy surface.

Table 1. Nominal chemical composition (in wt.%) of alloys cited in this paper

Material	C	Cr	Ni	Mn	Si	Mo	Al	Fe	Other
304	0.08	18.3	8.1	1.5	0.27	0.27	-	Bal[a]	-
316	0.05	17.4	13.8	1.5	0.73	2.2	-	Bal	-
310	0.07	25.0	18.7	1.21	0.64	0.002	-	Bal	-
800	0.08	20.1	31.7	0.96	0.24	0.30	0.39	Bal	Ti 0.31
GE 1541	-	15.2	-	0.001	0.07	-	4.95	Bal	Y 0.7
RV 8413	-	18.5	0.06	0.001	0.025	-	5.91	Bal	Hf 0.5
HR 160	0.05	28.0	Bal	0.5	2.75	–	–	4.0	Co 27.0
Alloy 556	0.10	22.0	20.0	1.5	0.4	3.0	-	Bal	Co 20.0, W 2.5
253 MA	0.10	20.7	10.9	0.3	1.8	-	–	Bal	Ce 0.03
FA 186	-	2.2	-	-	-	-	15.9	Bal	-
FAS	-	2.2	-	-	-	-	15.9	Bal	B 0.01
FA129	-	5.5	-	-	-	-	15.9	Bal	Nb 1.0, C 0.05
FAL	-	5.5	-	-	-	-	15.9	Bal	Zr 0.1, B 0.05
FAX	-	5.5	-	-	-	-	15.9	Bal	Nb 1.0, Mo 1.0, Zr 0.15, B 0.04
Fe-25Cr-20Ni	-	24.8	19.9	<0.01	<0.01	-	0.01	Bal	-
Fe-25Cr-6Al	-	24.6	<0.01	<0.01	<0.01	-	5.9	Bal	-
Fe-12Al	-	-	-	-	-	-	12.0	Bal	-
Fe_3Al	-	-	-	-	-	-	13.9	Bal	-
FeAl	-	-	-	-	-	-	34.0	Bal	-

[a]Indicates balance.

CORROSION IN MULTIOXIDANT ENVIRONMENTS

Protection of Fe aluminides from corrosion and environmental effects that arise from reaction with multicomponent gases and condensed products is best afforded either by formation of stable surface oxides (in this case, alumina) that are slow growing, sound, and adherent to the substrate, or by deposition of coatings that contain or develop oxides with similar characteristics. This is especially true for application of the intermetallics in integrated combined-cycle coal-gasification, low-NO_x systems, and pulverized-coal-fired and fluidized-bed combustion systems, and in gas turbine environments that are of interest in the development of fossil energy systems. In coal-gasification and low-NO_x systems, and in the first stage of magnetohydrodynamic systems, the gas environment is characterized by low pO_2 and moderate-to-high S partial pressure (pS_2), and the S is present as H_2S.[14] In combustion atmospheres and gas turbine environments, pO_2 is generally high and pS_2 is low, and the sulfur is present as SO_2. However, if combustion occurs near metal surfaces, e.g., in a bubbling fluidized bed, the local environment can be reducing and is dictated by the S sorbent equilibria, which are determined by stability fields of the $CaO/CaSO_4$-phase equilibrium.[14]

Extensive studies have been conducted on the corrosion performance of alumina-forming alloys in O/S mixed-gas environments.[15-19] Thermogravimetric studies on oxidation of Fe-base alloys with differing Al concentrations and Fe aluminide alloys showed that a minimum Al level of 12 wt.% is needed to develop a continuous alumina scale that is resistant to sulfur attack. A detailed comparison has been made of the corrosion performance of alumina- and chromia-forming alloys exposed to O/S mixed-gas environments. Weight change data, summarized in Fig. 5, show accelerated corrosion for chromia-forming alloys such as high-purity Fe-25Cr-20Ni and 310 stainless steel. Data for the Fe-25Cr-20Ni alloy show that Cr concentration at the high level of 25 wt.% does not improve sulfidation resistance of the alloy, which develops a scale (consisting of a mixture of Fe and Cr sulfide) at a very high growth rate. In fact, the presence of Ni leads to the formation of the Ni-Ni_3S_2 eutectic if the test is run for a longer time. The composition of this ternary alloy is similar to the base composition of the commercially available Type 310 stainless steel and its behavior is similar.[15] Alloys containing Cr and Al (RV 8413, GE 1541, and Fe-25Cr-6Al), which form alumina scale in single-oxidant environments, also exhibit significant corrosion in O/S environments.

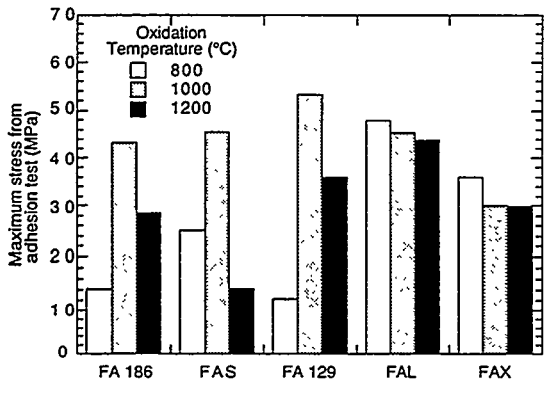

Figure 4. Maximum stress needed to pull scale from substrate for oxides that developed on several Fe-Al alloys oxidized at different temperatures (from Ref. 13)

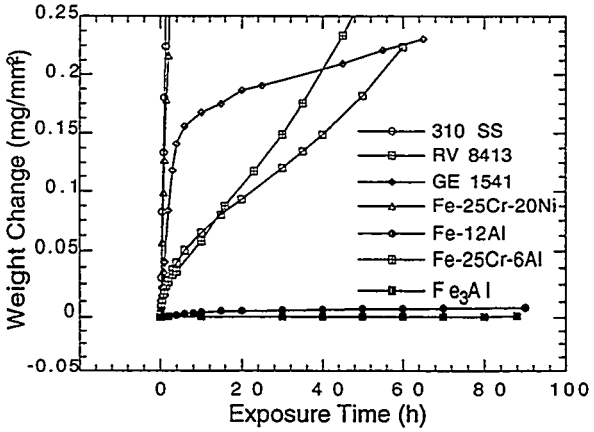

Figure 5. Weight change data for several chromia- and alumina-forming alloys tested in O/S environment with $pO_2 = 4.1 \times 10^{-18}$ and $pS_2 = 9.4 \times 10^{-7}$ atm at 875°C.

An addition of 6 wt.% Al to the Fe-25Cr alloy seems to reduce the corrosion rate somewhat but the external scale consists of Fe sulfide, which is not expected to offer protection against breakaway corrosion. The alloys GE 1541 and RV 8413 are Fe-based alloys with moderate Cr content and ≈5-6 wt.% Al. Corrosion performance of these alloys is not adequate for service in H_2S-containing environments. The binary Fe-12 wt.% Al alloy and Fe_3Al (with 13.9 wt.% Al) exhibit superior corrosion resistance in O/S mixed-gas atmospheres. The scales on these alloys were Al oxide and contained little S. The results indicate that a critical Al content in excess of 12 wt.%, which is present in Fe aluminides, is needed for alumina formation on the alloy surface in environments typical of coal conversion systems.

SURFACE ENRICHMENT WITH Al FOR CORROSION RESISTANCE

Even though the corrosion resistance of Fe-base alloys with high Al content is significant in environments that are prevalent in fossil energy systems, the use of these alloys as structural materials at elevated temperatures is very limited because of their inadequate strength properties and fabrication difficulties. Several approaches have been examined to enrich the surface regions of conventional structural alloys with Al that can form alumina scale during service, thereby offering improved corrosion protection. A promising approach for Al enrichment is the weld overlay process, in which claddings of high Al contents are produced by electrospark-deposition (ESD) and by gas tungsten arc and gas metal arc techniques. The ESD process is a microwelding technique that uses short-duration, high-current electrical pulses to deposit an electrode material on a metallic substrate. A principal advantage of the ESD process is that the overlay is fused to the metal surface with low heat input while the bulk substrate material remains at ambient temperature. This eliminates thermal distortion or changes in the metallurgical structure of the substrate. Because the overlay is alloyed with the surface, i.e., metallurgically bonded, it is inherently more resistant to damage and spalling than the mechanically bonded coatings produced by most other low–heat–input processes (such as detonation–gun, plasma–spray, and electrochemical plating). The use of welding to produce Fe aluminide layers leads to a loss of selected elements by vaporization and significant mixing of the filler metal and substrate alloys (dilution) during deposition. Because the substrates contain essentially no Al, the concentration of this element in the overlay is generally much lower than it is in the welding rod/wire used to produce the overlay.

Performance in Simulated Gasification Atmospheres

Several specimens with Al-enriched surfaces, applied on Type 316 stainless steel and Alloy 800 substrate alloys by the ESD process, were tested in simulated gasification environments that contained H_2S with or without HCl. In the first experiment, performance of the ESD coatings (which included Fe_3Al with differing bond coats of refractory metals and/or noble metals) was compared with that of uncoated austenitic alloys.[16] Figure 6 shows corrosion loss data obtained for specimens tested for 1000 h at 650°C in gas mixtures where $pO_2 = 1.2 \times 10^{-23}$, $pS_2 = 5.2 \times 10^{-10}$, $pCl_2 = 9.4 \times 10^{-17}$, and $pHCl = 2.1 \times 10^{-3}$ atm. All of the Fe aluminide coatings were resistant to sulfidation and chloride attack, whereas the base alloys were susceptible to general corrosion and pitting attack, especially in the HCl-containing environment. The weight change data and extensive microscopic analyses of tested specimens showed that the bond coats themselves do not significantly influence the corrosion process.

Further evaluation of Fe aluminide coatings was conducted with a Type 316 stainless steel substrate coated with either Fe_3Al or FeAl welding rod.[17] Coatings made with FeAl welding rod contained much more Al than those made with Fe_3Al welding rod. Type 316 stainless steel specimens with and without coatings and several commercial high-Cr alloys were exposed to O/S mixed-gas environments for up to 728 h

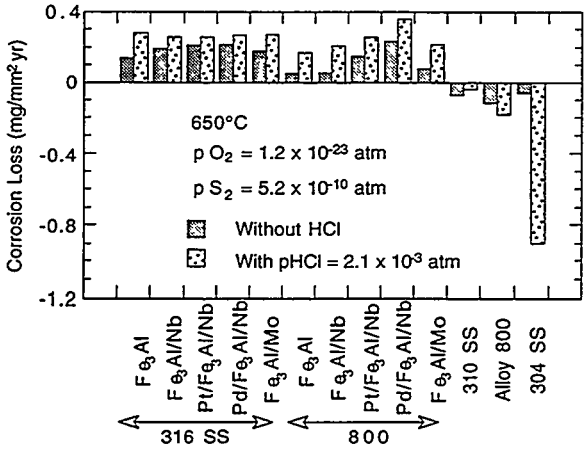

Figure 6. Corrosion loss data for several iron aluminide coatings and uncoated austenitic alloys after exposure in gas mixtures containing H_2S with and without HCl.

and periodically retrieved to measure weight changes at intermediate exposure times. Figure 7 shows weight change data for Alloy 800 and Type 316 stainless steel and for Fe_3Al- or FeAl-coated Type 316 stainless steel as a function of exposure time at 650°C to simulated gasification environments with or without HCl. The uncoated alloys exhibited some general corrosion and significant sulfidation and localized pitting corrosion. Weight gains and scaling rates were much lower for the aluminide-coated specimens than for the uncoated Type 316 stainless steel and Alloy 800.

Figure 8 shows similar weight change data for several commercial high-Cr alloys exposed together with FeAl-coated Type 316 stainless steel in O/S mixed-gas environments with and without HCl. The corrosion performance of the FeAl-coated specimen is comparable to or better than those of most other materials tested. Further, the cost of materials such as HR 160 and Alloy 556, which exhibit corrosion rates similar to FeAl layered specimen, will be a factor of 5 to 10 times higher than the FeAl coated specimen. Figure 9 shows corrosion loss data for several of these alloys and coatings calculated by parabolic kinetics.

Performance in Simulated Combustion Atmospheres

Specimens with Al-enriched surfaces, applied on Type 316 stainless steel and Alloy 800 substrate alloys by the ESD process, were also tested in simulated combustion environments that contained SO_2 with or without HCl. Specimens were tested for ≈900 h at 650°C in gas mixtures with $pO_2 = 6.7 \times 10^{-3}$, $pS_2 = 1.5 \times 10^{-35}$, $pCl_2 = 3.6 \times 10^{-4}$, and $pHCl = 1.7 \times 10^{-3}$ atm. Figure 10 shows weight change data for Alloy 800 and Type 316 stainless steel and for Fe_3Al- or FeAl-coated Type 316 stainless steel as a function of exposure time at 650°C to simulated combustion environments with or without HCl. In the absence of HCl, the uncoated alloys developed scales of (Fe, Cr) oxide or Fe oxide and tended to crack and spall, as evidenced by weight loss in Fig. 10. However, the absolute value for weight change after 900 h of exposure was <0.02 mg/mm^2. The aluminide-coated alloys showed a small weight gain due to the development of a thin, adherent alumina scale. In the presence of HCl, both the uncoated and coated alloys showed substantial weight loss at 650°C. The attack was most notable in the Fe_3Al-coated alloy, less notable in the uncoated alloys, and least notable in the FeAl-coated alloy. The primary cause for the increased corrosion of Fe_3Al-coated alloys seems to be a low concentration of Al in the coating that resulted from dilution of the deposit layer with substrate

ßconstituents. Even though Fe_3Al contained ≈14 wt.% Al, the coated alloy contained <8 wt.% Al after fabrication. The results also indicate that a threshold Al concentration of >12 wt.% is necessary to improve the corrosion resistance of structural alloys.

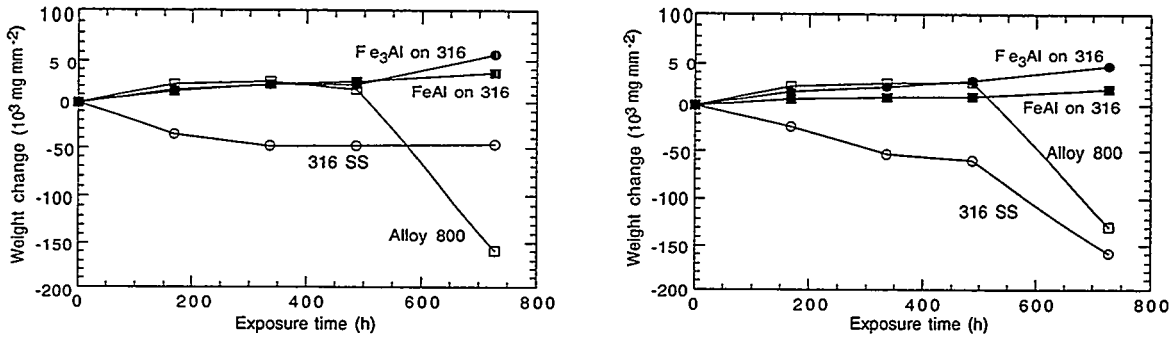

Figure 7. Weight change data for Type 316 stainless steel, Alloy 800, and Fe_3Al- and FeAl-coated Type 316 stainless steel after exposure in O/S mixed gas of composition $pO_2 = 1.2 \times 10^{-23}$ and $pS_2 = 5.2 \times 10^{-10}$ atm at 650°C (left) without HCl and (right) with pHCl = 2.1×10^{-3} atm.

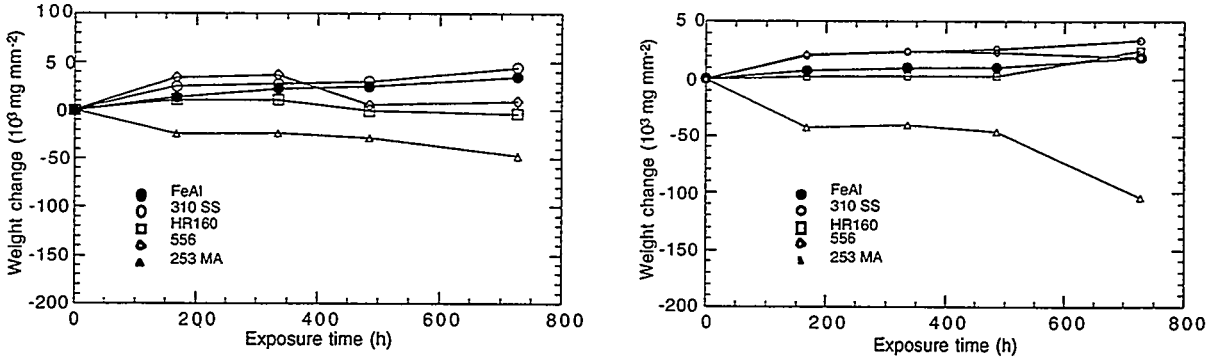

Figure 8. Weight change data for several commercial alloys and FeAl-coated Type 316 stainless steel after exposure in O/S mixed gas of composition $pO_2 = 1.2 \times 10^{-23}$ and $pS_2 = 5.2 \times 10^{-10}$ atm at 650°C (left) without HCl and (right) with pHCl = 2.1×10^{-3} atm.

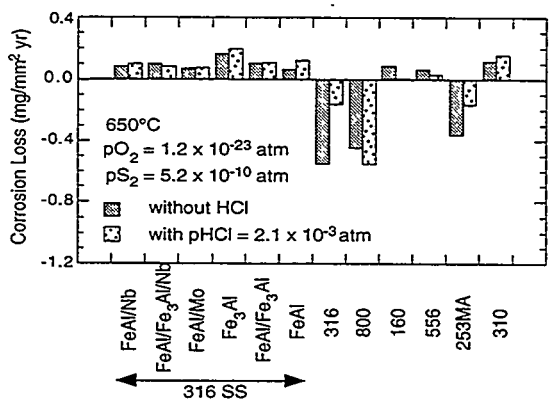

Figure 9. Corrosion loss data for iron aluminide coatings on Type 316 stainless steel and several uncoated high-Cr alloys after exposure in gas mixtures containing H_2S with and without HCl.

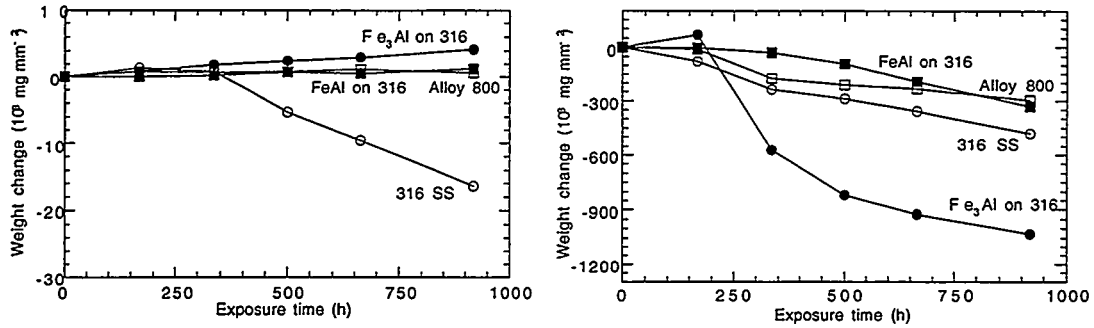

Figure 10. Weight change data for Type 316 stainless steel, Alloy 800, and Fe_3Al- and FeAl-coated Type 316 stainless steel after exposure in O/S mixed gas of composition $pO_2 = 6.7 \times 10^{-3}$ and $pS_2 = 1.5 \times 10^{-35}$ atm at 650°C (left) without HCl and (right) with $pHCl = 1.7 \times 10^{-3}$ atm.

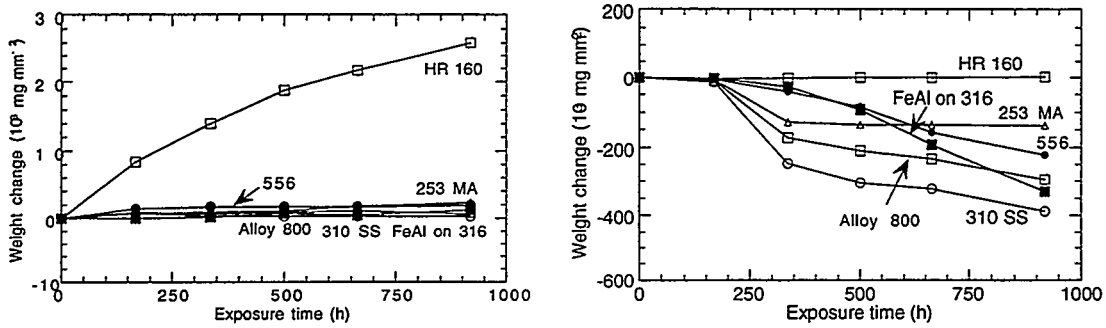

Figure 11. Weight change data for several commercial alloys and FeAl-coated Type 316 stainless steel after exposure in O/S mixed gas of composition $pO_2 = 6.7 \times 10^{-3}$ and $pS_2 = 1.5 \times 10^{-35}$ atm at 650°C (left) without HCl and (right) with $pHCl = 1.7 \times 10^{-3}$ atm.

Figure 11 shows similar weight change data for several commercial high-Cr alloys exposed together with FeAl-coated Type 316 stainless steel in simulated combustion environments with and without HCl. In the absence of HCl, all the alloys except HR 160 exhibited negligible weight gains and the scales were predominantly Cr_2O_3. HR 160 is the only alloy among those tested which contains ≈38 wt.% Ni and it is not known whether the higher Ni content of this alloy had contributed to higher oxidation in the alloy. However, the oxidation rate is still negligibly small. In the presence of HCl in the environment, all the alloys except HR 160 exhibited substantial weight loss during the 900 h exposure. HR 160 contains 2.75 wt% Si, which upon oxidation at the chromia/alloy interface, may act as a second barrier against cation migration outward and Cl penetration inward, resulting in negligible corrosive attack. MA 253, which contains 1.8 wt.% Si, exhibited weight loss for ≈300 h, beyond which the loss was negligible. Other chromia-forming alloys such as 310 stainless steel, Alloy 556, and Alloy 800 continued to lose weight during the 900 h exposure. The FeAl-coated Type 316 stainless steel, even though forming alumina scale, was found susceptible to corrosion in the HCl-containing combustion atmosphere and the rate was slightly higher than that of Alloy 556. Detailed microstructural and X-ray analyses of the corrosion-product layers from several of the tested specimens are in progress to evaluate the role of chlorine in the corrosion performance of these materials.

SUMMARY

Fe aluminides are being developed as structural materials and as cladding/overlay for conventional engineering materials. The present paper addresses the chemical compatibility aspects of these materials in

environments relevant to fossil energy systems. The raw gas environments that arise from gasification and combustion of coal have chemical compositions that are widely different in pO_2 and pS_2. In addition, presence of Cl in the gas as HCl, which is determined by the Cl content of the coal feedstock, can exacerbate the corrosion process. In single-oxidant environments, such as air and low-pO_2, the oxidation rates for these alloys are significantly lower than those for chromia-forming commercial alloys. However, the mechanical integrity of the alumina scales and the reformation characteristics are key to adequate protection in long-term service. In S-containing environments, Fe aluminides offer superior corrosion resistance. Experimental data on binary Fe-Al alloys showed that a threshold Al concentration of at least 12 wt.% is needed to minimize corrosion in these environments. Further, surface enrichment of conventional structural alloys with Al-enriched surfaces produced by electrospark deposition improved corrosion resistance in simulated coal conversion environments that contained S and/or Cl. Data are presented on the performance envelope for use of these materials in S-containing environments. In Cl-containing environments, pitting-type corrosion is the dominant mode of attack on Fe aluminides but, if S is present along with Cl in gasification atmospheres, the corrosion rate seems to be determined by sulfidation rather than by Cl. On the other hand, Cl seems to have a stronger degrading effect on corrosion of these materials. Additional work is needed to establish the threshold Cl levels in the environment beyond which corrosion of aluminides and alumina-forming alloys is accelerated at different exposure temperatures.

ACKNOWLEDGMENTS

D. L. Rink assisted in the corrosion tests and microstructural analysis of exposed specimens. This work was supported by the U.S. Department of Energy, Office of Fossil Energy, Advanced Research and Special Technologies Materials Program, Work Breakdown Structure Element ANL–4, under Contract W–31–109–Eng–38.

REFERENCES

1. G. C. Wood and F. H. Stott, in High Temperature Corrosion, ed. R. A. Rapp, NACE, Houston, TX, 1983.
2. H. Hindam and D. P. Whittle, Oxid. Met. 18, 245, 1982.
3. T. A. Ramanarayanan, M. Raghavan, and R. Petrovic-Luton, Trans. Jap. Inst. Met. 34, 199, 1983.
4. P. A. Lessing and R. S. Gordon, J. Mater. Sci. 12, 2291, 1977.
5. J. B. Wagner, Defects and Transport on Oxides, p. 283, Plenum, New York, 1973.
6. P. A. Mari, J. M. Chaix, and J. P. Larpin, Oxid. Met. 17, 315, 1982.
7. G. N. Irving, J. Stringer, and D. P. Whittle, Oxid. Met. 9, 427, 1975.
8. G. R. Wallwork and A. Z. Hed, Oxid. Met. 3, 171, 1971.
9. G. C. Wood and M. G. Hobby, Proc. 3rd Int. Cong. on Metallic Corrosion, Moscow, p. 102, 1966.
10. C. S. Wukusick and J. F. Collins, Mat. Sci. Stand., 637, 1964.
11. D. Delaunay and A. M. Huntz, J. Mater. Sci. 18, 189, 1983.
12. I. Pfeiffer, Z. Metallkunde, 53, 309, 1962.
13. K. Natesan, K. Klug, D. Renusch, B. W. Veal, and M. Grimsditch, Microstructural and Mechanical Characterization of Alumina Scales Thermally Developed on Iron Aluminide Alloys, Argonne National Laboratory Report ANL/FE-96/01, 1996.
14. K. Natesan and P. F. Tortorelli, Proc. Intl. Symp. on Nickel and Iron Aluminides: Processing, Properties, and Applications, ASM International, p. 265, 1997.

15. K. Natesan, in Proc. 7th Annual Conf. Fossil Energy Materials, ORNL/FMP-93/1, p. 249, 1993.

16. K. Natesan and W. D. Cho, in Proc. 8th Annual Conf. Fossil Energy Materials, ORNL/FMP-94/1, p. 227, 1994.

17. K. Natesan and R. N. Johnson, in Proc. 2nd Int. Conf. Heat-Resistant Materials, K. Natesan, P. Ganesan, and G. Lai, eds., p. 591, ASM International, Materials Park, OH, 1995.

18. P. F. Tortorelli and J. H. DeVan, Mater. Sci. and Eng., A153, 573, 1992.

19. K. Natesan, Materials at High Temperatures, 11, 36, 1993.

THE MICROSTRUCTURE AND MECHANICAL RELIABILITY OF ALUMINA SCALES AND COATINGS

K. B. Alexander, K. Prüßner, and P. F. Tortorelli

Oak Ridge National Laboratory
P. O. Box 2008
Oak Ridge, Tennessee 37831-6376

ABSTRACT

Alumina scales on iron-aluminides (Fe_3Al-based) and NiCrAl-based alloys were characterized in order to develop the knowledge to control the oxidation performance of alloys by controlling the microstructure and microchemistry of their scales. Plasma-deposited amorphous alumina coatings on iron-aluminides were used to study phase transformations, transport processes in the scales and sulfur segregation to the scale/metal interface. It was found, that during heat treatment in the absence of oxidation, amorphous coatings first transform to γ-Al_2O_3 and eventually α-Al_2O_3 nucleates at the scale/metal interface. Sulfur from the Zr-free alloy segregates to the scale/metal interface during heat treatment. Thermally-grown scales on Zr-doped iron-aluminides were compared to those formed after oxidation of a specimen with an alumina coating. Microstructural and gravimetric results showed that the primarily amorphous alumina coating promoted the nucleation and growth of metastable alumina phases, which resulted in more rapid oxidation. The thermally-grown oxide was found on top of the coating. The NiCrAl-based alloys formed columnar alumina scales underneath a layer of mixed oxides. Segregation of alloying elements like Y, Hf and Ta was found at both oxide grain boundaries and scale/metal interfaces.

INTRODUCTION

In many high-temperature fossil energy systems, corrosion and deleterious reactions with gases and condensable products in the operating environment often compromise materials performance. The presence of a stable surface oxide can effectively protect the materials from these reactions if the oxides are slow-growing, dense and adherent to the substrate. However, the various factors which control the scale/coating integrity and adherence are not fully understood. Of fundamental interest is the microstructure and microchemistry of the metal/oxide interface as well as oxide/oxide grain boundaries in the scale itself. In alumina scales, segregation of sulfur to the scale/metal interface was found to be detrimental to the oxidation performance, however the presence of reactive elements (RE) such as Y or Zr in the alloy can mitigate the effects of sulfur and thus improve the scale adherence.[1-5] Reactive elements segregate to the oxide/metal

interface and scale grain boundaries and modify the growth mechanisms and the microstructure.[6,7]

The Oak Ridge National Laboratory (ORNL) research described in this paper is being conducted in collaboration with work sponsored by the Department of Energy's Office of Fossil Energy at Argonne National Laboratory (ANL) and Lawrence Berkeley National Laboratory (LBNL) as well as in concert with on-going interactions that are part of the Office of Basic Energy Sciences' Center of Excellence for the Synthesis and Processing of Advanced Materials. The Center of Excellence on Mechanically Reliable Surface Oxides and Coatings includes participants from ORNL, ANL, LBNL, Idaho National Engineering Laboratory (INEL) and Lawrence Livermore National Laboratory (LLNL).

This report will discuss work on the oxidation of iron aluminides, with and without alumina coatings, as well as recent work on the oxidation and segregation behavior of NiCrAl-based alloys. Iron-aluminides (Fe_3Al-type) are known to have good oxidation resistance, if the protective alumina scale can be maintained. It has been shown that small amounts of zirconium significantly reduce the oxidation rate and improve scale adherence in short-term tests at 1000°C.[8,9] Zirconium-containing alloys form unconvoluted, uniform oxide scales with no evidence of spallation during thermal cycling, whereas a significant amount of spallation is observed after thermal cycling of a Zr-free alloy.[8,9] The influence of an applied coating on the oxidation behavior of the alloy should allow the operative transport mechanisms during oxidation to be better examined. The deposition of a plasma-synthesized alumina coating prior to oxidation promoted the growth of metastable aluminas and thus increased the oxidation rate.[10] Both coated and uncoated specimens have needle-like surface morphologies.[10]

Unlike iron-aluminides, NiCrAl-based alloys can result in complex oxide scales with mixed oxides formed in the initial oxidation stages and an alumina layer underneath.[12,13] NiCrAl-based alloys of different compositions, including a commercial superalloy as well as two model alloys were part of the study. Such alloys allow extension of the present work on alumina scales and coatings on Fe-based alloys to a class of Ni-based alloys that are of direct relevance to advanced turbine systems.

EXPERIMENTAL PROCEDURES

The alloys used for the iron aluminide studies were FAL (Fe-28 at. % Al-5 at. % Cr-0.1 at. % Zr + 0.05 at. B) and FA186 (Fe-28 at. % Al-5 at. % Cr), prepared by arc melting and casting. The bulk alloy sulfur content was ~ 40 ppm for both alloys. These alloys were rolled to

a final thickness of between 0.8 and 1.3 mm and rectangular specimens (typically 12 x 10 mm) were prepared from these sheets for coating and oxidation studies.

Oxidation experiments of coated or uncoated iron-aluminides were performed under isothermal and cyclic conditions for 96 h at 1000°C in static air. Gravimetric data were recorded during the cyclic oxidation by exposing coupons in individual pre-annealed alumina crucibles to a series of 24-h exposures. Heat treatments of deposited alumina coatings were performed for 0.5 and 2 h in He at 1000°C.

Alumina coatings on iron aluminides were deposited using a magnetically-filtered cathodic-arc plasma-synthesis process.[13] During the deposition process, the substrate was pulse-biased to a high ion energy (2 kV) in the initial phase of the deposition process to provide atomic mixing of the substrate and film at the interface. A substantially lower energy (0.2 kV) was used to deposit the remaining thickness of the coating.

Three NiCrAl-based alloys of different compositions (commercial superalloy René N5 (from General Electric Aircraft Engines), and ytrrium-doped ternary alloys with similar (NCA-S) as well as higher Cr and Al contents (NCA-H) - Table 1), which form complex oxide scales, were examined after isothermal oxidation in air at 1200°C for 100 h.

Table 1: Composition of NiCrAl-alloys (at %; except S in ppm)

at %	Ni	Cr	Al	Fe	Ta	Hf	W	Re	Si	Co	Mo	Y	Zr	S*	C
Rene N5	64.9	7.8	13.9	0.1	2.1	0.05	1.6	1.0	0.15	7.3	0.9	0.003	0.003	4	0.25
NCA-S	80.1	7.2	12.5	0.01					0.14			0.012		18	0.05
NCA-H	71.2	9.9	18.8	0.01					0.02			0.041		16	0.04

* sulfur contents in ppm

For all experiments, scanning electron microscopy (SEM) was performed on oxidized or heat treated coupons as well as on polished cross-sections through the scale and/or coatings. Field emission gun transmission electron microscopy/scanning transmission electron microscopy (FEG-TEM/STEM) of cross-sectional and plan-view specimens were used for the microstructural characterization of the scales. Energy dispersive x-ray spectroscopy (EDS) with high spatial resolution (1-2 nm probe) was used for the STEM studies of interfacial segregation.

RESULTS AND DISCUSSION

I. Oxidation Studies on Iron-Aluminides

1. Microstructure of Plasma-Deposited Alumina Coatings, As-Deposited

Plasma-deposited alumina coatings which were subsequently used for oxidation and segregation studies of iron-aluminides were primarily amorphous in the as-deposited state (as determined by x-ray diffraction). Auger Electron Spectroscopy (AES) and Rutherford Backscattering (RBS) analyses showed that the films are slightly cation-deficient Al_2O_3.[14] Cross-sectional TEM showed that most coatings had two distinctly different layers: an inner layer which exhibits contrast features perpendicular to the interface and an outer layer, which is featureless (Fig. 1).

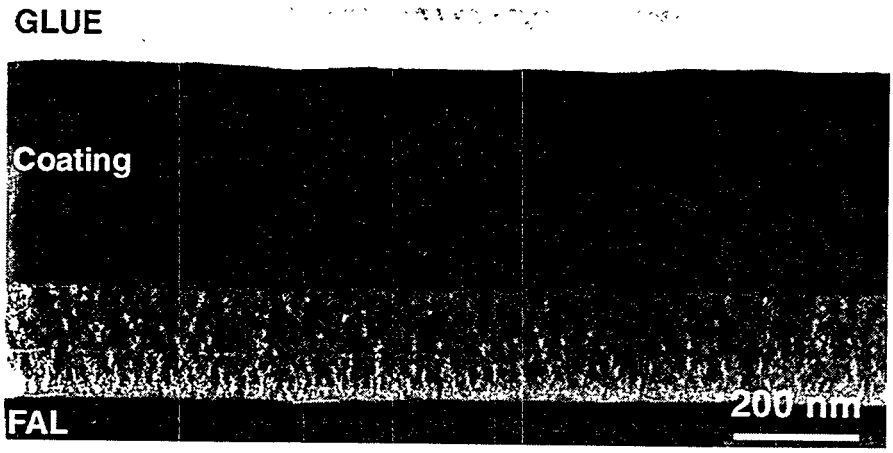

Fig. 1. TEM image of the structure of an as-deposited alumina coating (~ 0.7 μm thick).

The featureless portion was found by selected area diffraction (SAD) to be fully amorphous, whereas some fine-grained γ-Al_2O_3 was found in the inner part of the scale. The difference between the two regions was assumed to correlate with the change in pulse-biasing of the substrate from 2 kV to 0.2 kV during deposition. However, not all the coatings had these two layers. Further investigation of deposition parameter/structure correlations are underway.

2. Microstructural Development and Segregation During Heat Treatment of Alumina Coatings

Previous experiments concerning the segregation of sulfur to the scale/metal interface have only addressed segregation to interfaces between thermally-grown α-Al_2O_3 and an alloy.[3,4,15,16] Since α-Al_2O_3 grows by inward diffusion, the interface is not static but moving into the metal

during oxidation. Therefore diffusion of sulfur to the interface and migration of the interface in the opposite direction are counter-processes. In this study, alumina coatings (0.2 and 0.8 μm thick), plasma-deposited on FA 186, were used to study the segregation of sulfur to a static scale/alloy interface (in the absence of thermal oxidation) and thereby isolate the effect.[16] As-deposited alumina coatings were heat treated in a He-atmosphere at 1000°C (for 0.5 or 2 h) in order to crystallize the initially amorphous coating, while preventing the growth of a thermal oxide scale (if thermal oxidation occurs, oxide needles can clearly be seen on the coating surface by SEM, and this was not observed).

SEM imaging revealed that although the scale/gas interface remained smooth during crystallization, the scale/metal interface showed imprints of distinct oxide grains with associated cracks and cavities as shown in Fig. 2a. The 0.8 μm coating developed a network of cracks and spalled in several areas. The 0.2 μm coating didn't develop these large through-coating cracks. It can be concluded that for the 0.8 μm coating the critical scale thickness for accomodation of thermal and growth/transformation stresses was exceeded.

TEM investigations showed that the heat treatment resulted in the transformation of the coating to metastable alumina (γ-Al_2O_3 and θ-Al_2O_3) and eventually to the nucleation of α-Al_2O_3 at the scale/metal interface (Fig. 3). During the transformation to the metastable aluminas, both interfaces remained fairly flat. The formation of α-Al_2O_3 on the other hand, resulted in roughening of the scale/metal interface. The grains visible as imprints in the top-down SEM images (Fig. 2) could be correlated to faceted grains of α-Al_2O_3 which grew into the alloy. Cavities were formed next to the α-Al_2O_3 (Fig. 3b). Therefore considerable material transport seems to be associated with the phase transformation to α-Al_2O_3 although no thermal oxide growth occurs.

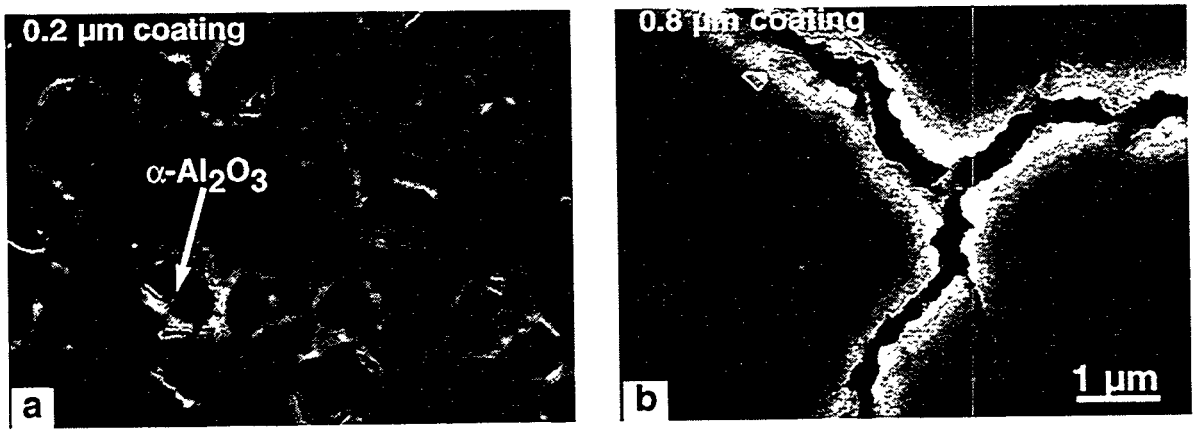

Fig. 2. SEM plan-views of the heat-treated coatings after 2 h in He at 1000°C. (a) 0.2 μm coating, revealing the scale/metal interface (b) 0.8 μm coating, revealing the gas/scale interface.

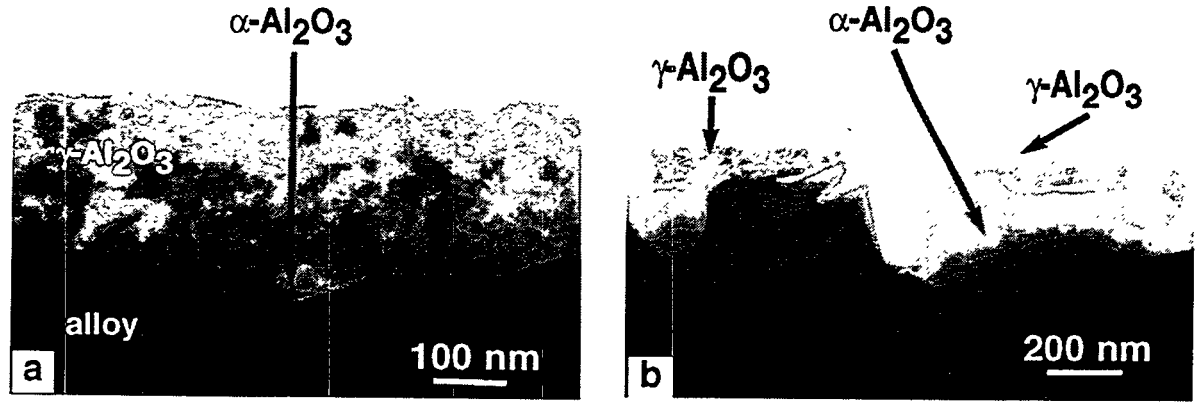

Fig. 3. (a) and (b) TEM cross-sections through heat-treated 0.2 μm thick coating after 2 h in He at 1000°C.

Studies with Auger electron spectroscopy (AES) on FA186/alumina coating interfaces that were freshly exposed by an in-situ scratch-technique, showed that sulfur segregated to the oxide/metal interface during the heat treatment.[16] The sulfur coverage of the interface increased with increasing annealing time and varied in different regions of the specimen. In order to study the correlation between different interface structures and the sulfur level at the interface, high spatial resolution EDS analysis of TEM cross sections was used. Segregation of sulfur was found at α-Al_2O_3/alloy interfaces as well as at γ-Al_2O_3/alloy interfaces (Fig. 4). No interfacial voids were observed in these areas. Quantification of these data is complicated by the roughness of the γ-Al_2O_3/alloy interface (in contrast to the facetted α-Al_2O_3/alloy interface) which made edge-on orientation of the interface impossible. Further analysis is underway to determine if the interfacial sulfur coverage is different for the two microstructures.

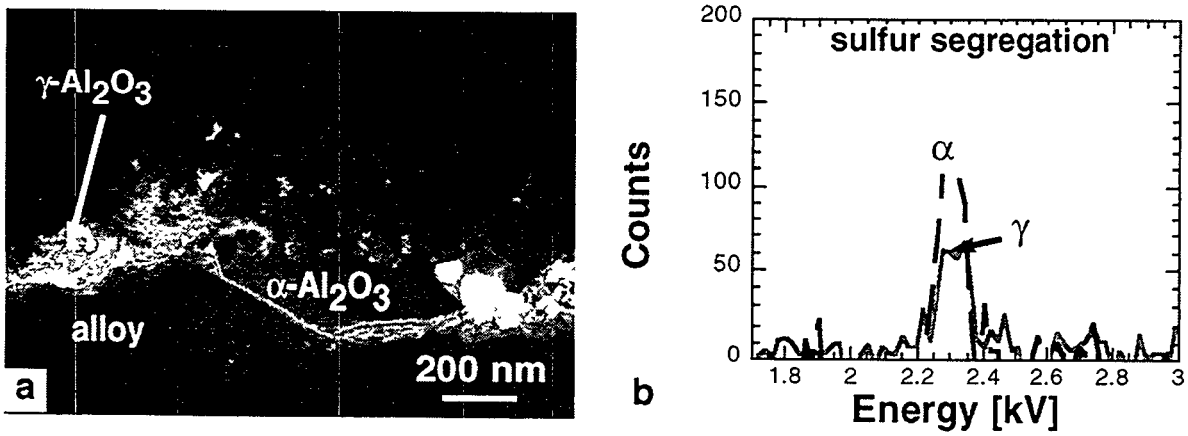

Fig. 4. a) STEM annular dark-field image of γ/alloy and α/alloy interface, b) EDS spectra showing segregation of sulfur at the γ/alloy and the α/alloy interface.

3. Influence of Alumina Coatings on Thermal Oxide Growth on Iron-Aluminides

To study the effect of an alumina coating applied prior to oxidation on the oxidation performance of iron-aluminides, FAL was coated on one side with a 0.1 μm alumina coating and oxidized in air at 1000°C for 96 h. On both the coated and the uncoated sides, oxide scales with a needle-like surface structure were formed (Fig. 5). Both oxide scales were adherent and did not spall. The recorded weight gain demonstrated that the coating increased the rate of oxidation. The oxide scale on the coated side was 1.5-2 μm thick, whereas on the uncoated side it was 0.8-1 μm (Fig. 6).

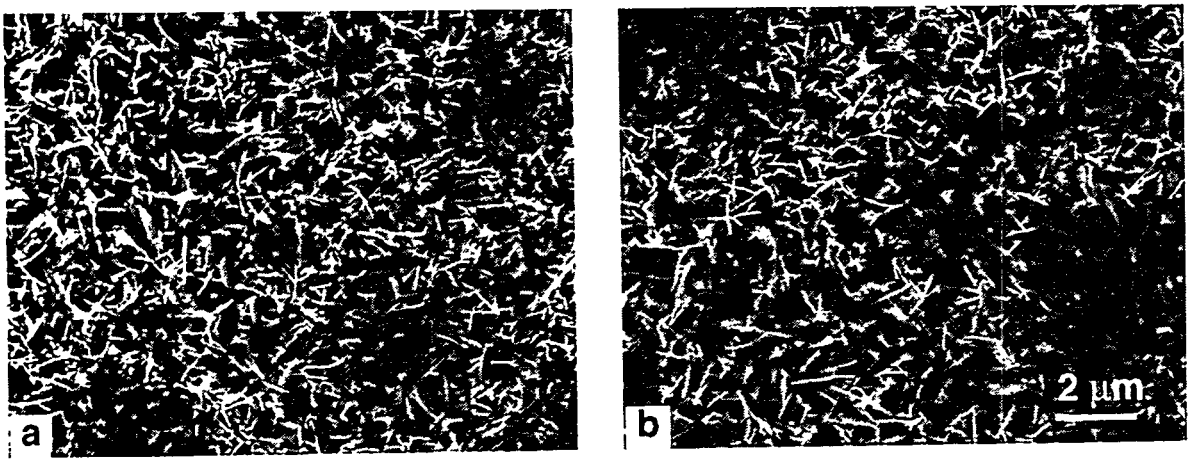

Fig. 5. SEM plan-view of oxidized surfaces exposed 96 h at 1000°C, a) FAL uncoated, b) FAL with 0.1 μm alumina coating.

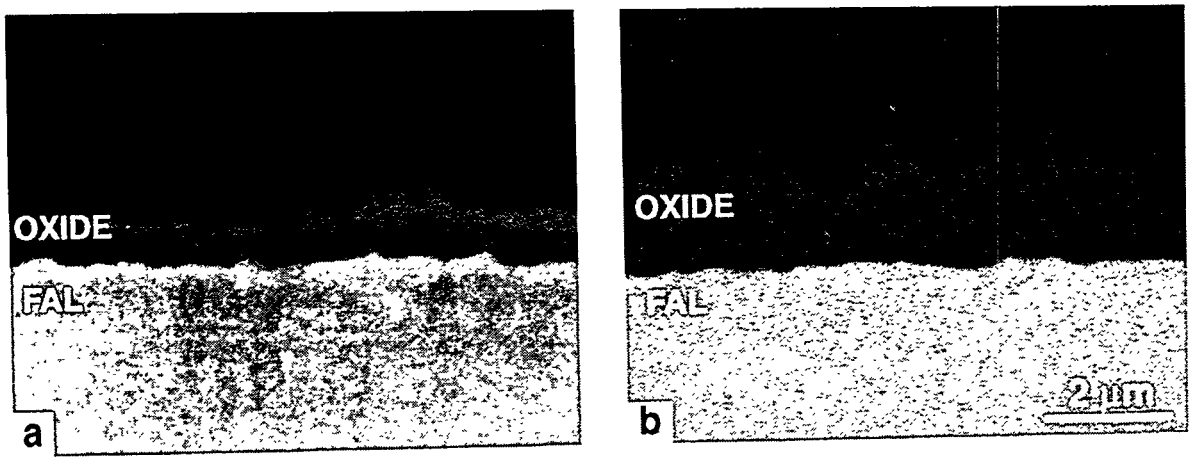

Fig. 6. SEM of polished cross-section after oxidation for 96 h at 1000°C, a) FAL uncoated, b) FAL with 0.1 μm alumina coating.

On the coated side, the original location of the coating can be discerned in the TEM cross-section shown in Fig. 7. The grain size in the area of the original coating is typically 100-150 nm. The grains were identified as nearly dense, equiaxed α-Al_2O_3. The thermally-grown oxide on top of the coating was also α-Al_2O_3 however, it had a much coarser grain structure. Selected-area diffraction showed all portions of the oxide scale, even the oxide needles at the scale/gas interface were α-Al_2O_3, consistent with the pseudomorphic transformation of the transient oxides to α-Al_2O_3 after 96h at 1000°C.

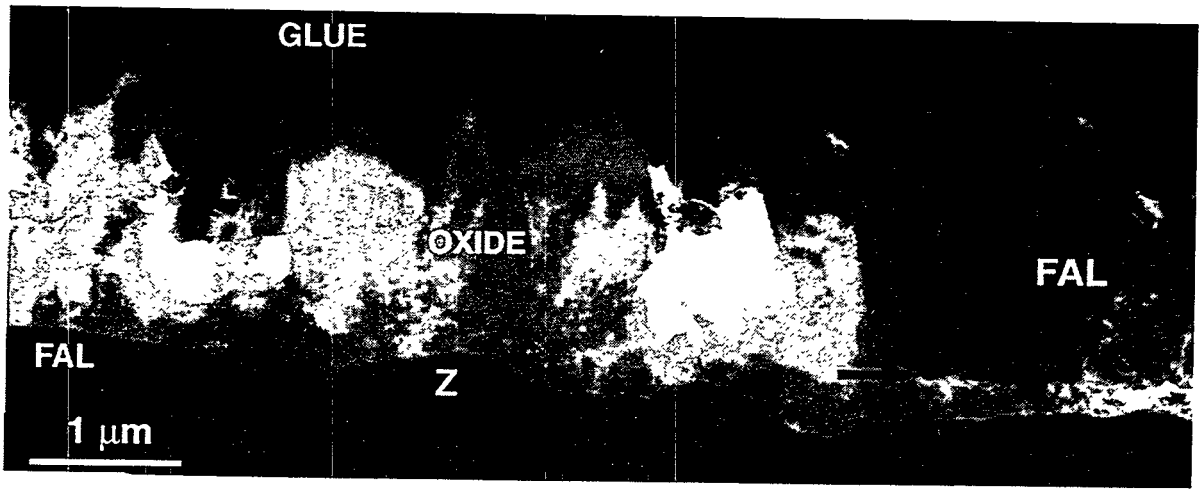

Fig. 7. STEM annular dark-field of coated-and-oxidized (96h at 1000°C) FAL. The location of the original coating is indicated by the arrow.

The identification of the original coating location in the bottom portion of the scale after oxidation implies that most of the scale growth on coated FAL occurred primarily by transport of aluminum through the coating. Although the scale/metal interface on the coated FALwas intact, it roughened during oxidation. This indicates that some transformation of α-Al_2O_3 at the metal/coating interface occurred (similar to that described in the previous section). On the coated surface, Zr-rich metallic particles (typical size: 0.5-1 μm) were found at the scale/metal interface (marked "Z" in Fig. 7). The particles at the scale/metal interface were, compared to the FAL alloy, rich in Zr but contained less Fe and Cr and no oxygen (as determined by STEM/EDS analysis). These particles were not observed at the scale/metal interface in the absence of the alumina coating. The fact that the Zr was not oxidized is consistent with the lack of inward diffusion of oxygen. It is proposed that the amorphous coating promotes the nucleation and growth of metastable alumina phases, resulting in slighly enhanced outwardly-growing oxidation and thicker scales. During the early stages of oxidation, the amorphous coating is therefore ineffective as a protective layer.

Fig. 8. Annular dark-field STEM image of cross-section through scale showing ZrO_2 particles within the scale.

Elemental analysis by EDS showed that zirconium segregated to oxide grain boundaries, both in the initial alumina coating and in the thermally-grown oxide. Segregation of zirconium at the scale/metal interface was also found, both in the coated and uncoated FAL. Auger analysis on metal/oxide interfaces exposed by scratching off the oxide in vacuo revealed the absence of sulfur at the metal/oxide interface.[14] In the portion of the scale near where the amorphous coating was originally located, ZrO_2 particles were found at grain boundaries as well as at the interface between the former coating and the thermally-grown oxide (Fig. 8). The formation of ZrO_2 particles within the oxide on coated-and-oxidized FAL must result from diffusion of zirconium into the coating and subsequent oxidation and/or formation of ZrO_2 during the growth of new oxide.

II. Oxidation Studies on NiCrAl-Alloys

Plan-view images of the three alloys after oxidation are shown in Fig. 9. Figure 10 shows the corresponding cross sections (polished or fractured). The oxide scale on René N5 (~5 μm) consists of columnar α-Al_2O_3 at the bottom (~4 μm) and a mixed layer of spinel (Ni, Co, Ta)(Al, $Cr)_2O_4$ and α-Al_2O_3 (~1 μm) at the top. The mixed oxide layer contains numerous precipitates of Ta,Y,Cr(Hf,Re)-oxides. These are concentrated at the interface between the columnar alumina and the mixed layer. This mixed layer of the scale is prone to spallation.

Similar oxide particles can also be found on the scale surface. Spallation of the complete scale exposing the bare alloy occurs only around particles in the alloy, which consist of Ta,Y,Cr(Hf,Re)-oxide in the center, surrounded by spinel (Ni, Co, Ta) (Al, $Cr)_2O_4$ and α-Al_2O_3. Using STEM/EDS analysis segregation of Ta and Y at oxide grain boundaries both in the alumina and in the spinel was found. Some oxide grain boundaries also exhibited segregation of Hf and Re.

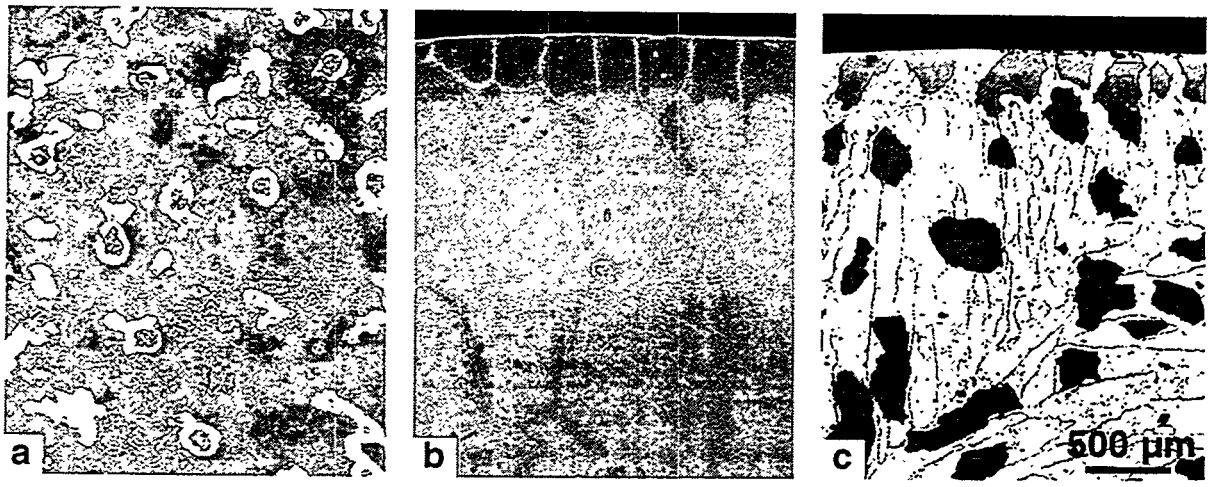

Fig. 9. SEM plan-view images of a) René N5, b) NCA-S and c) NCA-H after oxidation for 100 h at 1200°C.

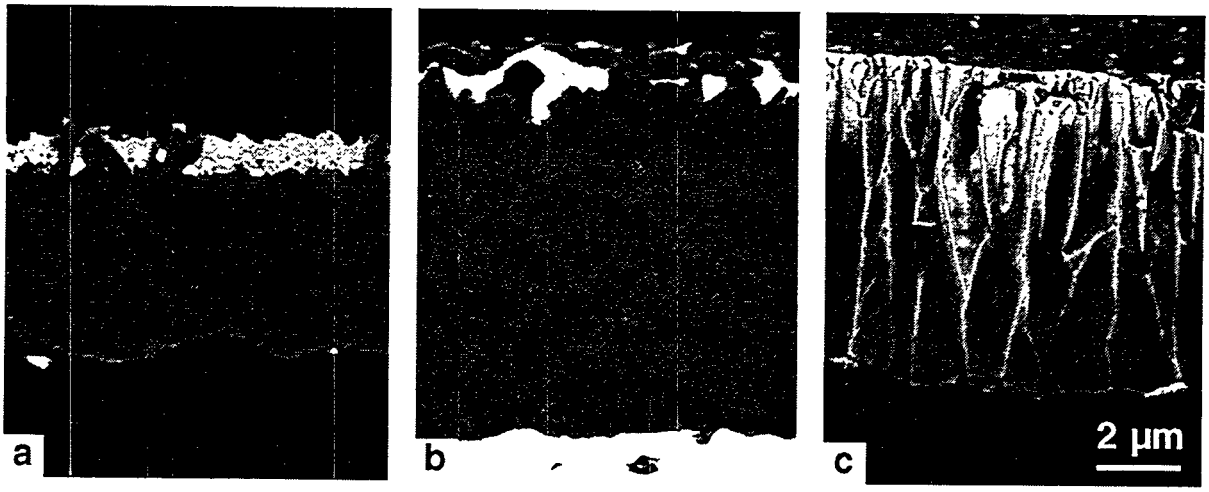

Fig. 10. SEM images of cross-sections of a) René N5, b) NCA-S and c) NCA-H after oxidation for 100 h at 1200°C.

On NCA-S, the scale (~9 µm) consists mainly of columnar Cr-doped α-Al_2O_3. The grain structure of the scale resembles that found on many reactive-element-doped alumina formers (e.g. - Refs. 6, 7, 18) and indicates alumina growth primarily by inward oxygen diffusion.[17] A thin, porous mixed layer of equiaxed spinel ($NiAl_2O_4$) and α-Al_2O_3, as well as some NiO formed on top of the alumina. Over time, NiO transforms to $NiAl_2O_4$ which eventually transforms to α-Al_2O_3; both transformations are pseudomorphic. Spallation of the scale occurred only in a few areas associated with the formation of Y_2O_3, $Y_3Al_5O_{12}$ (garnet) and α-Al_2O_3 at Y-rich alloy grain boundaries. Yttrium-rich oxide particles can be found on the scale surface. Using STEM/EDS analysis, yttrium was also found to be segregated at oxide grain boundaries and at the scale/metal interface.

The NCA-H alloy forms an oxide scale (~8 μm) that consists mainly of columnar Cr-doped α-Al_2O_3. Y-rich oxide particles can be found on the scale surface. The higher level of Y in this alloy results in the formation of Y-rich precipitates at all alloy grain boundaries. Preferential internal oxidation ultimately leads to the formation of Y_2O_3, $Y_3Al_5O_{12}$ (garnet) and α-Al_2O_3 at these grain boundaries. Due to the volume change and thermal mismatch associated with the formation of these phases, almost complete spallation of the oxide scale is initiated at these sites.

SUMMARY AND CONCLUSIONS

Alumina scales on iron-aluminides (Fe_3Al-based) and NiCrAl-based alloys were characterized in order to understand the relationship between the oxidation performance of alloys and the microstructure and microchemistry of their scales. Plasma-deposited amorphous alumina coatings on iron-aluminides were used to study phase transformations, transport processes in the scales and sulfur segregation to the scale/metal interface. It was found, that during heat treatment in the absence of oxidation, amorphous coatings first transform to γ-Al_2O_3 and eventually α-Al_2O_3 nucleates at the scale/metal interface. Sulfur from the Zr-free alloy segregates to the scale/metal interface during heat treatment. Thermally-grown scales on Zr-doped iron-aluminides were compared to those formed after oxidation of a specimen with an alumina coating. Microstructural and gravimetric results showed that the primarily amorphous alumina coating promoted the nucleation and growth of metastable alumina phases, which resulted in more rapid oxidation. The thermally-grown oxide was found on top of the coating. The NiCrAl-based alloys formed columnar alumina scales underneath a layer of mixed oxides. Segregation of alloying elements like Y, Hf and Ta was found at both oxide grain boundaries and scale/metal interfaces. The results from both alloy systems are consistent with previous results on primary alumina-formers. Reactive elements present in the alloy diffuse into the oxide scale and segregate to grain boundaries where they change the diffusion processes resulting in a columnar grain structure of the alumina scale.

ACKNOWLEDGMENT

The authors thank M. Howell for experimental support, B.A. Pint and I.G. Wright for technical discussions and E. A. Kenik for review of the manuscript. This research was sponsored by the Fossil Energy Advanced Research and Technology Development (AR&TD) Materials Program and the Division of Materials Science, U S. Department of Energy, DE-AC05-96OR22464 with Lockheed Martin Energy Research Corp. Research was performed in part with the SHaRE User Facilities at ORNL.

REFERENCES

1. J.G. Smeggil, A.W. Funkenbusch, N.S. Bornstein, Met. Trans. 17A (1986) 923.
2. E. Schumann, J.C. Yang, M.J. Graham and M. Rühle, Oxid. Met. 46 (1996) 37.
3. E. Schumann, Scripta Mater. 34 (1996) 1365.
4. C. Mennicke, E. Schumann, C. Ulrich and M. Rühle, Mat. Sci. Forum (1996) in press.
5. G.H. Meier, F.S. Pettit and J.L. Smialek, Mat. Corr. 46 (1995) 232.
6. B.A. Pint, Oxid. Met. 45 (1996) 1.
7. B.A. Pint and K.B. Alexander, submitted to J. Electrochem. Soc.
8. P.F. Tortorelli and K.B. Alexander, pp. 247-56 in *Proc. Ninth Annual Conf. Fossil Energy Materials*, N.C. Cole and R.R. Judkins (comp.), CONF-9505204, U. S. Department of Energy, August 1995.
9. P.F. Tortorelli and J.H. DeVan, pp. 257-70 in Processing, Properties, and Applications of Iron Aluminides, J.H. Schneibel and M.A. Crimp (eds.), The Minerals, Metals, and Materials Society, Warrendale, PA, 1994.
10. K.B. Alexander, K. Prüßner, P.Y. Hou and P.F. Tortorelli, 3rd Int. Conf. Microscopy of Oxidation, The Institute of Metals, London(1996) in press.
11. C.S. Giggins and F.S. Pettit, J. Electrochem. Soc. 118 (1971) 1782.
12. A. Kumar, M. Nasrallah and D.L. Douglass, Oxid. met. 8 (1974) 227.
13. I.G. Brown and Z. Wang, Proc. Ninth Annual Conf. Fossil Energy Materials, U.S. Department of Energy (1995) 239.
14. P.Y. Hou, Z. Wang, K. Prüßner, K.B. Alexander and I.G. Brown, 3rd Int. Conf. Microscopy of Oxidation, Cambridge (1996) in press.
15. P. Fox, D.G. Lees and G.W. Lorimer, Oxid. Met. 36 (1991) 491.
16. K. Prüßner, E. Schumann and M. Rühle, pp. 344-56 in Fundamental Aspects of High Temperature Corrosion, D. A. Shores, R. A. Rapp, and P. Y. Hou (eds.), Proc. Vol. 96-26, The Electrochemical Society, Pennington, New Jersey, 1997.
17. B. A. Pint, pp. 74-85 in Fundamental Aspects of High Temperature Corrosion, D. A. Shores, R. A. Rapp, and P. Y. Hou (eds.), Proc. Vol. 96-26, The Electrochemical Society, Pennington, New Jersey, 1997

MICROSTRUCTURAL AND MECHANICAL PROPERTY CHARACTERIZATION OF INGOT METALLURGY ODS IRON ALUMINIDE

V. K. Sikka and C. R. Howell

and

F. Hall* and J. Valykeo*

ABSTRACT

This paper deals with a novel, lower cost method of producing a oxide dispersion strengthened (ODS) iron-aluminide alloy. A large 250-kg batch of ODS iron-aluminide alloy designated as FAS was produced by Hoskins Manufacturing Company (Hoskins) [Hamburg, Michigan] using the new process. Plate and bar stock of the ODS alloy were the two major products received. Each of the products was characterized for its microstructure, including grain size and uniformity of oxide dispersion. Tensile tests were completed from room temperature to 1100°C. Only 100-h creep tests were completed at 800 and 1000°C. The results of these tests are compared with the commercial ODS alloy designated as MA-956. An assessment of these data is used to develop future plans for additional work and identifying applications.

INTRODUCTION

The Fe_3Al-based intermetallic alloys have been under development[1-5] at the Oak Ridge National Laboratory (ORNL) for a number of years. These alloys are attractive for coal gasification systems because of their excellent resistance[6] to high-temperature oxidation and sulfidation. To date, significant progress has been made in the development of alloy compositions with improved room-temperature ductility and high-temperature strength. However, the high-temperature strength at temperatures above 650°C continues to be a limiting factor in their applications to take full advantage of their excellent oxidation and sulfidation resistances. The oxide dispersion strengthening (ODS) is one possible method of improving the high-temperature strength of the iron aluminides. One method of producing the ODS materials is the attritor milling of alloy powder with Y_2O_3 powder, followed by consolidation, and grain-growth heat treatment. This method is the same as that used by Inco Alloys International, Inc. (Inco) [Huntington, West Virginia] to produce the commercial alloy MA-956. However, the cost

*Hoskins Manufacturing Company, 10776 Hall Road, Hamburg, Michigan.

of conventional processing of ODS materials is the limiting factor in their wide spread use. The purpose of this study was to ODS produce the Fe_3Al-based alloy by using an alternate low-cost method developed by Hoskins Manufacturing Company (Hoskins) [Hamburg, Michigan]. The low-cost method is designated as ingot metallurgy ODS iron aluminide. This paper will present the details of processing, microstructure, and properties of a heat of Fe_3Al-based alloy FAS that was ODS produced by Hoskins' method.

Processing

The Fe_3Al-based alloy FAS was chosen for this study. The FAS alloy consists of Fe-15.9 Al-2.2 Cr-0.01 B (weight percent) and has the best sulfidation resistance among the Fe_3Al-based alloys. A 500-kg heat of this alloy was prepared by air-induction melting at Hoskins. Table 1 is the chemical analysis of the heat which shows that it met the target composition extremely well. The alloy ingots were subsequently machined to remove any surface oxide and inert gas atomized to powder. The powder was blended with 0.5 wt % Y_2O_3 and processed by Hoskins' proprietary steps to billets that were subsequently processed to plate and bar. The plate was 15.9 mm thick, and the bar was 60.3 by 60.3 mm square with rounded corners. Figure 1 shows the plate and bar product received from Hoskins. The FAS + 0.5 wt % Y_2O_3 material is designated as 920 alloy, and its heat number is 21870.

A small section of the 15.9-mm plate was processed into 0.76-mm-thick sheet at ORNL. The processing steps consisted of hot rolling at 1100°C from 17.0 to 8.64 mm thickness, hot rolling at 800°C from 8.64 to 4.32 mm thickness, and warm rolling at 650°C from 4.32 to 0.76 mm thickness.

DISCUSSION OF CURRENT ACTIVITIES

The effort during this fiscal year continued to procure a large ingot metallurgy ODS iron-aluminide heat and characterize it for its mechanical and microstructural properties. The following activities were carried out and are briefly described below.

Testing Details

The 0.762-mm-thick sheet was die punched into 25.4-mm gage length tensile specimens. The specimens were tested after two heat treatments: 1 h at 700°C followed by oil quenching and 1 h at 1250°C in vacuum. Both sets of specimens were tensile tested from room temperature to 1000°C. Tensile specimens of 6.35 mm diam in the gage section were machined from the plate

Table 1. Comparison of target and check analyses of FAS alloy[a]

Element	Weight percent	
	Target	Powder
Al	15.9	16.0
Cr	2.2	2.17
B	0.01	0.010
C	--	0.014[b]
S	--	0.001[c]
Mo	--	0.01
Cb	--	<0.01
Zr	--	<0.01
N_2	--	0.005
O_2	--	0.030

[a]FAS alloy prepared by air-induction melting and used for oxide dispersion strengthening.

[b]Carbon was specified as 0.01 max.

[c]Sulfur was specified as 0.0020 max.

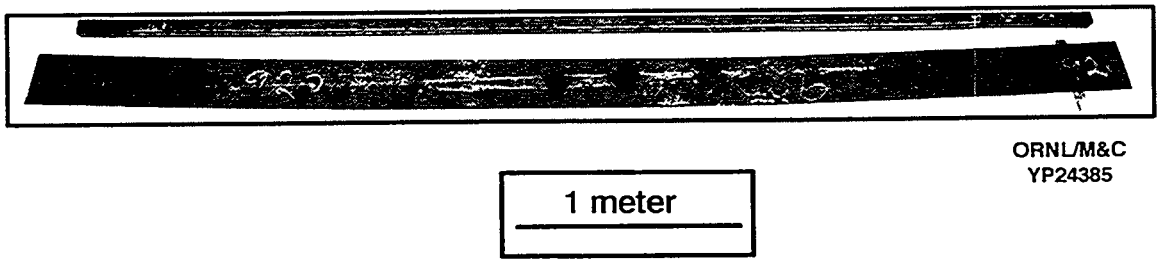

Figure 1. Hot-rolled plate and bar of 920 alloy. The plate is 15.9 mm thick by 210 mm wide, and the bar is 60.3 by 60.3 mm square with rounded corners.

and bar product. These were tensile tested in the as-hot rolled condition in the temperature range from room temperature to 1000°C. A limited number of creep tests were also conducted on the sheet, plate, and bar specimens. Optical and scanning electron microscopy were used to characterize the material.

Results

Tensile data on the sheet, plate, and bar are summarized in Table 2 and plotted in Figures 2 through 4. Data for the base FAS alloy is also included for comparison. These plots show the following:

1. The grain coursening treatment of 1250°C has a strong effect in reducing the room-temperature yield and ultimate tensile strengths. It also reduces the ductility by nearly 50%.
2. The large differences in yield strength between the grain coarsened sheet and the round specimens of plate and bar are associated with the specimen size.
3. The ultimate tensile strength, which is insensitive to the testing procedure, is more indicative of the true behavior. Data in Figure 3 shows that sheet has the highest strength in the fine-grained condition, which is reduced by the grain coarsening treatment of 1250°C for 1 h. The plate and bar of coarse-grained structure show even lower values at room temperature.
4. The yield and ultimate tensile strength properties are relatively unaffected by test temperatures of 600, 800, and 1000°C.
5. The room-temperature elongation is most affected by either grain coarsening treatment of the sheet or testing of coarse-grained hot-rolled plate and bar. It is interesting to note that the coarse-grained material has the highest ductility at temperatures ≥ 800°C and lowest at room temperature in comparison to fine-grained material that showed the highest ductility at room temperature and the lowest at ≥ 800°C. The elongation trends at intermediate temperatures of 600 and 800°C are not quite straightforward. In any event, the ductility at test temperatures of 600, 800, and 1000°C is sufficiently high to be of no concern.
6. At test temperatures of ≥ 600°C, the ODS produced material is consistently higher in strength than the base material. At 800°C, the yield and ultimate tensile strengths are higher by a factor of nearly two.

The creep rupture data for the sheet, plate, and bar are plotted as Larson Miller parameter in Figure 5 and shown in Table 3. Also included in this plot are the data for the base Fe_3Al alloys (FAS, FAL, and FA-129), a commercially produced mechanically alloyed MA-956 produced by Inco, and an ingot metallurgy Fe-Cr-Al-based ODS material (877) produced at Hoskins. This figure shows that while the Hoskins process significantly enhanced the creep properties of their Fe-Cr-Al alloy, it produced only a small effect for the FAS alloy. Note however that even though small, it is still a factor of nearly two improvement in creep rupture strength of the base FAS alloy.

Table 2. Tensile property data for 920 alloy (heat 21870) of FAS + 0.5 wt % Y_2O_3

Specimen no.	Test temperature (°C)	Heat treatment	Yield strength (MPa)	Tensile strength (MPa)	Total elongation (%)	Reduction of area (%)
2L[a]	23	Sheet Annealed 700°C/1 h OQ[b]	414	979	16.45	14.16
8L[a]	23	Sheet Annealed 1250°C/1 h Vacuum	370	775	7.37	8.84
14L[c]	23	Plate As rolled	515	578	2.18	2.23
22L[c]	23	Bar As rolled	491	572	1.91	3.34
4L[a]	600	Sheet Annealed 700°C/1 h Oq[b]	365	382	43.95	55.14
10L[a]	600	Sheet Annealed 1250°C/1 h Vacuum	356	402	42.00	62.80
15L[c]	600	Plate As rolled	394	399	46.53	70.04
23L[c]	600	Bar As rolled	386	393	59.84	77.76

Table 2. (Continued)

Specimen no.	Test temperature (°C)	Heat treatment	Yield strength (MPa)	Tensile strength (MPa)	Total elongation (%)	Reduction of area (%)
5L[a]	800	Sheet Annealed 700°C/1 h Vacuum	95	97	53.75	69.95
9L[a]	800	Sheet Annealed 1250°C/1 h	89	92	42.95	73.75
16L[c]	800	Plate As rolled	86	95	62.86	86.36
24L[c]	800	Bar As rolled	108	109	63.64	93.80
6L[a]	1000	Sheet Annealed 700°C/1 h OQ	17	20	79.30	81.99
11L[a]	1000	Sheet Annealed 1250°C/1 h Vacuum	18	18	102.10	71.80
17L[c]	1000	Plate As rolled	16	18	111.08	89.75
25L[c]	1000	Bar As rolled	17	18	111.20	--

[a]Strain rate: $3.33 \times 10^{-3} s^{-1}$.

[b]OQ = oil quenched.

[c]Strain rate: $2.67 \times 10^{-3} s^{-1}$.

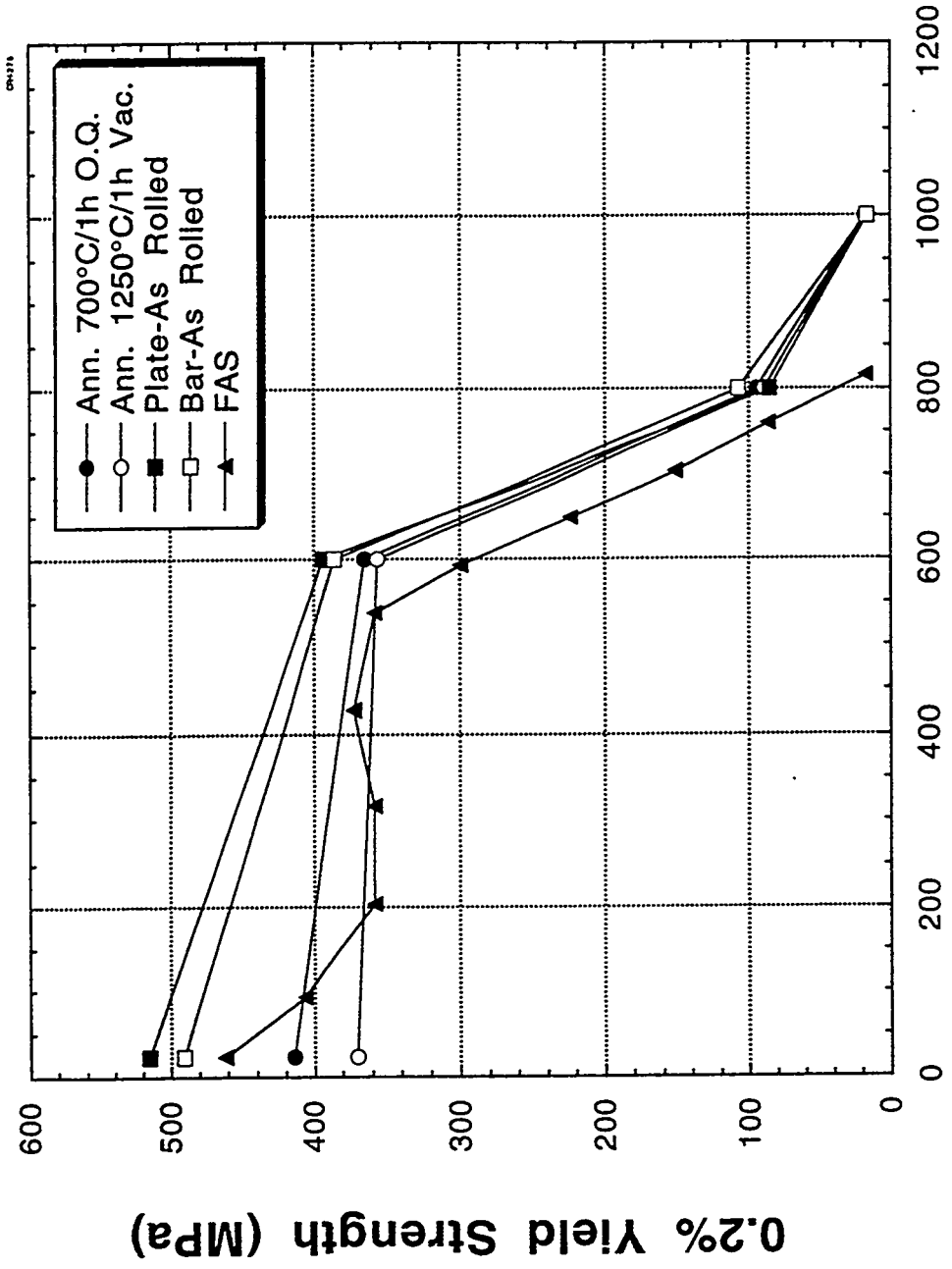

Figure 2. Yield strength (0.2% offset) as a function of test temperature for sheet, plate, and bar of 920 alloy.

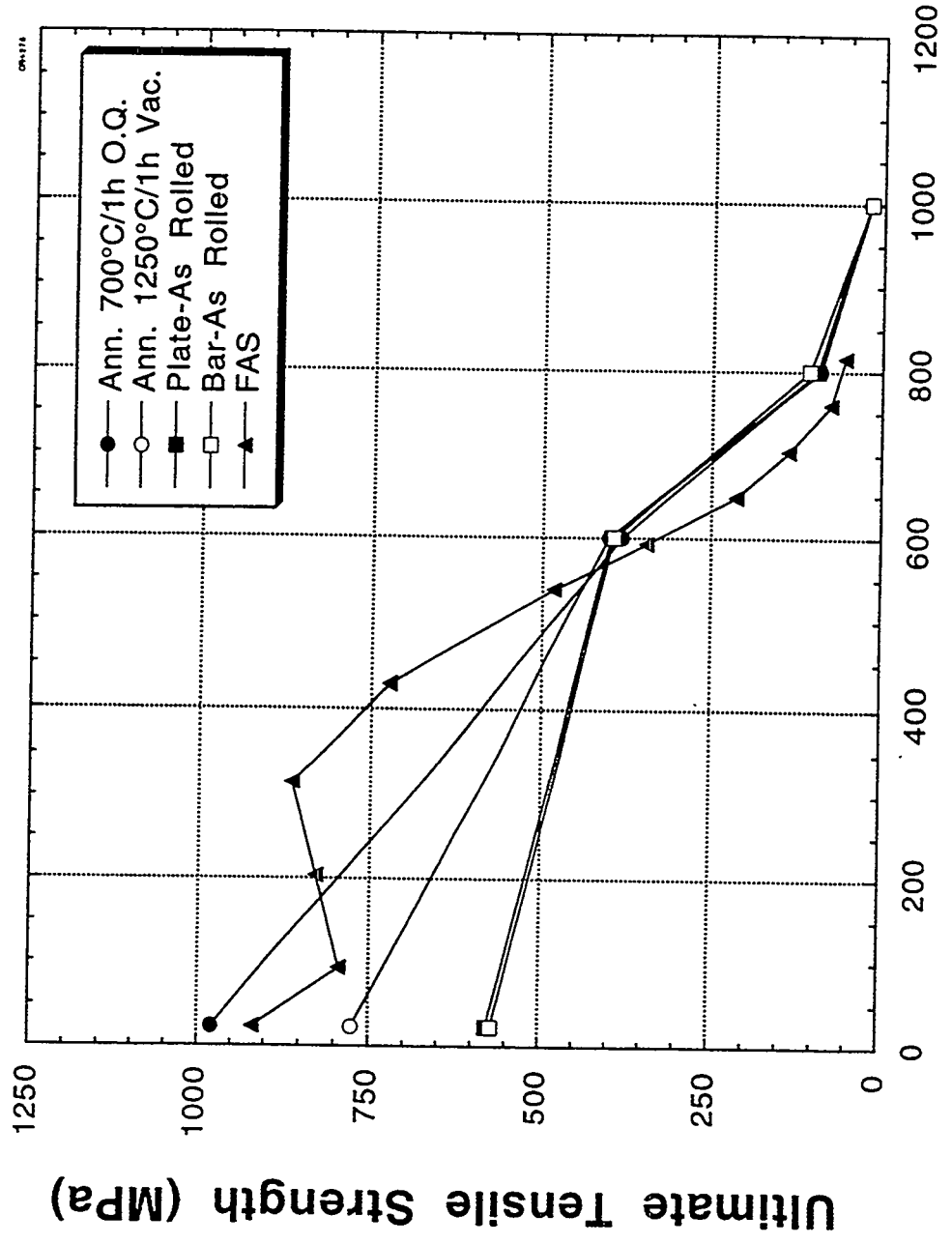

Figure 3. Ultimate tensile strength as a function of test temperature for sheet, plate, and bar of 920 alloy.

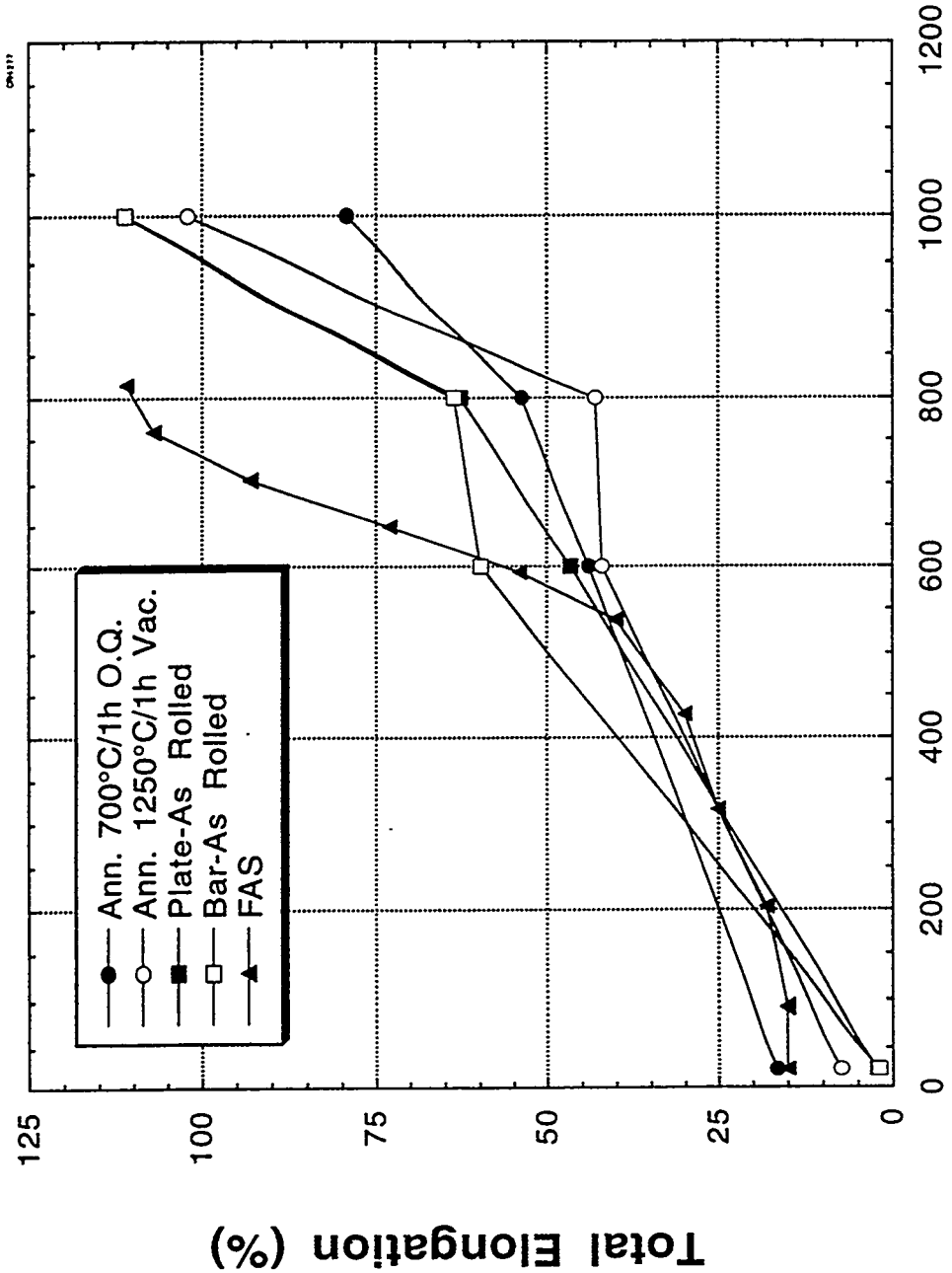

Figure 4. Total elongation as a function of test temperature for sheet, plate, and bar of 920 alloy.

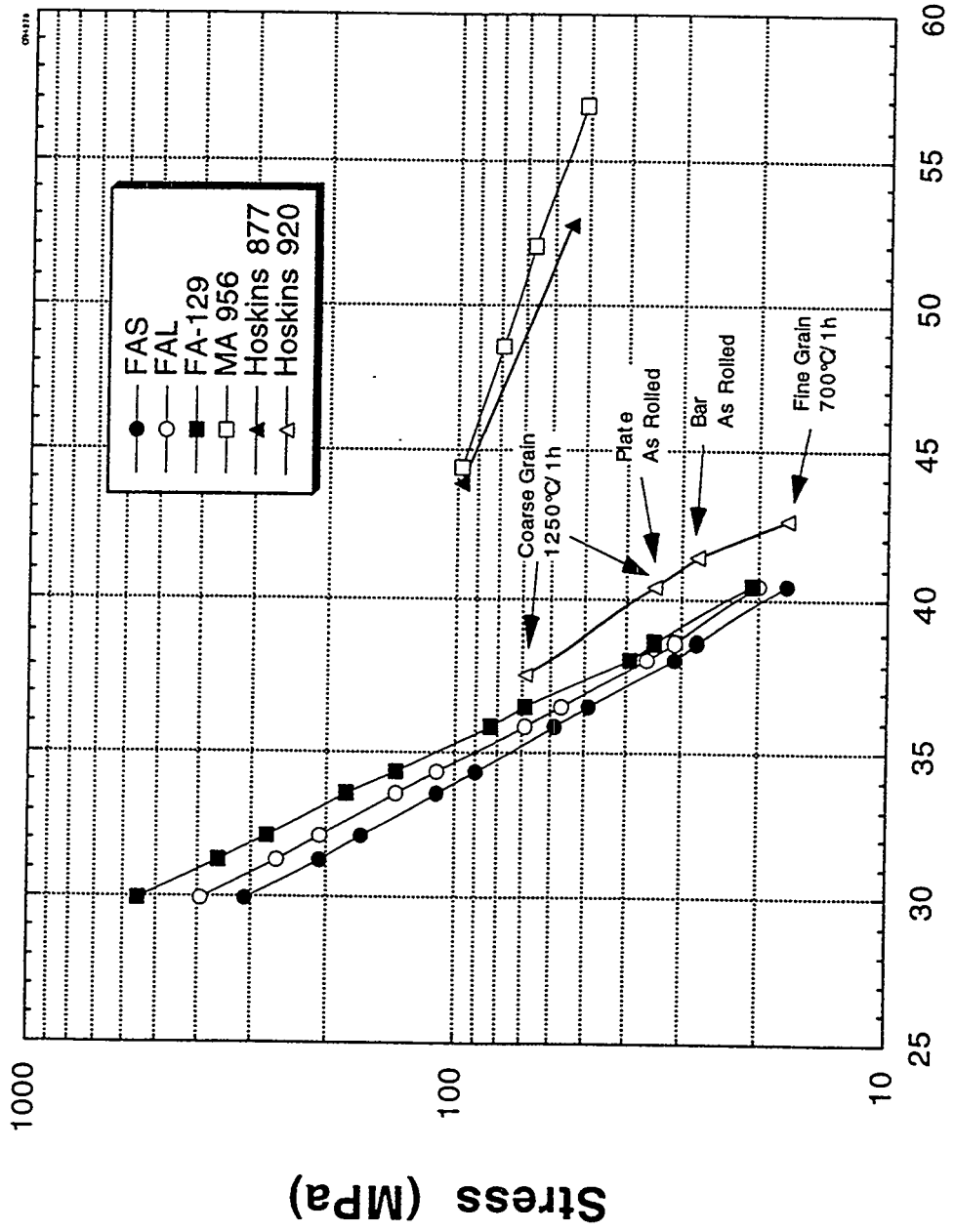

Figure 5. Larson Miller plot of creep rupture data for sheet, plate, and bar of 920 alloy.

Table 3. Creep property data for 920 alloy (heat 21870) of FAS + 0.5 wt % Y_2O_3

Specimen no.	Heat treatment	Test temperature (°C)	Stress (MPa)	Status[a]	Time (h)	Total elongation (%)	Reduction of area (%)
1L	Sheet Annealed 700°C/1 h OQ[b]	980	69	R	0.0	3.72	83.30
3L	Sheet Annealed 700°C/1 h OQ[b]	800	17	R	113.8	3.53	29.20
7L	Sheet Annealed 1250°C/1 h Vacuum	800	35	R	11.7	62.50	61.50
12L	Sheet Annealed 1250°C/1 h Vacuum	700	69	R	29.9	71.40	63.97
13L	Plate As rolled	800	35	R	6.0	126.37	85.33
21L	Bar As rolled	800	28	R	27.5	99.76	86.88

[a]R = ruptured.

[b]OQ = oil quenched.

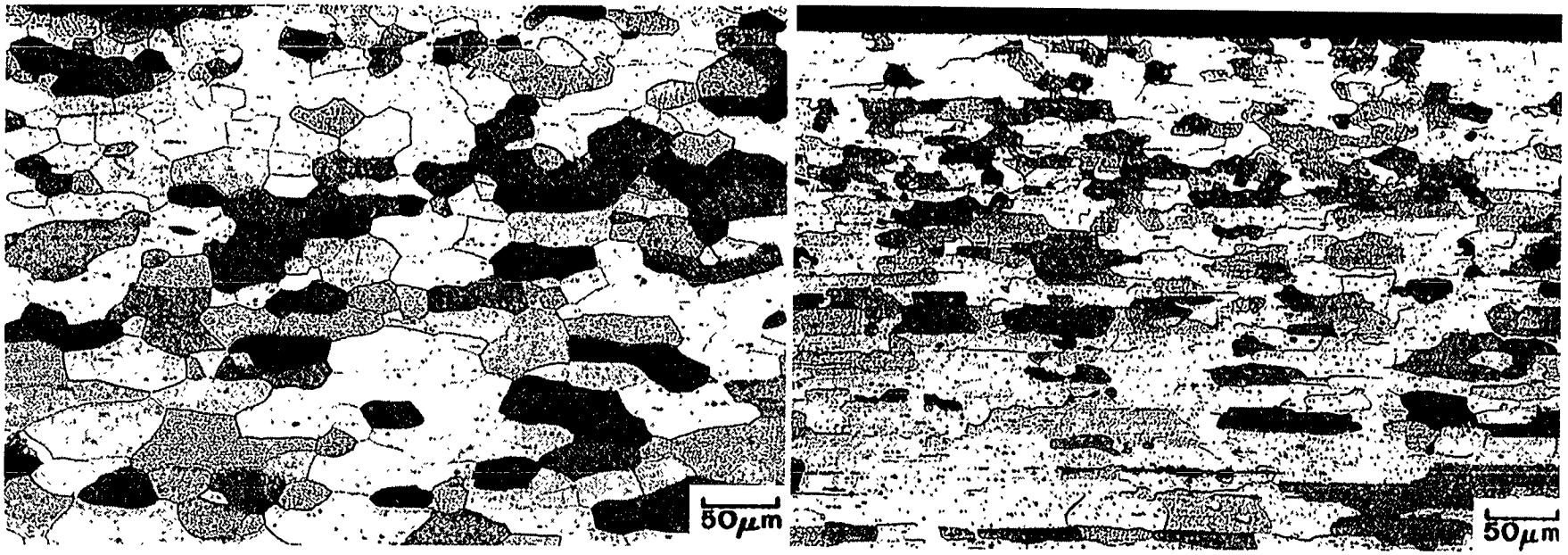

(*a*) 97-0524-10 (*b*) 97-0700-2

Figure 6. Optical microstructure of the longitudinal section of a 0.76-mm-thick sheet of ingot metallurgy oxide dispersion strengthened FAS alloy: (*a*) air annealed for 1 h at 700°C followed by oil quenching, and (*b*) vacuum annealed for 1 h at 1250°C. The magnification for both (*a*) and (*b*) is 200×.

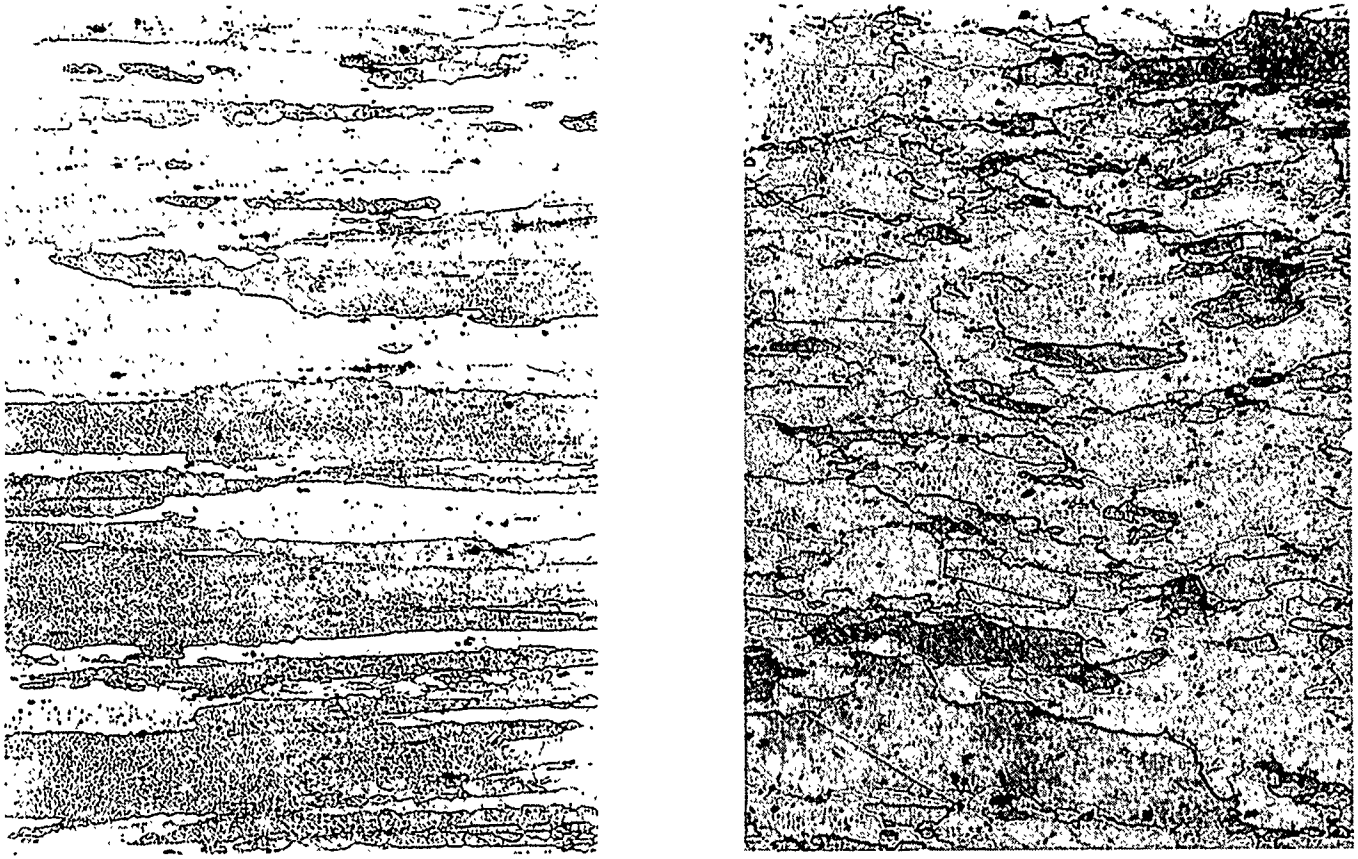

Figure 7. Optical micrographs of etched 15.9-mm-thick plate of ingot metallurgy oxide dispersion strengthened FAS alloy: (*a*) longitudinal and (*b*) transverse. The magnification for both (*a*) and (*b*) is 200×.

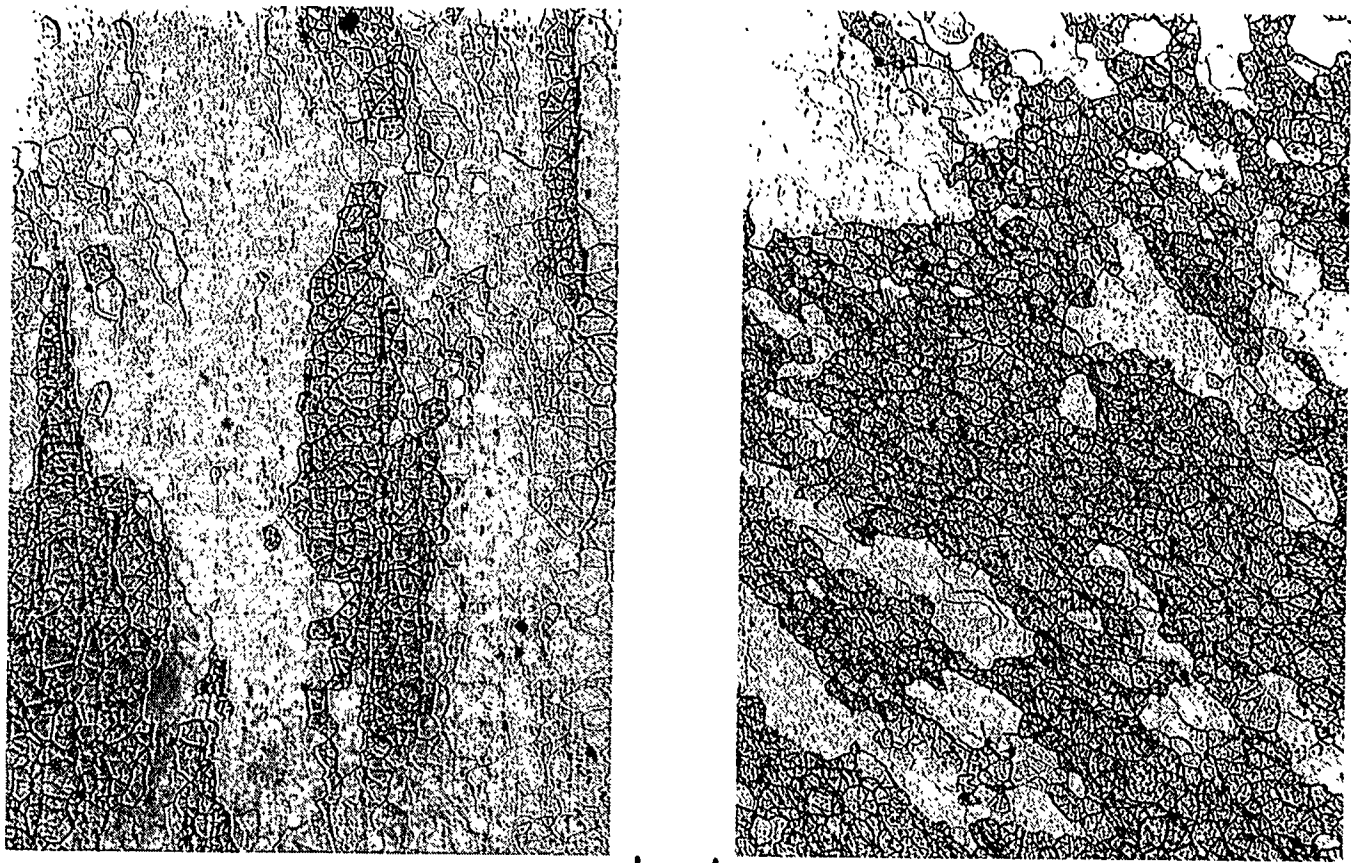

(*a*) 97-0469-003

(*b*) 97-0470-003

Figure 8. Optical micrographs of etched 60.3 mm rounded corner bar of ingot metallurgy oxide dispersion strengthened FAS alloy: (*a*) longitudinal and (*b*) transverse. The magnification for both (*a*) and (*b*) is 200×.

The optical microstructures of the sheet in the fine- and coarse-grained heat-treated conditions are shown in Figure 6. The microstructures of the plate and bar are shown in Figures 7 and 8. The sheet and plate show elongated grains in the rolling direction, and the microstructure is uniform across the thickness. The bar showed a inhomogeneous microstructure that consisted of large grains and large grains with colonies of fine grains, which may have resulted from the dynamic recrystallization process.

The backscattered electron micrographs of transverse sections of the plate and bar are shown in Figure 9. The low magnification micrographs show a fairly uniform distribution of Y_2O_3 particles. The higher magnification micrographs show the Y_2O_3 particles to be clusters. The porosity observed in the high magnification micrographs is a result of Y_2O_3 particle drop-out during metallographic specimen preparation.

Elemental mapping was carried out on one of the large particle areas to determine their composition (Figure 10). It is clear from these maps that the large particles consist of yttrium and oxygen and have no iron or aluminum associated with them.

DISCUSSION

The ingot metallurgy method for ODS, developed by Hoskins, has worked effectively for creep strengthening of their Fe-Cr-Al alloy. However, the same method when applied to the ORNL-developed Fe_3Al-based alloy FAS showed less benefit in improvement of creep strength. Detailed metallography has revealed that the primary cause for less improvement in the FAS material is the presence of Y_2O_3 agglomerates rather than the finer distribution that is required for strengthening. Even though the full property enhancement was not observed, the Y_2O_3-treated FAS alloy still showed nearly two times higher creep rupture strength values than the untreated material. The Y_2O_3-treated alloy also showed nearly a factor of two higher yield and ultimate tensile strengths at temperatures $\geq$ 600°C. A second heat of the alloy is planned to check if Y_2O_3 distribution can be refined to produce a finer uniform distribution.

The sheet produced by rolling the plate was used to determine if grain growth treatment resulted in further improvement of creep strength. Metallography of the sheet specimens with 700 and 1250°C treatments showed that the later treatment did not produce a significant increase in grain size. Work is currently under way to look at heat-treatment temperatures of 1350 and 1400°C for 1 h. The specimens heated for grain growth will be subjected to creep testing to determine the resulting strength improvement.

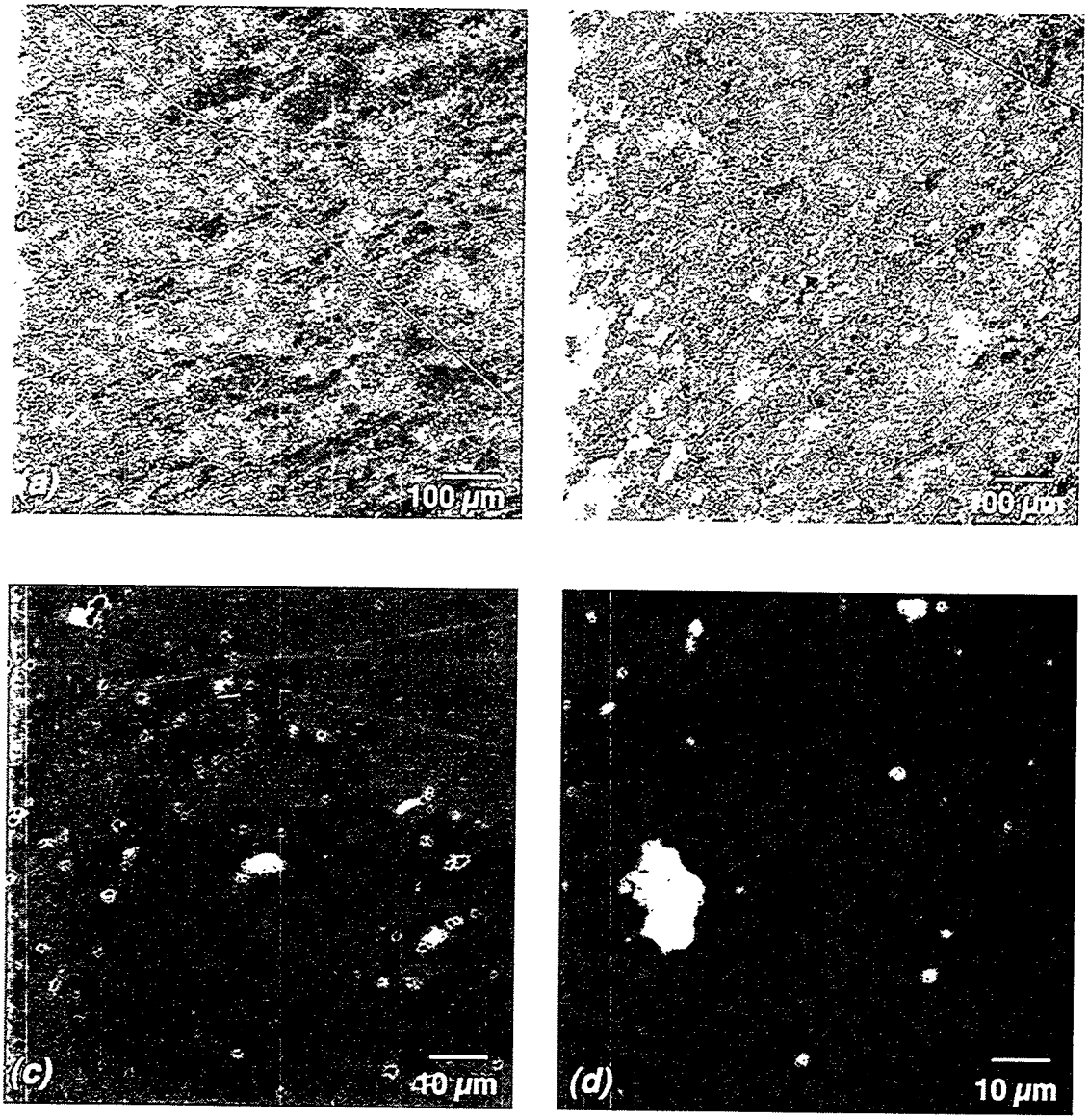

Figure 9. Scanning electron micrographs of transverse sections of plate and bar products of ingot metallurgy oxide dispersion strengthened FAS alloy: (*a*) plate and (*b*) bar are low magnification, and (*c*) plate and (*d*) bar are high magnification.

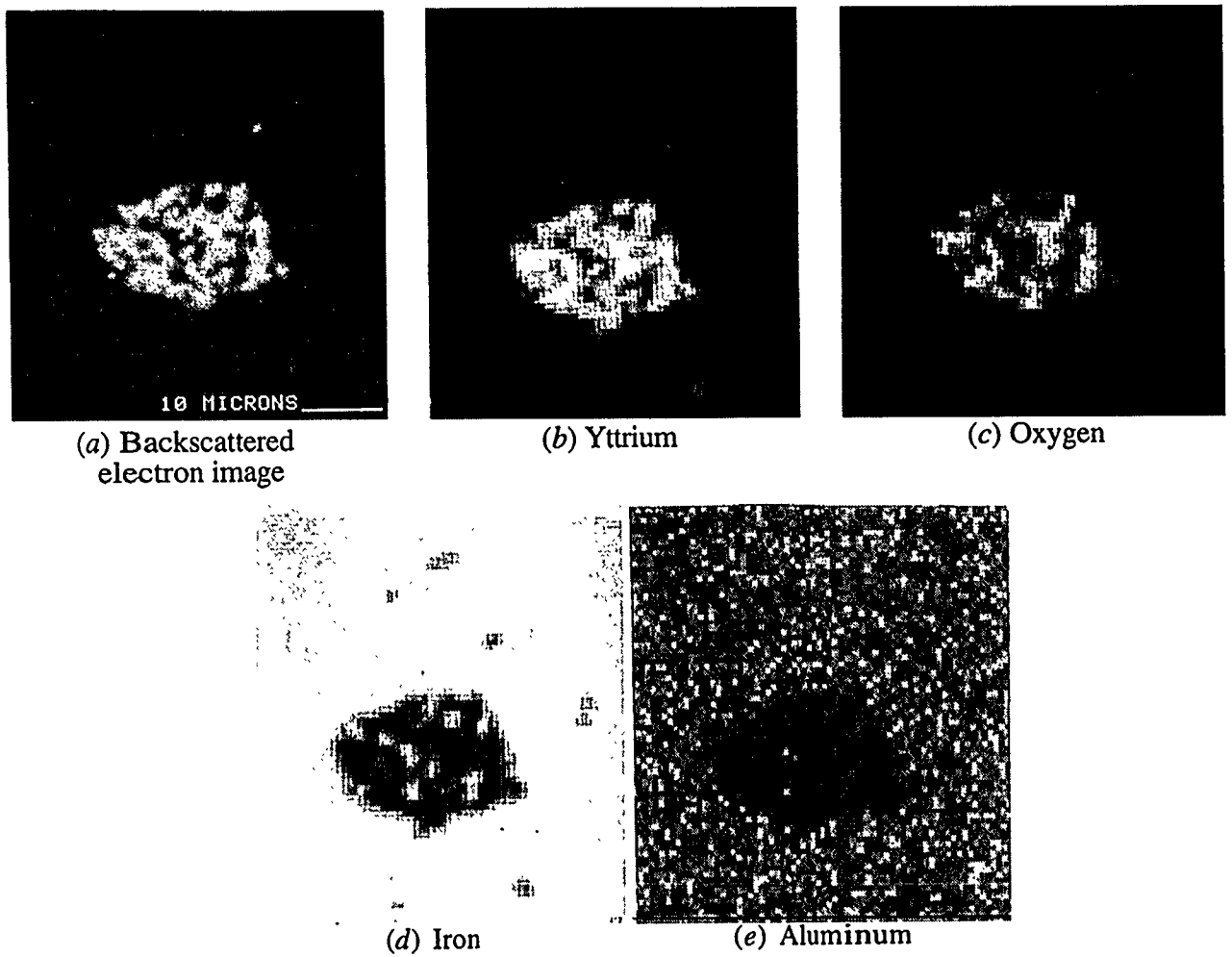

(*a*) Backscattered electron image

(*b*) Yttrium

(*c*) Oxygen

(*d*) Iron

(*e*) Aluminum

Figure 10. Scanning electron micrographs showing: (*a*) backscattered electron image of the particles in ingot metallurgy oxide dispersion strengthened FAS. Elemental maps of yttrium, oxygen, iron and aluminum are shown in (*b*), (*c*), (*d*), and (*e*), respectively.

SUMMARY AND CONCLUSIONS

A lower cost method developed by Hoskins was used to produce an ODS heat of Fe_3Al-based alloy FAS. The alloy contained 0.5% Y_2O_3 and was processed into plate, bar, and sheet. Tensile, creep, and metallography were carried out on all three products. To date, data have shown only moderate improvement in creep properties as opposed to Y_2O_3-free material. It is also shown that the Hoskins process works for a Fe-Cr-Al alloy (877). It is believed that Y_2O_3 particle clusters are the cause for limited improvement observed in creep properties. A second heat of FAS is being planned by Hoskins' method.

ACKNOWLEDGMENTS

The authors thank Dave Harper and Ken Blakely for cutting and processing the ingots, Hu Longmire for optical metallogjraphy, Larry Walker for scanning electron microscopy work, and Millie Atchley for preparing the manuscript.

Research for this work was sponsored by the U.S. Department of Energy, Office of Fossil Energy, Advanced Research and Technology Development Materials Program [DOE/FE AA 15 10 10 0, Work Breakdown Structure Element ORNL-2(H)], under contract DE-AC05-96OR22464 with Lockheed Martin Energy Research Corp.

REFERENCES

1. C. G. McKamey, J. H. DeVan, P. F. Tortorelli, and V. K. Sikka, *J. Mater. Res.*, **6**, 1779-805 (1991).
2. V. K. Sikka, S. Viswanathan, and S. Vyas, *High Temperature Ordered Intermetallic Alloys V*, Vol. 288, p. 971, Materials Research Society, Pittsburgh, Pennsylvania, 1993.
3. V. K. Sikka, S. Viswanathan, and C. G. McKamey, *Structural Intermetallics*, p. 483, The Minerals, Metals and Materials Society, Warrendale, Pennsylvania, 1993.
4. C. G. McKamey and D. H. Pierce, *Scr. Metall. Mater.*, **28**, 1173-6 (1993).
5. P. G. Sanders, V. K. Sikka, C. R. Howell, and R. H. Baldwin, *Scr. Metall. Mater.*, **25**, 2365-9 (1991).
6. K. Natesan and P. F. Tortorelli, *International Symposium on Nickel and Iron Aluminides: Processing, Properties, and Applications*, p. 265, ASM International, Materials Park, Ohio, 1997.

SIMULTANEOUS ALUMINIZING and CHROMIZING of STEELS to FORM $(Fe,Cr)_3Al$ COATINGS and Ge-DOPED SILICIDE COATINGS of Cr-Zr BASE ALLOYS

Minhui Zheng, Yi-Rong He and Robert A. Rapp

Department of Materials Science and Engineering
The Ohio State University
Columbus, Ohio 43210 (U.S.A.)

A halide-activated cementation pack involving elemental Al and Cr powders has been used to achieve surface compositions of approximately Fe_3Al plus several percent Cr for low alloy steels (T11, T2 and T22) and medium carbon steel (1045 steel). A two-step treatment at 925°C and 1150°C yields the codeposition and diffusion of aluminum and chromium to form dense and uniform ferrite coatings of about 400μm thickness, while preventing the formation of a blocking chromium carbide at the substrate surfaces. Upon cyclic oxidation in air at 700°C, the coated steel exhibits a negligible 0.085 mg/cm^2 weight gain for 1900 one-hour cycles. Virtually no attack was observed on coated steels tested at ABB in simulated boiler atmospheres at 500°C for 500 hours. But coatings with a surface composition of only 8 wt % Al and 6 wt% Cr suffered some sulfidation attack in simulated boiler atmospheres at temperatures higher than 500°C for 1000 hours.

Two developmental Cr-Zr based Laves phase alloys (CN129-2 and CN117(Z)) were silicide/germanide coated. The cross-sections of the Ge-doped silicide coatings closely mimicked the microstructure of the substrate alloys. Cyclic oxidation in air at 1100°C showed that the Ge-doped silicide coating greatly improved the oxidation resistance of the Cr-Zr based alloys.

INTRODUCTION

Recent papers, e.g. by DeVan et al.[1,2] show that the alloy compositions based on Fe_3Al are very resistant to sulfidation and oxidation at high temperatures, but that a low Cr content is also required to provide resistance to room temperature aqueous corrosion (leading to hydrogen embrittlement) and resistance to high temperature hot corrosion by fused salt deposits, e. g. coal fly ash. Natesan and Johnson[3] reported that a threshold Al content in excess of 10 wt% is needed in Fe-Al alloys for adequate corrosion resistance in sulfur-containing atmospheres, while the Cr content in the alloy played a critical role for corrosion resistance in HCl-containing environments.

Geib and Rapp[4,5] and Miller et al.[6] codeposited Cr-Al diffusion coatings on low-alloy steels and stainless steels, respectively, using a 85Cr-15Al masteralloy powder as a pack component. The surface composition sought by those studies was Fe-20Cr-4.5Al. That process specified the use of a Cr-Al

masteralloy powder which is expensive and probably cannot be recycled or rejuvenated. A preferred pack cementation process would use a mixture of pure elemental powders, which are less expensive than masteralloy powders, and would incorporate a thermal processing schedule that would not impair the strength of the metal. The current study describes a pack cementation process which develops an Al-Cr coating on carbon-containing steels by a two-step temperature program. To avoid the formation of a chromium carbide blocking layer, the steel substrate is aluminized first at a lower temperature and then is chromized at a higher temperature. In this regard, the process is similar to that for codepositing Cr and Si diffusion coatings onto steels.[7,8]

The demand for higher strength and high service temperatures of structural materials had led to the consideration of Laves phase-based alloys.[9,10] A Laves phase compound with the AB_2 stoichiometry shows either the hexagonal C14 structure, the cubic C15 structure, or the hexagonal C36 structure. The complex crystal structures of the Laves phase make the compound inherently strong but brittle. In binary refractory-metal chromium systems such Cr-Ti, Cr-Zr, Cr-Hf, Cr-Nb and Cr-Ta, these Laves phases are in equilibrium with Cr via eutectic reactions. For the Cr-Zr binary system, the eutectic temperature is about 1630°C; the melting point of Cr_2Zr is about 1675°C. The Laves phase Cr_2Zr undergoes a polymorphic transformation from a low-temperature C14 structure to the high-temperature C15 structure at about 1000°C.[11]

Recently, two Cr-Zr based alloys (CN117(Z) and CN129-2) have been prepared and studied at Oak Ridge National Laboratory(ORNL) as possible advanced high-temperature structural materials. Preliminary isothermal oxidation tests at 950°C and 1100°C at ORNL show that the alloys exhibit only fair to poor isothermal oxidation resistance. Also, the CN129-2 alloy catastrophically failed a 6 cycle, 120 hour screening test at 1100°C. These results indicate the need for a protective coating of the alloys for high temperature applications. A previous study at OSU showed that a Ge-doped silicide coating can protect Cr-Nb based alloys from significant oxidation and from pesting under cyclic and isothermal oxidation conditions.[12] Therefore, the goal of this research is to develop a Ge-doped silicide coating on the Cr-Zr based alloys by the pack cementation technique, to characterize the coating, and to test its oxidation resistance.

THERMODYNAMIC CONSIDERATIONS

To understand the chemical reactions taking place during the pack cementation process, the equilibrium vapor pressures of the halides generated by the pack powder mixtures at 1200K and 1400K were calculated using the PC-compatible STEPSOL computer program modified by Morris et al. from the ITSOL program.[13,14] The program calculates the equilibrium vapor pressures in the pack by minimizing

the Gibbs energy of the system. In fact, the activity of Al and the AlCl vapor pressure must drop during the deposition process, not only because of Al uptake by the substrate, but especially due to alloying of Al with the Cr powder. The dominant deposition species are AlCl and $CrCl_2$. For a fluoride-activated pack, the effective deposition species is AlF, and the partial pressures for the Cr fluorides are too low for Cr deposition, so a chloride activator is always needed to chromize. Kung and Rapp[15] presented such calculations for coatings involving a single component. He, Wang and Rapp[16] examined the use of various mixed activator salts for Cr-Si codeposition.

The deposition and diffusion of Cr into a steel which contains carbon is often limited by the formation of chromium carbide. Menzies and Mortimer[17] classified the coating structures into two groups: those for steels with carbon contents below 0.2 wt% C, which exhibited carbide formation along grain boundaries and as precipitates within the grains of the ferritic coating, and steels containing more than 0.2 wt% C, which usually formed a continuous chromium carbide layer at the surface of the coating. Since the solubility of Al in austenite is restricted to a low wt%, introducing Al into a steel substrate produces a ferrite layer with very low carbon solubility at the surface. Therefore carbon is rejected into the austenite core. This process is illustrated schematically in Fig.1. After forming a low-carbon Al-rich ferrite case at a low temperature, the codeposition of Cr becomes possible at a higher temperature, especially because the Al powder has been depleted upon alloying with the Cr powder and the substrate.

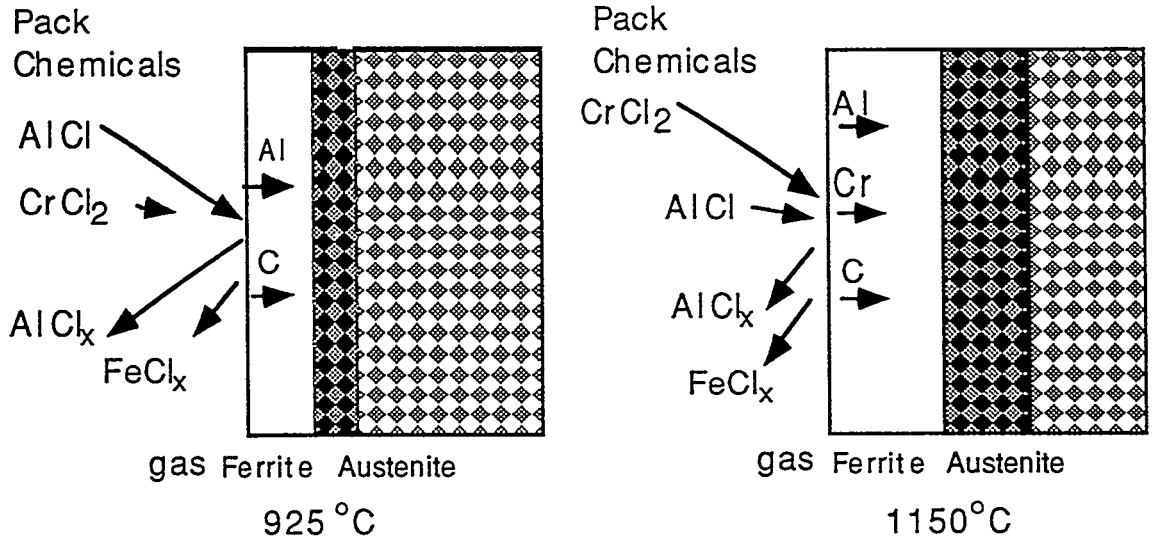

Fig. 1 Schematic of two-step pack cementation coating process. Longer arrows correspond to higher vapor pressures. The darkened area represents a zone of carbon enrichment in austenite. Microstructure of T11 steel coated in pack with 2Al-18Cr, $2CrCl_2$ at 925°C for 4 hours then at 1150°C for 3 hours.

From the STEPSOL program, the thermodynamic equilibria in the Cr-Al system containing various halide activators have been calculated. The presence of $CrCl_2$ is too low for significant transport at 1200K, but is much higher at 1400K. All chloride activators and their combinations generate higher AlCl vapor pressure and much lower vapor pressures for $CrCl_2$. Thus, a steel substrate will be aluminized preferentially at 1200K. Then upon raising the temperature to about 1400K, the substrate can gain chromium delivered by the $CrCl_2(g)$ species.

EXPERIMENTAL PROCEDURES

Coupons of T11 steel with composition Fe-1Cr-0.5Mo-0.15C or T2 steel with composition Fe-0.5Cr-0.5Mo-0.15C were cut from tubes or plates. The surface areas were about 1.5 cm^2. These coupons were ground through 600 grit SiC paper, cleaned, dried and weighed. The coupons were placed in an alumina crucible in contact with a mixed powder containing elemental Al and Cr powders, a chloride activator salt(s) and an inert alumina filler powder plus 2wt% cerium oxide. The alumina crucible was closed with an alumina lid using an alumina-base cement and then placed in a horizontal electric furnace purged with prepurified Ar. The furnace was heated to a desired temperature (±5°C) and held for the prescribed duration; for the current experimentation, an isothermal hold at 925°C for several hours was followed by a further hold at 1150°C. After cooling in the furnace, the crucible was opened and the coated substrates were cleaned and reweighed. The surface phase was identified with X-ray diffraction (XRD) using a SCINTAG diffractometer. An optical microscope was used to observe and photograph the coating cross-section. A scanning electron microscope (SEM) with an energy dispersive X-ray spectrometer (EDS) was used to determine the concentration profiles across the coating cross-section. Some coating compositions were also analyzed with a wave length dispersive X-ray spectrometer (WDS) to verify the reliability of the composition analyses.

Alloys of CN117(Z) and CN129-2 were used as the substrates. These alloys contain approximately 5-8 at.% Zr, and minor alloying additions of several other elements at concentrations less than 5 at.%. The EDM sliced CN117(Z) and CN129-2 alloys were prepared to a 600 grit finish. The as-cast CN129-2 coupons contained cracks. The cementation pack consisted of pure elemental powders of Si and Ge, NaF activator and Al_2O_3 inert filler. The detailed procedure for pack cementation was described in the previous study.[12] A 1-h cycle in air at 1100°C consisting of 45 min heated and 15 min cooled was used for cyclic oxidation study.

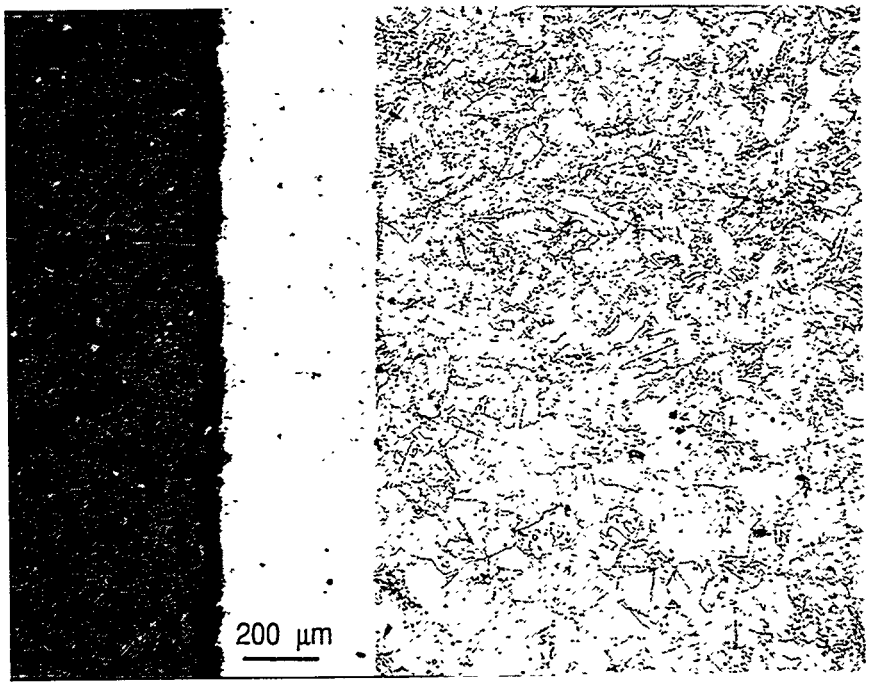

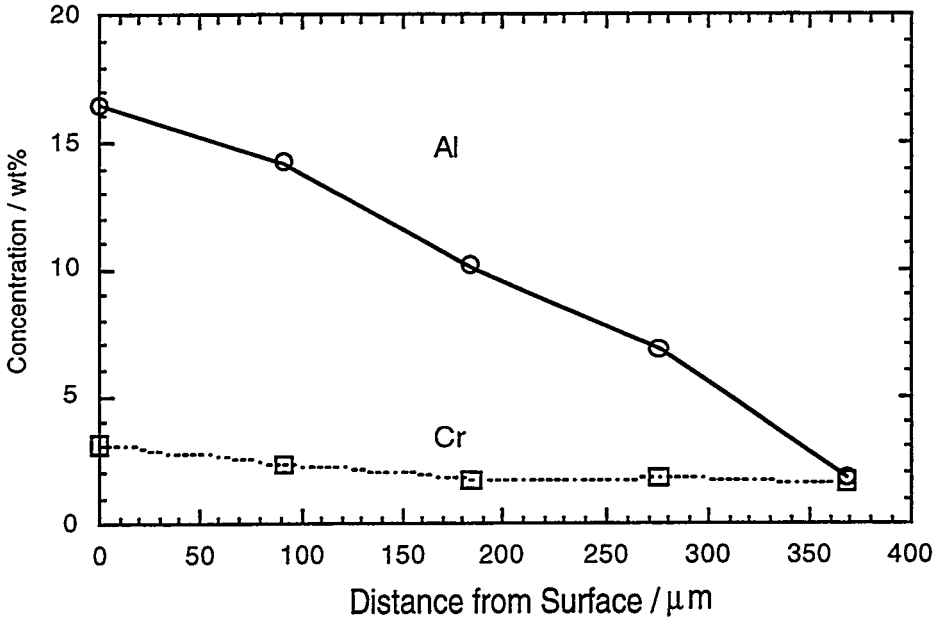

Fig. 2 Coating microstructure and EDS composition profile for T11 steel sample (NH_4F and $MgCl_2$ dual activators, heating sequence: 925°C for 8 hours, then at 1150°C for 4 hours).

RESULTS AND DISCUSSION

For the T11 steel samples, the phase transformation from ferrite to austenite occurs at about 888°C. Preliminary coating tests showed that at a temperature lower than about 920°C most T11 substrates lost weight by $FeCl_2$ evaporation and formed a porous coating. Thus, the temperature for the first-step treatment was set at 925°C. Other prior coating tests showed that a one-step treatment at 1150 °C resulted in chromium carbide layers on the substrates, accompanied by decarburization.

Figure 2 presents a representative coating microstructure and the corresponding composition profile for a T11 steel sample. A dual activator of 1 wt% NH_4F and 2 wt% $MgCl_2$ were used with Al_2O_3 plus 2 wt% CeO_2 as the filler. A two-step heating schedule consisted of 925°C for 8 hours followed by 4 hours at 1150°C. A dense ferrite layer of about 400μm thickness was formed, and the inward diffusion of carbon insured the absence of any denuded zone of decarburiztion. The surface composition was about 16 wt% Al, 3 wt% Cr. For all of the coatings produced in this work, the compositions at the external surface ranged from 13-17 wt% Al and 3-6 wt% Cr. Stoichiometric Fe_3Al has 13.8 wt% Al. Upon rather slow cooling from the 1150°C coating temperature, the ferrite grains of the coating grow inward to eliminate the coating/core interface which existed at the high temperature. Thus, the ferrite grains of the coating extend into the prior austenite core of the substrate, providing an excellent bond of the coating to the substrate. Indeed, after cooling, no interphase interface exists, only a discontinuity in the composition.

Table 1 presents the coating characteristics for some example packs with a mixture of elemental Al and Cr powders using single or dual activators and similar heating schedules. The surface compositions were consistently around 12-17 wt% Al and 6-3 wt% Cr. The cementation packs using NH_4Cl or NH_4F generally resulted in slightly higher aluminum content in the coatings. Although thermodynamic calculations indicate that CeO_2 can be partially reacted to form $CeCl_3$ (v), no Ce has been detected by EDS or WDS in the coatings produced using packs containing CeO_2 powder. Apparently the amount of Ce deposited into the coating was too small to be detected by the mentioned methods.

OXIDATION/CORROSION TESTING OF $(Fe, Cr)_3Al$ COATED STEELS

A coated T11 coupon, with surface composition of 15.9 wt% Al and 2.8 wt% Cr was tested in cyclic oxidation in air at 700°C for 1900 one-hour cycles, and a quite negligible weight gain of 0.085 mg/cm^2 was recorded, with an absence of scale spallation. Therefore, this coating composition forms a very adherent, very slow growing alumina scale in air oxidation.

Table 1 Contents of Example Cementation Packs and the Resulting Surface Concentrations of Diffusion Coatings.

Substrate Steels	Activator (wt%)	Metal Source (wt%)	Surface Comp. (wt%)	Coating Depth (μm)
T11	$1NH_4F$-$2MgCl_2$	2Al-18Cr	16.5Al-3.1Cr	400
T2	$1NH_4Cl$-$1.5MgCl_2$	2Al-18Cr	13.2Al-5.6Cr	440
T11	$1NH_4Cl$-$1.5MgCl_2$	2Al-18Cr	16.3Al-4.3Cr	400
T11	$2MgCl_2$	2Al-18Cr	12.4Al-3.8Cr	420
1045	$1NH_4Cl$-$1.5MgCl_2$	3.5Al-17Cr	18.9Al-2.8Cr	580

Table 2 ABB Corrosion Test Environments.

Oxidizing Gas			Reducing Gas		
1000 ppm SO_2	2.44 % H_2		1000 ppm H_2S	2 % H_2	
12.3 % CO_2	0.68 % O_2		7 % CO_2	N_2	balanced
8.6% CO	N_2	balanced	13% CO	(embedded in mid-western bituminous coal, 3.5 % S)	

Similarly coated T11 steel samples, with a surface composition of 12.4 wt% and 2.8 wt% Cr, were tested under oxidizing and reducing conditions of a low NO_X coal combustion environment at 500°C for a period of 500 hours at the ABB Power Plant Labs in Windsor, CT; and the gas compositions used for these tests are listed in Table 2.

Weight change measurements and microstructural observations showed that the Al-Cr coatings were virtually unattacked after 500 hour exposures to either the reducing or oxidizing testing conditions at 500°C. Some coatings with only 8 wt% Al and 6 wt% Cr at the surfaces were also tested at ABB in atmospheres containing higher hydrogen sulfide contents for longer times and the coatings showed attack. No preferential corrosion along grain boundaries was observed. The results show that the coatings with aluminum contents lower than that of Fe_3Al but with an increased amount of Cr are less resistant to sulfidation.

X-ray diffraction analysis of the coupon surface revealed only the $CrSi_2$ phase for both coated alloys. Figure 3(a) shows the surface morphology of a CN117(Z) alloy coated at 1050°C for 12 hours in a pack containing 12Si-12Ge (wt.%). EDS analysis showed the flat area (spot A) was composed of 71Si, 28Cr and 1Ge (at.%), indicating the formation of $Cr(Si,Ge)_2$. The nodule phase (spot B) consisted of 47O, 19Si, 17Al, 10Na, 7F, i.e., a residue from the pack coating process. Figure 3(b) presents the cross-section of Fig. 3(a). EDS results show that the dark phase has the composition of 29Cr, 1X1, 68Si, 1Ge, suggesting the formation of $(Cr,X1)(Si,Ge)_2$. The bright phase is composed of 34Cr, 2X2, 15Zr, 44Si, 5Ge, indicating the existence of (Cr,Zr,X2)(Si,Ge) monosilicide. The gray phase, which formed adjacent to the

coating/substrate interface, consists of 53Cr, 1X2, 3X1, 41Si and 2Ge, i.e., $(Cr,X1,X2)_3(SiGe)_2$. Figure 4 shows the cross-section of a coated CN129-2 alloy using the same treatment. EDS analyses again revealed the formation of $(Cr,X1)(Si,Ge)_2$, $(Cr,Zr,X2)(Si,Ge)$ and $(Cr,X1,X2)_3(Si,Ge)_2$ in the coating. X1 and X2 represent proprietary alloying elements added in the Cr-Zr based alloys.

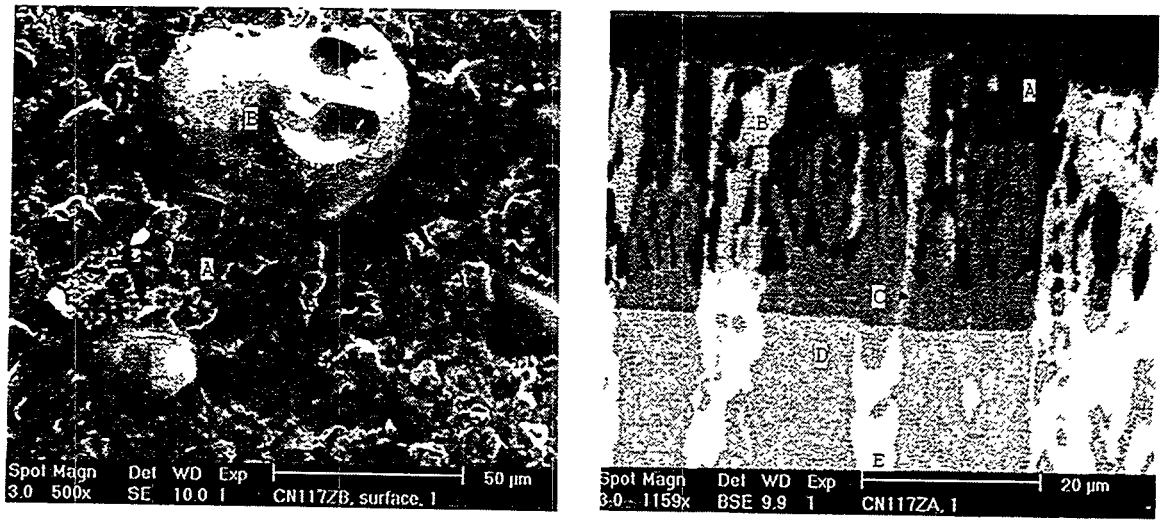

(a) (b)

Fig. 3(a) Surface morphology, 3(b) Cross-section of a CN117(Z) alloy coated at 1050°C for 12 hours in a pack containing 12Si-12Ge (wt.%)

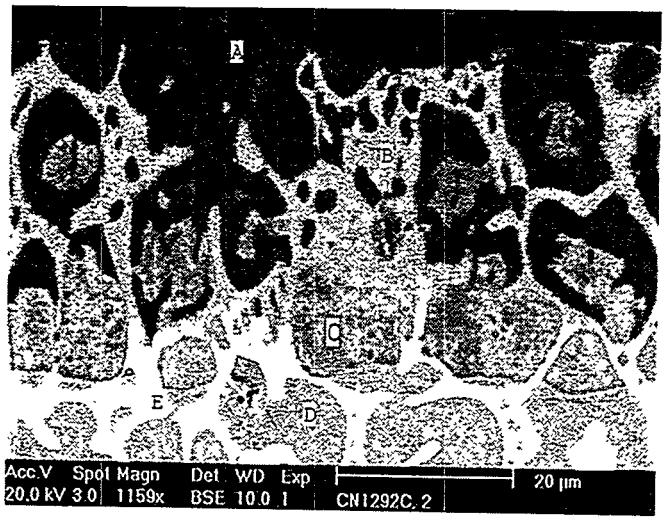

Figure 4 Cross-section of a CN129-2 alloy coated at 1050°C for 12 hours in a pack containing 12Si-12Ge (wt.%)

In each case, the microstructure of the coatings closely mimics the microstructure of the alloys, without any voids in the coating. Thus, the growth of the coating occurred the inward diffusion of Si and Ge. But the Ge content was not uniformly distributed among the three phases in the coating; the highest Ge concentration was found in the (Cr,Zr,X2)(Si,Ge) monosilicide phase. This is in consistent with the findings of previous study on Cr-Nb based alloys.[12]

Fissures were observed in the Ge-doped silicide coating on both alloys. These are generally the most significant defects in silicide coatings.[18] Because the silicides have a higher thermal expansion coefficient than the substrate, the thermal mismatch produces tension in the adherent coating upon cooling, which results in the inherent fissures. Then, for effective protection from oxidation, the coating must form oxides with sufficient fluidity to flow into fissures and exhibit a self-healing capability. The studies by Fitzer et al.[19] and Schlichting and Neumann[20] show that GeO_2 solute in a protective silica scale formed upon oxidation increases its fluidity and thermal expansion coefficient. Therefore the addition of Ge in the silicide coating is expected to help the healing of these fissures during isothermal and cyclic oxidation.

The cyclic oxidation studies underway at 1100°C already show the effectiveness of the Ge-doped silicide coatings in protection of CN117(Z) and CN129-2 alloys from significant oxidation. After 11 cycles, the average weight gains for the uncoated and coated CN117(Z) coupons are 8.9 and 1.5 mg/cm^2, respectively. The average weight gains for the uncoated and coated CN129-2 coupons are 12.5 and 1.6 mg/cm^2, respectively. These results clearly demonstrated that the Ge-doped silicide coating can greatly improve the cyclic oxidation resistance of the Cr-Zr based alloys, even when there are cracks in the substrate or coating.

CONCLUSIONS

A single-step halide-activated Cr-Al pack cementation process at 1150°C for low alloy steels produces a blocking chromium carbide layer and decarburization at the surface. A two-step process involving a first treatment at 925°C and a second at 1150°C results in a dense ferrite coating of composition $(Fe, Cr)_3Al$ which is very oxidation and corrosion resistant under both oxidizing and sulfidizing conditions. The reproducibilities of the composition and thickness of the coatings have been demonstrated.

Two Cr-Zr based Laves phase alloys were silicide/germanide coated using pack cementation technique. The microstructure of the Ge-doped silicide coatings closely mimicked the microstructure of the substrate alloys. Cyclic oxidation in air at 1100°C showed that the Ge-doped silicide coating greatly improved the oxidation resistance of the Cr-Zr based alloys.

ACKNOWLEDGMENTS

The authors wish to acknowledge the financial support from DOE, Oak Ridge National Laboratory (R. R. Judkins, project monitor), contract FWP-FEAA028. The earlier studies by Ge Wang led to the prospect for the aluminizing-chromizing process reported here. The oxidation testing in simulated combustion gas atmospheres was conducted by Juan Nava Paz of ABB Power Plant Labs.

REFERENCES

1. J. H. DeVan, *Oxidation of High-Temperature Intermetallics* (T. Grobstein and J.Doychak, Eds.), (1989), p.107.
2. P. F. Tortorelli, G. M. Goodwin, M. Howell, and J. H. DeVan, *Heat-Resistant Materials II* (K. Natesan, P. Ganesan and G. Lai, Eds.), ASM Intern., Materials Park, OH, (1995), p.585.
3. K. Natesan and R.N. Johnson, *Heat-Resistant Materials II* (K. Natesan, P.Ganesan and G. Lai, Eds.), ASM Intern., Materials Park, OH, (1995), p.591.
4. F. D. Geib and R.A. Rapp, *Processing and Manufacturing of Advanced Materials for High Temperature Applications* (V.A. Ravi, and T.S. Srivastan, Eds.) TMS, Warrendale, PA, (1991), p. 347.
5. F. D. Geib and R.A. Rapp, *Oxid. Metals* , 40, 213 (1993).
6. D. M. Miller, S. C. Kung, S. D. Scarberry and R.A. Rapp, *Oxid. Metals*, 29, 239 (1988).
7. R. A. Rapp and M. A. Harper, U. S. Patent No. 5,364,659, Nov. 1994.
8. R. A. Rapp, G. Wang and E. Pangestuti, U.S. Patent No. 5,492,727, Feb. 1996, and 5,589,220, Dec. 1996.
9. G. Sauthoff, *Z. Metallkde*, 79 (1988), 337.
10. K. S. Kumar and C. T. Liu, *JOM*, (1993), 28.
11. M. Hansen, K. Anderko, *Constitution of Binary Alloys*, Metallurgy and Metallurgical Engineering Series, McGraw-Hill Book Co., (1958), 573.
12. Y-R. He, R. A. Rapp and P. F. Tortorelli, *Materials Science and Engineering*, 222A (1997), 109
13. H. Flynn, A.E. Morris and D. Carter, Version 4.0, Released February, 1990.
14. H. Flynn, A.E. Morris and D. Carter, *Proc. of 25th Conference of Metallurgists*, TMS-CIM, Toronto, Ontario, 1996.
15. S-C Kung and R.A. Rapp, *Oxid. Metals*, **32**, 89 (1989).
16. N. He, G. Wang and R.A. Rapp, *High Temp. Materials Science*, **34**, 117 (1995).
17. I. A. Menzies and D.Mortimer, *Corr. Sci.*, **5**, 539 (1965).
18. C. M. Packer, *Oxidation of High-Temperature Intermetallics*, T. Grobstein and J. Doychak (eds.), TMS, (1988), 235.
19. E. Fitzer, H. Herbst and J. Schlichting, *Werkst. Korros.*, 24 (1973), 274.
20. J. Schlichting and S. Neumann, *J. Non-Cryst. Solids*, 48 (1982), 185.

ELECTRO-SPARK DEPOSITION TECHNOLOGY

Roger N. Johnson

Battelle, Pacific Northwest National Laboratory
P.O. Box 999, K3-59
Richland, Washington 99352

ABSTRACT

Electro-Spark Deposition (ESD) is a micro-welding process that uses short duration, high-current electrical pulses to deposit or alloy a consumable electrode material onto a metallic substrate. The ESD process was developed to produce coatings for use in severe environments where most other coatings fail. Because of the exceptional damage resistance of these coatings, and the versatility of the process to apply a wide variety of alloys, intermetallics, and cermets to metal surfaces, the ESD process has been designated as one of the enabling technologies for advanced energy systems. Protective coatings will be critical to the life and economy of the advanced fossil energy systems as the higher temperatures and corrosive environments exceed the limits of known structural materials to accommodate the service conditions.

Developments include producing iron aluminide-based coatings with triple the corrosion resistance of the best previous Fe_3Al coatings, coatings with refractory metal diffusion barriers and multi layer coatings for achieving functionally gradient properties between the substrate and the surface. A new development is the demonstration of advanced aluminide-based ESD coatings for erosion and wear applications. One of the most significant breakthroughs to occur in the last dozen years is the discovery of a process regime that yields an order of magnitude increase in deposition rates and achievable coating thicknesses. Achieving this regime has required the development of advanced ESD electronic capabilities. Development is now focused on further improvements in deposition rates, system reliability when operating at process extremes, and economic competitiveness.

Technology transfer activities are a significant portion of the ESD program effort. Notable successes now include the start-up of two new businesses to commercialize the ESD technology, the incorporation of the process into the operations of two major gas turbine manufacturers, major new applications in gas turbine and steam turbine protection and repair, and in military, medical, metal-working, and recreational equipment applications.

INTRODUCTION

The objective of this program is to develop an advanced coating process capable of meeting the surface treatment requirements for the next and future generations of advanced fossil energy systems. This includes the development and testing of new materials and coatings with the ability to operate in severe environments beyond current materials limits, and to provide improvements in performance, durability and cost effectiveness for both new and existing power systems. Ultimately new materials performance limits can enable new systems concepts.

A corollary objective is to further advance the Electro-Spark Deposition (ESD) technology and equipment, and to develop broad commercial applications through technology transfer activities.

Just as high performance jet engines would not be possible today without protective metallurgical coatings, so also does the next generation of high efficiency energy systems depend on protective coatings to survive the necessarily higher temperatures and more corrosive environments. The ESD coating process has been designated as one of the enabling technologies for such future systems. One of the reasons for this is that the exceptional structure produced in these metallurgically-bonded coatings makes them virtually immune to damage or spalling under severe service conditions and temperatures that destroy most other coatings. Additional attractions are that the process is portable (allowing coatings or surface treatments to be performed in the field), environmentally benign (creates no noxious wastes, fumes or effluents), and highly cost-effective.

BACKGROUND

The ESD process was developed to provide exceptionally robust coatings for use in nuclear reactor environments when all other commercially available coatings either failed to survive the severe conditions or failed to meet the performance requirements. The Fossil

Energy Program leveraged on that success to begin further developing the ESD process, coatings and applications to meet the demands of advanced fossil energy systems. Electro-spark deposition is a pulsed-arc micro-welding process that uses short-duration, high-current electrical pulses to weld a consumable electrode material to a metallic substrate. The short duration of the electrical pulse allows an extremely rapid solidification of the deposited material and results in an extremely fine-grained, homogeneous coating that may be amorphous for some materials. The microstructures thus produced are believed to be responsible for the superior corrosion and wear performance usually exhibited by the ESD coatings when compared to similar coatings applied by other processes.

The ESD process is one of the few methods available by which a fused, metallurgically-bonded coating can be applied with such a low total heat input that the bulk substrate material remains at or near ambient temperatures. This eliminates thermal distortions or changes in metallurgical structure of the substrate. Not only is the coating metallurgically-bonded, but it exhibits a functional gradient in composition and properties through the coating thickness. This eliminates the "metallurgical notch" associated with coatings that have an abrupt property change at the coating/substrate interface. The metallurgical bond and the elimination of this notch makes ESD coatings inherently more resistant to damage and spalling than the mechanically-bonded coatings produced by most other low-heat-input processes such as detonation gun, plasma spray, electro-chemical plating, etc. Nearly any electrically-conductive metal, alloy, intermetallic, or cermet can be applied by ESD to metal substrates.

Further background information on the ESD process is provided in Ref. 1 and 2.

DISCUSSION OF PRIOR ACTIVITIES

Chromium Carbide Experiments

ESD coatings usually show lower corrosion rates in most environments than the same material would in either bulk form or as a coating applied by other processes.[3] The superior performance of the ESD deposit is attributed to the fine-grained, nearly amorphous nano-structure inherent to the ESD coatings that is not normally achieved in other coating technologies.

In tests at Argonne National Laboratory (ANL), a nano-structured ESD chromium carbide-15% Ni coating showed (unexpectedly) four times better sulfidation resistance than Type 310 stainless steel at 875 C.[4] Normally, this composition would not be expected to perform that well because of the strong susceptibility of a nickel matrix to sulfidation attack. Again, the near amorphous structure is believed to be a major factor in the corrosion resistance. This observation is in agreement with other Fossil Energy Program work that indicates one mechanism of improving lifetimes of protective oxide films and scales is to maintain as fine a grain structure as possible.[5]

Iron Aluminide Coating Development

One of the most significant advances in ESD coatings for use in sulfidation environments has been the successful development of Fe_3Al as a coating material. Oak Ridge National Laboratory (ORNL) has demonstrated the exceptional corrosion properties of Fe_3Al in bulk form, but alloying to achieve acceptable mechanical properties while maintaining optimum corrosion resistance appears to be a challenge. One alternative is to use the most corrosion-resistant compositions as coatings. These iron aluminide compositions have proved to be nearly ideal for use in the ESD process. Consistent, defect-free coatings over 100 μm can be applied rapidly, uniformly and economically.

Sulfidation corrosion tests showed that weld-dilution effects with the substrate

material must be controlled to keep the aluminum content at the surface above the threshold 12% Al that appears to be necessary for good sulfidation resistance.[6,7] Three methods for increasing the aluminum content ultimately were tried. In the first, a simple process of alloying of the surface by ESD using an aluminum electrode was successful in producing aluminum enrichment, but the resulting structure was excessively cracked.[8] The second technique involved a preliminary coating (by ESD) of the substrate with a refractory metal, such as niobium or molybdenum. The higher melting material successfully served as a barrier to diffusion of the substrate material into the coating during subsequent ESD coating. This resulted in achieving a surface composition of good integrity undiluted with substrate elements, and doubled the corrosion resistance.[7] The third method was to use an electrode with a significantly higher Al content, such as FeAl.[9] This material also proved to be well-suited to the ESD process and resulted in the best corrosion performance achieved to date for coatings in coal combustion and coal gasification environments.[10]

DISCUSSION OF CURRENT ACTIVITIES

Process and Equipment Development

The advantages of the Electro-Spark Deposition process, summarized earlier, make it highly attractive for many advanced energy system applications, especially where it is often the only practical surface modification with adequate robustness to survive in severe service conditions. For applications involving limited areas of treatment, the ESD process also can be among the least expensive surface treatments available. But one of the process limitations is the relatively slow deposition rate for large areas compared to higher energy processes, such as thermal spray, conventional welding, diffusion coating, etc. The ESD's lower energy input that produces the unique nano-structures, attractive properties and low substrate effects also restricts the deposition rate.

A major thrust of current activities has been to identify methods of significantly increasing deposition rates while maintaining the properties and structure typical of the ESD

coatings. Achievement of higher rates will increase the number of fossil energy and other applications where ESD can be considered economically attractive.

Exploration of ESD welding parameters at and near the limits of our power supply capabilities has revealed a distinctly different deposition regime for some materials. When this regime is achieved, deposition rates increase by as much as an order of magnitude. The coating thickness limitations usually inherent to most ESD deposits appear to be eliminated. Whereas 100 microns (0.004 in) is normally considered a practical maximum under most circumstances, we have achieved coatings as thick as 1 mm (0.04 in).

This discovery sparked an effort to develop a next generation power supply that can consistently exploit this regime of deposition parameters without damage to the supply or its reliability. An improved prototype ESD power supply was developed that so far has improved deposition rates by 300 to 500% for most materials.

In addition to increased deposition rates, other improvements achieved include:

a) increased stability in the higher power regimes,

b) improved safety circuits for shock protection

c) improved computer controls, including replacement of chips to give non-volatile memory for key functions.

The power supply, of course, is only one element of the ESD system. Another important part is the device used to control the electrode-to-substrate motion and geometry. This is accomplished in the applicator head and controls, and typically has involved mounting servo-controlled motors directly on the applicator. A new design for an applicator that relocates the motor away from the head has been completed and fabrication of the prototype is in progress. The benefits expected are reduced mass of applicator, less operator fatigue for manual coating operations, and less stress on automated machine components in computer-controlled coating applications.

These advances mark the greatest improvements in the ESD technology in the past decade. Further improvements appear possible as more advanced and robust components capable of meeting our particular current and pulse duration requirements become commercially available.

Materials Development and Testing

Coatings of iron aluminides were successfully completed using a new, experimental (and less expensive) electrode fabricated by Stoody Co. The new electrode is formed by drawing or swaging an iron tube on to an aluminum core to produce an average cross sectional composition equivalent to the alloy composition desired in the final deposit. This avoids making a special heat of the alloy and then forming it into electrodes. Preliminary evaluations of the deposits show that the coatings are of equivalent quality to those made from pre-alloyed electrodes.

The first series of wear and erosion tests on candidate ESD coatings were completed. The coatings included iron aluminides, nickel aluminides, and titanium aluminides containing 0 to 10 wt.% TiB_2. The erosion tests (ASTM G-76) showed Ti_3Al to have the lowest erosion rate (0.13 mg/g of Al_2O_3 erodent) of the pure aluminide coatings, Ni_3Al to have the highest rate (0.40 mg/g), and Fe_3Al an intermediate erosion rate (0.30 mg/g). As expected, TiB_2 additions were beneficial in improving both wear and erosion resistance. The lowest erosion rate was achieved by an ESD coating of TiAl-10 wt.% TiB_2 (0.095 mg/g). Low stress abrasion tests (ASTM 1044) resulted in a similar ranking of the coatings. Further wear and erosion tests will be conducted on iron aluminide-base coatings containing TiC and TiB_2 when suitable electrodes being developed become available.

Technology Transfer Highlights

ESD coatings are seeing increasing use in fossil-fueled gas and steam turbine applications. Two major gas turbine manufacturers have qualified ESD coatings for use in several engine components and a steam turbine manufacturer has ESD coatings in long-term qualification tests.

The most recent ESD qualification to be placed in production involves the deposition of wear-resistant carbides to turbine blade tips for wear against abradable seals.

Such seals are critical to improved performance and fuel efficiency. The ESD coatings not only out-perform all previously used coatings, but they can be applied without affecting the single crystal structure of the advanced turbine blades used. Other turbine power plant ESD applications include:

a) build-up of high-value worn or mis-machined parts to acceptable tolerances,

b) Pt coating of blades on selected areas for subsequent incorporation into aluminide diffusion coatings,

c) repair of damaged aluminide diffusion coatings,

d) pre-placement of braze alloys for precision assembly of complex components,

e) coating of high-wear contact points in turbine assemblies,

f) elimination of stress-corrosion-cracking problems by surface treatment of critical high stress areas of components with special corrosion-resistant alloys.

Other successful applications, recently commercialized, where ESD coatings have out-performed all other surface treatments evaluated in combined corrosion and wear environments include:

a) coating of dies and cutter plates used in the extrusion and cutting of processed food products at 177 C (350 F) and 17.3 MPa (2500 psi),

b) pulp and paper mill plug screws and barrel extruders, where service lives have been increased from six months to two years at last report, and are still in service.

c) surface modifications to increase sparking resistance of components used in potentially explosive atmospheres.

ESD coatings now in test for severe service applications include: a) digging tools to be used by NASA's Mars Lander, b) cutters for multi-material chipping operations in recycling plants, c) tools user in the machining and metal working of titanium alloys, and d) seals and bearings used on tri-clone bits in deep well drilling for oil production.

REFERENCES

1. R.N. Johnson, "Principals and Applications of Electro-Spark Deposition," *Surface Modification Technologies*, T.S. Sudarshan and D.G. Bhat, eds., The Metallurgical Society, January 1988, p. 189-213.

2. R.N. Johnson, "Electro-Spark Deposited Coatings for High Temperature Wear and Corrosion Applications," *Elevated Temperature Coatings: Science and Technology I*, N. B. Dahotre, J.M. Hampikian, and J.J. Stiglich, eds., The Metallurgical Society, October 1994, p. 265-277.

3. R.N. Johnson, "Coatings for Fast Breeder Reactors," in *Metallurgical Coatings*, Elsevier Sequoia, S.A., New York, 1984, p. 31-47.

4. K. Natesan and R.N. Johnson, "Corrosion Resistance of Chromium Carbide Coatings in Oxygen-Sulfur Environments," *Surface and Coatings Technology*, Vol. 33, 1987, p. 341-351.

5. I.G. Wright and J.A. Colwell, "A Review of the Effects of Micro-Alloying Constituents on the Formation and Breakdown of Protective Oxide Scales on High Temperature Alloys at Temperatures Below 700 C," ORNL/Sub/86-57444/01, September 1989.

6. K. Natesan and R.N. Johnson, "Corrosion Performance of Fe-Cr-Al and Fe Aluminide Alloys in Complex Gas Environments," *Heat-Resistant Materials II - 2nd Int. Conf.*, ASM Int., 1995, p.591-600.

7. K. Natesan and R.N. Johnson, "Development of Coatings with Improved Corrosion Resistance in Sulfur-Containing Environments," *Surface and Coatings Technology*, Vol. 3/44, 1990, p. 821-835.

8. R.N. Johnson, "Electro-Spark Deposited Coatings for Fossil Energy Environments," in *Proceedings of the Seventh Annual Conference on Fossil Energy Materials*, ORNL/FMP-93/1, July 1993, p.289-295.

9. R.N. Johnson, "Electro-Spark Deposited Coatings for Protection of Materials," in *Proceedings of the Ninth Annual Conference on Fossil Energy Materials*, ORNL/FMP-95-1, August 1995, p. 407-413.

10. R. N. Johnson, "Electro-Spark Deposition Technology", in *Proceedings of the Tenth Annual Conference on Fossil Energy Materials,* ORNL/FMP-96/1, August 1996, p. 429-437.

INVESTIGATION OF AUSTENITIC ALLOYS FOR ADVANCED HEAT RECOVERY AND HOT-GAS CLEANUP SYSTEMS

R. W. Swindeman

Oak Ridge National Laboratory
P.O. Box 2008
Oak Ridge, TN 37831

ABSTRACT

Materials properties were collected for the design and construction of structural components for use in advanced heat recovery and hot gas cleanup systems. Alloys systems included 9Cr-1Mo-V steel, modified 316 stainless steel, modified type 310 stainless steel, modified 20Cr-25Ni-Nb stainless steel, and modified alloy 800. Experimental work was undertaken to expand the databases for potentially useful alloys. Types of testing included creep, stress-rupture, creep-crack growth, fatigue, and post-exposure short-time tensile tests. Because of the interest in relatively inexpensive alloys for service at 700°C and higher, research emphasis was placed on a modified type 310 stainless steel and a modified 20Cr-25Ni-Nb stainless steel. Both steels were found to have useful strength to 925°C with good weldability and ductility.

INTRODUCTION

The objective of the research is to provide databases and design criteria to assist in the selection of optimum alloys for construction of components needed to contain process streams in advanced heat recovery and hot gas cleanup systems. Typical components include: steam line piping and superheater tubing for low emission boilers (600 to 700°C), heat exchanger tubing for advanced steam (650 to 800°C), foil materials for recuperators on advanced turbine systems (700 to 750°C), and tubesheets, plenums, liners, and blowback systems for hot gas cleanup vessels (850 to 1000°C).

STEELS FOR LOW EMISSION BOILERS

Alloys such as vanadium-modified 2 1/4 Cr-1 Mo, 2 1/4Cr-1.5W, 9Cr-1Mo, 9Cr-1.5W and 12Cr-1.5W steels are candidates for the construction of piping, headers, and tubing in the low emission boiler (LEB) project supported by the Pittsburgh Energy Technology Center. However, these classes of steels exhibit a complex metallurgical constitutions that are not fully understood, and concerns exist about long-term embrittlement due to Laves

phase precipitation, degradation of weldments due to cavitation cracking, and susceptibility to creep-fatigue damage. Methods for on-line damage assessment are needed as an assurance against component failures. To assist the LEB project contractors in addressing these issues, damage accumulation mechanisms in 9Cr-1Mo-V steel are being studied. These studies involve the continuation of long-time creep testing on aged 9Cr-1Mo-V steel, the examination of correlation methods to relate mechanical behavior time-temperature-stress history, studies of thick-section weldment behavior, and the assessment of damage in service-exposed materials. Damage studies are being undertaken on T91 tubing removed from the superheater of a power boiler after sixteen years of service. The tubing included dissimilar metal welds between T91, T22, and 321 stainless steel. Metallurgical studies showed minor cracking at the joints in both the 321 stainless steel and T91. The Gr91 tubing retained good strength and ductility. When compared on the basis of the Larson Miller parameter, short-time stress-rupture data for T91 fell near the bottom of the scatterband for unexposed material. Data are plotted in Fig. 1. Such behavior was judged to be typical.

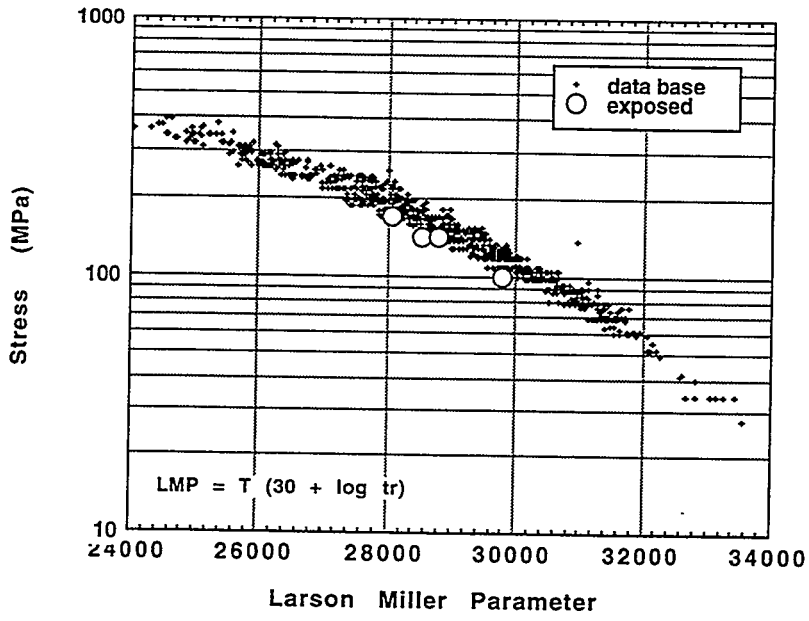

Fig. 1. Comparison of stress-rupture data for service exposed 9Cr-1Mo-V steel to the Larson-Miller scatterband for unexposed material.

Additional studies are needed to examine the performance heavy section weldments in the advanced ferritic alloys. Some welds in the T91 removed from the TVA boiler showed sign of type-IV cracking, and service failures have already occurred in components that were not properly fabricated. Exploratory fatigue and stress-rupture testing of weld in T91 piping has been completed at ORNL and the propensity for the acceleration of type IV cracking under cyclic stresses has been confirmed. For additional studies, and a heavy-section weld of T91 has been received from an industrial fabricator. Here section size effects on creep ductility and creep crack growth will be examined.

In the LEB, austenitic stainless steels will be used for tubing in the hotter, more corrosive sections of the superheater and reheater. Code-approved (ASME Sect. I) candidate steels include fine-grained 347 stainless steel (347FG), niobium-modified 310 stainless steel (310HCbN SS), and alloy 800H. Commercially available stainless steels for which a suitable database exists include a titanium-zirconium-modified 20Cr-25Ni-Nb stainless steel (NF709), a copper-niobium 18Cr-8Ni stainless steel (ST3Cu), and 17-14CuMo stainless steel (previously code-approved). Experimental alloys tested to long times in mechanical and corrosion probes include the modified 316 stainless steels (HT-UPS steels), modified alloy 800H, and Tantalum modified 310 stainless steel. The code-approved several stabilized grades stainless steels have cracked near welds and cold-formed regions, so Sect. I may impose requirements to re-anneal cold-worked tubing of the 347FG, 310HcbN, and alloy 800H. Further studies of these alloys are needed to establish fabrication guidelines for use in boiler construction of the LRB components. Also, further studies are needed to examine issues related to dissimilar metal welds between the advanced stainless steels and new ferritic alloys such as T23, T92, and T92. Under a CRADA with ABB-Combustion Engineering, work was begun to examine cold work effects in austenitic stainless steels. It was observed that the understabilized grades of steels, such as the HT-UPS alloys developed at ORNL, benefitted from cold work to levels of at least 10%. This was partly due to the stability of the microstructure and the resistance of the HT-UPS steels to grain-boundary creep cracking. A specimen examined after 60,000 h of creep at 700°C and 100 MPa was found to have a stable microstructure and no cavitation. The testing of the cold-worked stabilized grades has begun.

Welds in the advanced austenitic stainless steels are being examined in long-time testing. Both autogenous welds and filler metal welds are being investigated to further establish whether stress reduction factors will be needed for some types of weldments. Testing of some weldments has exceeded 30,000 hours. Filler metals include 308/CRE, 16-8-2/CRE, alloy 556, and alloy 117.

Of the austenitic stainless steels advanced steels studied to date, the mod. 20Cr-25Ni-Nb stainless steel appeared to have the best overall performance with respect to fabricability, strength, and corrosion resistance. A comparison of the rupture strength of this steel to 347 stainless steel is shown in Fig. 2, and it may be seen that the steel is significantly stronger than 347 stainless steel.

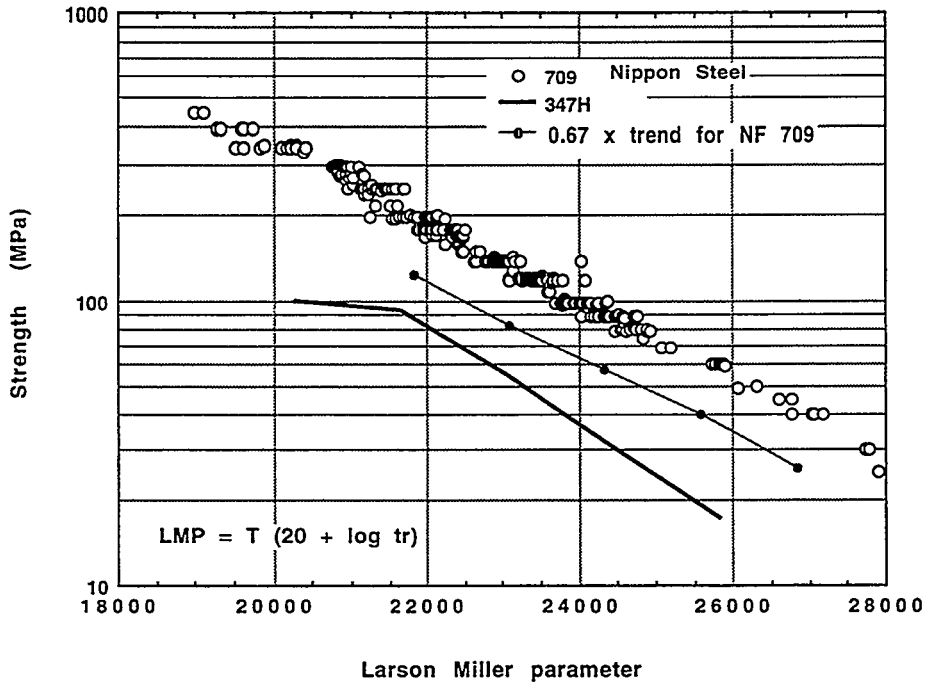

Fig. 2. Comparison of stress-rupture strength for modified 20Cr-25Ni-Nb stainless steel to 347 stainless steel on the basis of the Larson Miller parameter

STEELS FOR ADVANCED HEAT RECOVERY SYSTEMS

Austenitic alloys of interest for advanced heat recovery systems include 347 stainless steel, modified 316 stainless steels, modified 310 stainless steels, and modified 20Cr-25Ni-Nb stainless steels. Current emphasis has been on use of these materials for recuperators. Working on a CRADA with Solar Turbines, Inc., foil materials have been produced at ORNL and are being evaluated in the temperature range of 650 to 730°C. The goal of the development work is to define compositions and fabrication schedules that will produce good creep strength and adequate oxidation resistance in a very fine-grained material for times to beyond 20,000 h. The standard against which the alloy performance is compared is 347 stainless steel now used for service to 600°C. The creep behavior of the materials that have been produced are compared against 347 stainless steel in Fig. 3. Test conditions correspond to 75.8 MPa at 704°C. It is clear that the modified 310 stainless steel and the modified 20Cr-25Ni-Nb steels have significantly better strength for at least 1500 hours. The modified 347 stainless steel has not produced strength equivalent to the standard material.

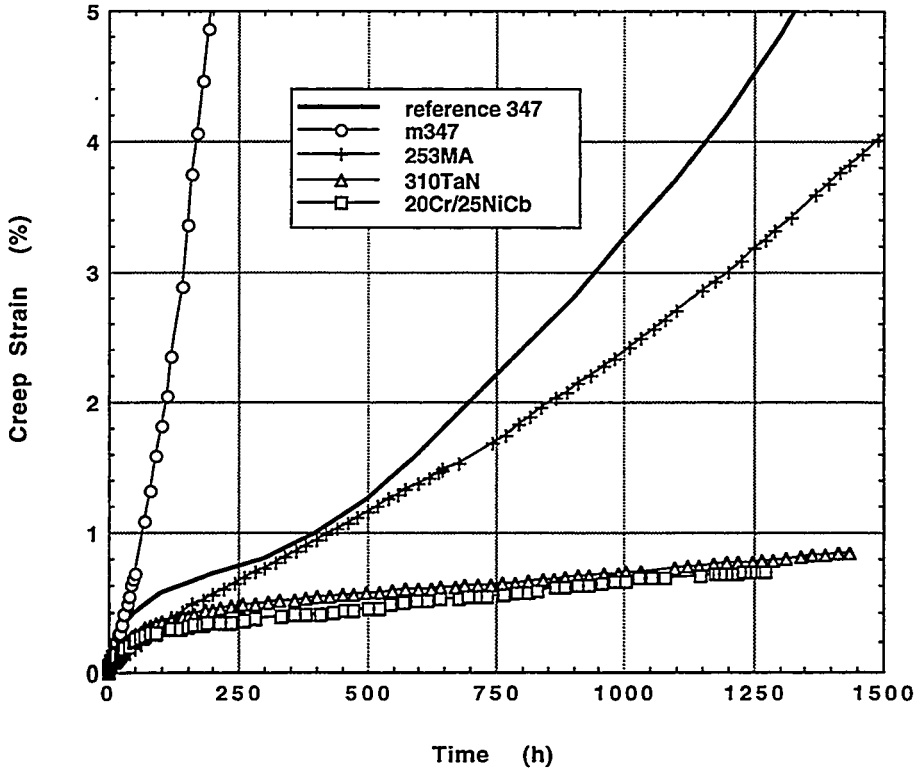

Fig. 3. Comparison of creep curves for candidate recuperator materials at 75.8 MPa and 704°C.

ALLOYS FOR HOT-GAS CLEANUP

Components in several advanced fossil energy systems are expected to experience very high temperatures, and the potential for creep damage, fatigue, thermal-fatigue, and creep-fatigue crack growth are significant. For both "code" alloys and developmental alloys, data for design at very high temperatures are often lacking. For these reasons, exploratory research on creep, creep-fatigue, fatigue, and crack growth of several candidate alloys has been in progress. Earlier work on alloy for hot-gas cleanup involved studies of alloy 333, alloy 556, and alloy 160, which were candidates for use in pressurized fluidized bed (PFBC) hot-gas cleanup systems at temperature above 815°C. More recently, evaluation was completed the heat of alloy 120 that is the tubesheet material in the hot-gas cleanup vessel installed at the Wilsonville PFBC facility. Testing of alloy 120 included creep, creep-crack growth, fatigue, and fatigue-crack growth. Efforts continued to evaluate the performance of modified 310 stainless steel and modified 20Cr-25Ni-Nb stainless steel. Creep testing of the modified 310 stainless steel has exceeded 40,000 h at 871°C, and the material has been found to exhibit good strength and ductility relative to standard 310 stainless steel and alloy 800HT. In Fig. 4. A creep curve is shown for a test at 17.5 MPa and 871°C. Creep strain exceeds 10% at 40,000 h, and a diminishing of the creep rate was observed. This diminishing creep rate is thought to be a manifestation of the influence of the air environment which produces nitriding effects near the free surfaces of the specimen.

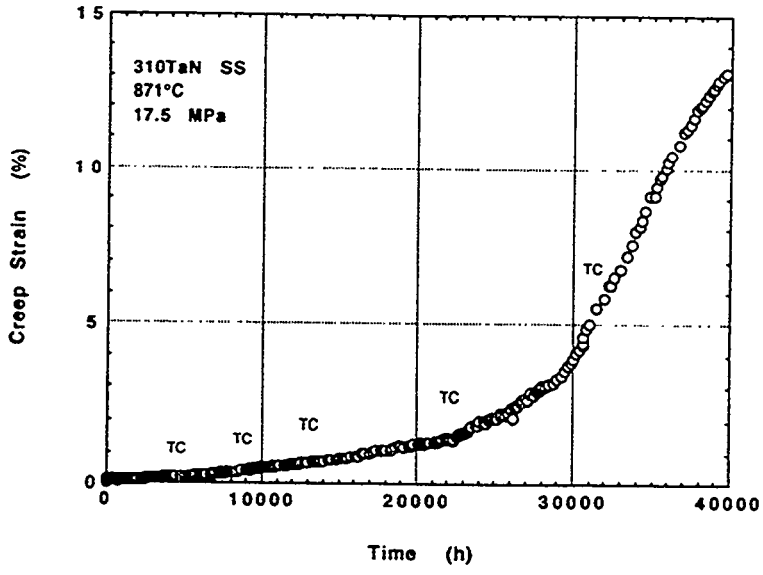

Fig. 4. Long-time creep curve for modified 310 stainless steel at 17.5 MPa and 871°C.

FIRESIDE CORROSION TESTING OF CANDIDATE SUPERHEATER TUBE ALLOYS, COATINGS, AND CLADDINGS - PHASE II

J. L. Blough
W.W. Seitz

Foster Wheeler Development Corporation
12 Peach Tree Hill Road
Livingston, NJ 07039

ABSTRACT

In Phase I a variety of developmental and commercial tubing alloys and claddings were exposed to laboratory fireside corrosion testing simulating a superheater or reheater in a coal-fired boiler. Phase II (in situ testing) has exposed samples of 347 RA-85H, HR3C, 253MA, Fe_3Al + 5Cr, 310 Ta modified, NF 709, 690 clad, and 671 clad for approximately 4,000, 12,000, and 16,000 hours to the actual operating conditions of a 250-MW coal-fired boiler. The samples were assembled on an air-cooled, retractable corrosion probe, the probe was installed in the reheater cavity of the boiler and controlled to the operating metal temperatures of an existing and advanced-cycle coal-fired boiler.

The results will be presented for the preliminary metallurgical examination of the corrosion probe samples after 16,000 hours of exposure. Continued metallurgical and interpretive analysis is still on going.

INTRODUCTION

High-temperature, fireside metal wastage in conventional coal-fired steam generators can be caused by gas-phase oxidation or liquid-phase coal-ash corrosion. Gas-phase oxidation is usually not a problem if tube and support materials are selected for their oxidation resistance at operating temperatures and for spalling, flaking, or other reactions to their environment. Coal-ash corrosion, on the other hand, usually results in accelerated attack and rapid metal wastage—even of stainless steels. The cause of this type of corrosion is generally accepted as the presence of liquid sulfates on the surface of the metal beneath an overlying ash deposit[1-4].

While substantial progress has been achieved through laboratory testing, actual utility service exposures are evidently necessary to verify any conclusions drawn from laboratory testing. A number of important environmental parameters cannot be fully simulated in the laboratory[5]:

- The actual composition of the deposits formed on the tubes is more complex than the composition of the simulated ash.
- The SO_3, formed by heterogeneous reaction on cooled surfaces, is variable.
- Very large temperature gradients occur within the ash deposits.
- The ash and flue gas move past tubes at high velocity; the rate varies with design.
- The composition of the corrosive deposits changes with time.

- Metal and flue-gas temperatures fluctuate.
- Fly-ash erosion removes the protective oxides, exposing a clean surface to fresh ash.

Foster Wheeler Development Corporation (FWDC) has performed a number of literature reviews and recent updates discussing the variables affecting the corrosion mechanism[6-8]. Additionally, Foster Wheeler is conducting two sizable research projects—one a laboratory and in situ field testing at three utilities of commercially available alloys[5,9-14] and this present project (ORNL-FW2)—combining laboratory and field testing to more completely cover the controlling variables for a longer duration[10].

PHASE I RESULTS

In Phase I of this ORNL program, "Fireside Corrosion Testing of Candidate Superheater Tube Alloys, Coatings, and Claddings," 20 commercial and developmental alloys were evaluated[10]. The coupons of the metals were exposed to synthetic coal ash and synthetic flue gases at 650 and 700°C (1202 and 1292°F) for up to 800 hours. The corrosion was evaluated as a function of alkali content in the ash, SO_2 concentration in the gas, and alloy content.

PHASE II CORROSION PROBE TESTING

In this project, the field tests comprise corrosion probe testing, coal characterization, and deposit/corrosion product analysis. The coals have been analyzed to provide fuel characterization, a deposit analysis data bank, and possibly a corrosivity index for predicting corrosivity under various combustion conditions. The equipment and the procedures for this phase have been previously used and perfected at three different utilities for over 3 years of in situ testing at each station.

The utility for test exposures should be burning an aggressive fuel to adequately evaluate the candidate alloys. The coal being burned at Tennessee Valley Authority's (TVA's) Gallatin Station had been previously analyzed, and numerous corrosion indices predicted high corrosivity in addition to the fact that installed T22 and Type 304SS tubing experienced about 7 years of life in the superheaters and reheaters of Units 1 and 2.

Selection of Materials for Corrosion Probes

FWDC tested 20 different materials[10] in the laboratory. Because this quantity was impractical from both an economic and a probe-length standpoint, fewer (the nine listed in Table 1) had to be selected for the field tests. These materials provide a range of compositions and cost for both the commercially available and developmental alloys and claddings.

Field Corrosion Probe Design

The corrosion probes were designed to provide realistic exposures of metal samples to both actual boiler environments and also at the higher anticipated metal temperatures of an advanced plant. The corrosion probes are independent from the main boiler; can be removed without a boiler outage; and have a fail-safe design, one that removes the probe from the boiler if there are any malfunctions. With these features, years of testing will not be compromised with a sudden system overheating.

The probes were exposed for approximately 4000, 12,000, and 16,000 hours. This was accomplished by utilizing two probe test locations. At one test location, the probe was exposed for 15,883 hours. At the other test location, the probe was removed after 4483 hours and a new probe inserted for the remaining 11,348 hours.

Each probe was a 2.56-m (8.4-ft)-long, 60.20-mm (2.37-in.)-OD tube that extended into the furnace for approximately 2.3 m (7.6 ft). Ring samples [38.1 mm (1.5 in.) wide] of the candidate alloys listed in Table 1 were installed at the end of the probe farthest from the furnace wall. The probe was cooled by air that flows in the annular region between the probe tube ID and the tapered inner tube OD. The tapered inner tube was designed to obtain two bands of temperature on the outer surface of the samples. The alloy samples were duplicated in such a manner as to expose each alloy to a temperature in each of the temperature bands [619 to 682°C (1146 to 1260°F) and 682 to 727°C (1260 to 1341°F)].

Table 1. Chemical Composition of Candidate Alloys (wt %)

Alloy	Cr	Ni	Others
Type 347	17-19	9-13	(Nb + Ta) = 10 × C (min.)
85 H	18	15	Al = 1, Si = 3.9
NF 709	20	25	Mo = 1.5, Mn = 1.0, Si = 0.6
690 Clad	30	58	
671 Clad	48	52	
Fe_3Al + 5% Cr	5	—	Al = 17
HR3C	25	20	Nb = 0.4
253 MA	21	11	Si = 1.7
310 Ta modified	25	20	1.5 Ta
800HT	21	32	Al + Ti = 1

Each probe had a retraction mechanism, and three K-type thermocouples in duplicate to monitor the mean tube wall at the beginning and end of each test section group. A 19.95-mm (3/4-in.)-OD thermowell with

sheathed thermocouple was mounted between the corrosion probes to measure flue-gas temperature. Each probe had its own cooling-air control valve.

The control system monitored the selected control thermocouple and modulated the airflow to maintain an average surface metal temperature for each temperature band. The probes retracted automatically if failure of the cooling-air supply system or any other malfunction (instrument signal, power failure, or computer failure) caused the probe temperature to exceed the set limit of 746°C (1375°F) for 2 minutes. FWDC personnel accessed the field computer automatically for probe status and temperature data each morning at 6 a.m. or manually through its modem.

The locations in this plant were chosen because of cavity access and because they best represent the locations for the reheater or superheater outlet on the "Advanced Cycle" unit.

The ideal coal-ash corrosion probe exposure is if only one coal is being burned at the plant. This practice is not common at many utilities; in fact, many are buying coal on the spot market. Gallatin burns a number of eastern high-sulfur coals, mainly Island Creek, Warrior, Dotiri, and Pattiki, which are known to be corrosive and prone to alkali-iron-trisulfate formation. The Borio Index for these coals typically range from 2.0 to 4.1, and the chloride level is 450 to 3000 ppm.

Post-Exposure Analysis

At 4000, 12,000, and 16,000 hours, the probes were removed and sent to FWDC for metallurgical evaluation. The 4,000-hour probe was removed and the analysis reported previously[17]. The 12,000- and 16,000-hour corrosion probes were removed during February 1997 from the reheater cavity of the TVA Gallatin Station Unit 2. The weighted average temperature was calculated for each test section in each of the two probes and is shown in Table 2.

Table 2. Average Exposure Temperature

Test Section	12,000-Hour Probe [°C (°F)]	16,000-Hour Probe [°C (°F)]
1	719-681 (1325-1260)	726-682 (1341-1260)
2	681-623 (1260-1153)	682-619 (1260-1146)

Macroscopic Examination

Both probes were received with a tan deposit on their outer surfaces. The deposits were removed and stored separately for later examination. Two 1/4-in.-long, transverse ring sections were removed from each sample on both probes. One of the ring sections was lightly grit blasted and used for thickness measurements, while the other was mounted for microscopic and SEM/EDX analysis.

Shallow pitting and some surface roughening are evident in some of the samples. The more prominent pitting was noted on samples 1* (RA85H), 5 (HR3C), 11 (RA85H), and 12 (347) from the upper (16,000-hour) probe, and 1 (RA85H) and 4 (RA253MA) in the lower (12,000-hour) probe. Post-exposure wall thickness readings were performed at the 45-, 135-, and 270-degree locations, and wall loss calculated for each sample. [Note: Further microexamination revealed that some of the wall loss in the clad samples 6, 7, 16, and 17 resulted from the oxidation of the inside surface which was a modified LSS (lean 316 stainless steel) and not from corrosion of the outside surface.] Further microscopic examination was performed to resolve these high wall losses and determine the actual corrosion from the outside coal-ash environment.

Microscopic Examination and EDX Analysis

Short sections from the 45-, 135-, and 270-degree locations of the samples were prepared for microscopic examination. [Note: After the evaluation it was noted that the samples from the upper probe (16,000 hours) contained the worst internal attack. Therefore, the discussion given in this report is from the upper probe.] Both probes were evaluated and detailed photomicrographs, SEM/EDX analysis, and interpretative discussions will be presented in the final report. A summary of the examination follows.

RA85H — The samples from both probes were very similar in terms of their intergranular penetration and general internal attack on the outside surface to a depth of approximately 1.5 to 2.0 mils. The worst attack was noted at the 135-degree location of sample 11, which operated at a higher temperature than sample 1. Along the surface the sample exhibited a two-part scale which consisted of a lighter scale on top of a darker scale. The lighter layer was mainly an iron-oxide scale with trace amounts of aluminum, silicon, calcium, and chromium. The darker layer was more of a chromium-rich oxide with nickel present and trace amounts of iron, aluminum, and silicon. Subsurface, the sample exhibited needle-like phases which consisted mainly of aluminum and iron with trace amounts of oxygen, silicon, chromium, and nickel. The gray phase noted at the sites of intergranular penetration were comprised of chromium, aluminum, and oxygen with small amounts of silicon, molybdenum, sulfur, titanium, vanadium, iron, and nickel. Also, the alloy displayed a very light gray phase in the form of a sphere, which was thought to be a penetrating sulfide. However, the EDX analysis revealed it was most likely a chromium carbide with minute amounts of silicon, sulfur, vanadium, iron, and nickel. In addition, the ID of samples 1 and 11 was examined and found to have suffered intergranular penetration to depths of 2.8 and 3.3 mils (upper probe) and 2.3 and 3.0 mils (lower probe), respectively.

347 — Both sets of samples contained a layer of scale, which was basically chromium oxide, on top of the corroded areas. The scale also displayed trace amounts of silicon, niobium, sulfur, calcium, iron and nickel. The gray nonmetallic phase which penetrated the subsurface of the material was found to be relatively the same

---

*Sample numbers 1 through 10 are on the hotter end of the probe, while 11 through 20 are on the colder end.

material as the scale layer. Sulfide penetration to a depth of approximately 3.0 mils was also evident in each of the samples. The sulfides contained iron, nickel, manganese, chromium, and oxygen. In addition, the samples of the upper probe suffered 2.3 and 4.0 mils of sulfur penetration along the ID surface.

NF 709 — All of the samples exhibited a thin scale layer along the outside surfaces. The scale was comprised of light and dark gray layers which gave the scale a striated appearance. The dark gray layers were chromium oxide with trace amounts of aluminum, silicon, sulfur, iron, and nickel. The light gray layers were comprised mainly of iron oxide and also contained traces of aluminum, sulfur, chromium, and nickel. The subsurface of the alloy displayed various nonmetallic phases. The amorphously shaped ones consisted of chromium, oxygen, iron, nickel, aluminum, silicon, and sulfur. The spherically shaped ones were revealed as sulfides which contained oxygen, chromium, manganese, iron, and nickel.

RA253MA — The RA253MA sample that was in the hotter section revealed a more roughened and irregular surface than its cooler counterpart. Both exhibited a two-layered scale along their outside surfaces; however, the hotter sample had the thicker layers. Beneath the scale the sample displayed sulfide penetration to a depth of approximately 4.5 mils. The outer layer of scale was basically an iron oxide with notable additions of aluminum, silicon, sulfur, calcium, chromium, and nickel. The inner layer was noted as being a chromium oxide with small amounts of silicon, sulfur, iron, and nickel present. The sulfide islands contained iron, nickel, chromium, manganese, and oxygen.

HR3C — The sample from the cooler section of the probe displayed a thin scale layer along its surface and a few localized areas of attack with subjacent internal oxidation and heavy penetration. The scale had remnant fly-ash particles in it but was still recognizable as a chromium oxide with trace amounts of sulfur, silicon, manganese, iron, and nickel. A white metallic phase was noted inside the scale. It was comprised mainly of sulfur, oxygen, iron, and nickel with small amounts of chromium and manganese. The sulfide islands noted subsurface of the scale were comprised of iron, chromium, nickel, manganese, and oxygen. The subsurface oxidation was a basic chromium oxide with notable additions of aluminum, silicon, sulfur, iron, nickel, and manganese. The depth of penetration was approximately 4 mils.

671 — Both samples from both probes displayed a broken, irregular scale along their outside surfaces. In addition, the samples exhibited some shallow pitting and localized areas of subsurface attack. The scale along the outside surface had two distinct layers—a light gray and dark gray one. The light gray was a chromium oxide with some small quantities of sulfur, iron, and nickel in it. The dark gray layer was an iron oxide with traces of aluminum, silicon, chromium, and nickel. The areas of localized attack had two distinguishable phases within their boundaries. One was a chromium-oxide phase with additional components such as aluminum, titanium, iron, and nickel also being observed. The other phase resembled a sulfide island; however, it was not a sulfur phase. Rather, it was a titanium-oxide phase with trace amounts of iron, nickel, and chromium. These internal corrodents penetrated to a depth of approximately 4 mils. In addition, both samples on both probes exhibited a scale along their inside surfaces (which consisted of LSS stainless steel material). The hotter sample (sample 16)

in the upper probe contained a 1.8-mil-thick scale while the cooler sample (sample 6) exhibited a 3-mil scale. In the lower probe, the hotter sample (sample 16) contained a 5.8-mil scale and the cooler sample (sample 6) had a 4.2-mil-thick scale.

690 — Some areas of scale exfoliaton were observed in each sample. Similar to the 671 samples, all of the 690 samples displayed a very thin, chromium-rich oxide layer on the outside surface. Internal oxidation and sulfidation were also evident in all of the samples; however, the hotter samples exhibited a deeper penetration (approximately 6 mils compared to 2 to 3 mils in the cooler sections). The inside surface (which also consisted of LSS stainless steel material) contained a 2.2-mil-thick scale in the hotter section (sample 17) and a 3.3-mil-thick scale in the cooler section (sample 7). The samples in the lower probe exhibited the same inside surface scale formation; sample 17 (hotter) had a 2-mil-thick scale, and sample 7 (cooler) had a 1-mil-thick scale.

Fe_3Al — Scale exfoliation was also observed at the ID surface. The outside surface of the samples exhibited a dark gray scale with intermittent layers of a lighter gray scale. The lighter gray scale was revealed to be chromium-rich oxide which had a substantial amount of iron mixed in as well. There were also traces of calcium, potassium, silicon, and aluminum found in the light gray scale. The dark gray scale was an aluminum-rich oxide with small amounts of chromium, iron, and sulfur. Beneath the scale layer, the surface of the metal was roughened and irregular with some definite evidence of shallow pitting. A needle-like phase was noted subsurface of the material throughout the entire thickness of all of the samples. The phases were high in iron, niobium, oxygen, and aluminum, with a small amount of chromium.

310 — The 310 Ta modified alloy sample in both probes contained a thin, chromium-rich scale with embedded fly-ash particles. Beneath the scale, the material suffered from internal oxidation and sulfidation which was more pronounced on the cooler samples. The depth of penetration for the upper probe was approximately 1.5 to 2 mils for the cooler sample (sample 9) and 2.5 mils for the hotter sample (sample 19). In the lower probe, the numbers were almost the same— 2 mils for the cooler (sample 9) and 2.2 mils for the hotter (sample 19).

800H — All of the 800H samples exhibited a two-layer scale/deposit along the outside surface with some minor internal oxidation and sulfidation. The depth of the internal penetration was noted as being deeper in the hotter sections of the upper and lower probes (sample 20: upper - 5.5 mils; lower - 5.3 mils). The cooler samples displayed penetration depths of 2 mils (upper) and 3 mils (lower). The outer layer was comprised of embedded fly-ash particles. The inner layer was predominantly chromium oxide. The sulfides contained manganese, chromium, iron, and nickel.

Wastage Determination

Wastage is considered the sum total of wall loss and metal rendered ineffective because of internal penetration of corrosive species (e.g., oxides, sulfides). Since only the wastage from the outside surface is of concern, wall loss from oxidation of the inside surface must be discounted. On this basis, the wastage of the specimens determined from the macroscopic and microscopic examinations is given in Figure 1.

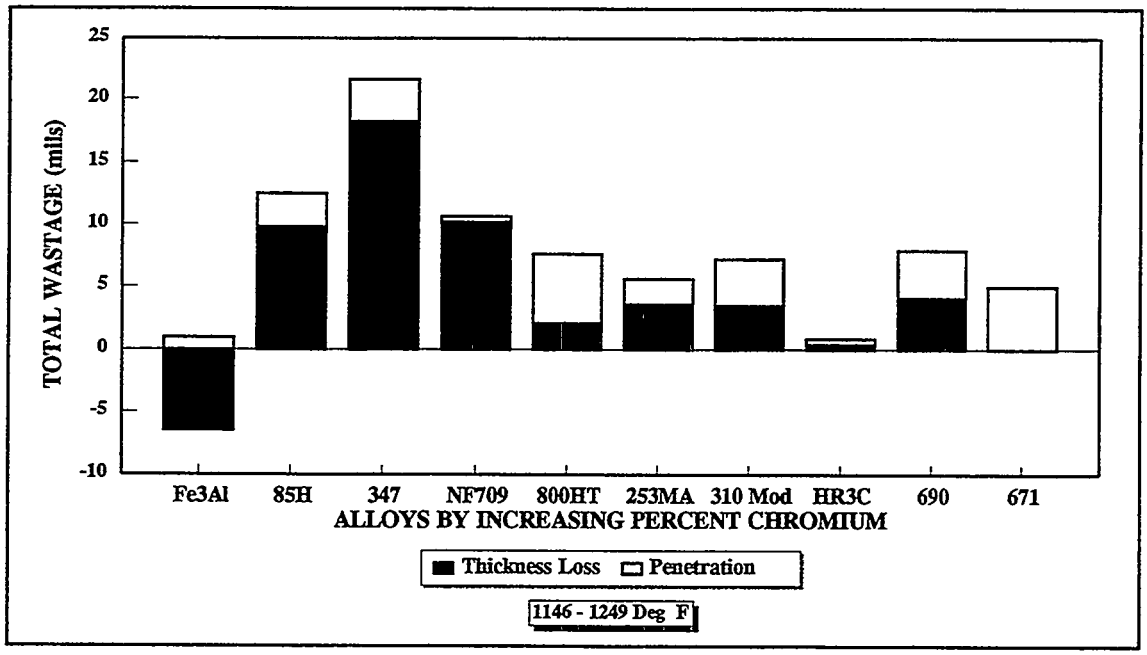

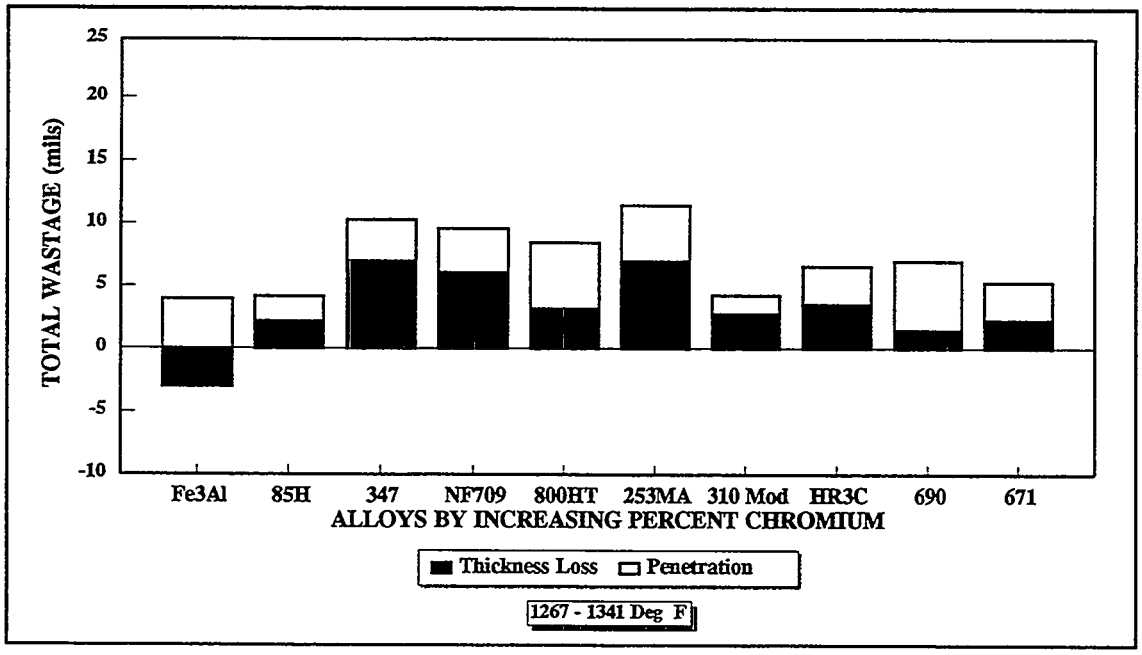

Figure 1

The upper graph lists the total wastage, including wall loss and penetration, for the samples on the 16,000-hour probe that were exposed to 1146-1249 deg F. The lower graph is for the same probe where the samples were exposed at 1267-1341 deg F.

The negative thickness losses in Figure 1 are caused by a swelling which occurred in the Fe_3Al specimens. This may be due to a phase transformation in that alloy, and further testing will have to be performed. The beneficial effect of Al and Si for the same chromium level can be observed when comparing RA85H to 347. Also, as chromium levels in the different alloys increase, there is a decrease in the corrosion rate. This is especially pronounced in the 1156 to 1249°F temperature range. Some alloys, notably RA85H, 347, and 310 Ta modified have higher corrosion rates at the lower temperature. Alloys HR3C and 253MA have a higher corrosion rate at the higher temperature, and the remaining alloys—NF 709, 800HT, 690, and 671—did not show a temperature relationship with total wastage.

These are the preliminary findings; more interpretative analysis is being performed.

CONCLUSIONS

The air-cooled, retractable corrosion probes worked successfully and provided 16,000-hour exposures of each of the nine alloys to two different temperatures.

The Fe3Al + 5Cr samples had a volume increase which is being further evaluated. The total wastage of the Fe3Al + 5Cr was 2 to 10 times lower than 347 stainless steel. The HR3C and 310 Ta modified alloy had total wastage values 2 to 3 times lower than 347 stainless steel. The 690 and the 671 samples had about the same total wastage, and the values were the same or slightly lower, respectively, than the HR3C and 310 Ta modified samples. More detailed analysis and interpretative analysis is being performed for the final report.

REFERENCES

1. W. Nelson and C. Cain, Jr., "Corrosion of Superheaters and Reheaters of Pulverized-Coal-Fired Boilers," *Transactions of the ASME, Journal of Engineering for Power,* July 1960, pp. 194-204.

2. W. T. Reid, "Formation of Alkali Iron Trisulphates and Other Compounds Causing Corrosion in Boilers and Gas Turbines," Project Review July 1, 1966-June 30, 1968, prepared by Battelle Memorial Institute, Columbus, OH, June 1968.

3. W. T. Reid, *External Corrosion and Deposits: Boilers and Gas Turbines,* American Elsevier Publishing Company, New York, 1974.

4. G. J. Hills, "Corrosion of Metals by Molten Salts," *Proceedings of the Marchwood Conference: Mechanism of Corrosion by Fuel Impurities,* Johnson and Littler, eds., Butterworths, London, 1963.

5. J. L. Blough, G. J. Stanko, M. Krawchuk, W. Wolowodiuk, and W. Bakker, "In Situ Coal Ash Corrosion Testing for 2 Years at Three Utilities," International EPRI Conference on Improved Technology for Fossil Power Plants New and Retrofit Applications, Washington, DC, March 1-3, 1993.

6. I. M. Rehn, "Fireside Corrosion of Superheater and Reheater Tubes," Palo Alto, CA: Electric Power Research Institute, 1980. CS-1653.

7. I. M. Rehn, "Fireside Corrosion of Superheater Alloys for Advanced Cycle Steam Plants," Palo Alto, CA: Electric Power Research Institute, 1987. EPRI 5195.

8. S. Van Weele and J. L. Blough, "Literature Search Update—Fireside Corrosion Testing of Candidate Superheater Tube Alloys, Coatings, and Claddings," Livingston, NJ: Foster Wheeler Development Corporation, September 1990. FWC/FWDC/TR-90-11.

9. W. Wolowodiuk, S. Kihara, and K. Nakagawa, "Laboratory Coal Ash Corrosion Tests," Palo Alto, CA: Electric Power Research Institute, July 1989. GS-6449.

10. S. Van Weele and J. L. Blough, "Fireside Corrosion Testing of Candidate Superheater, Tube Alloys, Coatings, and Claddings," Livingston, NJ: Foster Wheeler Development Corporation, August 1991. ORNL/SUB/89-SA187/02.

11. S. Kihara, K. Nakagawa, A. Ohtomo, H. Aoki, and S. Ando, "Simulating Test Results for Fireside Corrosion of Superheater & Reheater Tubes Operating at Advanced Steam Conditions in Coal-Fired Boilers, *High Temperature Corrosion in Energy Systems,* TMS/AIME, M. F. Rothman, ed., 1984, pp. 361-376.

12. W. Wolowodiuk, et al., "Coal-Ash Corrosion Investigations," *Proceedings of the First International Conference on Improved Coal-Fired Power Plants.* Palo Alto, CA: Electric Power Research Institute, November 1986.

13. J. L. Blough, M. T. Krawchuk, G. J. Stanko, and W. Wolowodiuk, "Superheater Corrosion Field Test Results," Palo Alto, CA: Electric Power Research Institute, November 1993. TR-103438.

14. J. L. Blough and W. T. Bakker, "Measurement of Superheater Corrosion Caused by Molten Alkali Sulfates," First International Conference on Heat-Resistant Materials, to be presented at the ASM International, Lake Geneva, WI, September 22-26, 1991.

15. T. Hammond, W. Wolowodiuk, J. L. Blough, J. Brooks, "Replacement of Reheater at TVA's Gallatin Station Unit 2," presented at the Third International Conference on Improved Coal-Fired Power Plants (ICPP), San Francisco, April 1991.

16. R. W. Borio and R. P. Hensel, "Coal-Ash Composition as Related to High-Temperature Fireside Corrosion and Sulfur-Oxides Emission Control," *Transactions of the ASME, Journal of Engineering for Power,* Vol. 94, 1972, pp. 142-148.

17. J. L. Blough, "Fireside Corrosion Testing of Candidate Superheater, Tube Alloys, Coatings, and Claddings," Livingston, NJ: Foster Wheeler Development Corporation, August 1996. ORNL/SUB/93-SM401/01.

PROCESSING AND PROPERTIES OF MOLYBDENUM SILICIDE INTERMETALLICS CONTAINING BORON

J. H. Schneibel, C. T. Liu, L. Heatherly, J. L. Wright, and C. A. Carmichael

Oak Ridge National Laboratory
P. O. Box 2008
Oak Ridge, Tennessee, U. S. A.

ABSTRACT

Molybdenum-silicon-boron intermetallics with the composition Mo-10.5 Si-1.1 B, wt% (Mo-26.7 Si-7.3 B, at. %) were fabricated by several processing techniques. Powder processing (PM) resulted in macrocrack-free material containing no or only few microcracks. The PM materials contained quasi-equilibrium pores and large concentrations of oxygen. Average room temperature flexure strengths of 270 MPa were obtained. At 1200°C in air, flexure strengths as high as 600 MPa were observed. These high values are attributed to crack healing and incipient plasticity. Ingot metallurgy (IM) materials contained much less oxygen than their PM counterparts. Depending on the cooling rate during solidification, they developed either mostly macrocracks or mostly microcracks. Due to the high flaw densities, the room temperature flexure strengths were only of the order of 100 MPa. However, the flexure strengths at 1200°C were up to 3 times higher than those at room temperature. Again, this is attributed to crack healing and incipient plasticity. The IM materials will require secondary processing to develop their full potential. A preliminary examination of secondary processing routes included isothermal forging and hot extrusion.

INTRODUCTION

The objective of this task is to develop new-generation corrosion-resistant Mo-Si alloys for use as hot components in advanced fossil energy combustion and conversion systems. The successful development of Mo-Si alloys is expected to improve the thermal efficiency and performance of fossil energy conversion systems through an increased operating

temperature, and to increase the service life of hot components exposed to corrosive environments at temperatures as high as 1600°C. While $MoSi_2$ is highly oxidation resistant at elevated temperatures, it is extremely brittle at ambient temperatures. Molybdenum compounds with lower Si contents, such as Mo_5Si_3, which are potentially less brittle, do however, not have the required oxidation resistance. As will be seen, boron additions are the answer to the oxidation problem.

As early as 1957, Nowotny et al.[1] pointed out that boron-containing silicides possess high oxidation resistance due to the formation of borosilicate glasses. Based on Nowotny et al's work, boron-containing molybdenum silicides based on Mo_5Si_3 were recently developed at Ames Laboratory.[2-4] These silicides consist of approximately 50 vol.% Mo_5Si_3 (T1), 25 vol.% Mo_5SiB_2 (T2), and 25 vol.% of Mo_3Si. They provide an exciting alternative to $MoSi_2$ for several reasons. First, they possess an oxidation resistance comparable to that of $MoSi_2$, and do not show catastrophic oxidization ("pest reaction") at intermediate temperatures such as 800°C.[4] Second, these three-phase materials may possess a higher fracture resistance than other high-temperature materials such as $MoSi_2$. Third, their creep strength is superior to that of $MoSi_2$.

At present, the mechanical properties of the new Mo-Si-B alloys have not been fully explored. One reason for this is simply the unavailability of sufficiently large test pieces. Due to the high processing temperatures and the high reactivity of Si, processing of Mo-Si-B alloys with good quality is a challenging task. Significant developmental work is, therefore, needed to produce sound Mo-Si-B material with controlled microstructures. At the same time the size of the material must be sufficient (e.g., 50 mm) to be able to characterize the mechanical properties. An interaction between processing, microstructural characterization, and mechanical property measurements is required in order to improve and optimize this new class of materials.

RESULTS AND DISCUSSION

Processing via powder metallurgy

A previous annual report for this program[5] focused on powder metallurgical (PM) processing. Some additional microstructural, mechanical property, and compositional work is reported here. Based on the composition Mo-10.5 Si-1.1 B (wt%), four PM alloys (see also Table I) were produced by hot-pressing. In several cases, carbon was

added to reduce the oxygen content. For the same reason, additions of Zr were made. The difference between the two approaches is that Zr removes oxygen in the form of internal oxides, while carbon additions remove oxygen in the form of gaseous CO/CO_2. Zirconium additions resulted in internal cracking, due to the formation of ZrO_2 particles and the associated thermal expansion mismatch. The Zr-containing alloys were therefore not further investigated.

The oxygen contents of several PM as well as cast Mo-Si-B materials are summarized in Table I. Several points are worth noting. First, the alloy MSB1, which was fabricated from $MoSi_2$ powder and addition of elemental powders, has by far the highest oxygen content. Second, as the carbon content is increased from 0.6 wt% (MSB2) to 1.0 wt% (MSB5), the oxygen content tends to decrease. This indicates that the carbon was indeed effective in deoxidizing the alloys. Third, as expected, the cast materials (MSB418 and MSB424) have much lower oxygen contents than the PM materials.

Table I. Compositions and oxygen contents of Mo-Si-B alloys

Sample ID	Processing*	Composition, wt%	Oxygen, wppm*
MSB1	PM/HP	Mo-10.5 Si-1.1 B-0.2 C	7482
MSB2, analysis #1	PM/HP	Mo-10.41 Si-1.09 B-0.60 C-0.20 Zr	3195
MSB2, analysis #2	PM/HP	"	2275
MSB3	PM/HP	Mo-10.4 Si-1.1B-1.0C	
MSB5	PM/HP	Mo-10.4 Si-1.1B-1.0C	
MSB5	PM/HP	Mo-10.4 Si-1.1 B-1.0 C	1938
MSB418 (center region)	IM(Cu mold)	Mo-10.5 Si-1.1 B	486
MSB418 (near surface)	IM (Cu mold)	"	222
MSB424	IM (C mold)	"	217
MSB425	IM (sand mold)	"	
MSB465	IM (Al_2O_3/SiO_2 mold)	"	

* processing by powder metallurgy (PM) and hot pressing (HP), or by ingot metallurgy (IM).

**The oxygen contents are courtesy M. J. Kramer, Ames Laboratory, Ames, Iowa

Figure 1 illustrates the microstructure of a polished and etched specimen of alloy MSB1, which contained 0.2 wt% C as deoxidizer. The scanning electron microscope (SEM) image in Fig. 1 shows no microcracks, although a more detailed examination of the specimen from which this micrograph was obtained, revealed occasional microcracks. Numerous pores are seen at the grain and interphase boundaries. Their quasi-equilibrium

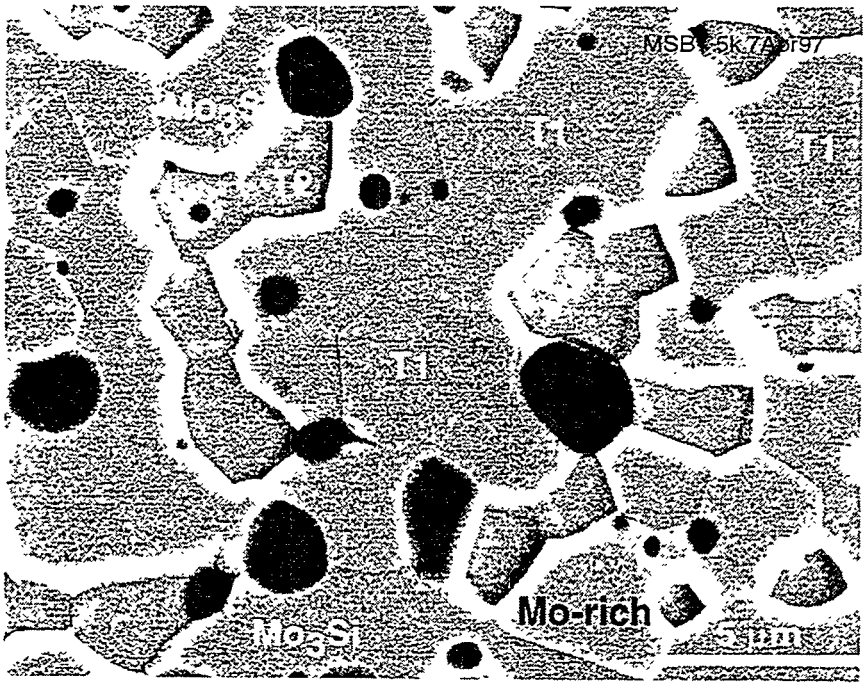

Fig. 1. SEM micrograph of alloy MSB1 (Mo-10.5 Si-1.1 B-0.2 C, wt%) after polishing and etching (Murakami's etch). Pores appear in black. The T2 phase (Mo_5SiB_2) is preferentially etched. In addition to Mo_3Si and Mo_5Si_3 (T1), a Mo-rich phase is found, which is either unreacted Mo or a boride of Mo.

shape suggests that they may have been stabilized by trapped CO/CO_2. The different phases were identified via energy dispersive spectroscopy (EDS) in the SEM. Since B was difficult to detect, identification was performed on the basis of the Si to Mo ratio. The T2 phase (Mo_5SiB_2) etched readily and was therefore easily recognized. Occasionally Mo-rich particles were found. These are either elemental Mo or borides of Mo. The fact that the three-phase Mo_3Si-T1-T2 equilibrium expected from the nominal composition[1] has not been reached is consistent with recent results by Perepezko et al.[6] These authors found that annealing of similar alloys for 150 h at 1600°C did not establish complete phase equilibrium. Since the hot-pressing in this work was carried out at 1600°C, it is not surprising that full equilibrium was not reached.

Processing via ingot metallurgy

Alloys with the composition Mo-10.5 Si-1.1 B (wt%) were drop-cast into molds made from materials with different thermal conductivities in order to examine the effect of the cooling rate on the microstructures that developed during solidification and cool-down. Casting into a 25 mm diam. Cu mold produced ingots which appeared to be uncracked as

judged by visual examination of their outside. However, sectioning and polishing of these ingots always revealed macroscopic cracking. The microstructure of a cast and annealed specimen is shown in Fig. 2. Voids were not detected, but microcracks were occasionally observed. As shown in Table I, the IM alloys contained much less oxygen than the PM alloys.

Casting Mo-10.5 Si-1.1 B into a 25 mm diam. SiO_2 (sand) mold resulted in much lower cooling rates and eliminated macroscopic cracking. An approximately 1 mm thick reaction zone was observed on the outside of the ingot. A typical microstructure is illustrated in Fig. 3. As compared to Fig. 2, more microcracking is seen. Although a quantitative analysis has not been carried out, it appears that the lower cooling rate enhances microcracking. Since Mo_5Si_3 exhibits anisotropic thermal expansion, slower cooling and the associated larger grain/phase sizes are likely to enhance microcracking.

Casting Mo-10.5 Si-1.1 B into a 25 mm diam. porous Al_2O_3/SiO_2 mold resulted in the slowest cooling rate. Solidification occurred so slowly, that the melt reacted extensively with the mold. After cool-down, the casting had a diameter of approximately 50 mm, instead of the initial mold diameter of 25 mm. As verified by qualitative EDS analysis, this alloy picked up significant amounts of oxygen. No macrocracks were observed, but many microcracks. Figure 4 illustrates the microcracks found in this material. Interestingly, the microcracks stopped often in the T2 phase. The microstructure is much coarser than that of the other alloys (compare for example Figs. 4 and 2). Therefore, while macrocracking was alleviated, microcracking was enhanced.

Isothermal forging

An attempt was made to isothermally forge a cylindrical section of an alloy cast into a sand mold (MSB425). This experiment was carried out in a hot-pressing unit. An initial pressure of 35 MPa was applied. Consistent with the excellent high temperature strength of this material no deformation occurred at temperatures up to 1800°C. At 1850°C, the specimen deformed by approximately 50% in 15 minutes . The external appearance of the deformed specimen suggested that the material was partially liquid during deformation.

Microstructural analysis showed that some voids and cracks had formed during the processing. Since the material was partially liquid, this is not surprising.

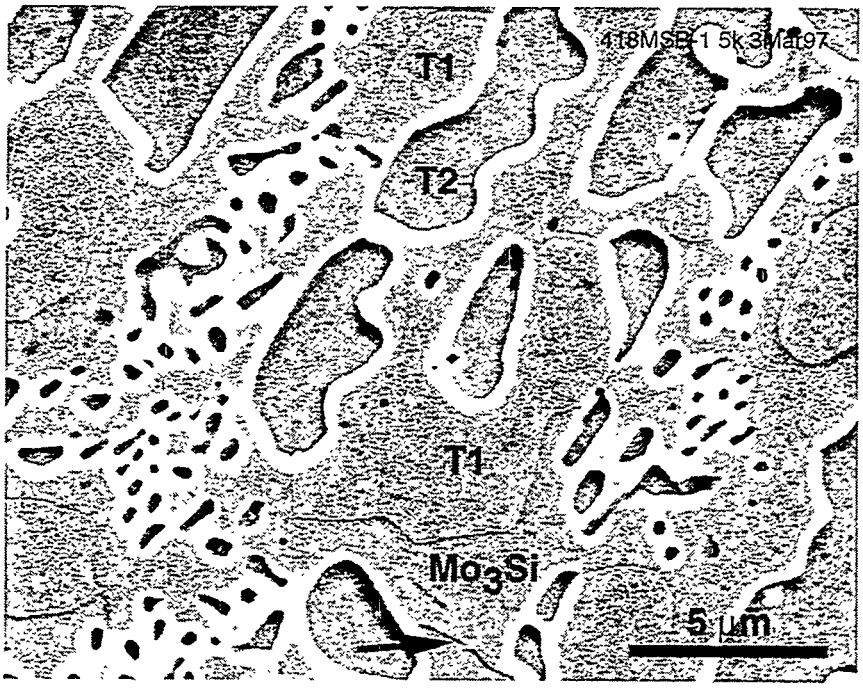

Fig. 2. SEM micrograph of polished and etched section of Mo-10.5 Si-1.1 B cast into a 25 mm diam. Cu mold and annealed for 24 h at 1400°C in vacuum (MSB418). The three phases expected according to the phase diagram[1] are all seen. The T2 phase is preferentially attacked by Murakami's etch. The absence of significant porosity is noted. A microcrack is indicated by an arrow.

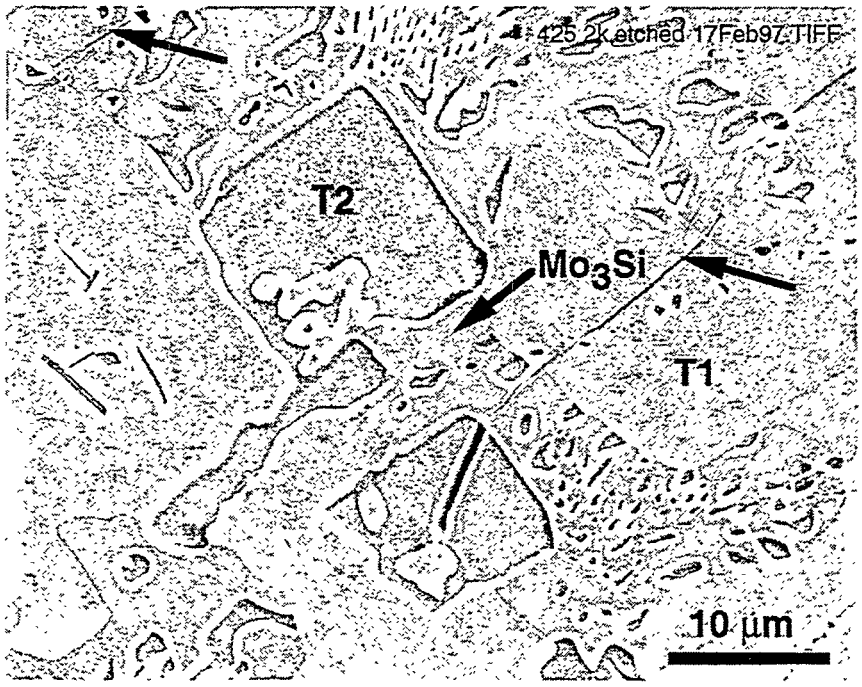

Fig. 3. SEM micrograph of polished and etched section of Mo-10.5 Si-1.1 B cast into a 25 mm diam. sand mold (MSB425). Several microcracks are indicated by arrows.

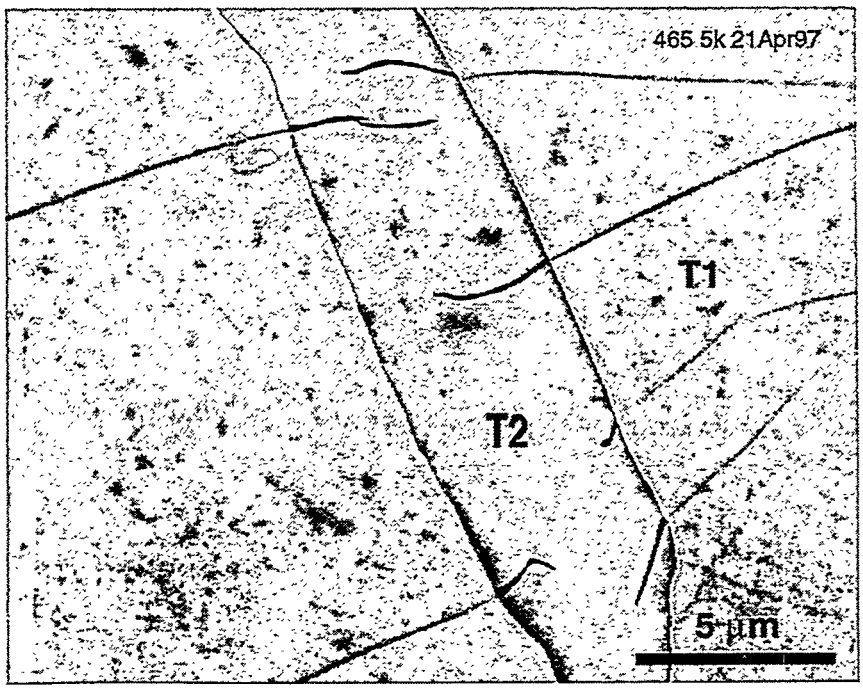

Fig. 4. SEM micrograph of polished and etched section of Mo-10.5 Si-1.1 B cast into a 25 mm diam. Al_2O_3/SiO_2 mold (MSB465).

Extrusion

A casting with the composition Mo-10.5 Si-1.1 B (MSB418) was encapsulated in an evacuated Mo can and extruded at 1800°C. The extrusion exhibited severe cracking and porosity and only small pieces were available for metallographic examination. Figure 5 shows an SEM of the extruded materials. According to EDS analysis, the microstructure consisted of particles of Mo_3Si (dark phase) in a multiphase matrix. In agreement with the EDS finding, x-ray analysis indicated Mo_3Si to be the majority phase. The x-ray analysis revealed also Mo and the T2 phase. The multiphase matrix found between the Mo_3Si particles is depicted in Fig. 6. Due to the small scale, a reliable EDS analysis was not possible. The x-ray analysis suggested that the matrix consists of Mo, Mo_3Si, and T2. Since the nominal composition of the extruded material should have resulted in a 3-phase mixture of Mo_3Si, T1, and T2, it appears that the Mo content of the extruded material increased by a reaction with the Mo can. Since liquid phase formation was observed during isothermal forging at 1850°C, and since the presence of Mo in the extrusion experiment may have reduced the liquidus temperature, liquid phase formation is plausible.

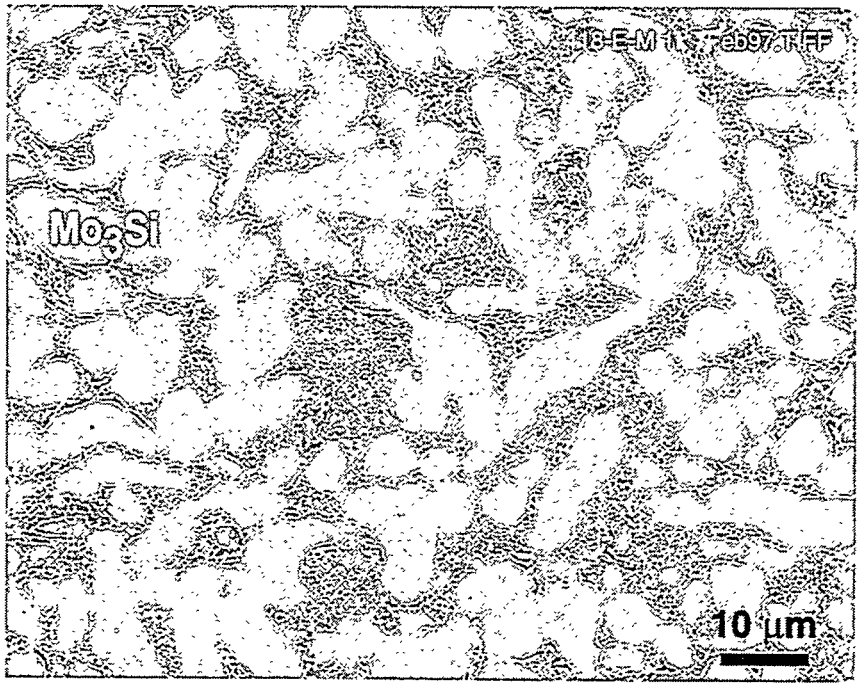

Fig. 5. SEM micrograph of a polished/etched section of extruded Mo-Si-B (MSB418-E).

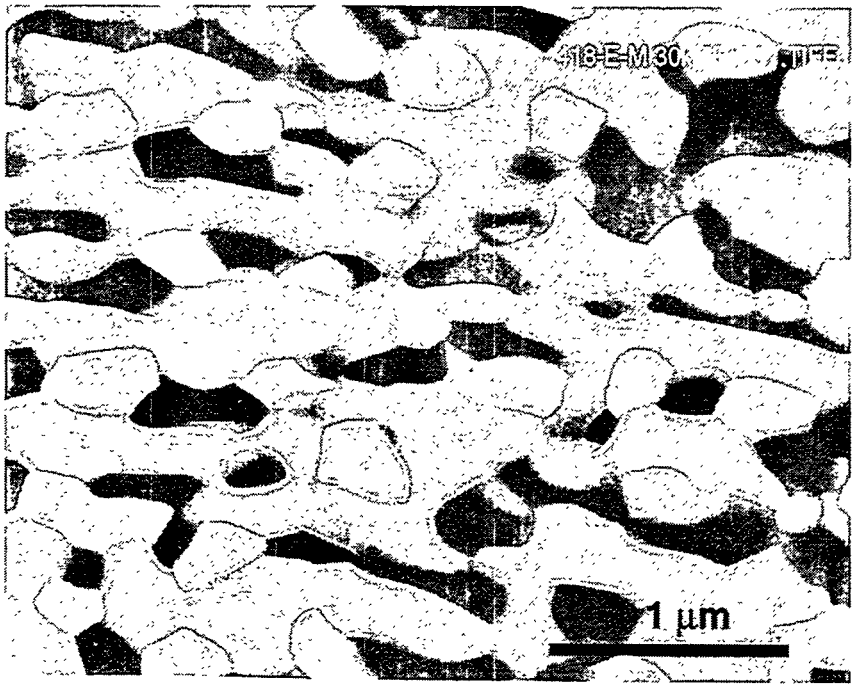

Fig. 6. High magnification SEM micrograph of matrix region of polished and etched section of extruded Mo-Si-B (MSB418-E).

It is, however, encouraging that the extrusion resulted locally in a very fine structure.

Mechanical properties

In a previous report[5] the room temperature tensile strength of the PM alloy MSB1 was determined to be 186 MPa. Since the silicides investigated in this work are flaw-sensitive, it was decided to carry out a larger number of flexure tests in order to obtain statistical information. The results are represented in the Weibull plot in Fig. 7. They indicate that flexure strengths of up to 300 MPa may be obtained. Since this particular material contained porosity (see Fig. 1) as well as a substantial concentration of oxygen (Table I), significantly better properties are expected for optimized processing. Table II shows that the flexure strength is substantially higher at 1200°C, where it reaches values as high as

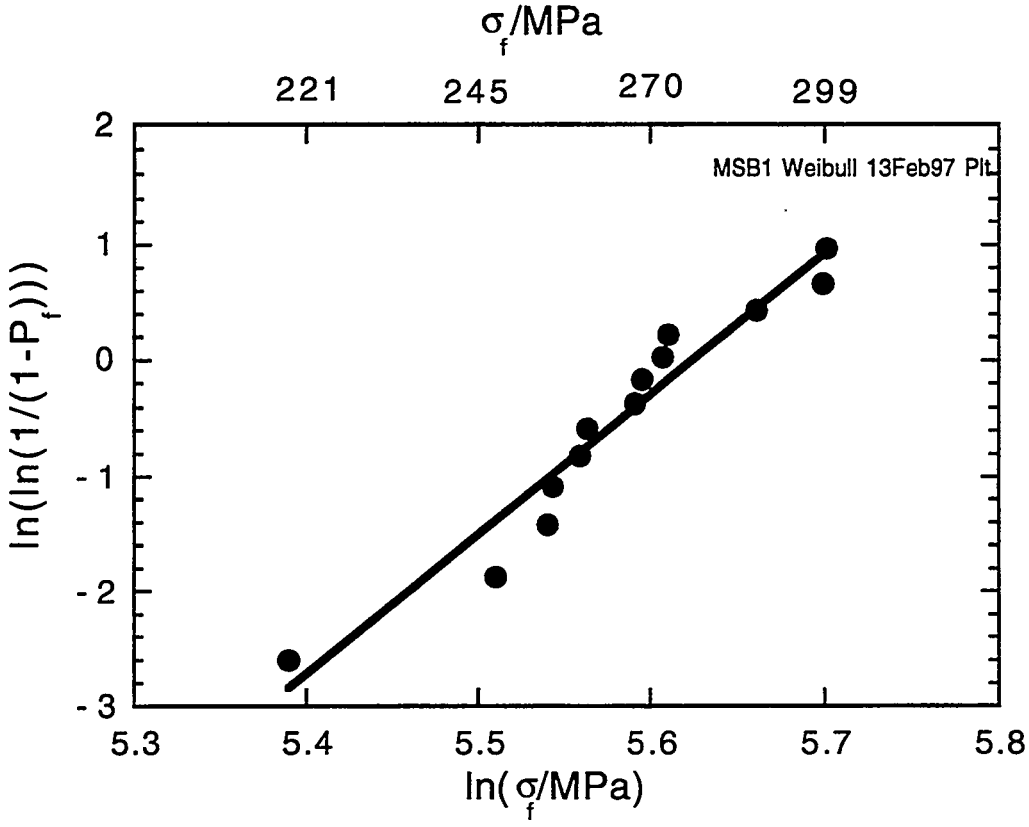

Fig. 7. Weibull Plot of the 3-point flexure strength of MBS1 (Mo-10.5 Si-1.1 B-0.2 C, wt%). P_f is the fracture probability, and σ_f the maximum outer fiber stress.

Table II. Three-point flexure strengths of Mo-10.5 Si-1.1 B (wt%)

Specimen Number	Processing*	Specimen Condition	Test Temperature, ℃	Fracture Strength, MPa
MSB1	PM	as-pressed, average of 13 specimens	20	270
"	PM	as-pressed	1200	460
"	PM	as-pressed	1200	604
MSB425	IM	as-cast	20	119
"	IM	as-cast	20	105
"	IM	as-cast	20	114
"	IM	isothermal forging at 1850°C	20	95
"	IM	isothermal forging at 1850°C	20	110
"	IM	as-cast	1200	221
"	IM	as-cast	1200	283

*PM:powder metallurgy, IM: ingot metallurgy

604 MPa. The high strength may be due to crack healing, borosilicate glass formation at crack tips, or incipient plasticity. The two specimens tested at 1200°C showed quite different strengths indicating that further processing improvements will be needed.

Whereas the PM processed silicides contain no or few microcracks, the cast silicides do. The cast materials are therefore expected to have lower room temperature strengths than the powder metallurgical ones. Table II shows this to be the case. Consistent with the observation of microcracks, isothermal forging at 1850°C (which did cause incipient melting) did not improve the room temperature strength. At elevated temperatures, the microcracks may not be as detrimental to the strength than at room temperature. This could be caused by crack healing, crack blunting, as well as borosilicate glass formation at crack tips. Consistent with this, the 1200°C flexure strengths determined in air are 2 to 3 times higher than those at room temperature, as demonstrated by the data in Table II. This result points out the continuing importance of optimizing the processing of these materials in order to achieve satisfactory mechanical properties. In the case of the IM materials, secondary processing is definitely required in order to minimize the size and number density of microcracks. Efforts are underway to improve the secondary processing.

SUMMARY AND CONCLUSIONS

Molybdenum-silicon-boron intermetallics with the composition Mo-10.5 Si-1.1 B (wt%) were fabricated by several processing techniques. Powder processing resulted in macrocrack-free material containing no or few microcracks. PM materials exhibited reasonably high room temperature strength and excellent strength at 1200°C in air. However, they contained quasi-equilibrium pores, and large concentrations of oxygen. Ingot metallurgy (IM) materials showed much lower oxygen concentrations. Depending on the cooling rate during solidification, they developed either mostly macrocracks or mostly microcracks. Due to the microcracks, the room temperature flexure strengths were low. However, the flexure strengths at 1200°C were up to 3 times higher than those at room temperature. This is attributed to processes such as crack healing, borosilicate glass formation, and incipient plasticity. The IM materials require secondary processing to develop their full potential. Preliminary examinations of secondary processing include isothermal forging and hot extrusion, and further work is in progress to improve the secondary processing.

ACKNOWLEDGMENTS

The authors would like to thank M. J. Kramer, Ames Laboratory, for kindly providing the oxygen concentration data. Thanks are due to J. A. Horton and C. G. McKamey for reviewing this manuscript. This research was sponsored by the Fossil Energy Advanced Research and Technology Development (AR&TD) Materials Program, U.S. Department of Energy, under contract DE-AC05-96OR22464 with Lockheed Martin Energy Research Corporation.

REFERENCES

1. H. Nowotny, E. Kimakopoulou, and H. Kudielka, "Untersuchungen in den Dreistoffsystemen: Molybdän-Silizium-Bor, Wolfram-Silizium-Bor und in dem System: VSi_2-$TaSi_2$," Mh. Chem. 88 (1957) 180
2. A. J. Thom, M. K. Meyer, Y. Kim, and M. Akinc, "Evaluation of $A_5Si_3Z_x$ Intermetallics for Use as High Temperature Structural Materials," in "Processing and Fabrication of Advanced Materials III, V. A. Ravi et al., eds., TMS, 1994, p. 413.
3. M. K. Meyer, M. J. Kramer, and M. Akinca [sic], "Compressive Creep Behavior of Mo_5Si_3 with the Addition of Boron," Intermetallics 4 (1996) 273.
4. M. Meyer, M. Kramer, and M. Akinc, "Boron-Doped Molybdenum Silicides," Adv. Mater. 8 (1996) 85.

5. Fossil Energy Program Annual Progress Report for April 1995 through March 1996, R. R. Judkins, Program Manager, ORNL-6902, pp. 157-167.
6. J. H. Perepezko, C. A. Nuñes, S.-H. Yi, and D. J. Thoma, "Phase Stability in Processing of High Temperature Intermetallic Alloys," in press, MRS Symposium Proceedings Vol. 460, C. C. Koch et al., eds.

APPENDIX A

FINAL PROGRAM

FINAL PROGRAM
CONFERENCE ON FOSSIL ENERGY MATERIALS
Knoxville, Tennessee
May 20-22, 1997

SESSION I - Ceramic Composites and Functional Materials

Tuesday, May 20, 1997

7:00 **Registration and Continental Breakfast**

8:00 *Welcome and Introductory Remarks*, Program Managers, Department of Energy and Oak Ridge National Laboratory

8:20 *Advanced Research Programs and AR&TD Materials Program Overview*- R.R. Judkins, Fossil Energy Program Manager, Oak Ridge National Laboratory

9:00 *Development of a Scale-Up CVI System for Tubular Geometries,* T. M. Besmann, Oak Ridge National Laboratory

9:30 *Mass Transport Measurements and Modeling for Chemical Vapor Infiltration,* T. L. Starr, Georgia Institute of Technology

10:00 **BREAK**

10:20 *Development of Oxidation-Resistant Composite Materials and Interfaces,* R.A. Lowden, Oak Ridge National Laboratory

10:50 *Corrosion Protection of SiC Based Ceramics with CVD Mullite Coatings,* V. Sarin, Boston University

11:20 *Thermal Cycling Characteristics of Plasma Synthesized Mullite Films*, I. Brown, Lawrence Berkeley National Laboratory

11:50 **LUNCH**

1:15 *Influence of Water Vapor and Slag Environments on Corrosion and Mechanical Properties of Ceramic Materials*, K. Natesan, Argonne National Laboratory

1:45 *Evaluation of an All-Ceramic Tubesheet Assembly for a Hot Gas Filter*, J. L. Bitner, Mallett Technology

2:15 *Development of Nondestructive Evaluation Methods for Structural Ceramics*, W. A. Ellingson, Argonne National Laboratory

2:45 **BREAK**

3:00 *Solid State Electrolyte Systems*, L. R. Pederson, Pacific Northwest Laboratory

3:30 *Activation and Micropore Structure Determination of Carbon-Fiber Composite Molecular Sieves*, M. Jagtoyen, University of Kentucky Center for Applied Energy Research

4:00 *A Carbon Fiber Based Monolithic Adsorbent for Gas Separation*, T. D. Burchell, Oak Ridge National Laboratory

4:30 **ADJOURN**

FINAL PROGRAM
CONFERENCE ON FOSSIL ENERGY MATERIALS
Knoxville, Tennessee
May 20-22, 1997

SESSION II - Ceramics, New Alloys, and Functional Materials

Tuesday, May 20, 1997
6:30 - 8:30 p.m.

POSTER PRESENTATIONS - BUFFET RECEPTION

Mechanical Performance of Hi-Nicalon/CVI-SiC Composites with Multilayer SiC/C Interfaces, W. A. Curtin, Virginia Polytechnic Institute and State University

Heat Treatment Effects for Improved Creep-Rupture Resistance of a Fe_3Al-based Alloy, C. G. McKamey, Oak Ridge National Laboratory

Effects of Humidity and Test Frequency on Environmental Embrittlement of Fe_3Al Alloys , N. S. Stoloff, Rensselaer Polytechnic Institute

Effects of Titanium and Zirconium on Iron Aluminide Weldments, G. R. Edwards, Colorado School of Mines

Effects of 1000 °C Oxide Surfaces on Room Temperature Aqueous Corrosion and Environmental Embrittlement of Iron Aluminides, R. A. Buchanan, University of Tennessee

Coal-Based Carbon Products: Processes, Applications, and Future Challenges, C. Irwin, West Virginia University

The Influence of Processing on Microstructure and Properties of Iron Aluminides, R. N. Wright, Idaho National Engineering Laboratory

Mechanisms of Defect Complex Formation and Environmental-Assisted Fracture Behavior of Iron Aluminides, B. R. Cooper, West Virginia University

Ultrahigh Temperature Intermetallic Alloys, C. T. Liu and M. Brady, Oak Ridge National Laboratory

Study of Fatigue and Fracture Behavior of Cr_2Nb-Based Alloys:Phase Stability in Nb-Cr-Ni Ternary Systems, P. Liaw, University of Tennessee

Iron-Aluminide Filters for IGCCs and PFBCs, P. F. Tortorelli, Oak Ridge National Laboratory

Weld Overlay Cladding With Iron Aluminides, G. M. Goodwin, Oak Ridge National Laboratory

SHS Processing and Properties of Intermetallic Alloys and Composites, R. Walters, Albany Research Center

Ceramic Membranes For High Temperature Hydrogen Separation, G. Roettger, East Tennessee Technology Park

High Temperature Corrosion Behavior of Iron-Aluminide Alloys and Coatings, P. F. Tortorelli, Oak Ridge National Laboratory

Corrosion-Resistant Coating Devlopment, D. P. Stinton, Oak Ridge National Laboratory

FINAL PROGRAM
CONFERENCE ON FOSSIL ENERGY MATERIALS
Knoxville, Tennessee
May 20-22, 1997

SESSION III - WORKSHOP

Wednesday, May 21, 1997

MORNING SESSION - Materials Issues in Low-Emission Boilers

7:00	**Registration and Continental Breakfast**
8:00	**Keynote Address: Mr. L. A. Ruth** **Federal Energy Technology Center** **Pittsburgh, Pennsylvania**
8:30	N. Birks, University of Pittsburgh
9:00	LEBS/T. B. Gibbons, ABB Combustion Engineering
9:20	LEBS/P. Daniel, Babcock & Wilcox
9:40	LEBS/Riley Stoker
10:00	**BREAK**
10:20	*Update on Low-NO_x Issues*, R. B. Dooley, EPRI
10:40	*Critical Materials Issues*, C. D. Lundin, University of Tennessee
11:00	Discussion
12:00	**LUNCH**

AFTERNOON SESSION - Materials Issues in High Efficiency Coal-Fired Cycles

1:30	*Review of UTRC's HIPPS Development*, John Holowczak
2:15	*Review of Foster Wheeler's HIPPS Development*, Jeff Blough
3:00	**BREAK**
3:20	*SiC-Based Ceramics in Coal Combustion Environments*, Kristin Breder, Oak Ridge National Laboratory
3:50	*Modifications of Slags and Monolithic Refractories to Reduce Corrosion Rates,* John Hurley, University of North Dakota Energy and Environmental Research Center
4:20	**ADJOURN**

FINAL PROGRAM
CONFERENCE ON FOSSIL ENERGY MATERIALS
Knoxville, Tennessee
May 20-22, 1997

SESSION IV - New Alloys

Thursday, May 22, 1997

7:30 **Registration and Continental Breakfast**

8:00 *Welcome and Introductory Remarks*

8:10 *Development of ODS Fe_3Al Alloys,* I.G.Wright , Oak Ridge National Laboratory

8:40 *Iron Aluminide Weld Overlay Coatings for Boiler Tube Protection in Coal-fired Low NOx Boilers*, J. N. DuPont, Lehigh University

9:10 *Corrosion Performance of Iron Aluminides in Fossil Energy Environments* K. Natesan, Argonne National Laboratory

9:40 *Microstructure of Mechanical Behavior of Alumina Scales and Coatings,* K. B. Alexander, Oak Ridge National Laboratory

10:10 **BREAK**

10:30 *Microstructural and Mechanical Property Characterization of Ingot Metallurgy ODS Iron Aluminum,* V. K. Sikka, Oak Ridge National Laboratory

11:00 *Simulataneous Aluminizing and Chromizing of Steels to Form $(Fe,Cr)_3Al$ Coatings and Ge-doped Silicide Coatings of Cr-Zr Base Alloys,* R. A. Rapp, Ohio State University

11:30 *Electro-Spark Deposition Technology,* R. N. Johnson, Pacific Northwest Laboratory

12:00 **LUNCH**

1:15 *Investigation of Austenitic Alloys for Advanced Heat Recovery and Hot-Gas Cleanup Systems,* R. W. Swindeman, Oak Ridge National Laboratory

1:45 *Fireside Corrosion Testing of Candidate Superheater Tube Alloys, Coatings, and Claddings - Phase II,* J. L. Blough, Foster Wheeler Development Corporation

2:15 *Processing and Properties of Molybdenum Silicide Intermetallics with Boron,* J. H. Schneibel, Oak Ridge National Laboratory

2:45 **ADJOURN**

APPENDIX B

LIST OF ATTENDEES

ATTENDEE LIST

Fossil Energy Materials Conference
May 20-22, 1997
Knoxville, Tennessee

A
Shawn Ailey
Oak Ridge National Laboratory
P.O. Box 2008
Oak Ridge, TN 37831-6064
(423) 576-5086
FAX 423-574-4913

Kathi Alexander
Oak Ridge National Laboratory
P.O. Box 2008
Oak Ridge, TN 37831-6376
(423) 574-0631
FAX 423-574-0641

David Alman
Albany Research Center
1450 Queen Avenue SW
Albany, OR 97321
(541) 967-5885
FAX 541-967-5845

Mark J. Andrews
U.S. Department of Energy
Oak Ridge National Laboratory
P.O. Box 2008
Oak Ridge, TN 37831-6069
(423) 241-4571
FAX 423-574-6098

B
Stephen W. Banovic
Lehigh University
Energy Research Center
Whitaker Laboratory
5 E Packer Avenue
Bethlehem, PA 18015
(610) 758-4270
FAX 610-758-4244

Paul Becher
Oak Ridge National Laboratory
P.O. Box 2008
Oak Ridge, TN 37831-6068
(423) 574-5157
FAX 423-574-6098

Barbara Bennett
Oak Ridge National Laboratory
P.O. Box 2008
Oak Ridge, TN 37831-6087
(423) 574-5220

Theodore Besmann
Oak Ridge National Laboratory
P.O. Box 2008
Oak Ridge, TN 37831-6063
(423) 574-6852
FAX 423-574-4913

Neil Birks
The University of Pittsburgh
Materials Science & Engineering Dept.
848 Benedum Hall
Pittsburgh, PA 15261
(412)624-9743
FAX 412-624-8069

Jerry Bitner
Mallett Technology
100 Park Drive
Suite 204
P.O. Box 14407
Research Triangle Park, NC
FAX 412-746-7001

Jeff Blough
Foster Wheeler Development Corp.
John Blizard Research Center
12 Peach Tree Hill Road
Livingston, NJ 07039-5701
(201) 535-2355
FAX 201-535-2242

Ron Bradley
Oak Ridge National Laboratory
P.O. Box 2008
Oak Ridge, TN 37831-6161
(423) 574-6095

Mike Brady
Oak Ridge National Laboratory
P.O. Box 2008
Oak Ridge , TN 37831-6115
(423) 576-2449
FAX 423-574-5118

Kristin Breder
Oak Ridge National Laboratory
P. O. Box 2008
4515, MS 6062
Oak Ridge, TN 37831-6062
(423) 574-5089
FAX 423-574-4913

Ian Brown
University of California
Lawrence Berkeley Laboratory
One Cyclotron Road
Bldg 53
Berkeley, CA 94720
(510) 486-4174
FAX 510-486-4374

R. A. Buchanan
The University of Tennessee
Department of Materials Science and Engineering
434 Dougherty Engineering Building
Knoxville, TN 37996-2200
(423) 974-4858

Tim Burchell
Oak Ridge National Laboratory
P. O. Box 2008
4508, MS 6088
Oak Ridge, TN 37831-6088
(423) 576-8595
FAX 423-576-8424

Nancy Cole
NCC Engineering, Inc.
10518 Raven Court
Knoxville, TN 37922
423-691-8011

Bernard R. Cooper
West Virginia University
Department of Physics
Morgantown, WV 26506-6315
(304) 293-3423
FAX 304-293-3120

Phil Daniel
Babcock & Wilcox
P.O. Box 351
Barberton, OH 44601
(330) 860-1953

R. B. Dooley
EPRI
3412 Hillview Avenue
Palo Alto, CA 94303
(415) 855-2458

John N. DuPont
Lehigh University
Energy Research Center
5 E Packer Avenue
Bethlehem, PA 18015
(610) 758-3942
FAX 610-758-4244

Glen R. Edwards
Colorado School of Mines
Center for Welding, Joining and Coatings Research
Golden, CO 80401-1887
(303) 273-3773
FAX 303-273-3795

Paul Eggerstedt
Industrial Filter and Pump
5900 Ogden Avenue
Cicero, IL 60804
(708) 656-7800
FAX 708-656-7806

William A. Ellingson
Argonne National Laboratory
9700 South Cass Avenue
Bldg. 212
Argonne, IL 60439
(708) 252-5068
FAX 708-252-4798

Jonathan Erpenbach
Oak Ridge National Laboratory
P.O. Box 2008
Oak Ridge, TN 37831-6087
(423) 576-2769

Douglas Fain
East Tennessee Technology Park
P. O. Box 2003
1004-L, MS 7271
Oak Ridge, TN 37831-7271
(423) 574-9932
FAX 423-576-2930

Thomas B. Gibbons
ABB Combustion Engineering
Power Plant Laboratories
2000 Day Hill Road
Windsor, CT 06095
(860) 285-3593

Fred M. Glaser
U.S. Department of Energy
Office of Advanced Research
FE-72
11901 Germantown Road
Germantown, MD 20874
(301) 903-2786
FAX 301-903-8350

G. M. Goodwin
Oak Ridge National Laboratory
P.O. Box 2008
4508, MS 6096
Oak Ridge, TN 37831-6096
(423) 574-4809
FAX 423-574-7721

Howard Halverson
Virginia Polytechnic Institute & State University
Department of Engineering Science and Mechanics
College of Engineering
Blacksburg, VA 24061-0219
(540) 231-7493
FAX 540-231-7187

John Holowczak
United Technologies
Research Center
411 Silver Lane
East Hartford, CT 06108)
FAX 860-610-7879

Linda Horton
Oak Ridge National Laboratory
P. O. Box 2008
4500S, MS 6132
Oak Ridge, TN 37831-6132
(423) 574-5081
FAX 423-574-4066

John P. Hurley
University of North Dakota
Energy & Environmental Research Center
P. O. Box 9018
Grand Forks, ND 58202-9018
(701) 777-5000
FAX 701-777-5181

Carl Irwin
West Virginia University
Department of Physics
P. O. Box 6064
Morgantown, WV 26506-6064
304-293-2867
(FAX) 304-293-3749

Marit Jagtoyen
The University of Kentucky
Center for Applied Energy Research
3572 Iron Works Pike
Lexington, KY 40511-8433
(606) 257-0213

Roger N. Johnson
Pacific Northwest National Laboratory
P. O. Box 999, K3-59
Battelle Boulevard
Richland, WA 99352
(509) 375-6906
FAX 509-375-3864

Roddie R. Judkins
Oak Ridge National Laboratory
P. O. Box 2008
4508, MS 6084
Oak Ridge, TN 37831-6084
(423) 574-4572
FAX 423-574-5812

Matthew June
PALL Corporation
3669 State Route 281
P.O. Box 2030
Cortland, NY 13045
(607-753-6041
FAX 607-753-1220

James Kelly
Rolled Alloys
125 West Sterns Road
P.o. Box 310
Temperance, MI 48182
(313) 847-0561
FAX 313-847-3227

Edgar Lara-Curzio
Oak Ridge National Laboratory
P.O. Box 2008
Oak Ridge, TN 37831-6064
(423) 574-1749
FAX 423-574-6098

Patrick H. Le
Federal Energy Technology Center
3610 Collins Ferry Road
Morgantown, WV 26507-0880
(304) 285-4324
FAX 304-285-4469

Peter Liaw
The University of Tennessee
Department of Materials Science and Engineering
430-C Dougherty Engineering Building
Knoxville, TN 37996-2200
(423) 974-2696
FAX 423-974-4115

C. T. Liu
Oak Ridge National Laboratory
P. O. Box 2008
4500S, MS 6115
Oak Ridge, TN 37831-6115
(423) 574-4459
FAX 423-574-7659

Rick Lowden
Oak Ridge National Laboratory
P. O. Box 2008
4508, MS 6087
Oak Ridge, TN 37831-6087
(423) 576-2769
FAX 423-576-8424

William D. Manly
Oak Ridge National Laboratory
P.O. Box 2008
Oak Ridge, TN 37831-6158
(423) 574-2556
FAX 423-574-5118

Claudette McKamey
Oak Ridge National Laboratory
P. O. Box 2008
4500S, MS 6115
Oak Ridge, TN 37831-6115
(423) 574-6917
FAX 423-574-7659

Theodore McMahon
Federal Energy Technology Center
MS C04
P.O. Box 880
Morgantown, WV 26507-0880
(304) 285-4865
FAX 304-285-4403

Othon Monteiro
Berkeley Laboratory
53-103
1 Cyclotron Road
Berkeley, CA 94720
(510) 486-6159
FAX 510-486-4646

Karren More
Oak Ridge National Laboratory
P.O. Box 2008
Oak Ridge, TN 37831-6064
(423) 574-7788
FAX 423-574-4913

K. Natesan
Argonne National Laboratory
9700 South Cass Avenue
Argonne, IL 60439
(708) 252-5103
FAX 708-252-3604

Dick Nixdorf
REMAXCO Technologies, Inc.
10425 Cogdill Road
Suite 300
Knoxville, TN 37932
(423) 675-1574
FAX 423-675-1581

Parvid Pasto
Oak Ridge National Laboratory
P.O. Box 2008
Oak Ridge, TN 37831-6062
(423) 574-5123
FAX 574-4913

L. R. Pederson
Pacific Northwest National Laboratory
MS K2/44
P. O. Box 999
Richland, WA 99352
(509) 375-2731
FAX 509-375-2186

Kent Probst
Oak Ridge National Laboratory
P.O. Box 2008
Oak Ridge, TN 37831-6063

Robert A. Rapp
Ohio State University
Department of Materials Science and Engineering
116 West 19th Avenue
Columbus, OH 43210-1110
(614) 292-6178
FAX 614-292-1537

Richard B. Read
Federal Energy Technology Center
P. O. Box 10940
Pittsburgh, PA 15236
(412) 892-5721
FAX 412-892-4604

Bill Riley
Albany Research Center
1450 Queen Avenue SW
Albany, OR 97321-2198
(541-967-5851
FAX 541-967-5991

George Roettger
East Tennessee Technology Park
P. O. Box 2003
1004-L, MS 7271
Oak Ridge, TN 37831-7271
(423) 574-7539
FAX 423-576-2930

John Ruether
Federal Energy Technology Center
P.O. Box 10940
Pittsburgh, PA 15236
(412) 892-4832
FAX 412-892-4775

Larry Ruth
Federal Energy Technology Center
P.O. Box 10940
Pittsburgh, PA 15236
(412) 892-4461
FAX 412-892-4822

Vinod K. Sarin
Boston University
College of Engineering
15 St. Mary's Street
Boston, MA 02215
(617) 353-6451
FAX 617-353-5548

Joachim H. Schneibel
Oak Ridge National Laboratory
P.O. Box 2008
Oak Ridge, TN 37831-6115
(423) 576-4644
FAX 423-574-7659

Vinod Sikka
Oak Ridge National Laboratory
P. O. Box 2008
4508, MS 6083
Oak Ridge, TN 37831-6083
(423) 574-5112
FAX 423-4-4357

Prabhu Singh
Westinghouse Electric Corporation
1310 Beulah Road
Pittsburgh, PA 15235-5098
(412) 256-2158
FAX 412-256-2002

Robert Smith
3M Company
Bldg. 203-1-01
3M Center
St. Paul, MN 55144-1000
(612) 733-2564
FAX 612-736-5484

Will Spint
Oak Ridge National Laboratory
P.O. Box 2008
Oak Ridge, TN 37831-6087
(423) 576-2769

Peter Stansberry
Department of Chemical engineering
423 Engineering Sciences Building
P.O. Box 6102
Morgantown, WV 26506-6102
(304) 293-2111, ext. 423
FAX 304-293-4139

Thomas L. Starr
Georgia Institute of Technology
School of Materials Science and
Engineering
Bunger-Henry Building, Room 276
Atlanta, GA 30332-0245
(404) 894-0579
FAX 404-894-9140

David P. Stinton
Oak Ridge National Laboratory
P. O. Box 2008
4515, MS 6063
Oak Ridge, TN 37831-6063
(423) 574-4556
FAX 423-574-4923

N. S. Stoloff
Rensselaer Polytechnic Institute
Materials Engineering Department
Troy, NY 12180-3590
(518) 276-6371
FAX 518-276-8554

Robert W. Swindeman
Oak Ridge National Laboratory
P. O. Box 2008
4500S, MS 6155
Oak Ridge, TN 37831-6155
(423) 574-5108
FAX 423-574-5118

Peter F. Tortorelli
Oak Ridge National Laboratory
P. O. Box 2008
4500S, MS 6156
Oak Ridge, TN 37831-6156
(423) 574-5119
FAX 423-574-5118

V Srinath Viswanathan
Oak Ridge National Laboratory
P.O. Box 2008
Oak Ridge, TN 37831-6083
(423) 576-9917
FAX 423-574-4357

W Rich Walters
Albany Research Center
1450 Queen Avenue SW
Albany, OR 97321-2198
(541) 967-5873
FAX 541-967-5991

Philip Way
Permeable Ceramics
Ferro Corporation
603 West Commercial St.
E. Rochester, NY 14445
(716) 586-8770
FAX 716-586-7154

Marvis White
U.T. Space Institute
MS-27
B. H. Goethert Parkway
Tullahoma, TN 37388
(615) 393-7502
FAX 615-455-7266

Ian Wright
Oak Ridge National Laboratory
P. O. Box 2008
4500S, MS 6157
Oak Ridge, TN 37831-6157
(423) 574-4451
FAX 423-574-5118

Richard N. Wright
Idaho National Engineering &
Environmental Laboratory
P. O. Box 1625
Idaho Falls, ID 83415-2218
(208) 526-6127
FAX 208-526-0690

Z John Zhu
University of Tennessee
Department of Materials Science and
Engineering
430-C Dougherty Engineering Building
Knoxville, TN 37996-2200
(423) 974-2696
FAX 423-974-4115

CONF-9705115
ORNL/FMP-97/1

INTERNAL DISTRIBUTION

1. K. B. Alexander
2. P. F. Becher
3. B. Bennett
4. T. M. Besmann
5. R. A. Bradley
6. M. Brady
7. K. Breder
8. T. D. Burchell
9. P. T. Carlson
10. J. R. DiStefano
11. J. Erpenbach
12. D. E. Fain
13. G. M. Goodwin
14. J. A. Haynes
15. L. L. Horton
16-19. R. R. Judkins
20. M. A. Karnitz
21. J. R. Keiser
22. E. Lara-Curzio
23. C. T. Liu
24. R. A. Lowden
25. P. J. Maziasz
26. C. G. McKamey
27. K. L. More
28. E. Ohriner
29. A. Pasto
30. B. Pint
31. K. Probst
32. G. E. Roettger
33 G. R. Romanoski
34. A. C. Schaffhauser
35. J. H. Schneibel
36. J. Sheffield
37. V. K. Sikka
38. W. Spint
39. D. P. Stinton
40. R. W. Swindeman
41. T. N. Tiegs
42. P. F. Tortorelli
43. S. Viswanathan
44. D. F. Wilson
45. I. G. Wright
46-47. Central Research Library
48. Document Reference Section
49. ORNL Patent Section
50-51. Laboratory Records Department
52. LRD-RC

EXTERNAL DISTRIBUTION

53. 3M COMPANY, 3M Center, St. Paul, MN 55144
R. G. Smith (Bldg 203-1-01)

54. A. AHLSTROM CORPORATION, Ahlstrom Pyropower, Kanslerinkatu 14, Fin 33720, Tampere, Finland
J. Isaksson

55. ABB Lummus Crest, 15 Broad St., Bloomfield, NJ 07003
M. Greene

56. ABB COMBUSTION ENGINEERING, 911 W. Main St., Chattanooga, TN 37402
D. A. Canonico

57 ABB COMBUSTION ENGINEERING, 2000 Day Hill Road, Windsor, CT 06095
T. B. Gibbons

58. ADIABATICS, INC., 3385 Commerce Dr., Columbus, IN 47201
P. Badgley

59. ADVANCED REFRACTORY TECHNOLOGIES, INC., 699 Hertel Avenue, Buffalo, NY 14207
K. A. Blakely

60. AEA INDUSTRIAL TECHNOLOGY, Harwell Laboratory, Materials Development Division, Bldg. 393, Didcot, Oxfordshire, OX110RA ENGLAND
H. Bishop

61. AIR PRODUCTS AND CHEMICALS, INC., 7201 Hamilton Blvd., Allentown, PA 18195-1501
P. Dyer

62-64. ALBANY RESEARCH CENTER, 1450 Queen Ave., SW, Albany, OR 97321-2198
D. Alman
W. Riley
R. Walters

65. ALBERTA RESEARCH COUNCIL, Oil Sands Research Department, P. O. Box 8330, Postal Station F, Edmonton, Alberta, CANADA T6H5X2
L. G. S. Gray

66. ALLEGHENY LUDLUM STEEL, Technical Center, Alabama and Pacific Avenues, Brackenridge, PA 15014
J. M. Larsen

67. ALLIEDSIGNAL, 2525 W 190th Street, Dept. 93140, Torrance, CA 90504-6099
N. Minh (MS T-41)

68. ALLIEDSIGNAL ENGINES, 111 S. 34th Street, Phoenix, AZ 85071-2181
T. Strangman (MS 553-12)

69. ALLISON ENGINE COMPANY, Materials Engineering, P.O. Box 420, Indianapolis, IN 46206-0420
L. E. Groseclose

70-71 ALLISON GAS TURBINE DIVISION, P. O. Box 420, Indianapolis, IN 46206-0420
P. Khandalwal (Speed Code W-5)
R. A. Wenglarz (Speed Code W-16)

72. ALON PROCESSING, INC., Grantham Street, Tarentum, PA 15084
W. P. Heckel, Jr.

73. ALON PROCESSING, INC., 900 Threadneedle, Vista Bldg, Houston, TX 77079-2990
K. A. Wynns

74. AMAX R&D CENTER, 5950 McIntyre St., Golden, CO 80403
T. B. Cox

75-76. AMERCOM, Advanced Material Division, Atlantic Research Corporation 8928 Fullbright Avenue, Chatsworth, CA 91311
J. O. Bird
W. E. Bustamante

77. AMOCO CHEMICAL COMPANY, P. O. Box 3011, D-2, Naperville, IL 60566-7011
N. Calamur

78. ANSTO, New Illawarra Rd, Lucas Heights NSW 2234 PMB, 1 Menai NSW 2234, Australia
A.B.L. Croker

79. APD INC., 2500 Pearl Buck Road, Bristol, PA 19007
F. Ko

80. A. P. GREEN REFRACTORIES COMPANY, Green Blvd.,
Mexico, MO 65265
J. L. Hill

81-82. ARGONNE NATIONAL LABORATORY, 9700 Cass Ave.,
Argonne, IL 60439
W. A. Ellingson
K. Natesan

83. BABCOCK & WILCOX, P.O. Box 351, Barberton, OH 44601
P. Daniel

84-86. BABCOCK & WILCOX, Lynchburg Research Center, P. O. Box 11165,
Lynchburg, VA 24506
R. Goettler
J. A. Heaney
W. Long

87. BABCOCK & WILCOX INTERNATIONAL, 581 Coronation Blvd.,
Cambridge, Ontario, Canada N1R 5V3
R. Seeley

88. BATTELLE COLUMBUS LABORATORIES, 505 King Ave.,
Columbus, OH 43201
D. Anson

89. BENNETT, Michael J., Three Chimneys, South Moreton Oxon, United Kingdom

90-91. BETHLEHEM STEEL CORPORATION, Homer Research Laboratories,
Bethlehem, PA 18016
B. L. Bramfitt
J. M. Chilton

92. BIRL, 1801 Maple Avenue, Evanston, IL 60201
D. Boss

93. BLACK & VEATCH, 11401 Lamar, Overland Park, KS 66211
M. Bary

94. BOSTON UNIVERSITY, 44 Washington Street, Boston, MA 02215
V. K. Sarin

95. BRITISH COAL CORPORATION, Coal Technology Development Division,
P. O. Box 199, Stoke Orchard, Cheltenham, Glocester,
ENGLAND GL52 4ZG
J. Oakey

96. BROWN UNIVERSITY, Division of Engineering, 182 Hope Street, Providence, RI 02912
K. Kumar

97. CANADA CENTER FOR MINERAL & ENERGY TECHNOLOGY, 568 Booth St., Ottawa, Ontario Canada K1A OG1
R. W. Revie

98. CARR, James P., 15005 Lear Lane, Silver Springs, MD 20905

99. CERAMEM SEPARATIONS, 952 Eat Fir Street, Palmyra, PA 17078
J. Vaklyes, Jr.

100. CHEVRON RESEARCH & TECHNOLOGY COMPANY, 100 Chevron Way, Richmond, CA 94802-0627
D. J. O'Rear

101. CIEMAT, Avda. Complutense, 22, 28040-Madrid (SPAIN)
G. M. Calvo

102. COAL & SYNFUELS TECHNOLOGY, 1616 N. Fort Myer Dr., Suite 1000, Arlington, VA 22209
J. Bourbin

103. COAL TECHNOLOGY CORPORATION, 103 Thomas Road, Bristol, VA 24201
R. A. Wolfe

104. COLORADO SCHOOL OF MINES, Dept. of Metallurgical Engineering, Golden, CO 80401
G. R. Edwards

105. CORNING INCORPORATED, SP-D V-1-9, Corning, NY 14831
P. Bardhan

106. DB Riley, Inc., 45 McKeon Road, Worcester, MA 01610
G. S. Gielda

107. DEVASCO INTERNATIONAL, INC., 9618 W. Tidwell, Houston, TX 77041
J. L. Scott

108. J. DOWICKI, P.E., 19401 Framingham Dr., Gaithersburg, MD 20879

109. DUPONT LANXIDE COMPOSITES, INC., Pencader Plant, Box 6100, Newark, DE 19714-6100
J. K. Weddell

110-111. DUPONT LANXIDE COMPOSITES, INC., 1300 Marrows Road,
P.O. Box 6077, Newark, DE 19714-6077
A. Z. Fresco
D. Landini

112. EC TECHNOLOGIES, INC., 3614 Highpoint Dr.,
San Antonio, TX 78217
D. J. Kenton

113. EG&G IDAHO, INC., Idaho National Engineering & Environmental Laboratory,
P.O. Box 1625, Idaho Falls, ID 83415
R. N. Wright

114-116. ELECTRIC POWER RESEARCH INSTITUTE, P.O. Box 10412,
3412 Hillview Avenue, Palo Alto, CA 94303
W. T. Bakker
R. B. Dooley
J. Stringer

117. ELECTRO PHYSICS, INC., 1400 Marshall Street, NE,
Minneapolis, MN 55413
D. Bell

118. ENERGY AND WATER RESEARCH CENTER, P. O. Box 6064
West Virginia University,
Morgantown, WV 26505-5054
P. G. Stansberry

119. ENVIRONMENTAL PROTECTION AGENCY, Global Warming Control
Division (MD-63), Research Triangle Park, NC 27711
K. T. Janes

120. ERC, INC., P. O. Box 417, Tullahoma, TN 37388
Y. C. L. Susan Wu

121-122. EXXON RESEARCH AND ENGINEERING COMPANY, Clinton Township,
Route 2 East, Annandale, NJ 08801
M. L. Gorbaty
S. Soled

123. FERRO CORPORATION, Permeable Ceramics, 603 West Commercial St.
E., Rochester, NY 14445
P. S. Way

124. FORSCHUUGS ZENTRUM JÜLICH GmbH, ICT, Postfach 1913, D-5170
Jülich, Germany
H. Barnert-Wiemer

125. FOSTER WHEELER DEVELOPMENT CORPORATION, Materials Technology Dept., John Blizard Research Center, 12 Peach Tree Hill Road, Livingston, NJ 07039
J. L. Blough

126. FRAUNHOFER-INSTITUT für WERKSTOFFMECHANIK, Wohlerstrass 11, 79108 Freiburg, West Germany
R. Westerheide

127. GAS RESEARCH INSTITUTE, 8600 West Bryn Mawr Avenue, Chicago, IL 60631
H. S. Meyer

128. GENERAL APPLIED SCIENCE LABS, 77 Raynor Avenue, Ronkonkoma, NY 11779
M. Novack

129. GENERAL ELECTRIC CORPORATE CR&D, P.O. Box 8, Bldg. K1, MB 265, Schenectady, NY 12301
G. Rowe

130. GEORGIA INSTITUTE OF TECHNOLOGY, Georgia Tech Research Institute, 123D Baker Bldg., Atlanta, GA 30332-0245
T. L. Starr

131. GRI, 8600 W. Bryn Mawr, Chicago, IL 60656
D. Scarpiello

132. HAYNES INTERNATIONAL, INC., 1020 W. Park Avenue, Kokomo, IN 46904
M. Harper

133. HOSKINS MANUFACTURING COMPANY, 10776 Hall Rd., Hamburg, MI 48139-0218
F. B. Hall

134. ILLINOIS INSTITUTE OF TECHNOLOGY, METM Dept., Perlstein Hall, IIT, Chicago, IL 60616
J. A. Todd-Copley

135. INCO ALLOYS INTERNATIONAL, INC., P. O. Box 1958, Huntington, WV 25720
S. Tassen

136. INDUSTRIAL FILTER & PUMP, 5900 Ogden Avenue, Cicero, IL 60804
P. Eggerstedt

137. INTECH, INC., 11316 Roven Dr., Potomac, MD 20854-3126
P. Lowe

138-139. IOWA STATE UNIVERSITY, Ames Laboratory, 107 Metals Development, Ames, IA 50011
D. J. Sordelet
Ozer Unal

140. JET PROPULSION LABORATORY, 4800 Oak Grove Dr., MS-79-21, Pasadena, CA 91020
R. L. Chen

141. LANXIDE CORPORATION, 1 Tralee Industrial Park, Newark, DE 19711
E. M. Anderson

142. LAVA CRUCIBLE-REFRACTORIES CO., P.O. Box 278, Zelienople, PA 16063
T. Mulholland

143-144. LAWRENCE BERKELEY LABORATORY, University of California, 1 Cyclotron Road, Berkeley, CA 94720
I. Brown - MS 53
O. Monteiro - 53-103

145. LAWRENCE LIVERMORE NATIONAL LABORATORY, P.O. Box 808, Livermore, CA 94551
J. H. Richardson (L-353)

146-147. LEHIGH UNIVERSITY, Energy Research Center, 5 E Packer Avenue, Bethlehem, PA 18015
S. W. Banovic
J. N. DuPont

148. LIQUID CARBONIC INDUSTRIAS S.A, Avenida Rio Branco, 57-6° Andar, Centro - 20090-004, Rio De Janeiro, Brazil
M. Saddy

149. LOCKHEED MARTIN-KAPL, P.O. Box 1072, MS G2-312, Schenectady, NY 12301
J. J. Letko (MS D2-121)

150. E. LORIA, 1829 Taper Drive, Pittsburgh, PA 15241

151. LOS ALAMOS NATIONAL LABORATORY, P.O. Box 1663, Los Alamos, NM 87545
R. G. Castro - MS G720

152. LURGI LENTJES BABCOCK, Duisburger Strasse 375, D-46041 Oberhausen, Germany
G. von Wedel

153-154. MALLETT TECHNOLOGY, 100 Park Drive, Suite 204, P.O. Box 14407, Research Triangle Park, NC 27709
R. Mallett
J. L. Bitner

155. MASSACHUSETTS INSTITUTE OF TECHNOLOGY, Department of Chemical Engineering, Room 66-456, Cambridge, MA 02139
J. Longwell

156. MICROCOATING TECHNOLOGIES, 430 Tenth St., NW, Suite N-108, Atlanta, GA 30318-5769
S. Shanmugham

157. MOBIL RESEARCH & DEVELOPMENT CORPORATION, P. O. Box 1026, Princeton, NJ 08540
R. E. Searles

158. NASA LEWIS RESEARCH CENTER, 21000 Brookpark Road, Cleveland, OH 44135
N. Jacobson - MS 106-1

159. NATIONAL INSTITUTE OF STANDARDS AND TECHNOLOGY, Materials Building, Gaithersburg, MD 20899
L. K. Ives (Bldg. 220, Rm. A-215)

160. NATURAL GAS AND OIL TECHNOLOGY PARTNERSHIP, 12434 Penthshire, Houston, TX 77024
R. M. Whitsett

161. NETHERLANDS ENERGY RESEARCH FOUNDATION ECN, P.O. Box 1, 1755 ZG Petten, The Netherlands
P. T. Alderliesten

162. NEW ENERGY AND INDUSTRIAL TECHNOLOGY DEVELOPMENT ORGANIZATION, 1800 K Street, N.W., Suite 924, Washington, DC 20006
T. Fukumizu

163-165. NEW ENERGY AND INDUSTRIAL TECHNOLOGY DEVELOPMENT ORGANIZATION, Sunshine 60 Bldg., P.O. Box 1151, 1-1 Higashi-Ikebukuro 3-Chome, Toshima-Ku, Tokyo, 170, Japan
S. Hirano
H. Narita
S. Ueda

166. NORCONTROL, Duran Marquina 20, 15080 La Coruna, Spain
S. Gomez

167. OFFICE OF NAVAL RESEARCH, Code 431, 800 N. Quincy St., Arlington, VA 22217
S. G. Fishman

168. OHIO STATE UNIVERSITY, Department of Metallurgical Engineering, 116 W. 19th Avenue, Columbus, OH 43210
R. A. Rapp

169-170. PACIFIC NORTHWEST NATIONAL LABORATORIES, P.O. Box 999, Richland, WA 99352
R. N. Johnson
L. R. Pederson

171. PALL CORPORATION, 3669 State Route 281, P.O. Box 2030, Cortland, NY 13045
M. June

172. PENNSYLVANIA STATE UNIVERSITY, 101 Steidle Building, University Park, PA 16802
R. Tressler

173. PSI TECHNOLOGY COMPANY, 20 New England Business Center, Andover, MA 01810
L. Bool

174. REMAXCO TECHNOLOGIES, INC., 10425 Cogdill Road, Suite 300 Knoxville, TN 37932
D. Nixdorf

175. RENSSELAER POLYTECHNIC INSTITUTE, Materials Engineering Department, Troy, NY 12180-3590
N. S. Stoloff

176. RIBBON TECHNOLOGY CORPORATION, P.O. Box 30758, Columbus, OH 43230
T. Gaspar

177. RISO NATIONAL LABORATORY, P.O. Box 49, DK-4000, Roskilde, DENMARK
Aksel Olsen

178. ROLLED ALLOYS, 125 West Sterns Road, Temperance, MI 48182
J. C. Kelly

179. SANDIA NATIONAL LABORATORIES, 7011 East Avenue, P.O. Box 969
Livermore, CA 94551-0969
J. E. Smugeresky (MS-9402)

180. SANDIA NATIONAL LABORATORIES, P.O. Box 5800,
Albuquerque, NM 87185
G. Carlson

181-182. SARGENT AND LUNDY, 55 E Monroe Street, Chicago, IL 60603
R. J. Kerhin
D. G. Sloat

183. SCIENCE APPLICATIONS INTERNATIONAL CORPORATION,
1710 Goodridge Dr., McLean, VA 22102
J. T. Bartis

184. SFA PACIFIC, INC., 444 Castro Street, Suite 920, Mountain View, CA 94041
N. Korens

185. SHELL DEVELOPMENT COMPANY, P.O. Box 1380,
Houston, TX 77251-1380
L. W. R. Dicks

186. G. SORELL, 49 Brookside Terrace, N. Caldwell, NJ 07006

187. SOUTHERN RESEARCH INSTITUTE, 2000 Ninth Avenue South,
Birmingham, AL 35202
H. S. Starrett

188. SOUTHWEST RESEARCH INSTITUTE, 6620 Culebra Road,
P.O. Drawer 28510, San Antonio, TX 78284
F. F. Lyle, Jr.

189. SRI INTERNATIONAL, 333 Ravenswood Avenue, Meno Park, CA 04025
Y. D. Blum

190. STANTON ENERGY INDUSTRY CONSULTANTS, INC., RD #1,
Liberty Court,
New Stanton, PA 15672-9621
R. J. Steffen

191. SUNDSTRAND, 4747 Harrison Ave., Rockford, IL 61125
D. Oakey

192. SUPERKINETICS, 2881 Tramway Place, NE,
Albuquerque, NM 87122
J. V. Milewski

193. TECHNIWEAVE, INC., 109 Chestnut Hill Road, Rochester, NH 03868
J. A. LeCoustaouec

194. TECHNOLOGY MANAGEMENT INC., 9718 Lake Shore Blvd., Cleveland, OH 44108
B. P. Lee

195. TELEDYNE ALLVAC, P.O. Box 5030, Monroe, NC 28110
A. L. Coffey

196-197. TENNESSEE VALLEY AUTHORITY, 3N66A Missionary Ridge Place, Chattanooga, TN 37402-2801
J. B. Brooks
C. M. Huang

198. TEXAS EASTERN TRANSMISSION CORPORATION, P.O. Box 2521, Houston, TX 77252
D. H. France

199. THE AMERICAN CERAMIC SOCIETY, INC., 735 Ceramic Place, Westerville, OH 43081
L. Sheppard

200. THE JOHNS HOPKINS UNIVERSITY, Materials Science & Engineering, Maryland Hall, Baltimore, MD 21218
R. E. Green, Jr.

201. THE MATERIALS PROPERTIES COUNCIL, INC., United Engineering Center, 345 E. Forty-Seventh St., New York, NY 10017
M. Prager

202. THE NORTON COMPANY, High Performance Ceramics Division, Goddard Road, Northboro, MA 01532-1545
N. Corbin

203. THE RALPH M. PARSONS COMPANY, 100 West Walnut St., Pasadena, CA 91124
J. B. O'Hara

204. THE TORRINGTON COMPANY, Advanced Technology Center, 59 Field Street, Torrington, CT 06790
W. J. Chmura

205. TRW, 1455 E. 195th Street, Cleveland, OH 44110
M. Kurup

206-207. UNITED TECHNOLOGIES RESEARCH CENTER, Materials Department, 411 Silver Lane, East Hartford, CT 06108
N. S. Bornstein
J. E. Holowczak

208. UNIVERSITY OF CALGARY, 2500 University Dr. NW, Calgary, Canada
S. X. Mao

209. UNIVERSITY OF CALIFORNIA, Department of Materials Science and Mineral Engineering, University of California, Building 66-Room 247, Berkeley, CA 94720
R. O. Richie

210-211. UNIVERSITY OF KENTUCKY, Center for Applied Energy Research, 3572 Iron Works Pike, Lexington, KY 40511-8433
F. Derbyshire
M. Jagtoyen

212. UNIVERSITY OF NORTH DAKOTA, P.O. Box 9018, University Station, Grand Forks, ND 58202
J. P. Hurley

213. UNIVERSITY OF PITTSBURGH, Materials Science & Engineering Department, 848 Brenedum Hall, Pittsburgh, PA 15261
N. Birks

214. UNIVERSITY OF SOUTH AUSTRALIA, Department of Metallurgy, The Levels SA 5095 Australia
K. N. Strafford

215-217. UNIVERSITY OF TENNESSEE, Department of Materials Science and Engineering, 434 Doughtery Engineering Building, Knoxville, TN 37996
R. A. Buchanan
P. Liaw
C. D. Lundin

218. UNIVERSITY OF TENNESSEE SPACE INSTITUTE, Tullahoma, TN 37388
M. White

219. UNIVERSITY OF WASHINGTON, Department of Materials Science and Engineering, 101 Wilson, FB-10, Seattle, WA 98195
T. G. Stoebe

220. UNIVERSITY OF WISCONSIN, Department of Materials Science and Engineering, 1509 University Avenue, Madison, WI 53706-1595
J. H. Perepezko

221. UOP, 50 E. Algonquin Road, Des Plaines, IL 60017-5016
G. J. Antos

222. VEBA OEL, P. O. Box 45, 4650 Gelsenkirchen-Buer, Germany
D. Fuhrmann

223-224. VIRGINIA POLYTECHNIC INSTITUTE AND STATE UNIVERSITY, Department of Materials Engineering, Blacksburg, VA 24061
W. Curtin
K. L. Reifsnyder

225. WESSEL, James K.,127 Westview Lane, Oak Ridge, TN 37830

226-228. WEST VIRGINIA UNIVERSITY, Mechanical & Aerospace Engineering Department, P.O. Box 6106, Morgantown, WV 26505
B. Cooper
B. Kang
P. Stansberry

229. WESTERN RESEARCH INSTITUTE, 365 N. 9th Street, P. O. Box 3395, University Station, Laramie, WY 82071
V. K. Sethi

230. WESTINGHOUSE ELECTRIC CORPORATION, 4400 Alafaya Trial, Orlando, FL 32826-2399
S. M. Sabol - MC 303

231-233. WESTINGHOUSE ELECTRIC CORPORATION, Research and Development Center, 1310 Beulah Road, Pittsburgh, PA 15235-5098
M. A. Alvin
G. Bruck
P. Singh

234. WORCESTER POLYTECHNIC INSTITUTE, 100 Institute Road, Worcester, MA 01609
E. Ma

235. DOE CHICAGO OPERATIONS OFFICE, 9800 S. Cass Ave., Argonne, IL 60439
J. Jonkouski

236. DOE IDAHO OPERATIONS OFFICE, 765 DOE Place, Idaho Falls, ID 83406
J. B. Malmo

237-251. DOE FEDERAL ENERGY TECHNOLOGY CENTER,
P.O. Box 880, Morgantown, W VA 26505
C. T. Alsup
R. A. Bajura
R. C. Bedick
D. C. Cicero
F. W. Crouse, Jr.
R. A. Dennis
U. Grimm
J. S. Halow
N. T. Holcombe
W. J. Huber
P. Lee
T. J. McMahon
H. M. Ness
J. E. Notestein
C. M. Zeh

252. DOE OAK RIDGE OPERATIONS OFFICE, Oak Ridge, P. O. Box 2008,
Oak Ridge, TN 37831-6269
M. A. Rawlins

253. DOE OFFICE OF BASIC ENERGY SCIENCES, Materials Sciences Division,
ER-131, 19901 Germantown Road, Germantown, MD 20874-1290
J. N. Mundy

254. DOE OFFICE OF ENERGY EFFICIENCY AND RENEWABLE ENERGY,
CE-12, Forrestal Building, Washington, DC 20545
J. J. Eberhardt

255-256. DOE OFFICE OF ENERGY RESEARCH, 14 Goshen Court,
Gaithersburg, MD 20882-1016
N. F. Barr
F. J. Wobber

257-262. DOE OFFICE OF FOSSIL ENERGY, Washington, DC 20585
H. Feibus (FE-23)
K. N. Frye (FE-13)
F. M. Glaser (FE-72)
S. C. Jain (FE-231)
T. B. Simpson (FE-231)
M. I. Singer (FE-70)

263. DOE OFFICE OF INDUSTRIAL TECHNOLOGIES, 1000 Independence Avenue
S.W., Washington, DC 20585
S. Dillich (EE-20)

264. DOE OFFICE OF NAVAL REACTORS, NE-60, Crystal City Bldg., N.C.-2, Washington, DC 20585
J. Mosquera

265. DOE OFFICE OF PETROLEUM RESERVES, Analysis Division, FE-431, 1000 Independence Ave., Washington, DC 20585
D. de B. Gray

266-279. DOE FEDERAL ENERGY TECHNOLOGY CENTER, P. O. Box 10940, Pittsburgh, PA 15236
A. H. Baldwin
J. L. Balzarini
R. A. Carabetta
R. C. Dolence
P. Goldberg
J. D. Hickerson
J. J. Lacey
S. R. Lee
M. E. Mather
G. V. McGurl
J. A. Ruether
L. Ruth
T. M. Torkos

280-281. DOE, OFFICE OF SCIENTIFIC AND TECHNICAL INFORMATION, P.O.Box 62, Oak Ridge, TN 37831

For distribution by microfiche as shown in DOE/OSTI-4500,
Distribution Category UC-114 (Coal Based Materials and Components)